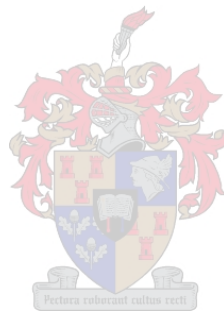


# Geochronology and Isotopic Characterisation of LCT Pegmatites from the Orange River Pegmatite Province

By: Shane William Doggart



*Thesis presented in partial fulfilment of the requirements for the degree of Master of Science in  
the Faculty of Science at Stellenbosch University*

Supervisor: Prof. Ian S. Buick  
Co-supervisors: Dr. Paul H. Macey and Prof Dirk Frei

April 2019

## Declaration

By submitting this thesis electronically, I declare that the entirety of the work contained therein is my own, original work, that I am the sole author thereof (save to the extent explicitly stated otherwise), that reproduction and publication thereof by Stellenbosch University will not infringe any third party rights and that I have not previously in its entirety or in part submitted it for obtaining any qualification.

Signature: \_\_\_\_\_

Date: April 2019

Copyright © 2019 Stellenbosch University  
All rights reserved

## Abstract

The pegmatites of the Orange River Pegmatite Belt (ORPB) form an extensive, ca. 450km long continuous W-E trending belt extending from Vioolsdrif to Kenhardt in South Africa, with the northern extent reaching into the southern Karas region of Namibia. This study attempts to explain the temporal and geochemical relationship of the pegmatites in the ORPB and the rocks of the Namaqua sector of the NNMP. In order to understand the evolution of the ORPB pegmatites this study uses: 1) in-situ high spatial resolution monazite (LA-Q-ICP-MS) geochronology to obtain pegmatite emplacement ages, and 2) in situ LA-MC-CP-MS isotopic tracing of monazite grains to determine the Sm-Nd isotope compositions and 2-stage depleted model ages for the pegmatites.

The geochronological data yielded U-Pb dates ranging from ~960 Ma to ~1038 Ma suggesting that the pegmatites of the ORPB were emplaced over a ~80 M.yr period. Additionally, the fact that the ORPB pegmatites are observed in the field to intrude metasediments of the Namaqua-Natal Metamorphic Belt, might be used to suggest that they were sourced via partial melting mechanism during late-stage  $D_4$  deformation of these metasediments. This is hard to envisage owing to the fact that the pegmatites that are emplaced into tectonic domains with vastly different metamorphic histories from greenschist- and amphibolite-facies in the ~1.9 Ga Richtersveld Magmatic Arc (RMA) to the poly-metamorphic granulite-facies Mesoproterozoic Kakamas Domain (KD).

The question is posed: how did these late-stage, highly fractionated granitic rocks originate? What was their emplacement history? If they are not linked to any late Namaqua age granitic plutons, is the source of the parental melts sourced via local anatexis of the metasedimentary country rocks of the RMA and KD?

Radiogenic data obtained give  $\epsilon_{Nd(1000)}$  values of ~ -15 to ~ -1, with the lowest values attributed to pegmatites within the RMA with  $\epsilon_{Nd_t}$  values increasing where pegmatites intrude into the more juvenile Mesoproterozoic KD.  $T_{2DM}$  model ages suggest that the pegmatites have similar sources to their host country rocks. However, metamorphic grades within the RMA never attained conditions conducive to partial melting and in the KD had reached peak, granulite-facies, metamorphic conditions ~200 Ma prior, and were hence refractory to further melting at ~1.0 Ga during the regional pegmatite emplacement.

The findings from this study indicate that the pegmatites within the RMA ( $T_{2DM}$ : ~2.7 – 2.1 Ga) were possibly sourced from anatexis occurring at depth of fertile metasediments in the tectonically underlying Bushmanland Subprovince (BSP;  $T_{2DM}$ : ~2.9 – 2.3 Ga) at ~1.0 Ga. Sm-Nd geochemistry from this study also suggests that the parental melts responsible for the pegmatites in the KD ( $T_{2DM}$ : ~1.8-1.7 Ga) are interpreted to have been sourced via anatexis of retrogressed granulite-facies KD country rocks at deeper crustal levels at around the same time, and possibly aided by fluid from anatexis of the BSP.

## Opsomming

Die pegmatiete van die Oranje Rivier Pegmatiet Gordel (ORPG) vorm 'n uitgebreide ca. 450 km-lange kontinue W–O-strekkende gordel vanaf Violsdrif tot Kenhardt in Suid-Afrika, met die noordelike uitbreiding wat die suidelike Karas area van Namibië bereik. Hierdie studie poog om die temporele en geochemiese verwantskap tussen die pegmatiete in die ORPG en die gesteentes van die Namakwa sektor van die NNMP te verklaar. Om die evolusie van die ORPG pegmatiete te verstaan, gebruik hierdie studie: 1) in situ hoë ruimtelike resolusie monasiet (LA-Q-ICP-MS) geochronologie om die inplasingsouderdomme te verkry en 2) in situ LA-MC-CP-MS isotoop natrekking van monasietkorrels om die Sm-Nd isotoop samestellings en 2-fase verarmde model ouderdomme van die pegmatiete vas te stel.

Die geochronologiese data het U-Pb datums wat vanaf ~960 Ma tot ~1038 Ma varieer, wat sou voorstel dat die pegmatiete van die ORPG ingeplaas is oor 'n tydperk van ~80 M.yr. Hierbenewens mag die feit dat die ORPG pegmatiete in die veld gesien word om die metasedimente van die Namakwa-Natal Metamorfe Gordel binne te dring, gebruik word om voor te stel dat hulle ontstaan het as gevolg van 'n gedeeltelike smeltingsmeganisme gedurende die laat-stadium  $D_4$  deformatsie van hierdie metasedimente. Dit is moeilik om voor te stel aangesien die pegmatiete ingeplaas is in tektoniese domeine wat ingrypend verskillende metamorfe geskiedenis het as die groenskis en amphibolite fasies in die 1.9 Ga Richtersveld Magmatiese Boog (RMB) tot die polimetamorfe granuliet fasies Mesoproterosoïese Kakamas Domein (KD).

Die vraag ontstaan nou: hoe het hierdie laat-stadium, hoogs gefraksioneerde granitiese gesteentes ontstaan? Wat was hulle inplasingsgeskiedenis? Indien hulle nie verwant is aan enige laat-stadium Namakwa-ouderdom granitiese plutone nie, het die stam smeltsels ontstaan via die lokale anatekse van die metasedimentêre newegesteentes van die RMB en die KD?

Beskikbare radiogene data het  $\epsilon Nd_{(1000)}$  waardes vanaf ~ -15 tot ~ -1 gelever, met die laagste waardes toegeken aan die meer juveniele Mesoproterosoïese KD.  $T_{2DM}$  model ouderdomme blyk voor te stel dat die pegmatiete 'n soortgelyke oorsprong as hulle newegesteentes sou hê. Nietemin, metamorfe grade binne die RMB het nooit toestande bereik wat gunstig sou wees vir gedeeltelike smelting nie en het in die KD piek granuliet-fasies metamorfe toestande bereik te ~200 Ma vooraf en was dus vuurvas met betrekking tot verdere smelting om en by ~1.0 Ga ten tye van die regionale pegmatiet inplasing.

Die bevindings van hierdie studie dui aan dat die pegmatiete binne die RMB ( $T_{2DM}$ : ~2.7 – 2.1 Ga) moontlik hul oorsprong vanuit anatekse mag hê wat plaasgevind het in 'n diep omgewing te midde van die vrugbare metasedimente in die tektonies onderliggende Boesmanland Subprovinsie (BSP;  $T_{2DM}$ : ~2.9 – 2.3 Ga) te ~1.0 Ga. Sm-Nd geochemie vanuit hierdie studie sou ook aandui dat die stamsmeltsels wat aanleiding gegee het tot die pegmatiete in die KD ( $T_{2DM}$ : ~1.8-1.7 Ga) geïnterpreteer sou kon word as afkomstig vanuit die anatekse van retrogressiewe granuliet facies KD newegesteentes in dieper kors lae omtrent terselfde tyd, en moontlik aangehelp is deur vloeistof vanuit die anatekse van die BSP.

## Acknowledgements

I would like to send out an enormous thank you and appreciation for my supervisor, Prof Ian Buick. The duration of this project has been met with hardships and obstacles we could never have imagined. Your support, wisdom, empathy and above all patience through this trying time has been greatly appreciated. It has pushed me to pull through the hard times and finish.

I would like to thank Dr. Paul Macey for your support with the project. Your advice and help at critical moments during this project have been greatly appreciated.

Prof. Dirk Frei at the University of the Western Cape, thank you for organising funding and assistance with analytical work. Thanks must also go to Dr Chris Lana at the Laboratório de Geoquímica Isotópica (LOPAG), Universidade Federal de Ouro Preto (UFOP) in Brazil.

I would like to extend my gratitude to my colleagues at the Council for Geoscience, Dr Robert Thomas, Chris Lambert, Hendrick Smith, for your help with samples, suggestions and encouragement.

To analytical and technical staff at CAF, Dr Rianna Roussow, Dr Madelaine Frazenberg and Mareli Moolman, for your assistance and patience with sample preparation and analysis.

I greatly extend my gratitude and appreciation to all the support I received from my girlfriend and family, without whom, the end of this project might not have been a reality.

Finally, to my late mother, thank you for teaching me courage and the tenacity to go out and accomplish the often impossible. I was without your guidance through much of this project but your “don’t give up attitude” was always remembered, sometimes frustratingly so.

## Table of Contents

<b>Declaration</b> .....	i
<b>Abstract</b> .....	ii
<b>Acknowledgements</b> .....	iii
<b>List of Figures:</b> .....	vii
<b>List of Tables:</b> .....	xii
<b>1 Introduction</b> .....	1
1.1 Background and rationale .....	1
1.2 General background on pegmatite classification, geochemistry and petrogenesis .....	5
1.3 Objectives and outcomes of this study .....	8
<b>2 Regional geological framework</b> .....	10
2.1 Lithostratigraphy of the Namaqua-sector of the Namaqua-Natal-Metamorphic Province .....	12
2.1.1 <i>Richtersveld Magmatic Arc (RMA)</i> .....	12
2.1.2 <i>Bushmanland Subprovince (BSP)</i> .....	17
2.1.3 <i>The Kakamas Domain (KD) and Areachap Domain (AD)</i> .....	18
2.1.4 <i>Kaaien Domain and Kheis Subprovince</i> .....	24
2.2 Tectono-metamorphic history .....	25
2.3 The Geology of the Orange River Pegmatite Belt .....	28
<b>3 Methods</b> .....	30
3.1 Sample preparation .....	30
3.2 Isotopic and chemical characterisation .....	31
3.2.1 <i>LA-Q-ICP-MS</i> .....	31
3.2.2 <i>LA-MC-ICP-MS</i> .....	32

<b>4</b>	<b>Results</b> .....	36
<b>4.1</b>	<b>Monazite U-Pb geochronology</b> .....	36
	Overview .....	36
4.1.1	Richtersveld Magmatic Arc .....	39
4.1.2	Lower Fish River Onseepkans Thrust Zone .....	68
4.1.3	Kakamas Domain .....	77
<b>4.2</b>	<b>Sm-Nd isotope systematics</b> .....	92
	Overview .....	92
4.2.1	Richtersveld Magmatic Arc .....	95
4.2.2	LFROTZ .....	98
4.2.3	Kakamas Domain .....	99
<b>5</b>	<b>Discussion</b> .....	100
5.1	The distribution of monazite U-Pb ages from pegmatites in the Orange River Pegmatite Belt .....	100
5.2	Sm-Nd isotope systematics of the Orange River Pegmatite Belt in relation to the Namaqua-Natal Metamorphic Province.....	105
5.3	The relationship between pegmatite Sm-Nd isotope compositions and country rocks of the Bushmanland Subprovince.....	111
5.4	Intrusion and source of the pegmatite melts in relation to the tectonic setting of the NNMP .....	112
<b>6</b>	<b>Conclusion</b> .....	121
	<b>References</b> .....	123
	<b>Appendix</b> .....	A.1
	Appendix A: Monazite Geochemistry.....	A.1
	Appendix B: Normalised monazite rare earth element (REE) geochemistry .....	A.33
	Appendix C: Monazite U-Th-Pb isotope data.....	A.51
	Appendix D: Monazite Sm-Nd isotope compositions.....	A.72
	Appendix E: Sm-Nd data for country rocks.....	A.81

## List of Figures:

Figure 1.1. A regional overview map of the Orange River Pegmatite Belt within the Namaqua Sector of the Namaqua-Natal-Province, southern Africa .....	2
Figure 2.1: Regional tectonostratigraphic map of the Namaqua-Natal Metamorphic Belt (NNMP).....	11
Figure 2.2: Simplified geological map of the Vioolsdrif Domain. ....	14
Figure 2.3: Simplified geological map of the Pella Domain, illustrating major structures, tectonic boundaries and pegmatite distribution. ....	17
Figure 2.4: Simplified geological map of the Kakamas Domain in the region west of Onseepkans and Riemvasmaak.....	20
Figure 2.5: Simplified geological map of the Kakamas Areachap and Kaaien Domains. ....	22
Figure 2.6: A field photograph illustrating the typical outcrop of the pegmatites intruding as a swarm into the Namaqua Natal Metamorphic Province country rocks.....	28
Figure 2.7: An elevated panoramic view of a pegmatite swarm intruding as a swarm into the intruding the metamorphic units of the LFROTZ in the Onseepkans area.....	29
Figure 4.1: Simplified geological map of the Namaqua-Natal metamorphic belt and the distribution of the Orange River Pegmatite Belt. Individual sample localities are indicated on the map .....	38
Figure 4.2: Field photograph of the 8m wide simple unzoned pegmatite (SD2015-10) that has intruded into ORG volcanics.....	40
Figure 4.3: Representative SEM BSE images of analysed monazite from pegmatite sample SD2015-10....	40
Figure 4.4 A) Chondrite-normalised REE diagram for sample SD2015-10. Wetherhill concordia diagram for monazite LA-Q-ICP-MS isotope data for pegmatite sample SD2015-10. ....	41
Figure 4.5: Field photograph of the sampled homogenous, unzoned pegmatite (SD2-15-11) that has intruded into Ramansdrif alkali granite. ....	42
Figure 4.6. A). Representative SEM BSE images of analysed monazite from pegmatite sample SD2015-11. B). Chondrite-normalised REE diagram for sample SD2015-11.....	43
Figure 4.7: Wetherhill concordia diagram for monazite LA-Q-ICP-MS isotope data for pegmatite sample SD2015-11 .....	44
Figure 4.8: A field photograph that highlights the complex zoning observed in this zoned LCT pegmatite of "Kokerboom Rand", with coarse- and fine-grained zones consisted of quartz, K-feldspar, with muscovite	



occurring in variable proportions within the coarse-grained zones. Zones with garnet-rich rims were present that had concentric zoning with respect to mineralogy containing K-feldspar rich mantles with the cores becoming quartz-rich. Li-rich zones were also present (not pictured).....	45
Figure 4.9. A) Representative SEM BSE images of analysed monazite from pegmatite sample SDORPB15-4B. B) Chondrite-normalised REE diagram for sample SDORPB15-4B. ....	46
Figure 4.10: A.) Wetherhill concordia diagram for monazite LA-Q-ICP-MS isotope data for pegmatite sample SDORPB15-4B. .B) Weighted mean $^{207}\text{Pb}/^{206}\text{Pb}$ diagram for pegmatite sample SDORPB15-4B.....	47
Figure 4.11: A): Photograph illustrating the mineralogical and textural zoning within the sampled pegmatite (SDORPB15-7d), the top zone is rich in K-feldspar with scattered muscovite books (~1-3cm in size); a muscovite rich zone (centre) contained large (~5-15cm) muscovite books with K-feldspar. The quartz-rich zone (bottom) hosted plagioclase and quartz and high proportion of blue apatite (~1-2cm crystals) that formed in scattered aggregate masses within the zone. B): Photograph of the lepidolite rich sample retrieved from this locality. C): Field photograph of the sampled pegmatite that has been worked out for the tourmaline by local gem miners. A characteristic of most of the mineralised pegmatites in the area.....	48
Figure 4.12. A.) Representative SEM BSE images of analysed monazite from pegmatite sample SDORPB15-7D. B) Chondrite-normalised REE diagram for sample SDORPB15-7D.....	49
Figure 4.13: A) Wetherhill concordia diagram for monazite LA-Q-ICP-MS isotope data for pegmatite sample SDORPB15-7D. B and C) Weighted mean $^{207}\text{Pb}/^{206}\text{Pb}$ spot date diagram for pegmatite sample SDORPB15-7D.....	50
Figure 4.14: Field photograph illustrating the zonation present in this sampled pegmatite (SDORPB15-9). The pegmatite is predominantly K-feldspar rich with zones that were rich in muscovite, quartz, plagioclase and garnet. Beryl is sparse but is present in the muscovite rich zones. ....	51
Figure 4.15. Representative SEM BSE images of analysed monazite from pegmatite sample SDORPB15-9. ....	52
Figure 4.16: A) Chondrite-normalised REE diagram for sample SDORPB15-9. B) Wetherhill concordia diagram for monazite LA-Q-ICP-MS isotope data for pegmatite sample SDORPB15-9. C) Weighted mean diagram for pegmatite sample SDORPB15-9.....	53
Figure 4.17.A.) Representative SEM BSE images of analysed monazite from pegmatite sample SDORPB16-4. B) Chondrite-normalised REE diagram for sample SDORPB16-4.....	54
Figure 4.18: A) Wetherhill concordia diagram for monazite LA-Q-ICP-MS isotope data for pegmatite sample SDORPB16-4. .B) Weighted mean $^{207}\text{Pb}/^{206}\text{Pb}$ spot date diagram for pegmatite sample SDORPB16-4.....	55

Figure 4.19: Field photograph of the sampled Li-rich pegmatite, “Spodumene Kop 1”. The zoned pegmatite contained K-feldspar rich zone (not pictures), quartz dominated zones with scattered, large pink spodumene crystals (top right zone in the picture), and lepidolite and spodumene rich zones that contained minor garnet, tourmaline, columbite and quartz. Spodumene crystals in the Li-rich zone varied in size from extremely large (50-80cm in length) to small (1-4 cm). .....	56
Figure 4.20: Representative SEM BSE images of analysed monazite from pegmatite sample SDORPB16-5. ....	57
Figure 4.21: A) Chondrite-normalised REE diagram for sample SDORPB16-5. B) Wetherhill concordia diagram for monazite LA-Q-ICP-MS isotope data for pegmatite sample SDORPB16-5. C) Weighted mean $^{207}\text{Pb}/^{206}\text{Pb}$ spot age diagram for pegmatite sample SDORPB16-5 .....	58
Figure 4.22. A) Representative SEM BSE images of analysed monazite from pegmatite sample RPGV14. B) Chondrite-normalised REE diagram for sample RPGV14. C) Wetherhill concordia diagram for monazite LA-Q-ICP-MS isotope data for pegmatite sample RPGV14. ....	60
Figure 4.23. A) Representative SEM BSE images of analysed monazite from pegmatite sample RPGV16. B) Chondrite-normalised REE diagram for sample RPGV16. C.) Weighted mean $^{207}\text{Pb}/^{206}\text{Pb}$ spot date diagram for pegmatite sample RPGV16. D) Wetherhill concordia diagram for monazite LA-Q-ICP-MS isotope data for pegmatite sample RPGV16. ....	62
Figure 4.24. A) Representative SEM BSE images of analysed monazite from pegmatite sample SDORPB15-10. B) Chondrite-normalised REE diagram for sample SDORPB15-10.....	64
Figure 4.25: Wetherhill concordia diagram for monazite LA-Q-ICP-MS isotope data for pegmatite sample SDORPB15-10. ....	65
Figure 4.26. A) Chondrite-normalised REE diagram for sample SD2015-13. B) Representative SEM BSE images of analysed monazite from pegmatite sample SD2015-13. C) Wetherhill concordia diagram for monazite LA-Q-ICP-MS isotope data for pegmatite sample SD2015-13. ....	66
Figure 4.27. A) Representative SEM BSE images of analysed monazite from pegmatite sample HS15HF1. B) Chondrite-normalised REE diagram for sample HS15HF1. C) Wetherhill concordia diagram for monazite LA-Q-ICP-MS isotope data for pegmatite sample HS15HF1.....	69
Figure 4.28 A) Representative SEM BSE images of analysed monazite from pegmatite sample SDORPB15-15C. B) Chondrite-normalised REE diagram for sample SDORPB15-15C. C) Wetherhill concordia diagram for monazite LA-Q-ICP-MS isotope data for pegmatite sample SDORPB15-15C.....	71
Figure 4.29. A) Representative SEM BSE images of analysed monazite from pegmatite sample SDORPB16-6. B) Chondrite-normalised REE diagram for sample SDORPB16-6.....	73

Figure 4.30: A.) Wetherhill concordia diagram for monazite LA-Q-ICP-MS isotope data for pegmatite sample SDORPB16-6. B.) Weighted mean diagram for $^{207}\text{Pb}/^{206}\text{Pb}$ spot dates for monazite from sample SDORPB16-6.....	74
Figure 4.31. A) Representative SEM BSE images of analysed monazite from pegmatite sample SDORPB16-7B. B) Chondrite-normalised REE diagram for sample SDORPB16-7B. C) Wetherhill concordia diagram for monazite LA-Q-ICP-MS isotope data for pegmatite sample SDORPB16-7B. ....	76
Figure 4.32: Field photograph of the simple, muscovite+K-feldspar rich zoned pegmatite (SDORPB15-17), that intrudes into the Twakputs gneiss in the Riemvasmaak area. Pictured centre is the relatively finer grained zone that was sampled at this locality.....	77
Figure 4.33. A) Representative SEM BSE images of analysed monazite from pegmatite sample SDORPB15-17. B) Chondrite-normalised REE diagram for sample SDORPB15-17. C) Wetherhill concordia diagram for monazite LA-Q-ICP-MS isotope data for pegmatite sample SDORPB15-17. ....	78
Figure 4.34. A) Representative SEM BSE images of analysed monazite from pegmatite sample SDORPB15-18. B) Chondrite-normalised REE diagram for sample SDORPB15-18. C) Wetherhill concordia diagram for monazite LA-Q-ICP-MS isotope data for pegmatite sample SDORPB15-18. ....	80
Figure 4.35. A) Representative SEM BSE images of analysed monazite from pegmatite sample SDORPB15-20. B) Chondrite-normalised REE diagram for sample SDORPB15-20. C) Wetherhill concordia diagram for monazite LA-Q-ICP-MS isotope data for pegmatite sample SDORPB15-20. ....	82
Figure 4.36. A) Representative SEM BSE images of analysed monazite from pegmatite sample SDORPB16-8. B) Chondrite-normalised REE diagram for sample SDORPB16-8. C) Weighted mean diagram for $^{207}\text{Pb}/^{206}\text{Pb}$ spot dates for sample SDORPB16-8. D) Wetherhill concordia diagram for monazite LA-Q-ICP-MS isotope data for pegmatite sample SDORPB16-8. ....	84
Figure 4.37. A) Representative SEM BSE images of analysed monazite from pegmatite sample SDORPB16-9. B) Chondrite-normalised REE diagram for sample SDORPB16-9. C) Weighted mean diagram for $^{207}\text{Pb}/^{206}\text{Pb}$ spot dates for sample SDORPB16-9. D.) Wetherhill concordia diagram for monazite LA-Q-ICP-MS isotope data for pegmatite sample SDORPB16-9.....	87
Figure 4.38: Field photograph of the large, zoned LCT pegmatite, "Jack no. 5". The pegmatite had large K-feldspar dominated, to often monomineralic zones and muscovite+garnet and muscovite+qtz+garnet rich "veins" or elongated lens shaped zones. ....	88
Figure 4.39. A) Representative SEM BSE images of analysed monazite from pegmatite sample SDORPB16-12. B) Chondrite-normalised REE diagram for sample SDORPB16-12. C) Wetherhill concordia diagram for monazite LA-Q-ICP-MS isotope data for pegmatite sample SDORPB16-12. ....	90
Figure 4.40. A and B) Weighted mean diagram for $^{207}\text{Pb}/^{206}\text{Pb}$ spot dates for sample SDORPB16-12. ....	91

Figure 4.41: $\epsilon\text{Nd}_{(t)}$ vs pegmatite magmatic U-Pb age for analysed monazites, where (t) is the respective monazite crystallisation age for each pegmatite sample. Error bars are smaller than the symbols used and thus are not shown. Included is the evolutionary curves for older Late-Archean/Paleoproterozoic Namaqua crust ( $T_{2\text{DM}} = \sim 2.8 - 2.1 \text{ Ga}$ ) and younger Paleoproterozoic Namaqua Crust ( $T_{2\text{DM}} = \sim 1.9-1.4 \text{ Ga}$ ). .....	93
Figure 4.42: Age histogram of monazite U-Pb crystallisation ages and monazite inheritance compared to the Sm-Nd two-stage depleted mantle model ages for the samples analysed. ....	93
Figure 5.1: Simplified geological map of the NNMP illustrating the distribution of monazite U-Pb emplacement ages for the pegmatites in the ORPB. ....	101
Figure 5.2: A simplified geological map of the NNMP illustrating the spatial distribution of Sm-Nd isotope compositions ( $\epsilon\text{Nd}_t$ ) from the studied pegmatites from across the ORPB. ....	106
Figure 5.3: $\epsilon\text{Nd}_t$ vs. time diagram showing Sm-Nd isotopic data for analysed monazite from pegmatites of the Orange River Pegmatite Belt. Time (t) or data from this study is the respective monazite crystallisation age. Monazite Sm-Nd isotope compositions are assumed to faithfully reflect the whole rock Sm-Nd isotope compositions of the Pegmatites (this study) $\epsilon\text{Nd}_t$ data for NNMP country rocks is from current literature have been recalculated using the preferred geological age (emplacement age) for the respective lithological units and the same CHUR and depleted mantle isotope compositions used to plot monazite data. ....	107

## List of Tables:

Table 1.1: The pegmatite classification scheme of Černý and Ercit (2005), modified to show the correlation between pegmatite classes and families. NYF = niobium-yttrium-fluorine family; LCT = lithium-caesium-tantalum family; HREE= heavy rare earth.....	6
Table 2.1: Summarised lithological features, geochemistry and geochronology of Richtersveld Magmatic Arc country rock. ....	16
Table 2.2 - Summarised lithological descriptions, geochemistry and geochronology of units within the Kakamas Domain.....	23
Table 3.1 - Summary of operational conditions for backscatter electron imaging of the monazite samples. Undertaken at the Central Analytical Facilities (CAF) at Stellenbosch University .....	30
Table 3.2 - Summary of primary and secondary reference materials used in U-Pb isotopic characterisation (LA-Q-ICP-MS).....	32
Table 3.3 Faraday cup configuration and instrument operating parameters for Nd isotopic analysis. ....	33
Table 4.1: Summary table for monazite U-Pb geochronology for pegmatite samples from the Orange River Pegmatite Belt., Includes descriptions of pegmatite mineralogy, structural placement and host rock. ....	37
Table 4.2 – Summary table of Sm-Nd isotope data for monazite from pegmatites of the Orange River Pegmatite Belt.....	94
Table 5.1: Summary table of U-Pb ages and Sm-Nd isotope compositions for country rocks and pegmatites for the studied tectonic domains of the Namaqua-Natal Metamorphic Province.....	107

# 1 Introduction

## 1.1 Background and rationale

The world has in the last few decades seen the increase in the importance of Li- (lithium) and Ta-ores (tantalum) due to the strong growth in the consumption for rechargeable batteries and high temperature and corrosion resistant capacitors. This growth in demand for Li- and Ta-ores has reactivated the interest in the studies of pegmatite fields (Beurlen *et al.*, 2014). The fact that globally, 25% of lithium and 100% of columbite-tantalite is sourced from pegmatites (Beurlen *et al.*, 2014), it is essential to understand the petrogenesis of pegmatite deposits and mineralisation of these economically important commodities.

The Namaqua-Natal-Province (NNMP) in Southern Africa hosts numerous (<45 000) pegmatite bodies across an extensive, ca. 450km long, continuous W-E trending belt, termed the Orange River Pegmatite Belt (ORPB; Figure 1.1). The belt extends from Vioolsdrif to Kenhardt in South Africa, with the northern extent reaching into the southern Karas region of Namibia (Figure 1.1; Gevers, 1936; Gevers *et al.*, 1937; Schutte, 1972; Hugo, 1970; Blignault, 1977, Cornell *et al.*, 2006; Cornell and Pettersson, 2007). The mineralogy of the pegmatites within the ORPB varies from simple, unzoned, quartz-feldspar-mica bearing pegmatites to complexly zoned, heterogeneous pegmatites with commonly exotic mineral assemblages (Hugo, 1969; Schutte, 1972). The structural setting of the pegmatite belt is not yet well constrained, and only locally described (e.g. Cameron. 1936, 1955; Lambert 2013). The belt has, however, been linked to tectonostratigraphic boundaries such as the Groothoek thrust (Cornell *et al.*, 2006) and the Southern Namaqua Front (Blignault, 1977; Beukes, 1973). The only detailed studies of the pegmatite belt have focused on their economic potential in South Africa (Hugo, 1970; Schutte, 1972; von Backstrom, 1976; Minnaar *et al.*, 2006).

Field mapping conducted by the Council for Geoscience (Macey *et al.*, 2015) with structural and limited geochronological studies were undertaken on ORPB pegmatites (Lambert, 2013) in the Skimmelberg Pegmatite Stockwork area of southern Namibia. These studies have determined that the distribution and concentration of pegmatites are largely controlled by structural features and fabrics created during deformation of the NNP, particularly during the late-stage development of transcurrent dextral shears (e.g. Marshall Rocks-Pofadder-Shear Zone and Eureka Shear Zone) in late- to post-tectonic Namaqua times (ca. 1000 Ma).

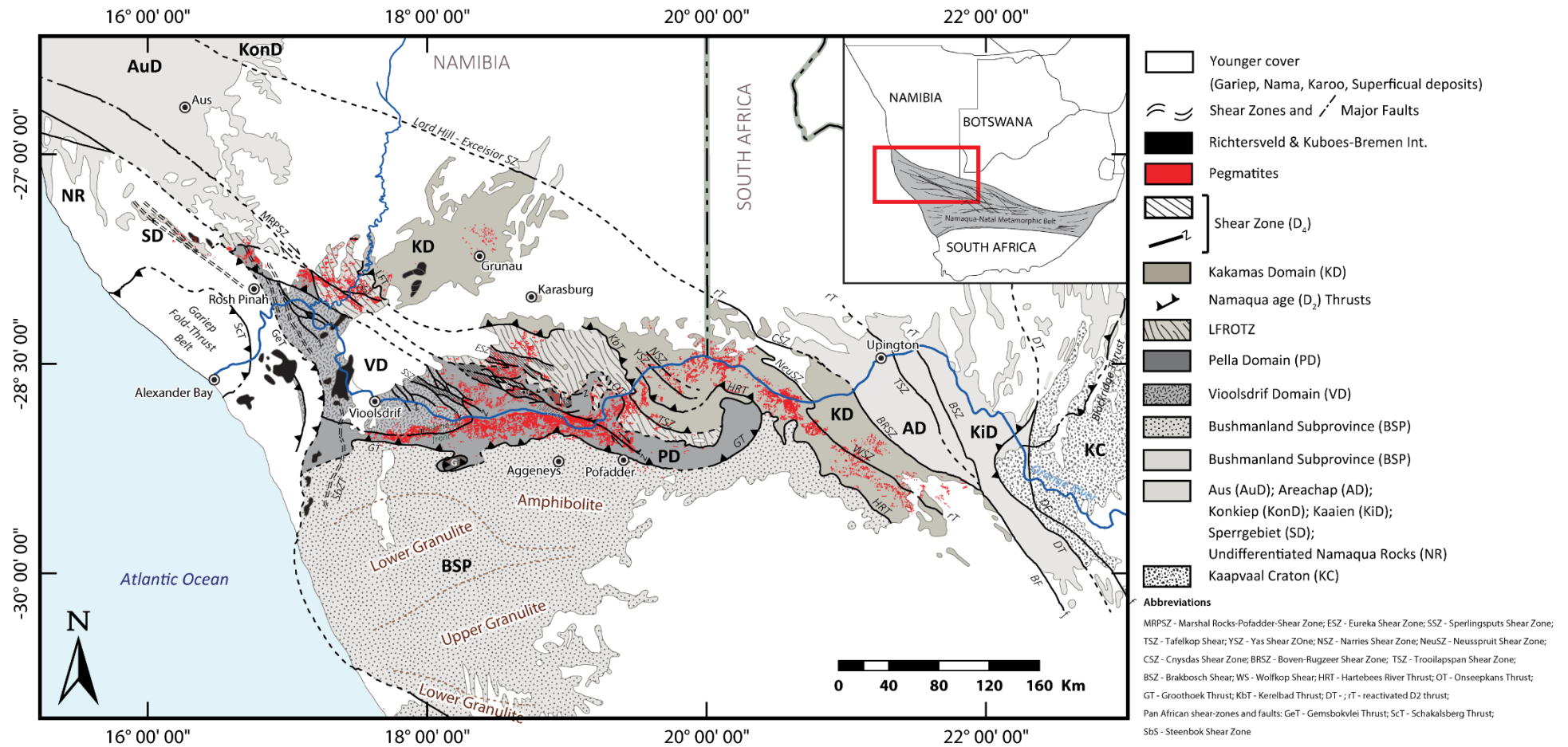


Figure 1.1. A regional overview map of the Orange River Pegmatite Belt within the Namaqua Sector of the Namaqua-Natal-Province, southern Africa (Map compiled from Hugo, 1970; Schutte, 1972; Lambert, 2013; Macey et al. 2015, 2018).

This begs the question on how did the production of numerous pegmatites, some of which must have been sourced from much more voluminous parental magmas (see chapter 1.2), over such an extended period, in a terrain that had previously experienced high-grade polymetamorphism (i.e. the NNMP)?

Currently, there are two hypotheses that are used to explain how rare-metal pegmatite-forming melts are generated: (a) by extended fractional crystallisation of granitic magma on a pluton scale and (b) the product of low-degree partial melting of crustal rocks, aided by the presence of fluids (London, 2005; Martin De Vito, 2005). Well-documented examples of rare-metal pegmatites that formed due to extended fractional crystallisation with genetic links to larger granitic plutons include: Separation Lake, Canada; Yichuan, China and the North Pilbara Craton, Western Australia (Pan *et al.*, 1997; Belkasmi *et al.*, 2000; Tindle *et al.*, 2000; Sweetapple *et al.*, 2002). On the contrary, there is an increase in the number of studies that describe pegmatites that are interpreted to be derived from direct partial melting including the Cape Cross-Uis pegmatite belt, Namibia; Fraser Lake area of Northern Saskatchewan, Canada; and the Moldanubian domain of the Bohemian Massif, Czech Republic (McKechnie *et al.*, 2012; Melleton *et al.*, 2012; Fuchsloch *et al.*, 2018). There are examples of some highly-fractionated, complexly-zoned LCT pegmatites that lack the evidence of a clear temporal or genetic link with surrounding granitic bodies, such as the Tanco pegmatite in the Bird River Greenstone Belt, Manitoba, Canada (Stilling *et al.*, 2006), and the Greenbushes pegmatite hosted in the Balingup Metamorphic Belt, Western Australia (Partington *et al.*, 1995).

These examples illustrate a problem that questions the validity in the assumption that if pegmatites cannot be proven to be spatially, temporally or genetically related to a parental granite body, does a granitic body exist unseen at deeper crustal levels (Shaw *et al.*, 2016). The hypotheses mentioned above are seen to represent two end-members, where pegmatite melt can be produced as a result of a combination of crustal melting and subsequent fractionation of small magmatic bodies (Shaw *et al.*, 2016).

A study by Buick *et al.* (2008) for example, looked at the temporal relationship between the long-lived and polyphase intraplate Alice Springs Orogeny that reworked the Harts Range Metamorphic Complex (HRMC) central Australia, and pegmatite emplacement within the country rocks of the orogenic zone. This study concluded from geochronological evidence that the pegmatites intruded into the Harts Range Metamorphic Complex (HRMC) over the entire duration of the polyphase ca. 450 – 300 Ma Alice Springs Orogeny. The previous understanding of this orogen was that the pegmatites were locally derived from partial melts of the country rocks. However, U-Pb monazite and zircon dates from anatexitic country rocks of the HRMC do not agree with the crystallisation ages determined from the pegmatites themselves. Thus it was concluded that the source of the melts responsible for the pegmatites must have been sourced from a much larger parental Alice Springs-age granites that exist at depth (Buick *et al.*, 2008).



Lithium-Caesium-Tantalum or LCT type pegmatites are a major source of economically crucial rare earth metals, e.g. Li, Cs, Ta and Nb. Understanding the petrogenesis of these pegmatites is difficult for many reasons. Determination of emplacement ages is commonly difficult because the main U/Pb target mineral, zircon, usually has a high uranium concentration, and as a result they are commonly metamict, and the U-Pb isotope data derived from them are highly discordant. Thus making it difficult to obtain precise and accurate age estimates from the zircons.

Additionally, isotopic and geochemical studies on pegmatites are uncommon. Factors such as: the large grain size (which may make bulk rock geochemical analysis unfeasible); oxygen and hydrogen isotope exchange between wall-rock and pegmatite melt; enrichment of Rb into micas and feldspars; and radiogenic Sr transfer into lower Rb/Sr minerals disturbing Rb-Sr systematics; can create erroneous results in whole rock geochemical analysis (von Blanckenburg, 1992; Tomascak *et al.*, 1998). The collection of samples from the wall-zone rocks along the exterior of the pegmatites has proved successful to some degree. The smaller grain size of the wall zone potentially allows for a modally representative sample to be obtained. However, sampling of the wall zone is still problematic in that accessory minerals are sparse and widely distributed. Moreover, hydrothermal alteration may preferentially disturb Sm-Nd systematics from the wall-zone samples (von Blanckenburg, 1992; Tomascak *et al.*, 1998), making their interpretation uncertain.

Monazite can be used as an alternative to dating pegmatites that often contains metamict zircon. Numerous studies have shown that monazite is a potent tool for studying crustal evolution, in general (McFarlane *et al.*, 2007; Dumond *et al.*, 2008, 2015; Thöni *et al.*, 2008; Gregory *et al.*, 2009; Clemens *et al.*, 2017), and pegmatites in particular (Tomascak *et al.*, 1998; Buick *et al.*, 2008; Mcfarlane *et al.*, 2013; Hammerli *et al.*, 2014; Gonçalves *et al.*, 2016; Liu *et al.*, 2017). Monazite self-anneals at low-temperatures and is therefore not affected by metamictisation (e.g. Seydoux-Guillaume *et al.*, 2018). Its high closure temperature for Pb (>900 °C) means that Pb diffusion is negligible up to high-grade metamorphic conditions (Cherniak *et al.*, 2004; Gardés *et al.*, 2006), thus favouring the preservation of U-Pb dates through high-temperature poly-metamorphism. Magmatic monazite commonly contains inherited cores, allowing U-Pb age information from source regions to be determined (e.g. Rubatto *et al.*, 2006; Crowley *et al.*, 2008), although this is less common than for zircon.

Monazite has high, near weight percent, concentrations of Sm and Nd (McFarlane *et al.*, 2007; Mcfarlane *et al.*, 2013; Goudie *et al.*, 2014; Gonçalves *et al.*, 2016) and its Nd isotope composition have proven to be a good proxy for the magmatic Nd isotope compositions of pegmatites. Whole-rock major element and Nd isotope compositions of pegmatites can often not be determined due to extreme coarse grain size, complex pegmatite compositional zonation, or a combination of the two (Tomascak *et al.*, 1998). Monazite Sm-Nd isotope compositions have proven a useful isotopic tracing tool for linking pegmatites to parental granites (Tomascak *et al.*, 1998). Previous studies have used monazite Sm-Nd isotope compositions to

trace the origin of isolated monazite megacrysts from different pegmatites in a pegmatites field (Gonçalves *et al.*, 2016), and to identify the source regions from which magmas parental to pegmatites were derived by anatexis (e.g. Shaw *et al.*, 2016; Müller *et al.*, 2017).

Monazite Nd-isotope tracing relies on the preservation of the original Sm-Nd isotopic composition through high-T overprinting. This is commonly the case (Montel and Seydoux, 1998; Hammerli *et al.*, 2014), but is hampered by the susceptibility of monazite to fluid mediated precipitation-dissolution reactions (Harlov *et al.*, 2011; Lo Pò *et al.*, 2016; Seydoux-Guillaume *et al.*, 2012), see section 4.1). This is a relatively common phenomenon in monazite from pegmatites due to the circulation of late-magmatic/hydrothermal fluids. It results in the development of highly porous monazite domains (e.g. Buick *et al.*, 2008) that need to be avoided in undertaking U-Pb or Sm-Nd isotope measurements. Lastly, monazite chondrite-normalised REE patterns have proven useful monitors of the crystallisation of major silicate phases (e.g. feldspars) or competition with other crystallising accessory phases (e.g. garnet, zircon, xenotime) during crystallisation of felsic anatectic rocks or magmas (e.g. Bea, 1996; Zhu and O’Nions, 1999b; Rubatto, Hermann and Buick, 2006; Buick *et al.*, 2010; Dumond *et al.*, 2015)

As a result of its utility in understanding magmatic process, this study employs high spatial U-Pb isotope, Sm-Nd isotope and major and trace element geochemical analyses of monazite found in the Orange River Pegmatite Belt (ORPB) to study and analyse the emplacement history of some of the numerous pegmatites within the Namaqua sector of the Namaqua-Natal Metamorphic Province.

## **1.2 General background on pegmatite classification, geochemistry and petrogenesis**

Pegmatites are texturally complex felsic rocks, mostly of granitic compositions (London, 2008), that can be distinguished from other igneous rocks by: 1) their extremely coarse-grained (> 20 mm) nature often, and common development of zoning defined by variations in grain size defined by internal zoning within the pegmatite body; 2) abundance of crystals with skeletal, graphic, or other strongly directional growth habits, or 3) an often prominent spatial zonation of mineral assemblages (London, 2018). There are two hypothesised mechanisms regarding the origin for parental melts for pegmatites (e.g. London, 2005; Simmons and Webber, 2008; Černý, London and Novak, 2012; London and Morgan, 2012): 1) through the formation of late-stage fractional crystallisation process associated with granitic plutons (London, 2005); 2) via partial melting of crustal rocks (e.g. Simmons *et al.*, 1995; Martin and De Vito, 2005). Pegmatites can occur as segregations in or near the top contacts of their source pluton, swarms of dykes that emanate from the source into the surrounding country rock, usually forming planar to intrusive lenticular bodies (London, 2018).

Table 1.1: The pegmatite classification scheme of Černý and Ercit (2005), modified to show the correlation between pegmatite classes and families. NYF = niobium-yttrium-fluorine family; LCT = lithium-caesium-tantalum family; HREE= heavy rare earth.

Class	Family	Subclass	Type	Subtype	Typical minor elements	Metamorphic environment of emplacement	Relation to Granites	
Abyssal (AB)	NYF	AB-HREE			HREE, Y, Nb, Zr, U, Ti	upper amphibolite to low- to high-P granulite facies: ~4 to 9 kbar, ~700 to 800°C	none(?) - segregations of anatectic leucosome	
		AB-LREE			LREE, U, Th, Ti			
	LCT	AB-U			U, Th, Zr, LREE			
Muscovite (MS)	NYF	AB-Be			B, Be	high-P, Barrovian amphibolite facies (kyanite-sillimanite), ~5 to 8 kbar, ~650 to 580°C	none - anatectic bodies (marginal and exterior)	
					no rare-element mineralisation (micas and ceramic minerals)			
Muscovite - Rare Element (MSREL)	NYF	MSREL-REE			Be, Y, REE, Ti, U, Th, Nb, Ta	moderate to high P, (T); amphibolite facies; ~3-7 kbar, ~650 to 520°C	interior to exterior; locally poorly defined	
	LCT	MSREL-Li			Li, Be, Nb			
Rare-Element - (REL)	NYF	REL-REE	allanite-monazite			Be, Y, REE, U, Th, Nb>Ta, F	Variable, largely shallow and postdating regional events affecting the host rocks	interior to marginal (rarely exterior)
			euxenite gadolinite					
	LCT	REL-Li	beryl	beryl-columbite		Li, Rb, Cs, Be, Ga, Sn, Hf, Nb, Ta, B, P, F	low-P, amphibolite-(andalusite sillimanite) to greenschist facies, ~2 to 4 kbar, ~650 to 450°C	(interior to marginal) exterior
			complex	beryl-columbite-phosphate spodumene petalite lepidolite elbaite amblygonite				
			albite-spodumene albite-spodumene					
Miarolitic (MI)	NYF	MI-REE	topaz-beryl gadolinite-fergusonite		Y, REE, Ti, U, Th, Zr, Nb, F	very low P, postdating regional events that affect host rocks	interior to marginal	
	LCT	MI-Li	beryl-topaz MI-spodumene MI-petalite MI-lepidolite		Li, Be, B, F, Ta>Nb	Low-P amphibolite to greenschist facies, ~3 to 4.5 kbar, 500 to 400°C	(interior to) marginal to exterior	

Pegmatite classification is complex and has seen controversy amongst researchers. However, the most widely accepted terminology has been devised by Černý (1991) and Černý and Ercit (2005), modified after Ginsburg *et al.* (1979). Their proposed classification scheme for pegmatites was loosely based on their depth of formation (Černý *et al.*, 2012) and has been subsequently reworked by Černý, (1991) and Černý and Ercit (2005) to include ten subclasses, each with differing types and subtypes, that is based on their

trace element signatures (Table 1.1; Černý *et al.*, 2012). The classification into the 10 subclasses relies heavily on the rare-element signatures of the pegmatites that is expressed by the pegmatites minor and accessory mineral assemblage.

The pegmatite classes imply a connotation to the geological environment within the country rocks at the time of pegmatite emplacement, i.e. the depth of formation or metamorphic conditions of the country rocks where pegmatites are emplaced (Černey and Ercit, 2005; Černý *et al.*, 2012). However, as pegmatites post-date their adjacent host rocks, the P-T conditions at which the pegmatites crystallise may have little or no correlations to the conditions of formation and the mineral assemblages of the host rocks (Černý *et al.*, 2012).

Černý (1991) has proposed that pegmatites can be divided into two distinct groups (“families”) based on their trace-element signatures. The pegmatite families are LCT (Li-Cs-Ta) and NYF (Nb-Y-F) and it is further stated that the signature of the family is only evident in the most highly fractionated members of a group in the form of their exotic minerals. It has also been recognised that the rare element budget is defined by both the composition and volume of the source material (Novak *et al.*, 2012). This classification scheme is proposed to imply a genetic relationship to the pegmatites and their parental magma (London, 2018).

LCT pegmatites are typically affiliated and show a chemical similarity to that of S-type granite (Chappell *et al.*, 2001) with progressive enrichment in Li, Rb, Cs, Be, Sn, Ta>Nb, and also in the volatiles B and F, with progressive fractionation of the melt (Černý and Ercit, 2005; Černý *et al.*, 2012; London and Morgan, 2012). The parental magmas in the LCT family have been suggested to form in two ways: a) anatexis of undepleted and juvenile, upper- to middle-crust metasedimentary and meta-volcanic protoliths; in response to crustal thickening associated with continental collisions, or b) by low-percentage of anatexis of (meta-) igneous rocks of the basement (Černý and Ercit, 2005 and references within). The LCT pegmatites and their parental granites lack deformation and foliation, and thus emplacement occurs in a post- to late-tectonic setting, after crustal thickening and possible accumulation of radiogenic heat sufficient to induce anatexis (Bea, 2012; Černý *et al.*, 2012; London, 2018).

NYF pegmatites are marked by an array of elements such as Nb>Ta, Ti, Y, Sc, REE, Zr, U, Th, with parental magmas inferred to be commonly subaluminous to metaluminous A- to I-type melts. However, some pegmatites have been linked to parental magmas of a weakly peraluminous and peralkaline composition (Černý and Ercit, 2005). Geological, isotopic, and geochemical evidence coupled with petrological-geochemical considerations have suggested several possible modes of origin for NYF magmas: a.) melting of middle- or lower-crust protoliths, modified by a previous melting causing LCT elements to be mobilised but NYF elements to be conserved; b.) melting of undepleted, juvenile, igneous lithologies in an orogenic setting. A combination of a.) and b.) above; or c.) melting of sialic crust pre-enriched in NYF elements by mantle-derived fluids (Černý, 2005; Martin and De Vito, 2005; Černý and Ercit, 2005; Černý *et al.*, 2012).

The vast majority of pegmatites are simple in their compositions and are close to the haplogranite minimum with minor quantities of micas and accessory minerals, e.g. garnet, apatite and tourmaline (London *et al.*, 2012; London, 2016, 2018). These simple “barren” pegmatites make up the vast majority of pegmatite bodies within a given pegmatite district, while the more fractionated and chemically “complex” pegmatites within the same district will be far less abundant (Černý *et al.*, 2012; London and Morgan, 2012; London, 2018). These simple-barren pegmatites have not been included in the classification schemes (Černý and Ercit, 2005) discussed here, but the chemical family of a pegmatite district may be evident in the rock-forming mineralogy and trace-element signature (London, 2018).

### 1.3 Objectives and outcomes of this study

The pegmatites of the ORPB (Figure 1.1) are not linked with plutons at current exposure level (Minnaar *et al.*, 2006). The vast number of pegmatites (<35 000) represent a range in pegmatite types (see section 1.2 above). The pegmatites range from “simple”, often muscovite or biotite bearing, unzoned to weakly zoned and barren pegmatites to chemically complex rare earth element (REL) class with exotic minerals rich in Be, Li, Ta, etc (Hugo, 1970; Schutte, 1972; Macey *et al.*, 2015). The REL-type pegmatites are mostly LCT in character. However, NYF pegmatites are found in the areas around Riemvasmaak and Kakamas in the Kakamas Domain. These complex REL-type pegmatite of the ORPB are found together in “swarms” that create an apparent regional zonation with respect to pegmatite mineralogy and chemistry, while the bulk of encountered pegmatites are simple and barren (Hugo, 1970; Schutte, 1972).

Given their mineralogy of LCT-type pegmatites within the ORPB (in particular, the occurrence of beryl and exotic lithium phases such as spodumene or lepidolite) at least some of the pegmatites must represent some final stage fractionates of much larger felsic magma bodies (Černý, 1991; Evensen *et al.*, 1999; Černý and Ercit, 2005). Additionally, the fact that the ORPB pegmatites are observed in the field to intrude metasediments of the Namaqua-Natal Belt might be used to suggest that they were sourced from partial melting of these metasediments during deformation of the NNMP at the time of pegmatite emplacement (see section 2.2).

There are few modern U-Pb geochronological data for these pegmatites, with and little known about the source regions from which they were derived. This raises the question about whether the pegmatites of the ORPB are as a result of local anatexis and melt segregation or whether they represent highly fractionated magmas derived from a much larger parental magma. Due to the lack of Sm-Nd isotope geochemistry, there is no idea about the character of the parental magma, whether they were sourced from an “evolved” or from some more “juvenile” source in the development of the OPRB.

From the facts of the ORPB mentioned above of the ORPB and despite their common occurrence within the Namaqua region, little is known about three critical questions.

- What was the timing of pegmatite intrusion for the pegmatites across the varying host tectonic domains?
- What is the nature of the source or sources for the late, fractionated melt responsible for the LCT-type pegmatites within the ORPB?
- What is the relationship between the ages and sources of the pegmatites within the context of the poly-metamorphic history of the different tectonic domains of the Namaqua-Natal-Province?

This study attempts to undertake a regional geological and isotope geochemical study across the length of the ORPB. To accomplish this aim, the study will use:

- in-situ high spatial resolution monazite (LA-Q-ICP-MS) to obtain U-Pb ages to constrain the emplacement ages and history for the pegmatites across the NNMP;
- in-situ high spatial resolution LA-MC-ICP-MS isotopic tracing of monazite grains to determine the Sm-Nd isotope compositions and 2-stage depleted model ages for the pegmatites.

These techniques used will help to constrain the crystallisation and emplacement history of selected pegmatites in the ORPB across the Namaqua Sector of the NNMP. Additionally, understanding the Sm-Nd isotope composition of the studied pegmatites will help constrain the source of the melt responsible for the numerous pegmatites in the ORPB.

Given the great number of pegmatites in the ORPB, and the time constraints of an MSc thesis, such a study can never claim to be exhaustive. However, to in part mitigate this problem the project will also draw on large existing U/Pb and whole rock Sm-Nd isotope geochemical datasets for potential source rocks in the Northern Cape (cf. Eglinton, 2006, and references therein).

## 2 Regional geological framework

The Namaqua-Natal Metamorphic Province (NNMP) forms part of a worldwide network of Mesoproterozoic, “Grenville-aged” orogenic belts. These “mobile-belts” formed during the amalgamation of the Rhodanian supercontinent (Li *et al.*, 2008), with the NNMP being associated with the formation of the Kalahari Craton (Jacobs *et al.*, 2008). The NMP forms a 400 km wide, 1800km long arcuate metamorphic crustal belt along the western and southern margins of the Kaapvaal Craton, that stretches from the west coast of southern Africa, (i.e. southern Namibia-north western South Africa) to the Kwazulu-Natal coast of south-east southern Africa (Hartnady *et al.*, 1985; Thomas *et al.*, 1994; Cornell *et al.*, 2009b). The belt is subdivided into an eastern (Natal) sector and the western (Namaqua) sector. The Mesoproterozoic Natal sector of the NNMP is chiefly comprised of juvenile crust formed by ca. 1200 Ma island arc system that was accreted to the Archean Kaapvaal craton at ca. 1100 (Thomas *et al.*, 1994). The western Namaqua sector, however, is much more complex, as it involves a Mesoproterozoic crust with a Paleoproterozoic heritage (Reid, 1997; Bailie *et al.*, 2017; Macey *et al.*, 2017, 2018 and references within).

The Namaqua sector (Figure 2.1) comprises of poly-deformed and poly-metamorphosed granitic gneisses and supracrustal rocks that developed during two major tectono-magmatic cycles in the Paleoproterozoic (~2050 Ma to 1800 Ma) and the Mesoproterozoic (~1350 Ma to 950 Ma; Clifford *et al.*, 2004; Cornell *et al.*, 2006, 2009; Eglington, 2006; Cornell and Pettersson, 2007b; Thomas *et al.*, 2016; Macey *et al.*, 2017). The Namaqua Sector is comprised of thin but laterally extensive thrust-bound crustal sheets that form different tectonostratigraphic domains. These domains are distinguished by their lithostratigraphic, tectonic and metamorphic histories (Figure 2.1; Hartnady *et al.*, 1985; Thomas *et al.*, 1994; Macey *et al.*, 2017).

In broad terms, the Namaqua sector (Figure 2.1) is subdivided from west to east into:

- The greenschist- amphibolite facies ~1.9 Ga Richtersveld Magmatic Arc (RMA; Macey *et al.*, 2017);
- the ~ 1.2-1.0 Ga, amphibolite- to granulite-facies Bushmanland Subprovince (BSP) to the south of the Richtersveld Magmatic Arc. The boundary with the Richtersveld Magmatic Arc to the north is termed the Groothoek Thrust (van Aswegen *et al.*, 1987; Colliston *et al.*, 1996). Amphibolite- to granulite-facies gneisses and granites in the BSP have been dated at ~ 1.2 - 1.02 Ga, and ~1.85 Ga migmatitic basement gneisses are locally preserved (Robb *et al.*, 1999; Cornell *et al.*, 2006; Eglington, 2006a);

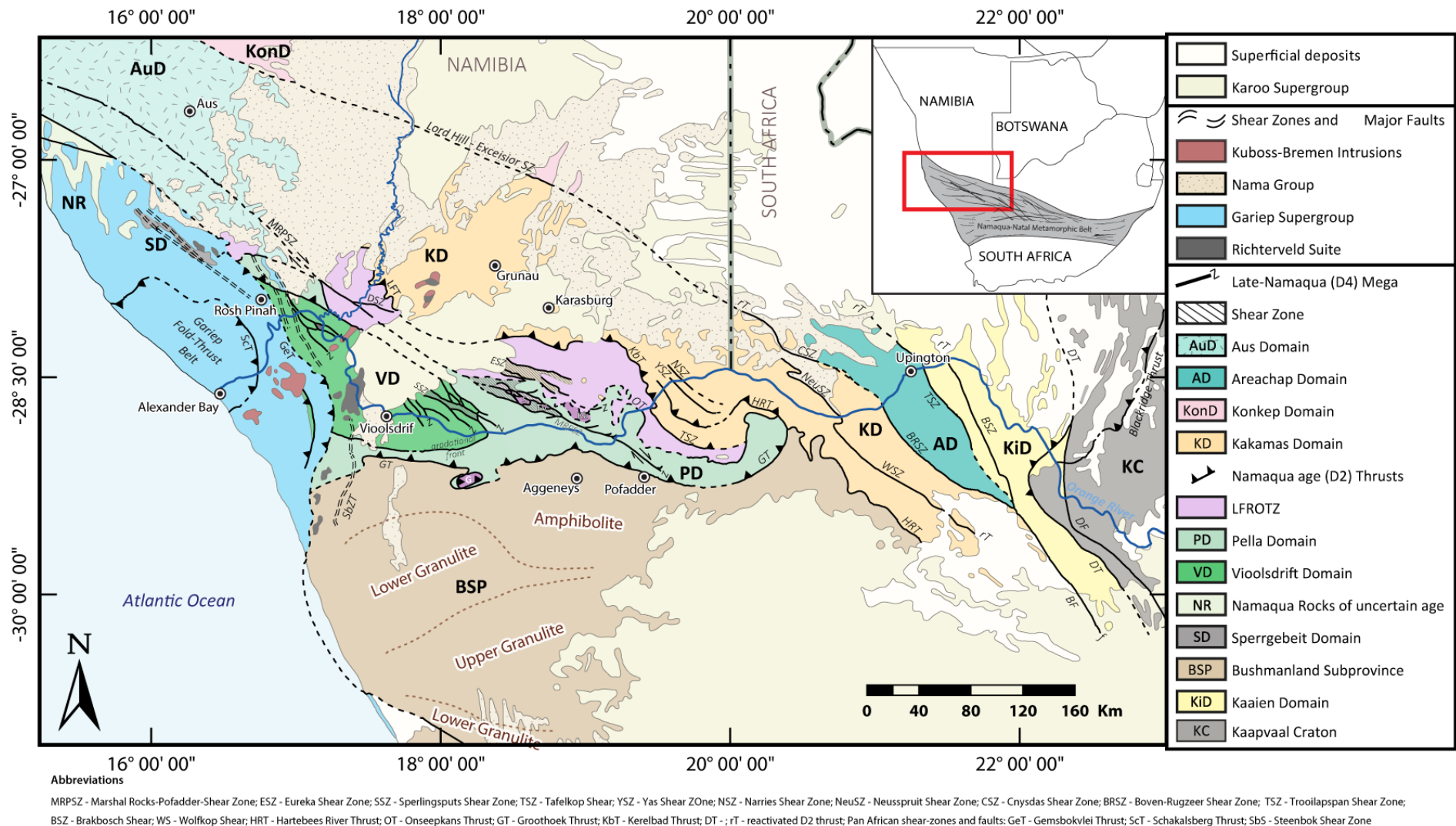


Figure 2.1: Regional tectonostratigraphic map of the Namaqua-Natal Metamorphic Belt (NNMP). Compiled from (Blignault et al., 1983; Hartnady et al., 1985; Colliston, 1990; Thomas et al., 2016, 1994; Moen et al., 2007b; Millar, R, 2008; Macey et al., 2015, 2017, 2018; Gresse et al., 2016).



- the ~1.2-1.09 Ga granulite-facies Kakamas Domain (KD). The supracrustal and intrusive rocks of the Kakamas Domain tectonically overly the RMA and BSP and is separated from the RMA by the recently recognised, wide zone of intense reworking and thrust-imbrication. This zone has been termed the Lower Fish River-Onseepkans-Thrust-Zone (LFROTZ; Macey *et al.*, 2015, 2017). It comprises amphibolite-facies mélange of thrust slices of exotic rocks, slivers of the RMA and granulite klippe of the KD;
- the east of the KD and separated by the Boven-Rugzeer Shear Zone is the upper-amphibolite facies ~1.3 to 1.22 Ga meta-volcanic, volcanoclastics and sedimentary rocks of the Areachap Domain, that is thought to represent a Mesoproterozoic volcanic arc succession (Cornell *et al.*, 2007b; Fransson, 2008; Bailie *et al.*, 2011a, 2011b; Bachmann *et al.*, 2015)
- the Kaaie Domain, a collection of ~1.77 Ga meta-quartzites and bimodal volcano-sedimentary rocks dated at ~1.37 to ~1.10 Ga with ~1.10 Ga granitic intrusions (Van Niekerk, 2006; Bailie *et al.*, 2012). This domain forms the tectonic transition zone between the Kheis Subprovince and the Kaapvaal and Craton further to the east; and
- the greenschist-facies Kheis Subprovince consists of Paleoproterozoic basement, which underwent Mesoproterozoic Namaqua Orogenic tectonic to form a thin-skinned fold and thrust belt (Eglington, 2006a; Van Niekerk, 2006; Moen *et al.*, 2008).

The late Namaqua-age (~1005-960 Ma) mega-shear zones such as the Marshal-Rocks-Pofadder (MRPSZ), Eureka (ESZ) and Sperlingsputs (SSZ) shear zones (Figure 2.1), provided extensional sites into which S-type leucogranites (Warmbad Granite) and pegmatites of the ORPB intruded (Hugo, 1970; Melcher *et al.*, 2008; Lambert, 2013).

## 2.1 Lithostratigraphy of the Namaqua-sector of the Namaqua-Natal-Metamorphic Province

### 2.1.1 Richtersveld Magmatic Arc (RMA)

The Richtersveld Magmatic Arc (RMA) forms a ~200km wide, wedge-shaped crustal block in the western parts of the NNMP (Figure 2.1). This tectonic domain comprises crustal material that was initially generated in a Paleoproterozoic island arc setting (Reid *et al.*, 1987; Reid, 1997). The magmatic arc is predominantly composed of felsic and mafic volcanics of the Orange River Group (ORG) (Blignault, 1977; Reid *et al.*, 1987; Reid, 1997) and sparse hyperbassal and voluminous plutonic rocks of the Vioolsdrif Suite (Blignault, 1977; Reid *et al.*, 1983; Reid, 1997), and their metamorphic equivalents (Macey *et al.*, 2017).

The RMA is composed of two parts that are distinct from each other based on metamorphic grade. A western part of Paleoproterozoic crust, termed the Vioolsdrif Domain (Figure 2.1; Table 2.1), consists of greenschist-facies crust that was largely excluded from the pervasive crustal re-working during the Mesoproterozoic Namaqua Orogeny. To the east, mostly but not limited to zones wrapped around the low-grade Vioolsdrif Domain, is the amphibolite-facies Pella Domain (Macey *et al.*, 2015, 2017, Figure 2.1). This belt is characterised by a pervasive Namaqua imprint that has converted the Paleoproterozoic volcanic and plutonic units into medium- to high-grade gneisses.

### *Vioolsdrif Domain - VD*

The ~1800 Ma Orange River Group (Figure 2.2) of the Vioolsdrif Domain represents a full suite of calc-alkaline volcanic rock types that range in composition from basalt to rhyolite (Reid, 1977, 1997; Reid *et al.*, 1987). The group predominantly contains variously textured aphanitic to porphyritic lavas although pyroclastic and volcanoclastic rocks do occur (Reid, 1977; Ritter, 1980; Gresse *et al.*, 2016). Quartzites and conglomerates occur as minor components (Macey *et al.*, 2017).

The Orange River Group is intruded by the voluminous plutonic and minor hyperbasal rocks of the Vioolsdrif Suite (Figure 2.2; Table 2.1). The Vioolsdrif Suite forms a calc-alkaline magma series that is subdivided into a number of units based on intrusive age relationships (Table 2.1). The mafic units of the Vuurdoed Gabbro (Strydom *et al.*, 1987; Figure 2.2; Table 2.1) and closely associated and slightly younger Goabis Diorite (Cilliers, 1989; Macey *et al.*, 2015; Figure 2.2; Table 2.1) forms a minor component within the Vioolsdrif Suite forming numerous isolated bodies within the VD.

The dominant unit of the Vioolsdrif Suite, the Gaarseep granodiorite (Figure 2.2; Table 2.1), is relatively heterogeneous in composition. It ranges from quartz diorite to granite but is dominated by granodiorite (Reid, 1977; Minnaar, 2012). Several, subvolcanic fsp±qtz porphyries bodies have been grouped as the Khoromous Porphyry. They are dioritic to granitic in composition and have been intruded by the Gaarseep granodiorite, has been (Minnaar, 2012; Macey *et al.*, 2017; Figure 2.2; Table 2.1). The youngest member of the Goodhouse Subsuite is the pink leucocratic Ramansdrif Alkali Granite (Figure 2.2; Table 2.1) that intrudes all the other members of the suite as small plutons, dykes and stockworks (Minnaar, 2012; Macey *et al.*, 2015; 2017).

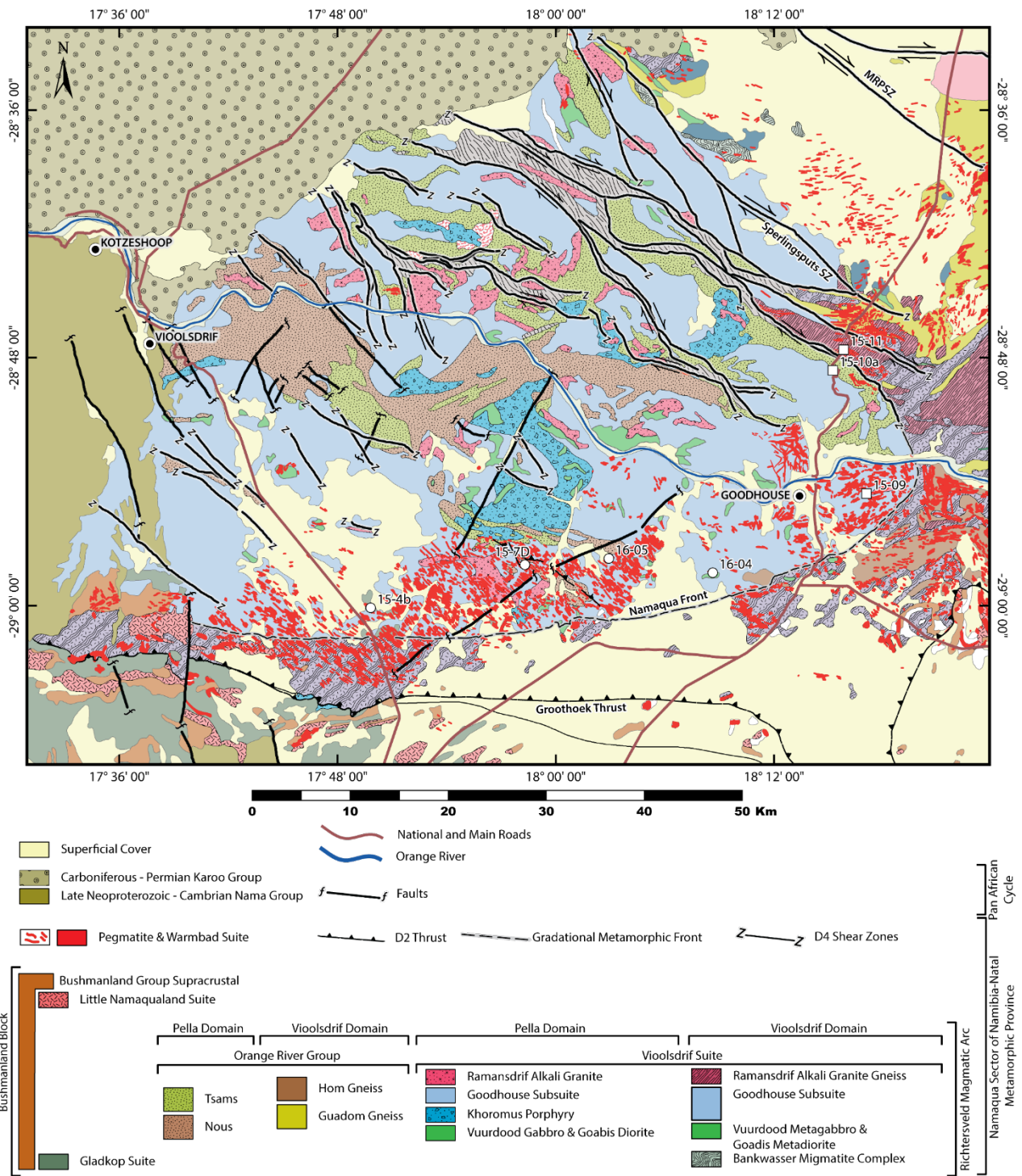


Figure 2.2: Simplified geological map of the Vioolsdrif Domain. Squares indicates monazite samples analysed for both U-Pb and Sm-Nd analysed samples, circles indicate monazite U-Pb only samples.. Compiled from maps: (Schutte, 1972; Moen et al., 2007b; Minnaar, 2012; Macey et al., 2015, 2017; Shifotoka et al., 2016). For the purpose of this illustration, pegmatite exposure has been exaggerated for clarity and are not to scale.

## *Pella Domain - PD*

The Pella Domain consists of units from the Vioolsdrif domain that were strongly reworked during the main Namaqua Orogenic event from ~1215 Ma to 980 Ma (Cornell *et al.*, 2006; Macey *et al.*, 2017) into supracrustals paragneisses (Orange River Group) and orthogneisses (Vioolsdrif Suite), with all original intrusive contacts now extensively tectonised (Macey *et al.*, 2015; 2017). This makes the relative stratigraphic ages between the units challenging to determine and many stratigraphic subdivisions have been proposed (Blignault, 1977; Strydom *et al.*, 1987; Cilliers, 1989; Colliston, 1990; Colliston *et al.*, 1996; Moen *et al.*, 2007b). Recent geochronological studies by Macey *et al.* (2017) propose a stratigraphic subdivision based on Strydom *et al.* (1987) in that the ORG of the Pella Domain can be subdivided into four lithodemic units: the Guadom, Umies, Gaidip and Hom Gneiss (Figure 2.3; Table 2.1).

The Guadom Gneiss is a heterogeneous succession of meta-volcanic and subordinate meta-sedimentary rocks that forms a belt across the southern and eastern parts of the Pella Domain. The Umies Gneiss is restricted to areas north of the Marshall Rocks-Pofadder-Shear Zone (MRPSZ) and consists of a banded, commonly strongly migmatitic grey gneisses. The leucocratic and quartzofeldspathic Gaidip Gneiss is thought to represent a meta-rhyolite (Cilliers, 1989; Macey *et al.*, 2017). The Hom Gneiss consists of intercalated quartzofeldspathic gneiss and biotite-hornblende gneiss.

Recent U-Pb geochemical studies in the southern Namibian parts of the NNMP (e.g. Macey *et al.*, 2015, 2017; Gresse *et al.*, 2016) has indicated that Paleoproterozoic orthogneisses of the Pella Domain are equivalent to the undeformed plutonic rocks of the Vioolsdrif Suite in the Vioolsdrif Domain. This observation is based on their matching geochemistry and overlapping U-Pb ages. Macey *et al.* (2017) have also further subdivided the Vioolsdrif Suite of the Pella Domain into several lithodemic orthogneiss units that largely retains the nomenclature of their low-grade equivalents in the Vioolsdrif Domain, namely the Goodhouse Subsuite and Ramansdrif Alkali Granite Gneiss (Figure 2.3; Table 2.1).

The Vuurdood Subsuite in the PD comprises meta-gabbros and hornblendite, which collectively forms a minor part of the Vioolsdrif Suite. The meta-dioritic to meta-gabbroic rocks of the Goabis Subsuite also represent a minor component of the Vioolsdrif Suite and occurs mostly in the western parts of the PD, typically in close association with the meta-gabbros of the Vuurdood suite. The southern and eastern parts of the PD hosts sheet-/dyke-like and plug-like bodies of amphibolite and associated calc-silicate (metasomatised equivalents of these mafic dykes) rocks of the Girtis Suite. The meta-basites are seen to represent swarms of metamorphosed mafic dykes that have been pulled into parallelism during the Namaqua Orogeny (Macey *et al.*, 2015).

The ~1.2 Ga D<sub>2</sub> thrusting saw the intrusion of the ~1220 Ma Orange Falls Suite of leucogranitic augen gneisses and leucogranite gneisses (Macey *et al.*, 2015), that is restricted to the northern and eastern parts

of the PD. The metaluminous to slightly peraluminous suite has geochemistry of this suite reflects evolved felsic magma that is interpreted to have been derived from melting of calc-alkaline rocks.

Table 2.1: Summarised lithological features, geochemistry and geochronology of Richtersveld Magmatic Arc country rock.

	Lithology and composition	Geochemical characteristics	Age of emplacement or relative age (Ma)	$\epsilon_{Nd}$	$T_{DM}$ (Ga)	References
<b>Vioolsdrif Domain</b>						
<b>Vioolsdrif Suite</b>						
Ramansdrif	alkali feldspar granite and aplite dykes	Calc-alkaline; meta-peraluminous; K-fsp+bt±ms	1844 ±26; 1886 ±8; 1882 ±8	-2.68	2.4	Macey <i>et al.</i> (2017)
<b>Goodhouse Subsuite</b>						
<i>Garseep</i>	Range from qtz diorite to granite; dominated by granodiorite	Calc - alkaline Island Arc intrusives; heterogenous	1902 ±10 Ma - 1869 ±14 Ma	-1.57 - 0.98	2.4 - 2.1	Macey <i>et al.</i> (2017)
Khoromous	Subvolcanic qtz±fsp porphyry; tonalitic to dioritic	Calc-alkaline; Metaluminous - slightly peraluminous; qtz+plag+or+bt±hbl±chl±ep	1893 ±10 Ma	-1.57	2	Macey <i>et al.</i> (2017)
Goabis Vuurdoed	Diorite Gabbro, meta-gabbro, hornblendite	Tholeiitic-calc alkaline; island Arc; metaluminous; opx+hbl+plag+qtz±cpx	1880 ±6 Ma	-0.33 -- 0.76	2.2	Macey <i>et al.</i> (2017)
<b>Pella Domain</b>						
<b>Vioolsdrif Suite</b>						
Ramansdrif Alkali granite gneiss	F-mg leucogranite gneiss C.g. leucogranite gneiss	High K calc-alkaline; metaluminous to peraluminous; alkali granite	1877 ±7 Ma - 1893 ±8 Ma	-2.97 - -2.2	2.8 - 2.3	Macey <i>et al.</i> (2017)
<b>Goodhouse Subsuite</b>						
	Leucogranite gneiss			-1.5	2.2	Macey <i>et al.</i> (2017)
	Bt-hbl granite augen gneiss			-1.47	2.2	Macey <i>et al.</i> (2017)
<i>Coboop Type</i>	Interlayered augen gneiss & leucogranite gneiss	Calc - alkaline Island Arc intrusives; heterogeneous	~ 1850 - ~1900 Ma	-3.12	2.3	Macey <i>et al.</i> (2017)
<i>Noudap Type</i>	Bt-hbl augen orthogneiss Bt-hbl equigranular granitic to tonalite gneiss			-2.26 -1.08	2.3 2.2	Macey <i>et al.</i> (2017) Macey <i>et al.</i> (2017)
Goabis Vuurdoed	Meta-diorite Meta-gabbro, hornblendite	Tholeiitic-Calc alkaline; Island Arc; Metaluminous	1880 ±6 Ma			Macey <i>et al.</i> (2017)
Orange Falls	f.g - m.g. equigranular leucogranite gneiss, c.g. equigranular granite gneiss, leucogranite augen gneiss, bt augen gneiss	Highly acidic, High-k calc-alkaline; metaluminous - mod. Peraluminous; evolved felsic magma derived from melting calc-alkaline source (Vioolsdrif suite and ORG)	1238 ±10Ma - 1196 ±4 Ma	-12.5 -- -9.3	2.5 - 2.2	Macey <i>et al.</i> (2015)

Abbreviations: f.g = fine grained; m.g. = medium grained; c.g. = coarse grained; mod. = moderate

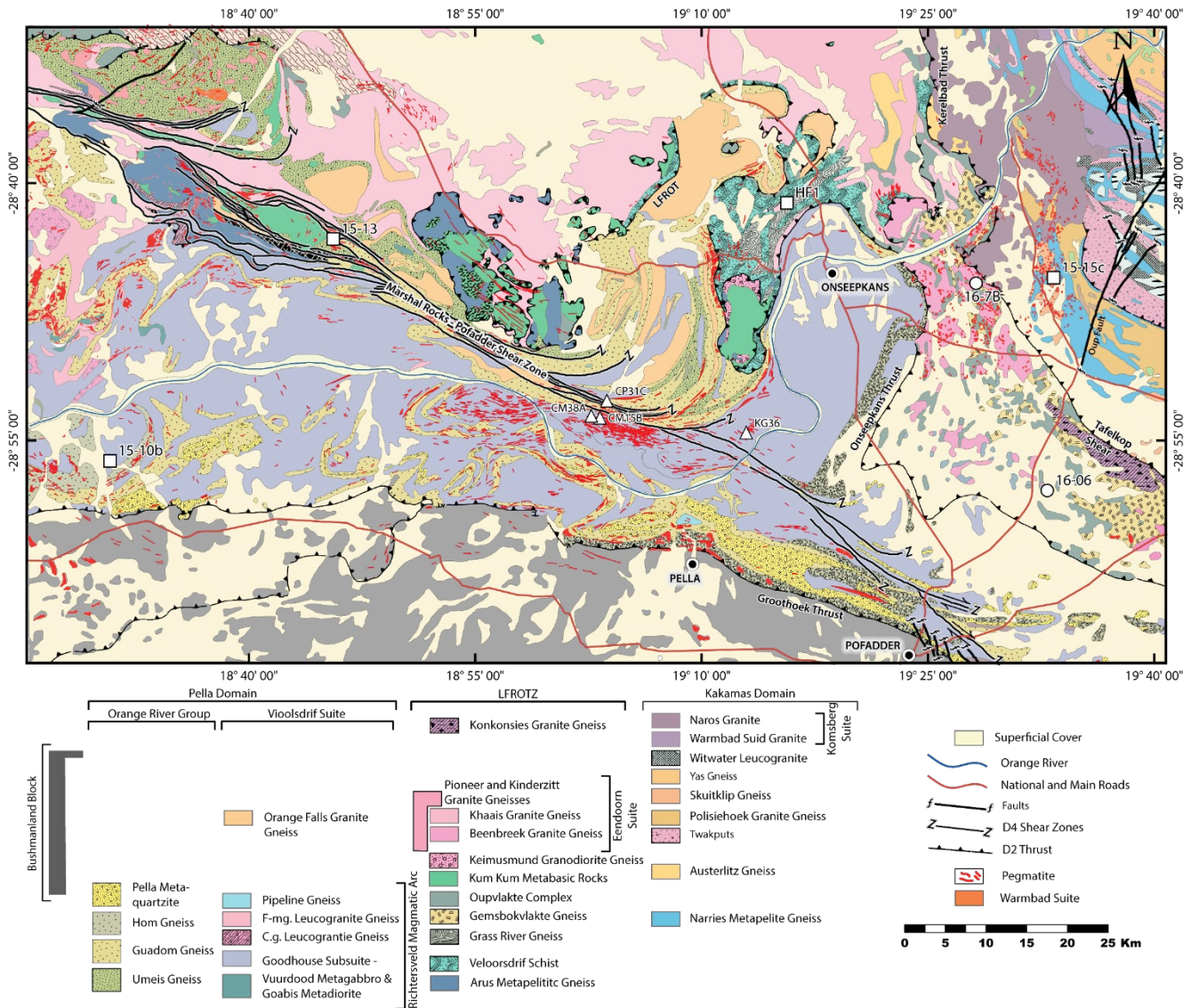


Figure 2.3: Simplified geological map of the Pella Domain, illustrating major structures, tectonic boundaries and pegmatite distribution. Squares indicate monazite samples analysed for both U-Pb and Sm-Nd analysed samples, circles indicate monazite U-Pb only samples and triangles indicate samples analysed for Sm-Nd only. Compiled from maps by Hugo (1970), Schutte *et al.* (1972), Moen (1988), Moen and Toogood (2007), Agenbacht (2007), Macey *et al.* (2015 and 2017).

## 2.1.2 Bushmanland Subprovince (BSP)

The Bushmanland Subprovince (BSP) forms the most southerly and structurally lowermost tectonic domain of the Namaqua sector. In the north-west the BSP is dominated by ~1850 Ma granitic gneisses and migmatites of the Gladkop Suite (Robb *et al.*, 1999). Vast volumes of pre- and post-tectonic Mesoproterozoic granites that are interleaved with thin sheets and discontinuous belts of high-grade paragneisses dominate the rest of the BSP (Marais *et al.*, 2001; De Beer *et al.*, 2002; Agenbacht, 2007; Moen *et al.*, 2007a; De Beer, 2010; Macey *et al.*, 2011).

The supracrustal units have been subdivided into the Bushmanland and Kamiesberg Groups (e.g. Agenbacht, 2007; De Beer, 2010; Macey *et al.*, 2011). However, recent studies on these supracrustal units

(McClung, 2006; Bailie *et al.*, 2007b; Cornell *et al.*, 2009b) yielded a range of detrital age spectra from different supracrustal gneisses that indicate that further subdivision is required.

The voluminous granitoids of the BSP can be separated in the field based on the presence or absence of a penetrative gneissic fabric. The ~1212 Ma and ~1191 Ma Little Namaqualand Suite (LNS) comprise the oldest pre-tectonic orthogneisses (Robb *et al.*, 1999; Clifford *et al.*, 2004; Macey *et al.*, 2011). Some minor plutons (e.g. the Landplaas Gneiss) yield younger magmatic crystallisation ages of ~1109 Ma (De Beer *et al.*, 2002; Raith *et al.*, 2003). The undeformed granitoids of the Spektakel Suite, which also includes charnokites, have been dated between ~1086 Ma and ~1033 Ma (Thomas *et al.*, 1996; Robb *et al.*, 1999; Clifford *et al.*, 2004; Macey *et al.*, 2018). Vast areas of the BSP are underlain by a “pink” quartz-feldspar gneiss that is collectively called the Lekkerdrink Gneiss, however, the protolith remains controversial (Macey *et al.*, 2011; 2017). Mafic units form a minor constituent of the intrusions of the western BSP. They are represented by a variety of pre-tectonic amphibolites and granulites, together with the economic Cu-bearing noritic bodies of the post-tectonic Koperberg Suite (~1030 Ma; Clifford *et al.*, 1995; Robb *et al.*, 1999; Clifford and Barton, 2012).

### 2.1.3 The Kakamas Domain (KD) and Areachap Domain (AD)

The Kakamas Domain tectonically overlies the Richtersveld Magmatic Arc, LFROTZ and Bushmanland Subprovince within the Namaqua Sector of the NNMP (Figure 2.1). Late Mesoproterozoic granulite-facies meta-sedimentary rocks dominate this high-grade metamorphic domain with a minimum depositional age from detrital zircons ranging from ~1220 Ma to ~1150 Ma (Cornell *et al.*, 2007b; Fransson, 2008). These supracrustal packages have been intruded by various ~1230 Ma to ~1080 Ma granites, anatectic leucogranites and minor gabbroic rocks (Pettersson *et al.*, 2007; Bial *et al.*, 2015a, 2015b, 2016; Macey *et al.*, 2017). The Kakamas Domain is viewed as a low-angle imbricate nappe stack separated from the Bushmanland Subprovince and Richtersveld Magmatic Arc by major thrust structures; Onseepkans, Hartebeest River, Lower Fish River and Kerelbad thrusts (Colliston *et al.*, 2015; Macey *et al.*, 2015; Macey *et al.*, 2017 and references within; Figure 2.1).

The granulite-facies meta-pelites and aluminous gneisses in the KD (e.g. Narries Suite, Figure 2.4; Figure 2.5 and Table 2.2; Beukes, 1973; Du Plessis, 1979; Moen and Toogood, 2007a; Macey *et al.*, 2015) are viewed as the oldest metasedimentary successions and occur in the north-western parts of the Kakamas Domain. Peak metamorphism of these supracrustals occurred at ~1230 Ma and ~1180 Ma during a period of magmatism in the western parts of the Kakamas Domain (Bial *et al.*, 2015). This period of magmatism is broadly contemporaneous with widespread magmatism of the Little Namaqua Suite within the Bushmanland Subprovince further to the west (Bailie *et al.*, 2007a; Cornell *et al.*, 2009b; Macey *et al.*, 2018).

In the western Kakamas Domain, ~1230 Ma to ~1180 Ma magmatism also resulted in the intrusion of the voluminous Eendoorn Suite (i.e. the ~1208 Ma Twakputs porphyritic gneiss, Figure 2.4; Table 2.2; Macey *et al.*, 2015) into the western KD. This period of intense magmatism and thrusting was accompanied by the intrusion of sheeted porphyritic granite (~ 1200 Ma Pioneer, Beenbreek, Khaais and Kinderzitt gneisses; Table 2.2; Figure 2.3 and Figure 2.4). These granites intruded into the LFROTZ during D2 thrusting and docking of the Kakamas Domain onto the Richtersveld Magmatic Arc (Macey *et al.*, 2015). This event culminated with the intrusion of parental magmatic rocks to augen gneisses and leucogranitic gneisses of the Yas, Shuitdrif and Skuitklip gneisses (Figure 2.3 and Figure 2.4; Table 2.2) into the western parts of the Kakamas Domain.

The Hartebees River Thrust represents the tectonic boundary separating the Kakamas Domain and the Bushmanland Subprovince (Colliston *et al.*, 2015; Figure 2.1 and Figure 2.5). The Vyfbeker Metamorphic Suite is situated in the adjacent hanging wall rocks of the KD and grades from the metapelites of the Narries Suite in the north into a variable package of amphibolites and migmatitic biotite gneisses of the ~1200 Ma Kenhardt Formation (Slabbert *et al.*, 1999; Cornell *et al.*, 2007b; Fransson, 2008; Table 2.2; Figure 2.5). These supracrustal rocks of the Kenhardt Formation were in turn metamorphosed during the intrusion of magmatic protolith to the Banks Vlei gneiss (Praekelt *et al.*, 1986; Table 2.2; Figure 2.5) at around ~1188 Ma (Pettersson, 2008) during the final stages of the amalgamation of the Bushmanland Subprovince and Kakamas Domain (Bailie *et al.*, 2017).

The Korannaland Group makes up the dominant supracrustals package in the eastern parts of the Kakamas Domain (Figure 2.5), occurring as a northwest trending belt of outcrops. Detrital zircon studies by Fransson (2008) revealed the minimum deposition age for a package of metamorphosed psammites, pelites and quartzites within the Goedehoop Formation to around ~1166 Ma, with a subsequent metamorphic event at ~1100 Ma. The Wolfkop Shear Zone represents the western boundary of the Korannaland Group separating it from the Narries metapelitic gneiss and Vyfbeker Metamorphic Suite (Figure 2.5). The southern parts of the Kakamas Domain is dominated by the amphibolite-facies metasediments of the Jacomynspan Formation (Slabbert *et al.*, 1999; Figure 2.5), a supracrustal succession of quartzites, metapelitic gneisses, felsic gneisses, minor calc-silicate gneisses and migmatites (Slabbert *et al.*, 1999; Cornell and Pettersson, 2007a).

The RMA is separated from the overlying Kakamas Domain by a wide, extensive imbricate zone known as the Lower Fish-Onseepkans Thrust Zone (LFROTZ). The LFROTZ is comprised of a mainly amphibolite-facies mélangé of exotic thrust slices but includes several granulite klippe (Kum Kum Suite and Arus metapelitic gneiss; Macey *et al.*, 2015), slivers of RMA rocks (Macey *et al.*, 2015; 2017) and the ~1200 Ma Eendoorn stitching pluton. It also contains a range of rock types that are restricted to the LFROTZ itself, e.g. ~1220 Ma bimodal gneisses of the Oupvlakte Complex (Moen and Toogood, 2007b; Macey *et al.*, 2015; Figure 2.3); the ~1220 Ma garnet-bearing Grass River Gneiss (Toogood, 1976; Figure 2.3) and the ~1218



Ma leucogranitic Gemsbokvlakte Gneiss (Macey *et al.*, 2015; Figure 2.3). Recent mapping has identified a suite of sheared and variably re-equilibrated pelitic to semi-pelitic Veloorsdrif schists, gneisses and migmatites (maximum deposition age of ~1165 Ma; Macey *et al.*, 2015; Figure 2.3).

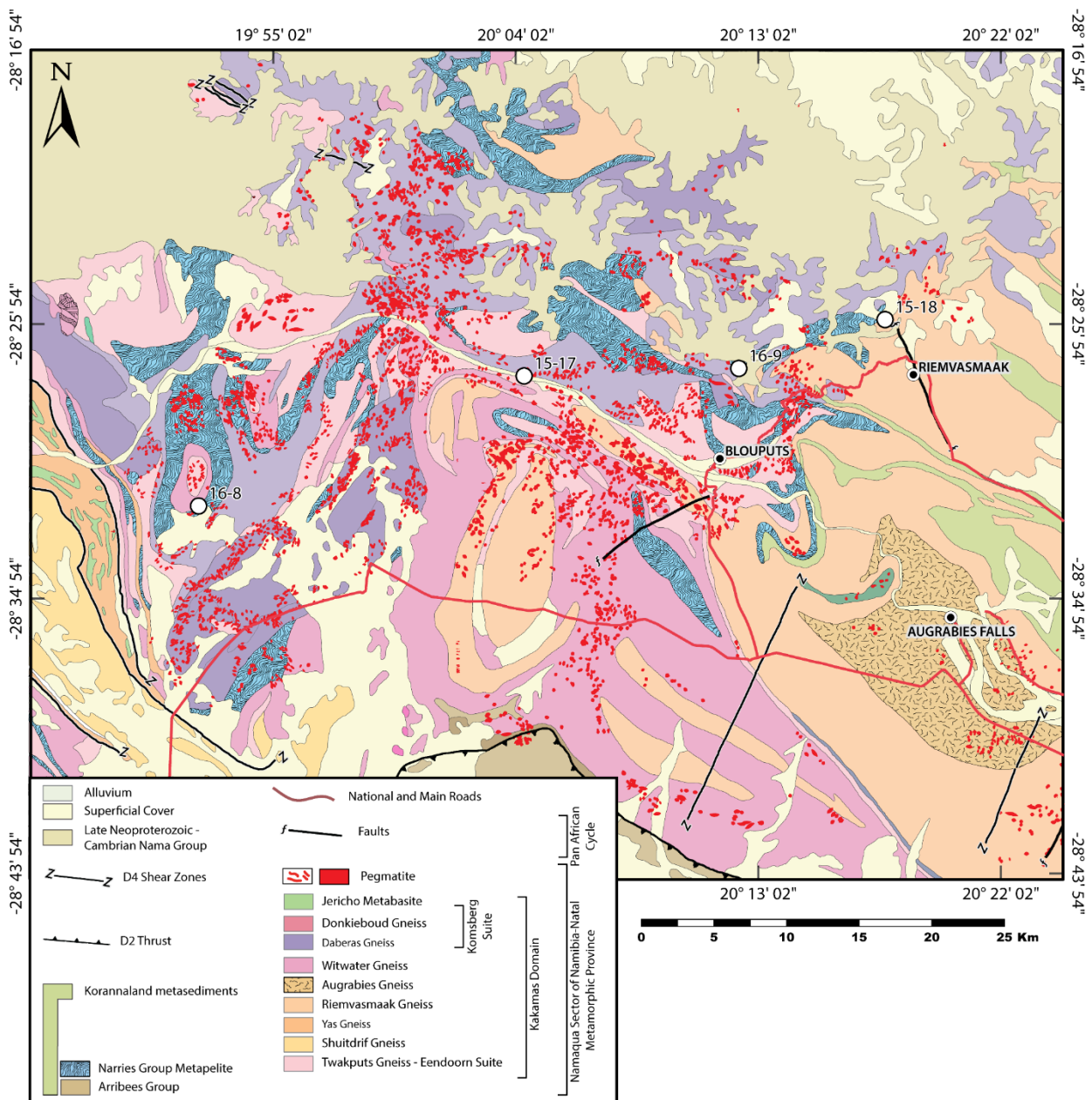


Figure 2.4: Simplified geological map of the Kakamas Domain in the region west of Onseepkans and Riemvasmaak. Circles indicate monazite samples analysed for U-Pb. Compiled from maps by (Moen, 2007; Moen and Toogood, 2007; Bial *et al.*, 2015a; Colliston *et al.*, 2015; Macey *et al.*, 2015; Bailie *et al.*, 2017b)

The Areachap Domain (AD), which is situated to the east of the Kakamas Domain (Figure 2.1), is dominated by ~1300 Ma to ~1220 Ma volcanoclastic, volcanic and sedimentary rocks of the Areachap Group (Figure 2.5). This supracrustal sequence represents a metamorphosed juvenile Mesoproterozoic volcanic arc succession (Geringer *et al.*, 1986, 1994; Pettersson *et al.*, 2007; Bailie *et al.*, 2011a, 2017; Cornell *et al.*, 2012) that was intruded by a younger ~1200 Ma to ~1090 Ma granitoids (Pettersson *et al.*, 2007; Bailie *et al.*,

2011b; Cornell *et al.*, 2012). This extensive juvenile magmatism with dominantly Mesoproterozoic Nd model ages has been proposed to have been as a result of eastward-directed subduction (Figure 2.1; Bailie *et al.*, 2010; 2017). This proposed interpretation relies on the subduction-arc geochemical signatures (Geringer *et al.*, 1994; Pettersson *et al.*, 2007), with little field evidence and needs further investigation. The Areachap Domain is bounded to the west by the Boven Rugzeer Shear Zone ,BRSZ (van Bever Donker, 1991; Miller, 2012), whereas its eastern boundary with the Kaaie Domain and Kheis Province is marked by the Trooilapspan shear zone (TLSZ) and the Brakbosch Fault (Figure 2.1; Moen, 1999).

The Areachap Domain and adjacent Kakamas Domain were affected by upper amphibolite- to lower granulite-facies regional metamorphism (Cornell *et al.*, 1992) during several thermal events associated with the closure of the Areachap ocean (Pettersson *et al.*, 2007). Extensive magmatism within the eastern Kakamas Domain and Areachap Domain is characterised by the intrusion of the syn-tectonic granite between ~1175 Ma and ~1146 Ma (Colliston *et al.*, 2015; Bailie *et al.*, 2017). These syn-tectonic granites (Figure 2.4; Figure 2.5 and Table 2.2) are the Vaalputs Granite Gneiss (~1146 Ma), Riemvasmaak Gneiss (1156 Ma; Pettersson, 2008) and Augrabies Gneiss (~1168 Ma; Colliston *et al.*, 2015). The timing of emplacement of these intrusions corresponds with a reported age of migmatitisation and deformation of the Areachap group at ~1165 Ma (Pettersson *et al.*, 2007). The syn-tectonic granite gneisses intrude across the major tectonic boundary between the Areachap and Kakamas Domains, indicating that juxtaposition of these two domains occurred before ~1160 Ma (Bailie *et al.*, 2017).

This period of magmatism and deformation was associated with granulite-facies metamorphism within the central and western parts of the Kakamas Domain. Granulite-facies metamorphism resulted in the dehydration melting of the Narries Suite metapelites to form the ~1140 Ma and ~1120 Ma garnet-bearing, syn-tectonic leucogranite protolith to the Witwater Gneiss (Moen, 2007; Macey *et al.*, 2015; Figure 2.4; Table 2.2). The Komsberg Suite of I-type granitoids intruded late into the western Kakamas Domain at ~1120 Ma - ~1105 Ma (Bial *et al.*, 2015a; Macey *et al.*, 2015; Figure 2.3; Figure 2.4; Table 2.2)

Late- to post-tectonic magmatism in the Kakamas and Areachap Domains resulted in the intrusion of megacrystic granitoids and charnockites of the Keimoes Suite at ~1110 Ma to ~1080 Ma (Cornell *et al.*, 2012; Lambert *et al.*, 2016; Bailie *et al.*, 2017; Figure 2.5). The Keimoes Suite is restricted to areas between the Trooilapspan Shear and Neusspruit-Wolfkop Shear zones (Bailie *et al.*, 2017; Figure 2.5).

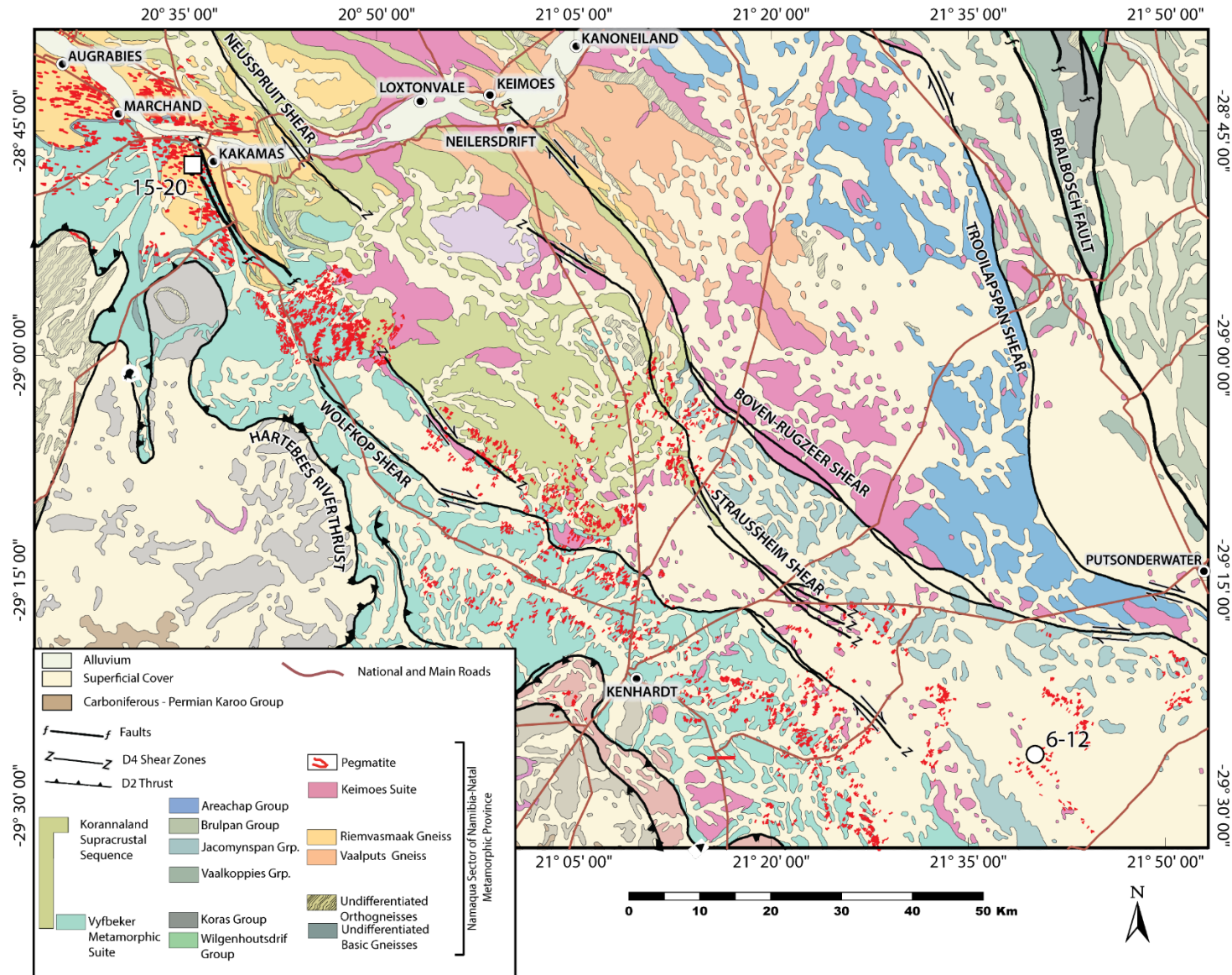


Figure 2.5: Simplified geological map of the Kakamas Areachap and Kaaien Domains. Squares indicate monazite samples analysed for both U-Pb and Sm-Nd analysed samples; circles indicate monazite U-Pb only samples. Compiled from maps by Slabbert et al. (1999); Moen (2007); Colliston et al., (2015) and Bailie et al. (2017).

Table 2.2 - Summarised lithological descriptions, geochemistry and geochronology of units within the Kakamas Domain

	Lithology and Composition	Geochemical Characteristics	Age of emplacement or relative age (Ma)	$\epsilon_{Nd}$	$T_{DM}$ (Ma)	References
<b>Kakamas Domain</b>						
Austerlitz	Equigranular m.g. leucogranite gneiss, leucogranite, bt granite augen gneiss		1244 ±14 Ma			Macey <i>et al.</i> (2015)
Kum Kum Suite	Gabbro, gabbroonorites, olivine gabbroonorites, olivine gabbros, troctolites, pyroxenites, ultramafic rocks (incl. metamorphic equivalents)	Sub-alkaline gabbroic to alkaline gabbroic	1213 ±4 Ma - 1212 ±11Ma; 1878 ±5 ma (inheritance)	-10.99	3.1 - 1.7	Macey <i>et al.</i> (2015)
<b>Eendoorn Suite - "Stitching pluton"</b>						
Kinderzitt Granite	Megacrystic granite - alkali feldspar granite		~1190-1193 Ma			Macey <i>et al.</i> (2015)
Pioneer Granite	Megacrystic granodiorite - granite		~1230 Ma	-8.15 - -3.41	2.2 - 1.9	Macey <i>et al.</i> (2015)
Khaais Granite Gneiss	Porphyroclastic granite gneiss	Intermediate to acidic; sub-alkaline to alkaline; peraluminous; A-type	~1190 Ma and ~1206 Ma			Macey <i>et al.</i> (2015)
Beenbreek Granite	Grt megacrystic - porphyritic granitic to granodioritic gneiss		1210; 1197 ±11 Ma (emplacement); 1091 ±8 Ma (metamorphic rim)	-0.17	1.4	Macey <i>et al.</i> (2015); Bial <i>et al.</i> (2015)
Twakputs	Grt megacrystic bt granite gneiss		~1208 Ma	-0.08	1.8	Macey <i>et al.</i> (2015)
Bokkiesbank Granite	Porphyritic granite/gneiss		~1214 Ma			
Keimusmund Granite	Porphyroblastic granodiorite gneiss	Sub-alkaline	1140 ±5 Ma (magmatic); ~1226 Ma - ~1220 Ma (inheritance)	-2.14 - -1.7	1.8 - 1.7	Macey <i>et al.</i> (2015)
Jerusalem	Metabasites, meta-gabbro, 2-px mafic granulites, amphibolites, grt amphibolites		1226 ±6 Ma (magmatic); ~1140 Ma (metamorphic rim)			Macey <i>et al.</i> (2015)
Skuitklip	Granite - granodiorite		1195 ±16 Ma (emplacement age); 1125 ±5 Ma (metamorphic age)			Bial <i>et al.</i> (2015)
Yas	Equigranular leucogranite gneiss, bt augen gneiss		~1188 Ma; ~1928 Ma - 1303 Ma (inheritance)	0.33	1.6	Macey <i>et al.</i> (2015)
Schuitdrif	C.g. bt augen gneiss, c.g. leucogranite augen gneiss, charnockite	Acidic, alkaline to sub-alkaline	1187 ±6 Ma; 1189 ±6 Ma; 1191 ±7 Ma (emplacement age); 1088 ±	1.51	1.6	Macey <i>et al.</i> (2015); Bial <i>et al.</i> (2015)
Witwater	Grt bearing m.g. to vc.g. granite and granodiorite	Strongly acidic, peraluminous, s-type	1126 ±22 Ma and 1142 ±11 Ma	-0.8	2.2	Macey <i>et al.</i> (2015); Pettersson (2008)

Abbreviations: f.g = fine grained; m.g. = medium grained; c.g. = coarse grained; mod. = moderate

Table 2.2 (continued): - Summarised lithological descriptions, geochemistry and geochronology of units within the Kakamas Domain

	Lithology and Composition	Geochemical Characteristics	Age of emplacement or relative age (Ma)	$\epsilon_{\text{Nd}}$	$T_{\text{DM}}$ (Ma)	References
<b>Komsberg Suite</b>						
Donkieboud	Granodiorite to granite gneiss, porphyritic bt±hbl granite gneiss, charnockitic in places		1107±5, 1108±6, 1118±6	-1.2 - -0.71	1.6 - 1.5	Macey <i>et al.</i> (2015)
Daberas	Hbl granodiorite, equigranular to porphyritic, charno-enderbites	Metaluminous, I-type/slight S-type character	1108 ±9 Ma; 1108 ±12 Ma (emplacement age); 1201 ±10 Ma; 1198 ±46 Ma (inheritance)			Bial <i>et al.</i> (2015)
Stolzenfels	Weakly porphyritic charno-enderbites, enderbites, diorite pods		1115±5	-0.74	1.6	Macey <i>et al.</i> (2015)
Naros	C.g. granodiorite, monzogranite, bt±hbl		1113±6, 1114±8; 1115 ±13 Ma; 1101 ±6 Ma (emplacement age)	-0.01	1.6	Macey <i>et al.</i> (2015); Bial <i>et al.</i> (2015)
Warmbad Suid	Megacrystic granite gneiss, grt bearing in places		1121±5	0.14	1.5	Macey <i>et al.</i> (2015)
Jericho	Metabasite dykes, sills and pods		1106 ±7 Ma			Macey <i>et al.</i> (2015)
<b>Augrabies Suite/Syntectonic Granite Gneisses</b>						
Riemvasmaak Gneiss	Quartzofeldspathic augen gneiss	S-type; metaluminous; Qtz+Mc+Plag+Bt+Mi	1156 ±8 Ma, 1151 ±14Ma	1.00 - 2.77	1.5 - 1.3	Pettersson (2008)
Augrabies Gneiss	Quartzofeldspathic gneiss;		1168 ±6 Ma (magmatic); 1090 ±16 Ma (metamorphic rim)			Colliston <i>et al.</i> (2015)
Vaalputs gneiss	Monzogranite	Peraluminous; S-type	1146 ±14 Ma (magmatic); 1062 ±27 Ma (metamorphic rim); ~1850 - 1297 Ma (inheritance)	-0.55 - 1.74	1.6	Pettersson (2008)
Elsie se Gorra Gneiss	Coarse grained leucogranite gneiss, granodiorites	Metaluminous; fractionated;	1175 ±18 Ma	1.25	1.6	Bailie <i>et al.</i> (2017)
Colston granite		Potassic, peraluminous granodiorite	1151 ±28 Ma	-1.6	1.9 - 1.8	Bailie <i>et al.</i> (2017)
Keimoes Suite	Monzogranite to granodiorites; charnockites	Ferroan, metaluminous; I type with A- type characteristics in maficity	~1110 Ma - 1078 ±12 Ma	-2.95 - 2.83	1.9 - 1.4	Bial <i>et al.</i> (2017); Cornell <i>et al.</i> (2012); Pettersson (2008)
<b>Vyfbeker Metamorphic Suite</b>						
Banks Vlei Gneiss	Equigranular grey gneiss	Peraluminous, volcanic arc source	1188 ±8 Ma (magmatic); 1041 ±15 Ma (metamorphic rim); 1215 ±24 Ma and 1214 ±26 Ma (inheritance)			Praekelt <i>et al.</i> (1986); Pettersson (2008)

Abbreviations: f.g = fine grained; m.g. = medium grained; c.g. = coarse grained; mod. = moderate

## 2.1.4 Kaaien Domain and Kheis Subprovince

The Kaaien Domain (Figure 2.1) and the Kheis Subprovince further to the west represent a thrust complex on the eastern margin of the Kaapvaal Craton. They comprise a complex foreland basin to the eastern Namaqua Sector (Cornell *et al.*, 2006). The Kaaien Domain largely consists of metasedimentary successions of the Brulpan and Vaalkoppies Groups (deposition occurring between 1800 Ma and 1300 Ma; Moen and Armstrong, 2008; Figure 2.5). The ~1290 Ma meta-volcanics of the Wilgenhoutsdrif Group (Moen and Armstrong, 2008; Bailie *et al.*, 2011; Figure 2.5) lies as a thick succession of tholeiitic metabasalts, meta-rhyolites and minor metasediments between the Vaalkoppies and Brulpan Groups. These are

unconformably overlain by the low-grade metamorphic succession of bimodal metavolcanics of the Koras Group (Bailie *et al.*, 2012; Figure 2.5). The Koras Group has been dated by Gutzmer *et al.* (2000) and Pettersson *et al.*, (2007) which indicates that the succession can be divided into a lower (~1170 Ma) succession and upper (~1100 Ma) succession.

The Trooilapspan Shear (Figure 2.1 and Figure 2.5) tectonically separates the greenschist-facies Kaaie Domain from the amphibolite grade Areachap Domain (Cornell *et al.*, 2006; Cornell and Pettersson, 2007). The Brakbosch-Blauwbospan Faults (Figure 2.1 and Figure 2.5) form the tectonic boundary between the Kaaie Domain with the Kheis Subprovince

## 2.2 Tectono-metamorphic history

Throughout the Namaqua sector of the NNMP, four main deformation events are recognised that accompany regional metamorphism (Joubert, 1986; Macey *et al.*, 2015,2017). In the western Namaqua Sector, the Vioolsdrif Domain of the Richtersveld Magmatic Arc was subjected to greenschist-facies metamorphism ( $M_1$ ) related to the ~1.9 Ga  $D_1$  Orange River Orogeny. This  $D_1$  created large scale, SW-trending isoclinal folds of  $S_0$  bedding with associated NW-dipping axial planar foliation and lineations (Blignault, 1977; Macey *et al.*, 2017).

The ~1200 Ma - ~1000 Ma Namaqua Orogeny ( $D_2$ - $D_3$ ) produced intense ductile deformation and amphibolite-facies metamorphism in the Pella and Areachap Domains, with amphibolite- to granulite-facies metamorphism within the Kakamas Domain and Bushmanland Subprovince. This polyphase, poly-metamorphic evolution led to the juxtaposition of the various Namaqua tectonic domains (Bachmann *et al.*, 2015; Bial *et al.*, 2016; Macey *et al.*, 2015; 2017).

The main  $D_2$  event occurred over a protracted period between ~1200 and ~1150 Ma (Miller, 2008; Pettersson, 2008; Bial *et al.*, 2015b, 2016). The timing, duration and number of sub-phases of this significant tectono-magmatic evolution have been contentious with arguments based mainly on evidence from zircon U-Pb ages (Clifford *et al.*, 1995, 2004, 2012; Macey *et al.*, 2018). Recent studies in the Kakamas Domain (Macey *et al.*, 2015) and the Bushmanland Domain (Macey *et al.*, 2018) have since subdivided the  $D_2$  Namaqua Orogeny into three distinct events ( $D_{2a}$ ,  $D_{2b}$  and  $D_{2c}$ ). This pervasive and poly-phase  $D_2$  deformational event in the Namaqua sector resulted in large scale isoclinal ( $F_2$ ) folding and thrusting. This developed an intense and regional penetrative, E-W striking, with moderate- to shallow-dipping  $S_2$ , gneissosity with a NE-plunging stretching lineation ( $L_2$ ) across the Kakamas, Areachap and Pella Domains as well as the Bushmanland Subprovince (e.g.; Praekelt, 1984; De Beer *et al.*, 2002; Macey *et al.*, 2015, 2018).

The main ~1.2 Ga tectono-magmatic event ( $D_{2a}$ ) is present in all the major tectonic domains apart from the relatively undeformed Vioolsdrif Domain of the RMA (Macey *et al.*, 2017). Within the BSP, LFROTZ, Kakamas and Areachap Domains, this ~1.2 Ga event was synchronous with voluminous magmatism and associated coeval metamorphic zircon growth (Pettersson *et al.*, 2008a; Bial *et al.*, 2015a; Macey *et al.*, 2015) under low-P, high-T metamorphic conditions).

Detrital zircon studies (e.g. Raith *et al.*, 2003; Fransson, 2008; Cornell *et al.*, 2009; Macey *et al.*, 2015) within supracrustals of the BSP and Kakamas Domain indicate a period of deposition with a minimum age of around ~1160 Ma. This provides evidence for a period of uplift, erosion and sedimentation within an extensional tectonic regime ( $D_{2b}$ ). The ~1170 Ma depositional age for the Koras Group (Evans *et al.*, 2007; Moen *et al.*, 2008) further records this depositional event along the eastern margin of the NS with the Kaapvaal Craton (Macey *et al.*, 2018)

Following  $D_{2b}$ , a second phase of ductile deformation ( $D_{2c}$ ) is considered to reflect a major thrusting and “shuffling” of the crust that resulted in the current SE-vergent thrust stack of the various domains in the Namaqua Sector (Macey *et al.*, 2015). Geochronological studies in the BSP (Macey *et al.*, 2018) and the Kakamas and Areachap Domains (Colliston *et al.*, 2015; Macey *et al.*, 2015; Bailie *et al.*, 2017) concluded that the termination of this event at around ~1105 Ma.

$D_3$  deformation within the NNMP created mega-scale  $F_3$  folds that re-orientated  $D_2$  structures into km scale open dome and basin structures with locally-developed  $S_3$  fabric (Macey *et al.*, 2018). The  $D_3$  deformation event is associated with the development of steep structures that host the ~1030 Ma Cu-bearing noritoids in the BSP (Gibson *et al.*, 1996; Clifford *et al.*, 2004). Geochronological studies on late- to post-tectonic granites of the Spektakel Suite (Macey *et al.*, 2018) and Keimoes Suite (Bailie *et al.*, 2017) have also proposed that the  $D_3$  deformation event is associated with tectono-magmatic events in the period ~1100 -1085 Ma in the Kakamas and Areachap Domains and ~1097 – 1033 Ma in the Bushmanland Subprovince (Macey *et al.*, 2018).

Large-scale, north-west trending, sub-vertical transcurrent shear zones with dextral movement cross-cut and re-orientate rocks and fabrics of Namaqua Sector (Macey *et al.*, 2015). This late ( $D_4$ ) event also involved re-activation and dextral strike-slip faulting along existing major regional shear zones and faults (i.e. Boven-Rugzeer Shear Zone, Trooilapspan Shear Zone, Hartebees River Thrust, etc.). Many of the major  $D_2$  structures show evidence of reactivation and retrograde greenschist-facies metamorphism during  $D_4$  with vertical and lateral movement (van Bever Donker, 1991). The largest of these, is the ~1,0 Ga Marshal Rocks-Pofadder Shear Zone (MRPSZ, Figure 2.1 and Figure 2.3; Macey *et al.*, 2015; Melosh *et al.*, 2018) cross-cuts and reworks lithologies within the Richtersveld Magmatic Arc.

Metamorphic studies in the Richtersveld Magmatic Arc have only been undertaken on units present within the Pella Domain where  $D_2$  deformation has strongly attenuated and reworked RMA lithologies into

gneisses. Peak metamorphic conditions took place under amphibolite facies conditions during D<sub>2</sub> thrusting and reached ~600 °C and 5-6 kbar (Macey *et al.*, 2017).

The Bushmanland Subprovince experienced the highest grade (M<sub>3</sub>) metamorphism at ~1030 Ma (Robb *et al.*, 1999; Eglinton and Armstrong, 2003; Bailie *et al.*, 2007b, 2007a; Cornell *et al.*, 2009). This high-grade metamorphism is characterised by a symmetrical zonation of metamorphic grade, defined by EW isograds. These isograds define a northern and southern amphibolite facies zone with metamorphic conditions reaching ~650°C and five kbar with an anticlockwise P-T path for the northern amphibolite facies zone near Aggeneys (Diener, 2014). These amphibolite facies zones bound a major low-P, High-T granulite facies metamorphism belt with peak conditions in the Garries and Kliprand area reaching ~750-870°C and 4.5-6 kbars, characterised by anti-clockwise P-T paths (Waters, 1986, 1989; Raith *et al.*, 1998).

The peak metamorphic conditions within the western Kakamas Domain close to Onseepkans reached 800 – 900 °C at ~5.0 kbar (Bial *et al.*, 2015b), synchronous with the onset of D<sub>2</sub> magmatism at around ~1200 Ma. Further north in the Aus region, Diener *et al.* (2013) calculated peak P-T conditions for high-T, low-P metamorphism to reach 825 °C at 5.5 kbar and having a clockwise P-T path. This metamorphic event occurred at ~1060 Ma, apparently much later than that further to the south. However, the latest metamorphic studies on Korannaland metasediments around the Keimoes area reveal that granulite-facies metapelites show evidence for polymetamorphism at ~1200 Ma and ~1090 Ma, with amphibolite facies andalusite-staurolite schist that underwent amphibolite-facies metamorphism at ~1035 Ma (Buick, pers. comm). Peak metamorphism within the Areachap Domain was determined by Cornell *et al.* (1992) to be around 730 °C at 4.1 kbar with a clockwise P-T path.

The recent studies (Bial *et al.*, 2015a,b; Bailie *et al.*, 2017; Macey *et al.*, 2018) highlight the fact that the domains of the Namaqua Sector have experienced poly-phase, low-P; high-T tectono-magmatic events at ~1.2 and between ~1,1 and 1.0 Ga. The low pressures experienced within the Namaqua Sector are incompatible with the previous collision orogenic tectonic models proposed in the past (e.g. Hartnady *et al.*, 1985; Cornell *et al.*, 2006) suggests that the Namaqua crust developed in response to long-lasting steady heat transfer from the mantle into thinned lithosphere in a continental back-arc mobile belt setting (Bial *et al.*, 2015a, 2015b). Furthermore, recent studies on magmatic rocks in the eastern Kakamas and Areachap Domains (e.g. Keimoes Suite; Bailie *et al.*, 2017) and Bushmanland Subprovince (Spektakel Suite; Macey *et al.*, 2018) have confirmed the continental back-arc model for at least the D<sub>2</sub>-D<sub>3</sub> events.



## 2.3 The Geology of the Orange River Pegmatite Belt

The pegmatites in the Namaqua Sector of the Namaqua-Natal Metamorphic Belt intrude as a roughly E-W trending ~400km long, belt along the Orange River (Figure 1.1). The belt extends from Vioolsdrif and Steinkopf in the western parts of the Namaqua-Natal Metamorphic Province, eastwards through the Karas region of southern Namibia towards the areas around Riemvasmaak and Kakamas in South Africa. Here the belt begins to curve to the SE towards Kenhardt and Putsonderwater. The pegmatite belt has been referred to as the Orange River Pegmatite Belt (ORPB) or the Bleskop Suite (Gevers, 1936; Hugo, 1969; Schutte, 1972; Blignault, 1977; Cilliers, 1989; Cornell *et al.*, 2006; Minnaar and Theart, 2006; Pettersson *et al.*, 2007; Lambert, 2013), the former term used in this study.

The ORPB cuts across numerous tectonic domains within the Namaqua-Sector of the NNMP that have a highly variable poly-metamorphic and tectono-magmatic history, from greenschist- to amphibolite-facies in the Richtersveld Magmatic Arc, and amphibolite- to granulite-facies in the LFROTZ and Kakamas Domains (see chapter 2.1 and 2.2 above). Pegmatites are absent from the higher metamorphic grade zones of the Bushmanland Subprovince (BSP), while there are a small number of pegmatite intrusions along the Groothoek Thrust within the amphibolite-facies zones of the BSP.



Figure 2.6: A field photograph illustrating the typical outcrop of the pegmatites (light brown to tan coloured) intruding as a swarm into the Namaqua Natal Metamorphic Province country rocks (dark brown). (photograph source: Macey *et al.*, 2015).

The abundant pegmatites occur as swarms (Figure 2.6 and Figure 2.7) or isolated bodies that exploit existing and newly-created anisotropies created during late-Namaqua shearing events (Lambert, 2013; Macey *et al.*, 2015) although some discordant bodies do occur. The sizes of individual bodies vary from a few tens of metres to ~5km in length, with shapes that can be elongated, rounded or irregular (Lambert, 2013; Macey *et al.*, 2015). The pegmatites vary drastically in composition and internal structure, ranging from simple, homogenous and unzoned quartz-feldspar-muscovite bearing assemblages to complexly zoned, heterogeneous bodies containing more exotic minerals (e.g. beryl, lepidolite, columbite-tantalite together with U- and REE-bearing minerals; Gevers, 1936; Hugo, 1969; Schutte, 1972; Minnaar and Theart, 2006; Lambert, 2013).



Figure 2.7: An elevated panoramic view of a pegmatite swarm (white, light brown to tan coloured) intruding as a swarm into the (dark brown) intruding the metamorphic units of the LFROTZ (dark brown) in the Onseepkans area.

The pegmatites are regionally zoned with respect to mineralogy and degree of trace-element enrichment, forming swarms of LCT rare-metal type pegmatites and a “sea” of simple-barren pegmatites within the country rock of the NNMP. LCT-type pegmatites occur as swarms along the gradational boundary between the Pella and Vioolsdrif Domains (Southern Namaqua Front), in the vicinity of the MRPSZ in close connection with the large granulite klippe (e.g. Tantalite Valley) and with a few isolated LCT pegmatites along the footwall between the LFROTZ and Kakamas Domain. A small percentage of the pegmatites of the ORPB are NYF in character and are more common in the Kakamas Domain in the Riemvasmaak and Kakamas areas. However, LCT pegmatites also occur in the areas around Putsonderwater and Kenhardt where pegmatites are associated with the Boven-Rugzeer Shear Zone. This regional zonation of pegmatites was observed by Hugo (1970) but he attributed the zoning to be host rock controlled.

The pegmatites have been used to date the timing of transcurrent shearing and deformation. Some pegmatitic bodies show variable degrees of deformation when near the major shears, thus indicating a prolonged emplacement during Late-Namaqua shearing episodes (Lambert, 2013). The geochronological studies on the pegmatites (Melcher and Graupner, 2009; Lambert, 2013; and this study) illustrate that the shearing event occurred over a protracted period from ~1060 Ma - ~950 Ma (Melcher *et al.*, 2008; Lambert, 2013; this study). The timing of pegmatite emplacement, coupled with the variability of deformation of the pegmatites within the shear zones, suggest that pegmatite intrusions occurred as multiple, progressive events, with D<sub>4</sub> structural features acting as magma traps for large scale, possible multiple, pulses of granitic magma through the Namaqua-Natal Metamorphic Province.

## 3 Methods

### 3.1 Sample preparation

Monazite concentrates were obtained from selected samples collected from pegmatites in the field (see Figure 4.1 for sample localities). Heavy mineral separation was undertaken at two different labs, the first batch was processed at the Council for Geoscience (CGS) heavy mineral separation lab, and the second was processed at the Central Analytical Facility (CAF, Stellenbosch University). Crushed samples were then milled (disk mill – CAF; two-roller mill – CGS) and sieved, and the  $\geq 450 \mu\text{m}$  fraction was collected. The retrieved heavy mineral fractions then underwent magnetic separation via a Franz magnetic separator before heavy liquid separation. Diiodomethane (density =  $3.32 \text{ g/cm}^3$ ) was used to undertake a density liquid separation on paramagnetic and non-magnetic fractions. Monazite grains were handpicked using a reflected light microscope and set in an epoxy mount. Polished grain mounts were imaged in backscatter electron (BSE) mode on either the Zeiss EVO MA15VP scanning electron microscope (SEM) or the Zeiss MERLIN SEM at the Central Analytical Facility (CAF) at the University of Stellenbosch. A summary of the SEM operational conditions is given in Table 3.1. The SEM imaging was undertaken prior to measurement of U-Pb or Sm-Nd isotope compositions to better characterise the internal compositional zoning and zones of alteration that was present in the monazite grains. Zones of alteration, identified by highly porous, locally cross-cutting domains in the monazite are interpreted to have formed by low-temperature fluid mediated recrystallisation (Seydoux-Guillaume *et al.*, 2012). These domains were systematically avoided during U-Pb and Sm-Nd isotope data collection, where possible.

Table 3.1 - Summary of operational conditions for backscatter electron imaging of the monazite samples. Undertaken at the Central Analytical Facilities (CAF) at Stellenbosch University

	Zeiss MERLIN SEM	Zeiss EVO MA15VP
Accelerating voltage	20 kV	20 kV
Working distance	9.5 mm	8.5 mm
Beam current	11.0 nA	10 nA

## 3.2 Isotopic and chemical characterisation

### 3.2.1 LA-Q-ICP-MS

Monazite samples in epoxy resin grain mounts were analysed in 3 sessions, with two at the ICP-MS facilities at CAF (University of Stellenbosch), and one at the Research School of Earth Sciences (RSES, The Australian National University (ANU), Canberra, Australia).

Monazite U-Pb geochronology and the determination of major and trace element concentrations of nine samples were undertaken at the Research School of Earth Sciences (RSES, The Australian National University [ANU] Canberra, Australia) using an Excimer 193 nm laser with a Helix dual volume sample cell coupled to an Argilent 7700 quadrupole laser ablation-inductively coupled plasma-mass spectrometer (LA-Q-ICP-MS). Samples were ablated using a 16  $\mu\text{m}$  laser spot size, at a repetition rate of 5 Hz, a laser power of 50 mJ and a fluence of 4 J/cm<sup>2</sup>. Background blanks were measured for 20 seconds, followed by a 30-second ablation of the unknowns. Helium carrier gas was used in the ablations, and the resulting aerosol was mixed with Ar prior to introduction into the ICP-MS via a signal-smoothing manifold (“squid”). The isotopes measured were <sup>29</sup>Si, <sup>31</sup>P, <sup>43</sup>Ca, <sup>88</sup>Sr, <sup>89</sup>Y, <sup>139</sup>La, <sup>140</sup>Ce, <sup>141</sup>Pr, <sup>146</sup>Nd, <sup>147</sup>Sm, <sup>153</sup>Eu, <sup>157</sup>Gd, <sup>159</sup>Tb, <sup>163</sup>Dy, <sup>165</sup>Ho, <sup>166</sup>Er, <sup>169</sup>Tm, <sup>172</sup>Yb, <sup>175</sup>Lu, <sup>206</sup>Pb, <sup>207</sup>Pb, <sup>208</sup>Pb, <sup>232</sup>Th, <sup>238</sup>U, with a dwell time of 100 ms for <sup>207</sup>Pb, <sup>208</sup>Pb, <sup>232</sup>Th and <sup>238</sup>U and 10 ms for all other isotopes. <sup>235</sup>U was calculated from <sup>238</sup>U counts via the natural abundance ratio  $^{235}\text{U}/^{238}\text{U} = 137.88$  (Jackson *et al.*, 2004). No correction was made for common Pb.

An additional 12 samples were analysed in two sessions for U-Pb geochronology and trace element concentrations at the ICP-MS facilities at the Central Analytical Facility (CAF) at the University of Stellenbosch. Apart from differences in analytical instruments used, the procedure for U-Pb isotope analysis via LA-Q-ICP-MS was similar, but slightly modified to that mentioned above. A Resonetics Resolution S155 Excimer (193nm) laser with an S155 Laurin Technic dual-volume sample cell was coupled to an Argilent 8800 triple quadrupole ICP-MS. Ablation pits were 12 – 15  $\mu\text{m}$  in diameter, undertaken at 5 Hz, with a laser power of 40 mJ and a fluence of 1.9 J/cm<sup>3</sup>. Background blank was measured for 20 s followed by a 20 s ablation.

USGS 44069 monazite (Aleinikoff *et al.*, 2006) was used as the primary calibration reference material at both CAF and ANU. Itambé (Gonçalves *et al.*, 2016), Managotry (Horstwood *et al.*, 2003) and/or Thompson Mine (Williams *et al.*, 2004) monazites were used as quality control standards. A summary of the results of the calibration and quality control standards for each analytical session are given in Table 3.2.

Table 3.2 - Summary of primary and secondary reference materials used in U-Pb isotopic characterisation (LA-Q-ICP-MS)

Analytical facility	Session	Standard	Standard age(measured during analytical session)		Reference age		
Central Analytical Facility - University of Stellenbosch	2016	Itembe	512.2 ± 3 Ma	Concordia age	506.4 ± 0.73 Ma <sup>b</sup> [ <sup>207</sup> Pb/ <sup>235</sup> U]	511.8 ± 0.52 Ma <sup>b</sup> [ <sup>206</sup> Pb/ <sup>238</sup> U]	
	2017	Itembe	513.1 ± 2.2 Ma	Concordia age	506.4 ± 0.73 Ma <sup>b</sup> [ <sup>207</sup> Pb/ <sup>235</sup> U]	511.8 ± 0.52 Ma <sup>b</sup> [ <sup>206</sup> Pb/ <sup>238</sup> U]	
		Thompson Mine	1766.6 ± 6.6 Ma	Concordia age	1766 Ma <sup>c</sup>		
			1722.9 ± 6.4 Ma	[ <sup>207</sup> Pb/ <sup>206</sup> Pb]			
Research School of Earth Sciences (RSES) - Australia National University	2016 a	USGS 44069	425.4 ± 2.1 Ma	Concordia age	424.9 ± 0.4 Ma <sup>a</sup>		
		Managotry	560.5 ± 3.3 Ma	Concordia age	555 ± 1 Ma <sup>d</sup>		
	2016 b	USGS 44069	426 ± 2.9 Ma	Concordia age	424.9 ± 0.4 Ma <sup>a</sup>		
		Managotry	560.3 ± 3.1 Ma	Concordia age	555 ± 1 Ma <sup>d</sup>		
	2016 c	USGS 44069	424.8 ± 2.6 Ma	Concordia age	424.9 ± 0.4 Ma <sup>a</sup>		
		Itembe	510.8 ± 3.5 Ma	Concordia age	506.4 ± 0.73 Ma <sup>b</sup> [ <sup>207</sup> Pb/ <sup>235</sup> U]	511.8 ± 0.52 Ma <sup>b</sup> [ <sup>206</sup> Pb/ <sup>238</sup> U]	

a.) Aleinikoff et al. (2006); b.) Gonçalves et al. (2016); c.) Williams et al. (1996); d.) Horstwood et al. (2003)

The standard bracketing procedure for samples analysed at ANU was the following: two analyses of 44069 reference monazite, 1-2 analyses of a quality control standard (Thompson Mine, Itembé and Managotry), one analysis of NIST 610 glass, eight analyses of unknowns, repeat. The bracketing procedure undertaken in the first session at CAF was two analyses of USGS 44069 reference monazite, two analyses of a quality control standard (Thompson mine, Itembé), one analysis of NIST 610 glass, ten unknowns, repeat. The second session at CAF the procedure was as follows, three analyses of USGS 44069 reference monazite, 2-4 analyses of a quality control standard, one analysis of NIST 610 glass, ten analyses of unknowns, repeat.

Data reduction was undertaken using the software package Glitter (Van Achterbergh *et al.*, 2001) in time-resolved mode. Final uncertainties on isotope ratios include a 1% uncertainty on the standard that was added in quadrature. Uncertainties on the spot isotope ratios and ages are given at the 1 $\sigma$  level. U-Pb isotope ratios were first reduced, and then the same time-resolved windows for the unknowns were used to reduce the monazite major and trace element data using NIST 610 as the external standard and assuming stoichiometric Ce (CeO<sub>2</sub> = 28.1 wt%) as the internal standard. U-Pb analyses were assessed statistically and plotted on Wetherill Concordia diagrams using the Isoplot Excel<sup>®</sup> plugin (Ludwig 2003). REE plots were normalised the chondritic values of (Sun *et al.*, 1989) and plotted in Grapher<sup>®</sup>. Depending on the degree concordancy of the U-Pb isotope data, dates were calculated either as upper intercepts, or concordia dates, using the relevant built-in Isoplot functions.

### 3.2.2 LA-MC-ICP-MS

The Sm-Nd isotope measurements were taken on a Thermo-Finnigan Neptune multi-collector-inductively coupled plasma-mass spectrometer (MC-ICP-MS) coupled with a 193 nm HellEx Photon-Machine laser ablation system at the Laboratório de Geoquímica Isotópica (LOPAG), Universidade Federal de Ouro Preto (UFOP) in Brazil. The Neptune MC-ICP-MS was operated in a static mode, using an 8 Hz repletion rate with an integration time of 0.524 seconds. Ablation pits had a diameter of 20  $\mu$ m, and the resulting aerosols were transported to the mass spectrometer using He carrier gas with N<sub>2</sub> gas mixed into the Ar sample carrier gas. The above procedure was undertaken to enhance the signal intensity and to reduce the

production of NdO<sup>+</sup> (Gonçalves *et al.*, 2016). A more in-depth description of experimental conditions and Faraday cup configurations are given in Table 3.3. An offline Excel® spreadsheet was used for data reduction and was supplied by Prof Axel Gerdes (Goethe University, Frankfurt). For a more thorough explanation of this procedure in the UFOP LOPAG, the reader may refer to Gonçalves *et al.* (2016 and 2018).

To simultaneously correct for instrument drift, mass bias and elemental fractionation the following approach was used, as is outlined below. All uncertainties are at the 2σ level and reported as 1SD for a given ratio. Following the procedure of Yang *et al.* (2008) and Fisher *et al.* (2011) the Sm isotopic values of 0.22332 for <sup>144</sup>Sm/<sup>149</sup>Sm (Isnard *et al.*, 2005) and 1.08680 for <sup>147</sup>Sm/<sup>149</sup>Nd (Dubois *et al.*, 1992) were used for the <sup>144</sup>Sm interference on <sup>144</sup>Nd instead of establishing instrument working values.

Table 3.3 Faraday cup configuration and instrument operating parameters for Nd isotopic analysis (Gonçalves *et al.*, 2016)

Faraday cup configuration									
Cups	L4	L3	L2	L1	Centre	H1	H2	H3	H4
Nominal mass	142	143	144	145	146	147	148	149	150
Measured elements	Nd	Nd	Nd	Nd	Nd	Sm	Nd	Sm	Nd
Natural abundance (%)	27.2	12.2	23.8	8.3	17.2	14.99	5.7	13.82	5.6
Interfering elements	Ce		Sm				Sm		Sm
Natural abundance (%)	11.11		3.07				11.24		7.38
Instrument parameters									
Thermo-finnigan Neptune	MC-ICP-MS				Photon Machine 193 nm HellFX Excimer				
Rf forward power	1200 W				Fluence	~4 J/cm <sup>2</sup>			
Cooling gas	15.5 L/min				Output power	~30 mJ			
Auxillary gas	0.85 L/min				Spot size	20 μm			
Sample gas	1.013 L/min				Pulse rate	8 Hz			
Mass resolution	400 (Low)				He gas cell	1.2 L/min			
Integration time	0.524 s								
Sensitivity on <sup>146</sup> Nd	15 V/ppm								
Acceleration Voltage	10 kV								

The exponential law of Russell *et al.* (1978) was used to correct for mass bias on Nd:

$$\frac{{}^{143}\text{Nd}}{{}^{144}\text{Nd}_{\text{corr}}} = \frac{{}^{143}\text{Nd}}{{}^{144}\text{Nd}_{\text{meas}}} \times \frac{M_{143}\beta_{\text{Nd}}}{M_{144}},$$

where <sup>143</sup>Nd/<sup>144</sup>Nd<sub>corr</sub> is the ratio for mass bias, <sup>143</sup>Nd/<sup>144</sup>Nd<sub>meas</sub> is the measured ratio corrected for the <sup>144</sup>Sm isobaric interference, M<sub>143</sub>/M<sub>144</sub> is the ratio of the exact atomic masses of the measured ratio, and β<sub>Nd</sub> is the mass bias correction factor:

$$\beta_{\text{Nd}} = \frac{\ln\left(\frac{{}^{146}\text{Nd}/{}^{144}\text{Nd}_{\text{ref}}}{{}^{146}\text{Nd}/{}^{144}\text{Nd}_{\text{meas}}}\right)}{\ln\left(\frac{M_{146}}{M_{144}}\right)},$$

where <sup>146</sup>Nd/<sup>144</sup>Nd<sub>ref</sub> is 0.7219 (Wasserburg *et al.*, 1981).

Steenkampskraal monazite reference material (Liu *et al.*, 2012a) was also used to correct for inter-element fractionation on the  $^{143}\text{Nd}/^{144}\text{Nd}$  ratio, instead of using the NIST 610 glass used in past studies. To accurately determine  $^{147}\text{Sm}/^{144}\text{Nd}$  ratio a similar approach to Foster and Vance (2006) and Fisher *et al.* (2011) was used, externally correcting the ratio of unknowns to the interference-corrected  $^{147}\text{Sm}/^{144}\text{Nd}$  of a bracketing calibration material, in this case, Steenkampskraal (Liu *et al.*, 2012).

$$\frac{^{147}\text{Sm}}{^{144}\text{Nd}_{\text{corr}}} = \frac{^{147}\text{Sm}}{^{144}\text{Nd}_{\text{meas}}} \times \frac{M_{147}}{M_{144}} \beta_{\text{Sm}/\beta_{\text{Nd}}}$$

where,

$$\beta_{\text{Sm}} = \frac{\ln\left(\frac{^{147}\text{Sm}/^{149}\text{Sm}_{\text{meas}}}{^{147}\text{Sm}/^{149}\text{Sm}_{\text{ref}}}\right)}{\ln\left(\frac{M_{147}}{M_{149}}\right)}$$

The influence of a matrix effect on  $^{147}\text{Sm}/^{144}\text{Nd}$  fractionations during LA-MC-ICP-MS analysis is controversial. Some studies have shown that a significant difference in fractionation of  $^{147}\text{Sm}/^{144}\text{Nd}$  between monazite and NIST glass in the same analytical session (Iizuka *et al.*, 2011). In contrast, a study by Fischer *et al.* (2011), observed no matrix effect on the Sm-Nd mass bias, implying that the use of a matrix matched reference material is not needed. Liu *et al.* (2012) did, however, observe differences in the  $^{147}\text{Sm}/^{144}\text{Nd}$  correction factors for monazite, LREE glass and apatite, illustrating a significant matrix effect when using NIST 610 glass. Gonçalves *et al.* (2016) assessed this using NIST 610 glass and Steenkampskraal (Namaqualand) monazite as an external reference material to analyse their Itambé monazite. This study showed that for the instrument conditions at UFOP, using NIST 610 or Steenkampskraal monazite as a reference material produced identical results within uncertainty for the analysed monazite unknowns.

Twenty-three Sm-Nd LA-MC-ICP-MS analyses of the Bannaneira monazite reference material (RM) obtained from the same analytical session as the pegmatites in this sample yielded an average  $\epsilon\text{Nd}_{507\text{ Ma}}$  of  $-3.0 \pm 0.51$  (1 SD), and 36 analyses of the Diamantina monazite RM yielded  $\epsilon\text{Nd}_{495\text{ Ma}}$  of  $-18.90 \pm 0.30$  (1 SD). These values are within error of the recommended values for these materials (Bannaneira: Gonçalves *et al.* (2016),  $-2.8 \pm 0.2$  (1 SD); Diamantine: Gonçalves *et al.* (2018),  $-18.70 \pm 0.5$  (1 SD)).

Epsilon Nd ( $\epsilon\text{Nd}_{(t)}$ ) values for monazite unknowns were calculated using the respective U-Pb (concordia or upper intercept) magmatic crystallisation dates that were calculated for each sample. Where inherited monazite xenocrysts were present in a sample, the  $^{207}\text{Pb}/^{206}\text{Pb}$  spot age was used for the respective monazite xenocryst. For all analysed samples the mean  $^{145}\text{Nd}/^{144}\text{Nd}$  values between  $0.34839 \pm 1$  (SD) and  $0.34841 \pm 1$  (SD) and all were in agreement with the canonical value of 0.348415 (Wasserburg *et al.*, 1981)

Two-stage model ages ( $T_{2DM}$ ) have been increasingly used for felsic igneous rocks (e.g. Liew and McCulloch, 1985). This method of calculating depleted model ages is used to correct for changes in the Sm/Nd ratios due to a possible second Sm-Nd fractionation in the course of intracrustal melting (Liew *et al.*, 1988). The calculation uses the measured  $^{147}\text{Sm}/^{144}\text{Nd}$  ratio taken back to the magmatic age of the sample with an assumed  $^{147}\text{Sm}/^{144}\text{Nd}$  ratio for calculating the sample evolution curve prior to the crystallisation age (Liew *et al.*, 1988; Champion, 2013). In this study, the assumed  $^{147}\text{Sm}/^{144}\text{Nd}$  ratio of 0.12 (Lieu and McCulloch, 1985) which is equivalent to the average upper continental crust was used to calculate 2-stage depleted mantle ( $T_{2DM}$ ) model ages using the calculation:

$$T_{2DM} = \left(\frac{1}{\lambda_{Sm}}\right) \ln \left\{ \frac{1 + [(^{143}\text{Nd}/^{144}\text{Nd})_{\text{sample}} - (^{143}\text{Nd}/^{144}\text{Nd})_{DM} - (e^{\lambda t}) [(^{147}\text{Sm}/^{144}\text{Nd})_{\text{sample}} - (^{147}\text{Sm}/^{144}\text{Nd})_{CC}]}{(^{147}\text{Sm}/^{144}\text{Nd})_{\text{sample}} - (^{147}\text{Sm}/^{144}\text{Nd})_{DM}} \right\}$$

Where  $(^{143}\text{Nd}/^{144}\text{Nd})_{DM} = 0.513151$ ;  $(^{147}\text{Sm}/^{144}\text{Nd})_{DM} = 0.219$ ;  $(^{147}\text{Sm}/^{144}\text{Nd})_{CC} = 0.12$  and  $\lambda_{Sm} = 6.54 \times 10^{-12}\text{y}^{-1}$  (Liew *et al.*, 1988)

Epsilon units ( $\epsilon_{Nd_t}$ ) were calculated using the appropriate magmatic age for the individual pegmatite samples for  $t$ , using the formula:

$$\epsilon_{Nd_t} = \left\{ \frac{(^{143}\text{Nd}/^{144}\text{Nd})_{\text{sample}}^t}{\left[ (^{143}\text{Nd}/^{144}\text{Nd})_{CHUR} - (^{147}\text{Sm}/^{144}\text{Nd})_{CHUR}^t \right] (e^{\lambda t})} \right\}$$

Where  $(^{143}\text{Nd}/^{144}\text{Nd})_{CHUR} = 0.51264$  and  $(^{147}\text{Sm}/^{144}\text{Nd})_{CHUR} = 0.1967$  (Jacobsen *et al.*, 1980)



## 4 Results

### 4.1 Monazite U-Pb geochronology

#### Overview

The pegmatites of the Orange River Pegmatite Belt were emplaced across the Namaqua Sector of the NNMP. They intrude into tectonic terranes of differing metamorphic grades and tectonic histories (Figure 4.1). One aim of the study was to determine the relative age of intrusion of the pegmatites within the Namaqua sector of the NNMP. This section serves as a brief overview discussion on the monazite U-Pb isotope geochemistry results and some observations on the monazite from the sampled pegmatites with respect to monazite composition, internal zoning in BSE imaging.

Monazite grain composition (as shown by BSE images) and texture varied from homogenous (both texturally and compositionally) to highly variable. For monazite that was compositionally zoned, the zoning varied from oscillatory zoning to polygonal sector zoning with varying degrees of complexity (e.g. Figure 4.24a and Figure 4.27a). These zoning patterns are interpreted to reflect the crystallisation of magmatic or anatectic monazite (e.g. Buick *et al.*, 2008; Dumond *et al.*, 2015; Clemens *et al.*, 2017), and as a result, the dates obtained from the analysed monazites are interpreted to date pegmatite crystallisation.

The difference in monazite zoning patterns do not reflect any link to the tectonic domain or pegmatite classification. In addition to magmatic zonation, monazite grains locally show evidence of “spongy”, locally crosscutting porous zones or rims. These alteration zones, which are inferred to reflect low-T fluid mediated alteration (Seydoux-Guillaume *et al.*, 2012), affect the grains in different samples to considerably different extents. These alteration zones were avoided, as low-T fluid mediated dissolution and reprecipitation is known to affect the monazite U-Th-Pb isotope system (Harlov *et al.*, 2011; Seydoux-Guillaume *et al.*, 2012; Taylor *et al.*, 2014; Lo Pò *et al.*, 2016).

Monazite chondrite-normalised REE patterns from different samples show significant variation in the extent of MREE to HREE fractionation, with HREE depletion but relatively little variation in LREE to MREE fractionation. Most of the samples have small variations in HREE concentrations that result in near parallel REE profiles on the chondrite-normalised REE distribution diagrams. Moderate to significant variations in HREE and Y concentrations were observed in several samples. This fanning of the HREEs in the REE patterns is the result from preferential partitioning of the HREE and Y into cogenetic accessory phases, such (e.g. garnet, xenotime, columbite-tantalite and zircon) during monazite crystallisation (Zhu *et al.*, 1999a; Hermann *et al.*, 2003; Buick *et al.*, 2006; Rubatto *et al.*, 2006; Gregory *et al.*, 2009). Monazite from all samples

show negative Eu anomalies. However, the extent of the Eu anomalies varies from sample to sample, from moderate ( $\text{Eu}/\text{Eu}^* = 0.5$ ) to very large ( $\text{Eu}/\text{Eu}^* = 0.001$ ).

Table 4.1: Summary table for monazite U-Pb geochronology for pegmatite samples from the Orange River Pegmatite Belt., Includes descriptions of pegmatite mineralogy, structural placement and host rock.

Sample	Latitude	Longitude	Host Domain	Host Rock	Structural emplacement	Pegmatite Mineralogy	Pegmatite description	Magmatic age	Xenocrystal monazite age
SD2015-10	18.2539	-28.8103	Vioolsdrif	Tsams - ORG	Concordant to D <sub>1/2</sub>	Qtz, Fsp, Ms, Grt, Mz, Cb, Ap	Unzoned REE class	1010 ± 4.4 Ma	
SD2015-11	18.2637	-28.7936	Vioolsdrif	Ramansdrif	Concordant to D <sub>4</sub>	Qtz, Fsp, Ms, Grt, Ap	Simple and unzoned	1038 ± 6.5 Ma	
SDORPB15-09	18.2847	-28.9097	Vioolsdrif	Goodhouse Subsuite	Discordant	Qtz, Fsp, Be, Cb, Tlm, Grt, Ap	Zoned REE Class type	LCT- 1004 ± 6 Ma	
SDORPB15-4b	17.8304	-29.0018	Vioolsdrif	Goodhouse Subsuite	Concordant to D <sub>1/2</sub>	Qtz, Fsp, Sp, Li, Grt, Cb, Ms, Bt, Ap	Complexly zoned LCT-type	1004 ± 13 Ma	
SDORPB15-7D	17.9717	-28.9670	Vioolsdrif	Ramansdrif	Discordant	Qtz, Fsp, Tlm, Li, Sp, Cb, Al	Zoned type	LCT- 1007 ± 5 Ma	1085 ± 30 Ma; 1209 ± 28 Ma
SDORPB16-04	18.1438	-28.9735	Vioolsdrif	Goodhouse Subsuite	Concordant to D <sub>1/2</sub>	Qtz, Fsp, Tlm, Be, Grt, Li, Sp, Cb,	Complexly zoned LCT-type	993 ± 12 Ma	
SDORPB16-05	18.0486	-28.9620	Vioolsdrif	Goodhouse Subsuite	Concordant to D <sub>1/2</sub>	Fsp, Qtz, Sp, Li, Grt, Cb-Ta	Complexly zoned LCT-type	1020 ± 11 Ma	
RPGV14	16.7093	-27.6456	Pella	Goodhouse Subsuite	Concordant to D <sub>2</sub> /D <sub>4</sub>	Fsp, Qtz, Ms, Bt	Simple and unzoned	973 ± 4 Ma	
RPGV16	16.7162	-27.6140	Pella	Goodhouse Subsuite	Concordant to D <sub>2</sub> /D <sub>4</sub>	Fsp, Qtz, Ms, Bt	Simple and unzoned	991.6 ± 6 Ma	1107 ± 14 Ma
SD2015-13	18.7599	-28.7211	Pella	Umeis	Concordant to D <sub>4</sub>	Qtz, Fsp, Ms, Bt, Grt, Ap.	Simple and unzoned	1005 ± 8 Ma	
SDORPB15-10	18.5134	-28.9363	Pella	Goodhouse Subsuite	Concordant to D <sub>2</sub>	Fsp, Qtz, Ms, Bt, Grt, Ap	Simple and unzoned	1016 ± 6 Ma	
HS15HF1	19.2610	-28.6859	LFROTZ	Veloorsdrif metapelitic gneiss	Discordant to D <sub>2</sub>	Fsp, Qtz, Ms, Grt, Mz, Ap	Simple and unzoned	966 ± 3 Ma	
SDORPB15-15c	19.5555	-28.7586	LFROTZ	Skuitklip	Concordant to D <sub>2</sub> /D <sub>4</sub>	Fsp, Qtz, Bt, Grt	Simple, zoned	976 ± 6 Ma	
SDORPB16-06	19.5485	-28.9652	LFROTZ	Oupvlakte	Discordant	Fsp, Ms, Qtz, Grt, Cb, Ta, Be	Zoned LCT-type	986 ± 4 Ma	1123 ± 9 Ma
SDORPB16-7B	19.4698	-28.7640	LFROTZ	Beenbreek	Concordant to D <sub>2</sub> /D <sub>4</sub>	Fsp, Qtz, Ms, Grt, Bt, Cb, Be	Zoned LCT-type	994 ± 3 Ma	
SDORPB15-17	20.0725	-28.4601	Kakamas	Twakputs	Concordant to D <sub>2</sub>	Fsp, Qtz, Ms, Grt	Zoned muscovite REE class	984 ± 4.2 Ma	
SDORPB15-18	20.2958	-28.4293	Kakamas	Donkieboud	Concordant to D <sub>2</sub>	Fsp, Qtz, Ms	Simple and unzoned	1015 ± 7 Ma	
SDORPB15-20	20.6005	-28.7880	Kakamas	Riemvasmaak	Concordant to D <sub>2/4</sub>	Fsp, Qtz, Be, Grt	Simple REE-class	990 ± 5 Ma	
SDORPB16-8	19.8711	-28.5312	Kakamas	Witwater/Narries contact	Discordant	Fsp, Qtz, Grt, Ms	Simple, zoned	994 ± 4 Ma	1219 ± 25 Ma
SDORPB16-9	20.2053	-28.4560	Kakamas	Narries/Donkieboud	Concordant to D <sub>2</sub>	Fsp, Qtz, Ms, Bt, Cb	Simple and unzoned; LCT-type	1019 ± 4 Ma	1212 ± 22 Ma
SDORPB16-12	21.6680	-29.4434	Kakamas	Jacomynspan Grp	Concordant to D <sub>2</sub>	Fsp, Qtz, Grt, Ta	Zoned LCT-type	993 ± 5 Ma	1092 ± 7 Ma, 1145 ± 4 Ma, 1199 ± 13 Ma

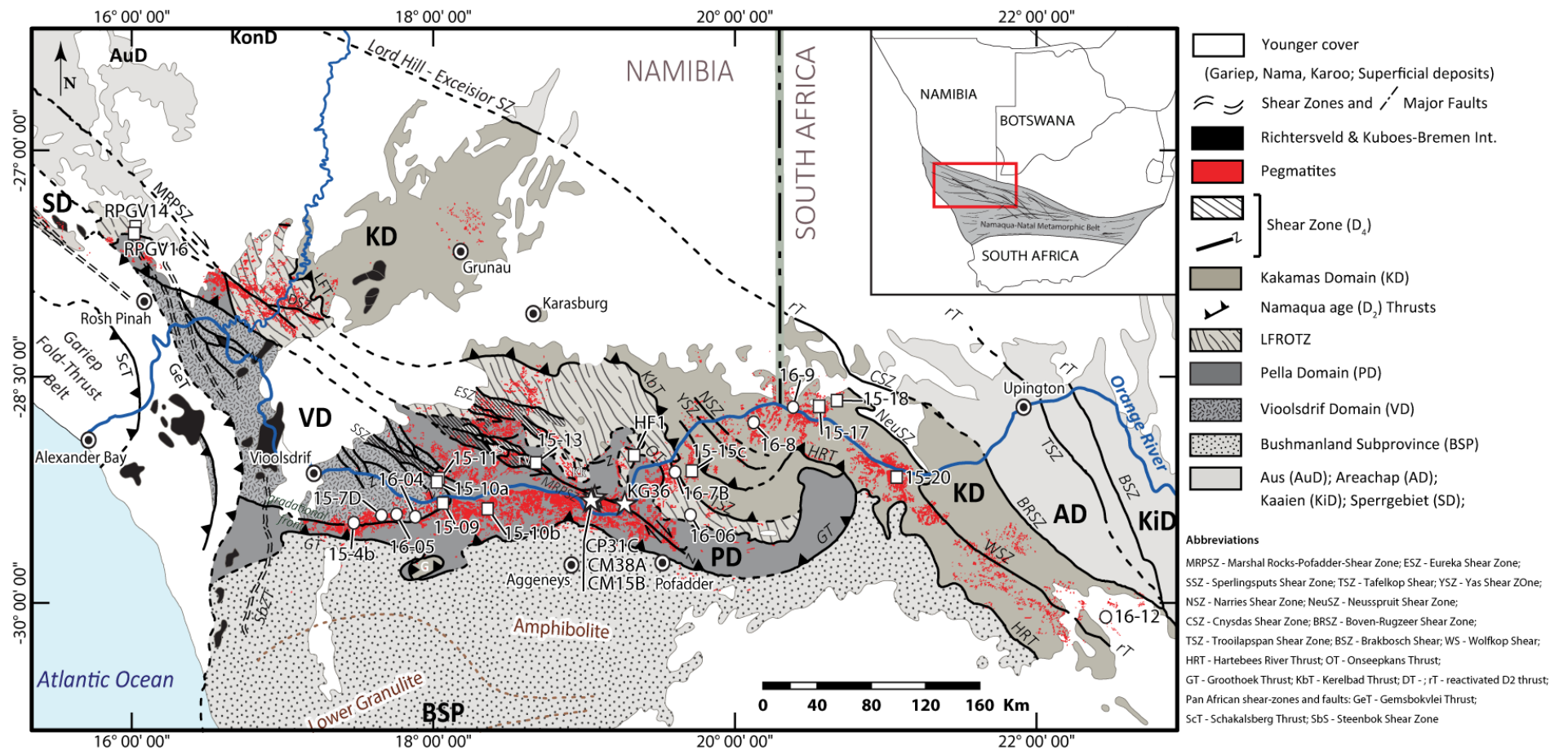


Figure 4.1: Simplified geological map of the Namaqua-Natal metamorphic belt and the distribution of the Orange River Pegmatite Belt. Individual sample localities are indicated on the map. Squares indicates monazite samples analysed for both U-Pb and Sm-Nd analysed samples; circles indicate monazite U-Pb only samples. An additional four samples (stars) were analysed for Sm-Nd isotopes only and were previously dated by Lambert (2013), (Map compiled from Hugo, 1970; Schutte, 1972; Lambert, 2013; Macey et al. 2015, 2018).

Concordia dates were calculated for the majority of samples in the sample set. Monazite from a subset of samples, defined linear discordant arrays for which upper intercept dates could be calculated that were in agreement with the date of a smaller number of concordant analyses. In some samples, xenocrystic monazite, with deviation in monazite geochemistry, grain morphology (as distinct different grains in the overall population or as inherited cores) with apparent spot dates between ~1200 and ~1090 Ma was present. The significance of these will be addressed in the following discussion chapter. The results from the U-Pb isotopic analyses in this study show that the pegmatites intruded into the Namaqua sector of the NNMP during an extended period of ~80 m.yr. from ~1038 Ma to ~958 Ma (Table 4.1). The new monazite U-Pb crystallisation ages came from pegmatites from across the majority of the belt and from the different tectonic domains.

## 4.1.1 Richtersveld Magmatic Arc

### 4.1.1.1. Vioolsdrif Domain

#### *SD2015-10*

This sample is from an 8m wide pegmatite (Figure 4.2) that intruded the meta-volcanics of the ~1885 Ma Orange River Group (ORG) near the contact between the ~1850 Ma Gaarseep granodiorite of the Vioolsdrif Suite and the Tsams meta-volcanic units. This sample was collected from a K-feldspar rich zone. It contains minor quartz with garnet, monazite, zircon, apatite and columbite as accessory minerals. Monazite is scarce in this sample, and only six usable grains were obtained. These grains vary in size from 100  $\mu\text{m}$  to 200  $\mu\text{m}$  in diameter with one subhedral grain being much bigger at ~360 $\mu\text{m}$  in diameter (Figure 4.4a). The grains were relatively homogenous BSE images, showing little internal magmatic zoning. The smaller grains show small patches of porous alteration and embayed grain boundaries (Figure 4.3).

Compositionally, the monazites can be grouped into three populations based on Ca and Y versus Pb, Th and U concentrations. 1) A low Ca (1015 ppm - 1181 ppm), high Y (10 384 - 14 822 ppm) monazite population with low Pb (1 951 - 2 247 ppm), moderate to low Th (20 605 - 24 212 ppm) and low U concentration from 596 ppm to 995 ppm (Appendix A.1.1.). 2). The high Ca (2 907 - 7 560 ppm); low Y (143 to 2 376 ppm) populations with elevated Pb (5 408 - 7 539 ppm), high Th (44 278 - 65 056 ppm) and higher U (2 078 - 3 392 ppm) concentrations (Appendix A.1.1.). 3) A third population with moderate Y (5 344 - 10 851 ppm) concentration, slightly elevated Ca (2 515 - 3 738 ppm) concentrations. These grains have variable Pb, Th and U concentrations from 3 289 to 7 762 ppm; 34 162 - 62 026 ppm and 991 - 4 868 ppm respectively (see Appendix A.1.1.).

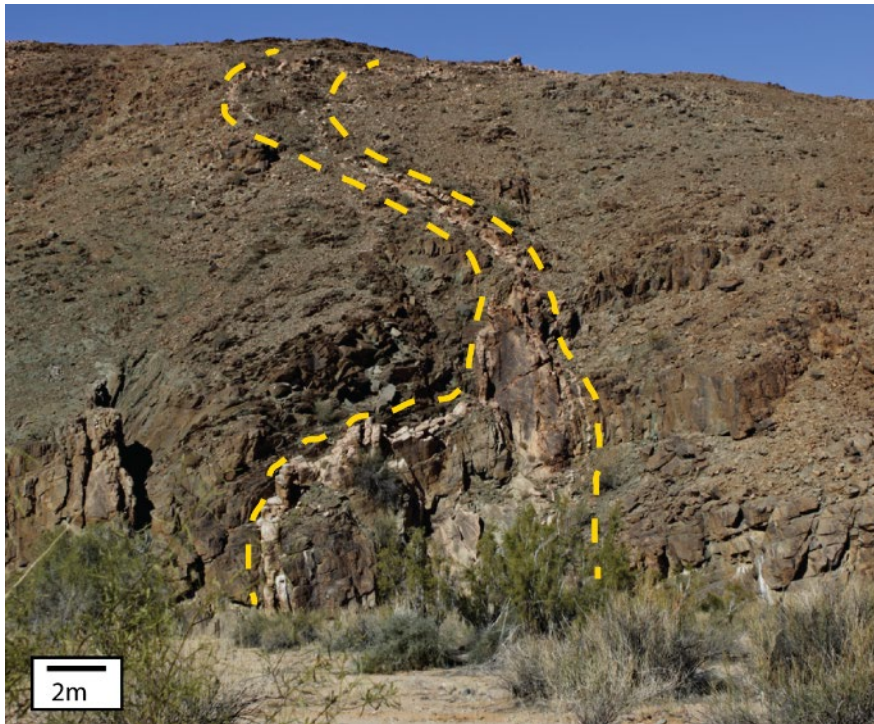


Figure 4.2: Field photograph of the 8m wide simple unzoned pegmatite (SD2015-10) that has intruded into ORG volcanics.

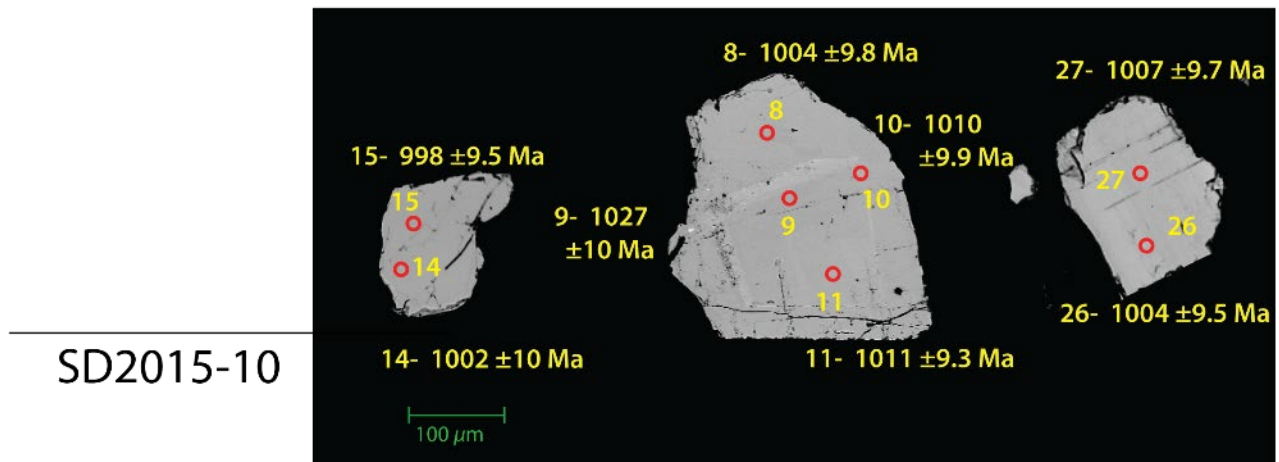


Figure 4.3: Representative SEM BSE images of analysed monazite from pegmatite sample SD2015-10. Red circles indicate positions of laser pits with a width of 15 $\mu$ m – 16  $\mu$ m (see text) in diameter. Spot dates indicated are  $^{206}\text{Pb}/^{238}\text{U}$  dates with uncertainties on the spot ages given at the 1 $\sigma$  level.

Monazite from this sample have chondrite-normalised REE patterns (Figure 4.4a) characterised by flat LREE-MREE profiles, ( $[\text{La}/\text{Sm}]_{\text{N}} = 0.7$  to 1.9; Appendix B.1.1), large negative Eu anomalies ( $\text{Eu}/\text{Eu}^* = 0.001 - 0.006$ ; Figure 4.4a, Appendix B.1.1) and steep but variable relative enrichment in the MREE over the HREE ( $[\text{Gd}/\text{Lu}]_{\text{N}} = 442$  to 26 315; Appendix B.1.1).

Despite the variability in monazite composition, a total of 13 out of 15 analyses defined a statistically homogenous population. The two excluded spot analyses were 93% to 95% concordant with older  $^{207}\text{Pb}/^{206}\text{Pb}$  spot dates from  $1072 \pm 24$  (1 $\sigma$ ) Ma to  $1068 \pm 28$  (1 $\sigma$ ) Ma (Appendix C.1.1) that is interpreted to

be a minor inherited monazite component. The U-Pb isotope data for the remaining thirteen analyses are concordant (98.3% to 101.5%) and yielded a small range in apparent  $^{207}\text{Pb}/^{206}\text{Pb}$  spot dates from  $1025 \pm 25(2\sigma)$  Ma to  $1004 \pm 24(2\sigma)$  Ma (Appendix C.1.1.). All 13 analyses could be combined to yield a concordia date of  $1009.7 \pm 4.4$  Ma ( $2\sigma$ , MSWD of concordance and equivalence (C+E) = 0.41; Figure 4.4b), which is interpreted as the monazite crystallisation age of this pegmatite.

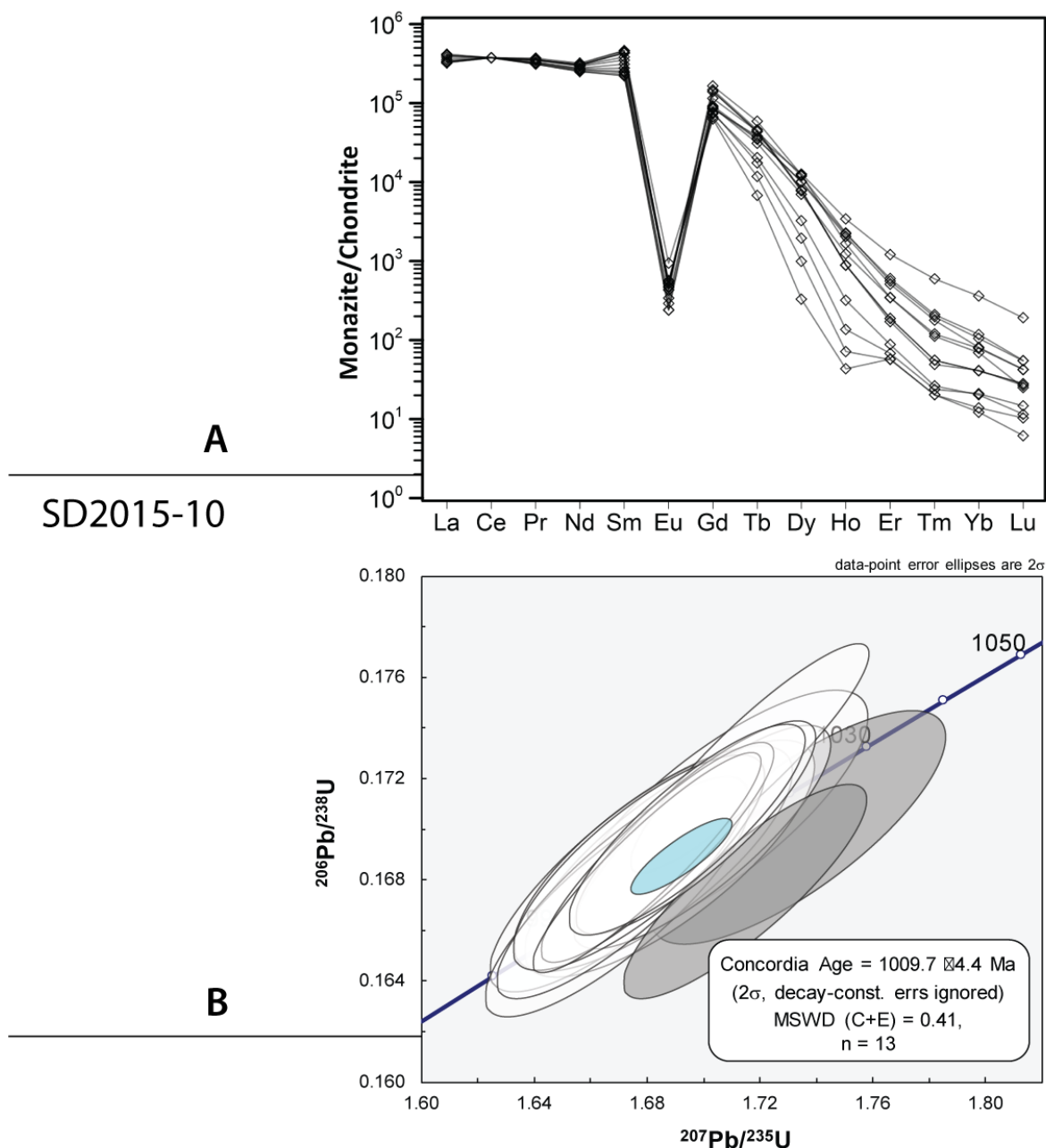


Figure 4.4 A) Chondrite-normalised REE diagram for sample SD2015-10. Normalised to values from Sun and McDonough (1989). B). Wetherill concordia diagram for monazite LA-Q-ICP-MS isotope data for pegmatite sample SD2015-10, errors are shown as  $2\sigma$  ellipses, excluded analyses are marked as grey ellipses.

## SD2015-11

Monazite from sample SD2015-11 is from a large unzoned barren pegmatite that intruded into the ~1880 Ma Ramansdrif alkali feldspar granite concordantly within the Sperlingsputs shear zone (Figure 4.5). The sample was from a fine-grained zone within the larger pegmatite body, consisting chiefly of K-feldspar with low proportions of muscovite and quartz. The accessory minerals present are monazite, zircon, garnet, columbite and apatite. The monazite extracted from this sample consists of predominantly small (55  $\mu\text{m}$  to 110  $\mu\text{m}$ ) anhedral fragments that commonly display embayed grain boundaries and rare altered cores. Internal zoning is present as fine-scale to broad sector zoning in some subhedral grains, with one grain having fine-scale polygonal sector zoning (Figure 4.6a).

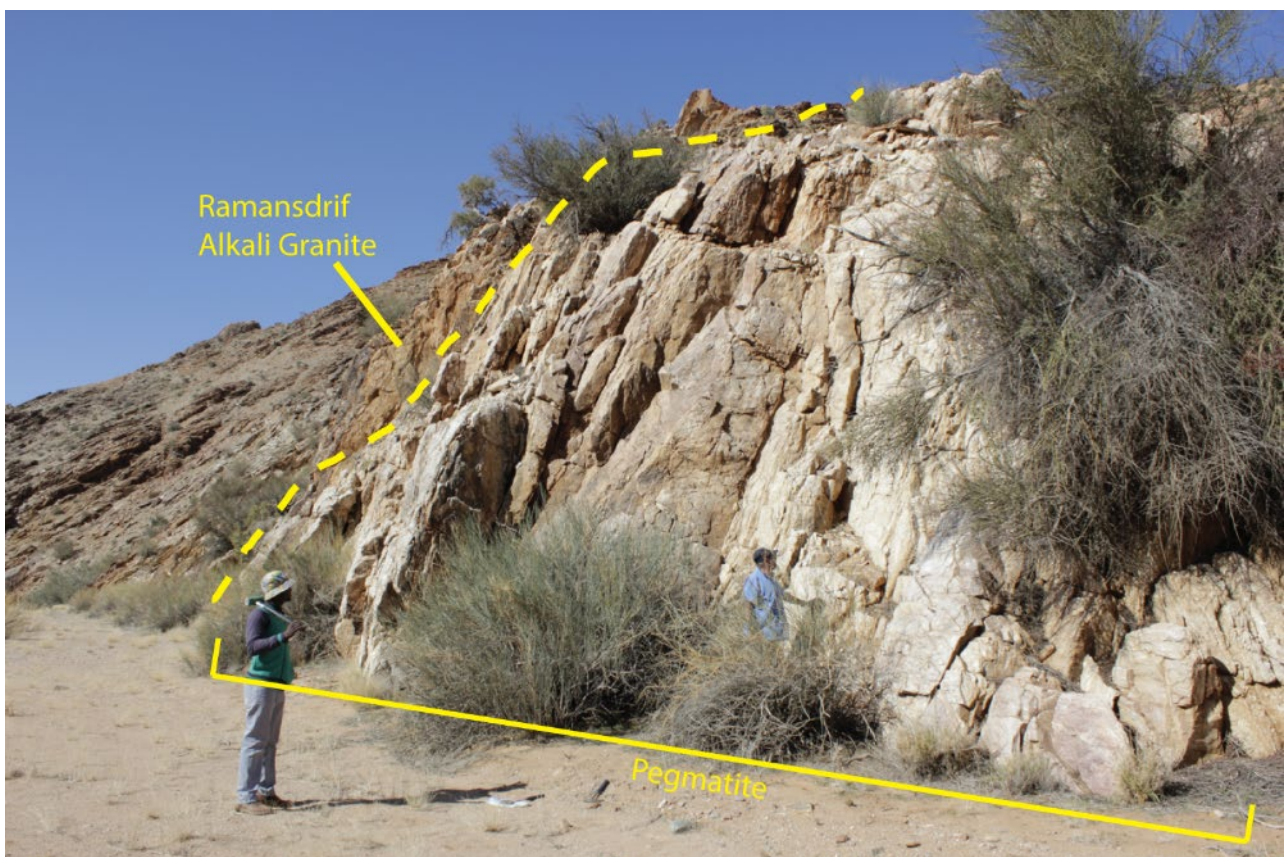


Figure 4.5: Field photograph of the sampled homogenous, unzoned pegmatite (SD2-15-11) that has intruded into Ramansdrif alkali granite.

Compositionally, the monazite from this sample is mostly homogenous with little variation in Y (13 042 – 15 382 ppm) and moderate variations in Ca (3 626 – 8 829 ppm) concentrations (Appendix A.1.2.). There is a small range in low U and high Th concentration (736 to 1319 ppm and 38 712 – 72 876 ppm, respectively). Th/U ratios vary between 50.2 and 73.9 (Appendix A.1.2). Chondrite-normalised REE (Figure 4.6b) show that monazite from this sample is characterised by flat LREE-MREE profiles with  $(\text{La}/\text{Sm})_N$  from 2.4 to 4

(Appendix B.1.2), a moderate negative Eu anomaly (mean  $\text{Eu}/\text{Eu}^* = 0.015$ , Appendix B.1.2; Figure 4.6b) and a relatively modest depletion of the HREE with respect to the MREE ( $[\text{Gd}/\text{Lu}]_N = 20$  to 40; Appendix B.1.2). Fifteen U-Pb analyses were taken from 7 grains. Five analyses were excluded due to not having  $^{207}\text{Pb}/^{206}\text{Pb}$  plateaus in the time-resolved signal. The lack of a  $^{207}\text{Pb}/^{206}\text{Pb}$  plateau may be due to the effects of fluid-mediated dissolution and precipitation (as seen in the porous zones in the BSE images, Figure 4.6a) resetting the U-Th-Pb isotope system. The remaining ten analyses are concordant (97 – 102% concordant; Appendix A.1.2) yielding a narrow range in apparent  $^{207}\text{Pb}/^{206}\text{Pb}$  spot dates ( $1018 \pm 24$  –  $1056 \pm 24$  Ma; uncertainties at  $1\sigma$ , Appendix A.1.2). All ten analyses could be statistically combined to yield a concordia date of  $1037.9 \pm 6.5$  Ma (95% c.l.,  $\text{MSWD}(\text{C}+\text{E}) = 1.04$ ,  $n=10$ ; Figure 4.7) which is interpreted to be the crystallisation of the monazite in this pegmatite.

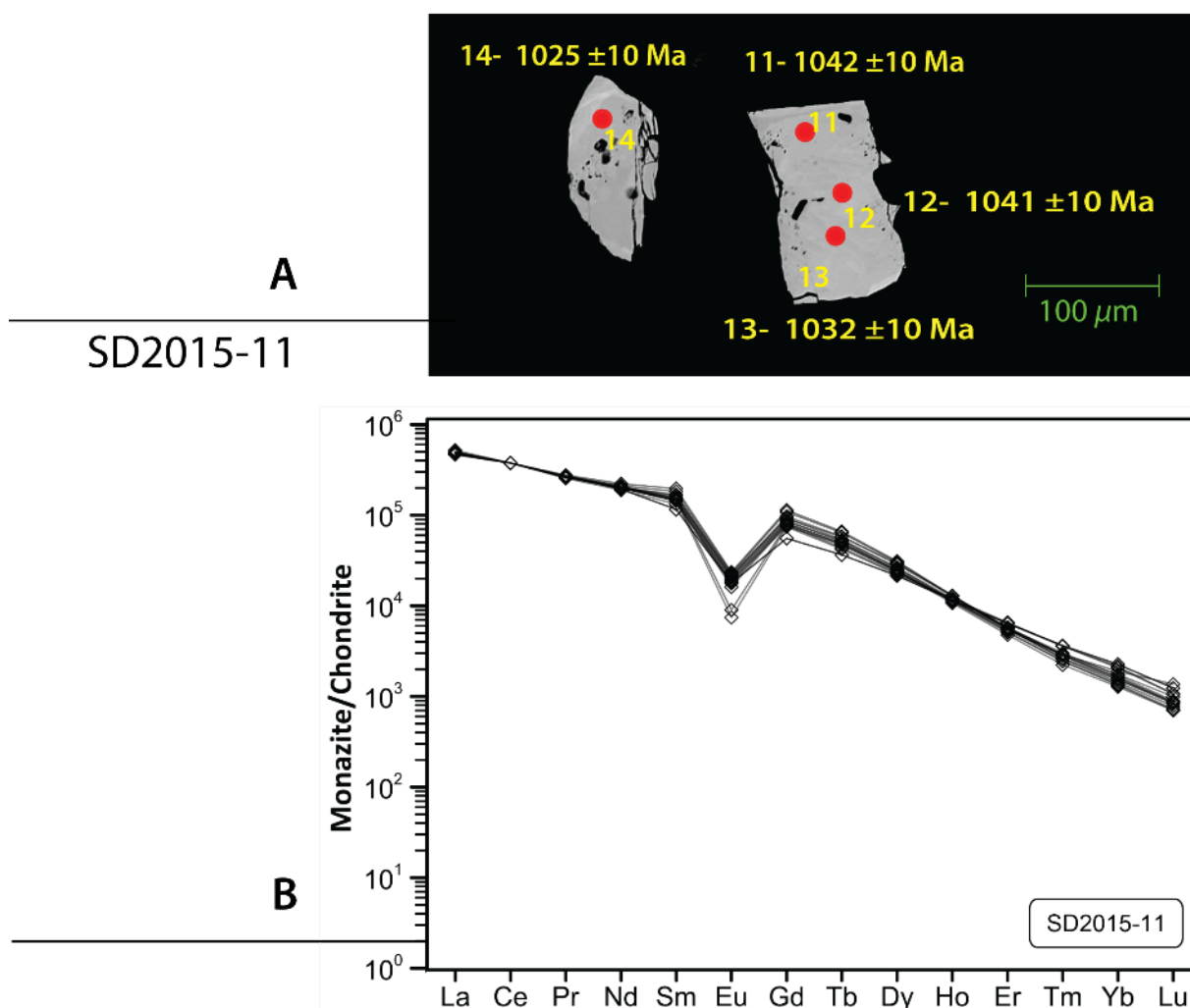


Figure 4.6. A). Representative SEM BSE images of analysed monazite from pegmatite sample SD2015-11. Red circles indicate positions of laser pits with a width of  $15\mu\text{m}$  –  $16\mu\text{m}$  (see text) in diameter. Spot dates indicated are  $^{206}\text{Pb}/^{238}\text{U}$  dates with uncertainties given at the  $1\sigma$  level. B). Chondrite-normalised REE diagram for sample SD2015-11. Normalised to values from Sun and McDonough (1989).



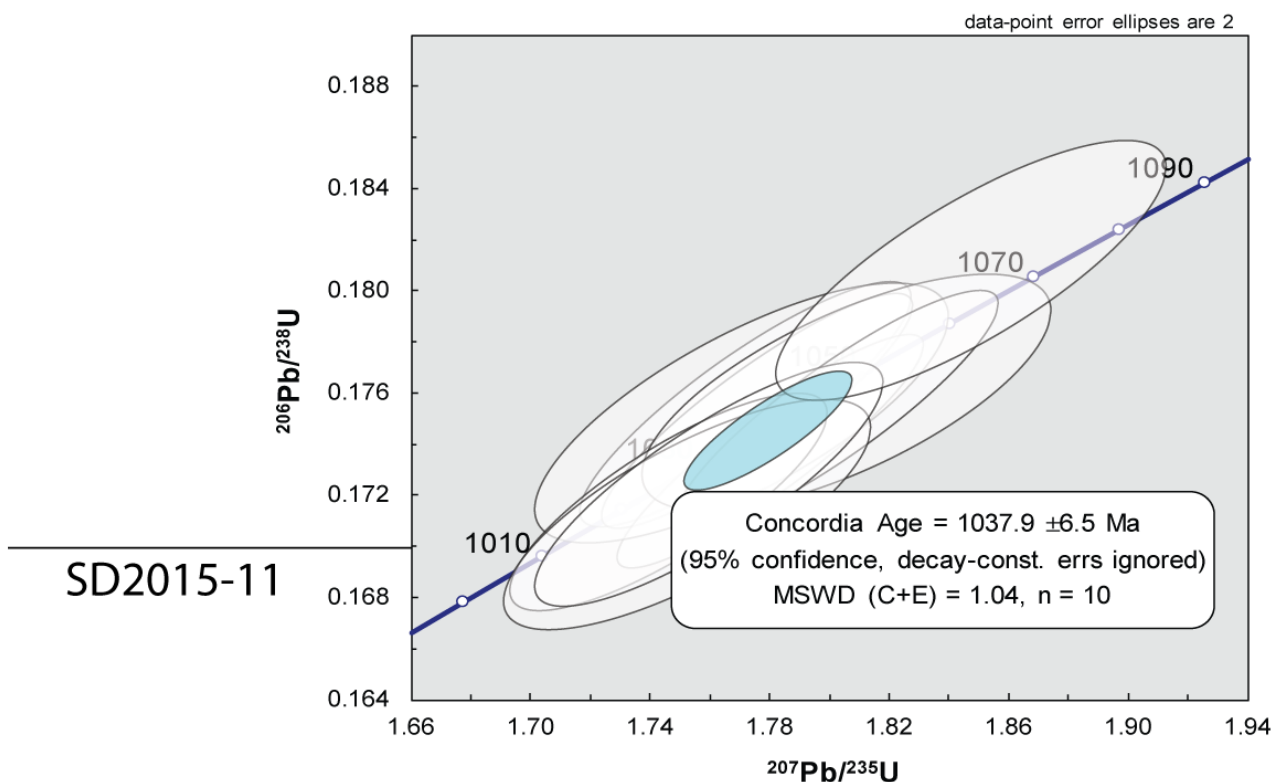


Figure 4.7: Wetherhill concordia diagram for monazite LA-Q-ICP-MS isotope data for pegmatite sample SD2015-11, errors are shown as 2 $\sigma$  ellipses

### SDORPB15-4b

This sample is from a large, complexly zoned, LCT-type pegmatite in the Steinkopf pegmatite field (Figure 4.8). The pegmatite is locally called “Kokerboom Rand” due to a prominent hill nearby with numerous “kokerboom” or quiver trees. The pegmatite was mined in the past for beryl, columbite-tantalite, spodumene and lepidolite and has been mostly mined out. It intrudes the ~1800 Ma Gaarseep Granodiorite of the Vioolsdrif Suite and appears concordant with the regional NE-SW striking foliation. The sample taken from this pegmatite contains feldspar and quartz in equal amounts with lithium micas, spodumene and as accessory minerals garnet, zircon, columbite-tantalite, apatite and monazite.

Monazite from this sample are mostly anhedral to subhedral and ~70-230  $\mu$ m in diameter. Subhedral grains are tabular in shape. They show homogenous centres; mantles characterised by polygonal sector zoning and minor alteration along the grain rims (Figure 4.9a). Concentrations of Si, Ca and Y vary between the rims and cores within the monazite grains (Appendix A.1.3). BSE light monazite rims have higher Si (3 016 – 8391 ppm). The anhedral grains exhibit a higher degree of alteration, characterised by spongy and patchy zones due to low-T fluid-mediated dissolution and precipitation along fractures, rims and zones within the grains. However, unaltered cores and zones are preserved (Figure 4.9a).

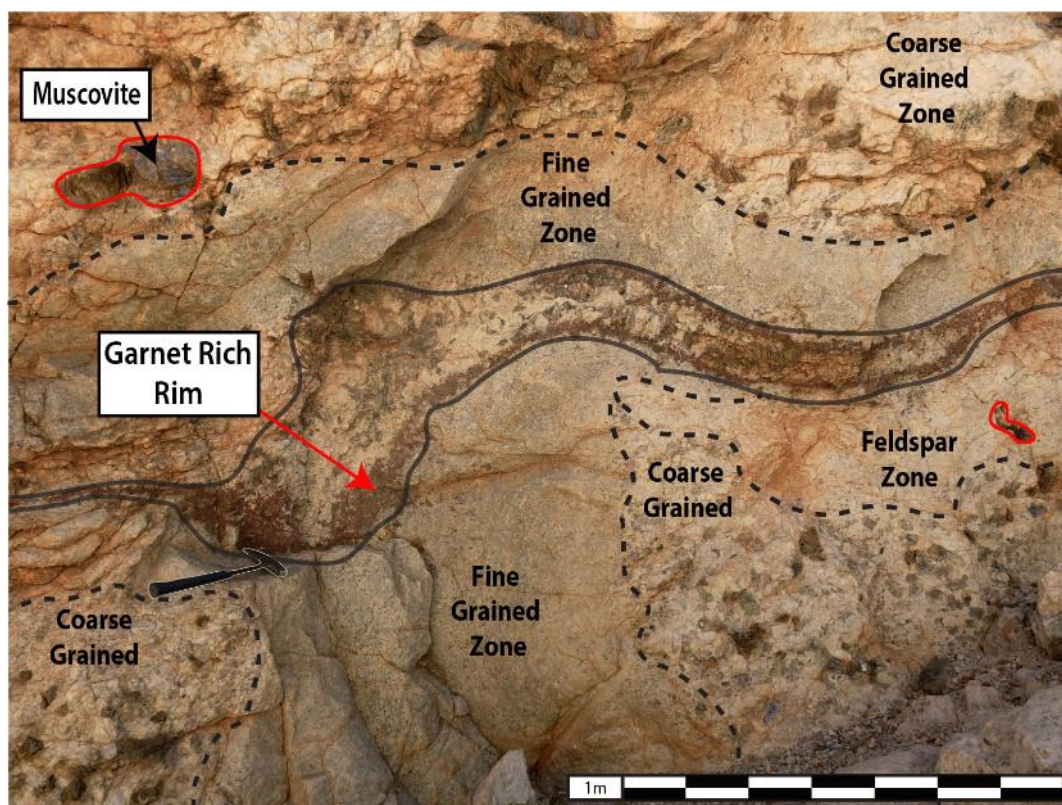


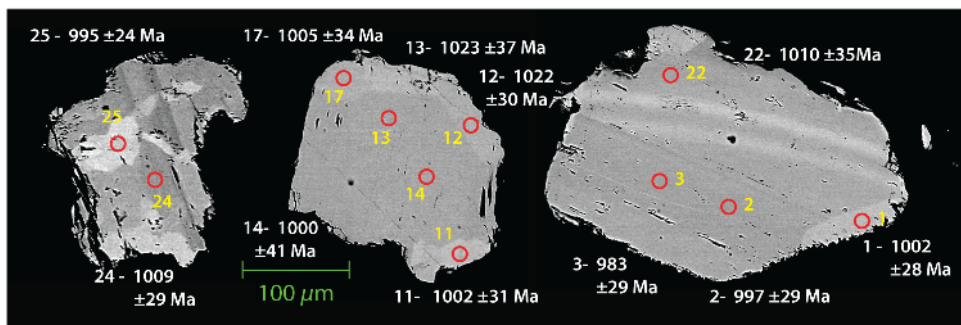
Figure 4.8: A field photograph that highlights the complex zoning observed in this zoned LCT pegmatite of “Kokerboom Rand”, with coarse- and fine-grained zones consisted of quartz, K-feldspar, with muscovite occurring in variable proportions within the coarse-grained zones. Zones with garnet-rich rims were present that had concentric zoning with respect to mineralogy containing K-feldspar rich mantles with the cores becoming quartz-rich. Li-rich zones were also present (not pictured).

Compositional variations between rim and core are minimal with similar Ca and Y contents (4 112 to 7258 ppm and 6 109 to 11 984 ppm, respectively; Appendix A.1.3). U and Thorium concentrations are low with higher Th/U for the cores (U = 680 – 1039 ppm; Th = 19 339 – 32 477 ppm; Th/U = 23 – 31) in comparison to the rims (U = 1 172 – 1 418 ppm; Th = 25 793 – 37 069 ppm; Th/U = 22 – 25; Appendix A.1.3). The composition of the anhedral monazite is much more variable with a wide range in Y (1 715 – 15 391 ppm) and Ca (1 960 – 22 780 ppm) contents, with moderate to high U contents (431 – 4222 ppm) and a range in Th content from 20 877 to 122 878 ppm (Appendix A.1.3). Altered monazite show a range in Th/U ratios from 15 to 66.

Monazite from this sample has chondrite-normalised REE patterns (Figure 4.9b) characterised by a strong relative LREE enrichment over the MREE ( $[La/Sm]_N = 6 - 16$ ; Appendix B.1.3), a variable negative Eu anomaly ( $Eu/Eu^* = 0.05 - 0.5$  Figure 4.9b) and a steep and variable relative depletion of HREE over MREE ( $[Gd/Lu]_N = 14 - 196$ ; Appendix B.1.3). The euhedral monazite has higher, and less variable chondrite-normalised HREE abundances compared to the anhedral monazite that has a higher variation in chondrite-normalised HREE abundances and larger range in negative Eu anomalies (Figure 4.9b)

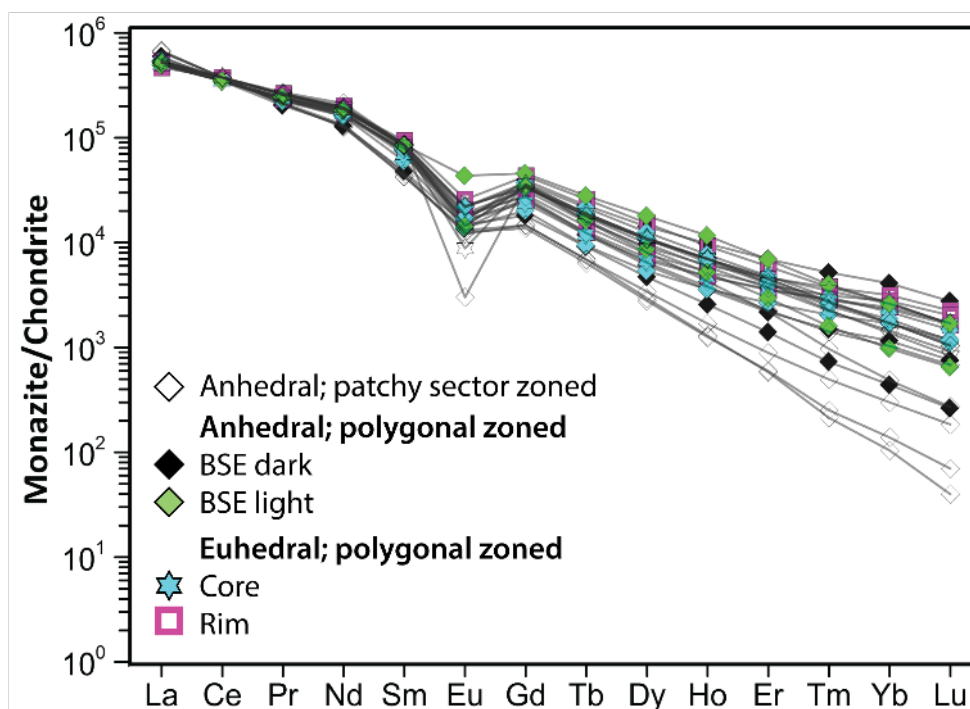
Monazite from this sample is variably (68-100 %) concordant (Appendix C.1.3) with the U-Pb isotope data from 24 analyses defining a discordant line segment with upper and lower intercept dates of  $1003 \pm 19$  Ma and  $7 \pm 260$  Ma, respectively (MSWD = 0.36, Figure 4.10a); the latter suggesting recent Pb loss. A weighted

mean  $^{207}\text{Pb}/^{206}\text{Pb}$  date of  $1004 \pm 13$  (95% c.i.; MSWD = 0.17; probability of 1.0; Figure 4.10b) from all 22 analyses was within error of the upper intercept date. Based on its lower uncertainty of the weighted mean  $^{207}\text{Pb}/^{206}\text{Pb}$  date is preferred as the crystallisation age of monazite in this pegmatite.



A

SDORPB15- 4b



B

Figure 4.9. A) Representative SEM BSE images of analysed monazite from pegmatite sample SDORPB15-4B. Red circles indicate positions of laser pits with a width of  $15\mu\text{m} - 16\mu\text{m}$  (see text) in diameter. Spot dates indicated are  $^{206}\text{Pb}/^{207}\text{Pb}$  dates with uncertainties on the spot ages given at the  $1\sigma$  level. B) Chondrite-normalised REE diagram for sample SDORPB15-4B. Normalised to values from Sun and McDonough (1989).

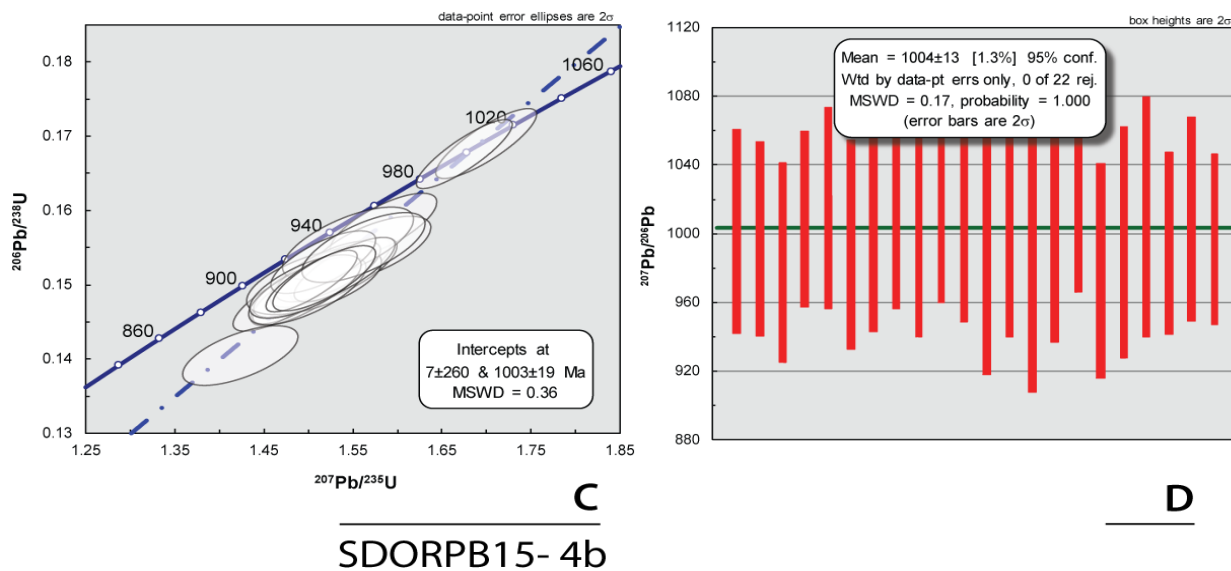


Figure 4.10: A.) Wetherill concordia diagram for monazite LA-Q-ICP-MS isotope data for pegmatite sample SDORPB15-4B, errors are shown as  $2\sigma$  ellipses. D) Weighted mean  $^{207}\text{Pb}/^{206}\text{Pb}$  diagram for pegmatite sample SDORPB15-4B where red boxes are plotted as  $2\sigma$  errors, with spot analyses that were excluded in the weighted mean are blue in colour.

### SDORPB15-7d

This sample is also from a zoned LCT pegmatite that intruded the ~1880 Ma Ramansdrif alkali feldspar granite (Figure 4.11a; Figure 4.11b) emplaced discordantly to the regional foliation. The pegmatite contains abundant lepidolite, tourmaline, and columbite-tantalite. The lepidolite-rich zone was sampled (Figure 4.11c), with the sample additionally containing plagioclase, quartz and garnet as major mineral phases. Zircon, xenotime, apatite and monazite occurs as accessory minerals. The monazite in this sample is highly altered. The alteration is characterised in BSE images by patchy and spongy domains that embay unaltered monazite, along fractures and permeating into the grains. The grains are anhedral to subhedral (~100 – 250  $\mu\text{m}$ ), some grains have embayed grain boundaries (Figure 4.12a). Away from the zones of alteration, the monazite grains are mostly homogenous in BSE images, except for one grain that has a narrow (~6  $\mu\text{m}$  wide) Th-rich, BSE-light rim. This rim was too narrow to analyse. Badly altered grains and zones of alteration were avoided during LA-Q-ICP-MS isotope data collection.

Nineteen LA-Q-ICP-MS U-Pb analyses were obtained from eight monazite grains in the sample. Based on apparent spot  $^{207}\text{Pb}/^{206}\text{Pb}$  dates, the U-Pb isotope data suggests three age populations (Figure 4.12c; Appendix C.1.4). Twelve spot analyses gave a population that is near concordant (99-104% concordant), with a range of moderate U concentrations (3 500-4 677 ppm), high Th (8 634 ppm – 1.3 wt%) and moderate Th/U ratios (Th/U = 27-37; Appendix A.1.4). These 12 analyses show a small range in apparent  $^{207}\text{Pb}/^{206}\text{Pb}$  spot dates ( $987.8 \pm 32\text{Ma}$  –  $1013 \pm 24\text{Ma}$ ; uncertainties are  $1\sigma$ ; Appendix C.1.4.) and could be combined to yield a concordia date of  $1007.2 \pm 5\text{Ma}$  ( $2\sigma$ , MSWD (C+E) = 1.6; Figure 4.13a).

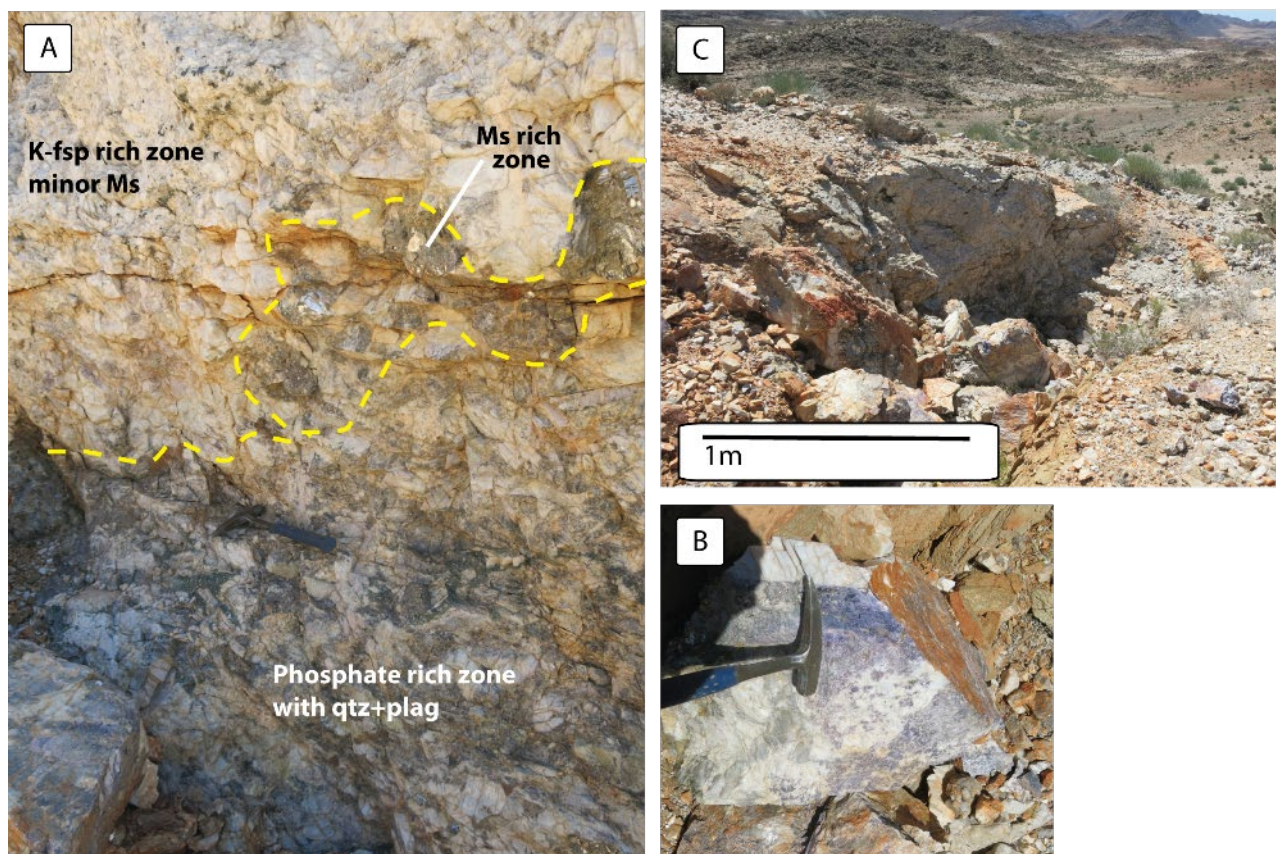


Figure 4.11: A): Photograph illustrating the mineralogical and textural zoning within the sampled pegmatite (SDORPB15-7d), the top zone is rich in K-feldspar with scattered muscovite books (~1-3cm in size); a muscovite rich zone (centre) contained large (~5-15cm) muscovite books with K-feldspar. The quartz-rich zone (bottom) hosted plagioclase and quartz and high proportion of blue apatite (~1-2cm crystals) that formed in scattered aggregate masses within the zone. B): Photograph of the lepidolite rich sample retrieved from this locality. C): Field photograph of the sampled pegmatite that has been worked out for the tourmaline by local gem miners. A characteristic of most of the mineralised pegmatites in the area.

The two older populations can be divided based on their degree of discordance, with a slightly discordant population of three analyses (91-98% concordance) and a discordant population of again three analyses (75-84% concordance). The slightly discordant population has a wide range in U concentrations (U = 5 042 ppm – 1.2 wt%; Appendix A.1.4.), low to moderate Th/U ratios (19 – 36; Appendix C.1.4.) and range in apparent  $^{207}\text{Pb}/^{206}\text{Pb}$  dates of  $1071 \pm 32$  Ma to  $1092 \pm 26$  Ma (Appendix C.1.4). An imprecise weighted mean  $^{207}\text{Pb}/^{206}\text{Pb}$  date was calculated for the three analyses to be  $1085 \pm 30$  Ma (95% c.i., MSWD = 0.14, probability = 0.87; Figure 4.13b).

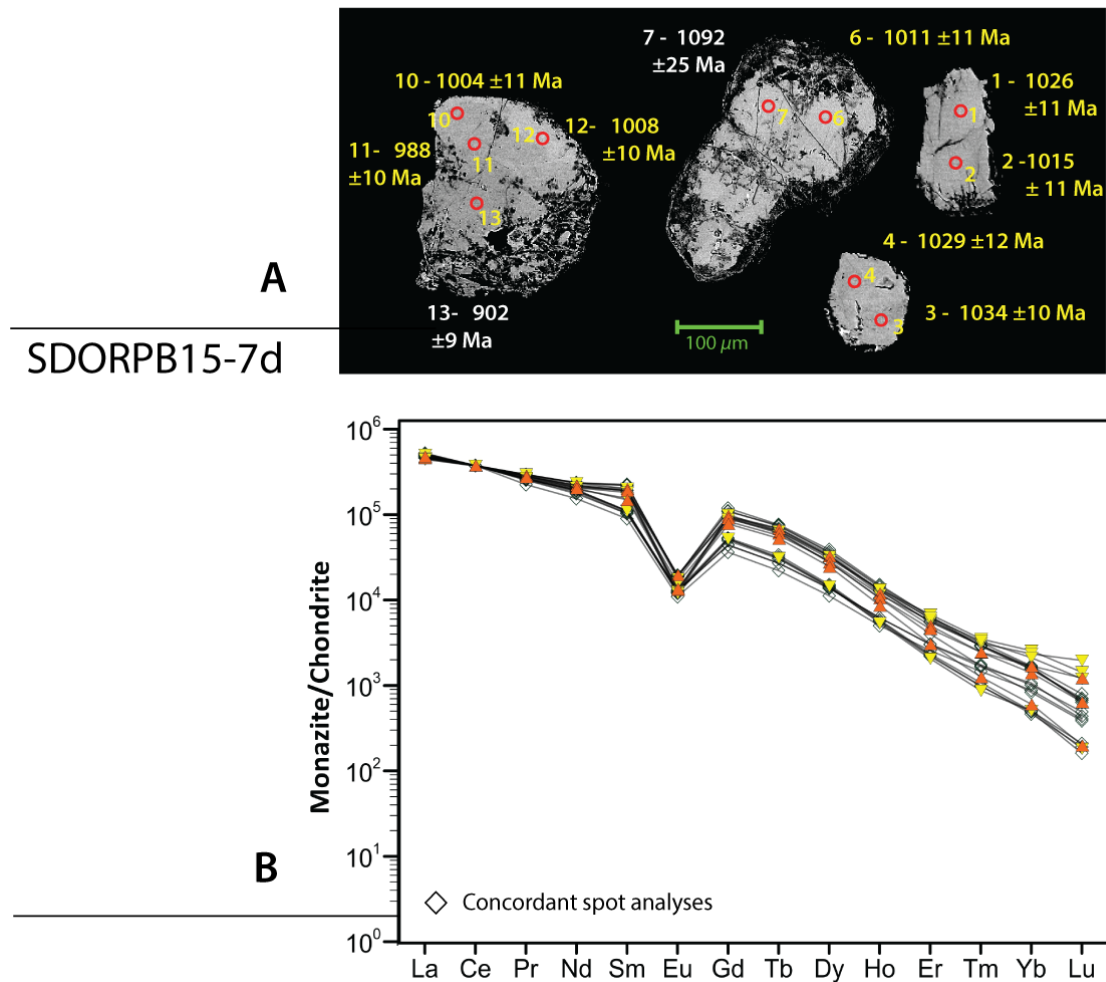


Figure 4.12. A.) Representative SEM BSE images of analysed monazite from pegmatite sample SDORPB15-7D. Red circles indicate positions of laser pits with a width of  $15\mu\text{m} - 16\mu\text{m}$  (see text) in diameter. Spot dates indicated are (white text)  $^{206}\text{Pb}/^{207}\text{Pb}$  dates and (yellow text)  $^{206}\text{Pb}/^{238}\text{U}$  dates with uncertainties on the spot ages given at the  $1\sigma$  level. B) Chondrite-normalised REE diagram for sample SDORPB15-7D. Normalised to values from Sun and McDonough (1989).

The more discordant population of 3 analyses has a wide range in U concentrations and Th/U ratios (U = 3 211 – 1.03 wt%; Th/U = 13 – 45; Appendix A.1.4) but has a narrow range in apparent  $^{207}\text{Pb}/^{206}\text{Pb}$  dates from  $1223 \pm 25$  Ma to  $1202 \pm 23$  Ma (uncertainties at  $1\sigma$ ; Appendix C.1.4). The three spot ages give a weighted mean  $^{207}\text{Pb}/^{206}\text{Pb}$  date of  $1209 \pm 28$  Ma (95% c.l., MSWD = 0.23, probability = 0.79; Figure 4.13c).

Compositional variations between the different monazite populations show that the discordant and older monazite domains have higher and more variable Si (4 188 – 14 022 ppm) and Ca (21 349 – 42 810 ppm) concentrations compared to the concordant populations with lower Si (2 013 – 6 860 ppm). The concordant monazite population could be subdivided on the basis of differing Y, Ca and HREE content. One group has higher Y (17 165 – 24 259 ppm), Ca (24 933 – 36 915 ppm) and  $\Sigma\text{HREE}$  (~50 000 ppm) contents (Appendix A.1.4). The other population has appreciably lower Y (7 903 – 9 529 ppm), Ca (15 118 – 19 355 ppm) and  $\Sigma\text{HREE}$  of around ~47 000 ppm (Appendix A.1.4).

Despite the significant compositional variations, monazite chondrite-normalised REE patterns (Figure 4.12b) for all analyses is characterised by strong relative enrichment of LREE over the variable MREE enrichment that produces a flat to gentle decrease in normalised abundances toward the M- and HREE, resulting in a range of  $[La/Sm]_N$  values from 2 to 6 (Appendix B.1.4.; Figure 4.12d). Variations in the  $[La/Sm]_N$  slope is due to the high Y/Ca monazite being slightly more enriched in the MREEs (Appendix B.1.4; Figure 4.12b). The REE pattern has a moderate and negative Eu anomaly ( $Eu/Eu^* = 0.1 - 0.2$ ; Appendix B.1.4; Figure 4.12b) with a moderate and variable relative depletion in HREE ( $[Gd/Lu]_N = 42 - 391$ ; Appendix B.1.4) with the high Y+Ca monazite being slightly more enriched in HREE.

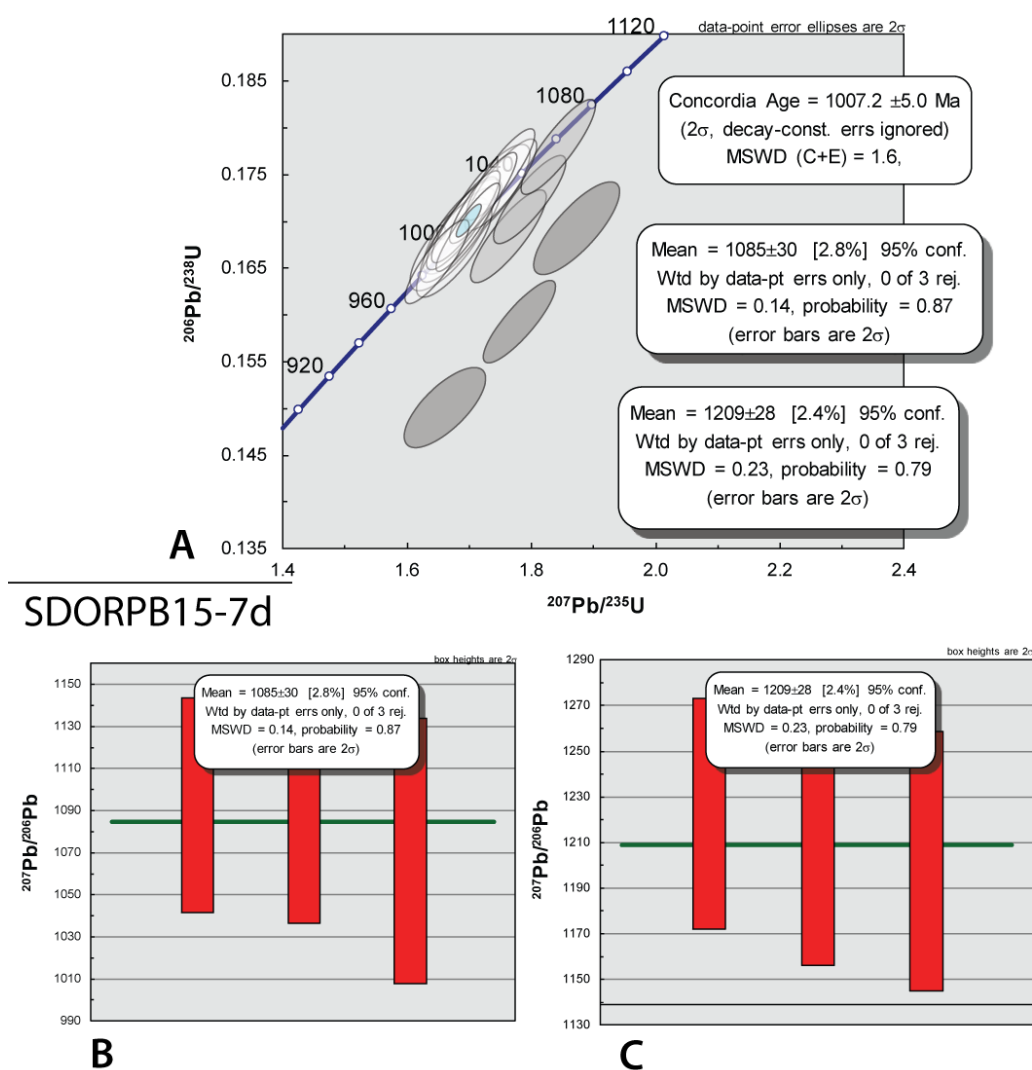


Figure 4.13: A) Wetherhill concordia diagram for monazite LA-Q-ICP-MS isotope data for pegmatite sample SDORPB15-7D, errors are shown as  $2\sigma$  ellipses. B and C) Weighted mean  $^{207}Pb/^{206}Pb$  spot date diagram for pegmatite sample SDORPB15-7D where red boxes are plotted as  $2\sigma$  errors.

**SDORPB15-9**

The sample is from a columbite-tantalite and beryl-bearing REE class, LCT-type pegmatite (Figure 4.14), that intrudes the ~1890 Ma Garseep granodiorite of the Vioolsdrif Suite near the Goodhouse settlement. The sample contains predominantly K-feldspar with subordinate quartz and muscovite, and garnet, monazite, columbite-tantalite, zircon and apatite as accessory minerals. Monazite from this sample is subhedral to anhedral in shape and approximately 90–250  $\mu\text{m}$  in diameter (Figure 4.15). Twelve LA-Q-ICP-MS U-Pb analyses were taken from nine monazite grains. U concentrations and Th/U ratios revealed two monazite populations: 1) A high Th/U, low Y group with low to moderate U contents (U = 1 447–2596 ppm; Th/U = 56 – 70), with higher Si (5 315 – 16 573 ppm), lower Ca (4 612 – 10 000 ppm), Y (5 491 – 10 350 ppm) and high Th contents (81 008 – 151 571 ppm; Appendix A.1.5). 2) A low Th/U, high Y group with moderate to high U contents (U = 4 608–6 649 ppm) higher Th (81 008 – 129 511 ppm) contents and with lower Si (2 120 – 3 472 ppm), higher Ca (10 014 – 14 133 ppm) and Y (21 102 - ppm) contents (Appendix A.1.5).

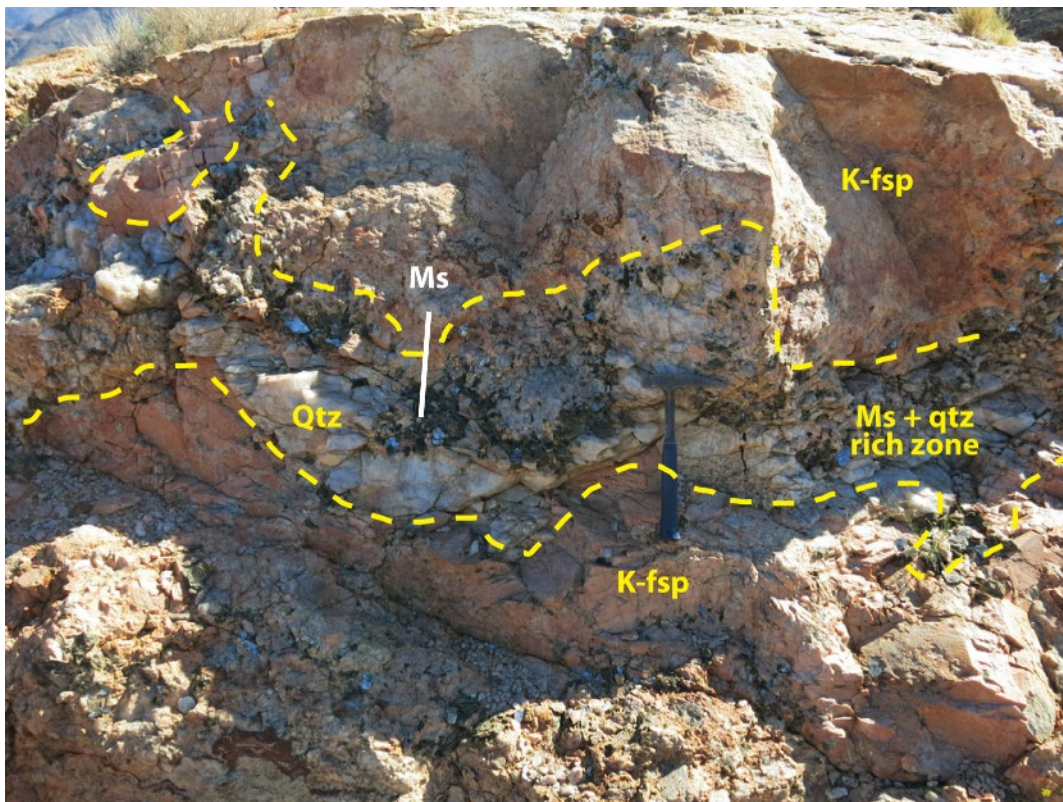


Figure 4.14: Field photograph illustrating the zonation present in this sampled pegmatite (SDORPB15-9). The pegmatite is predominantly K-feldspar rich with zones that were rich in muscovite, quartz, plagioclase and garnet. Beryl is sparse but is present in the muscovite rich zones.



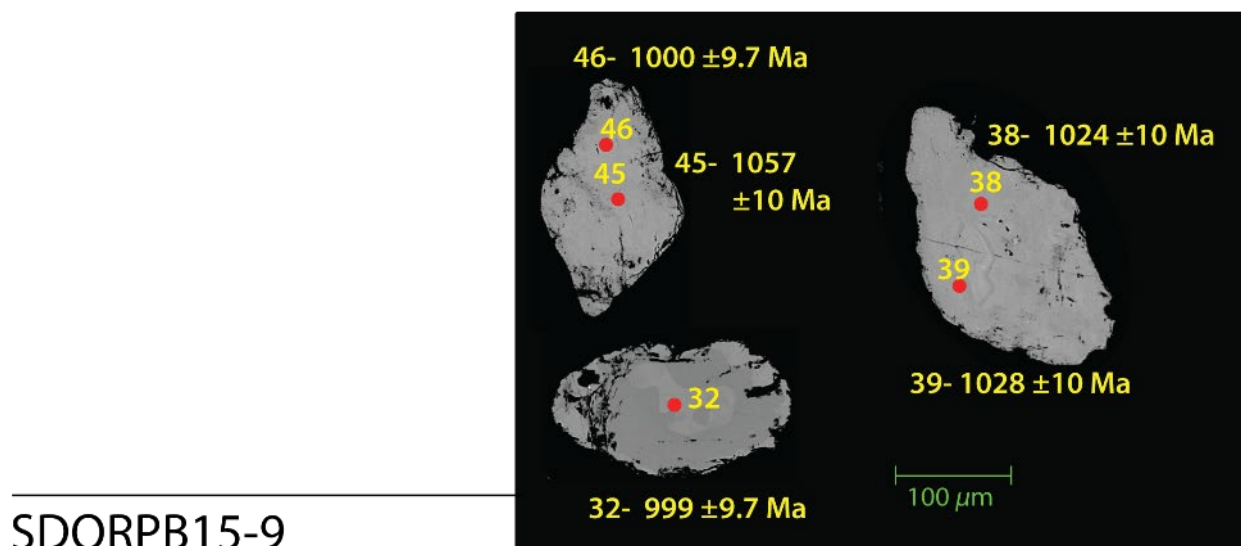


Figure 4.15. Representative SEM BSE images of analysed monazite from pegmatite sample SDORPB15-9. Red circles indicate positions of laser pits with a width of  $15\mu\text{m} - 16\mu\text{m}$  (see text) in diameter. Spot dates indicated are  $^{206}\text{Pb}/^{238}\text{U}$  dates with uncertainties on the spot ages given at the  $1\sigma$  level.

The trend in monazite compositional heterogeneity can be observed in the chondrite-normalised REE patterns (Figure 4.15d). Both monazite populations are characterised by generally flat REE patterns from the LREE to the MREE ( $[\text{La}/\text{Nd}]_{\text{N}} = \sim 1.1$ ; Appendix B.1.5; Figure 4.16a) except for a slight relative enrichment at Sm ( $[\text{La}/\text{Sm}]_{\text{N}} = \sim 0.4$ ; Appendix B.1.5; Figure 4.15b). Eu anomalies are variable (large to extreme) and negative with the high Th/U population having the largest anomalies ( $\text{Eu}/\text{Eu}^* = \sim 0.01/0.002-0.004$ ; low Th/U monazite/High Th/U monazite; Appendix B.1.5; Figure 4.16a). The REE patterns of both monazite types have a steep but variable relative enrichment in the MREE over the HREE ( $[\text{Gd}/\text{Lu}]_{\text{N}} = 911 - 1249 / 1863 - 5207$ ; low Th/U / high Th/U; Appendix B.1.5; Figure 4.16a).

Irrespective of monazite composition and texture, LA-Q-ICP-MS U-Pb isotope data for this sample cluster close to the concordia line (concordance = 98 – 104%; Figure 4.16b; Appendix C.1.5), with apparent  $^{207}\text{Pb}/^{206}\text{Pb}$  spot dates that vary between  $1018 \pm 22 \text{ Ma}$  ( $1\sigma$ ) and  $961 \pm 21 \text{ Ma}$  ( $1\sigma$ ) (Appendix C.1.5). The U-Pb isotope data for the 12 analyses show too much scatter above the concordia line for a concordia age to be calculated (Figure 4.16b). However, 11 of the 12 analyses have the same  $^{206}\text{Pb}/^{238}\text{U}$  spot dates within uncertainty allowing a weighted mean  $^{206}\text{Pb}/^{238}\text{U}$  date of  $1004 \pm 6 \text{ Ma}$  (95% c.i.; MSWD = 0.88; Probability of 0.56;  $n=11$  of 12; Figure 4.16c) to be calculated, and is interpreted to be the best estimate for the crystallisation age of this pegmatite.

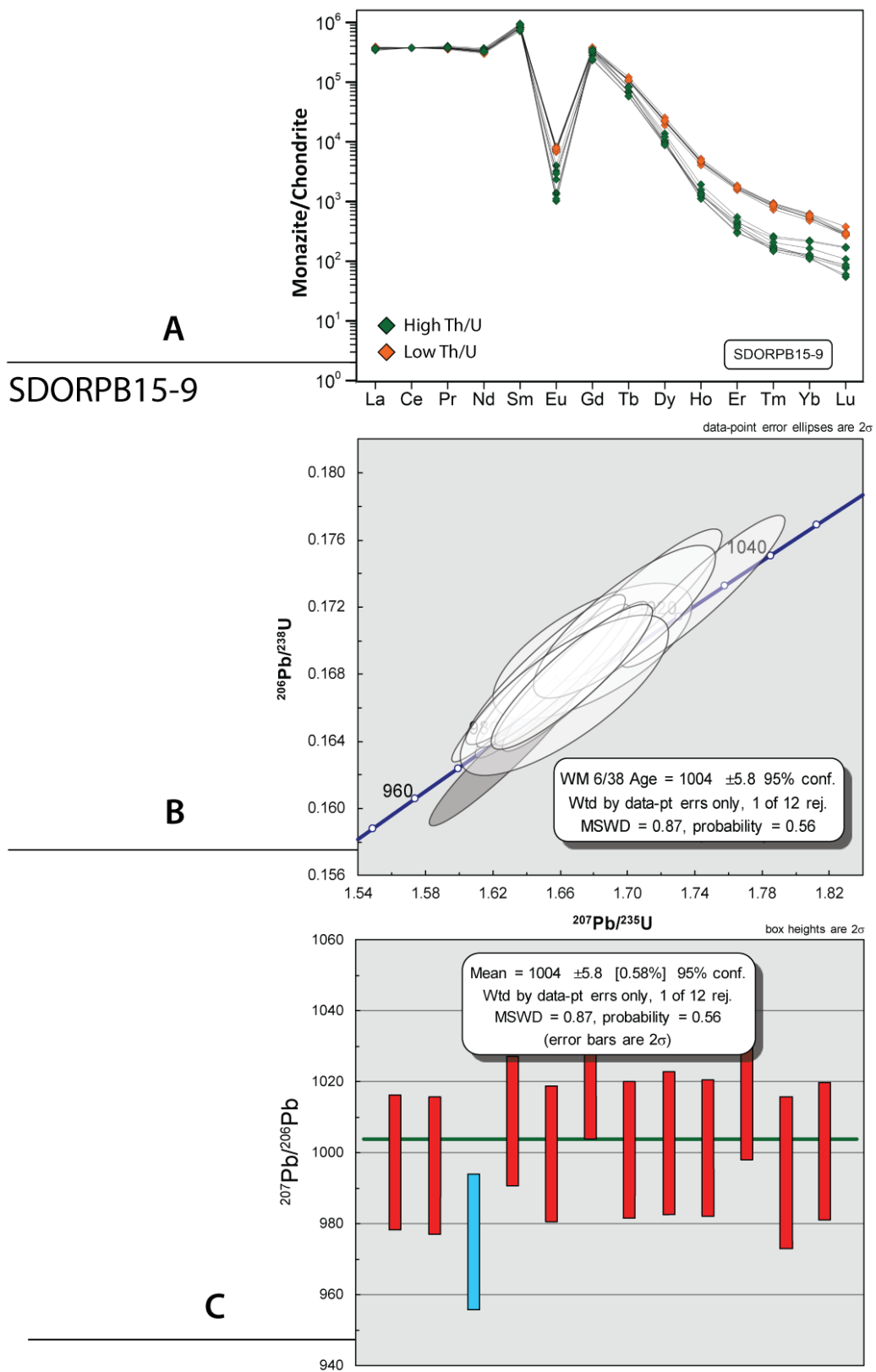


Figure 4.16: A) Chondrite-normalised REE diagram for sample SDORPB15-9. Normalised to values from Sun and McDonough (1989). B) Wetherhill concordia diagram for monazite LA-Q-ICP-MS isotope data for pegmatite sample SDORPB15-9, errors are shown as  $2\sigma$  ellipses. C) Weighted mean diagram for pegmatite sample SDORPB15-9 where red boxes are plotted as  $2\sigma$  errors, with spot analyses that were excluded in the weighted mean is blue.

## SDORPB16-4

The monazite from this sample came from a large (~900 m long, ~20 m wide) LCT pegmatite that intruded the mafic meta-volcanic rock of the ~1890 Ma Nous Formation and ~ 1880 Ma Garseep granodiorite. The pegmatite is located upon a prominent black weathering hill locally known as “Swartkop” near the settlement of Henkries along the Orange River. This pegmatite, formally known as Swartkop, had been mined for beryl, feldspar, micas and columbite-tantalite but has since ceased operation. The pegmatite also contains abundant tourmaline, muscovite and garnet with accessory zircon, apatite and xenotime.

The sample yielded many anhedral rounded monazite grains and angular fragments (>~200  $\mu\text{m}$ ) of larger monazite crystals (Figure 4.17a). The rounded monazite grains are slightly equant to elongated (~80 – 180  $\mu\text{m}$ ; X:Y = 1:1.5) and anhedral. The majority of these grains are unzoned in BSE images, while a minority show polygonal sector zoning. The large anhedral monazite fragments are homogenous in BSE images. Both monazite types are locally affected by porous alteration zones that are interpreted to be as a result of late low-T hydrothermal dissolution and precipitation.

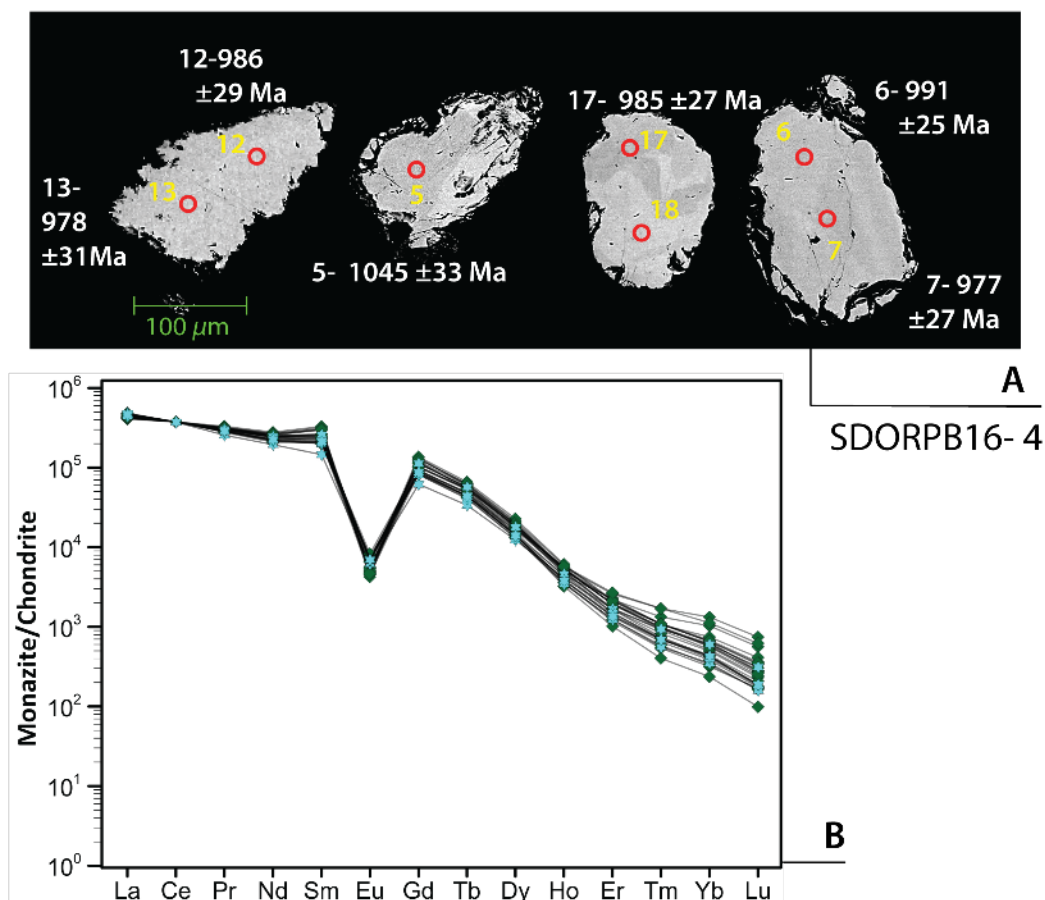


Figure 4.17. A) Representative SEM BSE images of analysed monazite from pegmatite sample SDORPB16-4. Red circles indicate positions of laser pits with a width of 15  $\mu\text{m}$  – 16  $\mu\text{m}$  (see text) in diameter. Spot dates indicated are (white text)  $^{206}\text{Pb}/^{207}\text{Pb}$  dates with uncertainties on the spot ages given at the  $1\sigma$  level. B) Chondrite-normalised REE diagram for sample SDORPB16-4. Normalised to values from Sun and McDonough (1989).

Fourteen monazite from this sample grains were selected and analysed by LA-Q-ICP-MS. Despite their textural differences the two monazite populations overlap in their chemical compositions, with a broad range of concentrations in Si (2 991 – 34 888 ppm), Ca (5 712 – 12 906 ppm), Y (12 534 – 21 653 ppm) and Th (42 991 – 104 852 ppm). U concentrations are low and moderately variable U (1 103 – 2 747 ppm; Appendix A.1.6), and Th/U ratios varied between 21 and 56 (Appendix A.1.6). The chondrite-normalised REE patterns for the sample is characterised by little relative fractionation of LREE over the MREE ( $[La/Sm]_N = 1 - 2$ ; Appendix B.1.6) with small variations in MREE normalised abundances (Figure 4.17b). The monazites have large negative Eu anomalies ( $Eu/Eu^* = 0.02 - 0.05$ ; Figure 4.17b) with a moderate to steep but variable relative depletion of HREE over the MREE ( $[Gd/Lu]_N = 165 - 1204$ ; Appendix B.1.6; Figure 4.17b).

Monazite from this sample is variably (86 to 98 %; Appendix C.1.6) concordant, with the U-Pb isotope data from 20 analyses, obtained from both monazite types, defining a discordant line segment with an upper intercept of  $986 \pm 35$  Ma and a lower intercept at  $-81 \pm 490$  Ma (MSWD = 0.24; Figure 4.18a), respectively. The lower intercept date is interpreted to indicate recent Pb loss. A weighted mean  $^{207}Pb/^{206}Pb$  date of  $993 \pm 12$  Ma (95% c.l., MSWD = 0.104, probability of 1.000; Figure 4.18b), within the error of the upper intercept date, was calculated from all 20 analyses. Based on its lower uncertainty, the weighted mean  $Pb^{207}/Pb^{206}$  date is preferred as the best estimate of the crystallisation age of the monazite in this pegmatite.

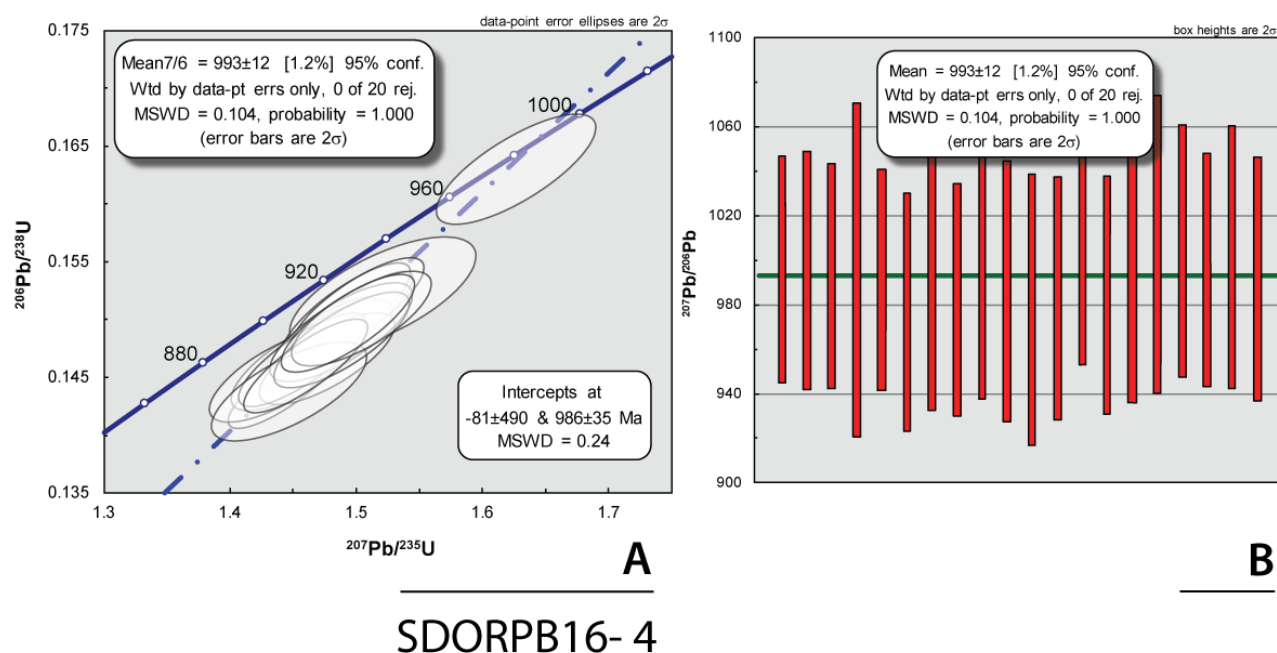


Figure 4.18: A) Wetherhill concordia diagram for monazite LA-Q-ICP-MS isotope data for pegmatite sample SDORPB16-4, errors are shown as  $2\sigma$  ellipses. B) Weighted mean  $^{207}Pb/^{206}Pb$  spot date diagram for pegmatite sample SDORPB16-4 where red boxes are plotted as  $2\sigma$  errors.

**SDORPB16-5**

This sample comes from a zoned LCT-type pegmatite (Figure 4.19) that intruded the ~1880 Ma Garseep granodiorite and is locally known as Spodumene Kop 1 pegmatite. The pegmatite was previously mined for lithium minerals (spodumene and lepidolite) as well as columbite-tantalite and feldspar. The main pegmatite mineral assemblage consisted of quartz, K-feldspar, muscovite, spodumene (notably large crystals; Figure 4.19), lepidolite and garnet. The pegmatite also contains the accessory minerals tourmaline, columbite-tantalite, xenotime, zircon, monazite and apatite. The sample did not yield much monazite; only two grains were extracted and analysed.

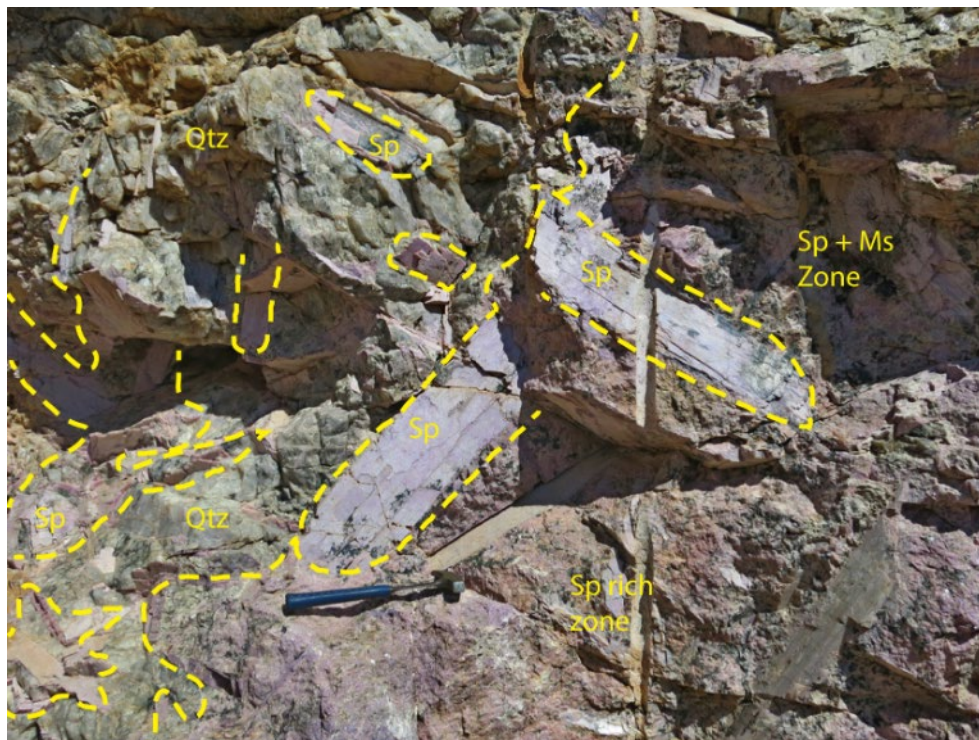


Figure 4.19: Field photograph of the sampled Li-rich pegmatite, "Spodumene Kop 1". The zoned pegmatite contained K-feldspar rich zone (not pictures), quartz dominated zones with scattered, large pink spodumene crystals (top right zone in the picture), and lepidolite and spodumene rich zones that contained minor garnet, tourmaline, columbite and quartz. Spodumene crystals in the Li-rich zone varied in size from extremely large (50-80cm in length) to small (1-4 cm).

The grains are anhedral and ~100 µm in size. Grain 1) is equant, with a porous, altered rim and lacked any compositional zoning (Figure 4.20). This monazite has low U (~222 to 280 ppm), and Th (13 565 – 18 629 ppm) contents with a high average Th/U ratio of 62 (Appendix A.1.7). The other anhedral grain has minor sector zoning with zones of "spongy" alteration due to fluid-mediated dissolution and precipitation. The grain has very high U, and high Th from 14 922 – 19 149 ppm and 93 319 – 107 668 ppm respectively with a low Th/U ratio (5 – 7) (Appendix A.1.7). The concentrations of Ca, Y and HREEs exhibited similar compositional variations seen with U and Th; where the low Th/U monazite has high Ca (~19 000 ppm) and Y (22 601 – 28 282 ppm) contents (appendix A.1.7). The high Th/U monazite has appreciably lower Ca (660 – 1 227 ppm), Y (159 – 2 081 ppm) and ΣHREE (13 212 – 20 968 ppm) concentrations (Appendix A.1.7).

The chondrite-normalised REE diagram (Figure 4.21a) further illustrated the differences in REE concentrations where there is markedly differing relative depletion of the HREE with respect to the MREE for the two grains. Both monazites have similar flat LREE to MREE profiles with  $(\text{La}/\text{Gd})_N$  of 1 to 2 (Appendix B.1.7) with the high Th/U grains showing MREE enrichment over the low Th/U monazite. Both grains show pronounced negative Eu anomalies for both grains ( $\text{Eu}/\text{Eu}^* = \sim 0.03$ ). The low Th/U monazite is characterised by much less relative depletion of the HREE with respect to the MREE than the high Th/U grain, as shown by  $[\text{Gd}/\text{Lu}]_N$  (144 – 336 versus 4800 – 6800, respectively). The differences in the values, together with differences in Y concentrations in the two monazite grains, suggest that the low Th/U monazite crystallised before HREE rich mineral phases such as garnet, xenotime, columbite-tantalite and possibly zircon.

Eight analyses were obtained from the two monazite grains. The analyses are concordant to moderately discordant (102 – 90% concordant), with a narrow spread in  $^{207}\text{Pb}/^{206}\text{Pb}$  dates from  $1025 \pm 22$  Ma ( $1\sigma$ ) to  $990 \pm 60$  Ma ( $1\sigma$ ) (Appendix C.1.7). The older and more concordant spot dates come from the “U rich” monazite. Regardless of their compositional difference all of the analyses define a discordant line segment with an upper intercept of  $1020 \pm 11$  Ma and lower intercept of  $48 \pm 300$  Ma (MSWD = 0.21; Figure 4.21b), the latter of which suggests recent Pb loss. A weighted mean  $^{207}\text{Pb}/^{206}\text{Pb}$  date of  $1017 \pm 22$  Ma (95% c.i., MSWD = 0.094, probability of 0.999; Figure 4.21c) was calculated for all the analyses ( $n=8$ ). The weighted mean estimate is in agreement with the error of the upper intercept date. As with previous samples, the more precise weighted mean date is regarded as the best estimate of the crystallisation of this pegmatite.

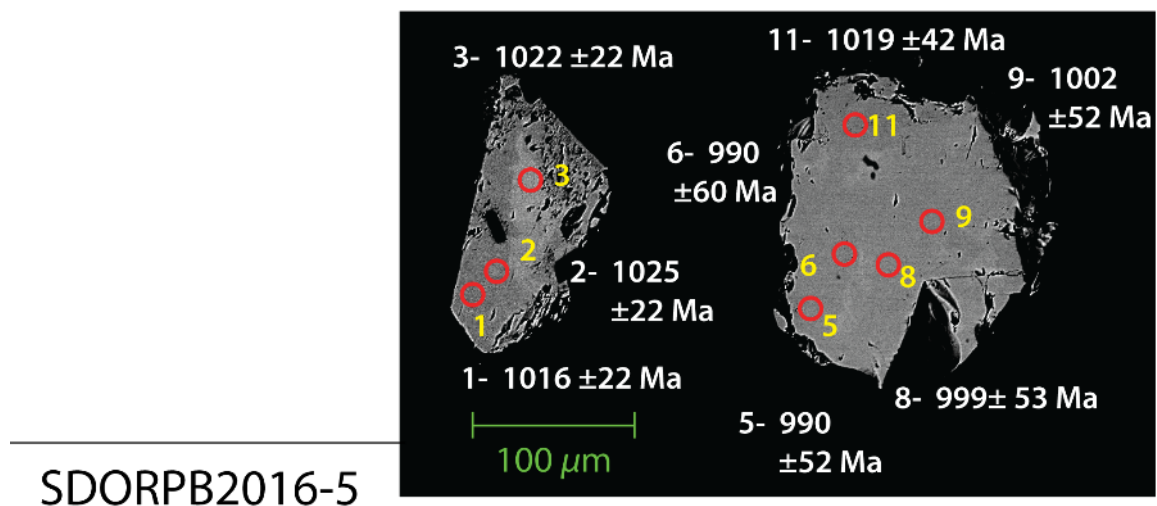


Figure 4.20: Representative SEM BSE images of analysed monazite from pegmatite sample SDORPB16-5. Red circles indicate positions of laser pits with a width of  $15\mu\text{m} - 16\mu\text{m}$  (see text) in diameter. Spot dates indicated are (white text)  $^{206}\text{Pb}/^{207}\text{Pb}$  dates with uncertainties on the spot ages given at the  $1\sigma$  level

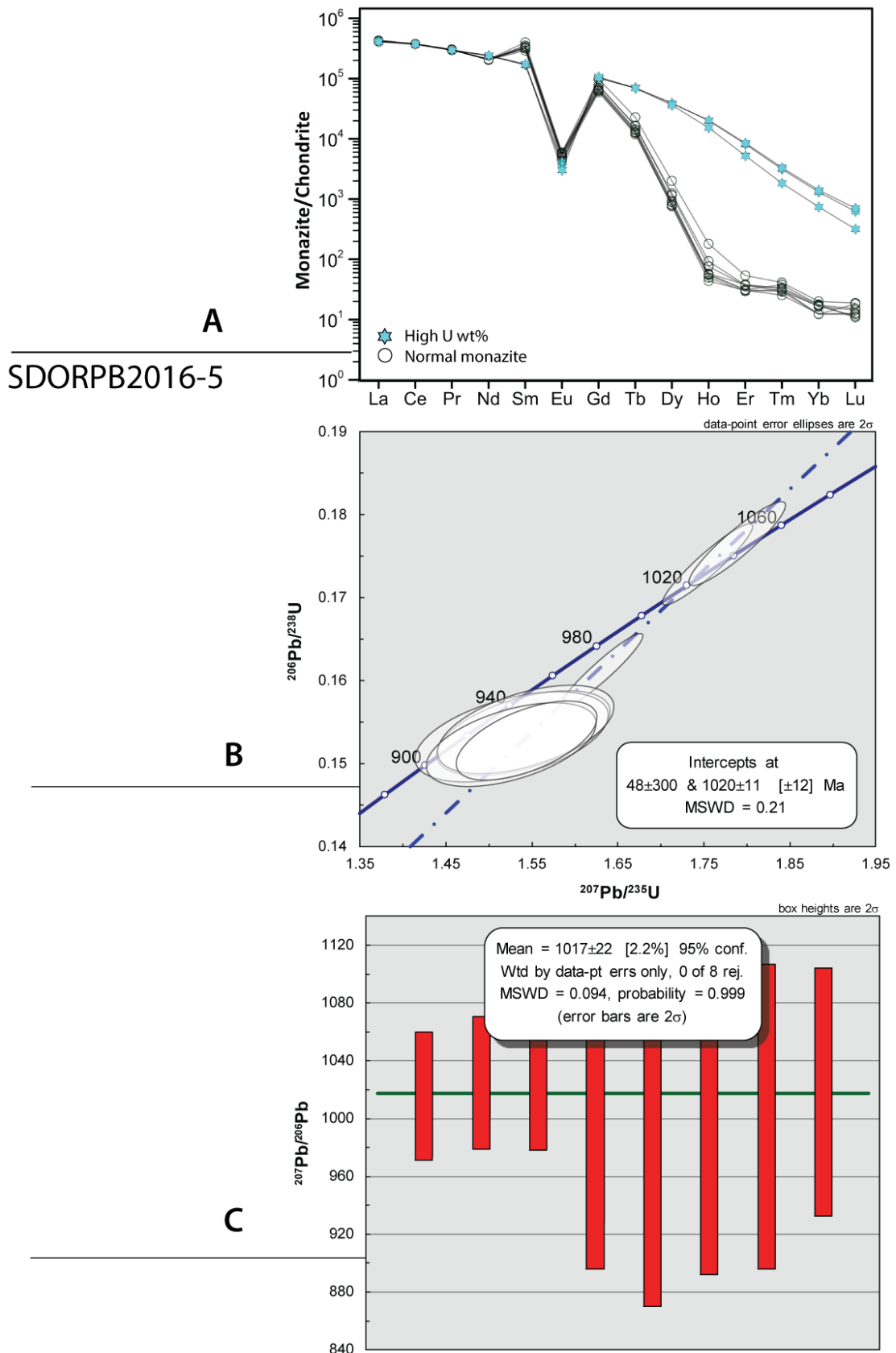


Figure 4.21: A) Chondrite-normalised REE diagram for sample SDORPB16-5. Normalised to values from Sun and McDonough (1989). B) Wetherill concordia diagram for monazite LA-Q-ICP-MS isotope data for pegmatite sample SDORPB16-5, errors are shown as  $2\sigma$  ellipses. C) Weighted mean  $^{207}\text{Pb}/^{206}\text{Pb}$  spot age diagram for pegmatite sample SDORPB16-5 where red boxes are plotted as  $2\sigma$  errors

#### 4.1.1.2. Pella Domain

##### *RPGV14*

This sample was obtained from a homogeneous pegmatite that intruded the “Noudap type”, biotite-hornblende augen gneiss of the ~1890 Ma Goodhouse Subsuite in the Namusklauff area near Rosh Pinah, southern Namibia. The sample had a mineralogy of K-feldspar and quartz with subordinate muscovite, and with monazite, zircon, and apatite as accessory minerals. The monazite grains are pale yellow with a “frosted” appearance. The grains are small (50-120  $\mu\text{m}$  in diameter) and range in shape from tabular and euhedral, to rounded and subhedral. Some separated grains are small fragments. Broad compositional sector zoning and limited and weak oscillatory zoning is present in some grains (irrespective of grain morphology). Some grains have BSE darker cores with BSE bright rims that reflect slight differences in Th content. However overall, most grains appear homogenous (Figure 4.22a). A limited number of grains have a porous zone or rim due to fluid mediated recrystallisation; these zones were not analysed.

Monazite U contents are high and varied from 4 901 to 14 053 ppm; while Th has a wide range in concentrations from 14 363 to 67 860 ppm. Th/U ratios varied from 1 – 12 (Appendix A.2.1). The monazite chondrite-normalised REE patterns (Figure 4.22b) are characterised by strong relative enrichment of the LREE with a progressive and smooth decrease in normalised abundances towards the M- and HREE ( $[\text{La}/\text{Sm}]_N = 3\text{-}4$ ; Appendix B.2.1; Figure 4.22b). Eu anomalies are moderate and negative ( $\text{Eu}/\text{Eu}^* = 0.1\text{-}0.3$ ; Appendix B.2.1.; Figure 4.22b), with one grain having an almost negligible Eu anomaly ( $\text{Eu}/\text{Eu}^* = 0.8$ ; Figure 4.22b). The analysis from this grain has a much lower Th/U ratio than the other spot analyses ( $\text{Th}/\text{U} = 1.0$ ; Appendix A.2.1). REE patterns are characterised by modest relative depletion of the HREE with respect to the  $[\text{Gd}/\text{Lu}]_N$  ratio of 25 – 49 (Appendix B.2.1).

Twenty-five U-Pb isotope analyses were taken from 25 monazite grains. Of these, 23 analyses are sub-concordant to concordant (99 – 104 % concordant). The two additional grains are either normally discordant (84% concordant) or reversely discordant (119% concordant), possibly due to disturbances in the U-Th-Pb isotope system due to fluid-mediated recrystallisation (Appendix C.1.7). The 23 concordant U-Pb isotope analyses clustered tightly on the concordia line with a range of apparent spot  $^{207}\text{Pb}/^{206}\text{Pb}$  dates between  $993 \pm 29 \text{ Ma}$  ( $1\sigma$ ) to  $946.4 \pm 26 \text{ Ma}$  ( $1\sigma$ ) (Appendix C.2.1). These analyses can be statistically combined to yield a Concordia date of  $973.3 \pm 4 \text{ Ma}$  ( $2\sigma$ , MSWD 0.48(C+E); Figure 4.22c), which is interpreted to be the monazite crystallisation age of this pegmatite.



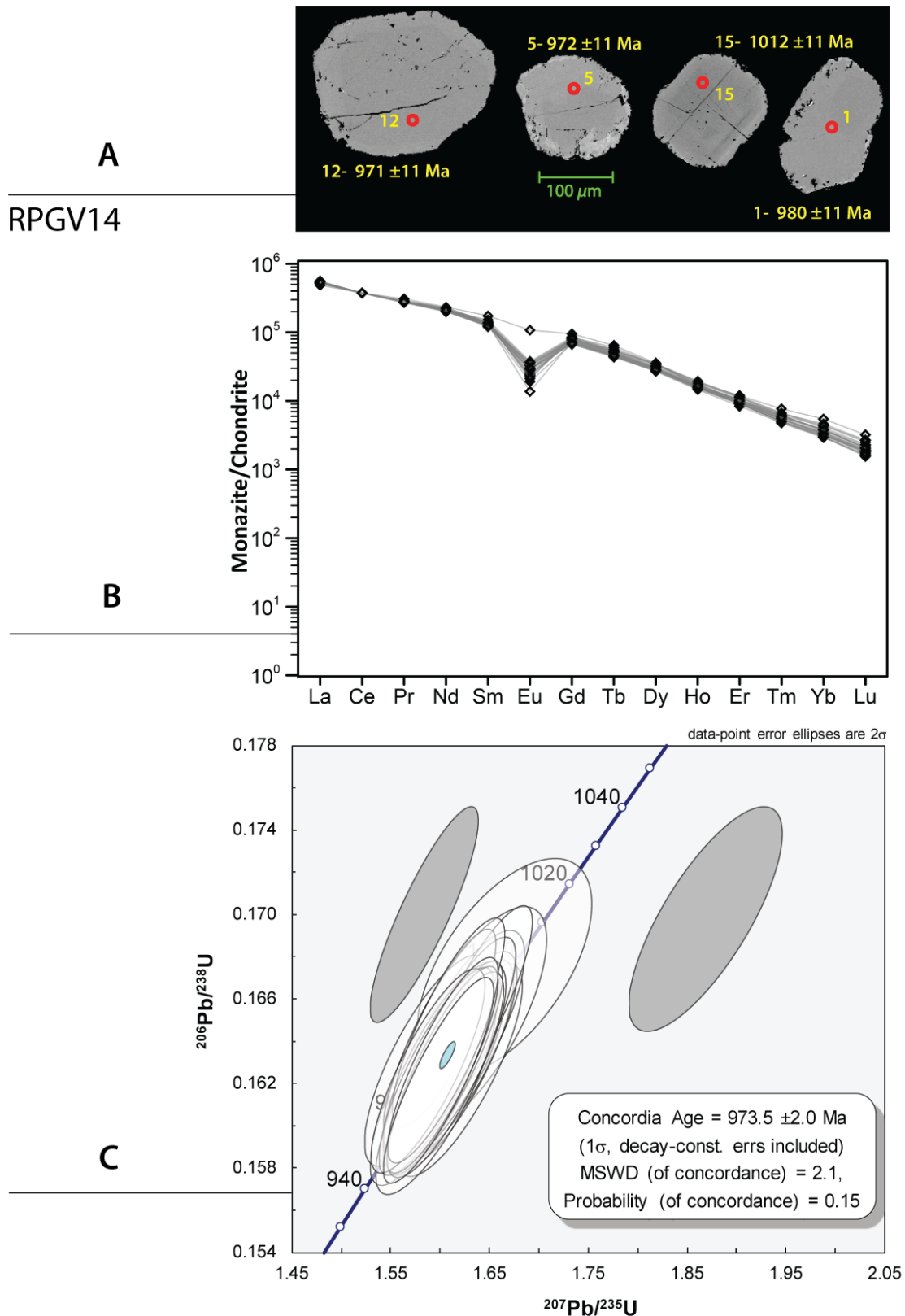


Figure 4.22. A) Representative SEM BSE images of analysed monazite from pegmatite sample RPGV14. Red circles indicate positions of laser pits with a width of  $15\mu\text{m} - 16\mu\text{m}$  (see text) in diameter. Spot dates indicated are  $^{206}\text{Pb}/^{238}\text{U}$  dates with uncertainties on the spot ages given at the  $1\sigma$  level. B) Chondrite-normalised REE diagram for sample RPGV14. Normalised to values from Sun and McDonough (1989). C) Wetherhill concordia diagram for monazite LA-Q-ICP-MS isotope data for pegmatite sample RPGV14, errors are shown as  $2\sigma$  ellipses, excluded analyses are marked as grey ellipses.

## RPGV16

This sample was also obtained from a homogeneous pegmatite that intruded the same rock-type as RPGV14 (above). The sample consists predominantly of K-feldspar with minor quartz and muscovite and contained zircon, monazite and apatite as accessory minerals. Monazite is scarce in this sample, and only a few grains were able to be separated. The grains are generally pale yellow in colour, with a pearly lustre. A subset of grains have a “frosty” (i.e. drusy) appearance, and some grains show an orange-brown Fe coating. The grains are euhedral to subhedral and tabular ( $x=180\ \mu\text{m}$ ,  $y=100\ \mu\text{m}$ ) to equant and rounded ( $120\ \mu\text{m}$  to  $50\ \mu\text{m}$ ) in shape, with some anhedral grains. Internal textures shown in BSE images (Figure 4.23c) range from broad sector compositional zoning to otherwise homogenous grains with a BSE-bright rim. Porous domains, interpreted to be a result from fluid-mediated recrystallisation are evident in all grains, to some degree. However, intact cores of affected grains were analysed, and the porous zones were avoided. Grains with a low degree of alteration commonly exhibited a  $5\ \mu\text{m}$  to  $12\ \mu\text{m}$  wide, BSE bright rim that reflects a higher Th content (Figure 4.23c). This rim was too narrow to analyse.

Monazite U and Th contents vary considerably in the sample; however, the variability is associated with monazite morphology. The majority of euhedral to subhedral grains have moderate U contents ( $U = \sim 164 - 4\ 038\ \text{ppm}$ ) with a broad range in Th concentrations from moderate to very high ( $\text{Th} = \sim 35\ 319 - 174\ 269\ \text{ppm}$ ) and with Th/U in the range of  $\sim 11 - 30$  (Appendix A.2.2). Anhedral and unaltered grains with lower Th/U ratios ( $5 - 7$ ) have high U and Pb contents compared to the monazite mentioned above ( $U = 7\ 303 - 14\ 501\ \text{ppm}$ ) (Appendix A.2.2). Two spots, V16-12 and V16-25, both from a single subhedral grain have similar U, Pb and Th contents but with very high Th/U ratios (66 and 73) (Appendix A.2.2).

The monazite chondrite-normalised REE patterns (Figure 4.23b) are characterised by strong relative enrichment of the LREE with a progressive and smooth decrease in normalised abundances towards the M- and HREE with variable enrichment within the MREEs resulting in a range of  $[\text{La}/\text{Sm}]_N$  values ( $[\text{La}/\text{Sm}]_N = 2-7$ ; Appendix B.2.2; Figure 4.23b). Negative Eu anomalies are variable from moderate to large ( $\text{Eu}/\text{Eu}^* = 0.03 - 0.1$ ; Appendix B.2.2; Figure 4.23b). The monazite REE patterns show variable relative enrichment of the MREE over the HREE ( $[\text{Gd}/\text{Lu}]_N = 22 - 48$ ; Appendix B.2.2). The inherited xenocrystic monazite component (see below) has a higher relative enrichment in MREE over the LREE with a higher and more variable relative depletion of HREE with respect to the MREE compared to the magmatic monazite patterns ( $[\text{Gd}/\text{Lu}]_N = 24 - 973$ ; Appendix B.2.2; Figure 4.23b). This monazite component has a similar negative Eu anomalies ( $\text{Eu}/\text{Eu}^* = 0.03 - 0.1$ ) to that of the magmatic monazite.

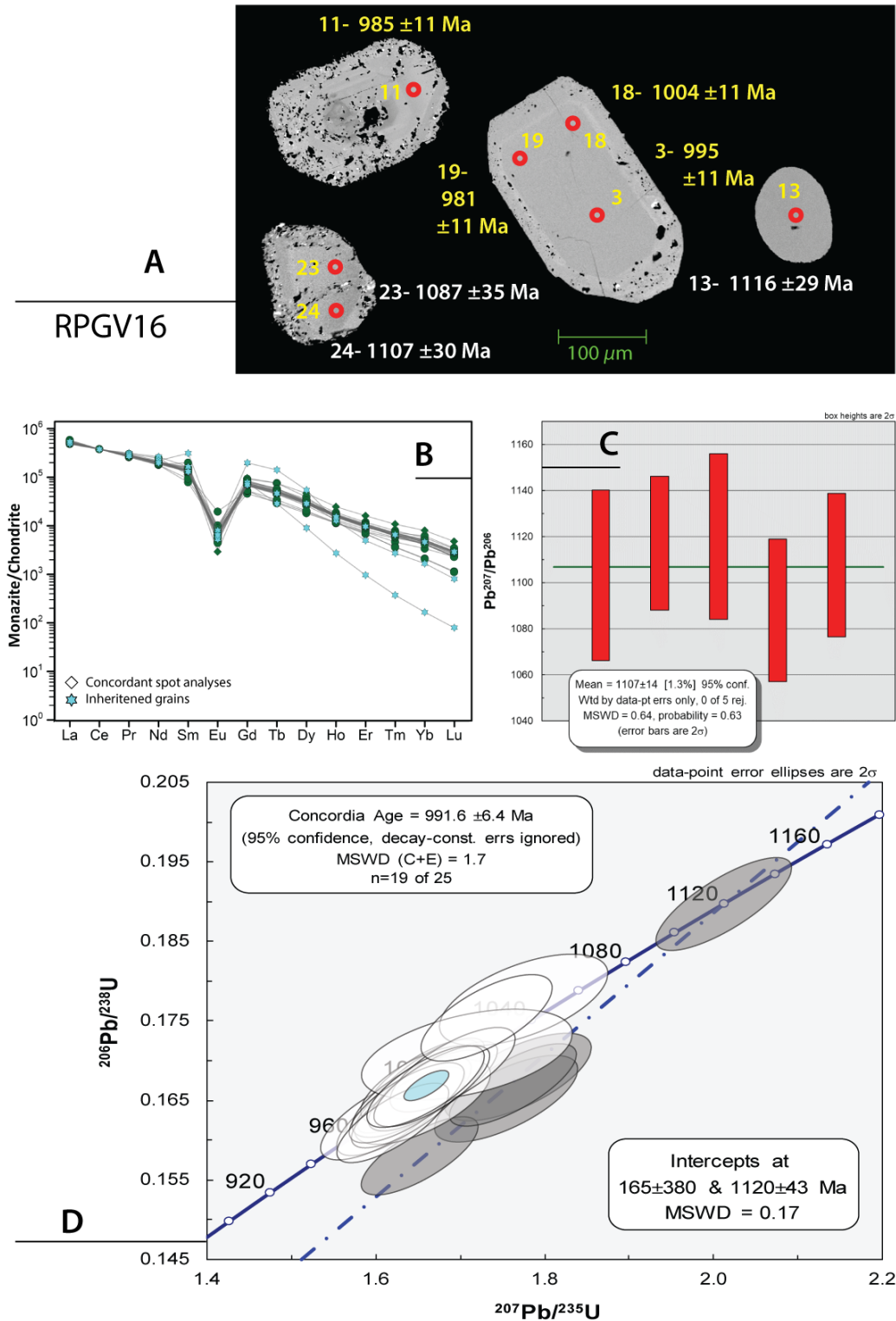


Figure 4.23. A) Representative SEM BSE images of analysed monazite from pegmatite sample RPGV16. Red circles indicate positions of laser pits with a width of 15 μm – 16 μm (see text) in diameter. Spot dates indicated are (yellow text)  $^{206}\text{Pb}/^{238}\text{U}$  dates and (white text)  $^{206}\text{Pb}/^{207}\text{Pb}$  dates with uncertainties on the spot ages given at the 1σ level. B) Chondrite-normalised REE diagram for sample RPGV16. Normalised to values from Sun and McDonough (1989). C.) Weighted mean  $^{207}\text{Pb}/^{206}\text{Pb}$  spot date diagram for pegmatite sample RPGV16 where red boxes are plotted as 2σ errors. D) Wetherhill concordia diagram for monazite LA-Q-ICP-MS isotope data for pegmatite sample RPGV16, errors are shown as 2σ ellipses.

Despite the compositional heterogeneity exhibited in the monazite grains from this sample, most of the U-Pb isotope data cluster tightly on the concordia diagram. This allowed the analyses to be statistically combined to yield a concordia date of  $991.6 \pm 6.4$  Ma ( $2\sigma$ ,  $\text{MSWD}(\text{C+E}) = 1.7$ ,  $n = 19$  of 25; Figure 4.23d), which is interpreted to this date to be the age of crystallisation of monazite in this pegmatite. It is slightly older than the crystallisation age obtained from RPVG14 (above), which intruded the same country rocks.

Five of the monazite U-Pb isotope analyses do not plot with the main concordant group, but instead, define a discordant line segment (84 – 100 % concordant) on the concordia diagram and have older apparent  $^{207}\text{Pb}/^{206}\text{Pb}$  dates from  $1119 \pm 36$  Ma ( $1\sigma$ ) to  $1087 \pm 31$  Ma ( $1\sigma$ ) (Appendix C.2.2). These analyses are interpreted to represent a xenocrystic monazite component, and a linear regression through the discordant data points gave an upper intercept of  $1120 \pm 43$  Ma and lower intercept of  $165 \pm 380$  Ma ( $\text{MSWD} = 0.17$ ; Figure 4.23d). The lower intercept age is consistent with recent Pb loss. A weighted mean  $^{207}\text{Pb}/^{206}\text{Pb}$  age of  $1107 \pm 14$  Ma (95% confidence;  $\text{MSWD} = 0.65$ , probability = 0.63, Figure 4.23c) was calculated for the inherited component. Due to its higher precision, the weighted mean date is interpreted to be the age of crystallisation of the xenocrystic monazites in this pegmatite.

### *SDORPB15-10*

This sample is from a homogenous pegmatite that intruded the ~1870 Ma Goodhouse subsuite gneisses. This relatively small (5m thick) pegmatite intruded the host gneisses concordantly along the regional foliation and is composed chiefly of feldspar, quartz, centimetre-scale (1 – 3 cm) garnets with minor muscovite. Zircon, apatite, monazite and magnetite occur as accessory phases. This sample contains small (~80 - 135  $\mu\text{m}$  in diameter) anhedral to subhedral, equant monazite grains. In BSE images (Figure 4.24a), the grains show broad sector- to polygonal zoning. Some grains have a homogenous core with Th-rich, BSE-bright rims. The grains generally show little alteration except for local development of spongy porous rims that are interpreted to represent late fluid-mediated replacement (Figure 4.24a).

The composition of the analysed monazite is highly variable with no distinct trend with respect to monazite compositional zoning. The monazite has concentrations of U (~1 412 – 7 354 ppm) and Th concentrations (46 849 – 229 071 ppm), with Th/U ranging from 14 to 64 (Appendix A.2.3). The variations in Si, Ca and Y followed this trend being highly variable with concentrations of 669 – 13 707 ppm, 7 216 – 34 211 ppm and 13 756 – 40 601 ppm respectively. Monazite chondrite-normalised REE patterns (Figure 4.24b) show a minor relative enrichment of LREE over the MREE with  $[\text{La}/\text{Sm}]_{\text{N}}$  values between 3 and 5 (Appendix A.2.3). Moderate negative Eu anomalies characterise the REE patterns ( $\text{Eu}/\text{Eu}^* = 0.2 - 0.3$ ; Appendix A.2.3; Figure 4.24b) and show variable but parallel relative enrichment of the MREE over the HREE ( $[\text{Gd}/\text{Lu}]_{\text{N}} = 21 - 56$ ; Appendix B.3.4).

Fifteen U-Pb isotopic analyses were taken from 12 monazite grains. Two of those analyses had to be excluded due to a lack of domains of uniform  $^{207}\text{Pb}/^{206}\text{Pb}$  in the time-resolved analyses, possibly due to multiple inclusions of other U-bearing minerals. The remaining 13 straddled the concordia line (98 – 103 % concordant, Figure 4.24c; Appendix C.2.3) with a range in apparent  $^{207}\text{Pb}/^{206}\text{Pb}$  spot dates from  $1052 \pm 28$  Ma ( $1\sigma$ ) to  $984.6 \pm 25$  Ma ( $1\sigma$ ) (Appendix C.2.3). These 13 spot analyses could be combined to yield a concordia age of  $1016 \pm 5.7$  Ma (95% c.l.,  $\text{MSWD}(\text{C}+\text{E}) = 1.7$ ; Figure 4.25), which is interpreted to date monazite crystallisation in the pegmatite.

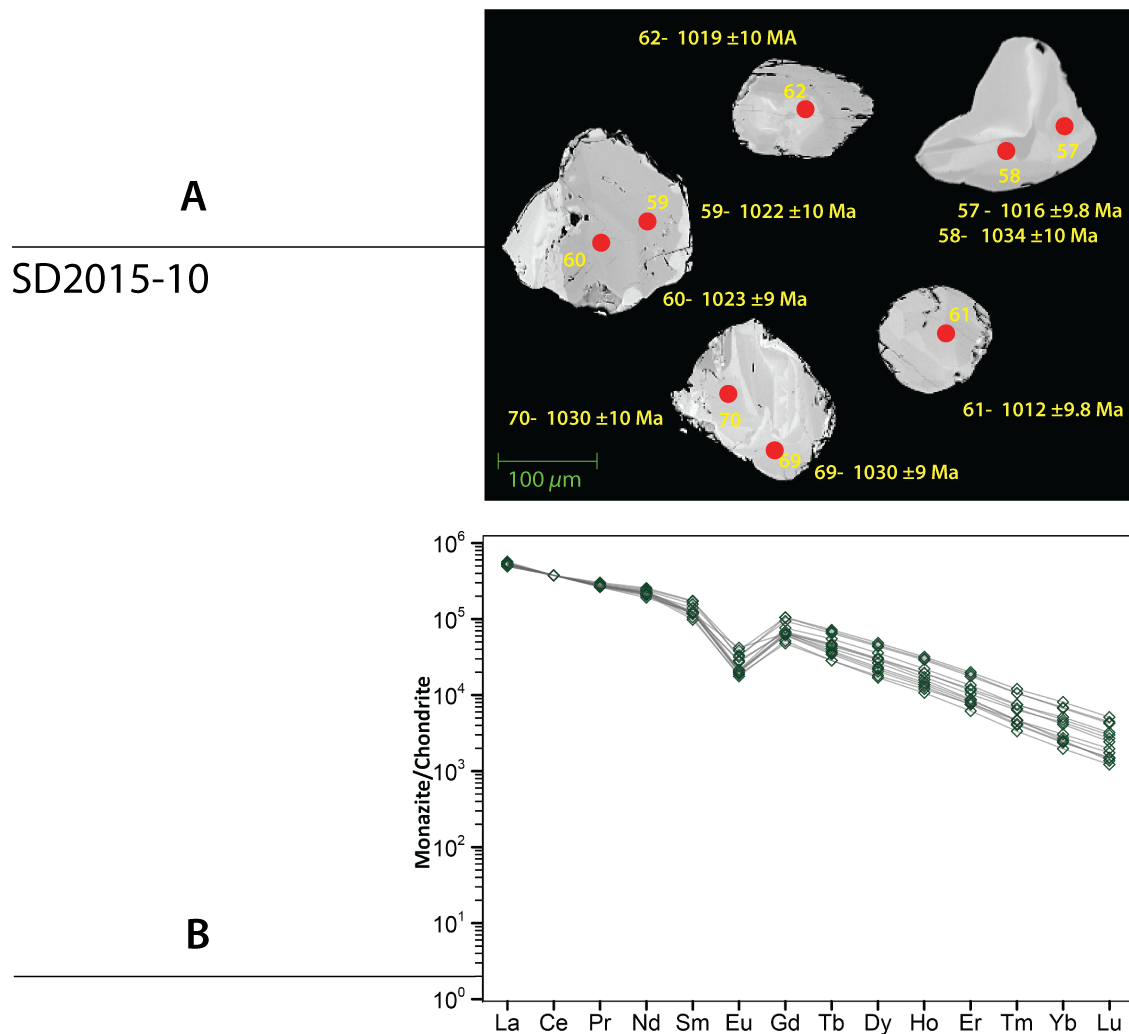


Figure 4.24. A) Representative SEM BSE images of analysed monazite from pegmatite sample SDORPB15-10. Red circles indicate positions of laser pits with a width of  $15\mu\text{m} - 16\mu\text{m}$  (see text) in diameter. Spot dates indicated are  $^{206}\text{Pb}/^{238}\text{U}$  dates with uncertainties on the spot ages given at the  $1\sigma$  level. B) Chondrite-normalised REE diagram for sample SDORPB15-10. Normalised to values from Sun and McDonough (1989).

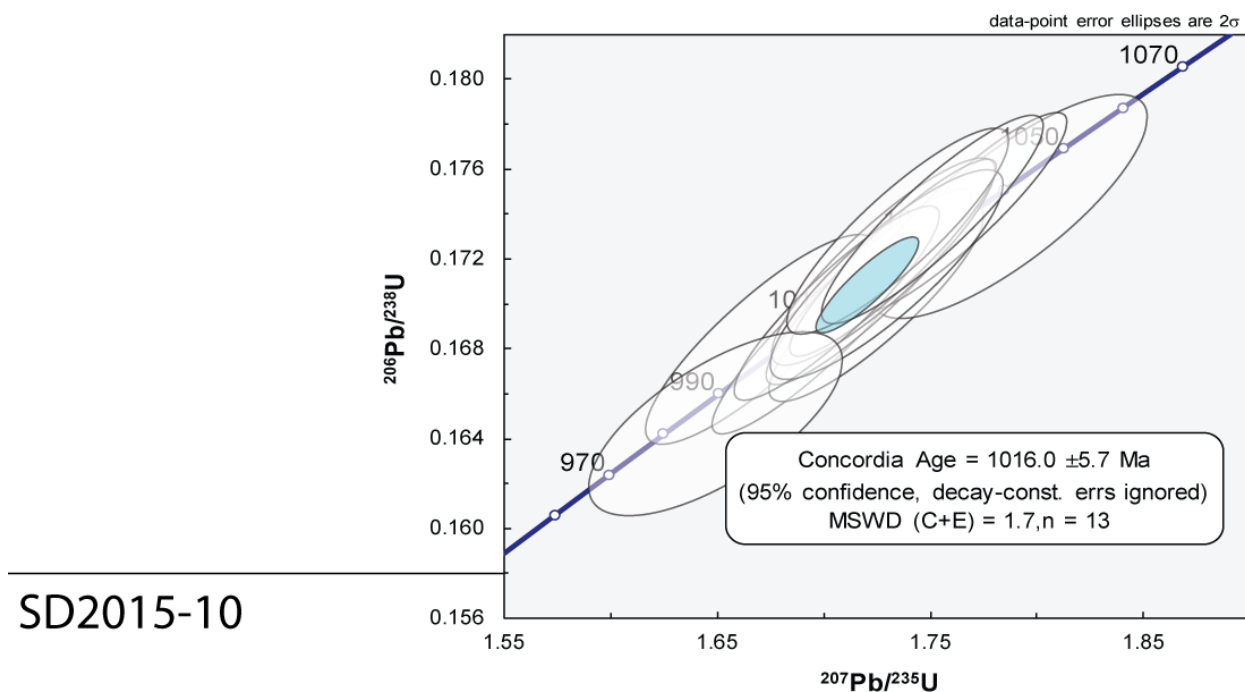


Figure 4.25: Wetherhill concordia diagram for monazite LA-Q-ICP-MS isotope data for pegmatite sample SDORPB15-10, errors are shown as  $2\sigma$  ellipses.

### SD2015-13

This sample was obtained from a pegmatite that intruded migmatitic hornblende-biotite-quartz-feldspar gneiss of the  $\sim 1875$  Ma Umies gneiss of the Goodhouse Subsuite. The sample locality is situated along the road towards the "Homestead" of the Tantalite Valley pegmatite mine within reworked gneisses that were reworked adjacent to the a major D4 Marshal Rocks Pofadder Shear Zone. K-feldspar and muscovite dominated the main pegmatite mineralogy with a minor quartz component. Accessory minerals present are garnet, zircon, apatite and monazite.

Accessory minerals are rare in this sample, and only a few anhedral grains of monazite were retrieved. These anhedral, rounded to angular grains vary in size from  $50 \mu\text{m}$  to  $120 \mu\text{m}$  in diameter and locally display embayed grain boundaries. Internal compositional zoning is present as either fine- or broad-scale sector zoning, with many grains having multiple fractures (Figure 4.26a). Two grains exhibit porous to patchy alteration zones due to fluid-mediated recrystallisation.

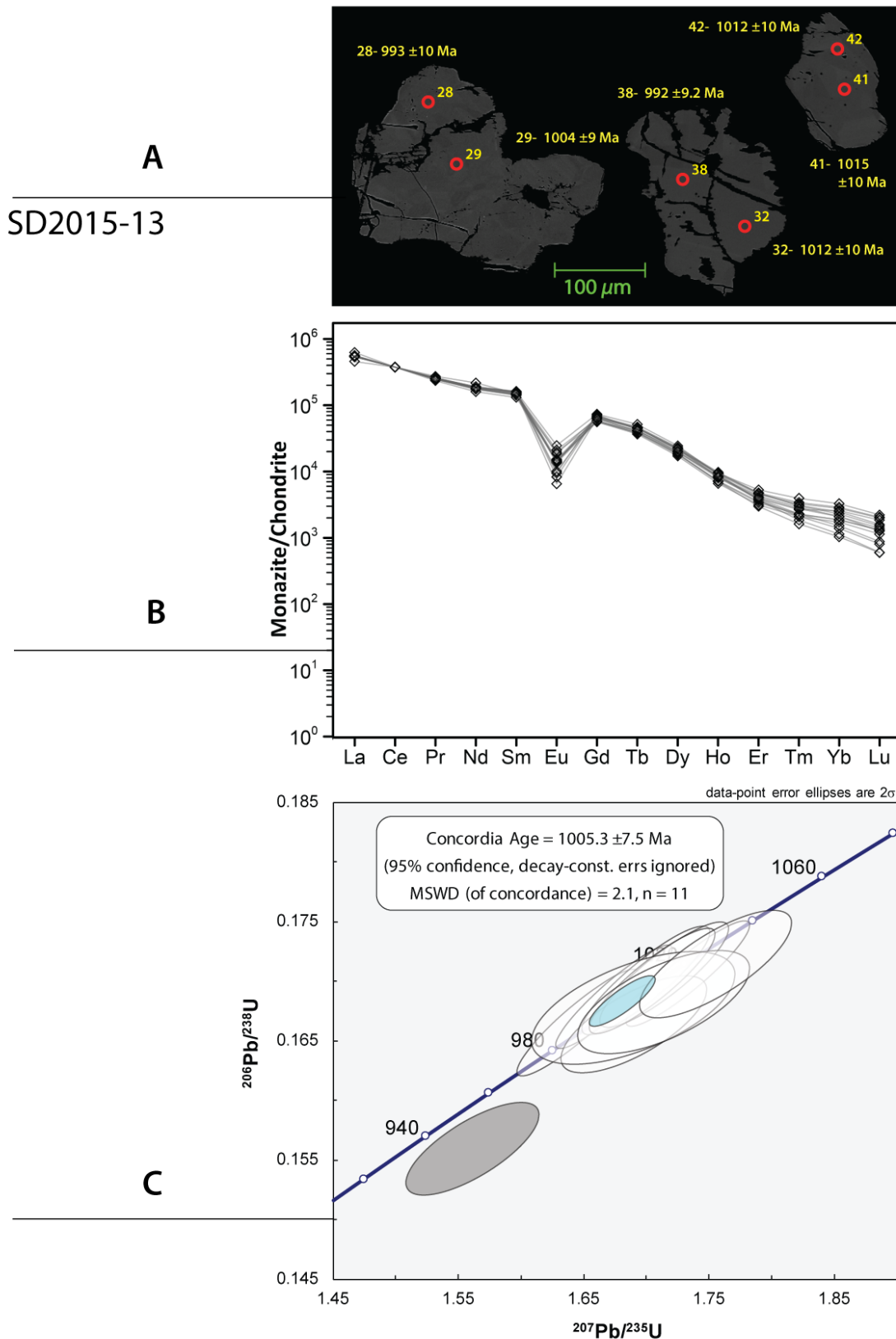


Figure 4.26. A) Chondrite-normalised REE diagram for sample SD2015-13. Normalised to values from Sun and McDonough (1989). B) Representative SEM BSE images of analysed monazite from pegmatite sample SD2015-13. Red circles indicate positions of laser pits with a width of  $15\mu\text{m} - 16\mu\text{m}$  (see text) in diameter. Spot dates indicated are  $^{206}\text{Pb}/^{238}\text{U}$  dates with uncertainties on the spot ages given at the  $1\sigma$  level. C) Wetherhill concordia diagram for monazite LA-Q-ICP-MS isotope data for pegmatite sample SD2015-13, errors are shown as  $2\sigma$  ellipses, excluded analyses are marked as grey ellipses..

The monazite grains show a range in Si (2 414 – 6 983 ppm), Ca (1 614 – 4 912 ppm) and Y (7 849 – 13 163 ppm) concentrations. The chondrite-normalised REE patterns (Figure 4.26b) are characterised by a relative enrichment of L-MREE over HREE, with the LREEs having a progressive decrease in abundances towards the MREE with  $(La/Sm)_N$  from 3-5 (Appendix B.2.4). Eu anomalies are moderate and negative with variable  $Eu/Eu^*$  from 0.06 to 0.2 (Appendix B.2.4; Figure 4.26b). Relative enrichment of the MREE over the HREE is moderate but quite variable (Figure 4.26b) of the REE patterns at the HREE end ( $[Dy/Lu]_N = 32 - 122$ ; Appendix B.3.1).

Fourteen U-Pb isotope analyses were obtained from 8 grains that have minimal fracturing and alteration. However, three analyses that are highly discordant (45 to 75% concordant, Appendix C.2.4) were discarded due to not having  $^{207}Pb/^{206}Pb$  plateaus in the time-resolved signal. This may be due to the effects of fluid-mediated dissolution and precipitation as these grains are heavily altered. Another one U-Pb isotope analysis was excluded from further consideration due to being 93 % concordant (Appendix C.2.4) and suffering possible lead loss.

The remaining 10 spots have a moderate variation with respect to U and Th concentrations ( $U = \sim 751 - 2\ 036$  ppm,  $Th = \sim 2.3 - 3.4$  wt%; Appendix C.2.4) with one spot (043d1311) having very high U and Th concentrations ( $U = \sim 8\ 283$  ppm,  $Th = \sim 26$  wt%). Despite the high U and Th concentrations for 043d1311, the Th/U ratio ( $Th/U = 31$ ) are within the range of the remaining analyses ( $Th/U = 11 - 47$ ; Appendix C.2.4). These ten analyses could be combined to yield a concordia date of  $1\ 005 \pm 7.5$  Ma (95% c.i., MSWD of concordance = 2.1, probability of concordance = 0.61;  $n=10$ ; Figure 4.26c), which is interpreted to be the age of crystallisation of monazite in this pegmatite.



## 4.1.2 Lower Fish River Onseepkans Thrust Zone

### *HS15HF1*

The monazite from sample HS15HF1 came from a simple and homogenous pegmatite that intruded the variably sheared and re-equilibrated meta-pelitic schists and gneisses of the Veloursdrif paragneiss succession within the LFRÖTZ. The sample was obtained close to the footwall of the Lower Fish River-Onseepkans thrust. The mineral assemblage of the sample is predominantly K-feldspar and quartz with minor muscovite, with accessory magnetite, garnet, monazite, zircon and apatite.

Monazite from this sample is transparent and pale yellow in colour. Most grains are subhedral to round, with some having a euhedral, tabular habit. BSE images show that most of the grains exhibit magmatic oscillatory zoning, are in general inclusion free and lack visible fractures or zones of recrystallisation (Figure 4.27a). Zoning is present mostly in the euhedral grains and in some subhedral and rounded grains. Subhedral and elongated grains lacking oscillatory zoning exhibit compositional zonation as either broad compositional sector zoning (observed in BSE images as BSE bright and BSE dark zones) or homogenous BSE dark cores with BSE bright rims. A number of grains have a thin but very bright Th rich rims that were too narrow (~5µm) to analyse using laser ablation. Tabular equant grains are ~180 µm in diameter, while the rounded grains range in size from 80 µm to 120 µm.

Despite apparent zoning in the monazite grains, the major-element composition of the monazite is relatively homogenous with little to no range in total LREE of ~52 wt% across all the grains and zones. Monazite Th/U ratios range from 3 to 11 reflecting variations in Th and U concentrations from 49 680 to 122 022 ppm and 8 438 to 18 939 ppm respectively (Appendix A.3.1). The chondrite-normalised REE patterns (Figure 4.27b) are characterised by a relative enrichment of L-MREE over HREE, with the LREEs having a nearly flat profile with  $(La/Sm)_N$  of ~1.7 (Appendix B.3.1). Chondrite-normalised abundances decreased monotonically from the MREE to the HREE ( $(Dy/Lu)_N$  of ~86; Appendix B.3.1). Eu anomalies are large and negative with  $Eu/Eu^*$  of 0.01 (Appendix B.3.1; Figure 4.27b).

Despite varying U and Th concentrations within and between the different grains, there is very little dispersion of U-Pb isotope compositions and apparent  $^{207}Pb/^{206}Pb$  and  $^{206}Pb/^{238}U$  ages; from  $985 \pm 31$  Ma ( $1\sigma$ ) to  $936 \pm 24$  Ma ( $1\sigma$ ) and  $984 \pm 11$  Ma ( $1\sigma$ ) to  $943 \pm 11$  Ma ( $1\sigma$ ), respectively (Appendix C.3.1). All 25 analyses clustered on the concordia diagram (97 to 104% concordant), yielding a concordia date of  $966 \pm 3.5$  Ma ( $2\sigma$ ,  $MSWD(C+E) = 0.66$ ,  $n = 25$ ; Figure 4.27c). This date is interpreted to represent the monazite crystallisation age of this pegmatite.

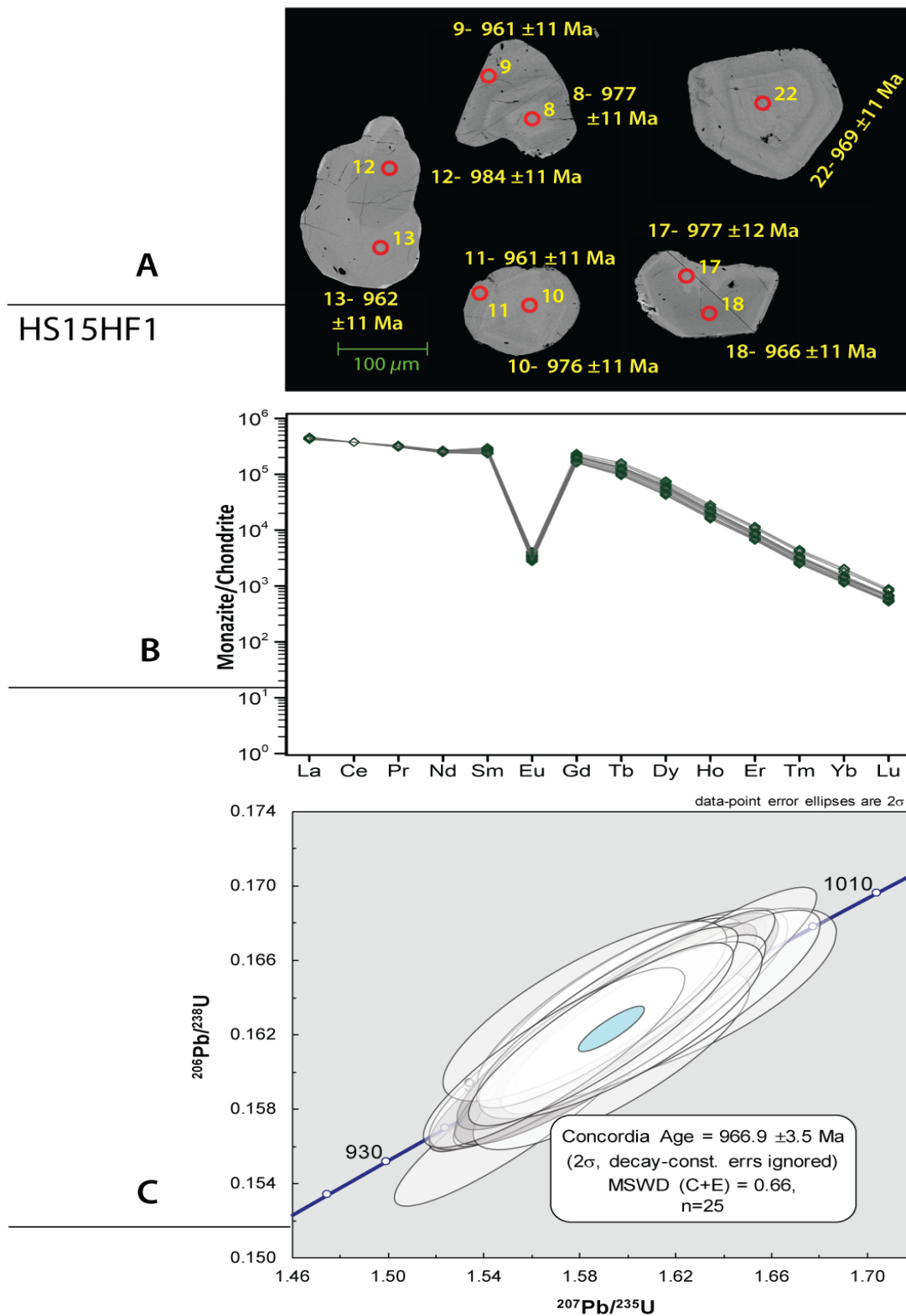


Figure 4.27. A) Representative SEM BSE images of analysed monazite from pegmatite sample HS15HF1. Red circles indicate positions of laser pits with a width of 15 μm – 16 μm (see text) in diameter. Spot dates indicated are  $^{206}\text{Pb}/^{238}\text{U}$  dates with uncertainties on the spot ages given at the 1σ level. B) Chondrite-normalised REE diagram for sample HS15HF1. Normalised to values from Sun and McDonough (1989). C) Wetherhill concordia diagram for monazite LA-Q-ICP-MS isotope data for pegmatite sample HS15HF1, errors are shown as 2σ ellipses.

*SDORPB15-15c*

Sample SDORPB15-15c was taken from a pegmatite that intruded the ~1200 Ma Schuitklip megacrystic biotite augen gneiss (meta-granodiorite) within the LFROTZ. This simple pegmatite sample contained K-feldspar and quartz, minor muscovite and with monazite, zircon and apatite as accessory minerals. The mineral separation yielded low amounts of accessory minerals, and only six usable monazite grains were recovered. Monazite grains obtained from this sample are pale green-yellow in colour with an orange-brown Fe stained exterior that gave the grains an earthy to waxy lustre.

Four of the six grains are euhedral to subhedral and tabular in shape with one of the four grains being equant. These grains show irregular broad sector compositional zoning under BSE imaging. The two larger grains in this subset, exhibit patchy alteration zones due to fluid-mediated recrystallisation (Figure 4.28a). Fracturing within the grains is present to a limited degree. The BSE dark sectors in the monazite have relatively low to moderate U concentrations (1 082 – 1 556 ppm), moderate to high Th (28 894 – 49 452 ppm) and a small range in Si (2 418 – 3 917 ppm) and Ca (1 867 – 4 109 ppm) concentrations (Appendix A.3.2), with moderate Th/U ratios (20 – 34; Appendix A.3.2). BSE bright sectors in these monazites have a higher overall Th (71 815 – 96 204 ppm), U (1 973 – 2426 ppm), Si (4 508 – 6 460 ppm) and Ca (6 247 – 7 849) concentrations (Appendix A.3.2), with slightly higher Th/U ratios (36 to 40; Appendix A.3.2). The two remaining monazite grains of the group of six are anhedral. One of these is highly altered with recrystallisation textures and embayed grain boundaries. It has lower U (899 to 1 063 ppm) concentrations with Si (2 769 – 4 107 ppm), Ca (1 853 – 2 547 ppm) and Th (27 485 – 40 439 ppm) concentrations (Appendix A.3.2) similar to the other four subhedral to euhedral grains.

Monazite chondrite-normalised REE patterns (Figure 4.28b) are tightly grouped and characterised by strong relative enrichment of LREE with a progressive and smooth decrease in normalised abundances towards the HREE apart from minor variations in the MREE abundances (Sm and Gd). This trend in normalised REE abundances results in a range of  $[La/Sm]_N$  values from 3 to 9 (Appendix C.3.3.) with the anhedral grains having lower relative M-REE enrichment (Figure 4.28b). All REE patterns have a moderate negative Eu anomalies ( $Eu/Eu^* = 0.1 - 0.2$ ; Appendix C.4.1; Figure 4.28b) with a moderate relative depletion in HREE with respect to the MREE ( $[Gd/Lu]_N = 20 - 42$ ; Appendix C.4.1).

Fifteen spot U-Pb analyses were taken from the six monazite grains; of these, two spot analyses were omitted due to them being more than 10% discordant due to extensive recrystallisation. The remainder (n=12) clustered on the concordia line and yielded apparent  $^{207}Pb/^{206}Pb$  and  $^{206}Pb/^{238}U$  dates ranging from  $998 \pm 34$  Ma ( $1\sigma$ ) to  $961 \pm 23$  Ma ( $1\sigma$ ) and  $1004 \pm 10$  Ma ( $1\sigma$ ) to  $956 \pm 9$  Ma ( $1\sigma$ ), respectively (Appendix C.3.2). The twelve analyses could be combined to yield a concordia date of  $979 \pm 5.8$  Ma (95% c.i.,  $MSWD(C+E) = 1.6$ ; Figure 4.28c) which is interpreted to be the monazite crystallisation age in this pegmatite.

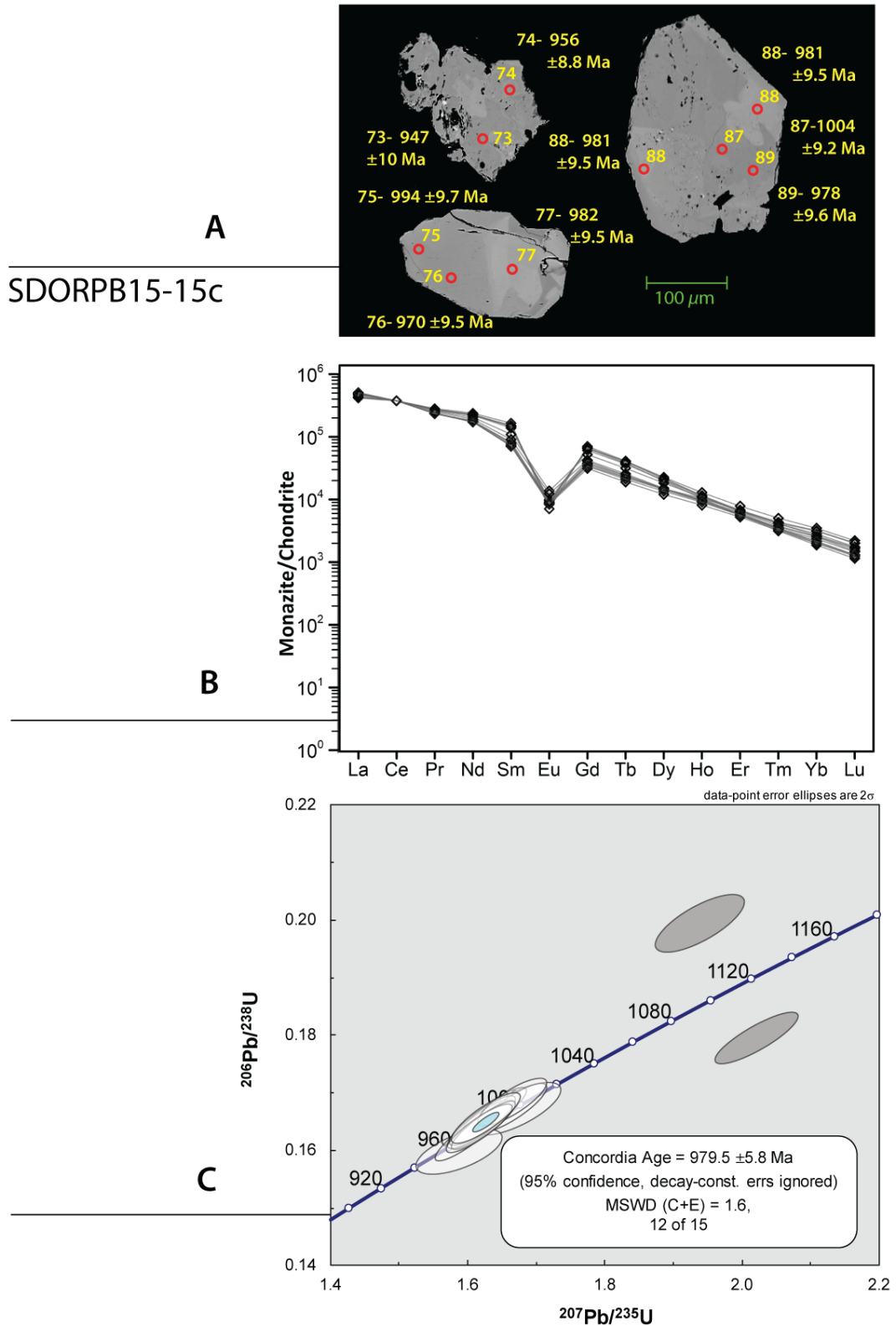


Figure 4.28 A) Representative SEM BSE images of analysed monazite from pegmatite sample SDORPB15-15C. Red circles indicate positions of laser pits with a width of  $15\mu\text{m} - 16\mu\text{m}$  (see text) in diameter. Spot dates indicated are  $^{206}\text{Pb}/^{238}\text{U}$  dates with uncertainties on the spot ages given at the  $1\sigma$  level. B) Chondrite-normalised REE diagram for sample SDORPB15-15C. Normalised to values from Sun and McDonough (1989). C) Wetherill concordia diagram for monazite LA-Q-ICP-MS isotope data for pegmatite sample SDORPB15-15C, errors are shown as  $2\sigma$  ellipses, excluded analyses are marked as grey ellipses.

## SDORPB16-6

This sample was taken from an LCT-type pegmatite, known as Konkonsies, that intruded the ~1220 Ma Oupvlakte meta-basites and ~1210 Beenbreek megacrystic granite gneiss close to the D2 Tafelkop Shear zone. This pegmatite has been mined in the past for tantalite as well as for beryl and feldspar with sporadic columbite also being recovered. It is a large zoned pegmatite, creating a small prominent hill. The sample came from a garnet and muscovite-rich zone within the quartz, K-feldspar-rich pegmatite and contains abundant garnet, monazite, zircon, columbite-tantalite, apatite and xenotime. The pegmatite has been mined out so full details of its heterogeneity, zoning and complete mineralogy were difficult to determine.

Monazite from the sample has two distinct forms. One population is euhedral and tabular to prismatic ( $n=3$ ). The other population is anhedral and rounded ( $n=4$ ). The euhedral population are large and tabular ( $x/y = \sim 120 - 200 \mu\text{m} / \sim 100 - 170 \mu\text{m}$ ). The grains have weak oscillatory compositional zoning and altered rims due to fluid-mediated dissolution and recrystallisation (Figure 4.29a). Compositionally, the monazite in this population has high Si (15 279 – 22 530 ppm), low Ca (1 219 – 4 532 ppm), high Y (17 509 – 23 504 ppm) concentrations. U/Th ratios have values between 14 and 22 reflecting high Th (106 542 – 167 999 ppm) and moderate U (6 374 – 7 643 ppm) concentrations (Appendix A.3.3).

The monazite chondrite-normalised REE patterns (Figure 4.29b) for this population are characterised by a moderate enrichment of LREE over the MREE with a near flat profile towards the MREE ( $[\text{La}/\text{Sm}]_N = \sim 2$ ; Appendix B.3.3), a large negative and variable Eu anomaly ( $\text{Eu}/\text{Eu}^* = 0.01 - 0.0005$ ; Figure 4.29b) and moderate depletion of the HREE over the MREE ( $[\text{Gd}/\text{Lu}]_N = 72 - 80$ ; Appendix B.3.3). Monazite U-Pb isotope analyses for these monazite grains are 100 to 103% concordant resulting in a narrow range in apparent  $^{207}\text{Pb}/^{206}\text{Pb}$  dates from  $992 \pm 22 \text{ Ma}$  to  $962 \pm 24 \text{ Ma}$  ( $1\sigma$ ; Appendix C.3.3).

From the euhedral monazite grains, one grain has higher HREE concentrations due to a relatively lower and variable depletion in the HREE over MREE ( $[\text{Gd}/\text{Lu}]_N = 4 - 31$ ; Appendix B.3.3; Figure 4.29b). This monazite grain also has much higher Y (20 731 – 133 545 ppm) and Ca (6 561 – 40 712 ppm) concentrations than the main monazite population. U-Pb isotope data for this grain is variably discordant (17 – 87% concordant) with much older  $^{207}\text{Pb}/^{206}\text{Pb}$  spot dates from  $2 437 \pm 18 \text{ Ma}$  to  $1 782 \pm 24 \text{ Ma}$  ( $1\sigma$ ; Appendix C.3.3). Based on their high discordancy, they were not considered for further statistical calculations.

The rounded anhedral monazite grains (100 to 150  $\mu\text{m}$  in diameter) exhibit sector compositional zoning that is embayed by zones of fluid-mediated recrystallisation (Figure 4.29a). One monazite grain is homogenous and lacked the zoning patterns mentioned above. Compositionally, these monazites have a range in Si (2 826 – 10 747 ppm), Ca (2 934 – 15 171 ppm) and Y (1 179 – 17 678 ppm) concentrations (Appendix A.3.3). Th and U concentrations are generally lower, ranging from 38 128 – 110 616 ppm and 791 – 9 359 ppm, respectively, with a spread in Th/U ratios from 7.9 to 48 (Appendix A.3.3).

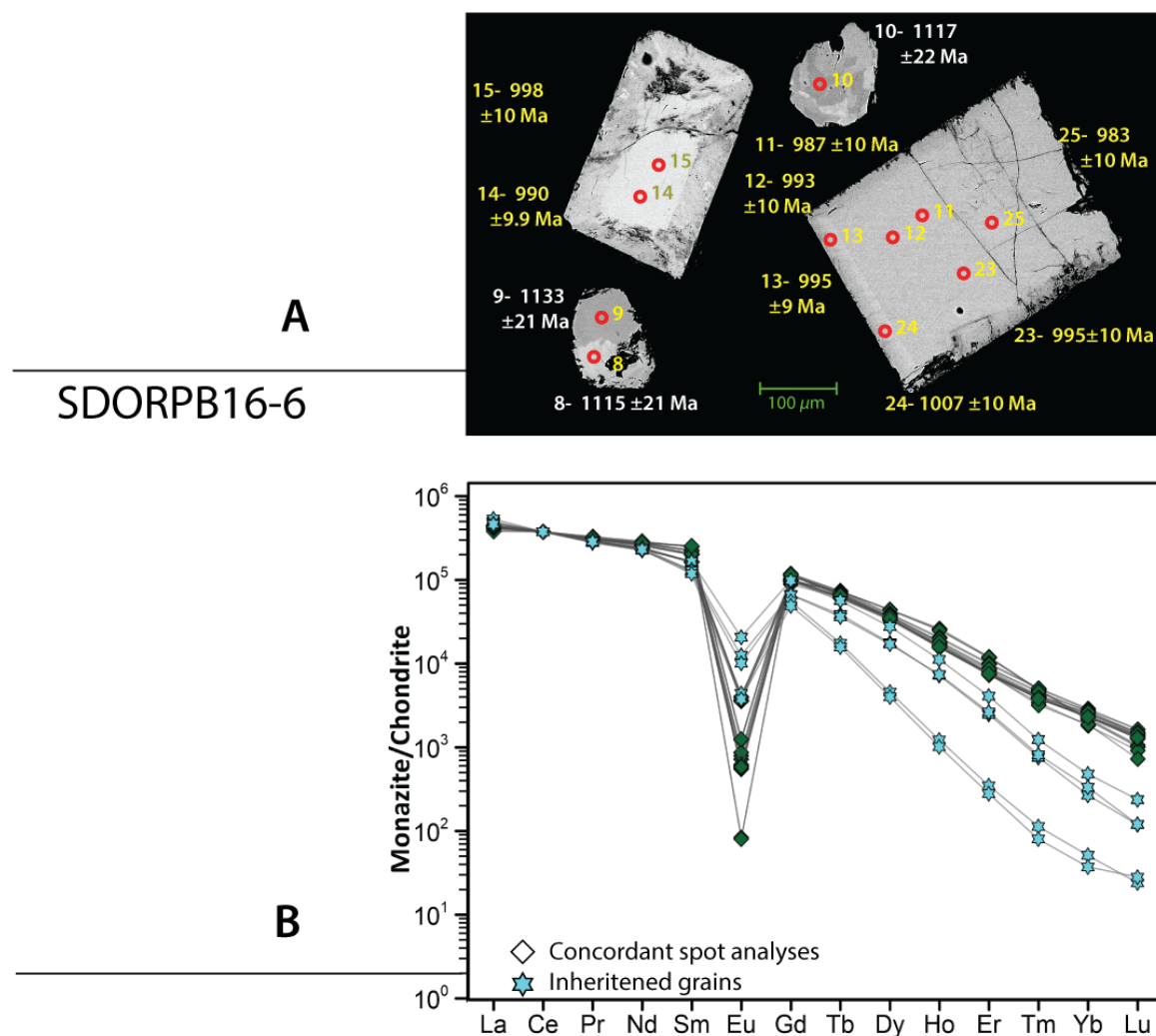


Figure 4.29. A) Representative SEM BSE images of analysed monazite from pegmatite sample SDORPB16-6. Red circles indicate positions of laser pits with a width of  $15\mu\text{m} - 16\mu\text{m}$  (see text) in diameter. Spot dates indicated are (yellow text)  $^{206}\text{Pb}/^{238}\text{U}$  dates and (white text)  $^{206}\text{Pb}/^{207}\text{Pb}$  dates with uncertainties on the spot ages given at the  $1\sigma$  level. B) Chondrite-normalised REE diagram for sample SDORPB16-6. Normalised to values from Sun and McDonough (1989).

The monazite chondrite-normalised REE patterns (Figure 4.29b) for this population are characterised by a moderate enrichment of LREE of MREE with a near flat profile towards the MREE with a drop in Sm normalised abundances resulting in higher  $[\text{La}/\text{Sm}]_N$  values of  $\sim 4$  (Appendix B.3.3). The REE patterns are characterised by large to moderate negative Eu anomalies ( $\text{Eu}/\text{Eu}^* = 0.01 - 0.1$ ; Figure 4.29b) and a large but variable higher depletion of the HREE over the MREE ( $[\text{Gd}/\text{Lu}]_N = 415 - 2310$ ; Appendix B.3.3). Monazite U-Pb isotope data for this monazite population are 84 to 102 % concordant with two distinct ranges apparent for  $^{207}\text{Pb}/^{206}\text{Pb}$  spot dates, one at  $973 \pm 25 \text{ Ma}$  to  $972 \pm 26 \text{ Ma}$  ( $1\sigma$ ,  $n=2$ ; Appendix C.3.3) and another from  $1134 \pm 21 \text{ Ma}$  to  $1108 \pm 26 \text{ Ma}$  ( $1\sigma$ ,  $n=5$ ; Appendix C.3.3). The younger age population is from a rounded anhedral grain that lacked any compositional zoning and have much higher Y concentrations.

Twelve U-Pb isotope spot analyses from the euhedral monazite and the younger two from the anhedral monazite could be combined statistically to yield a concordia date of  $986 \pm 3.9$  Ma ( $2\sigma$ , MSWD (C+E) = 1.2,  $n=14$ ; Figure 4.30a), which is interpreted to be the crystallisation age of the magmatic monazite component. The five U-Pb isotope analyses from the anhedral monazite resulted in a line segment through the discordant data points that gave an upper intercept date of  $1123 \pm 9.4$  Ma and lower intercept of  $41 \pm 180$  Ma (MSWD = 1.4;  $n=5$ ; Figure 4.30a). As with the other samples, the lower intercept is interpreted to indicate recent Pb loss. The upper intercept date is within error of the weighted mean  $^{207}\text{Pb}/^{206}\text{Pb}$  date of  $1121 \pm 110$  (95% conf.; MSWD = 0.006; probability = 1.0; Figure 4.30b). Due to the higher precision, the upper intercept date is interpreted to be the best estimate for the crystallisation age of this xenocrystic monazite component.

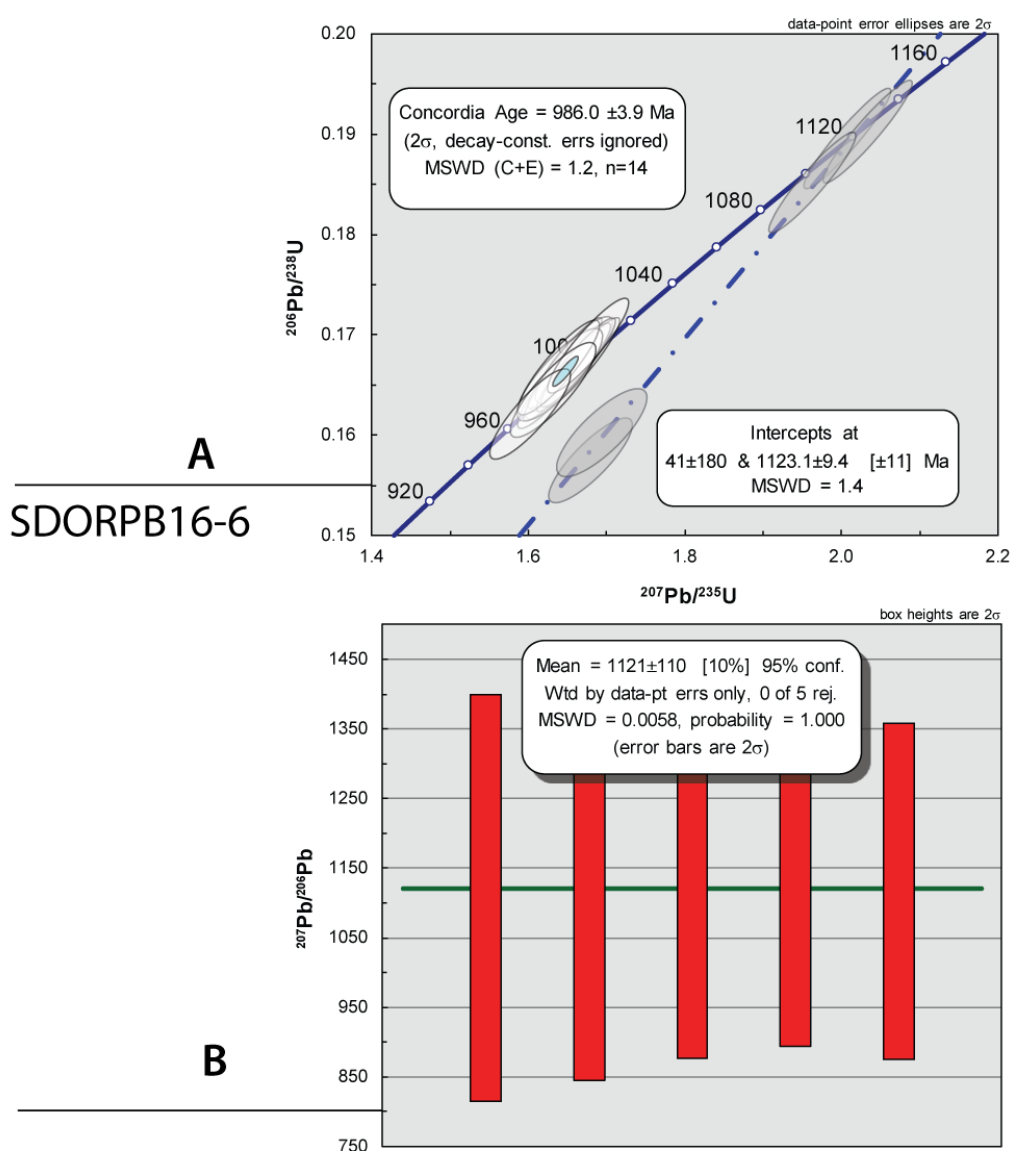


Figure 4.30: A.) Wetherhill concordia diagram for monazite LA-Q-ICP-MS isotope data for pegmatite sample SDORPB16-6, errors are shown as  $2\sigma$  ellipses. B.) Weighted mean diagram for  $^{207}\text{Pb}/^{206}\text{Pb}$  spot dates for monazite from sample SDORPB16-6 where red boxes are plotted as  $2\sigma$  errors.

## SDORPB16-7b

This sample comes from a pegmatite that intruded the ~1200 Ma Beenbreek garnet-bearing megacrystic granite gneiss within the LFROTZ, close to the D2 Tafelkop Shear zone. This zoned, REE-enriched pegmatite was once mined for columbite-tantalite and beryl and hosts plagioclase, K-feldspar, quartz, garnet, muscovite and biotite, with monazite, zircon and apatite as accessory minerals.

The monazite recovered from this sample generally consists of anhedral grain fragments (~200 µm in diameter), although rounded, anhedral to subhedral (~80 – 150 µm in diameter) grains are also present. Limited and weak broad compositional and polygonal sector zoning is present in some grains in BSE images. Most grains have embayed grain boundaries and highly altered rims due to fluid-mediated recrystallisation (Figure 4.31a). Similar alteration, characterised by porous zones, occur along fracture planes.

Despite the differing grain morphologies, the U and Th concentrations show no systematic differences between different grains. U and Th concentrations are moderate to high (~3 907 – 8 522 ppm and ~65 016 – 139 126 ppm respectively), and Th/U ratios vary from 9 to 20 (Appendix A.3.4). Y (16 923 – 30 648 ppm) and Ca (8 316 – 17 603 ppm) show moderate ranges in concentrations (Appendix A.3.4). Monazite chondrite-normalised REE patterns (Figure 4.31b) are flat from the LREE to the MREE ( $[La/Sm]_N = 1-2$ ), with a large negative Eu anomaly ( $Eu/Eu^* = 0.002 - 0.003$ ; Figure 4.31b) and show variable relative enrichment of the MREE over the HREE ( $[Gd/Lu]_N = 24 - 64$ ; Appendix B.3.4).

Thirty spot analyses were obtained from 22 monazite grains. Twenty-nine U-Pb analyses are concordant to near-concordant (98 to 103% concordant; Appendix C.3.4). One analysis is discordant (88% concordant) and was omitted from the final age calculation. The remaining 29 analyses cluster on the concordia line, with a range in apparent spot  $^{207}Pb/^{206}Pb$  dates from  $1011 \pm 24$  Ma ( $1\sigma$ ) to  $954 \pm 26$  Ma ( $1\sigma$ ) (Appendix C.3.4). All 29 analyses could be combined statistically to yield a concordia date of  $994 \pm 3.2$  Ma ( $2\sigma$ , MSWD (C+E) = 0.81, n = 29; Figure 4.31c) that is interpreted to be the age of crystallisation of monazite in this pegmatite.



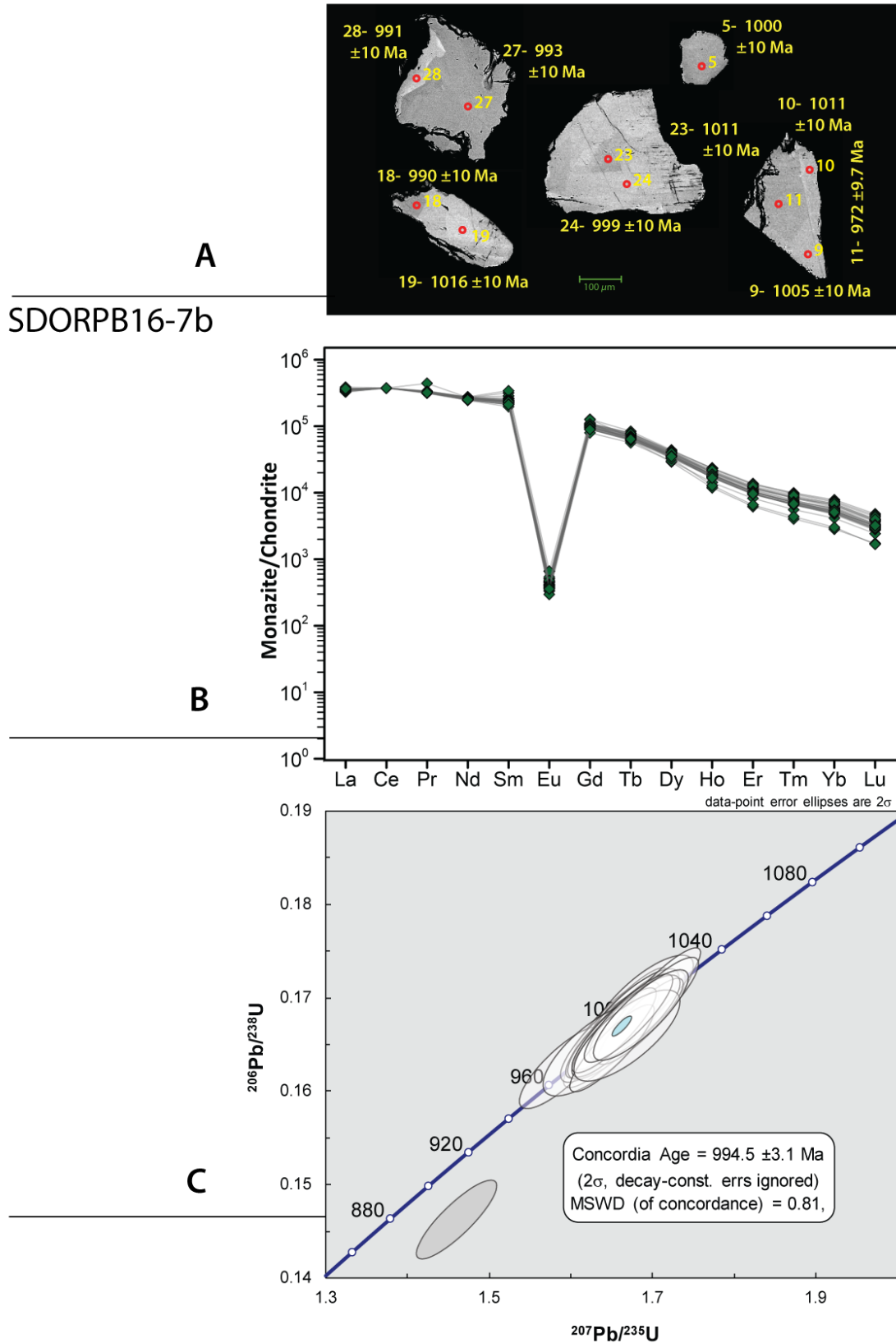


Figure 4.31. A) Representative SEM BSE images of analysed monazite from pegmatite sample SDORPB16-7B. Red circles indicate positions of laser pits with a width of  $15\mu\text{m} - 16\mu\text{m}$  (see text) in diameter. Spot dates indicated are  $^{206}\text{Pb}/^{238}\text{U}$  dates with uncertainties on the spot ages given at the  $1\sigma$  level. B) Chondrite-normalised REE diagram for sample SDORPB16-7B. Normalised to values from Sun and McDonough (1989). C) Wetherhill concordia diagram for monazite LA-Q-ICP-MS isotope data for pegmatite sample SDORPB16-7B, errors are shown as  $2\sigma$  ellipses.

### 4.1.3 Kakamas Domain

#### *SDORPB15-17*

This sample is from a zoned muscovite-rich REE-type pegmatite located in the rugged hills near Riemvasmaak (Figure 4.32). It intrudes the ~1208 Ma Twakputs garnet-bearing megacrystic biotite gneiss of the Eendoorn Suite within the eastern Kakamas Domain. The mineralogy of the sample from this pegmatite consists chiefly of K-feldspar and muscovite with minor quartz and garnet. Monazite, zircon and apatite occur as accessory minerals. The monazite extracted from this sample is mostly euhedral to subhedral and equant (260  $\mu\text{m}$  – 100  $\mu\text{m}$ ) in shape, with a limited number of rounded subhedral (150  $\mu\text{m}$  – 75  $\mu\text{m}$ ) and anhedral angular fragments (150  $\mu\text{m}$  – 70  $\mu\text{m}$ ). Magmatic oscillatory zoning is present in some euhedral grains, but the majority of the grains displayed weak broad sector compositional zoning or are homogenous in BSE images (Figure 4.33a). Some grains show cores that are affected by porous zones of alteration and fracturing occurs in the largest grains.

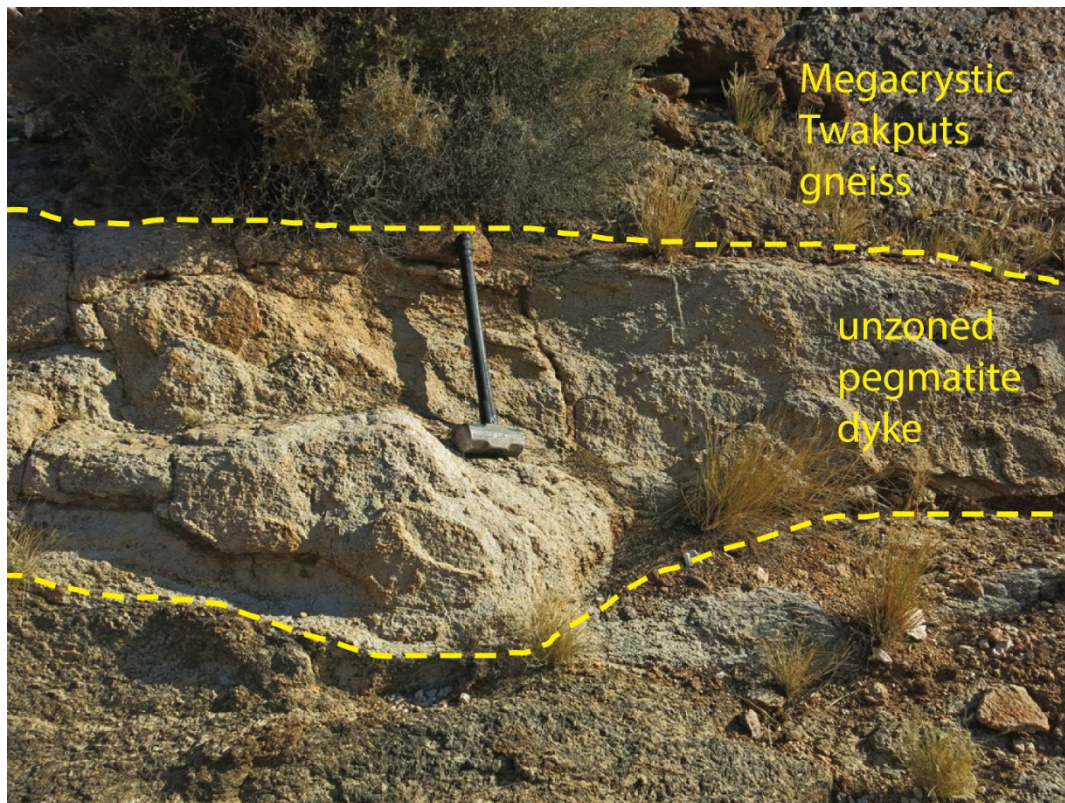


Figure 4.32: Field photograph of the simple, muscovite+K-feldspar rich zoned pegmatite (*SDORPB15-17*), that intrudes into the Twakputs gneiss in the Riemvasmaak area. Pictured centre is the relatively finer grained zone that was sampled at this locality.

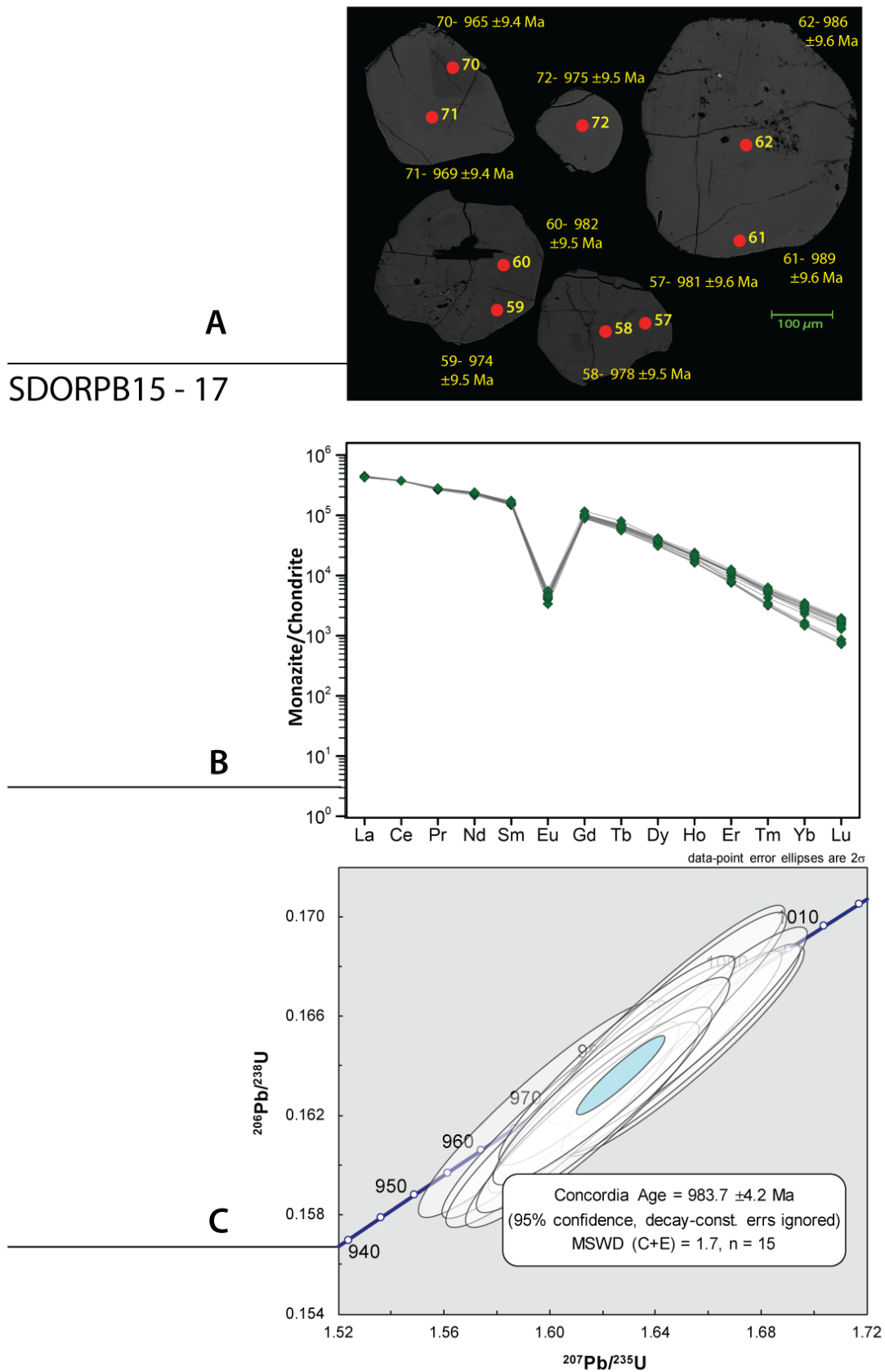


Figure 4.33. A) Representative SEM BSE images of analysed monazite from pegmatite sample SDORPB15-17. Red circles indicate positions of laser pits with a width of  $15\mu\text{m} - 16\mu\text{m}$  (see text) in diameter. Spot dates indicated are  $^{206}\text{Pb}/^{238}\text{U}$  dates with uncertainties on the spot ages given at the  $1\sigma$  level. B) Chondrite-normalised REE diagram for sample SDORPB15-17. Normalised to values from Sun and McDonough (1989). C) Wetherhill concordia diagram for monazite LA-Q-ICP-MS isotope data for pegmatite sample SDORPB15-17, errors are shown as  $2\sigma$  ellipses.

The monazite in this sample has a narrow range in Ca and Y content from 9 888 to 14 717 ppm and 21 767 to 33 133 ppm, respectively (Appendix A.4.1.) The monazite show little variation in very high U (9 604 - 20 082 ppm) with a large range in moderate to high Th concentrations (42 815 – 83 087 ppm; Appendix A.4.1.), and a range of relatively low Th/U ratios from 2 to 7 (Appendix A.4.1). The lowest monazite Th/U ratios were obtained from BSE dark zones. Monazite chondrite-normalised REE patterns (Figure 4.33b) are tightly grouped and characterised by strong relative enrichment of LREE with a progressive and smooth decrease in normalised abundances towards the HREE ( $[La/Sm]_N = \sim 3$ ; Appendix C.4.1.) with strong and uniform negative Eu anomaly ( $Eu/Eu^* = 0.03-0.04$ ; Appendix C.4.1). The REE pattern has a moderate but variable relative depletion in HREE with respect to the MREE ( $[Gd/Lu]_N = 48 - 159$ ; Appendix C.4.1). The lowest HREE normalised abundances reflect lower Y content in the monazite rims.

The U-Pb isotope data from 15 analyses obtained from 10 monazite grains are shown in Figure 4.33c and Appendix C.4.1. The analyses cluster on the concordia line (97 to 101% concordant) and yield a narrow range of apparent  $^{207}Pb/^{206}Pb$  spot dates between  $1006 \pm 22$  Ma ( $1\sigma$ ) and  $967 \pm 22$  Ma ( $1\sigma$ ) (Appendix C.4.1). All 15 analyses could be statistically combined to yield a concordia date of  $984 \pm 4.2$  Ma (95% c.l.,  $MSWD(C+E) = 1.7$ ,  $n = 15$ ; Figure 4.33c), that is interpreted to date monazite crystallisation in this pegmatite.

### *SDORPB15-18*

This sample is from a simple and unzoned pegmatite within the Riemvasmaak hills that intruded the  $\sim 1110$  Ma Donkieboud porphyritic biotite-hornblende granodioritic gneiss of the Komsberg suite. The sample contained abundant K-feldspar and quartz with minor muscovite. Monazite, xenotime, garnet, zircon and apatite occur as accessory minerals. This sample yielded very little monazite with only two useable grains were collected in total. These two grains are large ( $\sim 500$   $\mu m$  across), anhedral, highly altered and fractured (Figure 4.34a). The grains appear to be homogenous in BSE images except for localised porous and patchy fluid-mediated recrystallisation textures along the rims and similar porous zones that follow fractures (Figure 4.34a).

Compositionally, monazite from this sample has little variation in Ca concentrations (10 183 – 11 800 ppm), but a moderate range in Y (12 987 – 29 382 ppm) and Si (5 170 – 17 476 ppm) contents (Appendix A.4.2). Monazite chondrite-normalised REE patterns (Figure 4.34b) are tightly grouped and characterised by strong relative enrichment of LREE with a progressive and smooth decrease in normalised abundances towards the HREE ( $[La/Sm]_N = \sim 4$ ; Appendix C.4.2.), and a moderate to strong and uniform negative Eu anomaly ( $Eu/Eu^* = 0.04 - 0.09$ ; Appendix C.4.2). The REE pattern has a moderate but variable relative depletion in the HREE over the MREE with a parallel slope ( $[Gd/Lu]_N = 7 - 40$ ; Appendix C.4.2; Figure 4.34b), with a trend where analyses with low Y contents are more relatively depleted in HREE.

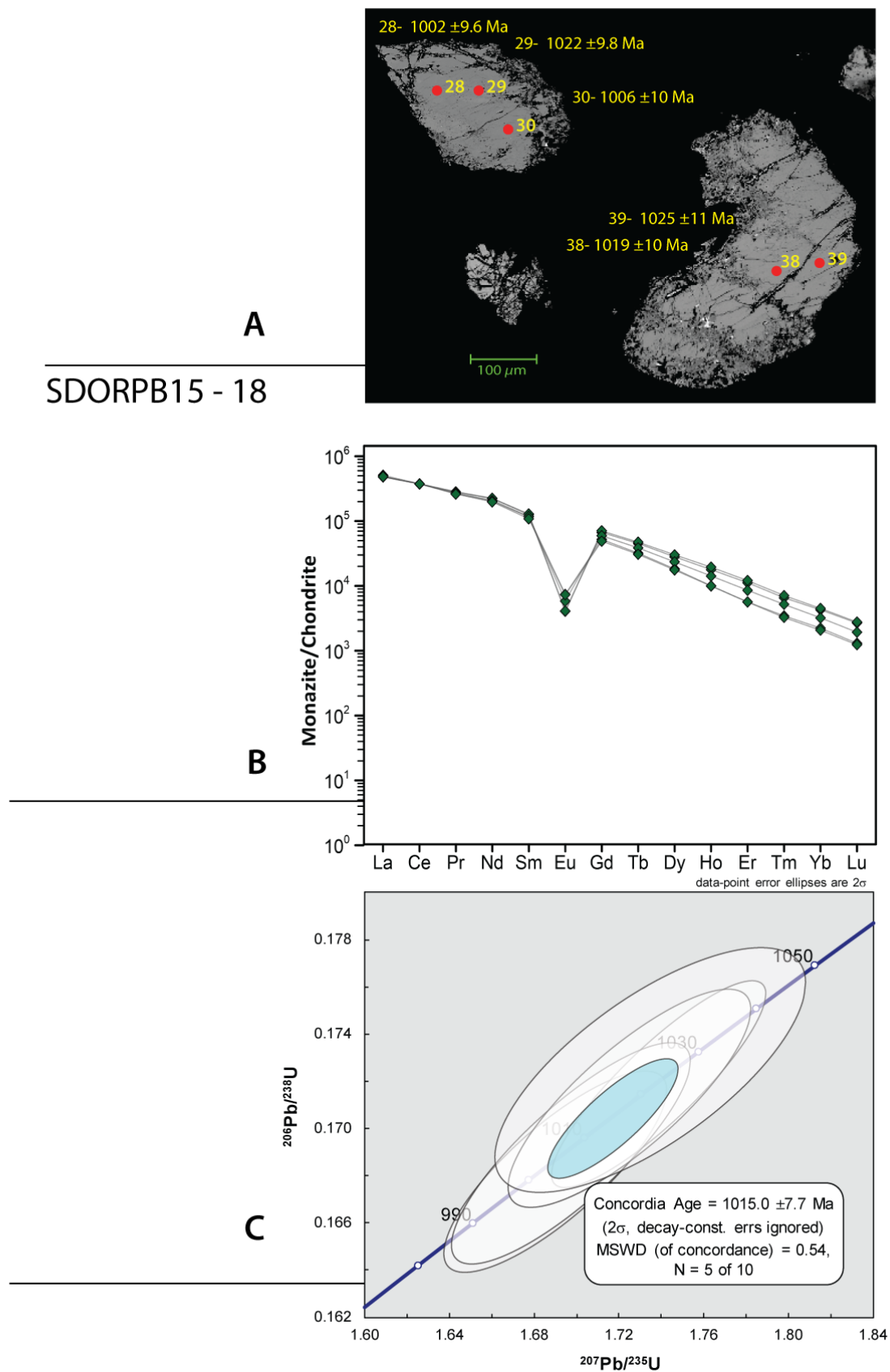


Figure 4.34. A) Representative SEM BSE images of analysed monazite from pegmatite sample SDORPB15-18. Red circles indicate positions of laser pits with a width of  $15\mu\text{m} - 16\mu\text{m}$  (see text) in diameter. Spot dates indicated are  $^{206}\text{Pb}/^{238}\text{U}$  dates with uncertainties on the spot ages given at the  $1\sigma$  level. B) Chondrite-normalised REE diagram for sample SDORPB15-18. Normalised to values from Sun and McDonough (1989). C) Wetherill concordia diagram for monazite LA-Q-ICP-MS isotope data for pegmatite sample SDORPB15-18, errors are shown as  $2\sigma$  ellipses.

Considerable effort was taken to avoid zones of alteration; however, three of the total eight analyses had to be excluded due to their lack of a useable  $^{207}\text{Pb}/^{206}\text{Pb}$  plateau in the time-resolved signal. This problem possibly reflects isotopic disturbance due to fluid-mediated recrystallisation. The remaining five analyses have moderate U (~2 059 to 5 632 ppm) and very high Th (~100 594 – 140 917 ppm) contents, and a range of moderate Th/U ratios (~25 to 50). These five analyses are 99 to 101% concordant with a narrow range in apparent  $^{207}\text{Pb}/^{206}\text{Pb}$  spot dates of  $1023 \pm 24$  Ma ( $1\sigma$ ) to  $1010 \pm 26$  Ma ( $1\sigma$ ) (Appendix C.4.2). These analyses group tightly on a concordia line yielding a concordia date of  $1015 \pm 7.7$  Ma ( $2\sigma$ , MSWD (C+E) = 0.54; Figure 4.34c). This date is interpreted to be the crystallisation age of monazite in the pegmatite.

### *SDORPB15-20*

Sample SDORPB15-20 was obtained from a simple and homogeneous pegmatite that intruded the ~1156 Ma quartzofeldspathic Riemvasmaak augen gneiss, adjacent a major shear zone associated with the Hartebees River thrust and Wolfkop shear zone in the Kakamas Domain. The sample contains K-feldspar and quartz predominantly with minor muscovite. Garnet, monazite, zircon, tourmaline, beryl and apatite occur as accessory minerals. The sample yielded abundant, yellow-orange monazite grains that are ~100  $\mu\text{m}$  to 120  $\mu\text{m}$  in diameter. The monazite is anhedral with a few grains having weak and broad polygonal compositional zoning in BSE images (Figure 4.35b). The majority of the grains are transparent with limited fracturing. Grain boundaries of many grains are embayed slightly while three grains have a spongy texture on the rims inferred to have formed by low-T, fluid-mediated recrystallisation (Figure 4.35a).

The monazite from this sample is characterised by a small range in the concentrations of Si (1 968 – 7 539 ppm) and Y (18 667 – 26 593 ppm), and a larger range in Ca content from 2 959 to 13 959 ppm (Appendix A.4.3). High relative LREE abundances characterise Chondrite-normalised REE patterns (Figure 4.35b) with a progressive and smooth decrease in normalised abundances towards the HREE ( $[\text{La}/\text{Sm}]_{\text{N}} = 3 - 4$ ), and generally moderate negative Eu anomalies ( $\text{Eu}/\text{Eu}^* = 0.04 - 0.06$ ; Appendix B.4.3; Figure 4.35b). The REE patterns show that monazite in this sample is moderately depleted in HREE with small variations in  $[\text{Gd}/\text{Lu}]_{\text{N}}$  from 38 to 45 (Appendix B.4.3).

Monazite analyses are characterised by high U (~2 892 to 7 046 ppm; average = ~4 581 ppm) with moderate to high Th concentrations (~39 592 – 89 270 ppm; Appendix A.4.3), and a narrow range in Th/U ratios of 13 – 22. Fifteen U-Pb isotope analyses were obtained from 10 monazite grains. Of these, 13 that are 99 to 103% concordant. Two of the analyses had no usable  $^{207}\text{Pb}/^{206}\text{Pb}$  plateaus and were highly discordant. The latter were therefore omitted from further consideration. The apparent  $^{207}\text{Pb}/^{206}\text{Pb}$  spot dates of the remaining 13 concordant analyses yield a narrow range from  $999 \pm 21$  Ma ( $1\sigma$ ) to  $964 \pm 22$  Ma ( $1\sigma$ ) (Appendix C.4.3). All 13 of these analyses could be combined statistically to yield a concordia date of  $990 \pm 4.9$  Ma (95% c.l., MSWD(C+E) = 2.1;  $n = 13$ ; Figure 4.35c). As with previous samples, this is interpreted to be the age of crystallisation of monazite in this pegmatite.

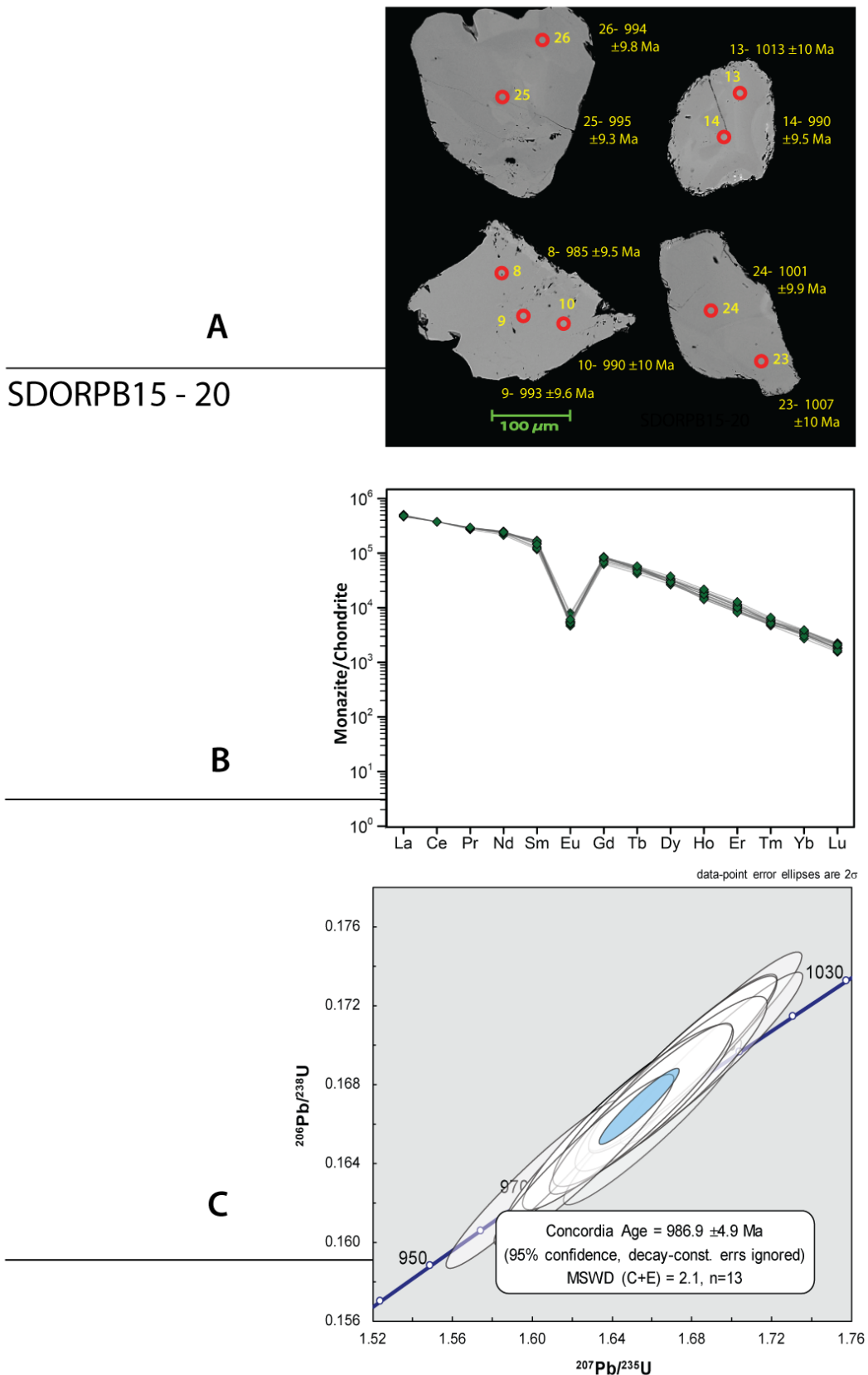


Figure 4.35. A) Representative SEM BSE images of analysed monazite from pegmatite sample SDORPB15-20. Red circles indicate positions of laser pits with a width of  $15\mu\text{m} - 16\mu\text{m}$  (see text) in diameter. Spot dates indicated are  $^{206}\text{Pb}/^{238}\text{U}$  dates with uncertainties on the spot ages given at the  $1\sigma$  level. B) Chondrite-normalised REE diagram for sample SDORPB15-20. Normalised to values from Sun and McDonough (1989). C) Wetherill concordia diagram for monazite LA-Q-ICP-MS isotope data for pegmatite sample SDORPB15-20, errors are shown as  $2\sigma$  ellipses.

## *SDORPB16-8*

Sample SDORPB16-8 comes from a small discordant pegmatite that intruded into the Narries pelitic granulite gneiss situated close to a contact with the ~1120 Ma Witwater garnet-bearing leucogneiss. The pegmatite appears to be broadly homogenous in composition, based on mineral modes but shows apparent zoning due to variations in grain size. The sample from this pegmatite contains K-feldspar, quartz and large garnets (0.5 to 2 cm in diameter) with minor muscovite. Accessory minerals present are monazite, zircon and apatite. Monazite recovered from this sample is abundant and variable in shape, size and internal zoning (Figure 4.36a).

A total of 16 monazites grains were selected, and these exhibit a range of grain shapes and textures. Six grains are subhedral with a tabular to prismatic habit. These grains are ~150 to 200  $\mu\text{m}$  in length with an overall width to length ratio of 1:2 (Figure 4.36a). They show broad oscillatory or polygonal sector zoning in BSE images and some embayment of grain boundaries. Alteration textures are present on grains with a BSE dark core and BSE bright rim, with the porous alteration by possible low-T fluid mediated recrystallisation occurring in the rims and on one grain permeating into the core. These grains have moderate to high U (4 392 ppm – 8 978 ppm) and highly variable Th (76 174 – 108 738 ppm) concentrations (Appendix A.4.4). The Th/U ratios have a broad but low range of 5 and 16 (Appendix A.4.4). There is no apparent trend between Th/U ratios between BSE-dark or -light zones. One subhedral grain is anomalous with appreciably higher U concentrations (~22 000 ppm) and a much lower Th/U ratio of 2 (Appendix A.4.4). The monazite have variable concentrations of Ca (4 641 – 20 355 ppm) and Si (895 – 10 821 ppm) with a small range in Y concentration (18 691 – 33 160 ppm; Appendix A.4.4), that, like U and Th contents have no observable trend relating to monazite compositional zoning.

There were also eight anhedral grains and fragments of larger monazite grains. These are varied in size and shape with mostly being equant (~100 to 130  $\mu\text{m}$ ), but two grains are elongated and about ~200 to ~250  $\mu\text{m}$  in length. These grains have variable porous alteration zones and rims due to inferred low-T fluid mediated recrystallisation (Figure 4.36a). The less altered grains have broad compositional sector zoning in BSE images. The unaltered grains have variable U and high Th concentrations (~3 158 – 13 453 ppm and 10 910 – 152 998 ppm, respectively) with a broad range on Th/U ratios (1 to 29) (Appendix A.4.4). Concentrations of Ca, Si and Y varied greatly, ranging from 3 335 to 30 533 ppm, 729 to 12 849 ppm and 14 135 to 31 478 ppm, respectively (Appendix A.4.4), again with no apparent link to monazite compositional zoning.



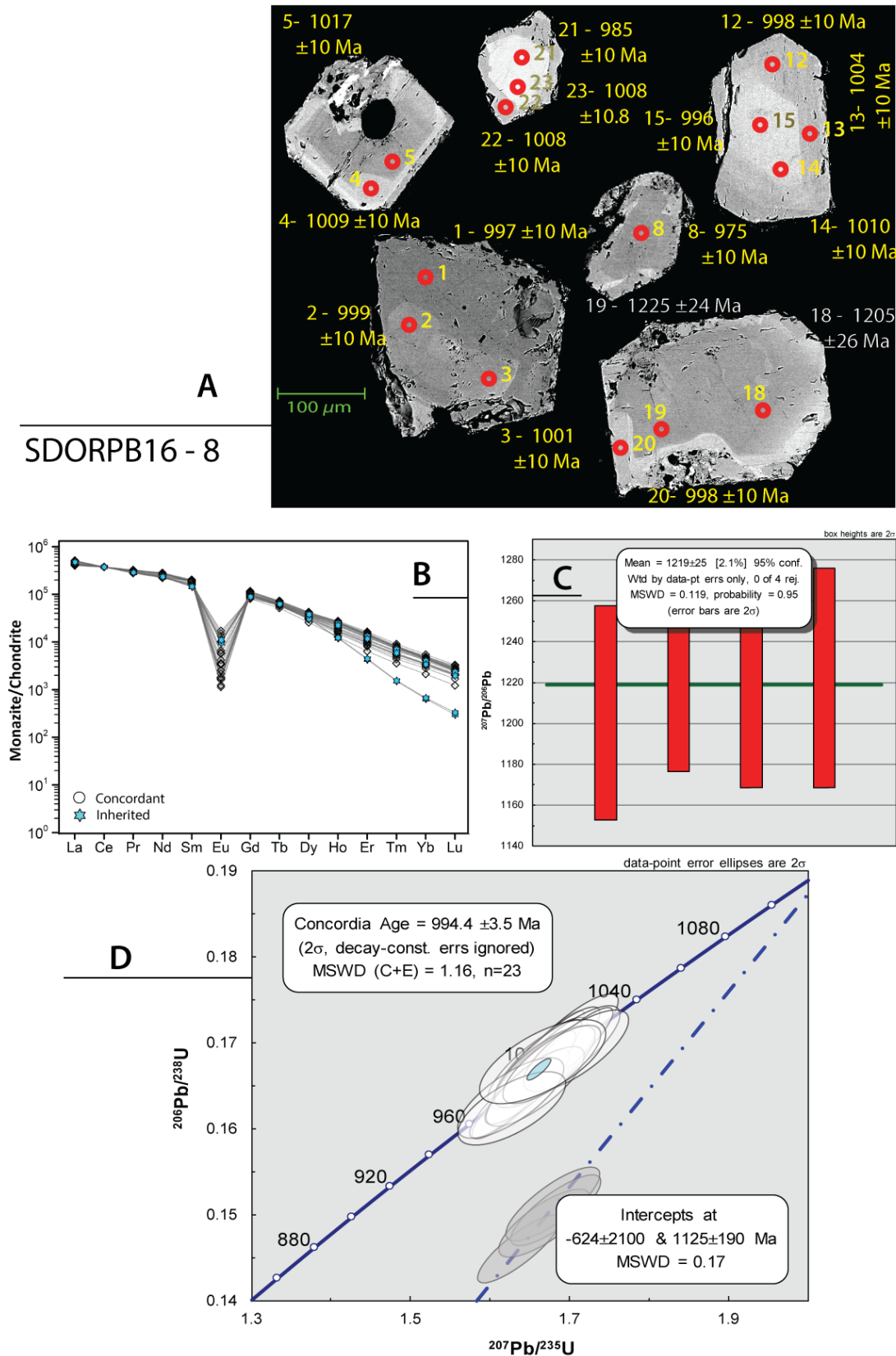


Figure 4.36. A) Representative SEM BSE images of analysed monazite from pegmatite sample SDORPB16-8. Red circles indicate positions of laser pits with a width of 15 μm – 16 μm (see text) in diameter. Spot dates indicated are (white text)  $^{206}\text{Pb}/^{207}\text{Pb}$  dates and (yellow text)  $^{206}\text{Pb}/^{238}\text{U}$  dates with uncertainties on the spot ages given at the  $1\sigma$  level. B) Chondrite-normalised REE diagram for sample SDORPB16-8. Normalised to values from Sun and McDonough (1989). C) Weighted mean diagram for  $^{207}\text{Pb}/^{206}\text{Pb}$  spot dates for sample SDORPB16-8 where red boxes are plotted as  $2\sigma$  errors. D) Wetherill concordia diagram for monazite LA-Q-ICP-MS isotope data for pegmatite sample SDORPB16-8, errors are shown as  $2\sigma$  ellipses

One large anhedral grain (~400  $\mu\text{m}$  in diameter) was present and also analysed and is homogenous in BSE imaging. The grain is fractured with porous alteration zones of possible low-T fluid-mediated recrystallisation on the rim and interior of the grain (Figure 4.36a). The large monazite grain has high U (47 981 to 50 163 ppm) and low average Th (~40 000 ppm) concentrations with a very low Th/U ratio of 1 (Appendix A.4.4).

Chondrite-normalised REE patterns (Figure 4.36b) for the majority of the spot analyses are characterised by strong relative LREE enrichment with a progressive and smooth decrease in normalised abundances towards the M- and HREE ( $[\text{La}/\text{Sm}]_{\text{N}} = 2 - 3$ ) with a variable, moderate to high, negative Eu anomaly ( $\text{Eu}/\text{Eu}^* = 0.01$  to  $0.1$ ; Appendix B.4.4; Figure 4.36b). The sample is moderately depleted in HREE with small variations in  $[\text{Gd}/\text{Lu}]_{\text{N}}$  from 31 to 66 (Appendix B.4.4). The large anhedral grain with low Th/U ratios (mentioned above) is variably more strongly depleted in HREE with a steeper slope ( $[\text{Gd}/\text{Lu}]_{\text{N}} =$  of 287 – 318; Appendix A.4.4; Figure 4.36b).

Twenty-seven U-Pb isotope spot analyses were obtained from the 16 grains. The ranges in apparent  $^{207}\text{Pb}/^{206}\text{Pb}$  spot dates show two age populations in this pegmatite (Figure 4.36d, Appendix C.4.4). The younger population of concordant (98-101% concordant, Appendix C.4.4) analyses is characterised by  $^{207}\text{Pb}/^{206}\text{Pb}$  spot dates between  $1021 \pm 30$  Ma ( $1\sigma$ ) and  $974 \pm 26$  Ma ( $1\sigma$ ) (Appendix C.4.4). Twenty-three U-Pb isotope analyses in this population could be combined to yield a concordia date of  $994 \pm 3.5$  Ma ( $2\sigma$ ,  $\text{MSWD}(\text{C}+\text{E}) = 1.16$ ,  $n = 23$ ; Figure 4.36d).

In contrast, an older population, defined by four U-Pb spot analyses, defines a discordant line segment on the concordia diagram, with imprecise upper and lower intercepts of  $1125 \pm 190$  Ma ( $\text{MSWD} = 0.17$ ; Figure 4.36d) and  $-624 \pm 2100$  Ma respectively. A weighted mean  $^{207}\text{Pb}/^{206}\text{Pb}$  date from the four analyses of  $1219 \pm 25$  Ma (95% c.l.,  $\text{MSWD} = 0.119$ , probability = 0.95,  $n = 4$ ; Figure 4.36c) was calculated. The weighted mean age is within error of the upper intercept age and, based on its much higher precision, is preferred as the best estimate of the age of crystallisation for the older monazite. These older U-Pb dates come from two monazite grains, where one is the larger anhedral grain with higher U concentrations and low Th/U ratio (see above), the other came from the core of a euhedral grain with BSE dark core and BSE light rim (Figure 4.36a). The large population of concordant analyses is interpreted to date magmatic crystallisation in the pegmatite to  $994 \pm 4$  Ma, whereas the smaller, older, and discordant population is interpreted to date monazite inheritance from  $1219 \pm 25$  Ma.

## SDORPB16-9

This sample is from a small subsidiary pegmatite near the Mostertshoek pegmatite mine in the Riemvasmaak area. The pegmatite group in the area is of the REE class of the LCT type pegmatite classification. This pegmatite is mined today for its abundant rose quartz but was mined in the past for beryl and feldspar. Columbite-tantalite was recovered locally from the main Mostertshoek pegmatite during these operations. The sample from this pegmatite contains K-feldspar with quartz and muscovite in low proportions. Accessory minerals present are monazite, pyrite (altered to limonite), zircon and apatite. The pegmatite intruded the equigranular ~1120 Ma Daberas granodiorite of the Komsberg Suite. The monazite recovered from the pegmatite varies from euhedral grains that are either tabular or prismatic (~100 – 250  $\mu\text{m}$  diameter) to rounded subhedral and anhedral grains (~100-150  $\mu\text{m}$ ). Anhedral fragments of larger monazite grains are also present (~80 to 150  $\mu\text{m}$  in length). Internal zoning in BSE images is limited to a few grains and present as fine patchy sector zoning. The majority of the grains are strongly altered, with a patchy “sponge” alteration along the rims of grains and also present in alteration zones that developed along fractures (Figure 4.37a).

Compositionally, the monazite from this sample has a wide range in Si (862 – 6 383 ppm) and smaller ranges in Ca (11 825 – 22 035 ppm) and a narrow range in Y (20 180 – 34 198 ppm; Appendix A.4.5) concentrations. It has moderate to high U (4 250 – 23 618 ppm) and high Th (67 302 – 120 806 ppm) contents (Appendix A.4.5). Th/U ratios are low, ranging from 4 – 15 with one anomalously high Th/U ratio of 27 (Appendix A.4.5). The later comes from a relatively U poor monazite grain (~4 250 ppm U). The chondrite-normalised REE patterns (Figure 4.37b) are characterised by strong relative LREE enrichment with a progressive and smooth decrease in normalised abundances towards the M- and HREE ( $[\text{La}/\text{Sm}]_N = 2 - 3$ ) and large, negative Eu anomalies ( $\text{Eu}/\text{Eu}^* = 0.02 - 0.04$ ; Appendix B.4.5; Figure 4.37b). Relative HREE depletion with respect to the MREE are variable, with a range in  $[\text{Gd}/\text{Lu}]_N$  values from 64 to 315 (Appendix B.4.5.)

A total of 27 spot U-Pb analyses were obtained from 20 monazite grains in this sample, and an additional three compositional analyses could be extracted from 3 spot analyses where the laser had ablated through to another crystal domain. Overall, 24 analyses are concordant (97 to 101%, Appendix C.4.5) with a narrow range in apparent  $^{207}\text{Pb}/^{206}\text{Pb}$  spot dates of  $1033 \pm 25$  Ma ( $1\sigma$ ) to  $1006 \pm 29$  Ma ( $1\sigma$ ) (Appendix A.4.5). All 24 could be statistically combined to yield a concordia date of  $1019 \pm 3.6$  Ma ( $2\sigma$ , MSWD (C+E) = 0.69; Figure 4.37d). The apparent  $^{207}\text{Pb}/^{206}\text{Pb}$  spot dates of the remaining five analyses range from  $1209 \pm 23$  Ma ( $1\sigma$ ) to  $1198 \pm 26$  Ma ( $1\sigma$ ) (Appendix C.4.5). The analyses did not show enough dispersion to define a statistically meaningful discordant line segment on the concordia diagram. However, a weighted  $^{207}\text{Pb}/^{206}\text{Pb}$  date was calculated for these five analyses at  $1203 \pm 21$  Ma (95% c.l., MSWD = 0.04, Probability = 0.9;  $2\sigma$  error bars; Figure 4.37c). The younger concordant monazite population is interpreted to be the magmatic age for this

pegmatite while the older discordant population is interpreted to be the age of inheritance for a xenocrystic monazite component in this pegmatite.

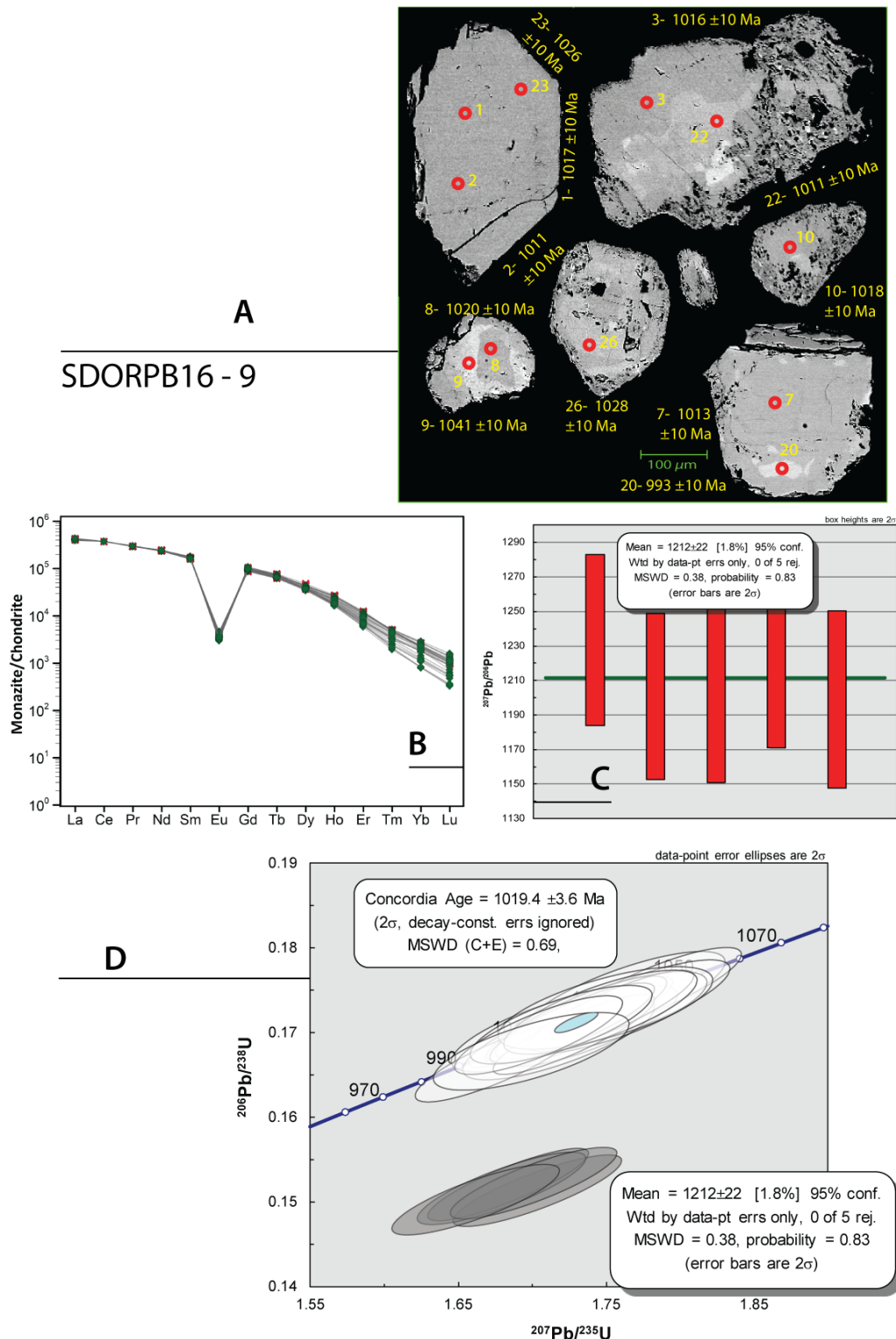
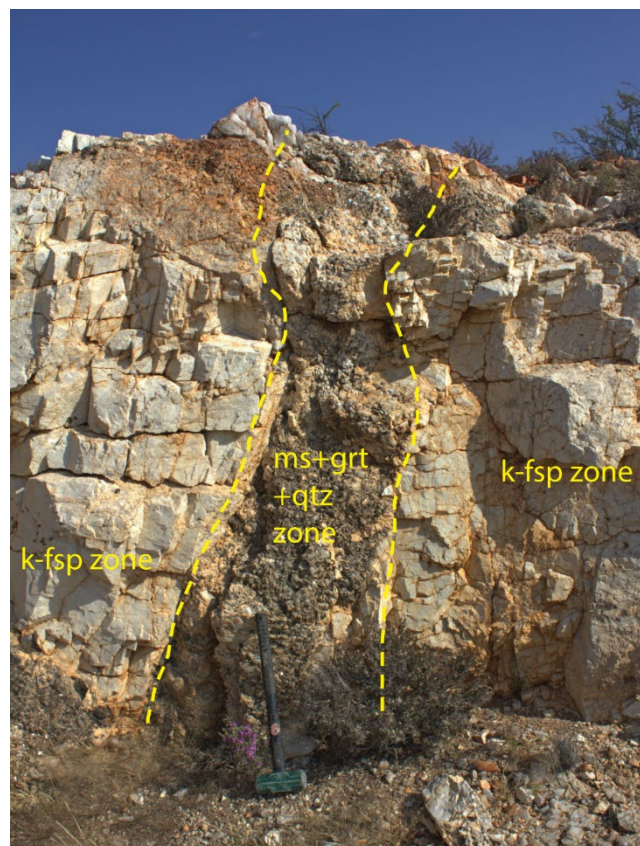


Figure 4.37. A) Representative SEM BSE images of analysed monazite from pegmatite sample SDORPB16-9. Red circles indicate positions of laser pits with a width of 15 μm – 16 μm (see text) in diameter. Spot dates indicated are (white text)  $^{206}\text{Pb}/^{207}\text{Pb}$  dates and (yellow text)  $^{206}\text{Pb}/^{238}\text{U}$  dates with uncertainties on the spot ages given at the 1σ level. B) Chondrite-normalised REE diagram for sample SDORPB16-9. Normalised to values from Sun and McDonough (1989). C) Weighted mean diagram for  $^{207}\text{Pb}/^{206}\text{Pb}$  spot dates for sample SDORPB16-9 where red boxes are plotted as 2σ errors. D.) Wetherill concordia diagram for monazite LA-Q-ICP-MS isotope data for pegmatite sample SDORPB16-9, errors are shown as 2σ ellipses.

*SDORPB16-12*

This monazite sample is from a zoned LCT type pegmatite locally named “Jack no. 5” (Figure 4.38) in an old pegmatite-mining district near Putsonderwater and Kenhardt in the Northern Cape. The pegmatite field was once mined for beryl, lepidolite, spodumene and columbite-tantalite. The pegmatite intruded into quartzites and felsic paragneiss units of the Jacomynspan Group in the Kakamas domain, within the D4 Strausheim Shear Zone.

The sample proved difficult to date as all data points spread out across the concordia line with a majority of analyses being variably discordant (Figure 4.39c). However, four age populations were determined from the data. The U-Pb isotope data from this sample show that there is a younger concordant population and a series of successively older monazite populations that are variably discordant with one older concordant population (Appendix C.4.6; Figure 4.39c).



*Figure 4.38: Field photograph of the large, zoned LCT pegmatite, “Jack no. 5”. The pegmatite had large K-feldspar dominated, to often monomineralic zones and muscovite+garnet and muscovite+qtz+garnet rich “veins” or elongated lens shaped zones.*

The youngest age population of two analyses came from one anhedral, rounded monazite grain (Figure 4.39a). The homogenous grain is about 140  $\mu\text{m}$  by 90  $\mu\text{m}$  with small ranges in concentrations of Ca and Y from 12 794 to 14 047 ppm and ~36 000 ppm respectively (Appendix A.4.6). U and Th concentrations are also uniform at ~5 400 and ~10 000 ppm respectively (Appendix D.4.6) with a mean Th/U ratio of 18

(Appendix A.4.6). The chondrite-normalised REE pattern for this youngest monazite population (Figure 4.39b) have a strong relative LREE enrichment with a smooth and progressive relative depletion in normalised abundances towards the MREE ( $[La/Sm]_N \sim 3$ ; Appendix B.4.6), a moderate to strong negative Eu anomaly ( $Eu/Eu^* = 0.04$ ; Figure 4.39b), and a smooth and progressive relative depletion in HREE over the MREE ( $[Gd/Lu]_N \sim 32$ ; Appendix B.4.6). The monazite grain has a narrow range in apparent  $Pb^{207}/Pb^{206}$  spot ages of  $985 \pm 24$  Ma to  $996 \pm 23$  Ma ( $1\sigma$ ; Appendix C.4.6) that are  $\sim 100\%$  concordant at  $\sim 990$  Ma (Appendix C.4.6).

Eleven analyses defined the younger discordant population (Figure 4.39c) and were obtained from seven monazite grains that vary in size and shape. Two larger grains (160 to 230  $\mu m$ ) are rounded with variably altered and fractured rims and compositional sector zoning (Figure 4.39a). The other nine monazite grains are smaller (75 to 110  $\mu m$ ), rounded and anhedral. Fracturing and alteration are minimal but variable, and these grains lack any visible zoning in BSE images (Figure 4.39a). Compositionally, the grains have highly variable Ca and Y concentrations from 1 812 to 11 918 ppm and 1 705 to 29 776 ppm (Appendix A.4.6) respectively. U and Th concentrations also vary widely from 308 to 2 572 ppm and 25 531 to 59 251 ppm respectively (Appendix A.4.6) with a range of Th/U ratios from 7 to 192. The eleven analyses in this group are variably discordant (87 to 101% concordant; Figure 4.39c), defining a line segment with lower and upper intercepts of  $-385 \pm 260$  Ma and  $1092 \pm 7$  Ma (MSWD = 1.6) respectively (Figure 4.39c). The same analysis yielded apparent  $^{207}Pb/^{206}Pb$  spot dates from  $1134 \pm 23$  Ma to  $1077 \pm 22$  Ma ( $1\sigma$ ; Appendix C.4.6) that could be combined to give a weighted mean  $^{207}Pb/^{206}Pb$  date of  $1102 \pm 82$  Ma (95% conf.; MSWD = 0.019; Prob. = 1.0;  $n=11$ ; Figure 4.40a).

The older concordant monazite population (Figure 4.39c) was obtained from four analyses from four monazite grains. These grains are small (80 to 110  $\mu m$  in diameter), anhedral and mostly rounded with one embayed grain. BSE zoning and evidence for fluid-related alteration is rare. Compositionally, the monazite is relatively homogenous with respect to Ca (6 031 – 9 359 ppm) but show a large range in Y (2 970 -13 412 ppm) concentrations (Appendix A.4.6). U concentrations have a narrow range from 2 489 to 3 109 ppm. Th concentrations varied from 30 831 to 46 810 ppm, which resulted in a range of Th/U ratios from 10 to 18 (Appendix A.4.6). The four analyses are concordant to slightly reversely discordant (99 to 101%) with a narrow range in apparent  $^{207}Pb/^{206}Pb$  spot dates from  $1150 \pm 22$  Ma to  $1128 \pm 22$  Ma ( $1\sigma$ ; Appendix C.4.6). These analyses could be combined to yield a concordia date of  $1145 \pm 4$  Ma ( $2\sigma$ ; MSWD = 0.79; Prob. = 0.37; Figure 4.39c).

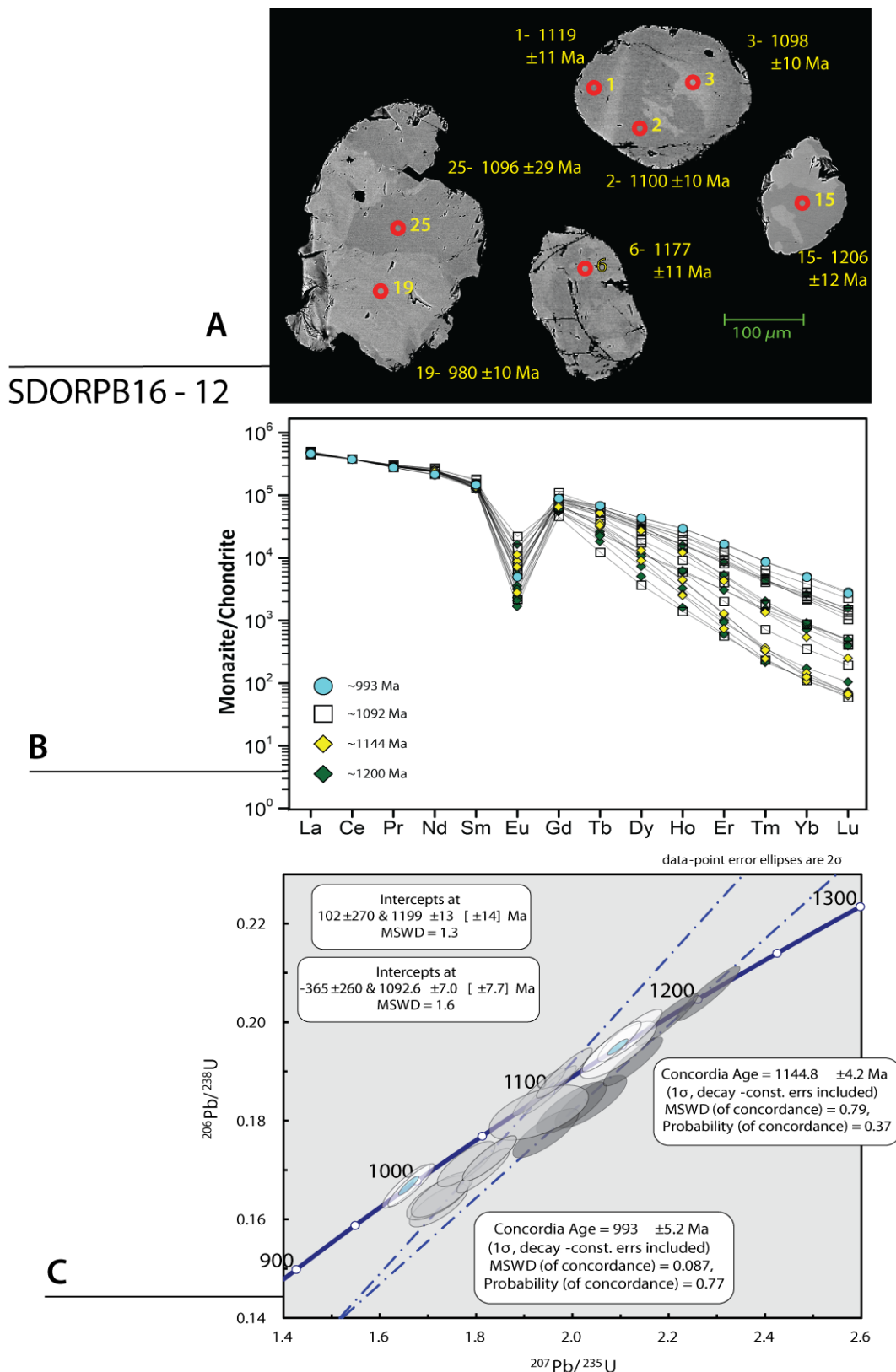


Figure 4.39. A) Representative SEM BSE images of analysed monazite from pegmatite sample SDORPB16-12. Red circles indicate positions of laser pits with a width of  $15\mu\text{m} - 16\mu\text{m}$  (see text) in diameter. Spot dates indicated are (white text)  $^{206}\text{Pb}/^{207}\text{Pb}$  dates and (yellow text)  $^{206}\text{Pb}/^{238}\text{U}$  dates with uncertainties on the spot ages given at the  $1\sigma$  level. B) Chondrite-normalised REE diagram for sample SDORPB16-12. Normalised to values from Sun and McDonough (1989). C) Wetherill concordia diagram for monazite LA-Q-ICP-MS isotope data for pegmatite sample SDORPB16-12, errors are shown as  $2\sigma$  ellipses.

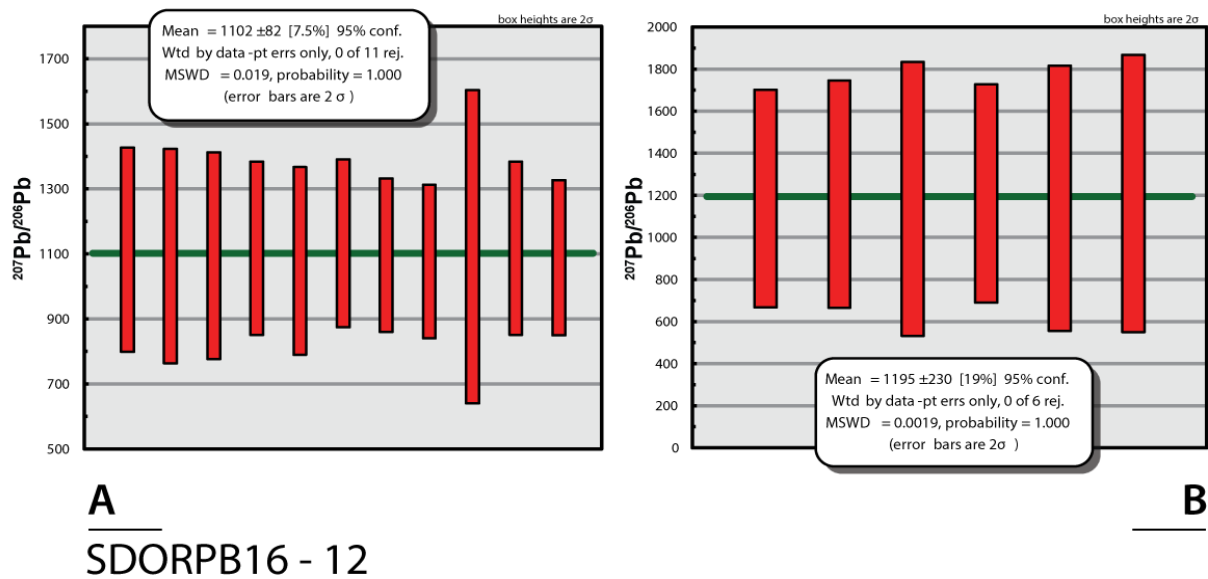


Figure 4.40. A and B) Weighted mean diagram for  $^{207}\text{Pb}/^{206}\text{Pb}$  spot dates for sample SDORPB16-12 where red boxes are plotted as  $2\sigma$  errors.

The oldest discordant population of monazite were obtained from five anhedral and rounded (~80 to 100  $\mu\text{m}$ ) and one subhedral and fractured grain. All grains have weak sector compositional zoning. Compositionally, these grains have narrow ranges in the concentrations of Ca (7 279 – 9 908 ppm); Th (39 486 – 45 937 ppm) and U (1 234 – 4 524 ppm), a range in Y 1 999 to 17 630 ppm and yielded Th/U ratios from 8.7 to 38. Six analyses from the six grains are invariably (89 to 100%) discordant to concordant and yield in apparent  $^{207}\text{Pb}/^{206}\text{Pb}$  spot dates from  $1207 \pm 27$  Ma to  $1181 \pm 28$  Ma ( $1\sigma$ ; Appendix C.4.6). These six spot ages define a discordant line segment on the concordia diagram, with a lower and upper intercept of  $102 \pm 270$  Ma and  $1199 \pm 13$  Ma (MSWD = 1.3) respectively (Figure 4.39c). The lower intercept date is inferred, as with other samples, to indicate recent Pb loss. The six analyses yield a weighted mean  $^{207}\text{Pb}/^{206}\text{Pb}$  date of  $1195 \pm 230$  Ma (95% conf.; weighted by data-point errors only;  $n = 6$ ; MSWD = 0.002, probability = 1; Figure 4.40b).

The chondrite-normalised REE pattern for the older monazite populations (Figure 4.39b) had a similar strong relative LREE enrichment with a smooth and progressive relative depletion in normalised abundances towards the MREE ( $[\text{La}/\text{Sm}]_{\text{N}} = \sim 2 - 4$ ; Appendix B.4.6), a variable, moderate to large, negative Eu anomaly ( $\text{Eu}/\text{Eu}^* = 0.02 - 0.1$ ; Figure 4.39b), and a variable relative depletion in HREE over the MREE ( $[\text{Gd}/\text{Lu}]_{\text{N}} = 51 - 1151$ ; Appendix B.4.6).

This sample had a spread of ages that need to be addressed. The youngest concordant dates of ~990 Ma are interpreted to be the age of crystallisation of magmatic monazite in this pegmatite. The older ages are interpreted to represent a series of xenocrystic monazite components in the pegmatite with a wide range of inheritance at ~1199 Ma, ~1144 Ma and a ~1092 Ma. These dates correspond to tectono-magmatic events within the Namaqua-Natal Metamorphic Province. Their significance is discussed in Chapter 5.1.



## 4.2 Sm-Nd Isotope systematics

### Overview

The monazite grains collected from the pegmatites of the Orange River Pegmatite belt have systematic variations in  $^{147}\text{Sm}/^{144}\text{Nd}$ ,  $^{143}\text{Nd}/^{144}\text{Nd}$ ,  $^{143}\text{Nd}/^{144}\text{Nd}_i$  and  $\epsilon\text{Nd}_t$  (Table 4.2) between samples that reflect their host tectonic domains (see chapter 5.2). Monazite grain morphologies have been described in chapter 4.1 and will not be readdressed here. As was the case with U-Pb isotope analyses, spot ablations for Sm-Nd isotope compositions avoided zones of obvious late-stage monazite recrystallisation.

For each sample, Sm-Nd isotope spot analyses show some variability, typically yielding  $\epsilon\text{Nd}_t$  variations of 1 to 3 epsilon units. These variations could possibly be a natural product as a result of compositional or oscillatory zoning within individual monazite grains (e.g. Fisher *et al.*, 2011; Liu *et al.*, 2012), or due to possible fluid-mediated recrystallisation of the monazite (e.g. McFarlane and McCulloch, 2007). Similar variations have been observed in monazite Sm-Nd reference material as noted by Liu *et al.* (2012). Yang *et al.* (2008) observed significant variations in  $^{144}\text{Sm}/^{144}\text{Nd}$  and  $^{143}\text{Nd}/^{144}\text{Nd}$  from monazite analysed in their study and attributed this to late stage alteration or recrystallisation. Samples with the highest variation in  $\epsilon\text{Nd}_t$  values typically (in this study) occur in pegmatites that are more LCT in character.

Samples from the Vioolsdrif and Pella Domains (Richtersveld Magmatic Arc, RMA) have overall the lowest average  $\epsilon\text{Nd}_t$  (where  $t$  = the crystallisation age of monazite in a given sample) values, ranging from -15.4 to -7.2 (Table 4.2 and Figure 4.41). Samples from the Kakamas Domain (KD) have consistently higher average  $\epsilon\text{Nd}_t$  of -3.5 to -1.4 (Table 4.2 and Figure 4.41) The two samples from the LFROTZ have  $\epsilon\text{Nd}_t$  values slightly lower than KD samples with average  $\epsilon\text{Nd}_t$  from -5.8 to -2.2 (Table 4.2 and Figure 4.41).

Two-stage depleted model ages ( $T_{2\text{DM}}$ ) were calculated for each sample and summarised in the age distribution histogram, Figure 4.42. The  $T_{2\text{DM}}$  ages for pegmatites from the Richtersveld Magmatic Arc (Vioolsdrif and Pella domains) have early Paleoproterozoic to late Archean model ages, between  $\sim 2.1$  and  $\sim 2.7$  Ga (Figure 4.42). The inherited monazite xenocrysts from sample RPGV16 have a younger  $T_{2\text{DM}}$  reflecting Paleoproterozoic age of  $\sim 1.8$  Ga.

The samples from the Kakamas domain and LFROTZ gave younger Paleoproterozoic signatures with  $T_{2\text{DM}}$  ages between  $\sim 1.7$  and  $\sim 1.9$  Ga (Figure 4.42). Sm-Nd isotope data descriptions for individual samples are followed below. The  $T_{2\text{DM}}$  model ages and  $\epsilon\text{Nd}_t$  values of magmatic monazite in this study suggest that the pegmatites formed in a setting of crustal reworking of Mesoproterozoic to Archean rocks, with little evidence of juvenile magmatic addition of material during the time of pegmatite and emplacement in the late Mesoproterozoic.

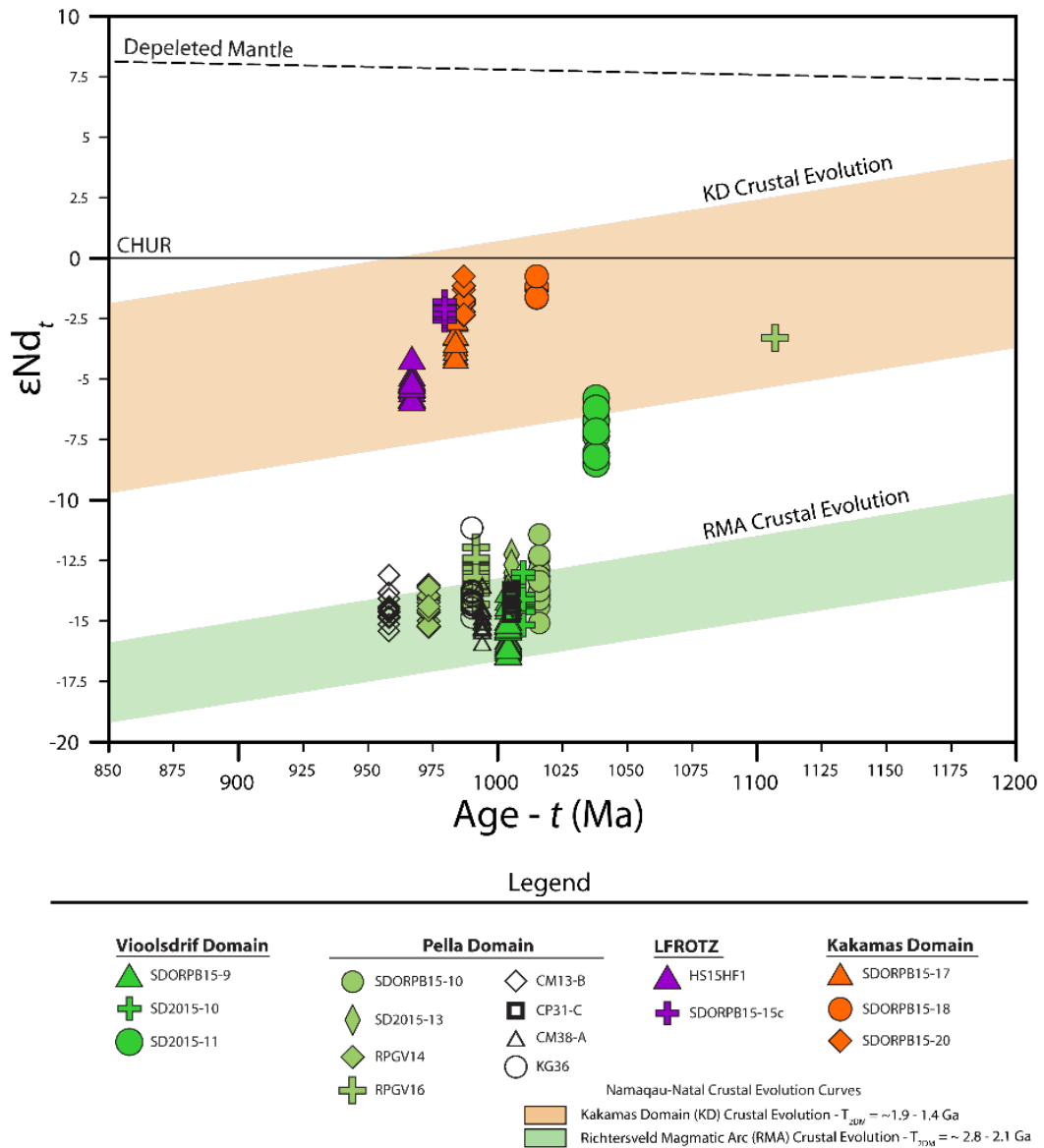


Figure 4.41:  $\epsilon Nd(t)$  vs pegmatite magmatic U-Pb age for analysed monazites, where (t) is the respective monazite crystallisation age for each pegmatite sample. Error bars are smaller than the symbols used and thus are not shown. Included is the evolutionary curves for older Late-Archean/Paleoproterozoic Namaqua crust ( $T_{2DM} = \sim 2.8 - 2.1$  Ga) and younger Paleoproterozoic Namaqua Crust ( $T_{2DM} = \sim 1.9 - 1.4$  Ga).

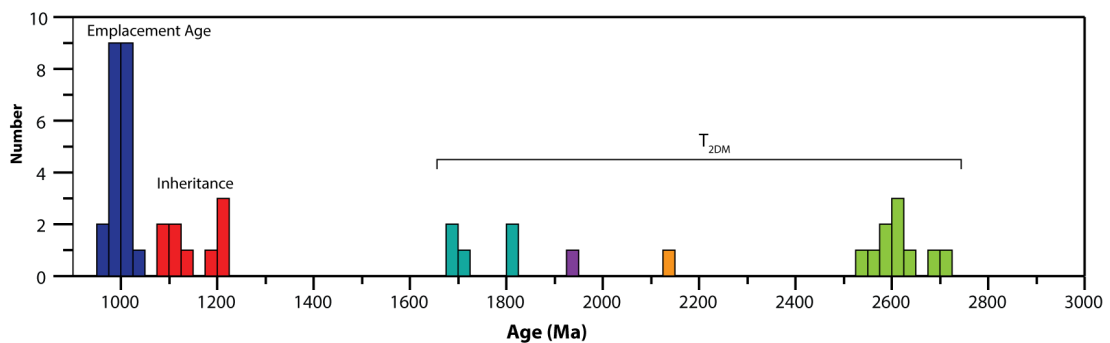


Figure 4.42: Age histogram of monazite U-Pb crystallisation ages and monazite inheritance compared to the Sm-Nd two-stage depleted mantle model ages for the samples analysed. Crystallisation ages - blue, inheritance - red;  $T_{2DM}$  ages: KD - cyan, LFROTZ - purple; SD2015-11 - orange; RMA - green.

Table 4.2 – Summary table of Sm-Nd isotope data for monazite from pegmatites of the Orange River Pegmatite Belt. Values for  $\epsilon Nd_t$  for individual samples represent arithmetic means of the values report in Appendix D.

Sample	U/Pb Age (Ma)	Nd <sub>tot</sub> [ppm]	<sup>147</sup> Sm/ <sup>144</sup> Nd <sup>a</sup>	$\pm 2s^b$	$\beta Nd^c$	<sup>143</sup> Nd/ <sup>144</sup> Nd <sup>a</sup>	$\pm 2s^b$	<sup>143</sup> Nd/ <sup>144</sup> Nd <sub>i</sub> <sup>e</sup>	$\epsilon Nd_t^f$	$\pm 2s^b$	$\epsilon Nd_0$	T <sub>2</sub> Dm [Ga]	f <sup>(Sm/Nd)</sup>
<i>Vioölsdrif Domain</i>													
SD2015-10	1010	36.5	0.26484	0.0012	-1.43	0.51236	0.00002	0.51061	-14	0.52	-5.3	2.6	0.35
SD2015-11	1038	24.4	0.15646	0.0011	-1.40	0.51200	0.00003	0.51093	-7.1	0.78	-12	2.1	-0.20
SDORPB15-9	1004	31.4	0.50489	0.0043	-1.43	0.51388	0.00003	0.51056	-15	0.76	24	2.6	-0.14
<i>Pella Domain</i>													
SD2015-13	1005	24.2	0.16816	0.0006	-1.39	0.51177	0.00002	0.51066	-13	0.56	-17	2.7	-0.14
SDORPB15-10	1016	22.3	0.12771	0.0008	-1.43	0.51149	0.00002	0.51064	-13	0.59	-22	2.6	-0.35
RPGV14	973	25.7	0.12017	0.0005	-1.45	0.51142	0.00002	0.51065	-14	0.56	-24	2.6	-0.39
RPGV16	992	24.7	0.13385	0.0005	-1.43	0.51157	0.00002	0.51069	-13	0.52	-21	2.5	-0.32
RPGV16*	992	35.4	0.11695	0.0004	-1.43	0.51195	0.00001	0.51119	-3.3	0.44	-13	1.8	-0.41
CM38A#	994	21.0	0.13323	0.0007	-1.00	0.51146	0.00001	0.51059	-15	0.45	-23	2.7	-0.32
CM13B#	958	21.6	0.16987	0.0007	-0.98	0.51173	0.00002	0.51066	-14	0.48	-18	2.6	-0.14
CP31C#	1005	22.9	0.10475	0.0004	-0.97	0.51131	0.00001	0.51062	-14	0.45	-26	2.6	-0.47
KG36#	990	23.0	0.15459	0.0004	-0.98	0.51166	0.00001	0.51065	-14	0.45	-19	2.6	-0.21
<i>LFROTZ</i>													
SDORPB15-15c	980	31.3	0.10968	0.0015	-1.40	0.51197	0.00002	0.51126	-2.2	0.54	-13	1.7	-0.44
HS15HF1	967	27.9	0.19742	0.0009	-1.44	0.51238	0.00002	0.51113	-5.2	0.53	-5.1	1.9	0.00
<i>Kakamas Domian</i>													
SDORPB15-17	984	27.6	0.14712	0.0007	-1.43	0.51214	0.00002	0.51119	-3.5	0.53	-10	1.8	-0.25
SDORPB15-18	1015	19.1	0.12124	0.0004	-1.45	0.51207	0.00002	0.51126	-1.4	0.54	-11	1.7	-0.38
SDORPB15-20	987	28.4	0.13591	0.0007	-1.43	0.51215	0.00002	0.51127	-1.8	0.51	-9	1.7	-0.31

\* = inherited monazite xenocryst

# = U-Pb age from Lambert (2013)

a Unweighted mean ratio corrected for inter-element fractionation using Steenkampskraal (Namaqualand; Liu et al, 2012)

b Uncertainty in the corrected ratio (expressed at 95% confidence interval)

c Mass bias correction factor using exponential law

e Initial ratio corrected according to U-Pb age

f t = calculated U-Pb age for the given sample in Ma

T<sub>2</sub>DM is the two-stage depleted model age (in Ga)

## 4.2.1 Richtersveld Magmatic Arc

### 4.2.1.1. Vioolsdrif Domain

#### *SD2015-10*

Ten analyses obtained from six monazite grains showed a wide range in high  $^{147}\text{Sm}/^{144}\text{Nd}$  ratios ( $0.20837 \pm 0.00002$  to  $0.32752 \pm 0.00002$ ;  $2\sigma$ ; Appendix D.1.1) with a mean  $^{147}\text{Sm}/^{144}\text{Nd}$  ratio of  $0.26484 \pm 0.0012$  ( $2\sigma$ ; Table 4.2). The measured, present-day  $^{144}\text{Nd}/^{143}\text{Nd}$  ratios for the sample have a narrower range, from  $0.51205 \pm 2$  to  $0.51273 \pm 0.00002$  ( $2\sigma$ ; Appendix D.1.1) and a mean ratio of  $0.51236 \pm 0.0002$  ( $2\sigma$ ; Table 4.2). Monazite  $\epsilon\text{Nd}_{1009\text{Ma}}$  values calculated for this sample are highly negative, ranging from  $-13 \pm 0.5$  to  $-15.2 \pm 0.6$  ( $2\sigma$ ; Appendix D.1.1; Figure 4.41), with a mean of  $-14.2 \pm 0.5$  ( $2\sigma$ ; Table 4.2). Monazite  $T_{2\text{DM}}$  model ages range from 2.5 to 2.7 Ga (Appendix D.1.1).

#### *SD2015-11*

Ten monazite LA-MC-ICP-MS Nd-isotope analyses were obtained from six monazite grains from this sample.  $^{147}\text{Sm}/^{144}\text{Nd}$  ratios vary from  $0.14506 \pm 10$  to  $0.17468 \pm 20$  ( $2\sigma$ ; Appendix D.1.2) with a mean  $^{147}\text{Sm}/^{144}\text{Nd}$  ratio of  $0.1563 \pm 56$  ( $2\sigma$ ; Table 4.2), and the measured  $^{144}\text{Nd}/^{143}\text{Nd}$  ratios for this sample have a narrow range from  $0.5119 \pm 2$  to  $0.5122 \pm 4$  ( $2\sigma$ ; Appendix D.1.2) with a mean of  $0.51120 \pm 0.0003$  ( $2\sigma$ ; Table 4.2). The monazite  $\epsilon\text{Nd}_{1038\text{Ma}}$  values range from  $-5.8 \pm 0.8$  to  $-8.2 \pm 1.1$  ( $2\sigma$ ; Appendix D.1.2; Figure 4.41) with a mean  $\epsilon\text{Nd}_{1038\text{Ma}}$  value of  $-7.1 \pm 0.8$  ( $2\sigma$ ; Table 4.2), and yield  $T_{2\text{DM}}$  model ages between 2.0 and 2.2 Ga (Appendix D.1.2).

#### *SDORPB15-9*

Eighteen LA-MC-ICP-MS Sm-Nd isotope analyses were obtained from 10 monazite grains in this sample. The  $^{147}\text{Sm}/^{144}\text{Nd}$  ratios vary from  $0.43915 \pm 0.015$  to  $0.55574 \pm 0.011$  ( $2\sigma$ ; Appendix D.1.3) with a mean of  $0.50489 \pm 0.004$  ( $2\sigma$ ; Appendix Table 4.2). The  $^{144}\text{Nd}/^{143}\text{Nd}$  values have a narrow range from  $0.51347 \pm 0.0001$  to  $0.51424 \pm 0.00006$  ( $2\sigma$ ; Appendix D.1.3) with a mean of  $0.51388 \pm 0.00003$  ( $2\sigma$ ; Table 4.2). The monazite  $\epsilon\text{Nd}_{1004\text{Ma}}$  values calculated for this sample is highly negative and ranged from  $-13.8 \pm 0.6$  to  $-16.4 \pm 0.6$  ( $2\sigma$ ; Appendix D.1.3; Figure 4.41) with a mean of  $-15.4 \pm 0.8$  ( $2\sigma$ ; Table 4.2). Corresponding monazite  $T_{2\text{DM}}$  model ages range from 2.6 to 2.7 Ga (Appendix D.1.3).

### 4.2.1.1. Pella Domain

#### *SD2015-13*

Ten LA-MC-ICP-MS monazite Sm-Nd-isotope analyses were obtained from six monazite grains in this sample.  $^{147}\text{Sm}/^{144}\text{Nd}$  ratios from individual analyses vary from  $0.14386 \pm 0.0004$  to  $0.18016 \pm 0.0005$  ( $2\sigma$ ; Appendix D.2.1) with a mean of  $0.16816 \pm 0.0006$  ( $2\sigma$ ; Table 4.2). The measured  $^{144}\text{Nd}/^{143}\text{Nd}$  ratios also have a very narrow range from  $0.5116 \pm 0.00002$  to  $0.5119 \pm 0.00003$  ( $2\sigma$ ; Appendix D.2.1) with a mean of  $0.51177 \pm 0.00002$  ( $2\sigma$ ; Table 4.2). Monazite  $\epsilon\text{Nd}_{1005\text{ Ma}}$  values are moderately negative and range from  $-12.2 \pm 0.8$  to  $-14.1 \pm 0.5$  ( $2\sigma$ ; Appendix D.2.1; Figure 4.41) with a mean of  $-13.2 \pm 0$ . ( $2\sigma$ ; Table 4.2), and yield monazite  $T_{2\text{DM}}$  model ages between 2.5 and 2.7 Ga.

#### *SDORPB15-10*

Thirteen Sm-Nd isotope analyses were obtained from seven monazite grains in this sample.  $^{147}\text{Sm}/^{144}\text{Nd}$  values from individual analyses vary from  $0.09463 \pm 0.0005$  to  $0.114907 \pm 0.0012$  ( $2\sigma$ ; Appendix D.2.2), with a mean of  $0.12771 \pm 0.0008$  ( $2\sigma$ ; Table 4.2).  $^{144}\text{Nd}/^{143}\text{Nd}$  values have a narrow range from  $0.51127 \pm 0.00002$  to  $0.51169 \pm 0.00004$  ( $2\sigma$ ; Appendix D.2.2) with a mean of  $0.51149 \pm 0.00002$  ( $2\sigma$ ; Table 4.2). The monazite  $\epsilon\text{Nd}_{1016\text{ Ma}}$  values are moderately negative and range from  $-12.3 \pm 0.7$  to  $-15 \pm 0.5$  ( $2\sigma$ ; Appendix D.2.2; Figure 4.41) with and a mean of  $-13.4 \pm 0.6$  ( $2\sigma$ ; Table 4.2). Corresponding  $T_{2\text{DM}}$  model ages varied from 2.5 to 2.7 Ga.

#### *RPGV14*

Sixteen Sm-Nd isotope analyses were obtained from fifteen monazite grains in this sample.  $^{147}\text{Sm}/^{144}\text{Nd}$  values from individual analyses vary from  $0.11769 \pm 0.0004$  to  $0.12522 \pm 0.003$  ( $2\sigma$ ; Appendix D.2.3) with a mean of  $0.12017 \pm 0.0005$  ( $2\sigma$ ; Table 4.2). The  $^{144}\text{Nd}/^{143}\text{Nd}$  values have a very narrow range from  $0.51137 \pm 0.00002$  to  $0.51149 \pm 0.00002$  ( $2\sigma$ ; Appendix D.2.3) with a mean of  $0.51142 \pm 0.00002$  ( $2\sigma$ ; Table 4.2). The monazite  $\epsilon\text{Nd}_{973\text{ Ma}}$  values are highly negative and ranged from  $-13.5 \pm 0.6$  to  $-15.2 \pm 0.6$  ( $2\sigma$ ; Appendix D.2.3; Figure 4.41) with a mean of  $-14.3 \pm 0.6$  ( $2\sigma$ ; Table 4.2). Monazite  $T_{2\text{DM}}$  ages are between 2.6 and 2.7 Ga for this sample.

#### *RPGV16*

Fifteen analyses were obtained from eleven monazite grains. Fourteen LA-MC-ICP-MS Nd-isotope analyses of magmatic monazite have  $^{147}\text{Sm}/^{144}\text{Nd}$  values that range from  $0.08613 \pm 0.0002$  to  $0.19418 \pm 0.004$  ( $2\sigma$ ), with a weighted mean of  $0.117 \pm 0.02$  ( $2\sigma$ , Appendix D.2.4). Measured  $^{144}\text{Nd}/^{143}\text{Nd}$  values have a narrow range from  $0.51121 \pm 0.00002$  to  $0.51195 \pm 0.00001$  ( $2\sigma$ ) with a mean of  $0.51155 \pm 0.00011$  ( $2\sigma$ ; Appendix D.2.4). The  $\epsilon\text{Nd}_{992\text{ Ma}}$  values are strongly negative, ranging from  $-11.9 \pm 0.5$  to  $-14.3 \pm 0.5$  ( $2\sigma$ ; Figure 4.41) yielding a weighted mean of  $-13 \pm 0.4$  ( $2\sigma$ ; Table 4.2). One xenocrystic monazite domain was also sampled.

It had a  $\epsilon\text{Nd}_{1120\text{ Ma}}$  value of  $-3.3 \pm 0.4$  ( $2\sigma$ ; Figure 4.41), significantly different from the magmatic monazite.  $T_{2\text{DM}}$  ages for the magmatic monazite population range from 2.5 to 2.6 Ga, whereas  $T_{2\text{DM}}$  age for the xenocrystic monazite is 1.81 Ga.

### CM38-A

Monazite from this sample had been previously dated in a study by Lambert (2013) who determined an age of  $994 \pm 3$  Ma that was interpreted to be the age of monazite crystallisation for this pegmatite. Thirteen LA-MC-ICP-MS Sm-Nd-isotope analyses were obtained from this monazite.  $^{147}\text{Sm}/^{144}\text{Nd}$  values from individual analyses vary from  $0.12247 \pm 0.0002$  to  $0.1421 \pm 0.0003$  ( $2\sigma$ ; Appendix D.2.5), with a mean of  $0.13323 \pm 0.0007$  ( $2\sigma$ ; Appendix D.2.5). Present day  $^{144}\text{Nd}/^{143}\text{Nd}$  values also have a narrow range from  $0.51134 \pm 0.00002$  to  $0.51154 \pm 0.00002$  ( $2\sigma$ ; Appendix D.2.5) with a mean of  $0.51146 \pm 0.00001$  ( $2\sigma$ ; Table 4.2). The  $\epsilon\text{Nd}_{994\text{ Ma}}$  values are highly negative, with values between  $-13.6 \pm 0.5$  and  $-16 \pm 0.5$  ( $2\sigma$ ; Appendix D.2.5; Figure 4.41) for this sample and gave a mean value of  $\epsilon\text{Nd}_{994\text{ Ma}} -15 \pm 0.3$  ( $2\sigma$ ; Table 4.2). Monazite  $T_{2\text{DM}}$  model ages for this sample were between 2.6 and 2.8 Ga (Appendix D.2.5).

### CM13-B

Fourteen LA-MC-ICP-MS Nd-isotope analyses were obtained from monazite from a pegmatite sample that had previously been dated at  $958 \pm 3$  Ma by Lambert (2013). The sample has a narrow range of  $^{147}\text{Sm}/^{144}\text{Nd}$  values ( $0.16013 \pm 0.0005$  to  $0.17989 \pm 0.002$ ;  $2\sigma$ ; Appendix D.2.6) with a mean  $^{147}\text{Sm}/^{144}\text{Nd}$  value of  $0.16987 \pm 0.0007$  ( $2\sigma$ ; Table 4.2). The present-day  $^{144}\text{Nd}/^{143}\text{Nd}$  values vary from  $0.51166 \pm 0.00001$  to  $0.5118 \pm 0.00002$  ( $2\sigma$ ; Appendix D.2.6) with a mean of  $0.51173 \pm 0.00002$  ( $2\sigma$ ; Table 4.2). The  $\epsilon\text{Nd}_{958\text{ Ma}}$  values are highly negative from  $-13.1 \pm 0.6$  to  $-15.4 \pm 0.5$  ( $2\sigma$ ; Appendix D.2.6; Figure 4.41), with a mean value  $-14.5 \pm 0.5$  ( $2\sigma$ ; Table 4.2) and yielded monazite  $T_{2\text{DM}}$  model ages between 2.5 and 2.7 Ga.

### CP31

Ten analyses were obtained from a pegmatite that was previously dated with a magmatic age of  $1005 \pm 5$  Ma (Lambert, 2013).  $^{147}\text{Sm}/^{144}\text{Nd}$  values from individual LA-MC-ICP-MS Sm-Nd vary from  $0.10116 \pm 0.0002$  to  $0.10708 \pm 0.0007$  ( $2\sigma$ ; Appendix D.2.7) with a mean  $^{147}\text{Sm}/^{144}\text{Nd}$  value of  $0.10475 \pm 0.0004$  ( $2\sigma$ ; Table 4.2). The present-day  $^{144}\text{Nd}/^{143}\text{Nd}$  values are between  $0.51127 \pm 0.00002$  and  $0.51133 \pm 0.00002$  ( $2\sigma$ ; Appendix D.2.7) with a mean of  $0.51131 \pm 0.00001$  ( $2\sigma$ ; Table 4.2). As with many other samples, the  $\epsilon\text{Nd}_{1005\text{ Ma}}$  are highly negative ( $-13.8 \pm 0.5$  to  $-14.7 \pm 0.4$  ( $2\sigma$ ; Appendix D.2.7; Figure 4.41) with a mean  $\epsilon\text{Nd}_{1005\text{ Ma}}$  of  $-14.1 \pm 0.45$  ( $2\sigma$ ; Table 4.2). Monazite  $T_{2\text{DM}}$  model ages are between 2.6 and 2.7 Ga.

## KG36

Twelve monazite Sm-Nd isotope analyses were obtained from this sample, which was previously dated by Lambert (2013) at  $990 \pm 4$  Ma. The  $^{147}\text{Sm}/^{144}\text{Nd}$  values from individual analyses range from  $0.14243 \pm 0.0003$  to  $0.17309 \pm 0.0004$  ( $2\sigma$ ; Appendix D.2.8) with a mean value of  $0.15459 \pm 0.0004$  ( $2\sigma$ ; Table 4.2). Present day  $^{144}\text{Nd}/^{143}\text{Nd}$  values vary from  $0.51156 \pm 0.00001$  to  $0.51178 \pm 0.00001$  ( $2\sigma$ ; Appendix D.2.8) with a mean value of  $0.51166 \pm 0.00001$  ( $2\sigma$ ; Table 4.2); with calculated  $^{144}\text{Nd}/^{143}\text{Nd}_i$  ratios varying from 0.51060 to 0.51079 (Appendix D.2.8) with a mean ratio of 0.51065 (Table 4.2).. The  $\epsilon\text{Nd}_{990 \text{ Ma}}$  values are again strongly negative ( $-11.1 \pm 0.6$  to  $-14.8 \pm 0.4$ ;  $2\sigma$ ; Appendix D.2.8; Figure 4.41) yielding a mean of  $-13.8 \pm 0.45$  ( $2\sigma$ ; Table 4.2). Monazite  $T_{2\text{DM}}$  model ages vary from 2.4 to 2.7 Ga (Appendix D.2.8; Table 4.2).

## 4.2.2 LFROTZ

### HS15HF1

Fourteen LA-MC-ICP-MS Sm-Nd analyses were obtained from this sample and have  $^{147}\text{Sm}/^{144}\text{Nd}$  from  $0.184 \pm 0.0016$  to  $0.2148 \pm 0.0004$  ( $2\sigma$ ; Appendix D.3.1), and has a mean value of  $0.19742 \pm 0.0009$  ( $2\sigma$ ; Table 4.2). Present-day  $^{144}\text{Nd}/^{143}\text{Nd}$  values have a narrow range from  $0.5123 \pm 0.00002$  to  $0.51251 \pm 0.00002$  ( $2\sigma$ ; Appendix D.3.1) and a mean value of  $0.51238 \pm 0.00002$  ( $2\sigma$ ; Table 4.2). The resulting  $\epsilon\text{Nd}_{967 \text{ Ma}}$  values have a narrow range of moderately negative values from  $-4.1 \pm 0.7$  to  $-5.7 \pm 0.5$  ( $2\sigma$ ; Appendix D.3.1; Figure 4.41) with a mean of  $-5.1 \pm 0.53$  ( $2\sigma$ ; Table 4.2). Monazite  $T_{2\text{DM}}$  model ages are between 1.9 and 2.0 Ga.

### SDORPB15-15c

Ten LA-MC-ICP-MS Sm-Nd isotope analyses taken from this sample gave  $^{147}\text{Sm}/^{144}\text{Nd}$  values between  $0.08676 \pm 0.0013$  and  $0.1555 \pm 0.0009$  ( $2\sigma$ ; Appendix D.3.2) with a mean of  $0.10968 \pm 0.0015$  ( $2\sigma$ ; Table 4.2). The present-day  $^{144}\text{Nd}/^{143}\text{Nd}$  values from this sample vary from  $0.51183 \pm 0.00002$  to  $0.51225 \pm 0.00002$  ( $2\sigma$ ; Appendix D.3.2) with a mean of  $0.51197 \pm 0.00002$  ( $2\sigma$ ; Table 4.2). The  $\epsilon\text{Nd}_{978 \text{ Ma}}$  values were small and negative, from  $-1.8 \pm 0.7$  to  $-2.5 \pm 0.5$  ( $2\sigma$ ; Appendix D.3.2; Table 4.2; Figure 4.41) with a mean of  $-2.2 \pm 0.54$  ( $2\sigma$ ; Table 4.2). Monazite  $T_{2\text{DM}}$  model ages vary little and have a mean  $T_{2\text{DM}}$  of 1.7 Ga (Appendix D.3.2; Table 4.2)

### 4.2.3 Kakamas Domain

#### *SDORPB15-17*

Ten LA-MC-ICP-MS Sm-Nd isotope analyses obtained from this sample have  $^{147}\text{Sm}/^{144}\text{Nd}$  values have a narrow range from  $0.1409 \pm 0.0005$  to  $0.1583 \pm 0.0005$  ( $2\sigma$ ; Appendix D.4.1), with a mean of  $0.14712 \pm 0.0007$  ( $2\sigma$ ; Table 4.2). The present-day  $^{144}\text{Nd}/^{143}\text{Nd}$  values has a narrow range from  $0.5121 \pm 0.00002$  to  $0.5123 \pm 0.00002$  ( $2\sigma$ ; Appendix D.4.1) with a mean of  $0.51214 \pm 0.00002$  ( $2\sigma$ ; Table 4.2). The resulting  $\epsilon\text{Nd}_{984\text{Ma}}$  values are small and negative ( $-2.6 \pm 0.7$  to  $-4.1 \pm 0.5$ ;  $2\sigma$ ; Appendix D.4.1; Figure 4.41) with a mean of  $-3.51 \pm 0.4$  ( $2\sigma$ ; Table 4.2). Monazite  $T_{2\text{DM}}$  model ages range from 1.7 to 1.9 Ga.

#### *SDORPB15-18*

Only six LA-MC-ICP-MS monazite Sm-Nd isotope analyses could be obtained from this sample and has  $^{147}\text{Sm}/^{144}\text{Nd}$  values varying from  $0.11199 \pm 0.0005$  to  $0.12323 \pm 0.0003$  ( $2\sigma$ ; Appendix D.4.2) with a mean value of  $0.12124 \pm 0.0004$  ( $2\sigma$ ) (Table 4.2). Present-day  $^{144}\text{Nd}/^{143}\text{Nd}$  values for this sample are homogenous with a narrow range from  $0.51204 \pm 0.00002$  ( $2\sigma$ ) to  $0.51210 \pm 0.00002$  ( $2\sigma$ ) (Appendix D.4.2), with a mean value of  $\sim 0.51207 \pm 0.0002$  ( $2\sigma$ ) (Table 4.2). The  $\epsilon\text{Nd}_{1015\text{Ma}}$  values also show a narrow range of very small negative values from  $-0.8 \pm 0.6$  to  $-1.7 \pm 0.6$  ( $2\sigma$ ; Appendix D.4.2; Figure 4.41) with a mean value of  $-1.4$ . Monazite  $T_{2\text{DM}}$  model ages range from 1.6 to 1.7 Ga.

#### *SDORPB15-20*

Twelve LA-MC-ICP-MS monazite Sm-Nd isotope analyses were obtained from this sample.  $^{147}\text{Sm}/^{144}\text{Nd}$  values vary from  $0.12069 \pm 0.0003$  to  $0.15761 \pm 0.0003$  ( $2\sigma$ ; Appendix D.4.3) with a mean value of  $0.13591 \pm 0.0007$  ( $2\sigma$ ; Table 4.2). The present-day  $^{144}\text{Nd}/^{143}\text{Nd}$  show a range from  $0.51204 \pm 0.0002$  to  $0.51226 \pm 0.00002$  ( $2\sigma$ ; Appendix D.4.3) with a mean of  $0.51215 \pm 0.00002$  ( $2\sigma$ ; Table 4.2). The  $\epsilon\text{Nd}_{987\text{Ma}}$  show a narrow range small negative values of  $-0.8 \pm 0.6$  to  $-2.4 \pm 0.5$  ( $2\sigma$ ; Appendix D.4.3; Figure 4.41), while monazite  $T_{2\text{DM}}$  ages range from 1.6 to 1.7 Ga.



## 5 Discussion

### 5.1 The distribution of monazite U-Pb ages from pegmatites in the Orange River Pegmatite Belt

Only two modern U-Pb geochronological studies have previously been undertaken on the pegmatites of the ORPB. One study concentrated on pegmatites along the Marshal Rocks-Pofadder Shear Zone (Lambert, 2013) and the other on the Homestead mine at Tantalite Valley, Namibia (Melcher *et al.*, 2008). Lambert (2013) dated five pegmatites by monazite LA-ICP-MS U-Pb geochronology and determined pegmatite crystallisation ages that ranged from ~1005 Ma to ~958 Ma. Melcher *et al.* (2008) obtained U-Pb crystallisation ages of ~985 Ma and ~981 Ma for tantalite from the Homestead mine.

As the studies mentioned above were from a small area within the ORPB, one aim of the present study was to date the pegmatites of the ORPB on a broader regional scale across the various tectonic domains to ascertain whether the pegmatites intruded in a single event or over an extended period. The results from the U-Pb isotopic analyses in this study, combined with those referenced above (Melcher *et al.*, 2008; Lambert, 2013), show that the pegmatites intruded into the Namaqua sector of the NNMP during an extended period of ~78 m.yr. from ~1038 Ma to ~958 Ma (Table 4.1). The range of crystallisation ages is significantly larger than the uncertainties on the crystallisation ages of individual pegmatites. Additionally, these pegmatites intrude into tectonic domains that have experienced a diverse and complex metamorphic and tectono-magmatic history over the ~1.0 Ga period, resulted in the development of the Namaqua-Natal Metamorphic Province.

Pegmatites that intrude into the Richtersveld Magmatic Arc along the gradational Southern Namaqua Front appear to be the oldest of the dated pegmatites (Figure 5.1), with U-Pb magmatic crystallisation ages between  $1038 \pm 7$  Ma and  $993 \pm 12$  Ma (Figure 5.1; Table 4.1). These pegmatites intrude into  $D_1$  and  $D_{1/2}$  ( $D_1$  structures reworked by  $D_2$  by  $D_2$  thrusting) structures along the transitional boundary between the greenschist-facies Vioolsdrif Domain and the amphibolite-facies Pella Domain. The oldest sample, SD2015-11 ( $1038 \pm 7$  Ma; Figure 5.1) intruded along structural sites opened up parallel to transcurrent  $D_4$  shearing in the Sperlingsputs Shear Zone (Indongo, 2017). Samples SDORPB15-4b, SDORPB15-7d, SDORPB15-9, SDORPB16-4 and SDORPB16-5 were weakly to strongly zoned, LCT-type pegmatites with a strong REE-class signature. They contain abundant Li minerals (spodumene and/or lepidolite), beryl, tourmaline and REE-phosphates. These dated pegmatites have ages ranging from  $1020 \pm 11$  Ma to  $993 \pm 12$  Ma and intruded conformably with  $D_{1/2}$  structures along the Southern Namaqua Front.

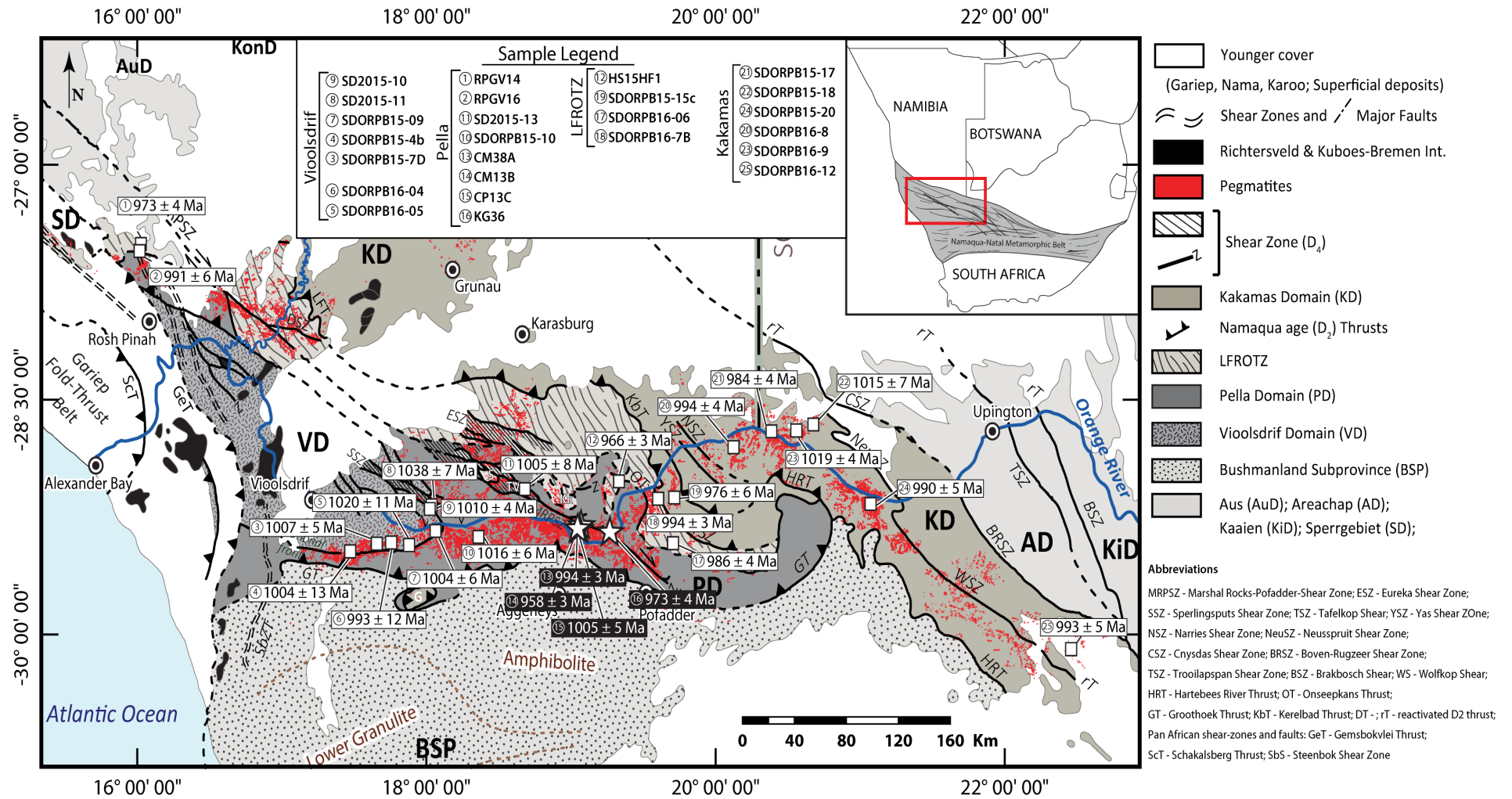


Figure 5.1: Simplified geological map of the NNMP illustrating the distribution of monazite U-Pb emplacement ages for the pegmatites in the ORPB. Samples analysed in this study are in white boxes while pegmatites dated by Lambert (2013) are in black boxes, (Map compiled from Hugo, 1970; Schutte, 1972; Lambert, 2013; Macey et al. 2015, 2018).

The pegmatites from the Pella Domain (PD; Figure 5.1) were predominantly sampled near the Marshall Rocks-Pofadder-Shear Zone (i.e. SD2015-13, RPGV14 and RPGV16) with one lone sample obtained from the interior of the PD (SDORPB15-10). All these pegmatites from the PD were relatively simple, weakly-zoned to unzoned and lacking in exotic mineral phases (e.g. spodumene, lepidolite and beryl) seen in the REE-class pegmatites in this study. With regards to samples RPGV14 and RPGV16, these pegmatites were located in the extension of the ORPB in the Namusklaaft area near Rosh Pinah (Figure 5.1), and yielded U-Pb crystallisation ages of  $973 \pm 4$  Ma and  $992 \pm 6$  Ma respectively. The sample SD2015-13 was from a weakly deformed pegmatite within the MRPSZ that yielded a U-Pb age of  $1005 \pm 8$  Ma (Table 4.1). This is similar to an age determined by Lambert *et al.* (2013) for a pegmatite within D<sub>4</sub> structures of the MRPSZ that he determined was the maximum age for deformation of this large transcurrent dextral shear-zone. Sample SDORPB15-10 yielded a slightly older age of  $1016 \pm 6$  Ma (Table 4.1; Figure 5.1), which is interpreted to be in close relation to the pegmatites of the Vioolsdrif Domain to the west.

The Orange River Group (ORG) and the Vioolsdrif Suite in the Vioolsdrif Domain experienced only greenschist-facies metamorphism during the D<sub>1</sub> Orange River Orogeny at ~1800 Ma and was largely unaffected to subsequent metamorphism throughout the pervasive D<sub>2</sub>-D<sub>3</sub> tectono-metamorphic events of the Namaqua Orogeny at ~1200 to 1080 Ma (Macey *et al.*, 2017). However, monazite recovered from the pegmatites in this domain were magmatic and yielded, in some cases (i.e. SD2015-10, SD2015-11 and SDORPB15-7d) concordant U-Pb ages. It is apparent that the parental magma for the pegmatites of the VD was sourced from elsewhere, and that the pegmatites intruded into country rocks that were well below even the wet solidus for quartzofeldspathic or pelitic rocks at the time of pegmatite emplacement.

A similar scenario is present with respect to the pegmatites emplaced into the country rocks of the Pella Domain of the RMA. The PD was reworked during the main ~1.2 Ga (D<sub>2</sub>) deformation event of the Namaqua Orogeny, which resulted in peak metamorphism at amphibolite-facies conditions, subsequently forming the para- and ortho-gneisses of the ORG and Vioolsdrif Suite (see chapter 2; Macey *et al.*, 2017). The pegmatites that were emplaced in the PD ~200 Ma after this peak metamorphic event into country rock that is still below the wet solidus for quartzofeldspathic or pelitic rocks at the time of pegmatite emplacement. Again, it is apparent that the parental magma for these pegmatites were sourced from elsewhere.

This study also sampled four pegmatites from the recently described Lower Fish River-Onseepkans-Thrust Zone (Macey *et al.*, 2015) that is a tectonised zone between the Kakamas and Pella Domains. The pegmatites from this zone of pervasive and intense deformation are the youngest dated within this study. Monazite U-Pb crystallisation ages ranged from  $994 \pm 3$  Ma to  $966 \pm 3$  Ma (Table 4.1; Figure 5.1). The two oldest pegmatites from the LFROTZ (SDORPB16-6 and SDORPB16-7b) were weakly to strongly zoned LCT-type pegmatites with monazite crystallisation ages of  $994 \pm 3$  Ma and  $986 \pm 4$  Ma respectively. A further

two simple, unzoned pegmatites (SDORPB15-15c and HS15HF1) are younger with interpreted pegmatite crystallisation ages of  $976 \pm 6$  Ma and  $966 \pm 3$  Ma (Table 4.1).

Additionally, peak metamorphic conditions in the LFROTZ has been estimated for Veloorsdrift amphibolites to be  $\sim 5$ - $7$  kbar and at  $600$ - $670$  °C (Macey *et al.*, 2015), with peak metamorphism occurring during  $D_{2a}$  thrusting at  $\sim 1100$  Ma. The maximum temperatures in the LFROTZ at  $\sim 1100$  Ma barely exceed the maximum required temperature for water-saturated melting of quartzofeldspathic or pelitic parent rock types ( $\sim 650$ - $660$  °C at  $\sim 6$  kbar; Luth *et al.*, 1964). It is clear from the relatively young crystallisation ages ( $\sim 990$  Ma to  $960$  Ma ( $\sim 960$  –  $990$  Ma) that the pegmatites in this tectonic domain post-date the peak of metamorphism and deformation in the LFROTZ (see section 2.1.3) by more than  $\sim 100$  Ma. Furthermore, reported hornblende  $^{40}\text{Ar}/^{39}\text{Ar}$  for the country rocks of the RMA and KD indicates that the currently exposed crust had cooled to below  $500$ °C at  $\sim 1026$  Ma to  $990$  Ma (Pettersson, 2008; Büttner *et al.*, 2013), with the crust experiencing further cooling to below the  $^{40}\text{Ar}/^{39}\text{Ar}$  closure temperatures for muscovite ( $\sim 350$  °C) at around  $\sim 960$ . Thus, it follows that the pegmatites could not have been sourced locally by anatexis of the country rocks of the LFROTZ at  $\sim 1000$  Ma, which had reached peak metamorphic conditions to upper amphibolite facies metamorphism at  $\sim 1100$  Ma (Macey *et al.*, 2015).

Six pegmatites were also sampled and dated from the granulitic Kakamas Domain (KD). The pegmatites within the KD, notably around the Riemvasmaak and Kakamas areas, are of a mixed LCT- and NYF-family of pegmatites due to the high abundance of fluorite, yttrium-rich minerals (gadolinite and euxenite) and Nb-rich columbite-tantalite in a number of the pegmatites. Pegmatite samples SDORPB15-17, SDORPB15-18 and SDORPB16-9 (Table 4.1; Figure 5.1) were from pegmatites in a mixed LCT- and NYF-type pegmatite field around the Riemvasmaak area. SDORPB15-18 and SDORPB16-9 were from simple and weakly- to unzoned pegmatites. Variably altered monazite grains from these pegmatites yielded U-Pb monazite crystallisation ages of  $1015 \pm 7$  Ma and  $1019 \pm 4$  Ma, respectively; at the older end of the spectrum of ages obtained from the ORPB. In the same vicinity, SDORPB15-17, a muscovite-rich REL-class pegmatite containing pristine magmatic monazite was dated yielding a younger magmatic age of  $984 \pm 4$  Ma.

The Kakamas Domain pegmatites, to the south of those described above, in the pegmatites fields around Kenhardt and Putsonderwater, have mineral assemblages that reflect clearer LCT-type affinity. These pegmatites are more abundant in Li-bearing minerals (chiefly lepidolite) and have a higher abundance of Ta-rich columbite-tantalite. It was only possible to date one sample from a pegmatite in this region (SDORPB16-12; Figure 5.1), and even this sample proved difficult to date, due to the abundance of inheritance in the recovered monazite. However, a magmatic age was calculated at  $993 \pm 5$  Ma (Table 4.1) from one monazite grain.

Six pegmatite samples yielded older xenocrystic monazite ages (Table 4.1) that reflect ages that are synchronous with magmatic and metamorphic events within the Namaqua-Natal Metamorphic Province.

These xenocrystic monazite components from RMA pegmatites came from both an LCT-type pegmatite (SDORPB15-7d) within the Vioolsdrif Domain and a simple pegmatite (RPGV16) in the Pella Domain.

The inherited xenocrystic monazite crystals are enigmatic as sample SDORPB15-7d (Table 4.1) was taken from a tectonic domain that only ever reached greenschist-facies metamorphic conditions throughout the ~1.2-1.0 Ga Namaqua Orogeny. The other pegmatite (RPGV16; Table 4.1) is within the amphibolite-facies Pella Domain, which did experience  $M_2$  metamorphism during  $D_2$  deformation events. However, the main tectono-magmatic event associated with the ~1100 – 1120 Ma magmatic event was restricted to the Kakamas Domain and LFROTZ (i.e. intrusion of the Komsberg and Keimoes Suites; Macey *et al.*, 2015; Bial *et al.*, 2015b; Bailie *et al.*, 2017; Table 2.2). Monazite inheritance was also observed in a sample from the LFROTZ (SDORPB16-6; Table 4.1) with a xenocrystic monazite component dated at  $1123 \pm 9$  Ma. The samples from the Kakamas domain contain a xenocrystic monazite component that is older (Table 4.1) than those noted above, and reflect the initial  $D_{2a}$  tectono-magmatic event at the onset of the ~1.2-1.0 Ga Namaqua Orogeny. Pegmatite samples SDORPB16-8, SDORPB16-9 and SDORPB16-12 all contain ~1200 Ma inheritance (Table 4.1). Additionally, sample SDORPB16-12 contained another group of xenocrystic ages at  $1145 \pm 4$  and  $1092 \pm 7$  Ma (Table 4.1). These ages reflect  $D_{2c}$  and  $D_3$  tectono-magmatic events within the Kakamas Domain, responsible for the intrusion of syn-tectonic granites at ~1140 Ma and supracrustal deposition at ~1160 Ma with subsequent  $D_3$  metamorphism at ~1090-1100 Ma (Colliston *et al.*, 2015, Bailie *et al.*, 2017).

To summarise, the pegmatites of the Orange River Pegmatite Belt have intruded into tectonic domains that reached maximum metamorphic conditions that vary from greenschist- to granulite-facies, reached these peak metamorphic grades at different times, and experienced multiple metamorphic and tectono-magmatic events prior to pegmatite emplacement. Although the dated pegmatites are just small sample set of the thousands of pegmatites that make up the swarm. There is an apparent zonation concerning pegmatite emplacement in the different domains. The pegmatites that intruded the boundary zone between the Vioolsdrif and Pella Domains appear to be the oldest. The pegmatites of the Orange River Pegmatite Belt intrude into structural sites that are predominantly concordant to regional deformational structures (Lambert, 2013; Macey *et al.*, 2015).

## 5.2 Sm-Nd isotope systematics of the Orange River Pegmatite Belt in relation to the Namaqua-Natal Metamorphic Province

The monazite Sm-Nd-isotope compositions of the analysed pegmatite samples from the Orange River Pegmatite Belt have been plotted on a  $\epsilon\text{Nd}_t$  versus time diagram (Figure 5.3), where  $t$  (time) is the appropriate geological age for the respective suite or unit. Included in this diagram are the Sm-Nd isotope compositions from the literature for the various NNMP country rocks and magmatic rocks that could conceivably be source rocks for the pegmatites. The compiled literature Sm-Nd isotope composition data includes lithologies within the Richtersveld Magmatic Arc, Kakamas Domain, LFROTZ as well as the Bushmanland Subprovince (Table 5.1; references within). A full table of Sm-Nd isotope compositions and lithology descriptions for the NNMP can be found in Appendix E. Sm-Nd isotope compositions, and  $\epsilon\text{Nd}_t$  values for individual samples are reported as arithmetic means of the individual analysed monazites from the sample set.

The ~2000 – 1900 Ma Orange River Group volcanics in the Vioolsdrif Domain and their metamorphic equivalents in the Pella Domain have very similar Sm-Nd isotopic compositions with  $\epsilon\text{Nd}_t$  (calculated using their respective geological age,  $t$ ) from -2.5 to 2.3 (Table 5.1 and Figure 5.3; Reid, 1997; Macey *et al.*, 2017). A similar range in  $\epsilon\text{Nd}_t$  occurs for the ~1890 Ma Vioolsdrif Suite in both the Vioolsdrif and Pella Domains, where the granitoids and gneisses have similar Sm-Nd isotopic ratios with  $\epsilon\text{Nd}_t$  values between -3.0 and 1.1 (Figure 5.3 and Table 5.1; Reid, 1997; Pettersson *et al.*, 2009; Macey *et al.*, 2015; 2017). The ~1220 Ma Orange Falls Suite (Chapter 2; Macey *et al.*, 2015) have unradiogenic Sm-Nd compositions that yield  $\epsilon\text{Nd}_t$  values between -12.4 to -9.3 (Figure 5.3). The isotopically “evolved” felsic rocks of the Orange Falls Suite are thought to be derived from melting of the calc-alkaline Richtersveld Magmatic Arc rocks or similar calc-alkaline source during  $D_{2a}$  thrusting (Macey *et al.*, 2015). The  $\epsilon\text{Nd}_t$  vs time diagram (Figure 5.3), where the Sm-Nd isotope data for Orange Falls Suite indicate that the suite lies on the evolutionary line through the RMA country rock isotope compositions agreeing with the proposition of an RMA source for the Orange Falls Suite.

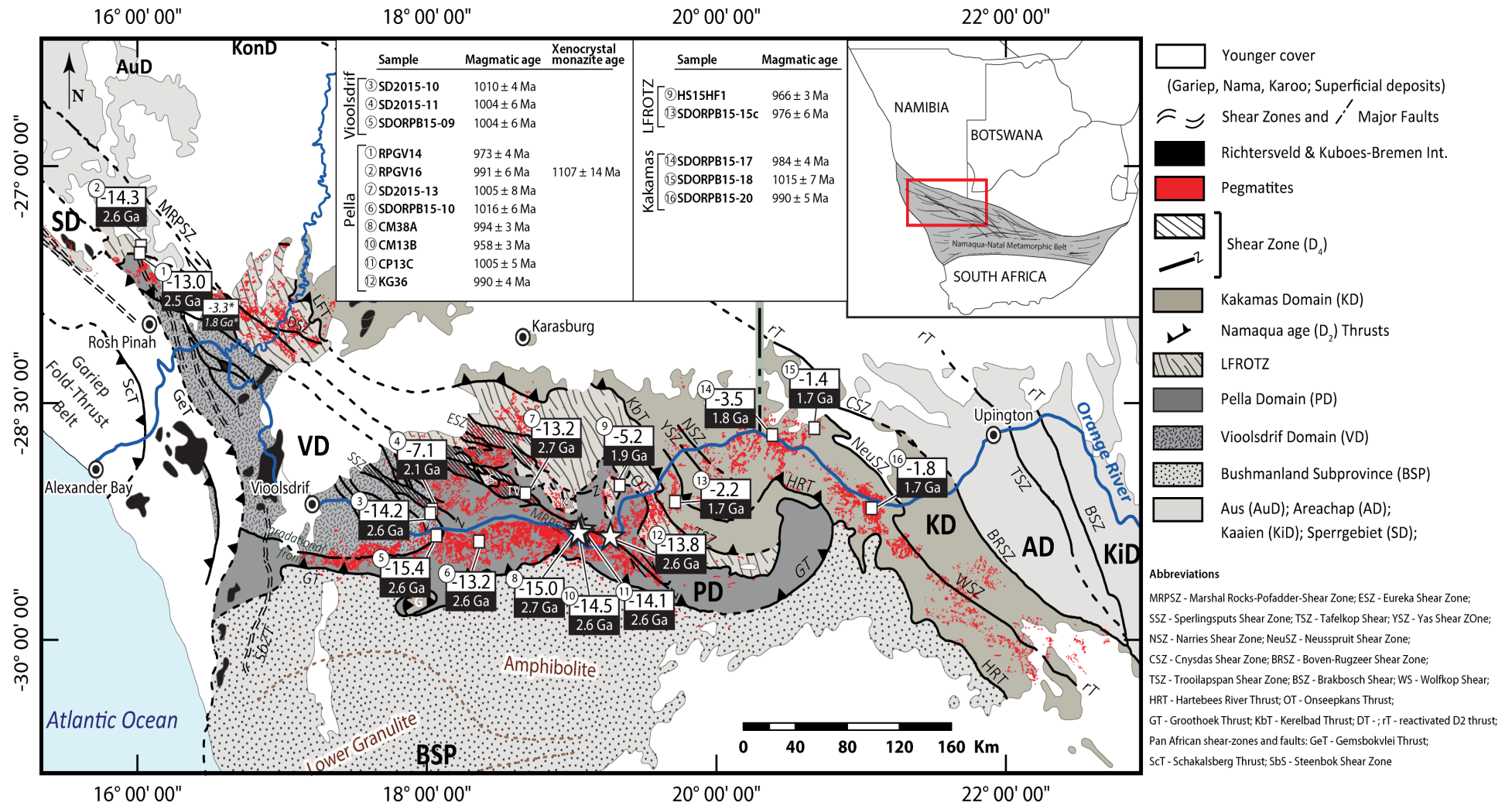


Figure 5.2: A simplified geological map of the NNMP illustrating the spatial distribution of Sm-Nd isotope compositions ( $\epsilon Nd_t$ ) from the studied pegmatites from across the ORPB. Epsilon units for the samples are in white boxes above the 2-stage depleted mantle model ages (black boxes). \* represents the inherited monazite component observed in sample RPGV16).

The majority of the pegmatites that have been emplaced into the Vioolsdrif Domain were unradiogenic (“evolved”) Sm-Nd isotope compositions with a narrow range of  $\epsilon\text{Nd}_t$  values between -14.2 and -15.4 (Table 5.1; Figure 5.2 and Figure 5.3). The same is true for pegmatites that intruded into the Pella Domain, which have slightly higher but similar range in  $\epsilon\text{Nd}_t$  values between -13.0 and -15.0 (Table 5.1; Figure 5.2 and Figure 5.3). These pegmatites lie within the crustal evolutionary trend lines of the Richtersveld Magmatic Arc (Figure 5.3), which suggests that the pegmatites are possibly derived from melting of rocks of similar composition. The possible scenario is that the pegmatite melts were sourced by reworking of Paleoproterozoic crust or Richtersveld Magmatic Arc type source rocks.

Two-stage depleted model ages ( $T_{2\text{DM}}$ ; calculated assuming  $^{147}\text{Sm}/^{144}\text{Nd} = 0.12$ ) were calculated for each sample (Table 4.2). The  $T_{2\text{DM}}$  ages for pegmatites from the Richtersveld Magmatic Arc, (Vioolsdrif and Pella domains) vary between  $\sim 2.1$  and  $\sim 2.8$  Ga (Table 5.1; Figure 5.2). These ages are in agreement with  $T_{2\text{DM}}$  ages for units from the Richtersveld Magmatic Arc (Table 5.1) or an early Paleoproterozoic crust. This suggests that the parental magmas responsible for the pegmatites within the RMA were derived from reworking of late Archean to early Paleoproterozoic crust. The Archean isotope signature could be due to an inherited signature from the RMA lithologies that have an inherited Archean component.

Within the Pella Domain and parts of the LFROTZ occurs a young, undeformed granite suite of peraluminous S-type leucogranites and biotite-muscovite granites collectively termed the Warmbad Suite (Macey *et al.* 2015). The granites of this suite have proven difficult to date, and only limited U-Pb and Sm-Nd isotope data exist. Its cross-cutting field relationships and sparse U-Pb dates indicate that this granite is a late intrusion into the NNMP at  $\sim 1.0$  Ga (Macey *et al.* 2015).  $\epsilon\text{Nd}_t$  values from -13.9 to -12.8 (Macey *et al.*, 2015; Table 5.1, Figure 5.3) for the Warmbad Suite falls within the range obtained from pegmatites within the RMA. This suggests, uniquely in the context of the Namaqua Sector of the NNMP, that exposed Warmbad Suite could be a possible source for late-fractionated melts responsible for the pegmatites within the RMA. However, field observations show that the pegmatites have been intruded by Warmbad Suite (Macey *et al.*, 2015) and could possibly be younger or its emplacement contemporary with the emplacement of the pegmatites. Further investigation of the Warmbad Suite granites themselves is needed to confirm this link.

Limited Sm-Nd isotope studies have been undertaken for units in the LFROTZ and granulite klippe associated with the  $D_2$  thrust zone (e.g. Macey *et al.*, 2015). The megacrystic granodiorites of the Eendoorn and the mafic Kum Suites (Chapter 2; Table 5.1) that intruded at  $\sim 1230 - 1193$  Ma during  $D_{2a}$  thrusting show similar Sm-Nd isotope compositions, with  $\epsilon\text{Nd}_t$  values ranging from -8.1 to 3.4 and -8.1 to -4.4, respectively (Table 5.1, Figure 5.3; Macey *et al.*, 2015). The mafic and felsic sheets of the Oupvlakte Complex have similar Sm-Nd isotope compositions to the Eendoorn and Kum Suites but have not been grouped together in studies by Macey *et al.* (2015). Two samples from the Oupvlakte Complex analysed by Macey *et al.* (2015) had  $\epsilon\text{Nd}_t$  of -9.4 and -1.3, respectively (Table 5.1, Figure 5.3).



Table 5.1: Summary table of U-Pb ages and Sm-Nd isotope compositions for country rocks and pegmatites for the studied tectonic domains of the Namaqua-Natal Metamorphic Province. Country rock data compiled from: (a) Clifford et al., 1995; (b) Reid, 1997; (c) Yuhara et al., 2001; (d,f,h) Bailie et al., 2007b,2001; 2017b; (e) Pettersson et al., 2009; (g,i,j) Macey et al., 2015, 2017, 2018)

Tectonic Domain	Suite/Group	Lithology	Magmatic Age	$\epsilon\text{Nd}_t$	$T_{2DM}$
<b>Vooldsdrif Domain</b>	Orange River Group <sup>b,g,i</sup>	Rhyolite, Basaltic andesites, dacites, rhyodacites, andesites	~2085 Ma	-2.5 to 2.3	~2.5 - 2.3 Ga
	Vooldsdrif Suite <sup>b,g,i</sup>	Tonalite, granodiorite, monzogranite, granite, alkali granite	~1998 - 1885 Ma	-2.8 to 1.0	~2.6 - 2.4 Ga
	Vuurdoed Suite <sup>b</sup>	Troctolite, gabbro	~1998 Ma	-0.3 to 0.8	~2.5-2.4 Ga
	Orange River Pegmatite <sup>k</sup>	Simple unzoned and REL-type (LCT)	~1038 - 993 Ma	-15 to -7.1	~2.6 - 2.1 Ga
<b>Pella Domain</b>	Goodhouse Subsuite <sup>b,e,g,i</sup>	(No Suggestions) orthogneiss, Augen gneiss, bt granite gneiss, equigranular gneiss	~1885 Ma	-3.0 to -1.1	~2.5 - 2.6 Ga
	Guadom gneiss <sup>g,i</sup>	Bt+Hbl gneiss	~1875 MA	-2.5	~2.5 Ga
	Orange Falls Suite <sup>g</sup>	Granitic augen gneiss, granitic gneiss, equigranular granite gneiss	~1238 - 1196 Ma	-12.4 to -9.3	~2.6 - 2.8 Ga
	Girtis Suite <sup>g</sup>	Amphibolite	~1220 Ma	-10.6	~2.7 Ga
	Warmbad Granite <sup>g</sup>	unfoliated granite	~1003 Ma	-13.9 to -12.8	~2.7 - 2.8 Ga
	Orange River Pegmatite <sup>k</sup>	Simple unzoned and zoned	~1016 - 973 Ma	-14 to -13	~2.7 - 2.5 Ga
<b>LFROTZ</b>	Eendoorn Suite <sup>g</sup>	Megacrystic granodiorite	~1230 - 1193 Ma	-8.1 to -3.4	~2.5 - 2.1 Ga
	Oupvlakte Complex <sup>g</sup>	quartzofeldspathic gneiss	~1210 Ma	-9.4 to -1.3	~2.6 - 1.9 Ga
	Kum Kum Suite <sup>g</sup>	Gabbro, metagabbro, olivine gabbro	~1220 - 1212 Ma	-8.1 to -4.4	~2.5 - 2.2 Ga
	Orange River Pegmatite <sup>k</sup>	Simple unzoned and zoned REL-type (LCT)	~994 - 966 Ma	-5.1 to -2.2	~1.9 - 1.7 Ga
<b>Kakamas Domain</b>	Josling Gneiss <sup>h</sup>	leucogranite gneiss	~1217 Ma	1.8 to 3.7	~1.5 - 1.7 Ga
	Eendoorn Suite <sup>g</sup>	Bt megacrystic augen gneiss, megacrystic granite gneiss	~1200 - 1113 Ma	-2.0 to -1.0	~1.9 - 1.7 Ga
	Witwater Gneiss <sup>e</sup>	Bt-grt gneiss	~1203 Ma	-0.8	~1.9 Ga
	Austerlitz Gneisses <sup>g</sup>	Bt augen gneiss, leucogranite gneiss	~1190 Ma	0.3 to 1.5	~1.7 - 1.8 Ga
	Cnydas Gneiss <sup>h</sup>	monzogranite gneiss	~1159 Ma	1.2 to 1.4	~1.6-1.7 Ga
	Syn-tectonic gneisses <sup>e,f,g</sup>	granodioritic gneiss, crs-grained leucogranite gneiss, bt granite gneiss, hbl granite gneiss, porphyritic granite granodioritic gneiss	~1151 - 1140 Ma	-2.1 to 2.8	~1.9 - 1.5 Ga
	Komsberg Suite <sup>g</sup>	Granodioritic porphyritic gneiss, C.g. equigranular granite gneiss, granite gneiss, porphyritic enderbite	~1110 Ma	-1.2 to 0.1	~1.7 - 1.8 Ga
	Klienbegin Subsuite <sup>f,h</sup>	leucocratic granodiorite	~1101 - 1099 Ma	-8.5 to -7.5	~2.4 - 2.3 Ga
	Keimoes Suite <sup>h</sup>	Pyx-Hbl-Bt granite, charnockite, Bt monzogranite, granodiorite	~1110 - 1078 Ma	-3.0 to 1.8	~1.9 - 1.5 Ga
	Orange River Pegmatite <sup>k</sup>	Simple unzoned and REL-type (LCT+NYF)	~1019 - 984 Ma	-3.5 to -1.4	~1.8 - 1.7 Ga
<b>Bushmanland Subprovince</b>	Bushmanland Grp <sup>d</sup>	various supracrustals (schists, quartzites, etc.)	~1600 Ma	-9.6 to -2.0	~2.9 to 2.3 Ga
	Little Namaqualand Suite (North) <sup>a,c,e</sup>	Bt-Hbl granite gneisses, Bt granite gneisses, 2-pyx granulites	~1212 - 1199 Ma	-8.7 to -2.4	~2.5 - 2.0 Ga
	Little Namaqualand Suite (South) <sup>c,e</sup>	Bt-Hbl granite gneisses, Bt granite gneisses, 2-pyx granulites	~1212 - 1199 Ma	-1.6 to 1.4	~1.9 - 1.7 Ga
	Concordia Granite <sup>a,e</sup>	garnet leucogranite	~1170 - 1160 Ma	-8.7 to -6.5	~2.5 - 2.2 Ga
	Koperberg Suite <sup>a</sup>	Anorthositic, Bt diorites, Hypersthinites, melanorites, norites, leuconorites	~1061 - 1037 Ma	-11.2 to 7.1	~2.6 - 2.3 Ga
	Spektakel Suite <sup>c,e,j</sup>	Granites, Charnockites, monzogranites, charnockitic granites	~1080 - 1030 Ma	-2.3 to 0.5	~1.9 - 1.6 Ga

Abbreviations used: Bt – biotite; Hbl – hornblende; Pyx – pyroxene; Grt – garnet; C.g. – coarse grained; Grp. – group.

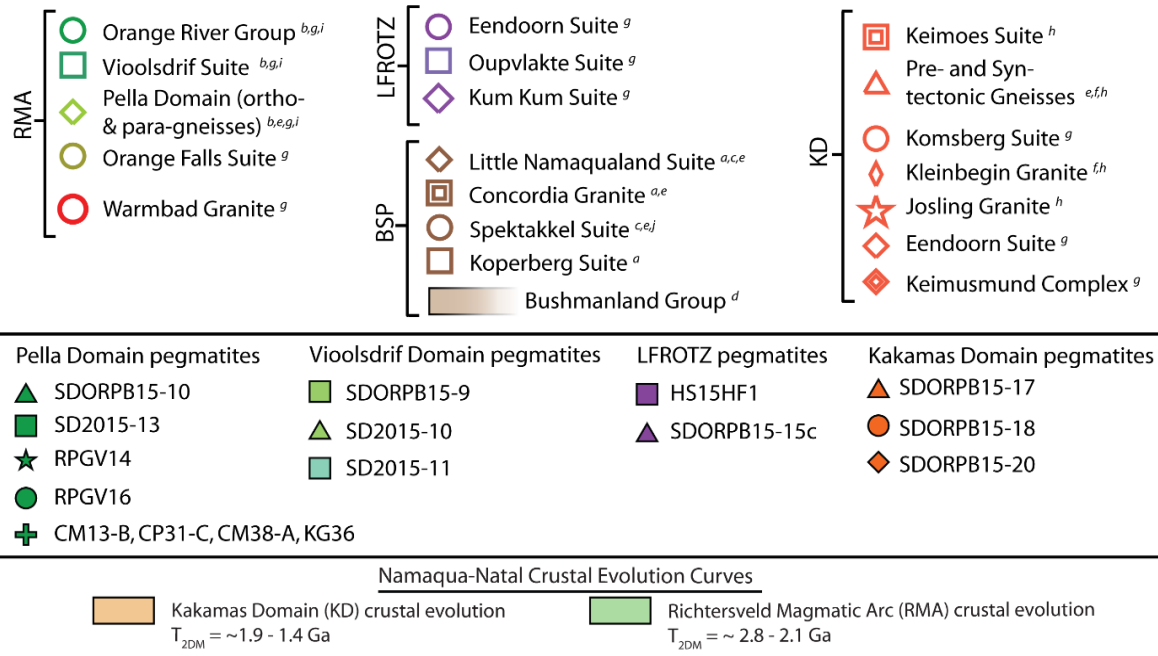
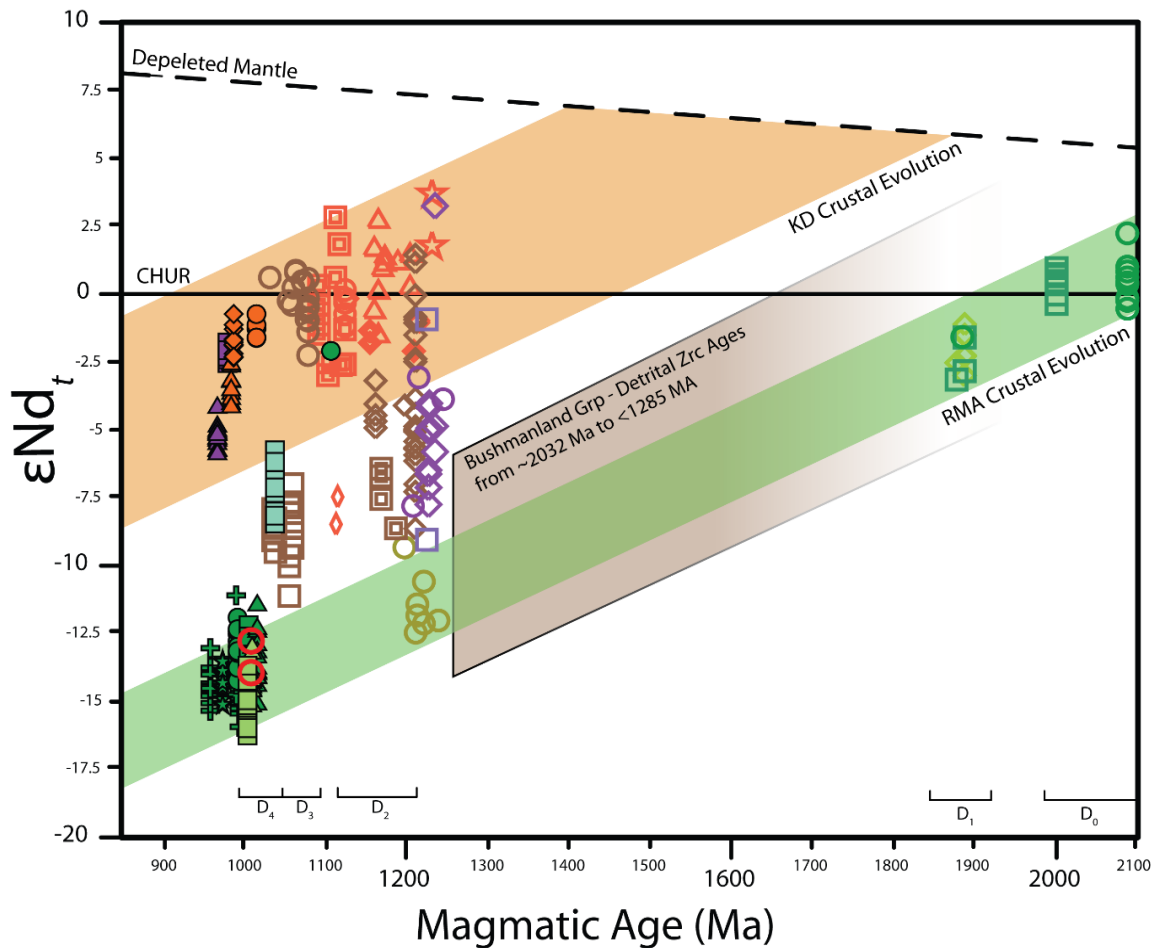


Figure 5.3:  $\epsilon Nd_t$  vs. time diagram showing Sm-Nd isotopic data for analysed monazite from pegmatites of the Orange River Pegmatite Belt. Time (t) or data from this study is the respective monazite crystallisation age. Monazite Sm-Nd isotope compositions are assumed to faithfully reflect the whole rock Sm-Nd isotope compositions of the Pegmatites (this study)  $\epsilon Nd_t$  data for NNMP country rocks is from current literature have been recalculated using the preferred geological age (emplacement age) for the respective lithological units and the same CHUR and depleted mantle isotope compositions used to plot monazite data. Country rock data sources: (<sup>a</sup> Clifford et al., 1995; <sup>b</sup> Reid, 1997; <sup>c</sup> Yuhara et al., 2001; <sup>d,f,h</sup> Bailie et al., 2007b,2001; 2017b; <sup>e</sup> Pettersson et al., 2009; <sup>g,i,j</sup> Macey et al., 2015, 2017, 2018).

Pegmatites emplaced into the LFROTZ have  $\epsilon\text{Nd}_t$  values between -5.2 and -2.2 (Table 5.1; Figure 5.2 and Figure 5.3). It is possible that the pegmatites could have been sourced from similar source-type rocks for some of the lithologies in the LFROTZ. However, the Sm-Nd isotope compositions for the country rocks of the LFROTZ are limited and mostly from the  $\sim 1.2$  Ga mafic intrusions of the Kum Kum Suite, the granodioritic Eendoorn Suite and scattered felsic dykes of the lithologically variable Oupvlakte Complex. The Eendoorn Suite has similar  $\epsilon\text{Nd}_t$  values (between -8.1 to -3.4; Table 5.1), hinting that the magmas that crystallised the pegmatites within the LFROTZ were from a similar source. The  $T_{2\text{DM}}$  model ages from the Eendoorn Suite and other country rocks in the LFROTZ are late Archean to early Paleoproterozoic ( $\sim 2.6 - 2.0$  Ga; Table 5.1) while the pegmatites have slightly younger, late Paleoproterozoic  $T_{2\text{DM}}$  model ages of  $\sim 1.9$  to 1.7 Ga (Table 5.1; Figure 5.2).

The Sm-Nd isotope composition of lithologies from the Kakamas Domain are, in general, relatively more radiogenic (“juvenile”) than those seen in the Richtersveld Magmatic Arc and LFROTZ. The granites and granite precursors to gneisses formed during  $D_{2a}$  thrusting at  $\sim 1.2$  Ga (i.e. Eendoorn Suite, Austerlitz gneisses, Josling gneiss and Witwater gneiss) have variable Sm-Nd compositions with a range in  $\epsilon\text{Nd}_t$  values from -2.0 to 3.7 (Table 5.1; Pettersson *et al.*, 2009; Macey *et al.*, 2015; Bailie *et al.*, 2017). Syn-tectonic orthogneisses (e.g. Augrabies Suite; Colliston *et al.*, 2015) in the Kakamas Domain have similar Sm-Nd compositions, with  $\epsilon\text{Nd}_t$  values ranging from -2.1 to 2.8 (Table 5.1, Figure 5.3; Pettersson *et al.*, 2009; Macey *et al.*, 2015; Bailie *et al.*, 2017). The relatively undeformed Komsberg and Keimoes Suites that intruded into the NNMP around  $\sim 1100 - 1080$  Ma (Pettersson *et al.*, 2009; Macey *et al.*, 2015; Bailie *et al.*, 2017) also have similar Sm-Nd isotope compositions with  $\epsilon\text{Nd}_t$  in the range of -1.2 to 0.1, and -2.6 to 2.8 respectively (Table 5.1, Figure 5.3).

The pegmatites that were emplaced into the Kakamas Domain have a mixed LCT- NYF-type signature (see chapter 2). Their Sm-Nd isotope compositions are similar to that of the Kakamas Domain country rocks, albeit with a range of slightly lower  $\epsilon\text{Nd}_t$  values from -3.5 to -1.4 (Table 5.1, Table 4.2). These values fall within the crustal evolution curve for the Kakamas Domain country rocks and for a young Paleoproterozoic crust (Figure 5.3). Two-stage depleted model ages ( $T_{2\text{DM}}$ ) for the KD pegmatites are from  $\sim 1.8$  to 1.7 Ga, suggesting that the parental magma for the pegmatites within the Kakamas Domain could have been sourced from the reworking of KD late Paleoproterozoic crustal materials with no juvenile magmatic input from the mantle.

One Sm-Nd isotope analysis from a xenocrystic monazite from sample RPGV16 dated at  $991 \pm 6$  Ma (see chapters 4.1 and 4.2; Table 4.1) has an inherited U-Pb apparent spot age of  $1107 \pm 14$  Ma (Table 4.1). This monazite grain has significantly different Sm-Nd isotope composition to the magmatic monazite in the same pegmatite (Table 4.2). This xenocrystic monazite had a  $\epsilon\text{Nd}_{1107\text{Ma}}$  value of -3.3 (Figure 5.3), which has a much younger  $T_{2\text{DM}}$  reflecting late Paleoproterozoic age of  $\sim 1.8$  Ga (Table 4.2); compared to the magmatic monazite component that has an average  $\epsilon\text{Nd}_{991}$  value of -13.0 (Table 4.2). The depleted model

ages and Sm-Nd compositions suggest that this monazite grain has a late Paleoproterozoic source similar to that for the Kakamas Domain and the pegmatites within it. This is enigmatic as this pegmatite is hosted in the amphibolite-facies country rocks of the Richtersveld Magmatic Arc that has a late Archean to early Paleoproterozoic heritage.

Pegmatite sample SD2015-11 (Figure 5.3; Figure 5.2), from the Vioolsdrif Domain, has monazite Sm-Nd isotopic compositions ( $\epsilon\text{Nd}_t \sim -7.1$ ; Figure 5.2) that lie between those of pegmatites hosted in the Richtersveld Magmatic Arc and the Kakamas Domain. Additionally, this pegmatite is the oldest dated pegmatite at  $\sim 1038$  Ma. Sm-Nd isotope data for the country rocks of the RMA and this pegmatite do not show any correlation, and it is possible that the pegmatitic melt was sourced from another reservoir, as observed in its differing  $\epsilon\text{Nd}_t$  values and younger  $T_{2\text{DM}}$  model age of  $\sim 2.1$  Ga, which suggests mixing between sources might have occurred. However, the lack of recognised early Paleoproterozoic or more radiogenic “juvenile crust” in this section of the NNMP, mixing with a younger source is not feasible.

### 5.3 The relationship between pegmatite Sm-Nd isotope compositions and country rocks of the Bushmanland Subprovince

The timing of the main Namaqua  $D_{2a}$  thrusting and initial juxtaposition of the tectonic domains in the Namaqua-sector occurred at  $\sim 1200$  Ma. During this  $D_{2a}$  event, the Richtersveld Magmatic Arc is interpreted to have been thrust over the Bushmanland Subprovince (BSP; e.g. Colliston and Schoch, 2000; Cornell *et al.*, 2006, 2009; Pettersson *et al.*, 2007; Macey *et al.*, 2015, 2017). On the basis of Sm-Nd isotope compositions, rocks in the BSP can be divided into an older, early Paleoproterozoic crust with some Archean heritage in the north and a younger, late Paleoproterozoic crust in the south (e.g. Yuhara *et al.*, 2001; Eglington, 2006; Pettersson *et al.*, 2009). Sm-Nd isotopic studies of igneous country rocks within the northern part of the BSP have yield latest Archean/Paleoproterozoic  $T_{2\text{DM}}$  model ages between  $\sim 2.5$  and  $2.0$  Ga, with  $\epsilon\text{Nd}_t$  values between  $-8.7$  and  $-2.4$  (Table 5.1; Figure 5.3). In contrast, Mesoproterozoic igneous country rocks of the Little Namaqualand Suite (Yuhara *et al.*, 2001; Peterson *et al.*, 2009) and the Spektakel Suite (Yuhara *et al.*, 2001; Pettersson *et al.*, 2009; Macey *et al.*, 2018) dominate the southern sectors of the BSP.

The northern Paleoproterozoic-dominated BSP country rocks include the pre-tectonic intrusions of the Little Namaqualand Suite (LNS) dated at  $\sim 1212$  to  $1199$  Ma (Robb *et al.*, 1999; Clifford *et al.*, 2004; Macey *et al.*, 2011). The LNS has a range in  $\epsilon\text{Nd}_t$  from  $-8.7$  to  $-2.4$  and  $T_{2\text{DM}}$  model ages between  $\sim 2.5$  Ga and  $\sim 2.0$  Ga (Table 5.1; Figure 5.3; Clifford *et al.*, 1995; Yuhara *et al.*, 2001; Pettersson *et al.*, 2009). The Sm-Nd

compositions for Concordia Granite, dated at ~1170 to 1160 Ma (Robb *et al.*, 1999; Clifford *et al.*, 2004; Macey *et al.*, 2018), has a range in  $\epsilon\text{Nd}_t$  values from -8.7 to -6.5 and late Archean/early Proterozoic  $T_{2\text{DM}}$  model ages of ~2.5 to 2.2 Ga (Clifford *et al.*, 1995; Pettersson *et al.*, 2009; Table 5.1; Figure 5.3). Limited isotope studies have been undertaken on the supracrustal gneisses of the northern BSP. A single study on the Bushmanland Group around Aggeneys (Bailie *et al.*, 2007) yielding  $\epsilon\text{Nd}_t$  values between -9.6 and -2.0 with  $T_{2\text{DM}}$  model ages between ~2.9 and 2.3 Ga (Table 5.1; Figure 5.3). The timing of deposition of the sedimentary precursors to these supracrustal gneisses (for which detrital U-Pb spot ages indicated sediment was sourced from a combination of the ~1.9 Ga Gladkop suite and the calc-alkaline Richtersveld Magmatic Arc) occurred earlier than ~1285 Ma (age of the youngest detrital zircons; Cornel *et al.*, 2009) and the onset of  $D_{2a}$  regional deformation.

The relationship between the RMA, northern Bushmanland Subprovince (both dominated with reworked early Paleoproterozoic crust), and the pegmatites can be seen in the  $\epsilon\text{Nd}_t$  versus time diagram (Figure 5.3), i.e. the Sm-Nd data for the pegmatites and the northern BSP rocks fall on the same Paleoproterozoic crustal evolutionary line. The oldest sample dated in this study (SD2015-11) sits within a mixing zone between the Mesoproterozoic and Paleoproterozoic evolutionary lines, with a strong relationship with the ~1030 Ma Koperberg suite within the BSP. There could be a genetic relationship as this pegmatite intruded into a  $D_4$  shear zone at ~1038 Ma. However, the geographic distance between the Koperberg Intrusion and this sample is vast, and thus the two cannot directly be related.

The Mesoproterozoic and early Paleoproterozoic country rocks are situated in the central and southern portions of the BSP crust. There is an apparent evolutionary relationship, observed in Figure 5.3, with the pegmatites that have intruded into the Kakamas Domain and the country rocks of the KD. However, as mentioned above for sample SD2015-11, there is a geographical problem in linking the two. Additionally, there is little-known evidence for a Mesoproterozoic or late Paleoproterozoic crustal component for the eastern parts of the BSP adjacent the Kakamas Domain. Therefore, Sm-Nd compositions indicate that the Kakamas Domain pegmatites are strongly related to their host country rocks.

## 5.4 Intrusion and source of the pegmatite melts in relation to the tectonic setting of the NNMP

In general, across the Namaqua sector of the NNMP, a comparison of the Sm-Nd isotope geochemistry (using monazite as an Sm-Nd isotope bulk compositional proxy) of the pegmatites and country rocks suggests that the pegmatites were derived from similar sources, if not the country rocks, where pegmatites are intruded into the various domains. The geochronology presented in this study shows that the pegmatites were emplaced over a protracted period of ~78 m.yr. (Lambert *et al.*, 2013; this study; Figure 5.1), and in all the cases were emplaced tens to hundreds of million years later than the timing  $D_2$ -

D<sub>3</sub> tectonic events and associated with voluminous igneous intrusions and amphibolite- to granulite-metamorphism.

The structural controls of the pegmatites of the ORPB have only been studied in detail for a small area around the Skimmelberg Pegmatite Stockwork (Lambert, 2013) and a small regional study in the area around Warmbad and Onseepkans (Beukes, 1973). An additional regional mapping study in southern Namibia by the Council for Geoscience (Macey *et al.*, 2015), has described the structural controls on a more regional basis in the southern Namibian sections of the NNMP. These studies have shown that the pegmatite emplacement is structurally controlled by D<sub>4</sub> structures, reworked and re-orientated D<sub>2</sub> thrust boundaries, and regional gneissosity at around ~1.0 Ga. A more in-depth regional structural study is needed for pegmatite swarms outside of these areas but is beyond the scope of this project. However, it can be stated from the above mentioned studies that the D<sub>4</sub> transcurrent shearing, subsequent reworking and re-orientation of D<sub>2</sub> thrust faults and gneissosity created a “plumbing network” to allow for pegmatite melt to intrude and be emplaced into structural anisotropies within the NNMP.

The lack of a clear temporal and spatial relationship between ORPB pegmatites and parental granites at current exposure levels in the Namaqua Sector highlights the problem of how and where the melts that were responsible for the pegmatites of the Orange River Pegmatite Belt formed. The answer is cryptic as the country rocks have either not experienced conditions conducive to melting, or they have not experienced such temperatures, during multiple tectono-metamorphic events that pre-date massive pegmatite emplacement by as much as ~100 m.yr to ~900 m.yr. The source of the pegmatite melt is as yet unknown. Is it possible the source of the pegmatites could have been from processes at depth, below current exposure levels?

If the pegmatite forming melt was sourced from the crust at deeper structural levels, what was the characteristics of the source? What mechanism could have initiated melting to produce the numerous pegmatites that were eventually emplaced into the NNMP at ~1.0 Ga? The current model for the source of melt for LCT-type pegmatites is understood to be as a result of fractionation of melt, derived from a metasedimentary source that has undergone partial melting or anatexis (i.e. S-type granite).

The hypothesis for a metasedimentary source for peraluminous rare-metal pegmatites has been shown by experimental studies on biotite and muscovite bearing metapelites (e.g. Harris and Massey, 1994; Gardien *et al.*, 1995). Biotite and muscovite in metapelites are hosts for elements that are concentrated in rare-metal pegmatites such as Be, Li, Rb, Cs, Nb and Ta (Bea *et al.*, 1994; London, 2008, 2018; Stepanov *et al.*, 2014), as well as an important source of H<sub>2</sub>O, F and Cl. During melting of metapelites, the characteristic elements mentioned above are typically partitioned into the melt (Icenhower *et al.*, 1995). The presence of Be and Li in the LCT and some rare-metal pegmatites within the RMA suggest that a large degree of fractionation had to have occurred to produce melts with the required Li and Be enrichment for these mineral phases to crystallise (London, 2016). Stewart (1978) estimated the most Li-rich pegmatites contain

~7000 ppm Li, while studies on the average Be contents of S-type granites (determined from experimental studies on the Macusani glasses) have shown to be ~4 ppm (MacDonald *et al.*, 1992, London and Morgen, 2017). Be concentrations seen in pegmatites range from 34 to 576 ppm with an average of 205 ppm (London, 2015), indicating that some degree of fractionation has occurred to enrich the melt in the lithophile elements.

Due to the bulk distribution coefficients of Li and Be in melts, and based on Rayleigh fractionation calculations, London (2016) suggests that 99.8% fractionation of a melt is needed to produce a Li and Be rich melts that can crystallise Be- and Li-rich mineral assemblages. This can be attributed to fractional differentiation of granitic melts (e.g. Evensen and London, 2002; London, 2015, 2018) from a much larger granitic body. However, the vast number of pegmatites observed in many pegmatite fields (e.g. the ORPB) leads to the idea that the primary granitic body would have to be extremely large.

This suggests that the LCT-type pegmatites of the ORPB require melting of a metasedimentary source (i.e. S-type magmas). The RMA and Kakamas Domain both contain metasedimentary rocks that are favourable sources for LCT-pegmatites, however, there the metamorphic grade recorded in the RMA (greenschist-amphibolite facies) and Kakamas Domain (granulite facies) were reached sometime before the massive emplacement of the ORPB pegmatites.

The pegmatites that were emplaced into the Richtersveld Magmatic Arc have similar Sm-Nd isotope compositions ( $\epsilon\text{Nd}_t$  units) to that of the host rocks of the RMA. Metamorphic conditions of the country rocks in the RMA reached amphibolite-facies (~600 °C; 5-6 kbar; Macey *et al.*, 2017) during D<sub>2</sub> thrusting at ~1.2 Ga, and never attained a temperature above the wet granite solidus at current exposure levels. This metamorphic event was restricted to the Pella Domain, with the Vioolsdrif Domain remaining relatively untouched and never reaching grades above greenschist-facies (Macey *et al.*, 2017) at any time. Thus, there is no clear evidence, at current crustal levels, of widespread partial melting of these country rocks that could have been responsible for the numerous pegmatites within the RMA. Furthermore, the predominance of the meta-volcanic units within the RMA that are relatively dry and might not be able to produce sufficient melt for the numerous pegmatites emplaced within the RMA. It is possible that some degree of melting could have taken place at depth, creating a limited amount of parental magma to fractionate, forming pegmatitic melts to a small degree.

It is possible that the involvement of the metasedimentary units of the BSP could have been a likely source for the pegmatites (as seen by the Sm-Nd isotope compositions, section 5.3). The largely amphibolite-facies northern sections of the Bushmanland Subprovince hosts numerous metasedimentary sequences (i.e. the metapelites and meta-quartzites of the ~1.2 Ga Bushmanland Group). The fertile metasediments of the northern BSP reflect similar Sm-Nd compositions to the pegmatites in the overlying Richtersveld Magmatic Arc (Figure 5.3; Table 5.1). These metasediments of the Bushmanland Group consists of a package of muscovite-rich schists, muscovite-biotite schists and biotite-garnet-sillimanite schists (e.g.

McClung, 2006; Agenbacht, 2007; Bailie *et al.*, 2007b) that are favourable protoliths for S-type granites (Chappell *et al.*, 2001). Metasedimentary protoliths and S-type granites a favourable source for LCT-type pegmatites (Cerny, 1991; Martin and De Vito, 2005; London, 2008, Cerny *et al.*, 2012), or for direct partial melt products of such metasedimentary rocks (Simmons, 2007).

The pegmatites within the Kakamas Domain have again, similar Sm-Nd compositions to their host country rocks in the KD (Figure 5.2; Figure 5.3; Table 5.1). Monazite Sm-Nd isotope compositions and  $T_{2DM}$  model ages suggest that the pegmatites emplaced in the KD country rocks were likely derived from melting of the KD supracrustal rocks. However, the KD country rocks are poly-metamorphic and reached granulite metamorphism during a) the ~1.2 Ga D2 event an associated  $M_2$ , low-P, high-T peak metamorphic conditions for metapelites in the domain reached ~800 to 900 °C at ~5.0 kbar (Bial *et al.*, 2015),  $M_2$ -D<sub>2</sub> was responsible for widespread partial melting of the supracrustal rock in the western KD; and b) a younger low-P, high-T metamorphic event has been recognised in other parts of the Kakamas Domain. In the Aus region of southern Namibia, this event reached peak conditions of 825 °C at 5.5 kbar at ~1060 Ma (Diener *et al.*, 2013). In the eastern KD, a second granulite event occurred at ~1090 Ma (Buick pers. comm. 2018), and was temporally related to the emplacement of granites and charnockites of the ~1100 Ma – 1090 Ma A- and I-type Keimoes Suite (Bailie *et al.*, 2017).

Moreover, at the highest grades in the eastern KD, the poly-metamorphic ~1.2 and ~1.09 Ga granulites are almost devoid of biotite and are extremely restitic in composition, rendering them infertile as a source of parental magmas to the later ORPB pegmatites. The Bushmanland Subprovince has been thrust under the KD along the Hartebeest River Thrust (Colliston *et al.*, 2015). However, the Kakamas Domain Sm-Nd compositions show that the KD is predominantly composed of Paleoproterozoic crust with a Mesoproterozoic heritage and have lower  $\epsilon Nd_t$  values and younger  $T_{2Dm}$  ages compared to the RMA (Table 5.1; Bailie *et al.*, 2011, 2017; Pettersson *et al.*, 2009). The Bushmanland Subprovince is however dominated by Paleoproterozoic crust in the northern parts, the southern and central parts have Mesoproterozoic signatures marked by younger  $T_{2Dm}$  model ages of ~1.9 – 1.6 Ga (Yuhara *et al.*, 2001; Pettersson *et al.*, 2009; Macey *et al.*, 2018). However, these more “juvenile” lithologies are separated geographically by some distance and have not been thrust underneath the KD.

It is plausible that the melting of low- to medium-grade BSP metasediments, underneath the Kakamas, Domain took place at depth, which resulted in volatile-rich fluids to move upwards through the crust and possibly interact with the over-riding Kakamas Domain to initiate partial melting of the now retrogressed country rocks. This is similar to a model proposed by Harris *et al.* (1986) and Shaw *et al.* (2016) for the pegmatites within Lewisian Gneiss Complex.

The above examples indicate the possibility that the melting of the Bushmanland Subprovince supracrustals at depth could have been the source for these pegmatite parental melts (as within the RMA). Additionally, this late stage event could have possibly resulted in fluids released from crystallising partial



melts at deeper crustal levels, which might have retrogressed the granulite-facies country rocks of the Kakamas Domain, allowing for subsequent melting during the time of major pegmatite generation and emplacement. However, the timing of melting is complicated due to the long period of pegmatite emplacement from ~1038 Ma to 973 Ma for pegmatites emplaced into the RMA.

There is some further evidence for a late magmatic event as seen in some young (~1020 Ma) U-Pb ages from zircon rims in metapelites within the BSP (Baillie *et al.*, 2007a; Cornell *et al.*, 2009c; Colliston *et al.*, 2015) indicating a late orogenic event as argued by Robb *et al.* (1999) and Raith *et al.* (2003). The mafic underplate driven melting of the Namaqua Sector possibly began during D<sub>3</sub> – M<sub>3</sub> tectono-magmatic events that culminated with the intrusion of the Koperberg Suite (Clifford *et al.*, 1995). The older ~1030 Ma age for the pegmatite (SD2015-11) emplaced along the D<sub>4</sub> Sperlingsputs shear zone (Indongo, 2017) suggests that melting of the source regions for pegmatite magmas was synchronous with the late D<sub>3</sub>-M<sub>3</sub> magmatism seen within the Bushmanland Subprovince and the intrusion of the Koperberg Suite (Clifford *et al.*, 1995; Macey *et al.*, 2018). The  $\epsilon\text{Nd}_t$  value of -7.1 for SD2015-11 (Table 4.2; Figure 5.2) is similar to that of the Koperberg Suite values of -11.2 to -7.1 (Table 5.1). This mafic underplate driven melting event might have been long lived and resulted in further melting of the NNMP crust at depth.

The pegmatites within the LFROTZ have similar  $\epsilon\text{Nd}_t$  values and late Paleoproterozoic  $T_{2DM}$  model ages that are similar to the Kakamas Domain country rocks (Figure 5.2; Figure 5.3; Table 5.1). The model of retrogression and re-fertilisation of the Kakamas granulite-facies metasediments might be able to explain the prevalence of these pegmatites with a younger heritage emplaced into country rock that has an older early Paleoproterozoic heritage of the LFROTZ. The pegmatites in the LFROTZ represent some of the youngest pegmatites emplaced in the Namaqua sector of the Namaqua-Natal Metamorphic Province. It might be plausible that the parental melts for the LFROTZ pegmatites were sourced from the KD at much deeper crustal levels, and subsequently emplaced into the adjacent LFROTZ into structural anisotropies created during D<sub>4</sub> transcurrent shearing. Another possible explanation for their emplacement history is that the parental magma could have been sourced from a tectonically imbricated thrust slice of the Kakamas Domain within the LFROTZ. As the LFROTZ represents a major thrust imbricated, tectonic mélange with various tectonised units of both the RMA and KD. This melting mechanism is likely, however further geochemical studies are needed to prove this hypothesis and ascertain a likely source.

The above hypothesis for melting of fertile crustal material at depth is not unique and studies in other pegmatite provinces where the answer to what source of the pegmatite melt is, has been cryptic. The problem of a temporal and genetic link between parental granites and large pegmatites belts seems to be a problem observed in a number of other pegmatite provinces. Studies on the polyphase ~450-300 Ma intra-plate Alice Springs Orogeny (ASO; Buick *et al.*, 2008) showed that the source of the melt for the pegmatites emplaced into the lower granulite-facies (~480 -40 Ma) Harts Range Metamorphic Complex (HRMC) and the upper amphibolite-facies (~340-320 Ma) Entia Gneiss Complex (EGC) were derived from

melting of fertile crustal material below the HRMC and EGC. The pegmatites were previously thought to have been derived from partial melts of the HRMC and EGC. Geochronological data (SHRIMP U-Pb zircon and monazite ages) from the pegmatites indicated that they were emplaced episodically throughout the entire ~140 Ma duration of the ASO. The pegmatite intrusive episodes correlated with the ages of major shear zone development (Cartwright *et al.*, 1999) in the ASO and with the deposition of syn-orogenic sedimentary rocks in the adjacent Centralian Superbasin (Buick *et al.*, 2008). Due to a lack of similar ASO ages present in the anatectic country rocks of the HRMC, Buick *et al.* (2008) suggested that the pegmatites could not have been derived via local partial melting. Buick *et al.* (2008) instead suggested that the above implies that a much larger Alice Springs-ages granites exist at depth that could be a parental source for the highly fractionated pegmatites. Episodic under thrusting and dehydration of unmetamorphosed Centralian Superbasin sedimentary rocks, allowing for crustal fertility to be maintained over a ~140 Ma period during the Alice Springs Orogeny was proposed as a mechanism by which repeated felsic magmatism could occur where all exposed country rock types had a previous high-T history (Buick *et al.*, 2008).

Shaw *et al.* (2016) has hypothesised a similar scenario in their study into the numerous pegmatites that occur within the Paleoproterozoic (~1900 – 1670 Ma) Lewisian Gneiss Complex (LGC) in north-west Scotland and the Hebrides. The pegmatites within this metamorphic complex were emplaced late in this event between ~1700 and 1650 Ma (Shaw *et al.*, 2016 and references within). Here, the numerous barren biotite-magnetite granitic pegmatites are considered to represent melting of the local Archean TTG host rocks in the presence of K-rich fluid (Castro, 2004; Watkins *et al.*, 2007), while the small number of LCT-type rare-metal pegmatites are spatially associated with the Harris Granulite Belt (Shaw *et al.*, 2016). Additionally, granulite-facies metamorphism of the Harris Granulite Belt (HGB) occurred at ~1890 Ma, predating the emplacement of pegmatites in the HGB by some ~190 Ma.

In this pegmatite province, the potential for the formation of large bodies of fertile S-type granite is significantly reduced by the predominance of the granulitic meta-igneous rocks (Shaw *et al.*, 2016). Due to this, the potential of LCT-type pegmatites that are attributed to fractionation of large S-type granitic bodies is non-existent. Additionally, there is no evidence to suggest that the HGB pegmatites were sourced by differing amounts of fractionation from a single parental granite (Shaw *et al.*, 2016). The explanation proposed by Shaw *et al.*, (2016) is that a late Laxfordian thrusting and crustal thickening with associated ~1870 Ma amphibolite metamorphism culminating in the development of extensional shear zones (e.g. Goodenough *et al.*, 2013) led to retrogression of the HGB and associated decompression occurred at ~1870 Ma. This retrogression event in the nearby Leverburgh Belt potentially played a role in re-fertilising the rocks of the HGB to allow subsequent melting due to decompression resulting in the LCT-type pegmatites to be emplaced within the HGB.

The above models for melting of a potential source rocks for the pegmatites of the ORPB within the RMA and KD are attributed to the formation of the LCT-type pegmatites within the belt. However, based on the pegmatite classification system of Černý and Ercit (2005), presence of NYF-type rare metal pegmatites in the areas around Kakamas and Riemvasmaak in the KD, suggest that these pegmatites formed either during a period of extension or in an anorogenic setting related to A-type magmatism. This might suggest that the pegmatites (at least the NYF pegmatites) within the Kakamas Domain are related to the largely A-, I-type igneous intrusion of the Keimoes Suite (Bailie *et al.*, 2017). The problem here is that these pegmatites post-date the intrusion by ~60 Ma, as shown by the oldest dated pegmatite in the KD (~1019 Ma; this study).

A study on the pegmatites from the Sveconorwegian province in southern Norway and southwest Sweden, which occur in a ~1.2 to ~0.9 Ga granulite- to amphibolite-facies Sveconorwegian (Grenville) Orogenic belt, where the pegmatites primarily have a NYF signature (Müller *et al.*, 2017). Müller *et al.* (2017) could not relate the pegmatites to any parental magma. They concluded that the majority of the Sveconorwegian NYF pegmatites are not attributed to anorogenic, A-type setting but formed due to anatexis by either crustal thickening or high-T orogenic extension (Müller *et al.*, 2017). Another conclusion from their study is that there may be a temporal gap between pegmatite and granite emplacement. Where the chemical similarities and spatial coincidence of pegmatite swarms with neighbouring granites might be similar in character but do not imply a genetic relationship (Müller *et al.*, 2017).

The above model could possibly explain the prevalence of NYF-type rare metal pegmatites within the Kakamas Domain. However, the source of the pegmatite melt is still cryptic. The Kakamas Domain experienced a poly-phase granulite and amphibolite-facies metamorphic history. The majority of the supracrustal gneisses that are predominantly metapelitic in origin dominate parts of the Kakamas Domain, especially along the western boundary of the KD, although migmatitic gneisses do occur. The majority of the metapelitic gneisses are seen as restitic, having most of their melt extracted during D<sub>2</sub>, high-T, low-P metamorphism (Bial *et al.*, 2015; Macey *et al.*, 2015). It is therefore hard to envisage that anatexis of these rocks at ~1.0 Ga could produce enough melt to produce the numerous pegmatites, where some of the rare-metal pegmatites indicate that some form of melt fractionation had occurred. The models proposed by Shaw *et al.* (2016) and Buick *et al.* (2008), where either fluid from melting of muscovite and biotite rich protolith or unmetamorphosed sediments could either themselves melt, or produce fluids that re-fertilise the overlying high grade rocks and allow them to undergo further melting, may be relevant to understanding pegmatite emplacement in the Kakamas Domain. Specifically, rehydration of the granulites to hydrous amphibolite facies assemblages, as also hypothesised in the Lewisian study of Shaw *et al.* (2016), may allow them to undergo further melting in an unrelated metamorphic event should a suitable heat source then be available. Evidence of the extent and effectiveness of such rehydration can be seen in the conversion of BSP granulite-facies metapelites into muscovite-biotite-staurolite-garnet-kyanite schists in the Pan-African West Coast Belt (Joubert *et al.*, 1980).

The granulite-facies country rocks of the Kakamas Domain contain garnet, monazite, rutile, zircon, apatite and monazite that are known to be important hosts for MREE, HREE and Y in metamorphic and magmatic systems (Bea, 1996). The rehydration of the KD proposed here could have led to the breakdown of these minerals acting as repositories of HFSE and REE elements and making these elements available during subsequent melting (e.g. Špaček *et al.*, 2013). This mechanism might explain the occurrence of the often Y and HREE enriched NYF rare-metal pegmatites in the Kakamas Domain. There is no evidence for this at the current exposure level, but might have occurred at depth, as the BSP is thrust to deeper levels of the crust where conditions allow for melting.

Invoking the idea of a magmatic source of S-type character suggests that there should be S-type granites of ~1.0 Ga in age throughout the NNMP. Indeed, there is the Warmbad Granite Suite that is S-type in character with a crystallisation age of ~1.0 Ga. The issue with the Warmbad Granite is that it is limited in its extent around the Warmbad area in Southern Namibia and has only been observed north of the MRPSZ (Macey *et al.*, 2015). A single and extremely large pluton or multiple granitic plutons at deeper structural levels might be a likely source for the pegmatites of the ORPB, and would limit the regional zonation of the emplaced pegmatites. Hence, there is still a problem understanding the magnitude of the parental magmatic source. Given the huge number of pegmatites within the ORPB, the parental granitic body would have to be massive in size.

To circumvent the need for an impossibly large parental granite, the study by Shaw *et al.* (2016) on the Lewisian pegmatites hypothesised that melting at depth of the HGB resulted in small volumes of melt that coalesced into small-scale magma lenses. These magma bodies may then have undergone further fractionation, with the more fractionated and fluid-rich melts rising upwards and then emplaced as pegmatites at higher crustal levels within the HGB (Shaw *et al.*, 2016). They further suggest that the wide range of metasediments within the HGB acted as variable sources of melt, which Shaw *et al.* (2016) uses to explain the variability seen within the pegmatites of a relatively small area. This might explain the regional zonation and occurrences of rare-metal LCT and NYF pegmatites within a sea of barren and simple pegmatites. Due to most studies of pegmatites concentrating on the more chemically and mineralogically complex pegmatites, the prevalence of the barren pegmatites within pegmatites field globally is still up for debate (London 2018).

The pegmatites of the ORPB are composed of a wide range of pegmatite types, from barren and simple pegmatites, to rare-metal pegmatites with both a LCT and NYF signature. On a regional scale, the pegmatites form areas or zones that have a higher proportion of LCT-type pegmatite than barren-simple pegmatites, or vice versa with a higher proportion of NYF-type pegmatites. In some areas, only barren and simple pegmatites are present without any observed rare-metal pegmatites. This hypothesis by Shaw *et al.* (2016) and Müller *et al.* (2017) of small volumes of melt being extracted from a large heterogeneous metasedimentary source might explain the regional variability in the chemical signature observed in

pegmatites belts. This is plausible as the general assumption that pegmatite mineralogy strongly reflects the composition of the protolith (c.f. Černý and Ercit, 2005 and Černý *et al.*, 2012). This is to propose that the melting of a heterogeneous metasedimentary package will create pockets of melts of variable size. These pockets of melt should vary compositionally, reflecting the chemical signature of their source within the supracrustal package.

Additionally, the above models by Shaw *et al.* (2016) and Müller *et al.*, (2017) propose that the pegmatites were sourced from S-type magmas, or widespread crustal anatexis at depth a period of continental orogeny with associated crustal thickening (e.g. Buick *et al.* 2008). The problem with the ORPB within the NNMP is that the major tectono-magmatic and metamorphic events attributed to the formation of the NNMP occurred much earlier, between ~1.2 and 1.09 Ga. There is added controversy in whether the NNMP represents major continental orogeny and crustal thickening as the recent metamorphic studies suggest. Metamorphic P-T studies (e.g. Bial *et al.*, 2015, 2016) indicate a high temperature, low-pressure regime that is not associated with traditional continental collision and crustal thickening, but point to a back-arc regime.

The presence of the widespread pegmatites of the ORPB and the largely S-type Warmbad Granite Suite that intruded the PD at ~1.0 Ga, at around the same time as major pegmatite emplacement within the NNMP suggests that a tectono-magmatic event occurred during the same time as D<sub>4</sub> shearing. Additionally, <sup>40</sup>Ar/<sup>39</sup>Ar cooling ages for muscovite, hornblende and biotite indicate that the western parts of the Namaqua Sector of the NNMP experienced uplift and had cooled to below ~350 °C at around ~960 Ma for the Kakamas Domain and Richtersveld Magmatic Arc (Eglington, 2006; Pettersson *et al.*, 2008). It is clear that the country rock at present exposure level, and emplacement level for the pegmatites of the ORPB, had cooled well below conditions associated with partial melting of the immediate country rock. The same study determined that the BSP was probably buried at deeper crustal levels at ~1040 – 1020 Ma and experienced a rapid cooling event of ~200 °C during this uplift event from ~1030 to 1000 Ma (Pettersson *et al.*, 2009).

The intrusion of the ~1.04 Ga Koperberg Suite and the Sm-Nd isotope compositional similarity with the oldest dated pegmatite in this study suggests that the mafic underplating responsible could have been a likely source of heat into the deeper reaches of the NNMP crust. It is unsure how long this event could of taken place to drive crustal anatexis, additionally, the regional extent of melting throughout the NNMP to produce the abundant pegmatites of the ORPB. The intrusion of the S-type Warmbad Granite and abundant pegmatites of the ORPB, with similar isotope compositions to metasedimentary rocks within the NNMP do point to a model of crustal anatexis at deeper structural levels. However, further investigations are needed, primarily in understanding the late-stage tectonic evolution of the NNMP at around ~1.0 Ga and associated D<sub>4</sub> transcurrent shear zones.

Furthermore, the fundamental controls of the genesis of LCT pegmatites are not particularly well understood. It is suggested by Bradley et al. (2016) that research into the subject of LCT-pegmatite genesis might develop a new kind of tectonic marker akin to other indicators such as blueschists in subduction zones. It is clear that understanding the genesis of the ORPB pegmatites further will yield new insight into the evolution of the NNMP during the late stages of development.

## 6 Conclusion

The Orange River Pegmatite Belt (ORPB) is a ~450 km long, ~40-80 km wide belt containing over 45 000 individual pegmatites that were emplaced in the Namaqua Sector of the Namaqua-Natal Metamorphic Complex. Within the ORPB, pegmatites of varying types, from barren, simple and unzoned to complexly zoned, rare-metal pegmatites of the LCT (with a small proportion of NYF) pegmatite family. In a given tectonic domain of the Namaqua Sector, the full range of pegmatite types may occur. The  $D_4$  shear deformation event, which reworked  $D_2$  thrust boundaries created pressure anisotropies to act as the “plumbing network” allowing the segregated pegmatite melts to rise up through the crust to cooler crust at higher crustal levels.

The ORPB pegmatites have been emplaced over a protracted (~80 Ma) period into differing tectonic domains that represent a vast array of lithologies. Within a given tectonic domain, pegmatites give U-Pb monazite emplacement ages that differ by tens of millions of years. There appears to be a progressive, but variable, trend in the emplacement ages with the oldest ages situated within the Vioolsdrif Domain and the eastern most pegmatites within the Kakamas Domain. The youngest pegmatites from this study are situated within the LFROTZ and in structural sites along the MRPSZ. The country rocks have experienced a complex poly-metamorphic history from greenschist-facies (Vioolsdrif Domain) to amphibolite-facies (Pella Domain and LFROTZ) to high-temperature, low pressure granulite-facies (Kakamas Domain), all of which pre-date pegmatite emplacement by at least 10-100 Ma.

Based on Sm-Nd isotope geochemistry, the parental melts responsible for the pegmatites within the Richtersveld Magmatic Arc have been sourced from reworking of Proterozoic crust. The source for the parental magmas responsible for the pegmatites of the Kakamas domain could have derived from reworked late Paleoproterozoic crust of the Kakamas Domain. Due to the metamorphic grade at present exposure level, the mechanism of crustal reworking responsible for the parental magmas in both tectonic domains must have occurred at deeper crustal levels.

Additionally, Sm-Nd isotope geochemistry suggests that the parental melts responsible for the pegmatites could have been sourced through anatexis of fertile, amphibolite-facies metasediments of the Bushmanland Subprovince (BSP). The BSP is overlain by the Kakamas Domain and Richtersveld Magmatic Arc due to SW directed thrusting during the main ~1.2-1.1 Ga Namaqua Orogeny. Additionally, the melting of the underlying BSP could have released fluid that retrogressed the overlying granulite-facies Kakamas Domain metasediments allowing for subsequent melting of these once restitic rocks.

Based on Sm-Nd isotope compositions, a possible link with the pegmatites and the ~1.0 Ga Warmbad Granite Suite has been identified in this study. However, the Warmbad Granite Suite is limited to areas in the northern parts of the Pella Domain and intruding into the Eendoorn Suite of the LFROTZ. Additionally, it has not been observed south of the major D<sub>4</sub> Marshall Rocks-Pofadder Shear Zone where numerous pegmatites have been emplaced. It could be a parental source for at least some of the pegmatites within the northern parts of the Pella Domain. However, further investigations are needed to confirm this link.

Additionally, the presence of such an S-type granite of similar age to the pegmatites of the ORPB suggests that melting of the NNMP crust at depth did occur. The regional extent of this melting must have been extensive to produce sufficient melt reservoirs to produce the numerous pegmatites of the ORPB. This melt event could be linked with the timing of mafic underplating responsible for the ~1.04 Ga Koperberg Suite. Further investigations into the late D<sub>4</sub> transcurrent shearing and tectono-magmatic events at ~1.0 Ga are needed to further understand the late-stage evolution of the NNMP. The ideas brought forward in this thesis regarding widespread pegmatite emplacement within the NNMP suggest that there was still some degree of tectonics at around ~1.0Ga. Due to the complexities of pegmatites and the current understanding of pegmatite genesis, further investigations into how the pegmatites of the ORPB formed might shed light on the late-stage evolution of the NNMP.

## References

- van Achterbergh, E., Ryan, C. G., Jackson, S. E. and Griffin, W. (2001) Data reduction software for LA- ICP-MS: appendix, in *Assoc. Canada (MAC) Short Course Series*, p. 239.
- Agenbacht, A. L. D. (2007) The geology of the Pofadder area. 1:250 000 map sheet explanation 2918. Council for Geoscience, p. 89.
- Aleinikoff, J. N., Schenck, W. S., Plank, M. O., Srogi, L. A., Fanning, C. M., Kamo, S. L. and Bosbyshell, H. (2006) Deciphering igneous and metamorphic events in high-grade rocks of the Wilmington complex, Delaware: Morphology, cathodoluminescence and backscattered electron zoning, and SHRIMP U-Pb geochronology of zircon and monazite, *Bulletin of the Geological Society of America*, 118(1–2), pp. 39–64. doi: 10.1130/B25659.1.
- Angombe, M. T. (2016) *The lithostratigraphy and structural components of the Eureka Shear*. University of Stellenbosch.
- van Aswegen, G., Strydom, D., Colliston, W. P., Praekelt, H. E., Schoch, A. E., Blignault, H. J., Botha, B. J. V. and van der Merwe, S. W. (1987) The structural-stratigraphic development of part of the Namaqua metamorphic complex, South Africa—An example of Proterozoic major thrust tectonics, in *Proterozoic Lithospheric Evolution*,. Vol.17, pp. 207–216. doi: 10.1029/GD017p0207.
- Bachmann, K., Schulz, B., Bailie, R. and Gutzmer, J. (2015) Monazite geochronology and geothermobarometry in polymetamorphic host rocks of volcanic-hosted massive sulphide mineralizations in the Mesoproterozoic Areachap Terrane, South Africa, *Journal of African Earth Sciences*. Elsevier Ltd, 111, pp. 258–272. doi: 10.1016/j.jafrearsci.2015.07.021.
- von Backstrom, J. W. (1976) The Geology and Mineral Deposits of Tantalite Valley, Warmbad District, South West Africa., *Atomic Energy Board, Pelindaba, Pretoria*, (April), p. 27.
- Bailie, R., Armstrong, R. and Reid, D. (2007a) Composition and single zircon U-Pb emplacement and metamorphic ages of the Aggeneys Granite Suite, Bushmanland, South Africa, *South African Journal of Geology*, 110(1), pp. 87–110. doi: 10.2113/gssajg.110.1.87.
- Bailie, R., Armstrong, R. and Reid, D. (2007b) The Bushmanland Group supracrustal succession, Aggeneys, Bushmanland, South Africa: Provenance, age of deposition and metamorphism, *South African Journal of Geology*, 110(1), pp. 59–86. doi: 10.2113/gssajg.110.1.59.
- Bailie, R., Gutzmer, J. and Rajesh, H. M. (2011a) Petrography, Geochemistry and Geochronology of the Metavolcanic rocks of the Mesoproterozoic Leerkrans Formation, Wilgenhoutsdrif Group, South Africa - back-arc basin to the Areachap Volcanic Arc, *South African Journal of Geology*, 114(2), pp. 167–194. doi: 10.2113/gssajg.114.2.167.
- Bailie, R., Gutzmer, J., Rajesh, H. M. and Armstrong, R. (2011b) Age of ferroan A-type post-tectonic granitoids of the southern part of the Keimoes Suite, Northern Cape Province, South Africa, *Journal of African Earth Sciences*. Elsevier Ltd, 60(3), pp. 153–174. doi: 10.1016/j.jafrearsci.2011.02.008.
- Bailie, R., Macey, P. H., Nethenzheni, S., Frei, D. and le Roux, P. (2017) The Keimoes Suite redefined: The geochronological and geochemical characteristics of the ferroan granites of the eastern Namaqua Sector, Mesoproterozoic Namaqua-Natal Metamorphic Province, southern Africa, *Journal of African Earth Sciences*. Elsevier Ltd, 134, pp. 737–765. doi: 10.1016/j.jafrearsci.2017.07.017.
- Bailie, R., Rajesh, H. M. and Gutzmer, J. (2012) Bimodal volcanism at the western margin of the Kaapvaal Craton in the aftermath of collisional events during the Namaqua-Natal Orogeny: The Koras Group, South Africa, *Precambrian Research*, 200–203, pp. 163–183. doi: 10.1016/j.precamres.2012.01.017.
- Bea, F. (1996) Residence of REE, Y, Th and U in granites and crustal protoliths; implications for the chemistry of crustal melts, *Journal of Petrology*, 37(3), pp. 521–552. doi: 10.1093/petrology/37.3.521.
- Bea, F. (2012) The sources of energy for crustal melting and the geochemistry of heat-producing elements,



*Lithos*. Elsevier B.V., 153, pp. 278–291. doi: 10.1016/j.lithos.2012.01.017.

Bea, F., Pereira, M. D. and Stroh, A. (1994) Mineral/leucosome trace-element partitioning in a peraluminous migmatite (a laser ablation-ICP-MS study), *Chemical Geology*, 117(1–4), pp. 291–312. doi: 10.1016/0009-2541(94)90133-3.

De Beer, C. H. (2010) The geology of the Garies area. 1:250 000 map sheet explanation 3017. Council for Geoscience, p. 110.

De Beer, C. H., Theron, J. N. and Almond, J. E. (2002) The geology of the Calvinia area. 1:250 000 map sheet explanation 3118. Council for Geoscience, p. 92.

Belkasm, M., Cuney, M., Pollard, P. J. and Bastoul, a (2000) Chemistry of the Ta-Nb-Sn-W oxide minerals from the Yichun rare metal granite (SE China): genetic implications and comparison with Moroccan and French Hercynian examples, *Mineralogical Magazine*, 64(3), pp. 507–523. doi: 10.1180/002646100549391.

Beukes, G. J. (1973) 'n Geologiese ondersoek van die gebied suid van Warm-bad, Suidwes-Afrika, met spesiale verwysing na die metamorf-magmatiese assosiasie van die Voorkambriese gesteentes. Univ. Orange Free State.

Beurlen, H., Thomas, R., da Silva, M. R. R., Müller, A., Rhede, D. and Soares, D. R. (2014) Perspectives for Li- and Ta-Mineralization in the Borborema Pegmatite Province, NE-Brazil: A review, *Journal of South American Earth Sciences*. Elsevier Ltd, 56, pp. 110–127. doi: 10.1016/j.jsames.2014.08.007.

van Bever Donker, J. M. (1991) A synthesis of the structural geology of a major tectonic boundary between a 1000 m.y. mobile belt and a 3000 m.y. craton, *Tectonophysics*, 196(3–4), pp. 359–370. doi: 10.1016/0040-1951(91)90330-U.

Bial, J., Büttner, S. and Appel, P. (2016) Timing and conditions of regional metamorphism and crustal shearing in the granulite facies basement of south Namibia: Implications for the crustal evolution of the Namaqualand metamorphic basement in the Mesoproterozoic, *Journal of African Earth Sciences*, 123, pp. 145–176. doi: 10.1016/j.jafrearsci.2016.07.011.

Bial, J., Büttner, S. H. and Frei, D. (2015a) Formation and emplacement of two contrasting late-Mesoproterozoic magma types in the central Namaqua Metamorphic Complex (South Africa, Namibia): Evidence from geochemistry and geochronology, *Lithos*. Elsevier B.V., 224–225(March), pp. 272–294. doi: 10.1016/j.lithos.2015.02.021.

Bial, J., Büttner, S. H., Schenk, V. and Appel, P. (2015b) The long-term high-temperature history of the central Namaqua Metamorphic Complex: Evidence for a Mesoproterozoic continental back-arc in southern Africa, *Precambrian Research*, 268, pp. 243–278. doi: 10.1016/j.precamres.2015.07.012.

von Blanckenburg, F. (1992) Combined high-precision chronometry and geochemical tracing using accessory minerals: applied to the Central-Alpine Bergell intrusion (central Europe), *Chemical Geology*, 100(1–2), pp. 19–40. doi: 10.1016/0009-2541(92)90100-J.

Blignault, H. J. (1977) Structural-Metamorphic imprint on part of the Namaqua Mobile Belt in South Africa, *Chamber of Mines Precambrian Research Unit*, 23, pp. 1–191.

Blignault, H. J., van Aswegen, G., van der Merwe, S. W. and Colliston, W. P. (1983) The Namaqualand geotraverse and environs: part of the Proterozoic Namaqua mobile belt, *Geological Society of South Africa, Special Publication*, 10, pp. 1–29.

Bradley, D., Shea, E., Buchwaldt, R., Bowring, S., Benowitz, J., O'Sullivan, P. and McCauley, A. (2016) Geochronology and Tectonic Context of Lithium-Cesium-Tantalum Pegmatites In the Appalachians, *The Canadian Mineralogist*, 54(4), pp. 945–969. doi: 10.3749/canmin.1600035.

Buick, I. S., Clark, C., Rubatto, D., Hermann, J., Pandit, M. and Hand, M. (2010) Constraints on the Proterozoic evolution of the Aravalli-Delhi Orogenic belt (NW India) from monazite geochronology and mineral trace element geochemistry, *Lithos*. Elsevier B.V., 120(3–4), pp. 511–528. doi: 10.1016/j.lithos.2010.09.011.

Buick, I. S., Hermann, J., Williams, I. S., Gibson, R. L. and Rubatto, D. (2006) A SHRIMP U-Pb and LA-ICP-MS trace element study of the petrogenesis of garnet-cordierite-orthoamphibole gneisses from the Central

- Zone of the Limpopo Belt, South Africa, *Lithos*, 88(1–4), pp. 150–172. doi: 10.1016/j.lithos.2005.09.001.
- Buick, I. S., Storkey, A. and Williams, I. S. (2008) Timing relationships between pegmatite emplacement, metamorphism and deformation during the intra-plate Alice Springs Orogeny, central Australia, *Journal of Metamorphic Geology*, 26(9), pp. 915–936. doi: 10.1111/j.1525-1314.2008.00794.x.
- Büttner, S. H., Sherlock, S., Fryer, L., Lodge, J., Diale, T., Kazondunge, R. and Macey, P. (2013) Controls of host rock mineralogy and H<sub>2</sub>O content on the nature of pseudotachylyte melts: Evidence from Pan-African faulting in the foreland of the Gariep Belt, South Africa, *Tectonophysics*. Elsevier B.V., 608, pp. 552–575. doi: 10.1016/j.tecto.2013.08.024.
- Cartwright, I., Buick, I. S., Foster, D. A. and Lambert, D. D. (1999) Alice Springs age shear zones from the southeastern Reynolds Range, central Australia, pp. 355–363.
- Castro, A. (2004) The source of granites: inferences from the Lewisian complex, *Scottish Journal of Geology*, 40(1), pp. 49–65. doi: 10.1144/sjg40010049.
- Černý, P. (1991) *Rare-element granitic pegmatites. Part I: anatomy and internal evolution of pegmatite deposits*, *Geoscience Canada*.
- Černý, P. (2005) Rare-element Granitic Pegmatites, *Geoscience Canada*, 18(2), pp. 49–81. Available at: <http://canmin.geoscienceworld.org/content/43/6/2005.short> (Accessed: 25 March 2015).
- Černý, P. and Ercit, T. S. (2005a) The classification of granitic pegmatites revisited, *Canadian Mineralogist*, 43(6), pp. 2005–2026. doi: 10.2113/gscanmin.43.6.2005.
- Černý, P. and Ercit, T. S. (2005b) THE CLASSIFICATION OF GRANITIC PEGMATITES REVISITED, *The Canadian Mineralogist*, 43(6), pp. 2005–2026. doi: 10.2113/gscanmin.43.6.2005.
- Černý, P., London, D. and Novak, M. (2012) Granitic Pegmatites as Reflections of Their Sources, *Elements*, 8(4), pp. 289–294. doi: 10.2113/gselements.8.4.289.
- Champion, D. C. (2013) *Neodymium depleted mantle model age map of Australia: explanatory notes and user guide*, *Record*. doi: 10.11636/Record.2013.044.
- Chappell, B. W. and White, A. J. R. (2001) Two contrasting granite types: 25 years later, *Australian Journal of Earth Sciences*, 48(4), pp. 489–500. doi: 10.1046/j.1440-0952.2001.00882.x.
- Cherniak, D. ., Watson, E. B., Grove, M. and Harrison, T. M. (2004) Pb diffusion in monazite: a combined RBS/SIMS study, *Geochimica et Cosmochimica Acta*, 68(4), pp. 829–840. doi: 10.1016/j.gca.2003.07.012.
- Cilliers, B. (1989) *'n Petrogenetiese studie van 'n gedeelte van die Namakwalandse Metamorfe Kompleks lands die Oranjerivier tussen die Ramansdrif- en Homriviere, Warmbad distrik, suidelike Suidwes-Africa/Namibia*. Univ. Oragne Free State.
- Clemens, J. D., Buick, I. S., Kisters, A. F. M. and Frei, D. (2017) Petrogenesis of the granitic Donkerhuk batholith in the Damara Belt of Namibia: protracted, syntectonic, short-range, crustal magma transfer, *Contributions to Mineralogy and Petrology*. Springer Berlin Heidelberg, 172(7). doi: 10.1007/s00410-017-1370-0.
- Clifford, T. N. and Barton, E. S. (2012) The O'okiep Copper District, Namaqualand, South Africa: a review of the geology with emphasis on the petrogenesis of the cupriferous Koperberg Suite, *Mineralium Deposita*, 47(8), pp. 837–857. doi: 10.1007/s00126-012-0403-x.
- Clifford, T. N., Barton, E. S., Retief, E. A., Rex, D. C. and Fanning, C. M. (1995) A Crustal progenitor for the intrusive Anorthosite-Charnockite kindred of the Cupriferous Koperberg Suite, O'okiep District, Namaqualand, South Africa: New isotope data for the country rocks and the intrusives, *Journal of Petrology*, 96(1), pp. 231–258.
- Clifford, T. N., Barton, E. S., Stern, R. A. and Duchesne, J.-C. (2004) U-Pb Zircon Calendar for Namaquan (Grenville) Crustal Events in the Granulite-facies Terrane of the O'okiep Copper District of South Africa, *Journal of Petrology*, 45(4), pp. 669–691. doi: 10.1093/petrology/egg097.
- Colliston, W. P. (1990) *A stratigraphic and structural investigation of part of the Namaqua mobile belt between*

*Dabenoris and Steyerskraal, South Africa*. Univ. Orange Free State.

Colliston, W. P., Cornell, D. H., Schoch, A. E. and Praekelt, H. E. (2015) Geochronological constraints on the Hartbees River Thrust and Augrabies Nappe: New insights into the assembly of the Mesoproterozoic Namaqua-Natal Province of Southern Africa, *Precambrian Research*. doi: 10.1016/j.precamres.2015.03.008.

Colliston, W. P. and Schoch, A. E. (2013) Wrench-shearing during the Namaqua orogenesis-Mesoproterozoic late stage deformation effects during Rodinia assembly, *Precambrian Research*. Elsevier B.V., 232, pp. 44–58. doi: 10.1016/j.precamres.2012.10.015.

Colliston, W. P. and Schoch, A. E. (1996) Proterozoic metavolcanic rocks and associated metasediments along the Orange River in the Pofadder Terrane, Namaqua metamorphic belt, *South African Journal of Geology*, 99(1), pp. 1–17.

Cornell, D. H., Pettersson, A., Whitehouse, M. and Scherstén, A. (2009a) A new chronostratigraphic paradigm for the age and tectonic history of the Mesoproterozoic Bushmanland ore district, South Africa, *Economic Geology*, 104(3), pp. 385–404. doi: 10.2113/gsecongeo.104.3.385.

Cornell, D. H. and Pettersson, A. (2007a) Ion probe dating of the Achab Gneiss, a young basement to the Central Bushmanland Ore District?, *Journal of African Earth Sciences*, 47(2), pp. 112–116. doi: 10.1016/j.jafrearsci.2006.11.002.

Cornell, D. H. and Pettersson, A. (2007b) Ion probe zircon dating of metasediments from the Areachap and Kakamas Terranes, Namaqua-Natal Province and the stratigraphic integrity of the Areachap Group, *South African Journal of Geology*, 110(4), pp. 575–584. doi: 10.2113/gssajg.110.4.575.

Cornell, D. H., Pettersson, A. and Simonsen, S. L. (2012) Zircon U-Pb emplacement and Nd-Hf crustal residence ages of the Straussburg Granite and Friersdale Charnockite in the Namaqua-Natal Province, South Africa, *South African Journal of Geology*, 44(4), pp. 465–484. doi: 10.2113/gssajg.115.4.65.

Cornell, D. H., Pettersson, A., Whitehouse, M. J. and Schersten, A. (2009b) A New Chronostratigraphic Paradigm for the Age and Tectonic History of the Mesoproterozoic Bushmanland Ore District, South Africa, *Economic Geology*, 104(3), pp. 385–404. doi: 10.2113/gsecongeo.104.3.385.

Cornell, D. H., Pettersson, A., Whitehouse, M. J. and Schersten, A. (2009c) A New Chronostratigraphic Paradigm for the Age and Tectonic History of the Mesoproterozoic Bushmanland Ore District, South Africa, *Economic Geology*, 104(3), pp. 385–404. doi: 10.2113/gsecongeo.104.3.385.

Cornell, D. H., Thomas, R. J., Moen, H. F. G., Reid, D. L., Moore, J. M. and Gibson, R. L. (2006) The Namaqua-natal province, in Johnson, M. R., Anhaeusser, C. R., and Thomas, R. J. (eds) *The Geology of South Africa*. South Africa: Geol. Soc. s. Africa and Council for Geoscience, pp. 325–379.

Cornell, D., Humphreys, H., Theart, H. and Scheepers, D. (1992) A collision-related pressure-temperature-time path for Prieska copper mine, Namaqua-natal tectonic province, South Africa, *Precambrian Research*, 59(1–2), pp. 43–71. doi: 10.1016/0301-9268(92)90051-O.

Crowley, J. L., Brown, R. L., Gervais, F. and Gibson, H. D. (2008) Assessing Inheritance of Zircon and Monazite in Granitic Rocks from the Monashee Complex, Canadian Cordillera, *Journal of Petrology*, 49(11), pp. 1915–1929. doi: 10.1093/petrology/egn047.

Depaolo, D. J. and Wasserburg, G. J. (1976) Nd isotopic variations and petrogenetic models, *Geophysical Research Letters*, 3(5), pp. 3–6.

Diener, J. F. A. (2014) Low-P-high-T metamorphism of the Aggeney's terrane, Namaqua Metamorphic Complex, South Africa, *South African Journal of Geology*, 117(1), pp. 31–44. doi: 10.2113/gssajg.117.1.31.

Diener, J. F. A., White, R. W., Link, K., Dreyer, T. S. and Moodley, A. (2013) Clockwise, low-P metamorphism of the Aus granulite terrain, southern Namibia, during the Mesoproterozoic Namaqua Orogeny, *Precambrian Research*, 224, pp. 629–652. doi: 10.1016/j.precamres.2012.11.009.

Dubois, J. C., Retali, G. and Cesario, J. (1992) Isotopic analysis of rare earth elements by total vaporisation of samples in thermal ionisation mass spectrometry, *International Journal of Mass Spectrometry and Ion Processes*. Elsevier, 120(3), pp. 163–177. doi: 10.1016/0168-1176(92)85046-3.

- Dumond, G., Goncalves, P., Williams, M. L. and Jercinovic, M. J. (2015) Monazite as a monitor of melting, garnet growth and feldspar recrystallisation in the continental lower crust, *Journal of Metamorphic Geology*, 33(7), pp. 735–762. doi: 10.1111/jmg.12150.
- Dumond, G., McLean, N., Williams, M. L., Jercinovic, M. J. and Bowring, S. A. (2008) High-resolution dating of granite petrogenesis and deformation in a lower crustal shear zone: Athabasca granulite terrane, western Canadian Shield, *Chemical Geology*, 254(3–4), pp. 175–196. doi: 10.1016/j.chemgeo.2008.04.014.
- Eglinton, B. and Armstrong, R. A. (2003) Geochronological and isotopic constraints on the Mesoproterozoic Namaqua–Natal Belt: evidence from deep borehole intersections in South Africa, *Precambrian Research*, 125(3–4), pp. 179–189. doi: 10.1016/S0301-9268(02)00199-7.
- Eglinton, B. M. (2006a) Evolution of the Namaqua-Natal Belt, southern Africa – A geochronological and isotope geochemical review, *Journal of African Earth Sciences*, 46(1–2), pp. 93–111. doi: 10.1016/j.jafrearsci.2006.01.014.
- Eglinton, B. M. (2006b) Evolution of the Namaqua-Natal Belt, southern Africa – A geochronological and isotope geochemical review, *Journal of African Earth Sciences*, 46(1–2), pp. 93–111. doi: 10.1016/j.jafrearsci.2006.01.014.
- Evans, D. M., Windrim, D. P. and Armstrong, R. a. (2007) Age of Metavolcanic rocks at the northern margin of the Namaqua-Natal Metamorphic Province in the Karas Mountains, Namibia, defined by SHRIMP U-Pb dating of zircons, *South African Journal of Geology*, 110(1), pp. 47–54. doi: 10.2113/gssajg.110.1.47.
- Evensen, J. M. and London, D. (2002) Experimental silicate mineral/melt partition coefficients for beryllium and the crustal Be cycle from migmatite to pegmatite, *Geochimica et Cosmochimica Acta*, 66(12), pp. 2239–2265. doi: 10.1016/S0016-7037(02)00889-X.
- Evensen, J. M., London, D. and Wendlandt, R. F. (1999) Solubility and stability of beryl in granitic melts, *American Mineralogist*, 84(5–6), pp. 733–745. Available at: [http://www.minsocam.org/msa/AmMin/toc/Articles\\_Free/1999/Evensen\\_p733-745\\_99.pdf](http://www.minsocam.org/msa/AmMin/toc/Articles_Free/1999/Evensen_p733-745_99.pdf) (Accessed: 25 March 2015).
- Fisher, C. M., McFarlane, C. R. M., Hanchar, J. M., Schmitz, M. D., Sylvester, P. J., Lam, R. and Longerich, H. P. (2011) Sm-Nd isotope systematics by laser ablation-multicollector-inductively coupled plasma mass spectrometry: Methods and potential natural and synthetic reference materials, *Chemical Geology*. Elsevier B.V., 284(1–2), pp. 1–20. doi: 10.1016/j.chemgeo.2011.01.012.
- Foster, G. L. and Vance, D. (2006) In situ Nd isotopic analysis of geological materials by laser ablation MC-ICP-MS, *Journal of Analytical Atomic Spectrometry*, 21(3), p. 288. doi: 10.1039/b513945g.
- Fransson, M. (2008) U-Pb zircon dating of metasedimentary rocks in the Areachap, Kakamas and Bushmanland Terranes in Namaqua Province, South Africa. University of Gothenburg.
- Fuchsloch, W. C., Nex, P. A. M. and Kinnaird, J. A. (2018) Classification, mineralogical and geochemical variations in pegmatites of the Cape Cross-Uis pegmatite belt, Namibia, *Lithos*. Elsevier B.V., 296–299, pp. 79–95. doi: 10.1016/j.lithos.2017.09.030.
- Gardés, E., Jaoul, O., Montel, J. M., Seydoux-Guillaume, A. M. and Wirth, R. (2006) Pb diffusion in monazite: An experimental study of  $\text{Pb}^{2+} + \text{Th}^{4+} = 2\text{Nd}^{3+}$  interdiffusion, *Geochimica et Cosmochimica Acta*, 70(9), pp. 2325–2336. doi: 10.1016/j.gca.2006.01.018.
- Gardien, V., Thompson, A. B., Grujic, D. and Ulmer, P. (1995) Experimental melting of biotite + plagioclase + quartz  $\pm$  muscovite assemblages and implications for crustal melting, *Journal of Geophysical Research: Solid Earth*, 100(B8), pp. 15581–15591. doi: 10.1029/95JB00916.
- Geringer, G. J., Botha, B. J. V., Pretorius, J. J. and Ludick, D. (1986) Calc-alkaline volcanism along the eastern margin of the Namaqua mobile belt, South Africa a possible middle Proterozoic volcanic arc, *Precambrian Research*, 33, pp. 139–170.
- Geringer, G. J., Humphreys, H. C. and Scheepers, D. (1994) Lithostratigraphy, proto-lithology and tectonic setting of the Areachap group along the eastern margin of the Namaqua mobile belt, South Africa., *South*

*African Journal of Geology*, 97, pp. 78–100.

Gevers, T. W. (1936) Phases of Mineralisation in Namaqualand pegmatites, *Transactions of the Geological Society of South Africa*, pp. 331–375.

Gibson, R. L., Robb, L. J., Kisters, A. F. M. and Cawthorn, R. G. (1996) Regional setting and geological evolution of the Okiep Copper District, Namaqualand, South Africa, *South African Journal of Geology*, 99, pp. 107–120.

Ginsburg, A. I., Timofeyev, I. N. and Feldman, I. G. (1979) Principles of Geology of Granitic Pegmatites, Nedra, Moscow, p. 296.

Gonçalves, G. O., Lana, C., Scholz, R., Buick, I. S., Gerdes, A., Kamo, S. L., Corfu, F., Marinho, M. M., Chaves, A. O., Valeriano, C. and Nalini, H. A. (2016) An assessment of monazite from the Itambé pegmatite district for use as U–Pb isotope reference material for microanalysis and implications for the origin of the ‘Moacyr’ monazite, *Chemical Geology*. Elsevier B.V., 424, pp. 30–50. doi: 10.1016/j.chemgeo.2015.12.019.

Gonçalves, G. O., Lana, C., Scholz, R., Buick, I. S., Gerdes, A., Kamo, S. L., Corfu, F., Rubatto, D., Wiedenbeck, M., Nalini, H. A. and Oliveira, L. C. A. (2018) The Diamantina Monazite: A New Low-Th Reference Material for Microanalysis, *Geostandards and Geoanalytical Research*, 42(1), pp. 25–47. doi: 10.1111/ggr.12192.

Goodenough, K. M., Crowley, Q. G., Krabbendam, M. and Parry, S. F. (2013) New U–Pb age constraints for the Laxford Shear Zone, NW Scotland: Evidence for tectono-magmatic processes associated with the formation of a Paleoproterozoic supercontinent, *Precambrian Research*. Elsevier B.V., 233, pp. 1–19. doi: 10.1016/j.precamres.2013.04.010.

Goudie, D., Fisher, C., Hanchar, J. M., Crowley, J. L. and Ayers, J. C. (2014) Simultaneous in situ determination of U–Pb and Sm–Nd isotopes in monazite by laser ablation ICP–MS, *Geochemistry, Geophysics, Geosystems*, pp. 1–26. doi: 10.1002/2014GC005431. Received.

Gregory, C. J., Buick, I. S., Hermann, J. and Rubatto, D. (2009) Mineral-scale trace element and U–Th–Pb age constraints on metamorphism and melting during the Petermann orogeny (Central Australia), *Journal of Petrology*, 50(2), pp. 251–287. doi: 10.1093/petrology/egn077.

Gresse, P. G., Macey, P. H., Smith, H. S., Hatnandy, M. I. and Frei, D. (2016) The Pre-Gariep geology east of Rosh Pinah, Karas Region, S. Namibia. Explanation to parts of 1:50 000 Geological Map Sheets 716DA, 2716Db, 2716DD, 2717CC, 2816BB and 2817AA. Geol. Surv. Namibia, Council for Geoscience S.A., Min. Mines and Energy, Namibia, p. 193.

Hammerli, J., Kemp, A. I. S. and Spandler, C. (2014) Neodymium isotope equilibration during crustal metamorphism revealed by in situ microanalysis of REE-rich accessory minerals, *Earth and Planetary Science Letters*. Elsevier B.V., 392, pp. 133–142. doi: 10.1016/j.epsl.2014.02.018.

Harlov, D. E., Wirth, R. and Hetherington, C. J. (2011) Fluid-mediated partial alteration in monazite: The role of coupled dissolution-reprecipitation in element redistribution and mass transfer, *Contributions to Mineralogy and Petrology*, 162(2), pp. 329–348. doi: 10.1007/s00410-010-0599-7.

Harris, N. B. W., Pearce, J. A. and Tindle, A. G. (1986) Geochemical characteristics of collision-zone magmatism, *Geological Society, London, Special Publications*, 19(1), pp. 67–81. doi: 10.1144/GSL.SP.1986.019.01.04.

Harris, N. and Massey, J. (1994) Decompression and anatexis of Himalayan metapelites, *Tectonics*, 13(6), pp. 1537–1546. doi: 10.1029/94TC01611.

Hartnady, C., Joubert, P. and Stowe, C. (1985) Proterozoic crustal evolution of Southwestern Africa, *Episodes*, 8(4), pp. 236–244.

Hermann, J. and Rubatto, D. (2003) Relating zircon and monazite domains to garnet growth zones: Age and duration of granulite facies metamorphism in the Val Malenco lower crust, *Journal of Metamorphic Geology*, 21(9), pp. 833–852. doi: 10.1046/j.1525-1314.2003.00484.x.

Horstwood, M. S. A., Foster, G. L., Parrish, R. R., Noble, S. R. and Nowell, G. M. (2003) Common-Pb corrected in situ U–Pb accessory mineral geochronology by LA–MC–ICP–MS, *J. Anal. At. Spectrom.* The Royal Society

of Chemistry, 18(8), pp. 837–846. doi: 10.1039/B304365G.

Hugo, P. J. (1970) Pegmatites of the Kenhardt, Gordonia districts, Cape Province, *Memoirs of the Geological Survey of South Africa*, p. 94.

Icenhower, J. and London, D. (1995) An experimental study of element partitioning among biotite, muscovite, and coexisting peraluminous silicic melt at 200 MPa (H<sub>2</sub>O), *American Mineralogist*, 80(11–12), pp. 1229–1251. doi: 10.2138/am-1995-11-1213.

Iizuka, T., Eggins, S. M., McCulloch, M. T., Kinsley, L. P. J. and Mortimer, G. E. (2011) Precise and accurate determination of <sup>147</sup>Sm/<sup>144</sup>Nd and <sup>143</sup>Nd/<sup>144</sup>Nd in monazite using laser ablation-MC-ICPMS, *Chemical Geology*. Elsevier B.V., 282(1–2), pp. 45–57. doi: 10.1016/j.chemgeo.2011.01.008.

Indongo, J. (2017) *The Lithological and Structural Characterisation of the Sperlingputs Shear Zone in Southern Namibia*. University of Stellenbosch.

Isnard, H., Brennetot, R., Caussignac, C., Caussignac, N. and Chartier, F. (2005) Investigations for determination of Gd and Sm isotopic compositions in spent nuclear fuels samples by MC ICPMS, *International Journal of Mass Spectrometry*, 246(1–3), pp. 66–73. doi: 10.1016/j.ijms.2005.08.008.

Jackson, S. E., Pearson, N. J., Griffin, W. L. and Belousova, E. A. (2004) The application of laser ablation-inductively coupled plasma-mass spectrometry to in situ U–Pb zircon geochronology, *Chemical Geology*. Elsevier, 211(1–2), pp. 47–69. doi: 10.1016/J.CHEMGEO.2004.06.017.

Jacobs, J., Pisarevsky, S., Thomas, R. J. and Becker, T. (2008) The Kalahari Craton during the assembly and dispersal of Rodinia, *Precambrian Research*, 160(1–2), pp. 142–158. doi: 10.1016/j.precamres.2007.04.022.

Jacobs, J., Thomas, R. and Weber, K. (1993) Accretion and indentation tectonics at the southern margin of the Kaapvall craton during Kibaran (Greenville) orogeny, *Geological Society Of America*, 21, pp. 203–206. doi: 10.1130/0091-7613(1993)021<0203.

Jacobsen, S. B. and Wasserburg, G. J. (1980) Sm–Nd isotopic evolution of chondrites, *Earth and Planetary Science Letters*, 50(1), pp. 139–155. doi: 10.1016/0012-821X(80)90125-9.

Joubert, P. and Waters, D. J. (1980) The occurrence of kyanite at Zoutpan and metamorphism in western Namaqualand, *Annual Report, Chamber of Mines Precambrian Research Unit, University of Cape Town*, 17, pp. 74–87.

Kinny, P. D., Friend, C. R. L. and Love, G. J. (2005) Proposal for a terrane-based nomenclature for the Lewisian Gneiss Complex of NW Scotland, *Journal of the Geological Society*, 162(1), pp. 175–186. doi: 10.1144/0016-764903-149.

Lambert, C. W. (2013) *Granitic melt transport and emplacement along transcurrent shear zones : Case study of the Pofadder Shear Zone in South Africa and Namibia*. University of Stellenbosch.

Lambert, C. W., Macey, P. H., Doggart, S., Nethenzheni, S. S. and Bailie, R. H. (2016) Lithostratigraphy of the Friersdale Charnockite (Keimoes Suite), South Africa, *South African Journal of Geology*, 119(4), pp. 691–698. doi: 10.2113/gssajg.119.4.691.

Li, Z. X., Bogdanova, S. V., Collins, A. S., Davidson, A., De Waele, B., Ernst, R. E., Fitzsimons, I. C. W., Fuck, R. A., Gladkochub, D. P., Jacobs, J., Karlstrom, K. E., Lu, S., Natapov, L. M., Pease, V., Pisarevsky, S. A., Thrane, K. and Vernikovsky, V. (2008) Assembly, configuration, and break-up history of Rodinia: A synthesis, *Precambrian Research*, 160(1–2), pp. 179–210. doi: 10.1016/j.precamres.2007.04.021.

Liew, T. C. and Hofmann, A. W. (1988) Precambrian crustal components, plutonic associations, plate environment of the Hercynian Fold Belt of central Europe: Indications from an Nd and Sr isotopic study, *Contributions to Mineralogy and Petrology*, 98(2), pp. 129–138. doi: 10.1007/BF00402106.

Liew, T. C. and McCulloch, M. T. (1985) Genesis of granitoid batholiths of Peninsular Malaysia and implications for models of crustal evolution: Evidence from a Nd and Sr isotopic and U–Pb zircon study, *Geochimica et Cosmochimica Acta*, 49(2), pp. 587–600.

Liu, X. C., Wu, Y. B., Fisher, C. M., Hanchar, J. M., Beranek, L., Gao, S. and Wang, H. (2017) Tracing crustal

evolution by U-Th-Pb, Sm-Nd, and Lu-Hf isotopes in detrital monazite and zircon from modern rivers, *Geology*, 45(2), pp. 103–106. doi: 10.1130/G38720.1.

Liu, Z. C., Wu, F. Y., Yang, Y. H., Yang, J. H. and Wilde, S. A. (2012a) Neodymium isotopic compositions of the standard monazites used in UThPb geochronology, *Chemical Geology*, 334(September), pp. 221–239. doi: 10.1016/j.chemgeo.2012.09.034.

Liu, Z. C., Wu, F. Y., Yang, Y. H., Yang, J. H. and Wilde, S. A. (2012b) Neodymium isotopic compositions of the standard monazites used in UThPb geochronology, *Chemical Geology*. Elsevier B.V., 334, pp. 221–239. doi: 10.1016/j.chemgeo.2012.09.034.

London, D. (2005) Granitic pegmatites: An assessment of current concepts and directions for the future, *Lithos*, 80(1–4 SPEC. ISS.), pp. 281–303. doi: 10.1016/j.lithos.2004.02.009.

London, D. (2008) Pegmatites. Mineralogical Association of Canada, p. 347.

London, D. (2015) Reading pegmatites: Part 1-what beryl says, *Rocks and Minerals*, 90(2), pp. 138–149. doi: 10.1080/00357529.2014.949173.

London, D. (2016) Reading Pegmatites—Part 2: What Tourmaline Says, *Rocks & Minerals*, 91(2), pp. 132–149. doi: 10.1080/00357529.2016.1113464.

London, D. and Morgan, G. B. (2017) Experimental crystallization of the Macusani Obsidian, with applications to lithium-rich granitic pegmatites, *Journal of Petrology*, 58(5), pp. 1005–1030. doi: 10.1093/PETROLOGY/EGX044.

London, D. (2018) Ore-Forming Processes Within Granitic Pegmatites, *Ore Geology Reviews*. Elsevier, 101(May), pp. 349–383. doi: 10.1016/j.oregeorev.2018.04.020.

London, D. and Morgan, G. B. (2012) The pegmatite puzzle, *Elements*, 8(4), pp. 263–268. doi: 10.2113/gselements.8.4.263.

MacDonald, R., Smith, R. L. and Thomas, J. E. (1992) Chemistry of the Subalkalic Silicic Obsidians, *USGS Professional Paper*, 1523, p. 214. doi: 1523.

Macey, P. H., Bailie, R. H., Miller, J. A., Thomas, R. J., de Beer, C., Frei, D. and le Roux, P. J. (2018) Implications of the distribution, age and origins of the granites of the Mesoproterozoic Spektakel Suite for the timing of the Namaqua Orogeny in the Bushmanland Subprovince of the Namaqua- Natal Metamorphic Province, South Africa, *Precambrian Research*. Elsevier, 312(March), pp. 1–35. doi: 10.1016/j.precamres.2018.02.026.

Macey, P. H., Minnaar, H., Miller, J. A., Lambert, C., Kisters, A. F. M., Diener, J., Thomas, R. J., Groenewald, C., Indongo, J., Angombe, M., Smith, H., Shifatoka, G., Le Roux, P. and Frei, D. (2015) The Precambrian Geology of the Warmbad Region, Southern Namibia. An Interim Explanation to 1:50,000 Geological Map Sheets of the 1:250 000 2818 Warmbad Sheet.

Macey, P. H., Siegfried, H. P., Minnaar, H. M., Almond, J. E. and Botha, P. M. W. (2011) The geology of the Loeriesfontein area. 1:250 000 map sheet explanation 3018. Council for Geoscience, p. 139.

Macey, P. H., Thomas, R. J., Minnaar, H. M., Gresse, P. G., Lambert, C. W., Groenewald, C. A., Miller, J. A., Indongo, J., Angombe, M., Shifotoka, G., Frei, D., Diener, J. F. A., Kisters, A. F. M., Dhansay, T., Smith, H., Daggart, S., Le Roux, P., Hartnady, M. I. and Tinguely, C. (2017) Origin and evolution of the ~1.9 Ga Richtersveld Magmatic Arc, SW Africa, *Precambrian Research*, 292, pp. 417–451. doi: 10.1016/j.precamres.2017.01.013.

Magni, V., Allen, M. B., van Hunen, J. and Bouilhol, P. (2017) Continental underplating after slab break-off, *Earth and Planetary Science Letters*. Elsevier B.V., 474, pp. 59–67. doi: 10.1016/j.epsl.2017.06.017.

Marais, J. A. H., Agenbacht, A. L. D., Prinsloo, M. and Basson, W. A. (2001) The geology of the Springbok area. 1:250 000 map sheet explanation, sheet 2916. Council for Geoscience, p. 103.

Martin, R. F. and De Vito, C. (2005) THE PATTERNS OF ENRICHMENT IN FELSIC PEGMATITES ULTIMATELY DEPEND ON TECTONIC SETTING, *The Canadian Mineralogist*, 43(6), pp. 2027–2048. doi: 10.2113/gscanmin.43.6.2027.

- McClung, C. R. (2006) Basin Analysis of the Mesoproterozoic Bushmanland Group of the Namaqua Metamorphic Province, South Africa, (November), p. 307.
- McFarlane, C. R. M. and McCulloch, M. T. (2007) Coupling of in-situ Sm-Nd systematics and U-Pb dating of monazite and allanite with applications to crustal evolution studies, *Chemical Geology*, 245(1–2), pp. 45–60. doi: 10.1016/j.chemgeo.2007.07.020.
- McFarlane, C. R. M. and Mckeough, M. (2013) Petrogenesis of the Kulyk Lake monazite-apatite-Fe (Ti) -oxide occurrence revealed using in-situ LA- (MC) -ICP-MS trace element mapping, U-Pb dating, and Sm-Nd isotope systematics on monazite †, *American Mineralogist*, 98(Mc), pp. 1644–1659.
- McKechnie, C. L., Annesley, I. R. and Ansdell, K. M. (2012) Medium- to low-pressure pelitic gneisses of Fraser Lakes Zone B, Wollaston Domain, Northern Saskatchewan, Canada: Mineral compositions, metamorphic P-T-t path, and implications for the genesis of radioactive abyssal granitic pegmatites, *Canadian Mineralogist*, 50(6), pp. 1669–1694. doi: 10.3749/canmin.50.6.1669.
- Melcher, F., Graupner, T., Henjes-Kunst, F., Oberthür, T., Sitnikova, M., Gäbler, E., Gerdes, A., Brätz, H., Davis, D. and Dewaele, S. (2008) Analytical fingerprint of columbite-tantalite (coltan) mineralisation in pegmatites - Focus on Africa, in *Australasian Institute of Mining and Metallurgy Publication Series*, pp. 615–624. Available at: <http://www.scopus.com/inward/record.url?eid=2-s2.0-58049135315&partnerID=40&md5=c8f4a3836e0d6f1a8fcc68085adf842>.
- Melcher, F. and Graupner, T. (2009) African Rare-Element Pegmatite Provinces: Mineralogy and Geochemistry of Nb-Ta Minerals, *Estudos ...*, 19(1992), pp. 217–222. Available at: <http://www.contabeis.ufpe.br/estudosgeologicos/paginas/edicoes/2009192/2009192t42.pdf> (Accessed: 25 March 2015).
- Melleton, J., Gloaguen, E., Frei, D., Novák, M. and Breiter, K. (2012) How are the emplacement of rare-element pegmatites, regional metamorphism and magmatism interrelated in the Moldanubian domain of the Variscan Bohemian Massif, Czech Republic?, *Canadian Mineralogist*, 50(6), pp. 1751–1773. doi: 10.3749/canmin.50.6.1751.
- Melosh, B. L., Rowe, C. D., Gerbi, C., Smit, L. and Macey, P. (2018) Seismic cycle feedbacks in a mid-crustal shear zone, *Journal of Structural Geology*. Elsevier Ltd, 112, pp. 95–111. doi: 10.1016/j.jsg.2018.04.004.
- Millar, R. M. (2008) *The geology of Namibia. Handbook*. Vol. 3. Geological Survey of Namibia.
- Miller, R. G. (2012) Review of Mesoproterozoic magmatism, sedimentation and terrane amalgamation in Southwestern Africa, *South African Journal of Geology*, 44(4), pp. 33–39. doi: 10.2113/gssajg.115.4.
- Minnaar, H. (2012) *Composition and Evolution of the Proterozoic Vioolsdrif Batholith (including the Orange River Group), northern Cape Province, South Africa*. University of the Free State.
- Minnaar, H. and Theart, H. F. J. (2006) The exploitability of pegmatite deposits in the lower Orange River area (Vioolsdrif - Henkries - Steinkopf), *South African Journal of Geology*, 109(3), pp. 341–352. doi: 10.2113/gssajg.109.3.341.
- Moen, H. F. G. and Armstrong, R. a. (2008) New age constraints on the tectogenesis of the Kheis Subprovince and the evolution of the eastern Namaqua Province, *South African Journal of Geology*, 111(1), pp. 79–88. doi: 10.2113/gssajg.111.1.79.
- Moen, H. F. G. and Toogood, D. J. (2007a) *The geology of the Onseepkans area. Map and explanation, sheet 2818 Onseepkans (1:250 000)*. Council for Geoscience.
- Moen, H. F. G. and Toogood, D. J. (2007b) *The Geology of the Onseepkans area. Map and explanation, sheet 2818 Onseepkans (1:250 000)*. Council for Geoscience, p. 101.
- Müller, A., Romer, R. L. and Pedersen, R.-B. (2017) The Sveconorwegian Pegmatite Province – Thousands of Pegmatites Without Parental Granites, *The Canadian Mineralogist*, 55(2), pp. 283–315. doi: 10.3749/canmin.1600075.
- Van Niekerk, H. S. (2006) *The origin of the Kheis Terrane and its relationship with the Archean Kaapvaal Craton and the Grenvillian Namaqua province in Southern Africa*. University of Johannesburg.



- Pan, Y. and Breaks, F. W. (1997) Rare-earth elements in fluorapatite, Separation Lake area, Ontario: Evidence for S-type granite - Rare-element pegmatite linkage, *Canadian Mineralogist*, 35(3), pp. 659–671.
- Partington, G. A., McNaughton, N. J. and Williams, I. S. (1995) A review of the geology, mineralisation, and geochronology of the Greenbushes Pegmatite, Western Australia, *Economic Geology*. GeoScienceWorld, 90(3), pp. 616–635. doi: 10.2113/gsecongeo.90.3.616.
- Pettersson, Å. (2008) *Mesoproterozoic crustal evolution in Southern Africa*. City of Gothenburg, Sweden. doi: <http://hdl.handle.net/2077/17269>.
- Pettersson, Å. and Cornell, D. H. (2008a) Regional granitoid geochronology in relation to the Namaquan Orogeny, *Lithos*.
- Pettersson, Å., Cornell, D. H. and Page, L. (2008b) Insights to the cooling history from Ar-dating in the (1.2–1.1 Ga) Namaqua Sector, South Africa, *Journal of African Earth Sciences*, pp. 1–10.
- Pettersson, Å., Cornell, D. H., Moen, H. F. G., Reddy, S. and Evans, D. (2007) Ion-probe dating of 1.2 Ga collision and crustal architecture in the Namaqua-Natal Province of southern Africa, *Precambrian Research*, 158(1–2), pp. 79–92. doi: 10.1016/j.precamres.2007.04.006.
- Pettersson, Å., Cornell, D. H., Yuhara, M. and Hirahara, Y. (2009) Sm-Nd data for granitoids across the Namaqua sector of the Namaqua-Natal Province, South Africa, *Geological Society, London, Special Publications*, 323(1), pp. 219–230. doi: 10.1144/SP323.10.
- Du Plessis, G. (1979) 'n Metamorf-magmatiese studie van 'n gedeelte van die Namak-walandse metamorfe kompleks langs die Oranjerivier, oos van Onseepkans. Univ. Orange Free State.
- Lo Pò, D., Braga, R., Massonne, H. J., Molli, G., Montanini, A. and Theye, T. (2016) Fluid-induced breakdown of monazite in medium-grade metasedimentary rocks of the Pontremoli basement (Northern Apennines, Italy), *Journal of Metamorphic Geology*, 34(1), pp. 63–84. doi: 10.1111/jmg.12171.
- Praekelt, H. E. (1984) *Die geologie van die gebied rondom Augrabies (2820 C)*. University of the Orange Free State, Bloemfontein, South Africa.
- Raith, J. G., Cornell, D. H., Frimmel, H. E. and De Beer, C. H. (2003) New insights into the geology of the Namaqua Tectonic Province, South Africa, from ion probe dating of detrital and metamorphic zircon, *Journal of Geology*, 111, pp. 347–366.
- Raith, J. G. and Harley, S. L. (1998) Low-P/high-T metamorphism in the Okiep Copper District, western Namaqualand, South Africa, *Journal of Metamorphic Geology*, 16, pp. 281–305.
- Reid, D. and Barton, E. S. (1983) Geochemical Characterization of Granitoids in the Namaqualand Geotraverse, *Geological Society of South Africa, Special Publication*, 10, pp. 67–82.
- Reid, D. L. (1977) Geochemistry of Precambrian igneous rocks in the lower Orange River region. Precamb. Res. Unit, Univ. Cape Town, p. 397.
- Reid, D. L. (1997) Sm\Nd age and REE geochemistry of Proterozoic arc-related igneous rocks in the Richtersveld subprovince, Namaqua Mobile Belt, Southern Africa, *Journal of African Earth Sciences*, 24(4), pp. 621–633. doi: 10.1016/S0899-5362(97)00084-5.
- Reid, D. L., Erlank, A. J., Welke, H. J. and Moyes, A. (1987) The Orange River Group: a Major Proterozoic Calcalkaline Volcanic Belt in the Western Namaqua Province, Southern Africa, *Geological Society, London, Special Publications*, 33(1), pp. 327–346. doi: 10.1144/GSL.SP.1987.033.01.22.
- Ritter, U. (1980) The Precambrian evolution of the eastern Richtersveld., *Bulletin of the Precambrian Research Unit, University of Cape Town*, 26, p. 276.
- Robb, L. J., Armstrong, R. a and Waters, D. J. (1999) The history of granulite-facies metamorphism and crustal growth from single zircon U-Pb geochronology: Namaqualand, South Africa, *Journal of Petrology*, 40(12), pp. 1747–1770. doi: 10.1093/ptro/40.12.1747.
- Rubatto, D., Hermann, J. and Buick, I. S. (2006) Temperature and bulk composition control on the growth of monazite and zircon during low-pressure anatexis (Mount Stafford, Central Australia), *Journal of*

*Petrology*, 47(10), pp. 1973–1996. doi: 10.1093/petrology/egl033.

Schutte, I. C. (1972) The main pegmatites of the area between Steinkopf, Vioolsdrif and Goodhouse, Namaqualand., *Memoirs Geological Survey of South Africa*, p. 20.

Seydoux-Guillaume, A.-M., Deschanel, X., Baumier, C., Neumeier, S., Weber, W. J. and Peugot, S. (2018) Why natural monazite never becomes amorphous: Experimental evidence for alpha self-healing, *American Mineralogist*, 103(5), pp. 824–827. doi: 10.2138/am-2018-6447.

Seydoux-Guillaume, A. M., Montel, J. M., Bingen, B., Bosse, V., de Parseval, P., Paquette, J. L., Janots, E. and Wirth, R. (2012) Low-temperature alteration of monazite: Fluid mediated coupled dissolution-precipitation, irradiation damage, and disturbance of the U-Pb and Th-Pb chronometers, *Chemical Geology*. Elsevier B.V., 330–331, pp. 140–158. doi: 10.1016/j.chemgeo.2012.07.031.

Shaw, R. A., Goodenough, K. M., Roberts, N. M. W., Horstwood, M. S. A., Chenery, S. R. and Gunn, A. G. (2016) Petrogenesis of rare-metal pegmatites in high-grade metamorphic terranes: A case study from the Lewisian Gneiss Complex of north-west Scotland, *Precambrian Research*. British Geological Survey, NERC, 281, pp. 338–362. doi: 10.1016/j.precamres.2016.06.008.

Shifotoka, G., Indongo, J., Thomas, R. J., Macey, P. H. and Miller, J. A. M. (2016) *1:50000 geological map of the Haib region. Portions of map sheets 2817DA, DB, DC, DD*.

Simmons, W. B., Foord, E. E., Falster, A. U. and King, V. T. (1995) Evidence for an anatectic origin of granitic pegmatites, western Maine, USA, in *Geological Society of America Annual Meeting*.

Simmons, W. B. S. and Webber, K. L. (2008) Pegmatite genesis: state of the art, *European Journal of Mineralogy*, 20(4), pp. 421–438. doi: 10.1127/0935-1221/2008/0020-1833.

Slabbert, M. J., Moen, H. F. G. and Boelema, R. (1999) Die geologie van die gebied Kenhardt. Explanation, sheet 2920. Council for Geoscience, South Africa, p. 123.

Špaček, P., Ackerman, L., Habler, G., Abart, R. and Ulrych, J. (2013) Garnet breakdown, symplectite formation and melting in basanite-hosted peridotite xenoliths from Zinst (bavaria, bohemian massif), *Journal of Petrology*, 54(8), pp. 1691–1723. doi: 10.1093/petrology/egt028.

Stepanov, A., Mavrogenes, J. A., Meffre, S. and Davidson, P. (2014) The key role of mica during igneous concentration of tantalum, *Contributions to Mineralogy and Petrology*, 167(6), pp. 1–8. doi: 10.1007/s00410-014-1009-3.

Stilling, A., Černý, P. and Vanstone, P. J. (2006) The Tanco pegmatite at Bernic Lake, Manitoba. XVI. Zonal and bulk compositions and their petrogenetic significance, *Canadian Mineralogist*, 44(3), pp. 599–623. doi: 10.2113/gscanmin.44.3.599.

Strydom, D., Colliston, W. P., Praekelt, H. E., Schoch, A. E., van Aswegen, G., Pretorius, J. J., Beukes, G. J., De Villiers, B., Watkeys, W. K. and Botes, F. J. (1987) The tectonic units of parts of Namaqualand, Bushmanland and southern Namibia. Map (1:250 000). Bushmanland Research Project, Dept. of Geology, Univ. Orange Free State.

Sun, S. and McDonough, W. F. (1989) Chemical and isotopic systematics of oceanic basalts: implications for mantle composition and processes, *Geological Society, London, Special Publications*, 42(1), pp. 313–345. doi: 10.1144/GSL.SP.1989.042.01.19.

Sweetapple, M. T. and Collins, P. L. F. (2002) Genetic framework for the classification and distribution of Archean rare metal pegmatites in the North Pilbara Craton, Western Australia, *Economic Geology*, 97(4), pp. 873–895. doi: 10.2113/gsecongeo.97.4.873.

Taylor, R. J. M., Clark, C., Fitzsimons, I. C. W., Santosh, M., Hand, M., Evans, N. and McDonald, B. (2014) Post-peak, fluid-mediated modification of granulite facies zircon and monazite in the Trivandrum Block, southern India, *Contributions to Mineralogy and Petrology*, 168(2), pp. 1–17. doi: 10.1007/s00410-014-1044-0.

Thomas, R. J., Agenbacht, A. L. D., Cornell, D. H. and Moore, J. M. (1994) The Kibaran of southern Africa: Tectonic evolution and metallogeny, *Ore Geology Reviews*, 9(2), pp. 131–160. doi: 10.1016/0169-

1368(94)90025-6.

Thomas, R. J., De Beer, C. H. and Bowring, S. A. (1996) A comparative study of the Mesoproterozoic late orogenic porphyritic granitoids of southwest Namaqualand and Natal, South Africa, *Journal of African Earth Sciences*, 23(3), pp. 485–508. doi: 10.1016/S0899-5362(97)00014-6.

Thomas, R. J., Macey, P. H., Spencer, C., Dhansay, T., Diener, J. F. A., Lambert, C. W., Frei, D. and Nguno, A. (2016) The Sperrgebiet Domain, Aurus Mountains, SW Namibia: A ~2020–850Ma window within the Pan-African Gariep Orogen, *Precambrian Research*, 286, pp. 35–58. doi: 10.1016/j.precamres.2016.09.023.

Thöni, M., Miller, C., Blichert-Toft, J., Whitehouse, M. J., Konzett, J. and Zanetti, A. (2008) Timing of high-pressure metamorphism and exhumation of the eclogite type-locality (Kupplerbrunn-Prickler Halt, Saualpe, south-eastern Austria): Constraints from correlations of the Sm-Nd, Lu-Hf, U-Pb and Rb-Sr isotopic systems, *Journal of Metamorphic Geology*, 26(5), pp. 561–581. doi: 10.1111/j.1525-1314.2008.00778.x.

Tindle, A. G. and Breaks, F. W. (2000) Columbite-tantalite mineral chemistry from rare-element granitic pegmatites: Separation Lake area, N. W. Ontario, Canada, *Mineralogy and Petrology*, 70, pp. 165–198.

Tomascak, P. B., Krogstad, E. J. and Walker, R. J. (1998) Sm-Nd isotope systematics and the derivation of granitic pegmatites in southwestern Maine, *Canadian Mineralogist*, 36(2), pp. 327–337. Available at: <http://canmin.geoscienceworld.org/content/36/2/327.short> (Accessed: 25 March 2015).

Wasserburg, G. J., Jacousen, S. B., DePaolo, D. J., McCulloch, M. T. and Wen, T. (1981) Precise determination of ratios, Sm and Nd isotopic abundances in standard solutions, *Geochimica et Cosmochimica Acta*, 45(Table 1), pp. 2311–2323. doi: 10.1016/0016-7037(81)90085-5.

Waters, D. J. (1986) Metamorphic zonation and thermal history of pelitic gneisses from western Namaqualand, South Africa, *South African Journal of Geology*, 89(2), pp. 97–102.

Waters, D. J. (1989) Metamorphic evidence for the heating and cooling path of Namaqualand granulites, *Evolution of metamorphic belts*, 43(43), pp. 357–363. doi: 10.1144/GSL.SP.1989.043.01.31.

Watkins, J. M., Clemens, J. D. and Treloar, P. J. (2007) Archaean TTGs as sources of younger granitic magmas: Melting of sodic meta-tonalites at 0.6–1.2 GPa, *Contributions to Mineralogy and Petrology*, 154(1), pp. 91–110. doi: 10.1007/s00410-007-0181-0.

White, R. W., Powell, R. and Holland, T. J. B. (2001) Calculation of partial melting equilibria in the system Na<sub>2</sub>O-CaO-K<sub>2</sub>O-FeO-MgO-Al<sub>2</sub>O<sub>3</sub>-SiO<sub>2</sub>-H<sub>2</sub>O (NCKFMASH), *Journal of Metamorphic Geology*, 19(2), pp. 139–153. doi: 10.1046/j.0263-4929.2000.00303.x.

Williams, I. S., Buick, I. S. and Cartwright, I. (2004) An extended episode of early Mesoproterozoic metamorphic fluid flow in the Reynolds Range, central Australia\*, *Journal of Metamorphic Geology*. Wiley/Blackwell (10.1111), 14(1), pp. 29–47. doi: 10.1111/j.1525-1314.1996.00029.x.

Yang, Y., Sun, J., Xie, L., Fan, H. and Wu, F. (2008) In situ Nd isotopic measurement of natural geological materials by LA-MC-ICPMS, *Science Bulletin*. SP Science in China Press, 53(7), pp. 1062–1070. doi: 10.1007/s11434-008-0166-z.

Yuhara, M., Kagami, H. and Tsuchiya, N. (2001) Rb-Sr and Sm-Nd systematics of granitic and metamorphic rocks in the Namaqualand Metamorphic Complex, South Africa: Implications for evolution of marginal part of Kaapvaal Craton, *National Institute of Polar Research, Special Issue, Memoirs*, 55, pp. 127–144.

Zhu, X. K. and O’Nions, R. K. (1999a) Monazite chemical composition: Some implications for monazite geochronology, *Contributions to Mineralogy and Petrology*, 137(4), pp. 351–363. doi: 10.1007/s004100050555.

Zhu, X. K. and O’Nions, R. K. (1999b) Zonation of monazite in metamorphic rocks and its implications for high-temperature thermochronology: A case study from the Lewisian terrain, *Earth and Planetary Science Letters*, 171(2), pp. 209–220. doi: 10.1016/S0012-821X(99)00146-6.

## Appendix

### Appendix A: Monazite Geochemistry.

Monazite geochemical data were collected in three runs at two institutions. Two runs were undertaken at the Central Analytical Facility (CAF) ICP-MS facilities using Resonetics Resolution S155 Excimer (193nm) laser with an S155 Laurin Technic dual-volume sample cell coupled to an Argilent 880 triple quadrupole ICP-MS. One run was undertaken at the Research School of Earth Sciences (RSES) at the Australian National University (ANU) using an Excimer (193nm) laser with a Helix dual-volume sample cell coupled to an Argilent 7700 quadrupole ICP-MS. For the list of the respective samples analysed during the various runs, please refer to table A.1.

*Table A-1: Summary table of monazite geochemistry analytical runs at the indicated ICP-MS facilities.*

<b>Run 1: Argilent 8800 triple Q-LA-ICP-MS</b>	<b>Run 2: Argilent 7700 Q-LA-ICP-MS</b>	<b>Run 3: Argilent 8800 triple Q-LA-ICP-MS</b>
<i>Central Analytical Facility; University of Stellenbosch</i>	<i>Research School of Earth Sciences; Australia National University</i>	<i>Central Analytical Facility; University of Stellenbosch</i>
RPGV14	SD2015-10	SDORPB15-4b
RPGV16	SD2015-11	SDORPB15-7d
HS15HF1	SD2015-13	SDORPB16-4
	SDORPB15-9	SDORPB16-5
	SDORPB15-10	SDORPB16-6
	SDORPB15-15c	SDORPB16-7b
	SDORPB15-17	SDORPB16-8
	SDORPB15-18	SDORPB16-9
	SDORPB15-20	SDORPB16-12

## A.1: Vioolsdrif Domain

## A.1.1: SD2015-10

Sample	SD2015-10															
Element	Type 1	Type 1	Type 1	Type 1	Type 2	Type 2	Type 2	Type 2	Type 3	Type 3	Type 3	Type 3	Type 3	Type 3	Type 3	Type 3
	016dog10b9	017dog10b10	023dog10b11	024dog10b12	025dog10b13	008dog10b1	009dog10b2	010dog10b3	011dog10b4	012dog10b5	013dog10b6*	014dog10b7	015dog10b8*	026dog10b14	027dog10b15	
Si	2 188	1 834	2 170	2 324	2 187	558	3 004	3 584	3 877	5 340	2 750	3 030	4 581	5 054	5 414	
P	101 058	102 479	98 398	106 614	107 565	120 842	110 308	112 945	118 022	132 005	107 361	99 920	113 969	127 474	123 096	
Ca	1 849	1 096	1 406	1 015	1 181	7 560	4 449	4 876	2 907	2 747	2 515	3 019	3 426	2 729	3 738	
Sr	2.2	0.32	0.52	0.17	2.4	9.5	6.2	19	5.0	31	21	2.2	21	12	9.1	
Y	14 822	11 776	10 854	10 384	11 547	143	509	1 182	2 376	10 851	5 344	6 511	10 160	5 949	6 049	
Pb*	2 247	1 951	2 193	2 078	2 037	7 539	5 486	5 758	5 408	7 762	3 289	4 280	5 047	6 636	7 127	
Th	21 976	20 605	24 212	21 476	20 897	65 056	48 717	48 690	44 278	50 280	34 162	44 830	47 733	56 383	62 026	
U	995	704	673	596	603	3 392	2 358	2 606	2 078	4 868	991	1 626	1 716	2 593	3 041	
La	99 103	90 374	95 464	95 033	95 165	76 311	78 792	80 450	84 713	79 533	83 679	95 355	94 223	78 821	78 483	
Ce	230 387	230 387	230 387	230 387	230 387	230 387	230 387	230 387	230 387	230 387	230 387	230 387	230 387	230 387	230 387	
Pr	28 788	30 405	28 863	29 564	29 634	34 349	33 035	31 987	30 609	32 813	32 297	29 486	29 219	32 695	33 280	
Nd	115 019	126 504	114 949	119 522	118 842	146 561	137 649	133 963	124 162	137 331	137 564	120 788	115 865	139 518	142 277	
Sm	32 591	46 088	33 968	35 991	34 882	68 566	56 698	51 871	40 994	65 503	58 271	37 608	36 381	63 566	68 473	
Eu	19	16	13	14	13	53	31	32	29	27	31	29	24	24	26	
Gd	16 809	22 806	17 334	18 307	17 782	12 552	13 250	15 295	14 656	32 862	23 426	17 634	18 560	27 939	29 413	
Tb	1 374	1 587	1 256	1 290	1 316	246	425	633	737	2 121	1 285	1 120	1 282	1 573	1 654	
Dy	3 132	2 926	2 505	2 447	2 651	81	246	480	799	3 036	1 670	1 727	2 401	1 904	1 961	
Ho	186	125	121	113	132	2.4	3.9	7.5	17	91	47	67	112	49	49	
Er	194	89	96	82	109	9.2	9.1	11	14	55	31	55	96	30	27	
Tm	15	4.9	5.2	4.4	6.2	0.50	0.50	0.59	0.65	3.0	1.4	2.8	5.9	1.4	1.2	
Yb	58	17	19	13	21	2.0	2.2	3.4	3.3	13	7.2	11	20	6.6	6.7	
Lu	4.7	1.3	1.4	1.1	1.6	0.15	0.25	0.36	0.28	1.0	0.63	0.62	1.5	0.7	0.7	
Th/U	22	29	36	36	35	19	21	19	21	10	34	28	28	22	20	
ΣLREE	505 888	523 758	503 632	510 498	508 910	556 174	536 561	528 658	510 866	545 568	542 199	513 624	506 076	544 987	552 900	
ΣHREE	21 773	27 557	21 337	22 258	22 019	12 893	13 937	16 430	16 228	38 182	26 469	20 618	22 480	31 502	33 112	
ΣREE + Y	542 501	563 108	535 837	543 153	542 489	569 262	551 037	546 302	529 499	594 628	574 044	540 782	538 740	582 463	592 088	

concentrations in ppm

\* = excluded U-Pb isotopic calculation

**A.1.2: SD2015-11**

Sample	SD2015-11														
Element	008d111*	009d112*	010d113*	011d114	012d115	013d116	014d117*	015d118	016d119*	017d1110	023d1111	024d1112	025d1113	026d1114	027d1115
Si	6 853	5 266	8 142	5 594	4 973	6 393	3 738	17 796	4 487	4 642	5 898	6 340	3 178	3 031	9 438
P	104 066	108 324	101 224	107 040	105 474	104 547	97 225	101 108	97 090	97 303	103 333	102 409	104 939	102 690	96 809
Ca	8 829	6 571	2 981	8 155	6 160	5 339	7 644	7 963	6 415	8 291	4 801	5 284	6 263	5 724	3 626
Sr	84	49	37	107	12	15	39	63	191	47	14	77	35	58	412
Y	15 382	15 027	14 034	15 593	13 844	13 580	13 335	14 224	13 063	13 042	13 359	13 029	14 878	14 441	13 920
Pb*	5 823	6 671	6 821	7 478	6 137	7 243	5 851	5 119	5 414	5 395	6 682	6 639	4 219	3 826	7 431
Th	57 716	65 478	65 379	76 691	61 882	72 876	57 789	43 620	54 737	57 897	67 284	68 705	43 200	38 712	76 004
U	968	1 155	1 180	1 069	936	1 137	835	736	901	738	1 057	930	852	771	1 319
La	117 090	111 429	114 546	114 179	117 318	118 130	110 410	121 201	118 205	123 490	116 649	116 251	115 926	115 054	112 078
Ce	230 387	230 387	230 387	230 387	230 387	230 387	230 387	230 387	230 387	230 387	230 387	230 387	230 387	230 387	230 387
Pr	24 819	25 705	25 224	24 924	24 803	24 492	24 915	24 567	24 375	23 646	24 310	24 172	24 278	24 323	24 357
Nd	96 740	101 611	95 608	93 811	92 323	90 597	88 409	91 030	90 362	86 433	91 395	91 091	93 197	92 063	91 972
Sm	26 975	29 016	22 271	23 159	22 066	21 299	17 137	22 363	23 067	19 586	21 200	21 459	24 835	24 434	21 391
Eu	1 283	1 326	506	1 184	1 089	990	1 003	1 199	1 145	1 029	909	1 071	1 199	1 249	418
Gd	21 575	22 656	15 547	18 200	16 986	16 229	11 019	17 520	17 280	15 013	15 777	16 105	19 303	18 427	14 781
Tb	2 302	2 384	1 570	2 084	1 898	1 768	1 318	1 986	1 854	1 707	1 690	1 764	2 101	1 948	1 524
Dy	7 446	7 639	5 615	7 244	6 475	6 192	5 277	6 550	6 021	5 862	5 857	6 029	7 016	6 463	5 466
Ho	699	711	658	711	631	636	631	636	612	586	628	605	697	659	632
Er	901	883	1 047	920	828	890	1 028	846	861	767	916	815	927	910	1 017
Tm	65	64	89	69	60	69	90	62	71	55	74	60	71	72	89
Yb	245	230	333	248	220	260	364	234	305	206	274	215	260	282	343
Lu	21	19	26	21	18	21	30	19	34	17	22	17	22	24	26
Th/U	60	57	55	72	66	64	69	59	61	78	64	74	51	50	58
ΣLREE	496 011	498 148	488 036	486 460	486 897	484 906	471 258	489 548	486 396	483 542	483 941	483 361	488 622	486 261	480 184
ΣHREE	33 253	34 586	24 885	29 497	27 116	26 065	19 757	27 852	27 038	24 213	25 239	25 610	30 396	28 786	23 878
ΣREE + Y	545 930	549 087	527 462	532 733	528 946	525 541	505 352	532 822	527 642	521 825	523 448	523 071	535 095	530 738	518 400

concentrations in ppm

\* = excluded U-Pb isotopic calculation

**A.1.3: SDORPB15-4B**

Sample	SDORPB15-4B												
Element	Eu; Poly Rim SD15-4B-1	Eu; Poly Rim SD15-4B-11	Eu; Poly Rim SD15-4B-12	Eu; Poly Rim SD15-4B-17	Eu; Poly Core SD15-4B-2	Eu; Poly Core SD15-4B-3	Eu; Poly Core SD15-4B-13	Eu; Poly Core SD15-4B-14	Eu; Poly Core SD15-4B-21	Eu; Poly Core SD15-4B-22	An; Alt Rim SD15-4B-4*	An; Alt Rim SD15-4B-5#	An; Alt Rim SD15-4B-6
Si	8 391	4 919	2 961	3 016	2 388	2 350	3 578	2 501	3 546	1 608	4 597	6 131	8 488
P	113 962	106 413	91 951	98 590	103 599	105 131	102 990	101 920	104 013	101 920	110 945	100 034	111 366
Ca	6 573	6 133	5 181	6 464	5 818	6 379	4 940	4 112	6 404	7 258	14 303	6 073	17 710
Sr	91	100	94	100	74	81	93	97	95	105	189	65	155
Y	11 984	7 965	6 109	6 825	8 977	9 360	6 502	5 129	11 066	10 291	1 777	8 257	8 594
Pb*	5 285	5 415	3 549	3 968	3 257	3 707	3 426	2 601	4 137	3 422	9 805	5 789	7 152
Th	37 069	37 982	25 793	30 463	25 099	29 053	25 621	19 339	32 477	26 163	90 008	27 614	68 682
U	1 481	1 666	1 173	1 374	858	937	1 120	680	1 186	1 040	2 602	415	1 780
La	127 898	119 989	111 777	124 634	138 109	139 174	127 821	133 259	132 961	132 629	157 680	128 289	134 803
Ce	230 469	230 469	230 469	230 469	230 469	230 469	230 469	230 469	230 469	230 469	230 469	230 469	230 469
Pr	24 091	24 640	21 868	24 505	22 472	22 845	23 794	23 025	23 860	23 173	19 534	24 454	23 475
Nd	86 437	92 068	80 158	87 448	79 468	82 551	83 998	79 772	86 583	83 814	58 419	89 351	84 726
Sm	13 960	12 875	10 755	12 146	12 075	12 533	11 051	9 615	12 831	12 326	6 346	12 346	12 695
Eu	1 470	1 093	929	1 012	1 016	1 045	981	845	1 305	1 330	708	496	1 219
Gd	8 673	6 301	5 159	5 725	7 111	7 340	5 133	4 332	8 375	7 976	2 726	7 174	7 137
Tb	941	569	459	516	715	745	464	366	887	839	230	682	685
Dy	3 782	2 240	1 769	1 927	2 854	2 948	1 798	1 428	3 497	3 337	684	2 729	2 678
Ho	510	335	262	289	384	403	278	212	488	453	68	384	378
Er	953	744	581	633	699	728	612	460	868	829	95	654	754
Tm	94	93	72	78	67	70	76	55	85	81	6.2	56	86
Yb	436	512	391	450	299	325	401	294	395	380	22	220	420
Lu	41	56	43	50	29	31	44	32	39	39	1.7	20	42
Th/U	25	23	22	22	29	31	23	28	27	25	35	67	39
ΣLREE	482 854	480 041	455 026	479 201	482 593	487 573	477 133	476 139	486 704	482 410	472 447	484 908	486 168
ΣHREE	15 430	10 851	8 735	9 668	12 158	12 591	8 806	7 178	14 633	13 933	3 834	11 921	12 179
ΣREE + Y	511 738	499 950	470 800	496 706	504 745	510 568	493 422	489 291	513 709	507 964	478 766	505 582	508 159

concentrations in ppm

An = anhedral

Eu = euhedral

eb = embayed

Alt = altered

Poly = polygonal zoning

homo = homogenous

# = excluded U-Pb isotopic calculation

## (SDORPB15-4b continued)

Sample	An; Alt Rim	An; Alt Rim	An; Alt Rim	An; Alt Rim	An; Alt Rim	An; Alt Rim	An; Alt Rim	An; Alt Rim	An; eb	An; eb	An; eb	An; eb	An; eb
Element	SD15-4B-7	SD15-4B-8#	SD15-4B-9	SD15-4B-10	SD15-4B-19#	SD15-4B-20#	SD15-4B-23	SD15-4B-15	SD15-4B-16#	SD15-4B-18	SD15-4B-24	SD15-4B-25	SD15-4B-25
Si	3 641	5 350	3 429	5 064	7 012	3 145	4 986	6 942	2 566	4 888	5 126	3 434	
P	108 856	107 775	109 356	100 000	113 811	99 036	110 087	108 135	93 954	99 178	109 898	125 086	
Ca	4 972	4 270	13 200	3 219	7 993	1 654	11 379	2 413	2 499	1 960	10 436	22 780	
Sr	78	68	122	54	94	16	122	33	34	33	145	181	
Y	8 369	8 243	2 221	4 116	13 519	4 362	1 715	6 181	4 231	6 785	15 391	3 519	
Pb*	4 191	4 430	9 332	2 643	7 366	2 196	8 689	5 302	3 521	3 770	4 379	15 436	
Th	29 402	31 793	80 956	20 827	62 064	14 231	79 038	39 730	27 636	28 510	35 353	122 878	
U	1 199	1 225	2 511	432	1 662	933	1 874	1 141	1 143	1 099	1 100	4 222	
La	126 170	123 188	160 352	126 977	125 922	122 421	155 137	125 821	128 698	122 995	133 550	153 231	
Ce	230 469	230 469	230 469	230 469	230 469	230 469	230 469	230 469	230 469	230 469	230 469	230 469	
Pr	24 173	24 258	19 580	23 946	24 121	25 104	20 061	24 396	24 211	24 242	24 103	20 402	
Nd	88 120	89 115	57 627	86 090	88 828	97 095	60 697	90 066	87 008	86 911	89 914	64 476	
Sm	12 569	12 907	6 302	11 531	14 242	12 745	6 757	13 473	11 751	12 393	13 668	7 692	
Eu	1 255	1 242	743	1 052	960	169	680	865	832	807	2 639	899	
Gd	6 695	6 683	2 907	5 423	8 467	7 108	2 928	7 309	5 526	6 830	9 824	3 888	
Tb	653	652	250	445	885	577	248	640	464	635	1 093	357	
Dy	2 652	2 599	840	1 579	3 781	1 973	724	2 308	1 624	2 398	4 770	1 253	
Ho	384	380	92	207	578	232	71	307	210	320	687	152	
Er	716	724	142	362	1 200	352	93	513	377	590	1 191	242	
Tm	69	66	12	35	138	24	5.3	43	40	55	106	19	
Yb	276	274	48	166	711	78	17	170	202	232	455	77	
Lu	25	26	4.5	17	73	6.7	0.98	17	20	23	45	7.0	
Th/U	25	26	32	48	37	15	42	35	24	26	32	29	
ΣLREE	481 502	479 937	474 330	479 012	483 582	487 833	473 121	484 224	482 136	477 010	491 703	476 270	
ΣHREE	11 470	11 404	4 296	8 235	15 833	10 351	4 086	11 306	8 463	11 083	18 170	5 996	
ΣREE + Y	502 596	500 825	481 590	492 416	513 894	502 716	479 601	502 576	495 662	495 685	527 903	486 684	

concentrations in ppm

An = anhedral

Eu = euhedral

eb = embayed

Alt = altered

Poly = polygonal zoning

homo = homogenous

# = excluded U-Pb isotopic calculation



**A.1.4: SDORPB15-07D**

Sample	SDORPB15-7D																								
																			1090 Ma	1090 Ma	1090 Ma	1200 Ma	1200 Ma	1200 Ma	1200 Ma
Element	SD15-7D-1	SD15-7D-2	SD15-7D-3	SD15-7D-4	SD15-7D-5	SD15-7D-6	SD15-7D-10	SD15-7D-11	SD15-7D-12	SD15-7D-14	SD15-7D-15	SD15-7D-17	SD15-7D-7	SD15-7D-9	SD15-7D-19	SD15-7D-8	SD15-7D-13	SD15-7D-16	SD15-7D-18						
Si	3 770	4 936	4 864	5 252	2 349	3 814	2 651	2 849	2 013	5 986	6 469	6 860	7 922	4 188	8 551	6 318	9 049	9 301	14 022						
P	149 482	143 155	122 989	118 059	109 019	148 983	143 769	159 507	146 603	117 483	114 175	112 238	151 479	155 539	136 042	148 835	161 885	118 171	125 918						
Ca	32 482	29 599	19 335	17 145	16 438	36 915	27 257	30 932	24 933	16 768	16 350	15 118	42 810	33 549	28 428	33 628	30 627	21 349	33 429						
Sr	117	80	126	94	142	101	90	244	74	125	149	209	600	183	157	208	1 094	395	517						
Y	22 686	21 781	9 529	9 461	7 903	17 165	24 259	23 460	22 747	9 821	9 388	8 933	17 765	20 782	16 065	21 504	21 205	8 618	20 518						
Pb*	23 631	22 535	15 552	15 157	11 867	27 284	23 282	24 112	20 963	14 191	13 940	13 934	26 221	23 892	20 651	22 331	16 398	13 791	20 405						
Th	177 332	178 189	126 570	130 982	94 957	201 418	153 008	145 735	129 673	130 996	130 561	130 971	222 143	178 297	180 797	174 032	133 365	145 251	209 052						
U	9 401	8 634	4 725	4 678	3 763	12 735	13 631	12 548	11 443	3 746	3 501	3 636	11 748	8 415	5 043	8 403	10 343	3 211	6 243						
La	113 735	114 319	122 838	124 237	119 177	112 869	111 110	109 621	108 756	118 745	117 439	121 776	111 254	108 902	113 567	106 340	110 876	120 716	107 816						
Ce	230 469	230 469	230 469	230 469	230 469	230 469	230 469	230 469	230 469	230 469	230 469	230 469	230 469	230 469	230 469	230 469	230 469	230 469	230 469						
Pr	26 061	26 335	23 537	23 775	20 848	26 024	27 365	27 378	27 290	24 437	24 402	24 235	26 437	26 458	25 529	25 268	27 635	24 479	25 013						
Nd	95 321	96 742	80 325	83 076	70 356	100 088	108 078	108 161	106 722	89 079	86 590	86 605	100 239	101 199	92 846	95 339	108 091	89 688	91 259						
Sm	28 547	28 562	15 258	15 220	13 273	28 092	33 384	32 258	32 701	16 462	16 280	15 833	28 196	29 604	22 004	27 166	30 200	16 517	23 225						
Eu	735	693	709	726	618	1 102	1 062	1 088	1 046	728	688	676	1 102	744	767	684	1 001	716	899						
Gd	18 727	18 558	8 798	8 733	7 231	18 573	23 688	21 674	22 038	10 594	10 323	9 888	18 073	19 346	15 516	17 815	19 987	10 440	16 693						
Tb	2 494	2 414	977	974	798	2 240	2 761	2 702	2 640	1 209	1 146	1 094	2 182	2 477	1 899	2 333	2 324	1 126	2 079						
Dy	8 465	8 096	3 359	3 411	2 765	6 865	9 610	9 032	8 896	3 731	3 598	3 471	6 792	8 046	6 048	8 048	7 609	3 567	7 143						
Ho	710	698	340	339	274	572	823	801	769	318	314	303	576	652	470	730	735	296	635						
Er	893	887	487	484	410	642	1 031	1 024	960	375	360	351	732	801	486	992	1 094	332	927						
Tm	73	73	43	41	36	42	71	79	72	27	25	24	61	60	31	83	88	22	78						
Yb	259	267	163	172	142	134	249	273	251	81	75	79	272	225	97	344	415	82	382						
Lu	17	16	12	11	10	10	17	20	17	5.2	4.7	4.0	30	16	4.9	30	35	4.5	49						
Th/U	19	21	27	28	25	16	11	12	11	35	37	36	19	21	36	21	13	45	33						
ΣLREE	494 133	496 425	472 427	476 777	454 124	497 542	510 406	507 887	505 938	479 192	475 179	478 917	496 593	496 632	484 415	484 582	507 270	481 867	477 782						
ΣHREE	31 637	31 009	14 180	14 165	11 665	29 078	38 251	35 603	35 644	16 339	15 846	15 214	28 718	31 624	24 552	30 374	32 286	15 869	27 986						
ΣREE + Y	549 191	549 908	496 845	501 129	474 309	544 886	573 978	568 038	565 374	506 079	501 101	503 740	544 178	549 782	525 799	537 144	561 762	507 071	527 184						

concentrations in ppm

xxx Ma = age of inheritance for analysis

**A.1.5: SDORPB15-9**

Sample	SDORPB15-9														
Element	Low Th/U 028dog91	Low Th/U 029dog92	Low Th/U 030dog93	Low Th/U 032dog95	Low Th/U 040dog98	Low Th/U 041dog99	Low Th/U 042dog910	High Th/U 031dog94	High Th/U 038dog96	High Th/U 039dog97	High Th/U 043dog911	High Th/U 044dog912	High Th/U 046dog914	High Th/U 045dog913*	High Th/U 047dog915#
Si	2 120	2 359	3 472	2 734	3 391	2 507	2 607	12 990	10 555	16 573	7 102	5 315	12 471	12 033	12 780
P	157 715	155 589	155 688	156 806	163 949	146 334	159 641	174 151	143 983	148 578	130 219	120 559	141 966	142 130	162 342
Ca	11 242	12 102	13 267	10 014	14 133	12 375	11 645	4 612	7 800	10 000	5 005	5 702	3 557	9 794	5 770
Sr	24	26	86	54	31	29	27	5.6	25	61	13	11	5.6	270	7
Y	26 964	26 339	27 337	21 102	31 420	27 107	28 179	6 453	8 154	10 350	8 075	9 245	5 491	5 880	7 072
Pb*	10 149	10 532	10 326	7 732	12 799	10 179	10 606	13 180	11 555	13 038	7 865	6 631	11 612	9 983	12 730
Th	74 936	80 255	86 561	57 038	100 183	84 606	78 602	125 634	129 511	151 571	87 286	81 008	125 626	121 936	122 304
U	5 778	6 042	5 775	4 609	6 649	5 446	6 042	2 007	1 840	2 596	1 461	1 447	1 894	1 385	2 116
La	86 937	87 672	88 904	86 297	88 588	92 825	87 596	80 602	87 708	89 161	86 782	86 826	81 494	86 562	84 066
Ce	230 469	230 469	230 469	230 469	230 469	230 469	230 469	230 469	230 469	230 469	230 469	230 469	230 469	230 469	230 469
Pr	33 812	34 054	34 048	34 726	33 434	32 810	34 196	35 351	34 673	34 670	35 059	34 085	36 242	37 307	35 194
Nd	146 532	144 413	143 956	149 752	143 049	136 518	144 942	159 205	152 609	153 038	149 078	145 483	162 005	169 018	156 871
Sm	122 133	123 247	120 830	134 370	123 854	113 791	121 658	141 426	131 216	124 957	112 045	105 873	132 907	136 444	117 976
Eu	429	414	428	381	466	402	443	62	133	225	164	181	57	78	74
Gd	68 378	69 233	68 672	76 085	74 126	64 262	68 642	70 666	66 289	62 700	48 972	46 485	61 296	62 103	56 440
Tb	3 904	3 884	3 943	3 754	4 363	3 816	3 944	2 971	2 982	3 038	2 085	2 127	2 540	2 481	2 435
Dy	5 444	5 336	5 593	4 653	6 266	5 351	5 618	2 576	2 983	3 370	2 157	2 268	2 326	2 316	2 473
Ho	247	245	259	222	284	251	261	60	85	105	72	76	62	68	72
Er	264	261	281	250	296	260	279	47	74	88	60	64	50	71	59
Tm	21	20	23	18	23	20	22	4.3	5.1	6.5	3.7	4.5	3.9	6.0	4.0
Yb	84	86	100	77	98	87	93	20	26	36	18	19	21	34	19
Lu	7.1	6.9	9.3	6.7	7.5	6.6	7.2	2.2	2.7	4.3	1.5	1.9	2.0	4.1	1.3
Th/U	13	13	15	12	15	16	13	63	70	58	60	56	66	88	58
ΣLREE	619 882	619 854	618 206	635 614	619 393	606 413	618 860	647 052	636 674	632 296	613 433	602 737	643 117	659 799	624 575
ΣHREE	78 349	79 071	78 879	85 065	85 463	74 055	78 867	76 348	72 447	69 347	53 368	51 046	66 299	67 084	61 503
ΣREE + Y	725 624	725 678	724 851	742 161	736 742	707 976	726 348	729 915	717 409	712 217	675 041	663 209	714 965	732 841	693 225

concentrations in ppm

\* = excluded U-Pb isotopic calculation

**A.1.6: SDORPB16-4**

Sample	SDORPB16-4												
	R; An; Zone	R; An; Zone	R; An; Zone	R; An; Zone	R; An; Zone	R; An; Zone	R; An; Zone	R; An; Zone	R; An; Zone	R; An; Zone	R; An; Zone	R; An; Zone	Aliquot
Element	SD16-4-1	SD16-4-2	SD16-4-5	SD16-4-6	SD16-4-7	SD16-4-17	SD16-4-18	SD16-4-22	SD16-4-23	SD16-4-24	SD16-4-25	SD16-4-3	
Si	25 678	23 456	9 972	12 753	21 666	2 991	6 361	3 702	5 318	8 066	16 783	27 221	
P	125 759	121 390	123 423	124 183	116 807	116 774	116 198	119 160	120 474	137 591	128 894	125 012	
Ca	9 568	7 515	11 169	9 072	7 552	6 398	6 827	8 851	9 556	12 433	12 496	12 134	
Sr	35	23	32	26	25	15	29	31	27	35	35	39	
Y	12 534	17 558	16 193	18 606	17 827	14 259	17 806	18 034	17 408	19 436	21 653	18 928	
Pb*	8 240	8 040	8 276	7 934	6 808	6 081	7 301	7 892	7 820	11 517	11 009	9 083	
Th	65 898	72 278	79 296	59 180	51 568	45 492	65 277	59 153	59 132	100 323	101 408	82 636	
U	2 512	1 675	1 449	2 254	2 155	1 871	1 452	2 390	2 330	2 308	2 375	2 062	
La	102 539	106 400	110 960	103 558	108 219	101 304	103 682	105 453	108 006	101 192	98 646	111 421	
Ce	230 469	230 469	230 469	230 469	230 469	230 469	230 469	230 469	230 469	230 469	230 469	230 469	
Pr	29 162	27 622	26 916	28 692	28 111	28 875	28 663	27 721	27 702	29 049	29 347	26 988	
Nd	116 741	110 600	104 118	115 263	110 830	115 946	113 629	109 853	109 481	118 412	121 883	105 203	
Sm	44 145	31 783	31 520	38 573	36 340	36 493	34 914	35 859	35 798	43 965	44 664	33 356	
Eu	263	255	395	391	367	274	274	321	308	268	279	466	
Gd	23 765	16 642	17 426	22 372	20 637	18 027	18 502	20 534	20 072	23 855	25 573	20 133	
Tb	1 933	1 582	1 592	2 051	1 938	1 574	1 728	1 956	1 899	2 179	2 265	1 964	
Dy	3 589	4 080	3 461	4 774	4 515	3 532	4 024	4 510	4 344	4 848	5 247	4 528	
Ho	177	316	209	292	285	243	278	272	263	298	324	298	
Er	163	430	218	308	311	363	352	274	266	305	339	339	
Tm	10	42	17	24	24	26	33	23	20	23	27	27	
Yb	38	181	69	91	98	120	166	83	80	95	106	106	
Lu	2.4	15	4.7	6.4	7.5	10	14	6.0	5.7	6.7	8.3	8.6	
Th/U	26	43	55	26	24	24	45	25	25	43	43	40	
ΣLREE	523 055	506 873	503 983	516 554	513 969	513 086	511 357	509 354	511 455	523 087	525 008	507 437	
ΣHREE	29 678	23 289	22 997	29 917	27 817	23 896	25 096	27 659	26 950	31 610	33 889	27 404	
ΣREE + Y	565 530	547 975	543 567	565 469	559 980	551 515	554 532	555 368	556 121	574 402	580 829	554 235	

concentrations in ppm

R = rounded monazite

Zone = zoned monazite

An = anhedral

(SDORPB16-4 continued)

Sample	SDORPB16-4												
Element	Aliquot SD16-4-4	Aliquot SD16-4-8#	Aliquot SD16-4-9	Aliquot SD16-4-10	Aliquot SD16-4-11	Aliquot SD16-4-12	Aliquot SD16-4-13	Aliquot SD16-4-14	Aliquot SD16-4-15	Aliquot SD16-4-16#	Aliquot SD16-4-19#	Aliquot SD16-4-20#	Aliquot SD16-4-21
Si	7 618	22 304	11 893	34 888	19 176	12 643	9 274	25 996	5 751	11 614	6 777	6 720	4 541
P	114 487	127 883	121 847	133 720	134 507	120 308	127 305	125 886	125 215	116 701	107 542	114 539	117 515
Ca	8 570	10 032	9 589	11 528	12 906	11 530	13 511	6 613	10 841	11 194	5 712	10 153	11 073
Sr	18	27	35	25	29	34	36	17	38	37	65	29	30
Y	17 630	16 808	18 480	20 275	22 654	16 731	15 422	21 267	14 754	14 583	12 577	16 490	15 985
Pb*	7 708	8 562	8 469	11 396	11 581	8 804	9 212	7 484	8 217	7 785	5 402	7 975	8 297
Th	57 780	67 421	69 490	99 296	104 852	85 045	83 084	57 796	75 265	76 810	42 991	81 011	84 019
U	2 747	2 320	2 728	2 466	2 612	1 875	1 823	1 748	1 436	1 378	1 103	1 512	1 643
La	100 631	104 940	107 414	98 505	98 297	113 821	113 209	96 712	111 997	113 257	115 375	110 256	111 409
Ce	230 469	230 469	230 469	230 469	230 469	230 469	230 469	230 469	230 469	230 469	230 469	230 469	230 469
Pr	28 623	28 246	28 835	29 437	29 814	26 260	25 746	30 622	26 195	26 578	23 960	27 101	27 066
Nd	112 542	112 566	114 652	120 280	123 212	98 471	95 288	127 408	99 716	101 050	89 578	102 355	103 230
Sm	38 380	38 505	39 164	45 250	47 147	30 683	30 241	48 704	29 646	29 852	21 718	31 524	33 949
Eu	293	392	367	284	306	426	420	238	388	385	352	402	408
Gd	18 396	22 571	22 845	25 358	27 177	17 764	16 699	26 575	16 286	16 376	12 429	17 349	18 562
Tb	1 756	2 081	2 040	2 256	2 389	1 686	1 608	2 146	1 517	1 480	1 224	1 612	1 714
Dy	4 253	4 397	4 762	5 042	5 601	3 739	3 450	4 763	3 251	3 237	3 051	3 508	3 495
Ho	305	252	275	297	334	235	212	286	195	190	225	214	195
Er	415	242	265	313	348	239	214	312	197	200	270	225	188
Tm	42	17	18	25	27	18	16	27	14	14	23	17	13
Yb	214	65	69	92	104	71	62	110	54	57	98	70	51
Lu	18	4.6	4.4	6.9	6.9	5.1	4.3	8.9	4.1	4.0	7.7	4.7	4.2
Th/U	21	29	25	40	40	45	46	33	52	56	39	54	51
ΣLREE	510 644	514 725	520 533	523 941	528 939	499 703	494 953	533 914	498 022	501 206	481 100	501 705	506 122
ΣHREE	25 399	29 631	30 279	33 389	35 987	23 756	22 265	34 227	21 519	21 558	17 328	23 000	24 221
ΣREE + Y	553 965	561 556	569 660	577 890	587 886	540 616	533 061	589 647	534 683	537 733	511 357	541 596	546 737

*concentrations in ppm**R = rounded monazite**Zone = zoned monazite**An = anhedral*

**A.1.7: SDORPB16-5**

Sample	SDORPB16-5										
Element	Type 1 SD16-5-4	Type 1 SD16-5-5	Type 1 SD16-5-6	Type 1 SD16-5-7	Type 1 SD16-5-8	Type 1 SD16-5-9	Type 1 SD16-5-10	Type 1 SD16-5-11	Type 2 SD16-5-1	Type 2 SD16-5-2	Type 2 SD16-5-3
Si	3 789	3 285	2 863	1 990	3 231	3 843	3 521	3 363	1 300	2 448	2 628
P	106 335	108 351	99 906	101 744	105 939	107 979	102 093	103 507	136 233	133 395	137 601
Ca	1 227	1 105	899	660	1 294	783	798	943	19 145	19 710	19 327
Sr	40	44	37	35	40	39	34	32	24	41	25
Y	363	847	239	159	218	420	164	129	28 091	22 601	28 282
Pb*	1 793	2 081	1 595	1 494	1 685	1 706	1 584	1 494	23 347	21 506	23 894
Th	16 062	18 629	14 686	13 565	14 874	15 028	14 472	13 225	94 291	107 668	93 913
U	246	280	238	221	242	237	230	222	18 246	14 922	19 149
La	100 060	97 382	100 054	101 947	101 456	99 841	101 810	101 135	101 082	97 116	101 099
Ce	230 469	230 469	230 469	230 469	230 469	230 469	230 469	230 469	230 469	230 469	230 469
Pr	28 073	27 839	27 624	28 233	27 822	27 859	28 001	27 758	27 982	27 613	27 594
Nd	95 723	95 653	95 005	93 818	94 654	94 389	95 329	93 842	111 787	111 584	109 835
Sm	51 957	59 012	48 878	46 692	48 034	51 474	46 722	43 115	25 450	26 014	25 309
Eu	329	337	307	279	312	320	284	249	206	172	233
Gd	15 302	19 630	13 840	12 551	13 519	15 373	12 776	11 844	20 402	21 309	20 761
Tb	591	821	519	454	498	597	467	429	2 524	2 543	2 553
Dy	286	493	230	197	219	306	199	186	9 667	8 952	9 662
Ho	4.2	10	3.2	2.7	3.0	5.1	3.1	2.4	1 119	840	1 109
Er	5.9	8.6	6.1	4.7	5.0	6.0	5.0	4.9	1 372	845	1 317
Tm	0.8	1.0	0.80	0.78	0.94	0.73	0.72	0.63	83	46	78
Yb	2.8	3.2	2.6	2.0	2.9	2.7	2.0	2.0	229	121	212
Lu	0.37	0.46	0.35	0.31	0.27	0.28	0.45	0.30	18	7.9	16
Th/U	65	66	62	61	61	63	63	60	5.2	7.2	4.9
ΣLREE	506 282	510 355	502 029	501 159	502 435	504 032	502 330	496 318	496 769	492 795	494 306
ΣHREE	16 194	20 968	14 603	13 212	14 248	16 291	13 453	12 470	35 414	34 663	35 708
ΣREE + Y	523 168	532 507	517 178	514 809	517 213	521 062	516 232	509 166	560 480	550 231	558 529

*concentrations in ppm*

**A.2: Pella Domain****A.2.1: RPGV14**

Sample RPGV14												
Element	V14_1	V14_2	V14_3	V14_4	V14_5	V14_6	V14_7	V14_8	V14_9	V14_10#	V14_11	V14_12
Si	-	-	-	-	-	-	-	-	-	-	-	-
P	-	-	-	-	-	-	-	-	-	-	-	-
Ca	-	-	-	-	-	-	-	-	-	-	-	-
Sr	-	-	-	-	-	-	-	-	-	-	-	-
Y	-	-	-	-	-	-	-	-	-	-	-	-
Pb*	15 009	6 660	10 148	11 606	7 514	12 466	12 502	16 480	11 211	23 278	10 225	7 039
Th	51 929	60 560	56 388	41 158	67 860	52 832	45 099	40 192	50 484	51 418	46 656	39 895
U	13 082	5 181	8 433	10 062	5 964	10 503	11 371	14 053	9 497	20 256	8 754	5 923
La	130 774	123 428	130 563	128 009	125 884	127 583	129 108	127 247	128 045	124 580	129 296	128 866
Ce	230 469	230 469	230 469	230 469	230 469	230 469	230 469	230 469	230 469	230 469	230 469	230 469
Pr	25 451	26 363	25 774	25 994	26 689	26 126	26 077	25 316	25 479	26 009	26 026	25 436
Nd	93 799	102 616	97 036	98 813	104 398	99 105	96 832	91 510	93 075	97 536	98 948	95 180
Sm	17 963	20 323	18 190	20 177	20 764	19 737	18 554	18 294	19 056	20 143	20 040	18 813
Eu	2 062	1 205	1 706	1 675	1 299	1 882	1 570	1 663	1 461	1 915	1 861	1 384
Gd	13 789	16 070	13 482	16 020	16 875	15 097	14 116	13 344	14 126	15 783	15 469	14 357
Tb	1 658	1 873	1 575	1 837	2 012	1 766	1 669	1 612	1 672	1 903	1 789	1 699
Dy	7 031	7 852	6 706	7 456	8 614	7 248	7 079	6 686	6 947	8 128	7 276	6 876
Ho	899	954	838	877	1 058	885	889	817	848	980	898	846
Er	1 629	1 621	1 568	1 467	1 831	1 539	1 569	1 444	1 488	1 785	1 630	1 446
Tm	143	138	153	125	152	133	135	124	133	163	163	119
Yb	604	532	700	490	611	554	544	516	530	716	747	483
Lu	51	43	66	40	50	46	45	45	45	62	66	39
Th/U	4.0	12	6.7	4.1	11	5.0	4.0	2.9	5.3	2.5	5.3	6.7
ΣLREE	498 455	503 197	502 031	503 461	508 205	503 020	501 040	492 836	496 124	498 737	504 780	498 763
ΣHREE	25 804	29 083	25 088	28 312	31 203	27 267	26 045	24 590	25 788	29 520	28 039	25 865
ΣREE + Y	526 321	533 485	528 826	533 448	540 707	532 170	528 656	519 090	523 373	530 172	534 679	526 011

concentrations in ppm

- (not analysed)

# = excluded U-Pb isotopic calculation

(RPGV14 continued)

Sample RPGV14													
Element	V14_13	V14_14	V14_15#	V14_16	V14_17	V14_18	V14_19	V14_20	V14_21	V14_22	V14_23	V14_24	V14_25
Si	-	-	-	-	-	-	-	-	-	-	-	-	-
P	-	-	-	-	-	-	-	-	-	-	-	-	-
Ca	-	-	-	-	-	-	-	-	-	-	-	-	-
Sr	-	-	-	-	-	-	-	-	-	-	-	-	-
Y	-	-	-	-	-	-	-	-	-	-	-	-	-
Pb*	16 039	10 317	3 044	12 911	14 218	9 961	13 505	10 061	6 225	13 016	5 797	16 580	7 356
Th	52 209	64 394	49 492	60 974	31 523	40 467	40 839	40 037	53 740	52 800	23 965	14 363	54 035
U	13 917	8 668	1 966	11 402	12 400	8 472	11 733	8 520	5 037	11 255	4 901	13 817	5 886
La	125 658	124 835	127 179	125 649	123 074	126 493	129 057	133 001	123 484	127 720	125 660	115 826	122 247
Ce	230 469	230 469	230 469	230 469	230 469	230 469	230 469	230 469	230 469	230 469	230 469	230 469	230 469
Pr	26 593	26 335	25 783	25 826	26 451	25 595	26 228	25 266	26 986	26 144	26 084	28 543	25 685
Nd	100 498	98 307	96 436	96 531	98 009	94 875	97 770	93 187	104 365	100 573	96 674	106 817	95 706
Sm	20 416	18 715	19 516	20 100	22 445	19 923	20 864	18 319	21 202	20 546	18 705	25 857	19 825
Eu	1 840	1 831	777	1 600	2 121	1 688	2 071	1 619	1 196	2 013	1 079	6 076	1 337
Gd	16 187	14 362	14 616	15 541	16 993	15 076	16 198	13 700	16 933	16 132	13 577	18 967	14 990
Tb	1 959	1 725	1 693	1 828	2 178	1 783	1 893	1 633	2 028	1 969	1 639	2 339	1 782
Dy	8 490	7 475	7 202	7 530	8 453	7 326	7 570	6 731	8 386	8 346	6 906	8 772	7 211
Ho	1 049	939	918	931	944	859	880	797	1 021	1 012	855	915	853
Er	1 878	1 680	1 687	1 637	1 550	1 460	1 516	1 343	1 793	1 918	1 486	1 544	1 480
Tm	165	148	150	146	138	125	132	118	154	189	124	143	126
Yb	663	617	616	606	562	513	531	471	573	883	477	625	503
Lu	57	51	53	51	47	43	48	41	48	79	38	56	45
Th/U	3.8	7.4	25	5.3	2.5	4.8	3.5	4.7	11	4.7	4.9	1.0	9.2
ΣLREE	503 635	498 661	499 382	498 574	500 447	497 354	504 388	500 241	506 506	505 451	497 593	507 511	493 932
ΣHREE	30 449	26 995	26 935	28 269	30 865	27 184	28 768	24 833	30 936	30 528	25 101	33 360	26 990
ΣREE + Y	535 924	527 487	527 093	528 443	533 433	526 226	535 227	526 693	538 637	537 993	523 773	546 948	522 258

concentrations in ppm

- (not analysed)

# = excluded U-Pb isotopic calculation

**A.2.2: RPGV16**

Sample	RPGV16													
	Eu; Zoned	Eu; Zoned	Eu; Zoned	Eu; Zoned	Eu; Zoned	Eu; Zoned	Eu; Zoned	Sub; alt. r	Sub; alt. r	Sub; alt. r	Sub; zoned	Sub; zoned	Sub; zoned	
Element	V16_1	V16_2	V16_20	Alt. rim V16_3	Alt. rim V16_11	Alt. rim V16_18	Alt. rim V16_19	V16_4	V16_5	V16_21	alt. r V16_6	V16_7	V16_8	inherited
Si	-	-	-	-	-	-	-	-	-	-	-	-	-	-
P	-	-	-	-	-	-	-	-	-	-	-	-	-	-
Ca	-	-	-	-	-	-	-	-	-	-	-	-	-	-
Sr	-	-	-	-	-	-	-	-	-	-	-	-	-	-
Y	-	-	-	-	-	-	-	-	-	-	-	-	-	-
Pb*	4 565	5 284	4 604	4 874	5 979	5 110	4 930	5 922	3 627	5 517	8 925	39 298	19 438	
Th	43 355	57 714	40 884	74 581	98 197	84 374	89 066	104 246	59 850	106 521	52 016	65 663	174 269	
U	3 520	4 002	3 699	3 288	4 039	3 455	3 271	3 900	2 661	3 502	7 303	33 742	15 350	
La	128 010	119 900	129 416	121 576	118 380	121 313	121 065	123 678	122 373	122 218	120 001	117 163	115 516	
Ce	230 469	230 469	230 469	230 469	230 469	230 469	230 469	230 469	230 469	230 469	230 469	230 469	230 469	230 469
Pr	25 063	26 140	24 751	25 559	26 063	25 914	25 769	25 715	25 624	26 005	26 068	25 861	27 425	
Nd	86 439	92 900	84 390	93 565	95 098	93 482	92 458	93 055	94 255	95 303	92 926	83 729	100 630	
Sm	19 522	22 135	19 004	19 335	22 708	19 842	19 457	20 848	19 049	20 391	23 866	29 158	46 043	
Eu	496	570	521	351	349	362	350	402	429	315	520	248	445	
Gd	13 969	16 310	13 505	14 145	16 767	14 679	13 972	15 098	13 531	15 012	18 968	18 138	39 399	
Tb	1 778	2 053	1 751	1 787	2 066	1 844	1 760	1 907	1 687	1 869	2 691	2 705	5 085	
Dy	7 252	8 017	7 175	7 346	8 554	7 505	7 221	7 690	6 976	7 813	11 354	9 559	13 334	
Ho	856	917	864	864	1 018	898	867	880	829	951	1 337	824	699	
Er	1 627	1 657	1 612	1 545	1 881	1 593	1 548	1 563	1 537	1 746	2 549	1 426	795	
Tm	168	165	172	152	194	155	149	152	161	173	264	178	67	
Yb	803	764	807	662	903	665	658	688	774	813	1 274	982	270	
Lu	72	68	74	56	81	56	58	57	70	72	116	85	20	
Th/U	12	14	11	23	24	24	27	27	22	30	7.1	1.9	11	
ΣLREE	489 503	491 543	488 029	490 504	492 718	491 019	489 217	493 764	491 770	494 386	493 330	486 380	520 082	
ΣHREE	26 524	29 950	25 960	26 557	31 466	27 395	26 234	28 034	25 564	28 450	38 552	33 898	59 669	
ΣREE + Y	516 523	522 063	514 510	517 412	524 532	518 776	515 801	522 201	517 762	523 151	532 402	520 526	580 196	

concentrations in ppm

- (not analysed)

# = excluded U-Pb isotopic calculation

Eu = Euhedral

Sub = Subhedral

An = Anhedral

Alt. rim = porous altered rim



## (RPGV16 continued)

Sample	RPGV16											
	Sub; zoned	An; zoned	An; zoned	rounded; sub	rounded; An	rounded; An	rounded; An	rounded; An	rounded; Ar	An; Alt. rim	An; Alt. Rim	An; Alt. Rim
Element	V16_10	V16_12	V16_25	Alt. rim V16_9	Alt. rim V16_15	Alt. rim V16_16	zoned V16_17	Alt. rim V16_22	inherited V16_13	inherited V16_14	inherited V16_23	inherited V16_24
Si	-	-	-	-	-	-	-	-	-	-	-	-
P	-	-	-	-	-	-	-	-	-	-	-	-
Ca	-	-	-	-	-	-	-	-	-	-	-	-
Sr	-	-	-	-	-	-	-	-	-	-	-	-
Y	-	-	-	-	-	-	-	-	-	-	-	-
Pb*	18 350	2 839	2 662	5 223	4 208	5 023	1 951	4 559	6 282	4 425	4 545	4 452
Th	73 769	89 877	80 445	85 910	47 208	91 251	35 319	80 279	42 494	73 713	81 061	71 791
U	14 501	1 231	1 212	3 708	3 212	3 263	1 164	2 981	4 225	3 052	3 130	2 941
La	120 099	137 087	134 709	117 941	128 140	121 596	112 581	119 755	114 720	126 662	126 168	126 304
Ce	230 469	230 469	230 469	230 469	230 469	230 469	230 469	230 469	230 469	230 469	230 469	230 469
Pr	25 096	23 959	23 750	25 816	24 793	25 705	27 612	25 886	29 137	25 231	25 269	25 023
Nd	82 829	81 496	81 074	93 223	85 992	92 603	112 090	94 172	120 525	89 720	89 598	89 853
Sm	24 273	13 601	11 505	21 594	18 938	20 075	16 588	20 382	24 206	19 312	19 463	19 167
Eu	164	496	478	358	312	263	1 098	416	299	359	402	389
Gd	15 550	10 426	9 038	15 887	13 092	14 358	10 348	14 941	15 349	13 824	13 601	13 388
Tb	2 123	1 229	1 093	1 977	1 595	1 830	1 040	1 867	1 032	1 683	1 684	1 650
Dy	7 440	4 960	4 746	8 089	6 303	7 451	4 420	7 541	2 213	6 996	6 919	6 774
Ho	694	633	613	911	731	899	614	901	149	825	839	818
Er	1 191	1 103	1 076	1 712	1 329	1 637	1 183	1 698	154	1 543	1 537	1 511
Tm	136	88	91	175	141	161	114	172	9.2	162	159	159
Yb	721	332	340	822	668	722	540	781	27	742	749	735
Lu	64	27	28	71	62	65	56	72	2.0	71	70	69
Th/U	5.1	73	66	23	15	28	30	27	10	24	26	24
ΣLREE	482 767	486 611	481 506	489 043	488 331	490 448	499 340	490 663	519 056	491 394	490 967	490 815
ΣHREE	27 918	18 798	17 025	29 644	23 921	27 123	18 316	27 973	18 935	25 845	25 558	25 103
ΣREE + Y	510 848	505 905	499 009	519 045	512 564	517 834	518 754	519 053	538 290	517 598	516 926	516 307

concentrations in ppm

- (not analysed)

# = excluded U-Pb isotopic calculation

Eu = Euhedral

Sub = Subhedral

An = Anhedral

Alt. rim = porous altered rim

**A.2.3: SDORPB15-10**

Sample	SDORPB15-10														
Element	Core; H	Core; H	Core; H	Core; H	Core; H	Core; Z	Core; Z	Core; Z	Core; BSE bright	BSE bright; Z	BSE bright; Z	BSE dark; Z	BSE dark; Z	BSE dark; Z	BSE dark; Z
	053dog10a1	054dog10a2	056dog10a4	061dog10a9	068dog10a11	059dog10a7	060dog10a8	072dog10a1	062dog10a10	057dog10a5	069dog10a12	058dog10a6	070dog10a13	071dog10a14	055dog10a3
Si	5 646	2 698	1 295	10 877	3 274	4 667	4 362	11 640	9 782	9 699	13 707	12 875	9 218	2 215	669
P	123 111	121 782	106 234	157 201	140 872	150 008	153 910	120 194	110 472	116 675	125 748	115 479	116 662	106 953	118 923
Ca	22 121	33 668	10 186	31 892	17 937	34 211	32 796	15 411	12 694	11 491	17 475	10 896	14 084	7 216	11 086
Sr	86	110	66	119	79	124	134	82	58	59	81	52	69	48	44
Y	29 201	25 795	20 641	40 601	23 300	42 867	38 399	19 683	17 949	16 473	18 917	13 756	17 401	18 162	24 128
Pb*	13 674	6 188	7 426	22 520	12 490	20 720	19 062	15 435	12 755	12 586	17 469	14 391	12 365	8 830	4 795
Th	157 361	50 692	55 249	229 071	110 263	201 609	174 770	168 264	142 987	124 718	185 382	155 569	136 598	53 497	46 849
U	3 284	3 431	5 117	5 122	3 994	7 354	6 487	2 820	2 753	3 042	3 034	2 458	2 108	2 996	1 412
La	117 427	134 729	128 317	117 320	122 807	117 121	121 877	126 560	124 615	127 635	125 444	127 914	129 253	116 865	123 193
Ce	230 469	230 469	230 469	230 469	230 469	230 469	230 469	230 469	230 469	230 469	230 469	230 469	230 469	230 469	230 469
Pr	25 880	24 616	25 238	28 016	24 535	27 188	26 642	26 048	25 741	24 959	25 992	25 513	25 510	26 304	25 717
Nd	99 884	93 097	95 828	117 254	86 978	112 954	108 387	105 588	103 169	96 083	106 816	100 189	102 345	102 105	99 006
Sm	20 650	17 412	17 440	25 829	18 399	25 307	23 222	18 543	17 969	14 584	18 576	15 618	17 516	20 671	18 254
Eu	1 218	1 607	2 367	1 781	1 172	2 174	1 872	1 185	1 141	1 056	1 174	994	1 121	1 967	1 541
Gd	15 190	13 233	12 715	20 864	12 830	20 946	18 749	13 097	12 333	9 485	13 153	10 286	12 174	14 948	13 563
Tb	1 979	1 591	1 476	2 480	1 679	2 608	2 352	1 374	1 313	1 030	1 360	1 028	1 247	1 829	1 698
Dy	8 817	7 248	6 549	11 163	7 205	11 950	10 733	5 710	5 387	4 424	5 598	4 188	5 044	7 177	7 513
Ho	1 214	1 054	870	1 647	942	1 736	1 581	799	752	659	790	583	705	832	1 067
Er	2 150	1 933	1 413	2 993	1 639	3 198	2 823	1 371	1 283	1 223	1 326	991	1 202	1 245	1 849
Tm	186	183	116	262	157	296	262	115	103	115	111	83	100	100	165
Yb	761	825	409	1 077	705	1 301	1 109	438	389	491	434	317	381	384	664
Lu	73	79	34	104	66	126	109	43	36	49	41	30	37	33	60
Th/U	48	15	11	45	28	27	27	60	52	41	61	63	65	18	33
ΣLREE	494 308	500 322	497 292	518 889	483 187	513 039	510 597	507 207	501 963	493 730	507 297	499 702	505 092	496 412	496 638
ΣHREE	30 370	26 146	23 581	40 590	25 223	42 161	37 719	22 945	21 597	17 475	22 812	17 506	20 890	26 549	26 579
ΣREE + Y	555 097	553 871	543 880	601 861	532 882	600 241	588 586	551 021	542 651	528 733	550 200	531 958	544 503	543 090	548 886

concentrations in ppm

H = homogenous

z = zoned

# = excluded U-Pb isotopic calculation

**A.2.4: SD2015-13**

Sample SD2015-13															
Element	028d131	029d132	030d133	031dh134#	032d135	038dh136	039d137#	040d138#	041d139	042d1310	043dh1311	044dh1312	045d1313#	046d1314#	047d1315
Si	2 488	2 435	2 614	2 419	2 632	2 702	6 963	2 450	2 447	2 414	bdl	2 601	6 032	2 573	2 822
P	97 680	98 231	98 798	100 441	101 904	99 032	99 881	100 092	98 423	99 808	98 058	98 689	107 263	94 368	96 073
Ca	1 693	1 733	1 614	2 584	2 608	3 684	4 912	3 620	3 469	3 097	3 199	4 591	4 191	4 349	4 435
Sr	3.6	2.3	2.6	12	57	111	114	53	4.8	4.3	6.3	29	68	34	29
Y	9 890	9 579	7 849	13 163	11 194	11 535	9 870	10 801	7 727	10 822	8 234	8 510	10 197	12 204	10 749
Pb*	3 267	3 382	3 181	3 017	3 229	3 283	6 278	26 548	3 541	3 231	27 718	3 286	3 523	3 767	3 335
Th	22 590	23 621	24 451	28 378	25 145	26 063	57 171	259 928	35 645	30 432	264 412	30 210	36 655	34 060	31 546
U	2 036	1 942	1 506	814	1 135	1 113	507	7 979	751	955	8 283	855	868	1 562	950
La	130 619	130 685	133 157	148 816	127 193	128 214	108 293	128 295	130 430	128 478	130 705	132 483	127 535	128 166	133 404
Ce	230 387	230 387	230 387	230 387	230 387	230 387	230 387	230 387	230 387	230 387	230 387	230 387	230 387	230 387	230 387
Pr	24 061	23 950	23 853	21 738	24 177	23 904	25 436	23 542	23 288	23 614	23 219	22 948	23 365	22 755	22 780
Nd	86 425	86 976	85 088	73 280	86 346	84 875	99 445	84 488	80 900	83 796	82 094	81 169	82 062	81 330	79 203
Sm	23 781	23 920	22 717	19 379	23 879	22 915	22 271	23 702	21 143	23 038	21 437	21 448	22 247	22 069	20 977
Eu	566	468	367	834	806	789	534	1 395	764	858	808	790	1 185	1 051	1 103
Gd	13 399	13 762	12 676	11 429	13 548	12 970	14 322	14 624	11 179	12 733	11 615	11 711	12 385	13 080	11 124
Tb	1 630	1 642	1 461	1 490	1 704	1 620	1 542	1 861	1 325	1 611	1 375	1 406	1 492	1 664	1 391
Dy	5 309	5 362	4 596	5 340	5 653	5 435	4 847	6 040	4 205	5 404	4 436	4 546	5 011	5 673	4 845
Ho	466	456	386	517	517	509	439	495	362	493	387	397	458	534	461
Er	624	601	477	847	749	762	626	596	504	726	542	564	655	761	687
Tm	57	52	40	97	76	84	66	46	51	81	55	57	68	75	72
Yb	245	223	166	526	397	466	415	183	277	448	303	299	336	370	339
Lu	22	20	15	55	39	50	46	15	28	49	32	32	34	37	31
Th/U	11	12	16	35	22	23	113	33	47	32	32	35	42	22	33
ΣLREE	495 273	495 919	495 203	493 600	491 982	490 296	485 833	490 414	486 148	489 313	487 843	488 435	485 597	484 706	486 751
ΣHREE	21 751	22 117	19 816	20 300	22 683	21 896	22 302	23 859	17 930	21 545	18 746	19 012	20 439	22 194	18 950
ΣREE + Y	527 481	528 083	523 235	527 896	526 665	524 516	518 539	526 469	512 568	522 537	515 631	516 747	517 417	520 155	517 553

concentrations in ppm

# = excluded U-Pb isotopic calculation

**A.3: LFROTZ****A.3.1: HS15HF1**

Sample	HS15HF1												
Element	HF1_1	HF1_2	HF1_3	HF1_4	HF1_5	HF1_6	HF1_7	HF1_8	HF1_9	HF1_10	HF1_11	HF1_12	HF1_13
Si	-	-	-	-	-	-	-	-	-	-	-	-	-
P	-	-	-	-	-	-	-	-	-	-	-	-	-
Ca	-	-	-	-	-	-	-	-	-	-	-	-	-
Sr	-	-	-	-	-	-	-	-	-	-	-	-	-
Y	-	-	-	-	-	-	-	-	-	-	-	-	-
Pb*	10 625	13 217	11 112	13 766	14 051	22 398	13 165	11 612	18 307	11 016	21 512	11 439	14 849
Th	81 939	122 022	95 798	109 818	118 917	104 097	113 492	94 007	85 890	96 223	109 789	87 076	111 001
U	8 438	10 777	8 884	11 330	11 291	17 837	10 496	9 088	15 916	8 453	18 498	9 150	12 059
La	102 449	102 849	107 973	104 686	102 737	98 662	101 849	105 383	102 017	106 166	102 248	108 616	101 861
Ce	230 469	230 469	230 469	230 469	230 469	230 469	230 469	230 469	230 469	230 469	230 469	230 469	230 469
Pr	28 641	29 479	28 692	29 557	29 731	29 643	29 222	28 527	30 684	29 211	29 827	28 598	29 939
Nd	112 574	119 477	111 952	117 463	121 369	118 489	118 694	112 844	123 983	117 902	119 647	112 703	121 473
Sm	35 952	43 571	34 088	38 864	40 427	42 070	39 956	34 558	44 819	34 913	43 498	36 238	41 569
Eu	165	180	154	171	196	208	187	157	234	178	225	165	201
Gd	32 470	39 193	31 571	37 236	40 146	42 496	39 756	32 319	47 535	32 027	45 616	33 849	41 281
Tb	3 645	4 470	3 388	4 232	4 666	5 371	4 566	3 480	5 733	3 458	5 865	3 870	4 844
Dy	11 221	14 064	10 322	13 331	14 241	16 652	14 206	10 574	18 254	10 257	18 742	11 854	15 292
Ho	952	1 167	856	1 117	1 196	1 437	1 188	917	1 556	871	1 569	956	1 268
Er	1 098	1 343	1 048	1 333	1 417	1 760	1 390	1 102	1 839	1 053	1 875	1 144	1 469
Tm	63	80	61	77	82	102	80	65	107	64	112	64	83
Yb	187	229	181	233	237	289	225	198	317	186	335	194	235
Lu	13	16	13	16	17	20	16	14	20	14	22	13	16
Th/U	10	11	11	10	11	5.8	11	10	5.4	11	5.9	10	9.2
ΣLREE	510 085	525 845	513 173	521 039	524 732	519 332	520 190	511 781	531 970	518 661	525 689	516 625	525 311
ΣHREE	49 650	60 562	47 440	57 576	62 001	68 127	61 426	48 668	75 361	47 931	74 136	51 945	64 489
ΣREE + Y	559 900	586 587	560 767	578 786	586 930	587 667	581 802	560 607	607 565	566 769	600 050	568 735	590 002

concentrations in ppm

- (not analysed)

(HS15HF1 continued)

Sample	HS15HF1											
Element	HF1_14	HF1_15	HF1_16	HF1_17	HF1_18	HF1_19	HF1_20	HF1_21	HF1_22	HF1_23	HF1_24	HF1_25
Si	-	-	-	-	-	-	-	-	-	-	-	-
P	-	-	-	-	-	-	-	-	-	-	-	-
Ca	-	-	-	-	-	-	-	-	-	-	-	-
Sr	-	-	-	-	-	-	-	-	-	-	-	-
Y	-	-	-	-	-	-	-	-	-	-	-	-
Pb*	13 774	12 270	14 185	11 282	18 594	11 214	15 203	22 603	12 291	14 938	11 419	13 532
Th	89 428	92 608	116 741	101 126	49 680	94 268	98 323	93 479	95 497	106 098	68 488	89 222
U	11 432	9 812	11 272	9 104	16 207	8 946	12 356	18 939	9 642	12 240	9 690	11 257
La	108 851	102 891	102 323	101 262	105 793	109 195	99 454	103 630	104 365	103 992	109 465	109 723
Ce	230 469	230 469	230 469	230 469	230 469	230 469	230 469	230 469	230 469	230 469	230 469	230 469
Pr	28 487	29 354	29 967	30 025	28 862	28 241	29 701	29 646	28 969	29 804	28 309	28 722
Nd	113 718	120 131	120 997	122 398	113 101	110 987	122 019	117 825	116 008	120 829	110 632	110 963
Sm	36 901	37 325	41 281	40 758	38 864	34 419	41 602	42 596	35 285	41 429	34 912	35 597
Eu	188	190	195	182	219	159	179	232	182	204	170	183
Gd	36 670	35 595	41 011	39 621	39 192	32 076	41 353	43 341	32 863	41 412	32 841	34 802
Tb	4 292	3 962	4 782	4 546	4 880	3 624	4 819	5 374	3 609	4 917	3 789	4 128
Dy	13 353	12 313	14 765	14 136	15 946	10 823	15 094	17 606	10 890	15 298	11 747	12 844
Ho	1 090	1 032	1 227	1 154	1 354	908	1 238	1 459	935	1 255	963	1 054
Er	1 245	1 290	1 427	1 310	1 666	1 073	1 475	1 798	1 162	1 444	1 132	1 191
Tm	72	77	82	74	99	62	85	106	71	83	67	69
Yb	207	233	234	218	293	180	250	320	213	228	195	207
Lu	14	17	16	15	20	13	17	21	16	16	13	14
Th/U	7.8	9.4	10	11	3.1	11	8.0	4.9	10	8.7	7.1	7.9
ΣLREE	518 425	520 170	525 035	524 912	517 089	513 310	523 244	524 165	515 097	526 523	513 786	515 474
ΣHREE	56 942	54 519	63 543	61 073	63 450	48 760	64 330	70 024	49 758	64 653	50 746	54 309
ΣREE + Y	575 555	574 878	588 773	586 166	580 758	562 229	587 753	594 421	565 037	591 380	564 703	569 966

concentrations in ppm

- (not analysed)

**A.3.2: SDORPB15-15c**

Sample	SDORPB15-15c														
	Eu; Zoned	Eu; Zoned	Eu; Zoned	Eu; Zoned	Sub; Zoned	Sub; Zoned	Sub; Zoned	Sub; Zoned	Sub; Zoned	Sub; Zoned	An; Alt.	An; Alt.	An, Zoned	An, Embayed	An, Embayed
Element	BSE dark	BSE dark	BSE dark	BSE bright	BSE dark	BSE dark	BSE dark c	BSE dark c	BSE dark c	BSE bright					
	087d1510	089d1512	086d159#	088d1511	075d153	076d154	083d156	084d157	085d158	077d155	073d151	074d152	092d1515	090d1513#	091d1514#
Si	3 675	3 281	6 460	4 508	3 035	3 917	3 067	3 075	2 418	6 457	2 769	2 901	3 065	3 886	4 107
P	96 313	97 837	101 916	97 151	91 620	94 198	89 030	90 625	89 446	105 435	89 179	88 827	90 693	84 232	83 598
Ca	4 109	2 860	7 721	6 247	1 982	3 104	1 867	2 046	2 294	7 849	2 546	1 853	2 146	1 995	2 538
Sr	9.2	9.4	16	9.0	11	13	7.2	7.0	7.8	12	11	14	7.8	11	22
Y	15 407	18 977	13 899	16 584	12 862	14 361	12 494	13 251	14 428	15 776	12 454	11 045	12 951	6 647	5 435
Pb*	5 125	4 555	9 044	6 881	3 582	4 503	3 485	3 724	3 114	9 356	3 597	2 875	3 833	4 200	6 580
Th	49 452	40 305	91 784	71 815	34 427	45 650	34 022	36 071	28 894	96 204	33 356	27 485	36 729	40 439	39 422
U	1 556	1 986	2 426	1 973	1 152	1 340	1 082	1 180	1 128	2 431	1 063	900	1 346	919	5 723
La	103 053	101 072	101 900	98 935	112 373	109 371	115 221	115 015	115 116	102 089	120 493	117 062	119 100	117 924	116 814
Ce	230 387	230 387	230 387	230 387	230 387	230 387	230 387	230 387	230 387	230 387	230 387	230 387	230 387	230 387	230 387
Pr	24 859	25 092	25 178	26 156	23 250	24 154	21 972	21 991	22 000	25 757	21 721	22 087	21 783	20 995	20 720
Nd	100 584	101 318	102 132	108 621	87 416	93 724	80 071	81 503	78 954	103 855	78 955	79 392	81 778	73 827	73 407
Sm	20 456	21 801	22 086	24 465	13 381	16 194	11 380	11 914	10 702	22 373	10 730	10 480	11 968	8 611	8 660
Eu	556	484	512	400	696	772	491	511	509	492	480	472	537	185	225
Gd	12 167	13 018	12 985	14 056	8 426	10 362	7 289	7 539	6 857	13 278	6 771	6 238	8 064	5 048	4 975
Tb	1 325	1 476	1 373	1 485	925	1 137	822	866	805	1 440	761	685	873	492	486
Dy	4 985	5 571	4 849	5 378	3 711	4 507	3 520	3 646	3 660	5 228	3 333	2 959	3 676	1 975	1 859
Ho	610	705	563	630	512	592	514	535	566	620	494	442	530	281	248
Er	1 037	1 251	909	1 073	893	1 022	900	981	1 086	1 052	902	842	937	475	416
Tm	101	125	89	108	85	94	78	86	102	105	83	79	83	41	37
Yb	454	562	412	513	379	407	301	345	424	503	345	324	324	156	168
Lu	43	54	40	50	36	37	28	32	42	49	32	31	32	15	18
Th/U	32	20	38	36	30	34	31	31	26	40	31	31	27	44	7
ΣLREE	479 339	479 669	481 683	488 563	466 808	473 830	459 032	460 810	457 159	484 462	462 286	459 408	465 015	451 744	449 988
ΣHREE	20 723	22 763	21 221	23 293	14 967	18 159	13 452	14 030	13 541	22 276	12 720	11 600	14 520	8 483	8 205
ΣREE + Y	516 026	521 893	517 316	528 841	495 333	507 122	485 468	488 602	485 637	523 005	487 941	482 526	493 023	467 058	463 853

concentrations in ppm

# = excluded from U-Pb age calculation

An = anhedral

Sub = subhedral

Eu = Euhedral

Alt = altered

**A.3.3: SDORPB16-06**

Sample	SDORPB16-6												
	Eu; zoned	Eu; zoned	Eu; zoned	Eu; zoned; Alt	Eu; zoned; Alt	Eu; zoned	Eu; zoned	Eu; zoned	Eu; zoned	Eu; zoned	Eu; zoned	Eu; zoned	Eu; zoned
Element	SD16-6-11	SD16-6-12	SD16-6-13	SD16-6-14	SD16-6-15	SD16-6-16	SD16-6-17	SD16-6-18	SD16-6-19	SD16-6-24	SD16-6-25	SD16-6-20 <sup>#</sup>	SD16-6-23
Si	18 523	15 279	17 719	16 803	16 395	22 043	22 530	20 878	16 153	17 800	18 475	20 988	18 728
P	108 050	106 754	124 791	112 403	114 343	126 544	121 487	115 816	115 425	114 648	107 978	141 259	106 822
Ca	3 442	2 652	4 322	1 291	1 347	4 302	4 532	3 070	2 844	3 844	3 236	19 084	3 073
Sr	1.8	0.7	29	0.34	0.44	8.7	8.0	24	1.3	15	1.7	1 106	0.64
Y	17 509	17 607	20 843	18 351	18 481	22 973	23 504	20 060	18 590	21 264	17 926	50 359	18 057
Pb*	17 205	17 247	19 940	15 793	16 104	21 619	21 774	20 090	17 962	18 736	17 529	14 606	17 619
Th	137 747	140 435	144 335	106 542	107 586	160 262	167 999	151 071	136 111	147 487	143 652	161 491	142 503
U	6 374	6 581	7 028	7 618	7 713	7 192	7 643	7 369	6 421	7 064	6 810	4 429	6 779
La	102 372	101 369	98 354	90 440	90 843	101 584	99 928	104 822	104 766	99 194	105 026	109 282	102 743
Ce	230 469	230 469	230 469	230 469	230 469	230 469	230 469	230 469	230 469	230 469	230 469	230 469	230 469
Pr	28 591	28 922	29 357	30 558	30 463	29 182	29 138	28 358	28 402	29 383	28 428	31 740	28 705
Nd	118 845	119 923	124 691	130 857	132 810	125 015	125 900	117 152	117 296	124 673	124 045	136 895	119 506
Sm	30 053	29 688	33 481	36 773	36 595	33 176	33 296	29 660	29 563	33 158	30 745	37 754	30 129
Eu	33	31	35	4.5	4.7	49	49	45	41	34	31	65	33
Gd	19 639	19 907	22 356	22 817	22 937	23 657	23 622	20 542	19 919	22 782	19 913	27 742	20 150
Tb	2 165	2 196	2 480	2 492	2 519	2 616	2 676	2 304	2 277	2 542	2 274	3 160	2 247
Dy	8 093	8 491	9 201	8 401	8 586	9 515	9 688	8 830	8 587	8 925	8 374	12 649	8 388
Ho	844	857	997	872	874	1 093	1 130	944	899	1 008	861	1 915	861
Er	1 186	1 208	1 386	1 224	1 231	1 572	1 611	1 342	1 285	1 428	1 195	3 991	1 218
Tm	95	96	114	101	101	124	126	104	99	112	95	457	97
Yb	372	373	426	401	414	449	466	400	377	434	379	2 774	381
Lu	31	33	36	37	35	40	40	35	34	37	34	356	33
Th/U	22	21	21	14	14	22	22	21	21	21	21	36	21
ΣLREE	510 329	510 371	516 351	519 097	521 179	519 426	518 730	510 460	510 495	516 877	518 713	546 140	511 551
ΣHREE	32 426	33 161	36 996	36 345	36 698	39 065	39 360	34 500	33 476	37 268	33 125	53 043	33 375
ΣREE + Y	560 297	561 170	574 225	573 797	576 363	581 512	581 643	565 065	562 602	575 443	569 794	649 607	563 016

concentrations in ppm

\* = inherited monazite xenocrysts

# = excluded from U-Pb age calculation

An = anhedral

Eu = Euhedral

Alt = altered

(SDORPB16-6 continued)

Sample	SDORPB16-6											
	Eu; zoned BSE Dark	Eu; zoned BSE Dark	Eu; zoned BSE Dark	Eu; zoned BSE Dark	Eu; zoned BSE Dark	An; Rounded Homo	An; Rounded Homo	An; rounded inherited	An; rounded inherited	An; rounded inherited	An; rounded inherited	An; rounded inherited
Element	SD16-6-1 <sup>#</sup>	SD16-6-2 <sup>#</sup>	SD16-6-3 <sup>#</sup>	SD16-6-4 <sup>#</sup>	SD16-6-21 <sup>#</sup>	SD16-6-7	SD16-6-22	SD16-6-5*	SD16-6-6*	SD16-6-8*	SD16-6-9*	SD16-6-10*
Si	9 643	12 800	23 561	32 246	15 776	6 631	7 701	7 869	10 474	4 845	4 511	2 826
P	128 913	123 732	145 319	184 335	134 844	124 327	124 339	100 837	104 512	123 123	116 019	117 617
Ca	11 588	6 561	21 227	40 712	18 064	16 437	10 460	2 934	4 038	15 171	9 588	6 569
Sr	472	281	496	1 536	628	1.8	1.1	6.3	21	66	48	43
Y	41 604	20 731	89 184	133 545	57 084	17 678	17 636	1 179	1 417	9 082	8 773	12 870
Pb*	8 658	8 328	7 265	16 130	9 172	11 608	11 300	5 136	7 396	20 387	13 649	8 448
Th	107 767	78 165	190 133	266 997	155 362	106 608	102 616	38 128	62 820	110 616	61 292	35 946
U	4 642	2 369	10 273	12 728	6 607	2 948	2 778	791	1 296	9 359	7 761	4 576
La	106 685	101 205	104 574	128 522	112 354	105 973	105 247	109 053	112 234	126 211	117 121	114 790
Ce	230 469	230 469	230 469	230 469	230 469	230 469	230 469	230 469	230 469	230 469	230 469	230 469
Pr	30 333	30 214	29 459	32 057	31 217	29 384	29 153	26 528	26 888	25 697	26 218	27 029
Nd	129 595	129 969	123 319	143 984	137 391	127 413	125 119	104 842	109 891	103 319	103 322	109 854
Sm	34 670	33 140	34 657	39 561	36 055	37 629	37 326	17 517	19 013	18 449	19 408	24 474
Eu	58	39	62	123	112	70	69	212	245	565	703	1 165
Gd	24 931	20 746	26 562	32 450	24 878	22 820	22 449	9 753	11 044	13 197	13 328	19 532
Tb	2 849	2 169	3 637	4 768	3 120	2 370	2 366	569	630	1 310	1 395	2 028
Dy	10 244	7 745	17 098	25 560	12 919	8 516	8 534	983	1 128	4 186	4 352	6 810
Ho	1 611	871	2 751	4 175	2 174	855	856	55	67	404	393	612
Er	3 173	1 431	7 169	9 720	4 775	1 204	1 166	45	55	421	396	650
Tm	369	137	883	1 375	560	94	95	2.0	2.8	20	19	30
Yb	2 152	758	5 424	8 262	3 342	371	368	6.0	8.2	53	43	77
Lu	285	81	728	1 140	467	32	31	0.69	0.59	2.9	2.9	5.8
Th/U	23	33	19	21	24	36	37	48	48	12	7.9	7.9
ΣLREE	531 751	524 996	522 478	574 592	547 486	530 867	527 314	488 408	498 495	504 144	496 536	506 616
ΣHREE	45 614	33 939	64 252	87 450	52 235	36 261	35 866	11 413	12 936	19 595	19 928	29 745
ΣREE + Y	619 027	579 706	675 977	795 710	656 918	584 876	580 885	501 211	513 094	533 386	525 940	550 396

concentrations in ppm

\* = inherited monazite xenocrysts

# = excluded from U-Pb age calculation

An = anhedral

Eu = Euhedral

Alt = altered



**A.3.4: SDORPB16-07b**

Sample	SDORPB16-7B															
	Zoned; A		Zoned; R		Zoned; A		Zoned; A		Zoned; A		Zoned; R		Zoned; A		Unzoned; R	
	BSE bright	BSE bright	BSE bright	BSE bright	BSE bright	BSE bright	BSE dull	BSE dull	BSE dull	BSE dull	BSE dull	BSE dull	BSE dull	BSE dull	BSE dull	BSE dull
Element	SD16-7B-6	SD16-7B-10	SD16-7B-19	SD16-7B-24	SD16-7B-28	SD16-7B-30	SD16-7B-7	SD16-7B-8	SD16-7B-9	SD16-7B-11	SD16-7B-18	SD16-7B-23	SD16-7B-27	SD16-7B-4	SD16-7B-5	
Si	8 483	7 563	9 422	7 817	8 263	8 856	5 207	3 575	7 231	7 181	4 663	3 890	3 803	5 003	4 819	
P	125 730	126 583	128 788	125 043	122 959	126 943	131 069	129 924	127 934	136 156	123 949	126 500	130 587	133 966	119 485	
Ca	12 995	10 127	13 139	11 608	10 783	17 603	12 846	12 784	11 686	10 223	8 316	9 637	12 091	10 377	10 917	
Sr	4.2	3.0	12	19	2.2	20	4.8	4.9	2.3	2.1	12	23	4.6	1.6	2.0	
Y	23 474	18 210	24 298	21 716	16 923	26 918	28 660	27 601	23 643	25 778	22 938	22 879	27 652	23 779	23 459	
Pb*	16 091	12 516	18 573	14 806	11 495	16 453	13 834	13 538	16 243	13 910	9 774	10 653	13 903	11 864	11 175	
Th	118 793	114 153	139 126	106 973	103 882	122 336	88 896	87 112	117 924	98 662	67 625	78 116	75 640	80 240	83 903	
U	6 795	3 052	7 028	6 270	2 790	6 896	7 243	6 748	6 459	5 648	3 957	4 202	8 369	4 946	4 966	
La	83 375	85 439	83 104	86 759	82 178	83 073	81 568	91 893	82 895	82 321	81 779	83 415	83 341	81 583	82 244	
Ce	230 469	230 469	230 469	230 469	230 469	230 469	230 469	230 469	230 469	230 469	230 469	230 469	230 469	230 469	230 469	
Pr	30 269	31 008	30 290	29 749	30 953	30 630	30 764	30 644	30 255	30 857	30 292	30 630	29 967	30 253	30 661	
Nd	118 128	126 553	119 037	114 142	123 626	121 017	122 535	120 870	119 375	121 635	119 999	121 225	117 562	118 942	120 777	
Sm	33 828	50 746	33 024	31 276	47 093	34 497	36 686	35 629	33 351	34 719	33 334	35 361	35 590	34 235	35 235	
Eu	24	37	23	22	29	24	27	26	22	23	23	25	29	23	21	
Gd	19 145	25 150	19 015	17 792	22 225	20 946	21 516	20 655	18 891	20 291	18 923	20 206	20 611	19 508	20 052	
Tb	2 454	2 477	2 458	2 307	2 200	2 589	2 789	2 707	2 457	2 582	2 344	2 457	2 709	2 457	2 567	
Dy	8 933	8 039	9 338	8 671	7 118	9 375	10 088	9 931	9 050	9 769	8 618	8 813	9 826	9 739	8 788	
Ho	995	701	1 032	922	652	1 118	1 194	1 148	1 011	1 082	977	948	1 140	1 033	1 018	
Er	1 640	1 048	1 726	1 514	993	1 885	2 006	1 931	1 655	1 786	1 591	1 536	1 937	1 675	1 635	
Tm	179	108	188	164	100	205	224	211	179	191	165	164	214	175	180	
Yb	887	487	928	802	458	974	1 096	1 049	856	912	788	761	1 104	859	856	
Lu	81	41	83	74	43	90	98	93	79	83	69	67	99	77	78	
Th/U	17	37	20	17	37	18	12	13	18	17	17	19	9.0	16	17	
ΣLREE	496 068	524 214	495 924	492 394	514 319	499 685	502 021	509 504	496 344	500 000	495 873	501 100	496 929	495 481	499 385	
ΣHREE	34 313	38 052	34 767	32 247	33 788	37 184	39 012	37 724	34 178	36 696	33 476	34 952	37 641	35 525	35 175	
ΣREE + Y	553 879	580 514	555 012	546 379	565 058	563 810	569 721	574 855	554 188	562 496	552 310	558 956	562 251	554 809	558 040	

concentrations in ppm

A = angular

R = rounded

(SDORPB16-7B continued)

Sample	SDORPB16-7B														
	Unzoned; R BSE dull	Unzoned; R BSE dull	Unzoned; R BSE dull	Unzoned; A BSE bright	Unzoned; A BSE bright	Unzoned; A BSE dull	Unzoned A BSE dull	Unzoned; A BSE dull	Unzoned; A BSE dull	Unzoned; A BSE dull	Unzoned; A BSE dull	Unzoned; A BSE dull	Unzoned; A BSE dull	Unzoned; A BSE dull	Unzoned; A BSE dull
Element	SD16-7B-12	SD16-7B-17	SD16-7B-14	SD16-7B-1	SD16-7B-22	SD16-7B-2	SD16-7B-13	SD16-7B-15	SD16-7B-16	SD16-7B-20	SD16-7B-21	SD16-7B-25	SD16-7B-26	SD16-7B-29	
Si	5 560	6 961	4 442	9 057	5 419	5 742	2 440	8 976	6 325	8 497	6 277	8 293	8 564	4 120	
P	119 765	126 224	129 378	127 926	114 972	121 705	128 934	127 034	121 987	131 372	115 944	140 588	134 435	123 130	
Ca	9 763	10 505	11 004	12 560	8 901	10 633	11 645	14 172	9 554	14 590	10 961	15 171	14 550	8 651	
Sr	12	5.5	2.1	16	15	8.9	4.5	4.4	2.0	3.1	35	2.2	31	4.6	
Y	21 960	23 581	24 081	22 685	18 423	21 696	26 771	29 698	22 596	30 631	21 692	26 821	30 648	24 013	
Pb*	10 825	13 345	12 097	16 101	9 506	14 074	13 564	17 530	11 081	18 275	11 632	16 785	16 322	10 555	
Th	79 382	98 102	88 173	113 631	71 128	103 931	65 016	132 367	83 534	127 004	86 650	112 592	115 387	74 908	
U	4 735	5 210	5 115	6 905	3 908	6 131	8 213	8 345	4 371	8 522	5 696	7 040	7 538	4 660	
La	84 104	83 044	77 648	86 514	86 478	86 546	83 888	83 053	81 919	82 100	87 008	78 257	78 420	82 696	
Ce	230 469	230 469	230 469	230 469	230 469	230 469	230 469	230 469	230 469	230 469	230 469	230 469	230 469	230 469	
Pr	29 942	30 498	31 167	29 823	29 128	29 694	29 909	31 038	30 361	40 925	29 287	31 474	31 326	30 693	
Nd	115 167	121 409	124 115	116 744	111 457	113 734	114 994	124 466	119 997	123 621	114 484	123 172	126 092	121 436	
Sm	31 908	33 785	38 083	31 627	29 154	31 476	35 524	36 235	33 612	36 364	31 332	38 792	42 176	34 328	
Eu	21	23	17	21	19	22	31	25	22	26	23	19	21	26	
Gd	18 139	19 291	21 065	18 292	15 845	17 785	21 719	21 893	18 951	21 877	17 978	21 760	25 309	19 685	
Tb	2 205	2 490	2 630	2 379	2 037	2 238	2 673	2 863	2 326	2 845	2 277	2 811	3 035	2 486	
Dy	8 124	9 022	9 223	8 806	7 376	8 630	9 534	10 586	8 429	10 473	8 481	10 277	10 834	9 121	
Ho	932	1 008	1 002	976	781	917	1 097	1 259	955	1 288	936	1 090	1 262	1 023	
Er	1 547	1 654	1 647	1 630	1 318	1 539	1 851	2 139	1 534	2 199	1 535	1 870	2 157	1 666	
Tm	166	175	181	176	138	162	205	235	161	243	168	209	246	175	
Yb	793	808	952	871	667	797	1 058	1 160	770	1 202	834	1 026	1 266	831	
Lu	72	72	83	78	60	72	95	107	69	112	80	93	118	76	
Th/U	17	19	17	16	18	17	7.9	16	19	15	15	16	15	16	
ΣLREE	491 589	499 204	501 483	495 176	486 684	491 919	494 783	505 260	496 356	513 479	492 579	502 164	508 483	499 622	
ΣHREE	31 979	34 518	36 783	33 206	28 221	32 142	38 232	40 242	33 198	40 239	32 287	39 136	44 227	35 061	
ΣREE + Y	545 549	557 328	562 363	551 089	533 348	545 779	559 816	575 225	552 172	584 375	546 580	568 139	583 379	558 722	

concentrations in ppm

A = angular

R = rounded

**A.4: Kakamas Domain****A.4.1: SDORPB15-17**

Sample	SDORPB15-17														
Element	Euhedral 053d171	Euhedral 055d173	Euhedral 059d177	Euhedral 060d178	Euhedral 061d179	Euhedral 062d1710	Euhedral 070d1713	Euhedral 071d1714	Subhedral 054d172	Subhedral 057d175	Subhedral 058d176	Subhedral 072d1715	Anhedral 056d174	Anhedral 068d1711	Anhedral 069d1712
Si	3 098	2 934	1 607	1 546	2 692	2 814	1 380	2 312	2 064	2 667	2 780	2 714	4 216	2 278	2 996
P	120 679	120 086	115 783	115 766	113 183	118 564	107 054	114 343	123 327	115 119	117 446	118 943	108 614	112 634	120 613
Ca	13 124	11 615	12 246	11 993	11 395	11 744	9 888	10 880	14 717	10 989	11 830	12 721	11 069	12 441	13 952
Sr	40	23	26	37	30	25	23	44	27	26	26	24	33	24	42
Y	30 004	29 442	25 171	25 970	21 767	29 911	28 925	30 974	26 516	29 102	29 088	30 257	22 179	22 923	33 133
Pb*	14 753	14 216	15 727	15 022	13 344	14 887	14 699	14 257	19 751	13 250	13 908	15 604	11 868	14 507	16 822
Th	75 495	74 601	65 571	61 872	74 297	74 538	42 815	62 954	73 296	70 302	72 280	77 741	69 526	74 224	83 087
U	12 320	11 375	14 951	14 028	10 206	12 523	16 994	13 574	20 082	10 739	11 442	13 348	9 604	12 469	14 361
La	101 889	101 523	103 738	103 004	101 585	101 276	107 090	100 634	103 746	102 091	101 980	100 774	104 844	101 484	101 413
Ce	230 387	230 387	230 387	230 387	230 387	230 387	230 387	230 387	230 387	230 387	230 387	230 387	230 387	230 387	230 387
Pr	26 221	26 328	25 508	25 830	25 548	26 012	24 421	25 343	26 198	25 551	26 061	25 613	25 632	25 206	25 870
Nd	110 445	109 728	103 466	105 009	103 733	108 391	97 997	106 291	106 043	108 234	108 600	107 592	105 480	102 815	109 265
Sm	24 414	24 124	22 877	22 943	22 215	24 416	21 808	23 414	25 900	23 058	23 275	24 026	22 523	22 381	24 232
Eu	253	240	308	314	193	235	281	264	313	236	254	246	189	225	266
Gd	20 330	20 278	18 914	18 555	17 644	20 695	17 693	19 529	23 313	19 080	19 362	20 332	18 095	18 318	20 612
Tb	2 382	2 411	2 280	2 200	2 028	2 484	2 220	2 404	2 911	2 273	2 319	2 439	2 034	2 146	2 530
Dy	9 571	9 423	8 479	8 483	7 620	9 806	8 974	9 590	10 350	9 233	9 197	9 691	7 644	8 075	10 249
Ho	1 200	1 197	997	1 041	888	1 206	1 138	1 216	1 089	1 165	1 154	1 197	913	918	1 318
Er	1 867	1 771	1 431	1 573	1 206	1 754	1 765	1 891	1 281	1 812	1 786	1 794	1 258	1 209	2 022
Tm	146	130	105	124	81	124	144	147	80	140	136	132	86	77	157
Yb	529	441	371	461	250	407	535	529	239	498	486	453	267	236	568
Lu	46	36	32	39	19	32	46	44	18	44	41	38	21	18	48
Th/U	6.1	6.6	4.4	4.4	7.3	6.0	2.5	4.6	3.6	6.5	6.3	5.8	7.2	6.0	5.8
$\Sigma$ LREE	493 356	492 090	485 976	487 174	483 467	490 481	481 702	486 069	492 274	489 321	490 303	488 392	488 867	482 274	491 167
$\Sigma$ HREE	36 071	35 688	32 608	32 475	29 738	36 509	32 515	35 349	39 280	34 245	34 481	36 075	30 318	30 997	37 505
$\Sigma$ REE + Y	559 685	557 460	544 063	545 934	535 164	557 135	543 423	552 656	558 384	552 904	554 126	554 970	541 553	536 419	562 070

concentrations in ppm

**A.4.2: SDORPB15-18**

Sample	SDORPB15-18							
Element	028dog181	029dog182	030dog183	038dog186	039dog187	031dog184#	032dog185#	040dog188#
Si	5 170	6 646	5 144	9 511	8 750	17 476	7 853	11 813
P	120 544	123 941	107 694	117 892	107 685	136 537	117 793	114 275
Ca	10 773	11 800	10 423	10 603	10 183	15 691	10 995	10 683
Sr	96	56	36	26	28	300	65	74
Y	12 987	19 704	13 589	26 948	24 853	29 382	21 576	28 530
Pb*	9 666	12 084	8 921	14 529	12 680	12 603	12 232	15 099
Th	100 594	119 365	104 725	140 917	137 890	158 762	122 595	157 776
U	2 066	3 454	2 059	5 632	4 957	4 686	4 125	6 046
La	114 274	113 625	115 765	114 600	120 754	120 610	116 782	116 681
Ce	230 387	230 387	230 387	230 387	230 387	230 387	230 387	230 387
Pr	24 266	24 976	24 991	26 399	25 968	26 987	25 370	26 866
Nd	90 356	95 413	92 498	102 815	101 709	106 046	99 536	106 307
Sm	16 055	17 364	17 175	19 059	18 473	19 368	17 809	20 002
Eu	413	329	416	231	228	384	230	280
Gd	9 759	11 832	10 385	14 062	13 321	13 363	12 571	14 613
Tb	1 108	1 392	1 156	1 707	1 630	1 624	1 476	1 760
Dy	4 329	5 772	4 507	7 423	6 905	7 283	6 199	7 902
Ho	543	778	547	1 062	974	1 140	859	1 133
Er	904	1 373	905	1 934	1 791	2 510	1 542	2 053
Tm	81	128	85	176	162	335	139	202
Yb	333	519	360	725	689	2 092	584	869
Lu	30	47	32	68	66	254	55	86
Th/U	49	35	51	25	28	34	30	26
$\Sigma$ LREE	475 338	481 765	480 817	493 260	497 291	503 399	489 884	500 243
$\Sigma$ HREE	17 088	21 841	17 977	27 157	25 537	28 600	23 424	28 617
$\Sigma$ REE + Y	505 826	523 638	512 798	547 596	547 909	561 765	535 114	557 671

concentrations in ppm

# = excluded from U-Pb age calculation

**A.4.3: SDORPB15-20**

Sample	SDORPB15-20														
Element	008dog201	009dog202	010dog203	013dog206	014dog207	015dog208	016dog209	017dog2010	023dog2011	024dog2012	025dog2013	026dog2014	027dog2015	011dog204#	012dog205#
Si	1 968	2 431	2 540	7 539	6 468	3 465	3 496	4 517	2 603	3 873	4 720	6 581	2 453	5 827	3 168
P	122 091	121 040	115 512	114 729	114 732	119 540	102 440	115 512	118 178	107 142	120 244	112 852	122 277	102 572	110 033
Ca	11 484	10 807	12 035	4 591	3 853	12 258	3 659	7 567	12 857	3 551	3 931	4 291	13 959	3 958	2 959
Sr	14	15	16	7.4	6.4	13	6.0	7.9	13	5.1	6.1	6.4	15	18	5.1
Y	19 183	18 667	19 991	24 138	23 362	22 465	19 118	20 734	19 614	23 746	23 365	24 795	22 244	26 593	21 826
Pb*	9 736	9 472	9 950	9 714	7 952	10 600	5 006	8 522	10 720	6 035	6 674	9 000	11 859	6 261	5 865
Th	73 873	71 722	81 691	83 135	66 368	89 270	39 592	75 228	93 053	47 002	49 403	74 449	92 872	48 556	45 477
U	5 442	5 306	5 529	4 335	3 597	5 658	2 893	3 487	5 011	3 424	3 280	4 545	7 046	4 145	2 987
La	112 384	111 898	113 712	115 135	112 432	110 447	119 837	110 890	112 219	114 210	110 789	115 762	111 039	114 383	115 914
Ce	230 469	230 469	230 469	230 469	230 469	230 469	230 469	230 469	230 469	230 469	230 469	230 469	230 469	230 469	230 469
Pr	26 638	26 882	27 204	27 272	26 893	27 190	25 169	26 831	26 770	26 936	27 103	27 200	27 167	27 475	26 327
Nd	106 847	106 643	108 624	114 557	114 423	112 343	98 303	107 978	106 745	106 569	114 316	114 777	109 273	111 264	105 476
Sm	24 636	24 446	25 141	21 677	21 572	24 394	17 272	21 981	23 701	19 327	21 704	22 235	25 295	21 649	18 303
Eu	317	315	322	303	306	316	282	262	416	317	298	308	451	343	296
Gd	16 230	15 961	16 633	16 143	16 025	17 137	12 532	14 762	15 854	14 354	16 272	16 452	16 885	16 795	13 524
Tb	1 884	1 861	1 936	1 892	1 885	2 016	1 523	1 792	1 873	1 782	1 912	1 973	2 066	2 086	1 672
Dy	7 030	7 003	7 238	8 013	7 988	7 938	6 526	7 175	7 310	7 851	8 104	8 461	7 958	9 247	7 223
Ho	793	776	837	1 070	1 049	943	856	879	860	1 049	1 039	1 115	944	1 193	967
Er	1 320	1 313	1 399	1 796	1 746	1 561	1 429	1 465	1 380	1 725	1 730	1 859	1 554	2 050	1 614
Tm	122	121	131	145	138	138	117	125	123	141	141	157	141	164	129
Yb	554	543	583	546	531	596	437	516	515	522	516	595	623	630	488
Lu	50	50	54	46	44	54	38	44	43	45	44	51	56	51	40
Th/U	14	14	15	19	18	16	14	22	19	14	15	16	13	12	15
ΣLREE	500 973	500 337	505 150	509 111	505 788	504 843	491 050	498 148	499 903	497 510	504 382	510 443	503 243	505 240	496 490
ΣHREE	27 981	27 627	28 809	29 652	29 406	30 384	23 457	26 759	27 959	27 469	29 759	30 662	30 227	32 217	25 658
ΣREE + Y	548 454	546 946	554 272	563 203	558 863	558 007	533 907	545 903	547 891	549 042	557 804	566 207	556 165	564 393	544 270

concentrations in ppm

# = excluded from U-Pb age calculation

**A.4.4: SDORPB16-08**

Sample	SDORPB16-8															
	Eu; zoned			Eu; Alt; Zoned		Eu; zoned; alt		Eu; zoned		Eu; zoned		inherited		inherited		
	BSE dark r	BSE dark r	BSE dark r	BSE Bright r	BSE bright r	BSE bright c	BSE bright c	BSE bright c	BSE bright c	BSE bright c	BSE bright c	BSE dark c	BSE dark c	BSE Dark c	BSE Dark	BSE dark
Element	SD16-8-12	SD16-8-13	SD16-8-17	SD16-8-4	SD16-8-20	SD16-8-14	SD16-8-28	SD16-8-30	SD16-8-15	SD16-8-16	SD16-8-18	SD16-8-19	SD16-8-5	SD16-8-1	SD16-8-29	
Si	7 177	8 636	2 455	5 543	2 666	10 821	9 102	8 519	11 271	8 552	1 686	895	2 672	729	bdl	
P	116 316	124 406	137 662	135 549	141 494	125 358	131 287	115 607	129 464	123 533	129 035	132 262	140 362	117 431	121 576	
Ca	3 936	5 240	18 917	8 345	20 355	5 025	7 526	4 790	6 095	4 641	13 269	12 744	14 665	4 301	3 335	
Sr	10	13	60	22	62	12	20	14	14	13	71	52	48	16	62	
Y	27 599	29 025	18 691	31 123	21 544	30 024	33 357	25 507	33 160	27 957	29 421	26 362	31 951	24 417	20 560	
Pb*	9 660	11 354	15 120	13 079	17 246	14 449	14 602	11 891	15 604	12 351	19 516	20 426	19 279	8 334	8 417	
Th	66 817	76 390	99 154	76 174	108 738	99 937	94 516	80 824	107 053	85 794	40 097	39 655	71 546	11 279	10 910	
U	4 392	5 257	7 978	6 607	8 978	6 403	7 240	6 452	7 135	5 622	21 586	22 946	15 059	8 981	8 780	
La	96 712	97 972	121 250	98 333	112 795	96 304	95 773	96 029	96 358	97 725	113 828	111 821	104 006	107 777	104 986	
Ce	230 469	230 469	230 469	230 469	230 469	230 469	230 469	230 469	230 469	230 469	230 469	230 469	230 469	230 469	230 469	
Pr	29 176	29 625	25 827	29 610	27 025	29 329	30 034	28 845	30 136	29 114	27 222	26 558	28 177	26 923	26 738	
Nd	123 741	124 685	102 459	126 177	108 573	125 567	128 468	124 090	129 308	124 950	110 731	107 146	115 076	101 540	101 606	
Sm	26 948	27 337	24 449	29 490	27 332	27 436	30 101	27 347	28 606	26 536	22 350	21 567	28 059	24 236	24 106	
Eu	92	91	749	143	573	95	122	122	103	99	657	619	371	323	335	
Gd	20 055	20 081	17 623	22 289	19 340	20 680	23 283	19 889	22 189	19 491	18 181	17 704	21 903	17 414	16 185	
Tb	2 166	2 247	2 141	2 503	2 257	2 335	2 586	2 099	2 528	2 219	2 335	2 247	2 653	2 171	2 168	
Dy	8 663	9 098	7 657	9 991	8 403	9 369	10 293	8 259	10 206	8 960	9 655	9 339	10 475	8 456	8 069	
Ho	1 280	1 335	878	1 402	1 004	1 376	1 463	1 169	1 504	1 277	1 350	1 218	1 425	1 075	938	
Er	2 189	2 290	1 366	2 269	1 603	2 370	2 494	1 984	2 621	2 237	2 110	1 868	2 302	1 775	1 536	
Tm	189	196	121	190	140	198	206	178	225	197	173	145	198	163	134	
Yb	736	796	506	710	582	780	793	720	877	791	649	548	765	670	562	
Lu	70	73	49	63	53	72	71	63	82	78	58	48	66	61	51	
Th/U	15	15	12	12	12	16	13	13	15	15	1.9	1.7	4.8	1.3	1.2	
ΣLREE	507 046	510 087	504 454	514 078	506 193	509 104	514 844	506 780	514 877	508 793	504 599	497 560	505 787	490 945	487 904	
ΣHREE	35 349	36 115	30 341	39 416	33 383	37 181	41 189	34 360	40 233	35 250	34 510	33 116	39 787	31 785	29 644	
ΣREE + Y	570 085	575 319	554 235	584 761	561 693	576 405	589 512	566 769	588 373	572 099	569 187	557 657	577 896	547 470	538 442	

concentrations in ppm

A = anhedral

Eu = euhedral

Alt = altered

c = core

r = rim

# = excluded

## (SDORPB16-8 continued)

Sample Element	SDORPB16-8															inherited	inherited						
	An; Alt; Zoned		An; Alt; Zoned		A; Alt; Zoned		A; Alt; Zoned		An; Alt; Zoned		An; Alt; Zoned		An; Alt; Homo		An; Alt; Homo		An; Alt; Homo		An; Alt; Homo		An; Alt; Homo		
	BSE dark c SD16-8-8	BSE dark r SD16-8-23	BSE Bright SD16-8-2	BSE Bright SD16-8-3	BSE bright c SD16-8-21	BSE bright c SD16-8-22	BSE bright c SD16-8-25	SD16-8-6	SD16-8-7	SD16-8-9#	SD16-8-10#	SD16-8-11	SD16-8-24#	SD16-8-26	SD16-8-27								
Si	3 615	12 849	2 164	963	12 080	3 505	2 446	12 357	12 177	6 795	3 669	2 715	5 510	bdl	1 678								
P	126 443	124 022	120 202	124 816	124 339	136 114	122 464	114 927	128 830	122 782	113 315	152 314	115 301	131 983	136 403								
Ca	10 994	6 522	6 267	5 635	7 711	19 647	14 251	3 779	4 297	3 215	1 540	30 533	1 641	17 240	18 694								
Sr	29	18	13	13	62	80	58	20	23	16	9.2	62	36	76	73								
Y	31 308	31 039	20 878	20 262	31 478	17 120	14 135	26 260	26 959	7 540	6 278	22 615	6 107	14 752	14 695								
Pb*	13 147	16 219	7 611	7 528	16 065	14 468	10 282	13 389	13 494	6 508	2 946	24 034	3 369	38 937	41 431								
Th	54 428	115 845	32 151	29 554	117 231	110 308	91 650	105 378	95 844	56 788	28 815	152 998	33 307	39 309	40 630								
U	10 436	7 149	5 402	5 222	7 345	6 141	3 158	5 559	5 188	267	51	13 453	77	47 981	50 163								
La	103 431	97 053	101 740	101 566	96 162	121 668	117 867	98 467	95 173	102 623	109 571	115 850	106 644	112 635	113 357								
Ce	230 469	230 469	230 469	230 469	230 469	230 469	230 469	230 469	230 469	230 469	230 469	230 469	230 469	230 469	230 469								
Pr	29 378	29 061	28 403	28 287	29 381	26 546	26 155	29 465	29 714	27 963	29 445	26 192	28 674	26 796	26 415								
Nd	117 599	127 198	111 776	110 617	126 277	104 306	103 964	121 667	125 632	120 287	121 411	102 392	123 629	106 205	104 772								
Sm	29 057	28 677	27 300	27 105	28 106	25 633	23 306	27 230	28 384	28 011	27 836	28 776	28 351	21 372	21 284								
Eu	236	102	200	190	100	854	960	64	70	566	562	563	519	542	546								
Gd	21 481	21 840	17 924	17 918	21 891	17 835	16 061	19 665	20 289	18 270	18 326	19 190	18 381	18 821	18 791								
Tb	2 569	2 397	2 032	2 137	2 429	2 107	1 861	2 185	2 340	1 639	1 673	2 470	1 670	2 229	2 285								
Dy	10 198	9 406	7 800	7 883	9 705	7 305	6 329	8 457	9 331	4 501	4 356	9 039	4 326	7 450	7 430								
Ho	1 362	1 421	931	919	1 417	821	701	1 202	1 233	372	344	1 050	343	671	654								
Er	2 229	2 357	1 525	1 498	2 386	1 297	1 024	2 058	2 084	442	339	1 694	348	710	684								
Tm	190	190	135	133	191	108	88	181	183	32	19	158	20	38	37								
Yb	746	699	558	544	738	453	342	716	718	101	53	713	65	108	103								
Lu	60	62	52	51	67	41	30	65	68	8.4	4.3	64	4.8	8.1	7.3								
Th/U	5.2	16	6.0	5.7	16	18	29	19	18	213	563	11	435	0.82	0.81								
ΣLREE	509 932	512 457	499 687	498 044	510 394	508 623	501 761	507 298	509 372	509 352	518 731	503 678	517 767	497 477	496 296								
ΣHREE	38 836	38 373	30 957	31 084	38 825	29 968	26 435	34 530	36 246	25 366	25 114	34 377	25 157	30 035	29 991								
ΣREE + Y	580 313	581 972	551 722	549 580	580 798	556 564	543 291	568 152	572 647	542 825	550 685	561 233	549 549	542 805	541 529								

concentrations in ppm

A = anhedral

Eu = euhedral

Alt = altered

c = core

r = rim

# = excluded

**A.4.5: SDORPB16-09**

Sample	SDORPB16-9													
Element	Eu; unzoned SD16-9-1E	Eu; unzoned SD16-9-2E	Eu; unzoned SD16-9-23	Eu; alt; z SD16-9-18#	Eu; alt; z SD16-9-26	Sub; alt; z SD16-9-20	Sub; alt; z SD16-9-24#	An; alt; Z SD16-9-3	An; rounded; Z SD16-9-4	An; rounded; Z SD16-9-5	A; rounded; Z SD16-9-6	Sub; alt; z SD16-9-7	An; rounded; Z SD16-9-8	
Si	bdl	1593	3088	6949	2983	3832	2908	2097	3525	2832	4779	2208	5844	
P	149312	138439	138270	130416	134475	141579	133688	135219	126825	134494	131872	137077	131763	
Ca	19428	18995	18751	14967	18999	19386	16504	17381	15068	17481	17528	15337	15712	
Sr	23	23	19	16	24	46	61	103	19	16	13	52	15	
Y	33176	34198	24994	22004	24610	31852	28865	24462	22209	24467	24785	27884	24165	
Pb*	26874	23770	21192	16611	22358	22914	21896	22035	15915	21553	16404	22610	18238	
Th	80754	85130	99478	125258	102677	98363	67302	71839	83012	84860	103216	74430	114825	
U	22652	22866	14606	5797	16310	17409	21413	19198	10535	16845	9078	19626	9247	
La	100944	101110	97766	95905	98952	97639	99267	104039	96939	99035	92569	100251	96482	
Ce	230469	230469	230469	230469	230469	230469	230469	230469	230469	230469	230469	230469	230469	
Pr	27478	27737	27822	27899	27186	27944	27540	27593	27514	27617	27435	27214	27669	
Nd	108674	111335	109795	108739	107948	111131	108650	111458	106929	109722	106873	106313	106734	
Sm	24237	24474	25503	25218	24112	25684	23752	23837	24827	24246	25130	23376	25159	
Eu	223	229	175	236	207	221	263	201	182	194	191	247	179	
Gd	19470	19818	20137	18343	18740	20019	17326	19627	19085	18472	18783	17956	19096	
Tb	2636	2637	2520	2384	2317	2649	2266	2368	2357	2280	2444	2297	2452	
Dy	10720	10860	9437	9071	9071	10773	9589	9161	8652	8885	9337	9396	9435	
Ho	1362	1438	955	1024	968	1343	1242	1003	886	941	1071	1197	1011	
Er	1897	1934	1098	1303	1209	1821	1777	1088	979	1162	1433	1572	1273	
Tm	119	121	63	90	79	119	128	53	59	71	106	106	86	
Yb	342	358	194	314	301	383	437	134	180	204	373	321	280	
Lu	25	26	13	23	18	28	33	9.0	14	14	27	25	22	
Th/U	3.6	3.7	6.8	22	6.3	5.7	3.1	3.7	7.9	5.0	11	3.8	12	
ΣLREE	491801	495125	491355	488229	488666	492867	489677	497396	486677	491088	482475	487622	486513	
ΣHREE	36570	37191	34417	32553	32703	37134	32799	33444	32211	32029	33573	32870	33654	
ΣREE + Y	561770	566743	550942	543021	546186	562074	551604	555503	541280	547777	541023	548623	544512	

concentrations in ppm

An = anhedral

Eu = euhedral

Sub = subhedral

Alt = altered

z = zoned

homo = homogenous

# = excluded



(SDORPB16-9 continued)

Sample Element	SDORPB16-9													
	An; rounded; Z	An; rounded; Z	An; Alt; homo	An; Alt; homo	Alt; homo	An; alt; z	An; alt; z	An; alt; z	An; alt; z	An; alt; z	A; alt; z	An; alt; z	An; alt; z	An; alt; z
	SD16-9-9	SD16-9-17	SD16-9-10	SD16-9-15	SD16-9-16	SD16-9-11	SD16-9-12#	SD16-9-13	SD16-9-14	SD16-9-21E	SD16-9-22	SD16-9-25	SD16-9-27	SD16-9-19
Si	5173	2955	2128	3587	4028	2788	1564	3947	4093	862	2893	1723	6383	4151
P	141965	133069	136171	131639	132924	138797	137064	134030	132564	150856	135146	129287	119928	138017
Ca	18838	17359	16163	20796	20636	16571	21015	18282	17997	18963	17072	15096	11825	22035
Sr	23	16	26	39	14	19	25	13	24	24	83	45	13	18
Y	25895	23986	23666	23915	28323	28732	36521	27091	25484	33301	23823	20180	20359	24538
Pb*	18760	17444	21458	18998	18279	19544	24505	17920	17230	26461	17139	19132	13831	23125
Th	120806	94514	70154	117927	113501	89245	89362	109371	111461	80738	95821	71595	115621	118518
U	8169	10658	17988	10859	10352	13649	23618	10084	8498	22692	10251	15481	4250	15362
La	95292	96228	101982	95970	93346	97065	99235	94750	96123	98207	96697	103548	96596	98812
Ce	230469	230469	230469	230469	230469	230469	230469	230469	230469	230469	230469	230469	230469	230469
Pr	27694	27494	27389	28062	28045	27921	27521	27782	27602	26976	27656	26811	27440	27419
Nd	109294	108395	110994	110428	110034	111632	114135	109138	107824	108325	109230	105863	105725	110215
Sm	25581	25282	23398	26350	26754	26147	25694	25971	25294	23872	24543	21285	24533	26385
Eu	197	188	248	178	199	178	241	198	187	226	206	250	200	168
Gd	19110	19012	18308	20662	20254	21445	20927	19596	18492	19053	18176	15624	17625	21638
Tb	2567	2408	2318	2590	2686	2735	2805	2591	2409	2640	2403	2012	2232	2712
Dy	10332	9018	9042	9359	10373	10374	11856	10064	9525	10853	9425	7788	8476	9704
Ho	1141	998	965	926	1258	1130	1505	1215	1104	1381	1042	836	918	898
Er	1548	1254	1044	1007	1719	1319	2013	1618	1489	1866	1385	932	1179	935
Tm	114	85	52	59	128	80	123	121	109	122	96	46	84	48
Yb	387	288	129	175	465	230	365	432	385	344	367	107	293	133
Lu	29	22	8.1	12	39	16	28	35	30	25	27	6.7	22	8.5
Th/U	15	8.9	3.9	11	11	6.5	3.8	11	13	3.6	9.3	4.6	27	7.7
ΣLREE	488330	487867	494230	491279	488648	493234	497052	488109	487311	487849	488595	487975	484762	493300
ΣHREE	35229	33085	31866	34790	36923	37327	39622	35672	33543	36285	32922	27351	30831	36077
ΣREE + Y	549651	545126	550011	550162	554093	559472	573436	551069	546525	557661	545546	535756	536152	554083

concentrations in ppm

An = anhedral

Eu = euhedral

Sub = subhedral

Alt = altered

z = zoned

homo = homogenous

# = excluded

**A.4.6: SDORPB16-12**

Sample	SDORPB16-12												
	R; Zoned	R; Zoned	R; Zoned	An; Embaye	R; Zoned	Sub; Zoned	An; Homo	An; Homo	An; Homo	An; Homo	An; Homo	An; Homo	An; Zoned
	BSE dark	BSE dark	BSE bright	Homo	BSE dull	BSE dark c							
	1092 Ma	1092 Ma	1092 Ma	1144 Ma	1144 Ma	1200 Ma	1144 Ma	1092 Ma	1200 Ma	1092 Ma	1200 Ma	1144 Ma	1092 Ma
Element	SD16-12-1	SD16-12-2	SD16-12-3	SD16-12-4	SD16-12-5	SD16-12-6	SD16-12-7	SD16-12-8	SD16-12-9	SD16-12-10	SD16-12-11	SD16-12-12	SD16-12-13
Si	bdl	1 475	2 075	1 896	bd	bdl	1 892	5 323	bdl	3 325	1 712	bc	5 470
P	124 522	128 129	118 534	114 748	114 068	118 113	104 801	119 412	116 243	111 147	108 853	110 253	124 011
Ca	11 918	11 602	11 371	7 838	9 359	8 462	8 583	7 901	9 150	9 598	7 916	6 031	9 556
Sr	32	29	35	14	25	37	36	37	25	35	24	25	19
Y	26 440	29 776	7 063	13 412	5 282	17 630	5 024	18 241	7 328	1 705	3 136	2 970	16 565
Pb*	12 451	12 497	10 631	7 634	8 639	9 346	7 421	7 457	9 590	6 622	6 572	6 747	8 603
Th	53 114	51 877	53 127	42 486	46 810	39 486	46 464	57 682	45 937	59 251	47 268	30 831	57 635
U	6 826	7 033	5 217	2 732	2 986	4 524	2 489	1 231	3 717	308	1 234	3 109	2 580
La	110 150	111 673	114 304	110 063	110 689	112 537	111 251	117 339	110 978	105 414	113 522	114 776	103 915
Ce	230 469	230 469	230 469	230 469	230 469	230 469	230 469	230 469	230 469	230 469	230 469	230 469	230 469
Pr	27 055	26 977	26 260	27 262	26 446	26 862	26 629	25 576	26 530	28 107	26 810	26 754	27 861
Nd	109 717	111 053	106 872	114 477	107 379	109 135	108 065	97 817	106 696	119 711	109 599	110 067	117 688
Sm	22 534	22 632	21 712	22 533	19 861	21 404	20 224	18 751	18 665	19 092	19 067	22 137	26 501
Eu	346	371	301	493	402	930	630	804	178	120	118	156	442
Gd	17 228	17 443	16 039	17 526	12 896	16 084	13 515	14 432	10 863	9 024	11 621	14 343	21 648
Tb	2 111	2 193	1 679	1 872	1 186	1 954	1 299	1 694	866	439	812	1 124	2 315
Dy	8 505	9 340	4 270	6 620	3 216	7 599	3 252	6 654	2 918	893	1 819	2 200	7 977
Ho	1 194	1 351	320	653	241	869	236	882	346	76	143	136	757
Er	1 756	2 030	319	686	206	1 359	199	1 407	492	89	148	117	815
Tm	112	138	18	33	8.2	107	9.0	110	35	5.7	8.8	6.0	45
Yb	342	438	56	86	20	425	23	397	116	18	28	17	137
Lu	25	36	4.7	6.1	1.6	39	1.7	33	10	1.5	2.6	1.5	10
Th/U	7.8	7.4	10	16	16	8.7	19	47	12	192	38	10	22
ΣLREE	499 924	502 804	499 617	504 803	494 843	500 406	496 637	489 951	493 337	502 793	499 466	504 203	506 434
ΣHREE	31 274	32 970	22 705	27 484	17 774	28 435	18 535	25 610	15 646	10 547	14 582	17 944	33 704
ΣREE + Y	557 984	565 921	529 686	546 191	518 301	547 402	520 826	534 606	516 489	515 165	517 302	525 273	557 146

concentrations in ppm

bdl = below detection limit

# = excluded from U-Pb age calculation

An = anhedral

Eu = Euhedral

c = core

R = rim

homo = homogenous

(SDORPB16-12 continued)

Sample	SDORPB16-12											
	An; Homo	An; zoned BSE dark	An; Homo	An; Homo	An; zoned	An; zoned BSE light	An; Homo	An; Homo	An; Homo	An; Homo	An; zoned	An; zoned BSE dark
	993 Ma	1200 Ma	1200 Ma	1200 Ma	1092 Ma	1144 Ma				1092 Ma	1092 Ma	1092 Ma
Element	SD16-12-14	SD16-12-15	SD16-12-16#	SD16-12-17	SD16-12-18	SD16-12-19	SD16-12-20	SD16-12-21#	SD16-12-22#	SD16-12-23	SD16-12-24	SD16-12-25
Si	7 031	1 982	3 888	3 186	4 523	22 880	8 495	-	6 133	3 530	5 773	14 027
P	128 875	120 391	113 825	108 252	106 951	107 852	131 388	bdl	99 731	125 577	121 484	111 787
Ca	12 794	9 908	10 260	7 279	8 132	1 812	14 047	-	3 556	9 961	3 174	4 200
Sr	20	30	16	26	29	4.6	37	561 819	19	54	6	11
Y	36 038	15 201	3 898	1 999	7 089	8 031	35 604	91 126	7 510	23 112	24 044	15 635
Pb*	13 999	10 347	8 691	6 575	6 709	3 610	13 466	161 680	7 012	8 073	5 715	4 848
Th	102 061	47 202	50 205	44 908	44 417	25 531	96 489	34 687	45 860	49 243	39 180	36 110
U	5 548	4 332	3 046	1 348	1 579	668	5 367	18 703	2 440	2 572	1 244	774
La	109 379	108 775	106 601	112 836	113 392	114 884	108 863	108 973	122 200	107 483	108 435	109 957
Ce	230 469	230 469	230 469	230 469	230 469	230 469	230 469	230 469	230 469	230 469	230 469	230 469
Pr	25 616	27 595	27 851	27 048	26 809	26 443	25 758	28 263	23 777	27 328	28 202	26 701
Nd	97 000	113 334	114 427	110 419	111 338	108 287	98 754	117 171	84 688	112 453	122 254	110 375
Sm	21 767	22 787	23 223	19 357	19 406	19 022	21 733	22 576	12 469	21 643	25 167	20 642
Eu	279	309	131	95	203	434	279	4 573	461	586	793	1 223
Gd	17 582	16 621	14 440	11 354	11 713	12 706	17 691	20 274	7 280	15 474	19 306	14 475
Tb	2 411	1 975	1 169	666	944	1 409	2 458	3 159	694	1 962	2 199	1 861
Dy	10 729	7 104	2 598	1 251	2 825	4 677	10 576	17 358	2 619	8 260	8 685	7 417
Ho	1 618	709	178	88	327	498	1 603	2 865	347	1 045	1 212	882
Er	2 688	859	161	97	491	640	2 642	9 455	572	1 500	1 955	1 283
Tm	216	51	8.2	5.3	37	43	212	1 043	46	107	157	100
Yb	818	148	21	19	137	139	791	6 253	181	357	615	380
Lu	70	12	1.8	1.7	12	12	67	808	16	30	55	33
Th/U	18	11	16	33	28	38	18	1.9	19	19	32	47
ΣLREE	484 231	502 960	502 570	500 128	501 414	499 105	485 576	507 453	473 602	499 375	514 527	498 143
ΣHREE	36 132	27 480	18 578	13 482	16 487	20 124	36 040	61 215	11 755	28 735	34 184	26 430
ΣREE + Y	556 680	545 949	525 176	515 705	525 193	527 694	557 499	664 367	493 328	551 808	573 547	541 432

concentrations in ppm

bdl = below detection limit

# = excluded from U-Pb age calculation

An = anhedral

Eu = Euhedral

c = core

R = rim

homo = homogenous

## Appendix B: Normalised monazite rare earth element (REE) geochemistry

### B.1: Vioolsdrif Domain

#### B.1.1: SD2015-10

Sample: SD2015-10																				
Analysis No.	La	Ce	Pr	Nd	Sm	Eu	Gd	Tb	Dy	Ho	Er	Tm	Yb	Lu	[La/Sm] <sub>N</sub>	[La/Nd] <sub>N</sub>	[Gd/Lu] <sub>N</sub>	[Dy/Lu] <sub>N</sub>	Eu/Eu*	
008dog10b1	321987	375836	370138	320702	463285	942	63077	6801	329	43	58	20	12.2	6.2	1	1	10208	53	0.006	
009dog10b2	332454	375836	355985	301201	383092	546	66584	11774	998	72	57	20	13.9	10.3	1	1	6449	97	0.002	
010dog10b3	339450	375836	344692	293136	350480	565	76859	17523	1950	137	68	24	21.0	14.7	1	1	5237	133	0.003	
011dog10b4	357440	375836	329834	271690	276988	515	73648	20424	3249	320	88	26	20.2	11.5	1	1	6379	281	0.003	
012dog10b5	335581	375836	353593	300506	442589	481	165134	58756	12343	1662	345	120	78.7	42.3	1	1	3906	292	0.002	
014dog10b7	402342	375836	317740	264306	254107	523	88612	31024	7020	1235	345	112	69.3	25.0	2	2	3539	280	0.003	
016dog10b9	418155	375836	310214	251684	220206	339	84469	38047	12732	3408	1215	596	361	191	2	2	442	67	0.002	
017dog10b10	381325	375836	327638	276815	311406	291	114605	43975	11894	2281	557	197	105	54.5	1	1	2104	218	0.001	
023dog10b11	402803	375836	311027	251530	229514	239	87107	34787	10184	2208	600	211	118	55.3	2	2	1576	184	0.002	
024dog10b12	400985	375836	318577	261536	243185	242	91997	35736	9948	2066	511	178	80.7	42.7	2	2	2155	233	0.001	
025dog10b13	401540	375836	319333	260047	235691	233	89357	36459	10776	2423	681	252	131	63.4	2	2	1409	170	0.001	
026dog10b14	332580	375836	352312	305291	429500	433	140396	43561	7738	891	188	55.5	40.7	28.2	1	1	4977	274	0.002	
027dog10b15	331150	375836	358624	311329	462654	464	147802	45816	7970	898	172	49.0	41.4	26.7	1	1	5543	299	0.002	

Raw concentration values have been normalised to values from Sun and McDonough (1989)

#### B.1.2: SD2015-11

Sample: SD2015-11																				
Analysis No.	La	Ce	Pr	Nd	Sm	Eu	Gd	Tb	Dy	Ho	Er	Tm	Yb	Lu	[La/Sm] <sub>N</sub>	[La/Nd] <sub>N</sub>	[Gd/Lu] <sub>N</sub>	[Dy/Lu] <sub>N</sub>	Eu/Eu*	
008d111	494052	375836	267449	211685	182262	22786	108417	63768	30268	12799	5634	2626	1520	837	3	2	130	36	0.2	
009d112	470166	375836	276994	222343	196054	23549	113847	66039	31052	13029	5518	2592	1428	784	2	2	145	40	0.2	
010d113	483314	375836	271814	209208	150479	8995	78127	43503	22827	12047	6542	3591	2067	1063	3	2	73.5	21	0.1	
011d114	481770	375836	268576	205275	156479	21022	91456	57726	29449	13014	5752	2808	1538	853	3	2	107	35	0.2	
012d115	495015	375836	267270	202019	149096	19336	85358	52563	26321	11562	5175	2445	1365	728	3	2	117	36	0.2	
013d116	498440	375836	263927	198243	143912	17578	81554	48973	25169	11645	5565	2809	1615	845	3	3	96.5	30	0.2	
014d117	465864	375836	268479	193456	115793	17812	55369	36502	21451	11557	6428	3640	2260	1235	4	2	44.8	17	0.2	
015d118	511397	375836	264730	199190	151100	21290	88042	55004	26626	11642	5289	2498	1450	761	3	3	116	35	0.2	
016d119	498755	375836	262666	197728	155855	20335	86833	51360	24474	11203	5383	2894	1897	1370	3	3	63.4	18	0.2	
017d1110	521053	375836	254806	189131	132341	18271	75444	47281	23830	10725	4794	2235	1277	701	4	3	108	34	0.2	
023d1111	492190	375836	261963	199988	143245	16146	79283	46817	23811	11498	5725	3013	1700	891	3	2	89.0	27	0.1	
024d1112	490512	375836	260474	199323	144995	19031	80928	48863	24510	11074	5091	2449	1335	705	3	2	115	35	0.2	
025d1113	489137	375836	261619	203931	167802	21299	96999	58193	28520	12771	5793	2881	1613	876	3	2	111	33	0.2	
026d1114	485459	375836	262106	201451	165093	22190	92600	53972	26273	12061	5690	2906	1750	996	3	2	93.0	26	0.2	
027d1115	472902	375836	262466	201251	144531	7424	74275	42203	22221	11573	6358	3589	2130	1072	3	2	69.3	21	0.1	

Raw concentration values have been normalised to values from Sun and McDonough (1989)

**B.1.3: SDORPB15-004B**

Sample:		SDORPB15-4B																		
Analysis No.	La	Ce	Pr	Nd	Sm	Eu	Gd	Tb	Dy	Ho	Er	Tm	Yb	Lu	[La/Sm] <sub>N</sub>	[La/Nd] <sub>N</sub>	[Gd/Lu] <sub>N</sub>	[Dy/Lu] <sub>N</sub>	Eu/Eu*	
SD15-004B-1	539653	375968	259601	189139	94323	26113	43584	26060	15376	9333	5954	3806	2710	1665	6	3	26	9	0.4	
SD15-004B-2	582740	375968	242158	173892	81585	18051	35732	19799	11603	7036	4367	2718	1858	1196	7	3	30	10	0.3	
SD15-004B-3	587232	375968	246176	180638	84686	18555	36887	20631	11985	7387	4552	2833	2017	1254	7	3	29	10	0.3	
SD15-004B-4	665316	375968	210491	127831	42880	12579	13698	6370	2781	1254	596	251	139	69.9	16	5	196	40	0.4	
SD15-004B-5	541304	375968	263508	195516	83416	8811	36052	18903	11094	7032	4091	2272	1367	830	6	3	43	13	0.1	
SD15-004B-6	568789	375968	252958	185397	85776	21652	35864	18972	10885	6920	4711	3463	2611	1695	7	3	21	6	0.4	
SD15-004B-7	532364	375968	260489	192824	84928	22290	33645	18093	10782	7032	4473	2773	1713	1035	6	3	33	10	0.4	
SD15-004B-8	519781	375968	261406	194999	87208	22060	33582	18070	10566	6957	4523	2687	1700	1051	6	3	32	10	0.4	
SD15-004B-9	676591	375968	210996	126099	42580	13200	14607	6927	3416	1685	888	496	299	185	16	5	79	19	0.5	
SD15-004B-10	535768	375968	258035	188381	77912	18682	27253	12337	6421	3791	2262	1413	1034	682	7	3	40	9	0.4	
SD15-004B-11	506284	375968	265518	201461	86995	19412	31662	15757	9107	6137	4652	3781	3179	2269	6	3	14	4	0.3	
SD15-004B-12	471634	375968	235646	175400	72667	16501	25923	12724	7192	4801	3629	2908	2428	1730	6	3	15	4	0.3	
SD15-004B-13	539331	375968	256395	183804	74672	17422	25792	12862	7310	5098	3822	3070	2488	1788	7	3	14	4	0.3	
SD15-004B-14	562274	375968	248111	174555	64965	15004	21768	10125	5804	3882	2877	2218	1829	1293	9	3	17	4	0.3	
SD15-004B-15	530889	375968	262885	197081	91036	15364	36728	17737	9380	5622	3207	1722	1054	701	6	3	52	13	0.2	
SD15-004B-16	543030	375968	260890	190390	79397	14782	27770	12845	6601	3852	2357	1612	1252	819	7	3	34	8	0.3	
SD15-004B-17	525884	375968	264060	191352	82065	17972	28768	14283	7835	5289	3954	3160	2797	2041	6	3	14	4	0.3	
SD15-004B-18	518968	375968	261229	190177	83737	14339	34322	17579	9748	5861	3686	2236	1443	922	6	3	37	11	0.2	
SD15-004B-19	531318	375968	259925	194373	96227	17044	42548	24508	15371	10580	7498	5603	4418	2983	6	3	14	5	0.2	
SD15-004B-20	516543	375968	270515	212462	86112	3007	35720	15973	8022	4253	2200	968	486	272	6	2	132	30	0.05	
SD15-004B-21	561018	375968	257108	189460	86699	23188	42087	24560	14215	8939	5423	3440	2451	1580	6	3	27	9	0.4	
SD15-004B-22	559616	375968	249713	183400	83281	23621	40079	23239	13564	8303	5179	3260	2359	1593	7	3	25	9	0.4	
SD15-004B-23	654585	375968	216173	132816	45658	12081	14712	6866	2943	1295	580	213	104	39.8	14	5	369	74	0.4	
SD15-004B-24	563502	375968	259726	196748	92349	46868	49365	30269	19389	12582	7443	4310	2825	1816	6	3	27	11	0.7	
SD15-004B-25	646546	375968	219845	141086	51971	15965	19540	9895	5092	2783	1513	787	477	284	12	5	69	18	0.4	

Raw concentration values have been normalised to values from Sun and McDonough (1989)

**B.1.4: SDORPB15-07D**

Sample: SDORPB15-7D																			
Analysis No.	La	Ce	Pr	Nd	Sm	Eu	Gd	Tb	Dy	Ho	Er	Tm	Yb	Lu	[La/Sm] <sub>N</sub>	[La/Nd] <sub>N</sub>	[Gd/Lu] <sub>N</sub>	[Dy/Lu] <sub>N</sub>	Eu/Eu*
SD15-007D-1	479895	375968	280831	208580	192887	13055	94105	69078	34409	12998	5584	2969	1607	671	2	2	140	51	0.1
SD15-007D-2	482357	375968	283778	211689	192984	12300	93254	66869	32912	12790	5546	2949	1657	638	2	2	146	52	0.1
SD15-007D-3	518302	375968	253637	175767	103093	12590	44209	27071	13656	6228	3045	1753	1014	493	5	3	90	28	0.2
SD15-007D-4	524207	375968	256200	181785	102839	12901	43883	26983	13865	6215	3027	1655	1070	439	5	3	100	32	0.2
SD15-007D-5	502857	375968	224659	153953	89684	10974	36334	22101	11238	5021	2561	1460	883	407	6	3	89	28	0.2
SD15-007D-6	476241	375968	280430	219012	189808	19567	93332	62062	27907	10477	4011	1701	831	386	3	2	242	72	0.1
SD15-007D-7	469425	375968	284876	219341	190511	19565	90821	60431	27610	10547	4575	2450	1692	1223	2	2	74	23	0.1
SD15-007D-8	448692	375968	272284	208619	183556	12156	89523	64612	32715	13364	6201	3358	2135	1207	2	2	74	27	0.1
SD15-007D-9	459501	375968	285109	221442	200030	13218	97218	68615	32709	11939	5005	2445	1400	637	2	2	153	51	0.1
SD15-007D-10	468816	375968	294884	236495	225570	18864	119033	76474	39067	15082	6447	2872	1549	678	2	2	176	58	0.1
SD15-007D-11	462536	375968	295023	236677	217957	19322	108914	74841	36714	14669	6399	3198	1694	796	2	2	137	46	0.1
SD15-007D-12	458885	375968	294078	233528	220955	18574	110742	73142	36162	14092	6003	2920	1556	707	2	2	157	51	0.1
SD15-007D-13	467830	375968	297787	236522	204057	17775	100440	64380	30929	13456	6836	3546	2575	1439	2	2	70	21	0.1
SD15-007D-14	501032	375968	263332	194922	111228	12929	53236	33479	15166	5832	2342	1078	502	209	5	3	254	72	0.2
SD15-007D-15	495521	375968	262952	189474	110000	12217	51877	31743	14627	5749	2250	994	465	191	5	3	272	77	0.2
SD15-007D-16	509350	375968	263777	196253	111599	12720	52463	31180	14502	5421	2075	879	510	183	5	3	287	79	0.2
SD15-007D-17	513824	375968	261154	189507	106978	12004	49690	30307	14108	5546	2194	982	490	161	5	3	309	88	0.2
SD15-007D-18	454922	375968	269536	199691	156929	15960	83883	57595	29037	11633	5793	3159	2370	1984	3	2	42	15	0.1
SD15-007D-19	479186	375968	275099	203165	148675	13631	77972	52616	24584	8602	3037	1255	600	200	3	2	391	123	0.1

Raw concentration values have been normalised to values from Sun and McDonough (1989)

**B.1.5: SDORPB15-09**

Sample: SDORPB15-9																			
Analysis No.	La	Ce	Pr	Nd	Sm	Eu	Gd	Tb	Dy	Ho	Er	Tm	Yb	Lu	[La/Sm] <sub>N</sub>	[La/Nd] <sub>N</sub>	[Gd/Lu] <sub>N</sub>	[Dy/Lu] <sub>N</sub>	Eu/Eu*
028dog91	366823	375968	364349	320638	825226	7612	343608	108149	22130	4518	1650	857	522	289	0.4	1.1	1189	77	0.01
029dog92	369923	375968	366956	316002	832748	7348	347904	107577	21693	4479	1631	828	532	278	0.4	1.2	1249	78	0.01
030dog93	375121	375968	366895	315003	816419	7604	345088	109212	22734	4742	1754	941	619	379	0.5	1.2	911	60	0.01
031dog94	340094	375968	380932	348370	955581	1109	355107	82294	10472	1107	296	172	124	87.4	0.4	1.0	4063	120	0.002
032dog95	364121	375968	374204	327686	907906	6763	382338	103976	18913	4059	1561	735	479	270	0.4	1.1	1414	70	0.01
038dog96	370074	375968	373628	333937	886596	2357	333111	82592	12128	1558	463	206	164	108	0.4	1.1	3081	112	0.004
039dog97	376207	375968	373603	334876	844306	3995	315076	84161	13698	1920	547	261	221	173	0.4	1.1	1819	79	0.01
040dog98	373789	375968	360276	313017	836849	8271	372494	120860	25470	5197	1851	914	611	303	0.4	1.2	1230	84	0.01
041dog99	391667	375968	353558	298726	768857	7137	322923	105705	21753	4603	1628	818	541	267	0.5	1.3	1207	81	0.01
042dog910	369602	375968	368492	317159	822011	7863	344937	109254	22839	4784	1743	882	578	291	0.4	1.2	1183	78	0.01
043dog911	366170	375968	377786	326211	757063	2920	246088	57769	8767	1311	375	148	110	59.8	0.5	1.1	4118	147	0.01
044dog912	366355	375968	367299	318344	715360	3214	233592	58930	9220	1400	402	180	117	76.4	0.5	1.2	3057	121	0.01
045dog913	365238	375968	402016	369843	921917	1390	312074	68736	9414	1250	444	244	213	167	0.4	1.0	1863	56	0.002
046dog914	343857	375968	390543	354496	898019	1021	308018	70352	9456	1128	310	156	129	79.7	0.4	1.0	3866	119	0.002
047dog915	354711	375968	379241	343263	797132	1322	283617	67456	10055	1314	370	163	115	54.5	0.4	1.0	5207	185	0.002

Raw concentration values have been normalised to values from Sun and McDonough (1989)

**B.1.6: SDORPB16-04**

Sample: SDORPB16-4																[La/Sm] <sub>N</sub>	[La/Nd] <sub>N</sub>	[Gd/Lu] <sub>N</sub>	[Dy/Lu] <sub>N</sub>	Eu/Eu*
Analysis No.	La	Ce	Pr	Nd	Sm	Eu	Gd	Tb	Dy	Ho	Er	Tm	Yb	Lu						
SD16-004-1	432655	375968	314248	255450	298274	4670	119424	53544	14590	3235	1019	402	237	99.2	1	2	1204	147	0.02	
SD16-004-2	448946	375968	297646	242013	214749	4527	83628	43826	16587	5792	2685	1702	1125	620	2	2	135	27	0.03	
SD16-004-3	470129	375968	290823	230204	225380	8281	101171	54406	18406	5465	2118	1073	661	348	2	2	290	53	0.05	
SD16-004-4	424603	375968	308436	246262	259323	5200	92443	48634	17290	5582	2592	1697	1327	746	2	2	124	23	0.03	
SD16-004-5	468184	375968	290048	227829	212972	7015	87568	44091	14069	3829	1362	697	431	190	2	2	461	74	0.05	
SD16-004-6	436952	375968	309181	252217	260628	6950	112420	56816	19408	5339	1925	971	563	259	2	2	433	75	0.04	
SD16-004-7	456620	375968	302921	242516	245541	6524	103702	53692	18354	5225	1946	989	610	305	2	2	340	60	0.04	
SD16-004-8	442784	375968	304378	246315	260169	6962	113423	57648	17876	4615	1512	705	406	188	2	2	603	95	0.04	
SD16-004-9	453224	375968	310725	250879	264619	6525	114800	56513	19358	5032	1658	742	429	179	2	2	642	108	0.03	
SD16-004-10	415631	375968	317209	263196	305744	5051	127426	62505	20497	5433	1953	1000	571	281	1	2	454	73	0.02	
SD16-004-11	414754	375968	321275	269611	318561	5441	136566	66168	22770	6112	2175	1098	648	280	1	2	487	81	0.02	
SD16-004-12	480256	375968	282970	215473	207317	7573	89269	46691	15198	4299	1493	718	442	208	2	2	430	73	0.05	
SD16-004-13	477677	375968	277436	208508	204333	7466	83912	44550	14024	3886	1339	649	384	174	2	2	481	80	0.05	
SD16-004-14	408069	375968	329978	278791	329081	4234	133543	59439	19361	5234	1951	1098	682	361	1	1	370	54	0.02	
SD16-004-15	472559	375968	282269	218196	200312	6893	81838	42027	13217	3579	1230	586	335	165	2	2	497	80	0.05	
SD16-004-16	477878	375968	286403	221117	201703	6836	82293	40986	13160	3480	1253	563	354	161	2	2	511	82	0.05	
SD16-004-17	427444	375968	311154	253711	246573	4865	90590	43591	14359	4443	2269	1065	747	411	2	2	220	35	0.03	
SD16-004-18	437478	375968	308866	248642	235908	4863	92974	47879	16356	5087	2199	1330	1028	562	2	2	165	29	0.03	
SD16-004-19	486813	375968	258195	196014	146744	6249	62455	33906	12402	4116	1690	947	608	315	3	2	198	39	0.06	
SD16-004-20	465215	375968	292041	223972	213000	7132	87182	44666	14258	3919	1407	704	434	190	2	2	459	75	0.05	
SD16-004-21	470078	375968	291656	225886	229386	7247	93275	47474	14207	3566	1173	540	318	169	2	2	553	84	0.04	
SD16-004-22	444951	375968	298713	240378	242290	5693	103188	54194	18334	4981	1714	912	518	245	2	2	422	75	0.03	
SD16-004-23	455720	375968	298516	239564	241876	5479	100863	52612	17657	4819	1662	828	496	231	2	2	437	76	0.03	
SD16-004-24	426969	375968	313033	259108	297062	4766	119875	60359	19706	5451	1908	947	593	272	1	2	440	72	0.02	
SD16-004-25	416227	375968	316237	266701	301786	4963	128506	62751	21328	5936	2117	1090	658	337	1	2	382	63	0.02	

*Raw concentration values have been normalised to values from Sun and McDonough (1989)*

**B.1.7: SDORPB16-05**

Sample:		SDORPB16-5																	
Analysis No.	La	Ce	Pr	Nd	Sm	Eu	Gd	Tb	Dy	Ho	Er	Tm	Yb	Lu	[La/Sm] <sub>N</sub>	[La/Nd] <sub>N</sub>	[Gd/Lu] <sub>N</sub>	[Dy/Lu] <sub>N</sub>	Eu/Eu*
SD16-005-1	426505	375968	301532	244610	171956	3667	102524	69927	39298	20493	8576	3346	1422	711	2	2	144	55	0.03
SD16-005-2	409771	375968	297558	244166	175767	3061	107079	70436	36390	15394	5278	1846	749	319	2	2	336	114	0.02
SD16-005-3	426579	375968	297353	240340	171006	4140	104328	70717	39278	20308	8230	3152	1318	630	2	2	166	62	0.03
SD16-005-4	422192	375968	302513	209460	351063	5849	76897	16373	1163	76.2	37.0	33.7	17.4	15.2	1	2	5071	77	0.03
SD16-005-5	410895	375968	299989	209307	398730	5989	98642	22756	2006	181	53.9	41.3	20.1	18.9	1	2	5230	106	0.02
SD16-005-6	422170	375968	297667	207888	330257	5453	69550	14372	937	57.9	38.3	32.3	16.4	14.3	1	2	4847	65	0.03
SD16-005-7	430155	375968	304237	205291	315489	4951	63070	12571	801	50.0	29.5	31.5	12.3	12.7	1	2	4957	63	0.03
SD16-005-8	428086	375968	299804	207120	324556	5541	67936	13796	890	54.9	31.4	37.9	17.8	10.9	1	2	6259	82	0.03
SD16-005-9	421270	375968	300202	206541	347799	5677	77251	16542	1242	93.6	37.4	29.6	16.8	11.4	1	2	6763	109	0.03
SD16-005-10	429578	375968	301734	208598	315686	5049	64201	12933	810	56.4	31.3	29.1	12.4	18.1	1	2	3541	45	0.03
SD16-005-11	426730	375968	299119	205343	291316	4421	59518	11895	756	43.8	30.5	25.5	12.5	12.2	1	2	4864	62	0.0

*Raw concentration values have been normalised to values from Sun and McDonough (1989)*



**B.2: Pella Domain****B.2.1: RPGV14**

Sample: RPGV14																			
Analysis No.	La	Ce	Pr	Nd	Sm	Eu	Gd	Tb	Dy	Ho	Er	Tm	Yb	Lu	[La/Sm] <sub>N</sub>	[La/Nd] <sub>N</sub>	[Gd/Lu] <sub>N</sub>	[Dy/Lu] <sub>N</sub>	Eu/Eu*
V14_2	520792	375968	284079	224542	137315	21400	80755	51892	31920	17471	10134	5567	3304	1736	4	2	47	18	0.2
V14_3	550898	375968	277738	212334	122903	30309	67748	43637	27259	15352	9801	6200	4349	2666	4	3	25	10	0.3
V14_4	540121	375968	280106	216221	136332	29744	80502	50894	30309	16068	9169	5045	3040	1640	4	2	49	18	0.3
V14_5	531158	375968	287598	228443	140299	23077	84799	55734	35014	19385	11444	6153	3794	2049	4	2	41	17	0.2
V14_6	538326	375968	281533	216860	133360	33435	75863	48907	29465	16215	9617	5397	3438	1863	4	2	41	16	0.3
V14_7	544759	375968	281006	211887	125363	27895	70933	46223	28777	16287	9804	5449	3380	1844	4	3	38	16	0.3
V14_8	536906	375968	272806	200241	123610	29539	67056	44664	27180	14960	9027	5037	3208	1839	4	3	36	15	0.3
V14_9	540276	375968	274557	203666	128753	25944	70987	46307	28239	15533	9297	5385	3289	1840	4	3	39	15	0.3
V14_10	525652	375968	280274	213427	136105	34014	79311	52711	33041	17953	11156	6613	4449	2501	4	2	32	13	0.3
V14_11	545554	375968	280457	216517	135406	33048	77734	49549	29578	16452	10185	6609	4641	2692	4	3	29	11	0.3
V14_12	543738	375968	274090	208271	127115	24576	72144	47053	27950	15493	9038	4831	3001	1596	4	3	45	18	0.2
V14_13	530205	375968	286567	219908	137949	32691	81343	54261	34514	19221	11735	6679	4120	2314	4	2	35	15	0.3
V14_14	526732	375968	283784	215113	126454	32513	72169	47773	30385	17206	10497	5972	3834	2063	4	2	35	15	0.3
V14_15	536619	375968	277831	211019	131866	13794	73447	46884	29278	16812	10547	6068	3824	2152	4	3	34	14	0.1
V14_16	530164	375968	278299	211227	135809	28421	78098	50635	30609	17048	10232	5899	3762	2059	4	3	38	15	0.3
V14_17	519302	375968	285028	214462	151652	37672	85390	60333	34360	17286	9691	5581	3491	1922	3	2	44	18	0.3
V14_18	533724	375968	275807	207604	134616	29973	75757	49403	29779	15729	9123	5048	3187	1743	4	3	43	17	0.3
V14_19	544543	375968	282629	213940	140976	36777	81399	52432	30772	16125	9473	5346	3299	1937	4	3	42	16	0.3
V14_20	561187	375968	272258	203909	123777	28761	68842	45233	27360	14602	8391	4779	2925	1656	5	3	42	17	0.3
V14_21	521031	375968	290792	228370	143259	21236	85089	56175	34088	18705	11207	6227	3559	1961	4	2	43	17	0.2
V14_22	538903	375968	281721	220073	138822	35759	81065	54556	33928	18529	11985	7666	5485	3204	4	2	25	11	0.3
V14_23	530213	375968	281080	211541	126385	19169	68227	45391	28072	15651	9287	5001	2965	1556	4	3	44	18	0.2
V14_24	488715	375968	307576	233735	174709	107928	95311	64793	35659	16765	9649	5781	3880	2262	3	2	42	16	0.8
V14_25	515809	375968	276781	209423	133952	23742	75328	49373	29312	15631	9249	5089	3122	1813	4	2	42	16	0.2

*Raw concentration values have been normalised to values from Sun and McDonough (1989)*

**B.2.2: RPGV16**

Sample: RPGV16																[La/Sm] <sub>N</sub>	[La/Nd] <sub>N</sub>	[Gd/Lu] <sub>N</sub>	[Dy/Lu] <sub>N</sub>	Eu/Eu*
Analysis No.	La	Ce	Pr	Nd	Sm	Eu	Gd	Tb	Dy	Ho	Er	Tm	Yb	Lu						
V16_2	505907	375968	281679	203282	149558	10128	81961	56858	32588	16787	10359	6685	4742	2761	3	2	30	12	0.1	
V16_3	512979	375968	275420	204738	130640	6234	71083	49499	29862	15827	9659	6140	4111	2262	4	3	31	13	0.1	
V16_4	521847	375968	277101	203622	140863	7146	75869	52818	31260	16119	9770	6139	4274	2297	4	3	33	14	0.1	
V16_5	516342	375968	276125	206246	128711	7611	67993	46727	28359	15186	9604	6504	4807	2836	4	3	24	10	0.1	
V16_6	506335	375968	280909	203339	161254	9237	95315	74542	46153	24494	15933	10678	7913	4700	3	2	20	10	0.1	
V16_8	487408	375968	295526	220197	311101	7909	197982	140868	54203	12802	4970	2723	1677	807	2	2	245	67	0.03	
V16_9	497640	375968	278189	203990	145906	6358	79834	54766	32882	16679	10701	7099	5103	2902	3	2	28	11	0.1	
V16_10	506749	375968	270433	181246	164008	2910	78139	58797	30244	12708	7444	5499	4477	2602	3	3	30	12	0.0	
V16_11	499496	375968	280849	208092	153431	6196	84258	57243	34771	18651	11756	7863	5612	3309	3	2	25	11	0.1	
V16_12	578427	375968	258181	178327	91895	8802	52390	34057	20162	11596	6891	3580	2062	1100	6	3	48	18	0.1	
V16_13	484053	375968	313973	263731	163551	5309	77130	28589	8997	2724	964	372	166	79.3	3	2	973	114	0.04	
V16_14	534440	375968	271886	196323	130488	6377	69465	46631	28438	15108	9642	6549	4607	2902	4	3	24	10	0.1	
V16_15	540676	375968	267165	188165	127960	5548	65790	44193	25622	13383	8306	5704	4146	2516	4	3	26	10	0.1	
V16_16	513061	375968	276995	202633	135644	4676	72152	50691	30289	16464	10228	6525	4486	2633	4	3	27	12	0.05	
V16_17	475027	375968	297543	245274	112082	19497	52002	28805	17968	11254	7392	4606	3355	2288	4	2	23	8	0.2	
V16_18	511869	375968	279245	204556	134065	6425	73765	51087	30508	16445	9953	6255	4133	2280	4	3	32	13	0.1	
V16_19	510821	375968	277682	202315	131467	6217	70212	48756	29355	15882	9676	6047	4084	2358	4	3	30	12	0.1	
V16_20	546061	375968	266711	184660	128406	9253	67863	48491	29167	15832	10078	6945	5011	3019	4	3	22	10	0.1	
V16_21	515690	375968	280226	208541	137775	5600	75439	51775	31761	17409	10912	7012	5052	2930	4	2	26	11	0.1	
V16_22	505295	375968	278941	206065	137719	7396	75082	51704	30653	16509	10610	6977	4851	2945	4	2	25	10	0.1	
V16_23	532356	375968	272300	196058	131505	7132	68347	46661	28124	15363	9608	6438	4649	2832	4	3	24	10	0.1	
V16_24	532928	375968	269640	196615	129503	6905	67275	45693	27537	14978	9442	6436	4564	2816	4	3	24	10	0.1	
V16_25	568391	375968	255927	177404	77739	8492	45418	30271	19295	11231	6726	3665	2110	1133	7	3	40	17	0.1	

Raw concentration values have been normalised to values from Sun and McDonough (1989)

**B.2.3: SD2015-13**

Sample: SD2015-13																[La/Sm] <sub>N</sub>	[La/Nd] <sub>N</sub>	[Gd/Lu] <sub>N</sub>	[Dy/Lu] <sub>N</sub>	Eu/Eu*
Analysis No.	La	Ce	Pr	Nd	Sm	Eu	Gd	Tb	Dy	Ho	Er	Tm	Yb	Lu						
028d131	551 136	375 836	259 275	189 113	160 682	10 054	67 333	45 161	21 581	8 527	3 900	2 292	1 521	878	3	3	77	25	0.09	
029d132	551 414	375 836	258 084	190 320	161 621	8 321	69 154	45 479	21 798	8 354	3 753	2 105	1 382	811	3	3	85	27	0.07	
030d133	561 843	375 836	257 041	186 189	153 496	6 510	63 697	40 476	18 683	7 064	2 980	1 622	1 032	596	4	3	107	31	0.06	
031dh134	627 914	375 835	234 248	160 350	130 938	14 805	57 430	41 284	21 706	9 471	5 292	3 943	3 267	2 221	5	4	26	10	0.16	
032d135	536 681	375 836	260 526	188 941	161 342	14 312	68 080	47 215	22 978	9 473	4 679	3 077	2 466	1 591	3	3	43	14	0.12	
038dh136	540 986	375 835	257 591	185 723	154 834	14 009	65 174	44 876	22 094	9 324	4 762	3 417	2 892	2 046	3	3	32	11	0.13	
039d137	456 934	375 836	274 098	217 605	150 479	9 492	71 970	42 701	19 703	8 037	3 913	2 673	2 576	1 850	3	2	39	11	0.09	
040d138	541 331	375 835	253 685	184 874	160 151	24 771	73 485	51 554	24 551	9 067	3 724	1 856	1 138	602	3	3	122	41	0.21	
041d139	550 339	375 835	250 946	177 024	142 859	13 562	56 174	36 696	17 092	6 623	3 149	2 083	1 723	1 140	4	3	49	15	0.14	
042d1310	542 100	375 836	254 458	183 362	155 662	15 238	63 985	44 624	21 969	9 027	4 537	3 263	2 781	1 993	3	3	32	11	0.14	
043dh1311	551 500	375 835	250 205	179 637	144 847	14 359	58 367	38 081	18 034	7 084	3 390	2 243	1 881	1 314	4	3	44	14	0.14	
044dh1312	559 000	375 835	247 286	177 612	144 917	14 031	58 851	38 940	18 478	7 277	3 526	2 297	1 860	1 302	4	3	45	14	0.14	
045d1313	538 122	375 835	251 780	179 567	150 320	21 052	62 237	41 322	20 370	8 384	4 094	2 747	2 086	1 394	4	3	45	15	0.20	
046d1314	540 783	375 835	245 203	177 964	149 114	18 659	65 727	46 082	23 063	9 772	4 758	3 045	2 297	1 502	4	3	44	15	0.17	
047d1315	562 885	375 835	245 474	173 311	141 734	19 589	55 900	38 527	19 695	8 438	4 296	2 901	2 107	1 257	4	3	44	16	0.20	

Raw concentration values have been normalised to values from Sun and McDonough (1989)

**B.2.4: SDORPB15-10**

Sample: SDORPB15-10																[La/Sm] <sub>N</sub>	[La/Nd] <sub>N</sub>	[Gd/Lu] <sub>N</sub>	[Dy/Lu] <sub>N</sub>	Eu/Eu*
Analysis No.	La	Ce	Pr	Nd	Sm	Eu	Gd	Tb	Dy	Ho	Er	Tm	Yb	Lu						
053dog10a1	495 471	375 968	278 877	218 564	139 524	21 632	76 329	54 832	35 842	22 228	13 438	7 540	4 725	2 979	4	2	26	12	0.2	
054dog10a2	568 476	375 968	265 257	203 713	117 651	28 550	66 497	44 066	29 464	19 302	12 082	7 425	5 123	3 206	5	3	21	9	0.3	
055dog10a3	519 800	375 968	277 123	216 643	123 337	27 378	68 156	47 032	30 540	19 541	11 558	6 661	4 127	2 426	4	2	28	13	0.3	
056dog10a4	541 422	375 968	271 960	209 690	117 835	42 034	63 896	40 879	26 622	15 929	8 830	4 700	2 538	1 378	5	3	46	19	0.5	
057dog10a5	538 544	375 968	268 957	210 247	98 541	18 752	47 664	28 521	17 983	12 065	7 643	4 666	3 049	1 975	5	3	24	9	0.3	
058dog10a6	539 722	375 968	274 922	219 232	105 526	17 663	51 691	28 471	17 023	10 680	6 195	3 351	1 969	1 222	5	2	42	14	0.2	
059dog10a7	494 180	375 968	292 979	247 165	170 994	38 608	105 258	72 238	48 576	31 787	19 989	11 998	8 081	5 130	3	2	21	9	0.3	
060dog10a8	514 249	375 968	287 091	237 171	156 908	33 243	94 217	65 164	43 630	28 962	17 643	10 590	6 888	4 441	3	2	21	10	0.3	
061dog10a9	495 022	375 968	301 900	256 574	174 523	31 631	104 844	68 702	45 379	30 158	18 708	10 589	6 690	4 246	3	2	25	11	0.2	
062dog10a10	525 801	375 968	277 384	225 753	121 415	20 274	61 976	36 360	21 897	13 780	8 021	4 177	2 418	1 469	4	2	42	15	0.2	
068dog10a11	518 172	375 968	264 387	190 324	124 317	20 815	64 470	46 522	29 289	17 244	10 243	6 361	4 379	2 694	4	3	24	11	0.2	
069dog10a12	529 300	375 968	280 091	233 733	125 514	20 858	66 094	37 662	22 755	14 472	8 286	4 505	2 694	1 660	4	2	40	14	0.2	
070dog10a13	545 369	375 968	274 890	223 949	118 351	19 905	61 178	34 531	20 505	12 910	7 511	4 041	2 367	1 504	5	2	41	14	0.2	
071dog10a14	493 099	375 968	283 445	223 425	139 666	34 932	75 116	50 675	29 175	15 236	7 781	4 050	2 388	1 333	4	2	56	22	0.3	
072dog10a15	534 009	375 968	280 691	231 046	125 289	21 055	65 813	38 052	23 210	14 631	8 569	4 636	2 717	1 740	4	2	38	13	0.2	

*Raw concentration values have been normalised to values from Sun and McDonough (1989)*

**B.3: LFROTZ**  
**B.3.1: HS15HF1**

Sample:	HS15HF1														[La/Sm] <sub>N</sub>	[La/Nd] <sub>N</sub>	[Gd/Lu] <sub>N</sub>	[Dy/Lu] <sub>N</sub>	Eu/Eu*
Analysis No.	La	Ce	Pr	Nd	Sm	Eu	Gd	Tb	Dy	Ho	Er	Tm	Yb	Lu					
HF1_1	432 276	375 968	308 628	246 333	242 919	2 929	163 167	100 964	45 615	17 430	6 863	2 567	1 164	541	2	2	302	84	0.01
HF1_2	433 963	375 968	317 666	261 437	294 397	3 205	196 947	123 834	57 172	21 375	8 392	3 234	1 424	634	1	2	311	90	0.01
HF1_3	455 582	375 968	309 186	244 971	230 323	2 730	158 646	93 864	41 960	15 684	6 550	2 451	1 121	533	2	2	297	79	0.01
HF1_4	441 715	375 968	318 504	257 030	262 595	3 039	187 115	117 236	54 192	20 465	8 332	3 127	1 448	644	2	2	290	84	0.01
HF1_5	433 489	375 968	320 372	265 577	273 155	3 490	201 736	129 250	57 890	21 901	8 856	3 317	1 474	685	2	2	294	84	0.01
HF1_6	416 293	375 968	319 427	259 276	284 254	3 701	213 550	148 770	67 692	26 318	11 000	4 134	1 794	815	1	2	262	83	0.01
HF1_7	429 743	375 968	314 888	259 724	269 975	3 328	199 777	126 484	57 746	21 756	8 687	3 247	1 395	634	2	2	315	91	0.01
HF1_8	444 655	375 968	307 406	246 923	233 500	2 790	162 408	96 386	42 984	16 787	6 887	2 646	1 231	563	2	2	289	76	0.01
HF1_9	430 450	375 968	330 644	271 297	302 828	4 150	238 868	158 814	74 204	28 501	11 491	4 326	1 968	830	1	2	288	89	0.02
HF1_10	447 957	375 968	314 773	257 992	235 899	3 166	160 940	95 784	41 696	15 957	6 581	2 603	1 158	556	2	2	289	75	0.02
HF1_11	431 425	375 968	321 414	261 809	293 907	3 991	229 228	162 470	76 187	28 729	11 718	4 530	2 083	902	1	2	254	84	0.02
HF1_12	458 297	375 968	308 173	246 615	244 855	2 930	170 098	107 209	48 187	17 509	7 151	2 593	1 204	548	2	2	311	88	0.01
HF1_13	429 794	375 968	322 623	265 805	280 873	3 578	207 442	134 189	62 164	23 232	9 179	3 363	1 458	665	2	2	312	93	0.01
HF1_14	459 287	375 968	306 975	248 835	249 328	3 336	184 270	118 887	54 282	19 967	7 783	2 902	1 284	553	2	2	333	98	0.02
HF1_15	434 140	375 968	316 314	262 868	252 198	3 371	178 871	109 746	50 053	18 893	8 061	3 120	1 446	699	2	2	256	72	0.02
HF1_16	431 741	375 968	322 916	264 763	278 923	3 464	206 083	132 458	60 020	22 466	8 921	3 336	1 451	650	2	2	317	92	0.01
HF1_17	427 265	375 968	323 544	267 830	275 391	3 231	199 099	125 918	57 463	21 129	8 185	3 014	1 355	598	2	2	333	96	0.01
HF1_18	446 385	375 968	311 015	247 485	262 594	3 898	196 943	135 185	64 821	24 792	10 415	4 011	1 822	809	2	2	243	80	0.02
HF1_19	460 739	375 968	304 321	242 859	232 561	2 828	161 185	100 394	43 996	16 636	6 706	2 511	1 121	519	2	2	311	85	0.01
HF1_20	419 637	375 968	320 050	267 000	281 091	3 186	207 803	133 484	61 357	22 683	9 220	3 445	1 551	673	1	2	309	91	0.01
HF1_21	437 258	375 968	319 460	257 822	287 808	4 117	217 793	148 872	71 567	26 726	11 237	4 279	1 986	857	2	2	254	84	0.02
HF1_22	440 360	375 968	312 169	253 847	238 415	3 230	165 141	99 972	44 268	17 128	7 260	2 855	1 325	645	2	2	256	69	0.02
HF1_23	438 786	375 968	321 164	264 396	279 924	3 626	208 100	136 203	62 188	22 989	9 024	3 359	1 416	643	2	2	324	97	0.01
HF1_24	461 878	375 968	305 052	242 082	235 893	3 028	165 030	104 952	47 752	17 642	7 076	2 706	1 209	517	2	2	319	92	0.02
HF1_25	462 968	375 968	309 508	242 807	240 522	3 251	174 887	114 338	52 213	19 299	7 441	2 789	1 285	584	2	2	300	89	0.02

*Raw concentration values have been normalised to values from Sun and McDonough (1989)*

**B.3.2: SDORPB15-15c**

Sample: SDORPB15-15C																[La/Sm] <sub>N</sub>	[La/Nd] <sub>N</sub>	[Gd/Lu] <sub>N</sub>	[Dy/Lu] <sub>N</sub>	Eu/Eu*
Analysis No.	La	Ce	Pr	Nd	Sm	Eu	Gd	Tb	Dy	Ho	Er	Tm	Yb	Lu						
073d151	508 410	375 835	234 059	172 769	72 498	8 530	34 024	21 072	13 549	9 044	5 635	3 366	2 144	1 301	7	3	26	10	0.2	
074d152	493 934	375 835	238 006	173 724	70 810	8 390	31 347	18 983	12 028	8 100	5 262	3 192	2 012	1 241	7	3	25	10	0.2	
075d153	474 149	375 835	250 543	191 283	90 411	12 365	42 344	25 620	15 083	9 380	5 583	3 431	2 356	1 456	5	2	29	10	0.2	
076d154	461 479	375 835	260 285	205 085	109 421	13 706	52 073	31 486	18 321	10 845	6 388	3 804	2 529	1 513	4	2	34	12	0.2	
077d155	430 756	375 835	277 557	227 255	151 169	8 740	66 724	39 895	21 253	11 349	6 575	4 248	3 126	1 996	3	2	33	11	0.1	
083d156	486 167	375 835	236 769	175 209	76 894	8 730	36 629	22 757	14 308	9 412	5 623	3 158	1 871	1 143	6	3	32	13	0.2	
084d157	485 295	375 835	236 972	178 343	80 501	9 076	37 885	23 988	14 820	9 798	6 133	3 477	2 141	1 304	6	3	29	11	0.2	
085d158	485 720	375 835	237 065	172 767	72 311	9 044	34 455	22 290	14 876	10 369	6 789	4 139	2 635	1 703	7	3	20	9	0.2	
086d159	429 958	375 835	271 316	223 483	149 229	9 099	65 252	38 041	19 710	10 307	5 683	3 616	2 561	1 637	3	2	40	12	0.1	
087d1510	434 821	375 835	267 880	220 097	138 218	9 882	61 143	36 696	20 264	11 177	6 480	4 100	2 821	1 764	3	2	35	11	0.1	
088d1511	417 448	375 835	281 851	237 682	165 301	7 099	70 635	41 135	21 863	11 532	6 708	4 361	3 186	2 029	3	2	35	11	0.1	
089d1512	426 464	375 835	270 385	221 702	147 303	8 596	65 419	40 875	22 647	12 920	7 821	5 048	3 489	2 203	3	2	30	10	0.1	
090d1513	497 569	375 835	226 238	161 546	58 185	3 279	25 366	13 640	8 029	5 144	2 969	1 652	968	598	9	3	42	13	0.1	
091d1514	492 885	375 836	223 276	160 628	58 511	4 001	24 998	13 449	7 557	4 533	2 600	1 485	1 045	723	8	3	35	10	0.1	
092d1515	502 530	375 835	234 726	178 945	80 865	9 535	40 525	24 182	14 943	9 702	5 859	3 340	2 015	1 309	6	3	31	11	0.2	

*Raw concentration values have been normalised to values from Sun and McDonough (1989)*

**B.3.3: SDORPB16-06**

Sample:	SDORPB16-6															[La/Sm] <sub>N</sub>	[La/Nd] <sub>N</sub>	[Gd/Lu] <sub>N</sub>	[Dy/Lu] <sub>N</sub>	Eu/Eu*
Analysis No.	La	Ce	Pr	Nd	Sm	Eu	Gd	Tb	Dy	Ho	Er	Tm	Yb	Lu						
SD16-006-5	460 138	375 968	285 860	229 414	118 356	3 761	49 008	15 758	3 995	1 016	278	80	37	28	4	2	1742	142	0.04	
SD16-006-6	473 562	375 968	289 739	240 462	128 469	4 360	55 499	17 460	4 585	1 225	346	113	51	24	4	2	2310	191	0.05	
SD16-006-7	447 143	375 968	316 639	278 803	254 249	1 250	114 676	65 653	34 617	15 657	7 522	3 797	2 301	1 294	2	2	89	27	0.01	
SD16-006-8	532 534	375 968	276 910	226 080	124 658	10 042	66 318	36 297	17 016	7 394	2 630	818	332	120	4	2	555	142	0.11	
SD16-006-9	494 181	375 968	282 517	226 087	131 133	12 485	66 973	38 630	17 692	7 199	2 474	760	268	119	4	2	564	149	0.13	
SD16-006-10	484 348	375 968	291 259	240 381	165 363	20 695	98 150	56 177	27 683	11 205	4 061	1 232	479	237	3	2	415	117	0.16	
SD16-006-11	431 949	375 968	308 092	260 054	203 062	583	98 689	59 986	32 900	15 458	7 411	3 848	2 308	1 266	2	2	78	26	0.004	
SD16-006-12	427 718	375 968	311 662	262 414	200 593	554	100 034	60 830	34 517	15 702	7 548	3 899	2 317	1 326	2	2	75	26	0.004	
SD16-006-13	414 997	375 968	316 343	272 846	226 223	621	112 342	68 699	37 401	18 264	8 664	4 620	2 645	1 475	2	2	76	25	0.004	
SD16-006-14	381 603	375 968	329 287	286 340	248 468	80	114 658	69 018	34 151	15 976	7 651	4 091	2 488	1 513	2	1	76	23	0.000	
SD16-006-15	383 304	375 968	328 263	290 612	247 262	83	115 263	69 780	34 904	16 004	7 694	4 096	2 574	1 433	2	1	80	24	0.000	
SD16-006-16	428 623	375 968	314 459	273 556	224 165	866	118 877	72 466	38 677	20 014	9 822	5 014	2 791	1 633	2	2	73	24	0.005	
SD16-006-17	421 635	375 968	313 986	275 493	224 970	868	118 706	74 125	39 384	20 700	10 068	5 100	2 894	1 639	2	2	72	24	0.01	
SD16-006-18	442 287	375 968	305 584	256 350	200 404	791	103 228	63 812	35 895	17 282	8 386	4 206	2 487	1 404	2	2	74	26	0.01	
SD16-006-19	442 050	375 968	306 058	256 665	199 748	720	100 093	63 067	34 908	16 464	8 031	3 996	2 344	1 375	2	2	73	25	0.005	
SD16-006-23	433 515	375 968	309 321	261 501	203 573	586	101 255	62 239	34 099	15 763	7 612	3 947	2 368	1 341	2	2	76	25	0.004	
SD16-006-24	418 541	375 968	316 623	272 808	224 043	605	114 483	70 406	36 281	18 469	8 926	4 543	2 693	1 491	2	2	77	24	0.004	
SD16-006-25	443 149	375 968	306 338	271 433	207 737	548	100 067	62 980	34 039	15 776	7 467	3 828	2 354	1 398	2	2	72	24	0.004	

Raw concentration values have been normalised to values from Sun and McDonough (1989)

**B.3.4: SDORPB16-07b**

Sample:	SDORPB16-7B															[La/Sm] <sub>N</sub>	[La/Nd] <sub>N</sub>	[Gd/Lu] <sub>N</sub>	[Dy/Lu] <sub>N</sub>	Eu/Eu*
Analysis No.	La	Ce	Pr	Nd	Sm	Eu	Gd	Tb	Dy	Ho	Er	Tm	Yb	Lu						
SD16-007B-1	365 037	375 968	321 371	255 457	213 694	379	91 918	65 906	35 796	17 869	10 185	7 115	5 407	3 158	2	1	29	11	0.002	
SD16-007B-2	365 173	375 968	319 982	248 870	212 678	396	89 371	61 993	35 083	16 803	9 622	6 547	4 953	2 941	2	1	30	12	0.003	
SD16-007B-3	366 596	375 968	319 823	250 940	212 771	358	89 677	63 962	34 992	16 810	9 602	6 807	5 085	3 202	2	1	28	11	0.002	
SD16-007B-4	344 231	375 968	326 002	260 266	231 319	412	98 032	68 067	39 591	18 912	10 471	7 102	5 338	3 142	1	1	31	13	0.003	
SD16-007B-5	347 020	375 968	330 401	264 283	238 073	369	100 765	71 106	35 725	18 638	10 221	7 292	5 316	3 188	1	1	32	11	0.002	
SD16-007B-6	351 794	375 968	326 171	258 486	228 565	425	96 204	67 983	36 312	18 225	10 248	7 238	5 507	3 304	2	1	29	11	0.003	
SD16-007B-7	344 170	375 968	331 504	268 128	247 879	480	108 123	77 257	41 007	21 877	12 540	9 074	6 807	3 987	1	1	27	10	0.003	
SD16-007B-8	387 735	375 968	330 211	264 485	240 736	464	103 792	74 990	40 370	21 026	12 067	8 543	6 517	3 772	2	1	28	11	0.003	
SD16-007B-9	349 767	375 968	326 021	261 215	225 342	398	94 931	68 066	36 789	18 524	10 343	7 229	5 318	3 194	2	1	30	12	0.002	
SD16-007B-10	360 501	375 968	334 135	276 921	342 878	664	126 380	68 623	32 680	12 841	6 549	4 373	3 028	1 679	1	1	75	19	0.003	
SD16-007B-11	347 345	375 968	332 514	266 159	234 585	403	101 964	71 523	39 712	19 808	11 161	7 722	5 664	3 393	1	1	30	12	0.002	
SD16-007B-12	354 870	375 968	322 650	252 006	215 594	369	91 149	61 080	33 026	17 063	9 671	6 736	4 925	2 932	2	1	31	11	0.002	
SD16-007B-13	353 956	375 968	322 296	251 628	240 024	544	109 141	74 033	38 756	20 089	11 569	8 314	6 570	3 853	1	1	28	10	0.003	
SD16-007B-14	327 630	375 968	335 850	271 587	257 321	298	105 854	72 857	37 493	18 351	10 295	7 318	5 911	3 376	1	1	31	11	0.002	
SD16-007B-15	350 433	375 968	334 460	272 355	244 828	446	110 017	79 300	43 031	23 053	13 368	9 521	7 204	4 356	1	1	25	10	0.003	
SD16-007B-16	345 648	375 968	327 163	262 575	227 106	399	95 231	64 445	34 266	17 498	9 590	6 538	4 785	2 821	2	1	34	12	0.002	
SD16-007B-17	350 396	375 968	328 638	265 666	228 276	415	96 939	68 974	36 673	18 460	10 336	7 083	5 016	2 915	2	1	33	13	0.003	
SD16-007B-18	345 059	375 968	326 421	262 580	225 233	401	95 089	64 936	35 034	17 895	9 947	6 687	4 896	2 805	2	1	34	12	0.003	
SD16-007B-19	350 651	375 968	326 400	260 474	223 136	406	95 554	68 090	37 959	18 895	10 788	7 602	5 763	3 364	2	1	28	11	0.003	
SD16-007B-20	346 412	375 968	441 006	270 506	245 704	457	109 936	78 798	42 574	23 583	13 745	9 832	7 467	4 564	1	1	24	9	0.003	
SD16-007B-21	367 121	375 968	315 588	250 512	211 702	401	90 340	63 072	34 474	17 140	9 594	6 784	5 178	3 244	2	1	28	11	0.003	
SD16-007B-22	364 884	375 968	313 875	243 888	196 984	339	79 621	56 433	29 984	14 300	8 235	5 585	4 143	2 429	2	1	33	12	0.002	
SD16-007B-23	351 963	375 968	330 068	265 262	238 924	451	101 538	68 061	35 825	17 356	9 599	6 659	4 725	2 737	1	1	37	13	0.003	
SD16-007B-24	366 073	375 968	320 567	249 763	211 325	384	89 405	63 896	35 248	16 894	9 464	6 659	4 982	3 016	2	1	30	12	0.003	
SD16-007B-25	330 200	375 968	339 162	269 522	262 106	332	109 345	77 871	41 776	19 960	11 687	8 472	6 372	3 797	1	1	29	11	0.002	
SD16-007B-26	330 887	375 968	337 560	275 913	284 974	369	127 182	84 060	44 039	23 107	13 483	9 972	7 861	4 811	1	1	26	9	0.002	
SD16-007B-27	351 649	375 968	322 922	257 247	240 473	514	103 575	75 038	39 943	20 887	12 107	8 657	6 858	4 035	1	1	26	10	0.003	
SD16-007B-28	346 743	375 968	333 545	270 516	318 195	512	111 684	60 940	28 935	11 937	6 205	4 045	2 845	1 736	1	1	64	17	0.002	
SD16-007B-29	348 927	375 968	330 746	265 725	231 945	454	98 917	68 865	37 079	18 727	10 413	7 070	5 158	3 073	2	1	32	12	0.003	
SD16-007B-30	350 518	375 968	330 060	264 808	233 088	419	105 258	71 728	38 111	20 477	11 784	8 296	6 050	3 652	2	1	29	10	0.002	

Raw concentration values have been normalised to values from Sun and McDonough (1989)



**B.4: Kakamas Domain****B.4.1: SDORPB15-17**

Sample: SDORPB15-17		La	Ce	Pr	Nd	Sm	Eu	Gd	Tb	Dy	Ho	Er	Tm	Yb	Lu	[La/Sm] <sub>N</sub>	[La/Nd] <sub>N</sub>	[Gd/Lu] <sub>N</sub>	[Dy/Lu] <sub>N</sub>	Eu/Eu*
053d171		429911	375835	282557	241673	164961	4498	102159	65994	38907	21973	11671	5900	3288	1854	3	2	55	21	0.03
054d172		437747	375835	282308	232042	174997	5566	117151	80632	42074	19937	8006	3225	1484	739	3	2	159	57	0.04
055d173		428368	375835	283708	240105	162997	4265	101897	66793	38307	21931	11071	5270	2740	1462	3	2	70	26	0.03
056d174		442382	375835	276208	230810	152184	3361	90932	56334	31072	16714	7864	3480	1658	870	3	2	105	36	0.03
057d175		430765	375835	275338	236835	155798	4188	95878	62972	37531	21344	11324	5678	3096	1776	3	2	54	21	0.03
058d176		430297	375835	280826	237636	157265	4510	97296	64240	37385	21138	11163	5486	3021	1682	3	2	58	22	0.04
059d177		437714	375836	274866	226403	154575	5464	95047	63147	34467	18263	8944	4248	2303	1284	3	2	74	27	0.04
060d178		434618	375836	278341	229780	155023	5572	93241	60938	34483	19062	9831	5018	2861	1596	3	2	58	22	0.04
061d179		428627	375835	275303	226986	150101	3420	88664	56191	30975	16264	7539	3286	1555	783	3	2	113	40	0.03
062d1710		427323	375835	280300	237179	164971	4169	103994	68819	39861	22091	10965	5023	2527	1310	3	2	79	30	0.03
068d1711		428202	375835	271620	224979	151225	3993	92050	59454	32827	16818	7554	3135	1463	721	3	2	128	46	0.03
069d1712		427901	375835	278775	239092	163729	4717	103578	70086	41664	24137	12639	6359	3525	1965	3	2	53	21	0.04
070d1713		451856	375835	263152	214436	147351	4982	88908	61507	36481	20839	11033	5843	3321	1859	3	2	48	20	0.04
071d1714		424616	375835	273089	232585	158203	4689	98137	66603	38984	22265	11816	5941	3283	1799	3	2	55	22	0.04
072d1715		425207	375835	276004	235430	162336	4367	102169	67565	39395	21918	11210	5333	2814	1548	3	2	66	25	0.03

Raw concentration values have been normalised to values from Sun and McDonough (1989)

**B.4.2: SDORPB15-18**

Sample: SDORPB15-18		La	Ce	Pr	Nd	Sm	Eu	Gd	Tb	Dy	Ho	Er	Tm	Yb	Lu	[La/Sm] <sub>N</sub>	[La/Nd] <sub>N</sub>	[Gd/Lu] <sub>N</sub>	[Dy/Lu] <sub>N</sub>	Eu/Eu*
028dog181		482170	375836	261486	197716	108477	7335	49043	30693	17597	9949	5652	3263	2069	1235	4	2	40	14	0.09
029dog182		479430	375836	269133	208781	117325	5845	59458	38553	23464	14245	8582	5185	3221	1929	4	2	31	12	0.07
030dog183		488461	375836	269303	202402	116048	7384	52183	32029	18320	10017	5658	3456	2235	1307	4	2	40	14	0.09
031dog184		508901	375836	290812	232049	130865	6826	67150	44982	29604	20886	15685	13549	12995	10308	4	2	7	3	0.07
032dog185		492752	375836	273384	217803	120328	4079	63169	40875	25200	15727	9637	5647	3628	2226	4	2	28	11	0.04
038dog186		483543	375836	284474	224978	128776	4098	70664	47293	30176	19445	12090	7108	4500	2771	4	2	25	11	0.04
039dog187		509510	375836	279826	222558	124816	4051	66938	45145	28068	17842	11196	6561	4278	2680	4	2	25	10	0.04
040dog188		492326	375836	289506	232620	135146	4980	73431	48751	32122	20742	12830	8190	5395	3485	4	2	21	9	0.05

Raw concentration values have been normalised to values from Sun and McDonough (1989)

**B.4.3: SDORPB15-20**

Sample: SDORPB15-20																[La/Sm] <sub>N</sub>	[La/Nd] <sub>N</sub>	[Gd/Lu] <sub>N</sub>	[Dy/Lu] <sub>N</sub>	Eu/Eu*
Analysis No.	La	Ce	Pr	Nd	Sm	Eu	Gd	Tb	Dy	Ho	Er	Tm	Yb	Lu						
008dog201	474193	375968	287049	233801	166459	5626	81556	52175	28576	14521	8249	4931	3439	2043	3	2	40	14	0.05	
009dog202	472142	375968	289674	233354	165178	5598	80207	51560	28466	14211	8204	4888	3371	2016	3	2	40	14	0.05	
010dog203	479797	375968	293148	237689	169872	5711	83581	53616	29423	15330	8745	5289	3618	2178	3	2	38	14	0.05	
011dog204	482631	375968	296063	243466	146277	6093	84399	57796	37590	21848	12812	6645	3911	2089	3	2	40	18	0.05	
012dog205	489090	375968	283699	230802	123672	5256	67958	46325	29364	17716	10086	5209	3033	1644	4	2	41	18	0.05	
013dog206	485803	375968	293884	250673	146468	5373	81121	52412	32574	19605	11223	5873	3392	1869	3	2	43	17	0.05	
014dog207	474395	375968	289792	250378	145760	5442	80527	52225	32470	19212	10914	5601	3296	1791	3	2	45	18	0.05	
015dog208	466020	375968	292995	245827	164826	5606	86115	55851	32266	17276	9758	5603	3700	2212	3	2	39	15	0.04	
016dog209	505641	375968	271223	215105	116700	5011	62973	42194	26527	15675	8929	4717	2715	1553	4	2	41	17	0.06	
017dog2010	467888	375968	289131	236275	148518	4653	74180	49636	29167	16108	9159	5079	3206	1781	3	2	42	16	0.04	
023dog2011	473496	375968	288467	233577	160145	7391	79666	51894	29716	15745	8624	4991	3202	1765	3	2	45	17	0.06	
024dog2012	481898	375968	290257	233194	130585	5631	72130	49358	31915	19219	10781	5705	3244	1815	4	2	40	18	0.06	
025dog2013	467465	375968	292059	250145	146651	5297	81769	52967	32945	19037	10810	5697	3207	1808	3	2	45	18	0.05	
026dog2014	488448	375968	293106	251152	150239	5465	82674	54649	34393	20424	11616	6340	3693	2077	3	2	40	17	0.05	
027dog2015	468520	375968	292751	239108	170914	8016	84849	57230	32351	17284	9712	5696	3871	2266	3	2	37	14	0.06	

*Raw concentration values have been normalised to values from Sun and McDonough (1989)*

**B.4.4: SDORPB16-08**

Sample: SDORPB16-8																[La/Sm] <sub>N</sub>	[La/Nd] <sub>N</sub>	[Gd/Lu] <sub>N</sub>	[Dy/Lu] <sub>N</sub>	Eu/Eu*
Analysis No.	La	Ce	Pr	Nd	Sm	Eu	Gd	Tb	Dy	Ho	Er	Tm	Yb	Lu						
SD16-008-1	454757	375968	290121	222188	163759	5732	87506	60139	34375	19697	11094	6590	4159	2478	3	2	35	14	0.05	
SD16-008-2	429281	375968	306069	244587	184458	3550	90072	56291	31708	17043	9533	5474	3467	2102	2	2	43	15	0.03	
SD16-008-3	428549	375968	304816	242051	183142	3369	90041	59201	32046	16827	9365	5366	3381	2091	2	2	43	15	0.02	
SD16-008-4	414906	375968	319075	276099	199255	2537	112006	69322	40613	25669	14184	7677	4408	2575	2	2	43	16	0.02	
SD16-008-5	438844	375968	303636	251807	189586	6589	110067	73495	42581	26098	14387	7997	4753	2687	2	2	41	16	0.04	
SD16-008-6	415474	375968	317508	266231	183986	1140	98821	60522	34380	22011	12862	7329	4448	2657	2	2	37	13	0.01	
SD16-008-7	401574	375968	320198	274907	191781	1234	101957	64822	37930	22577	13027	7396	4461	2768	2	1	37	14	0.01	
SD16-008-8	436416	375968	316568	257327	196332	4188	107946	71157	41457	24952	13934	7686	4635	2430	2	2	44	17	0.03	
SD16-008-11	488817	375968	282238	224052	194431	10008	96430	68414	36743	19226	10590	6383	4426	2621	3	2	37	14	0.07	
SD16-008-12	408066	375968	314395	270768	182083	1626	100779	60012	35217	23447	13681	7666	4573	2827	2	2	36	12	0.01	
SD16-008-13	413384	375968	319232	272833	184709	1622	100909	62244	36985	24453	14311	7925	4941	2967	2	2	34	12	0.01	
SD16-008-14	406346	375968	316044	274764	185376	1687	103920	64681	38087	25200	14814	8033	4847	2924	2	1	36	13	0.01	
SD16-008-15	406576	375968	324743	282950	193283	1837	111503	70036	41488	27554	16382	9124	5447	3320	2	1	34	12	0.01	
SD16-008-16	412341	375968	313729	273413	179294	1758	97946	61476	36424	23386	13978	7963	4912	3165	2	2	31	12	0.01	
SD16-008-17	511605	375968	278309	224198	165197	13307	88559	59299	31127	16076	8537	4895	3146	1997	3	2	44	16	0.1	
SD16-008-18	480286	375968	293344	242300	151010	11675	91359	64670	39247	24729	13185	7006	4033	2349	3	2	39	17	0.1	
SD16-008-19	471819	375968	286187	234454	145720	10989	88965	62244	37963	22305	11672	5872	3403	1962	3	2	45	19	0.09	
SD16-008-20	475928	375968	291213	237577	184678	10175	97188	62534	34159	18391	10019	5665	3618	2146	3	2	45	16	0.07	
SD16-008-21	405747	375968	316604	276317	189905	1785	110005	67291	39453	25945	14914	7751	4582	2741	2	1	40	14	0.01	
SD16-008-22	513369	375968	286060	228241	173196	15163	89625	58376	29695	15034	8106	4379	2814	1682	3	2	53	18	0.1	
SD16-008-23	409506	375968	313155	278333	193764	1820	109749	66412	38236	26018	14729	7688	4344	2539	2	1	43	15	0.01	
SD16-008-25	497330	375968	281842	227493	157472	17055	80707	51553	25726	12831	6401	3549	2123	1228	3	2	66	21	0.1	
SD16-008-26	475255	375968	288750	232396	144406	9620	94579	61734	30285	12297	4435	1548	669	330	3	2	287	92	0.08	
SD16-008-27	478298	375968	284646	229261	143810	9705	94429	63287	30203	11975	4278	1501	638	297	3	2	318	102	0.08	
SD16-008-28	404104	375968	323640	281112	203388	2164	116998	71643	41843	26794	15586	8357	4925	2872	2	1	41	15	0.01	
SD16-008-29	442978	375968	288120	222332	162880	5950	81332	60069	32799	17177	9602	5412	3491	2091	3	2	39	16	0.05	
SD16-008-30	405186	375968	310829	271533	184776	2162	99945	58141	33573	21419	12397	7198	4470	2565	2	1	39	13	0.02	

*Raw concentration values have been normalised to values from Sun and McDonough (1989)*

**B.4.5: SDORPB16-09**

Sample: SDORPB16-9																[La/Sm] <sub>N</sub>	[La/Nd] <sub>N</sub>	[Gd/Lu] <sub>N</sub>	[Dy/Lu] <sub>N</sub>	Eu/Eu*
Analysis No.	La	Ce	Pr	Nd	Sm	Eu	Gd	Tb	Dy	Ho	Er	Tm	Yb	Lu						
SD16-009-1	433135	375968	297588	243111	164225	4039	98918	71658	44387	25756	11987	4905	2161	1028	3	2	96	43	0.03	
SD16-009-2	422303	375968	298794	241444	161821	4099	96979	75053	43557	25430	12024	4845	2165	1023	3	2	95	43	0.03	
SD16-009-3	438985	375968	297340	243890	161059	3568	98630	65596	37241	18375	6799	2130	835	365	3	2	270	102	0.03	
SD16-009-4	409026	375968	296485	233980	167750	3234	95903	65279	35169	16227	6122	2391	1120	550	2	2	174	64	0.02	
SD16-009-5	417870	375968	297592	240092	163825	3439	92825	63150	36117	17226	7265	2880	1266	571	3	2	163	63	0.03	
SD16-009-6	390585	375968	295636	233857	169796	3392	94386	67692	37956	19610	8957	4272	2315	1113	2	2	85	34	0.03	
SD16-009-7	423000	375968	293254	232632	157943	4380	90232	63634	38197	21922	9824	4278	1994	1018	3	2	89	38	0.04	
SD16-009-8	407097	375968	298163	233553	169996	3187	95959	67910	38352	18519	7959	3500	1736	887	2	2	108	43	0.02	
SD16-009-9	402077	375968	298432	239156	172844	3491	96028	71114	42002	20889	9677	4607	2406	1196	2	2	80	35	0.03	
SD16-009-10	430303	375968	295136	242875	158092	4407	92001	64203	36756	17681	6526	2108	799	330	3	2	279	111	0.04	
SD16-009-11	409559	375968	300876	244270	176669	3161	107765	75753	42169	20699	8243	3228	1426	641	2	2	168	66	0.02	
SD16-009-12	418711	375968	296559	249748	173606	4283	105161	77704	48196	27559	12583	4981	2266	1120	2	2	94	43	0.03	
SD16-009-13	399789	375968	299372	238813	175478	3508	98473	71761	40912	22255	10112	4885	2683	1434	2	2	69	29	0.03	
SD16-009-14	405582	375968	297430	235938	170906	3325	92923	66744	38720	20221	9307	4398	2389	1215	2	2	76	32	0.03	
SD16-009-15	404939	375968	302395	241637	178038	3167	103829	71748	38046	16958	6292	2390	1085	479	2	2	217	79	0.02	
SD16-009-16	393865	375968	302211	240774	180772	3536	101779	74417	42165	23046	10741	5189	2890	1598	2	2	64	26	0.03	
SD16-009-17	406026	375968	296268	237189	170821	3333	95535	66708	36658	18271	7837	3455	1792	892	2	2	107	41	0.03	
SD16-009-18	404661	375968	300631	237941	170390	4196	92177	66048	36876	18754	8142	3645	1950	933	2	2	99	40	0.03	
SD16-009-19	416930	375968	295468	241170	178277	2989	108736	75130	39447	16447	5846	1943	824	346	2	2	315	114	0.02	
SD16-009-20	411980	375968	301118	243176	173540	3921	100598	73369	43793	24593	11381	4821	2380	1135	2	2	89	39	0.03	
SD16-009-21	422800	375968	293214	241419	163837	3992	98331	70802	44506	26361	12023	4840	2198	1000	3	2	98	45	0.03	
SD16-009-22	408006	375968	298021	239015	165831	3655	91336	66557	38314	19081	8659	3896	2281	1106	2	2	83	35	0.03	
SD16-009-23	412516	375968	299809	240252	172318	3112	101192	69814	38361	17490	6862	2550	1206	533	2	2	190	72	0.02	
SD16-009-24	418848	375968	296765	237747	160486	4671	87065	62780	38978	22754	11105	5200	2714	1352	3	2	64	29	0.04	
SD16-009-25	436912	375968	288908	231648	143817	4437	78511	55742	31657	15304	5827	1845	666	272	3	2	289	116	0.04	
SD16-009-26	417517	375968	292953	236210	162920	3683	94172	64188	36875	17726	7554	3178	1872	728	3	2	129	51	0.03	
SD16-009-27	407580	375968	295688	231345	165761	3561	88566	61835	34457	16822	7371	3417	1818	911	2	2	97	38	0.03	
SD16-009-1E	425922	375968	296097	237799	163763	3967	97838	73012	43577	24944	11857	4800	2124	1004	3	2	97	43	0.03	
SD16-009-2E	426623	375968	298893	243622	165365	4061	99588	73038	44148	26331	12085	4882	2223	1065	3	2	94	41	0.03	
SD16-009-21E	414377	375968	290690	237035	161295	4017	95745	73139	44119	25298	11660	4945	2136	1024	3	2	93	43	0.03	

Raw concentration values have been normalised to values from Sun and McDonough (1989)

**B.4.6: SDORPB16-12**

Sample: SDORPB16-12																[La/Sm] <sub>N</sub>	[La/Nd] <sub>N</sub>	[Gd/Lu] <sub>N</sub>	[Dy/Lu] <sub>N</sub>	Eu/Eu*
Analysis No.	La	Ce	Pr	Nd	Sm	Eu	Gd	Tb	Dy	Ho	Er	Tm	Yb	Lu						
SD16-012-1	464767	375968	291540	240081	152259	6142	86572	58483	34574	21877	10972	4540	2124	1023	3	2	85	34	0.05	
SD16-012-2	471194	375968	290702	243005	152922	6583	87653	60752	37969	24747	12688	5568	2723	1468	3	2	60	26	0.05	
SD16-012-3	482297	375968	282969	233856	146704	5350	80600	46508	17356	5858	1994	711	346	191	3	2	421	91	0.05	
SD16-012-4	464402	375968	293767	250496	152250	8754	88071	51861	26912	11961	4290	1346	534	248	3	2	355	109	0.07	
SD16-012-5	467041	375968	284981	234964	134194	7142	64805	32849	13072	4415	1286	334	124	67	3	2	972	196	0.07	
SD16-012-6	474840	375968	289463	238807	144622	16519	80822	54138	30889	15924	8494	4329	2639	1575	3	2	51	20	0.1	
SD16-012-7	469415	375968	286945	236465	136649	11197	67913	35976	13221	4329	1241	364	144	69	3	2	983	191	0.1	
SD16-012-8	495101	375968	275606	214041	126695	14286	72525	46936	27051	16158	8792	4439	2463	1355	4	2	54	20	0.1	
SD16-012-9	468260	375968	285888	233470	126115	3163	54590	23977	11863	6330	3077	1411	719	398	4	2	137	30	0.04	
SD16-012-10	444783	375968	302877	261951	129000	2133	45348	12160	3632	1392	559	231	109	59	3	2	769	62	0.02	
SD16-012-11	478997	375968	288896	239822	128833	2088	58396	22486	7393	2616	927	355	173	105	4	2	557	70	0.02	
SD16-012-12	484289	375968	288301	240847	149573	2771	72074	31145	8942	2492	730	243	107	63	3	2	1151	143	0.03	
SD16-012-13	438460	375968	300227	257523	179063	7855	108782	64137	32427	13861	5095	1829	852	402	2	2	270	81	0.05	
SD16-012-14	461514	375968	276034	212255	147076	4953	88352	66786	43614	29636	16798	8746	5082	2860	3	2	31	15	0.04	
SD16-012-15	458966	375968	297363	247997	153963	5491	83522	54715	28877	12990	5371	2049	922	494	3	2	169	58	0.05	
SD16-012-16	449792	375968	300118	250387	156911	2319	72560	32394	10562	3263	1008	330	133	73	3	2	997	145	0.02	
SD16-012-17	476099	375968	291469	241618	130788	1684	57056	18446	5084	1612	608	215	119	68	4	2	835	74	0.02	
SD16-012-18	478446	375968	288894	243628	131124	3600	58862	26162	11483	5981	3069	1514	853	493	4	2	119	23	0.04	
SD16-012-19	484744	375968	284951	236951	128525	7712	63851	39018	19013	9121	3998	1738	864	500	4	2	128	38	0.08	
SD16-012-20	459338	375968	277561	216091	146843	4957	88902	68075	42993	29368	16511	8599	4911	2703	3	2	33	16	0.04	
SD16-012-21	459803	375968	304563	256393	152539	81231	101877	87506	70563	52477	59092	42235	38839	32843	3	2	3	2	0.64	
SD16-012-22	515613	375968	256218	185312	84247	8186	36581	19212	10648	6362	3576	1866	1125	641	6	3	57	17	0.1	
SD16-012-23	453514	375968	294488	246067	146234	10408	77759	54346	33577	19145	9376	4313	2217	1203	3	2	65	28	0.09	
SD16-012-24	457531	375968	303899	267514	170049	14093	97014	60925	35305	22204	12216	6367	3818	2230	3	2	44	16	0.1	
SD16-012-25	463955	375968	287722	241521	139472	21722	72739	51558	30149	16146	8016	4061	2359	1347	3	2	54	22	0.2	

*Raw concentration values have been normalised to values from Sun and McDonough (1989)*

## Appendix C: Monazite U-Th-Pb isotope data

Monazite U-Th-Pb isotope data was collected in three runs at two institutions. Two runs were undertaken at the Central Analytical Facility (CAF) ICP-MS facilities using Resonetics Resolution S155 Excimer (193nm) laser with an S155 Laurin Technic dual-volume sample cell coupled to an Argilent 880 triple quadrupole ICP-MS. One run was undertaken at the Research School of Earth Sciences (RSES) at the Australian National University (ANU) using an Excimer (193nm) laser with a Helix dual-volume sample cell coupled to an Argilent 7700 quadrupole ICP-MS. For the list of the respective samples analysed during the various runs, please refer to table C.1.

Table 0-2: Summary table of monazite U-Th-Pb isotope analytical runs at the indicated ICP-MS facilities.

Run 1: Argilent 8800 triple Q-LA-ICP-MS <i>Central Analytical Facility; University of Stellenbosch</i>	Run 2: Argilent 7700 Q-LA-ICP-MS <i>Research School of Earth Sciences; Australia National University</i>	Run 3: Argilent 8800 triple Q-LA-ICP-MS <i>Central Analytical Facility; University of Stellenbosch</i>
RPGV14	SD2015-10	SDORPB15-4b
RPGV16	SD2015-11	SDORPB15-7d
HS15HF1	SD2015-13	SDORPB16-4
	SDORPB15-9	SDORPB16-5
	SDORPB15-10	SDORPB16-6
	SDORPB15-15c	SDORPB16-7b
	SDORPB15-17	SDORPB16-8
	SDORPB15-18	SDORPB16-9
	SDORPB15-20	SDORPB16-12

<sup>a</sup> U and Pb concentrations and Th/U ratios are calculated relative to NIST610 glass.

<sup>b</sup> Corrected for background and within-run Pb/U fractionation and normalised to reference monazite USGS 44069 (ID-TIMS values/measured value);  $^{207}\text{Pb}/^{235}\text{U}$  calculated using  $(^{207}\text{Pb}/^{206}\text{Pb}) / (^{238}\text{U}/^{206}\text{Pb} \times 1/137.88)$ .

<sup>c</sup> Rho is the error correlation defined as the quotient of the propagated errors of the  $^{206}\text{Pb}/^{238}\text{U}$  and the  $^{207}\text{U}/^{235}\text{U}$  ratio.

<sup>d</sup> percent Concordance defined by agreement between  $^{206}\text{Pb}/^{238}\text{U}$  and  $^{207}\text{Pb}/^{206}\text{Pb}$  spot ages.

## C.1: Vioolsdrif Domain

### C.1.1: SD2015-10

SD2015-10																					
Analysis No	Th <sup>a</sup>	U <sup>a</sup>	Th/U <sup>a</sup>	Apparent spot ages (Ma)																	
	(ppm)	(ppm)		<sup>207</sup> Pb/ <sup>206</sup> Pb <sup>b</sup>	2s <sup>206</sup> Pb/ <sup>238</sup> U <sup>b</sup>	2s <sup>207</sup> Pb/ <sup>235</sup> U <sup>b</sup>	2s <sup>208</sup> Pb/ <sup>232</sup> Th <sup>b</sup>	2s	r <sup>c</sup>	<sup>207</sup> Pb/ <sup>206</sup> Pb	2s <sup>206</sup> Pb/ <sup>238</sup> U	2s <sup>207</sup> Pb/ <sup>235</sup> U	2s <sup>208</sup> Pb/ <sup>232</sup> Th	2s	%Conc <sup>d</sup>						
008dog10b1	65 056	3392	19	0.07285	0.001	0.16868	0.002	1.69429	0.02	0.05110	0.001	0.92	1010	22	1005	9.8	1006	7.4	1007	10	100
009dog10b2	48 717	2358	21	0.07294	0.001	0.17279	0.002	1.73776	0.02	0.05155	0.001	0.91	1012	23	1028	10	1023	7.6	1016	11	101
010dog10b3	48 690	2606	19	0.07341	0.001	0.16969	0.002	1.71750	0.02	0.05136	0.001	0.83	1025	25	1010	9.9	1015	8.3	1012	10	99
011dog10b4	44 278	2078	21	0.07301	0.001	0.16997	0.002	1.71114	0.02	0.05102	0.0005	0.85	1014	24	1012	9.4	1013	7.6	1006	9.4	100
012dog10b5	50 280	4868	10	0.07314	0.001	0.17007	0.002	1.71495	0.02	0.04944	0.0005	0.85	1018	24	1013	9.5	1014	7.7	975	9.3	99
014dog10b7	44 830	1626	28	0.07267	0.001	0.16831	0.002	1.68637	0.02	0.05070	0.001	0.82	1005	26	1003	11	1003	8.9	1000	11	100
016dog10b9	21 976	995	22	0.07299	0.001	0.16714	0.002	1.68206	0.02	0.04924	0.001	0.83	1014	26	996	10	1002	8.5	972	11	98
017dog10b10	20 605	704	29	0.07331	0.001	0.17061	0.002	1.72422	0.03	0.05123	0.001	0.79	1023	28	1015	11	1018	9.6	1010	11	99
023dog10b11	24 212	673	36	0.07320	0.001	0.16885	0.002	1.70417	0.02	0.04995	0.001	0.78	1020	28	1006	11	1010	9.3	985	11	99
024dog10b12	21 476	596	36	0.07291	0.001	0.16884	0.002	1.69707	0.02	0.05007	0.001	0.77	1011	28	1006	10	1007	9.0	987	10	99
025dog10b13	20 897	603	35	0.07283	0.001	0.16769	0.002	1.68409	0.02	0.05008	0.001	0.84	1009	25	999	9.9	1003	8.1	988	10	99
026dog10b14	56 383	2593	22	0.07270	0.001	0.16869	0.002	1.69107	0.02	0.05068	0.001	0.81	1006	26	1005	9.5	1005	8.1	999	9.6	100
027dog10b15	62 026	3041	20	0.07285	0.001	0.16910	0.002	1.69868	0.02	0.05093	0.001	0.89	1010	23	1007	9.8	1008	7.5	1004	10	100
<b>Excluded</b>																					
013dog10b6	34 162	991	34	0.07498	0.001	0.17007	0.002	1.75804	0.03	0.05153	0.001	0.77	1068	28	1013	10.4	1030	9.3	1016	11	95
015dog10b8	47 733	1716	28	0.07512	0.001	0.16754	0.002	1.73537	0.02	0.04887	0.0005	0.86	1072	24	999	9.5	1022	7.7	964	9	93

<sup>a</sup> U and Pb concentrations and Th/U ratios are calculated relative to NIST610 glass.

<sup>b</sup> Corrected for background and within-run Pb/U fractionation and normalised to reference monazite USGS 44069 (ID-TIMS values/measured value); <sup>207</sup>Pb/<sup>235</sup>U calculated using (207Pb/206Pb)/(238U/206Pb × 1/137.88).

<sup>c</sup> Rho is the error correlation defined as the quotient of the propagated errors of the <sup>206</sup>Pb/<sup>238</sup>U and the <sup>207</sup>U/<sup>235</sup>U ratio.

<sup>d</sup> percent Concordance defined by agreement between <sup>206</sup>Pb/<sup>238</sup>U and <sup>207</sup>Pb/<sup>206</sup>Pb spot ages.

## C.1.2: SD2015-11

SD2015-11																					
Analysis No	Th <sup>a</sup>	U <sup>a</sup>	Th/U <sup>a</sup>	Apparent spot ages (Ma)																	
	(ppm)	(ppm)	<sup>207</sup> Pb/ <sup>206</sup> Pb <sup>b</sup>	2s <sup>206</sup> Pb/ <sup>238</sup> U <sup>b</sup>	2s <sup>207</sup> Pb/ <sup>235</sup> U <sup>b</sup>	2s <sup>208</sup> Pb/ <sup>232</sup> Th <sup>b</sup>	2s	r <sup>c</sup>	<sup>207</sup> Pb/ <sup>206</sup> Pb	2s <sup>206</sup> Pb/ <sup>238</sup> U	2s <sup>207</sup> Pb/ <sup>235</sup> U	2s <sup>208</sup> Pb/ <sup>232</sup> Th	2s %Conc <sup>d</sup>								
011d114	76 691	1069	72	0.07317	0.001	0.17559	0.002	1.77144	0.02	0.05239	0.001	0.87	1019	24	1043	11	1035	8.3	1032	11	102
012d115	61 882	936	66	0.07345	0.001	0.17532	0.002	1.77532	0.02	0.05240	0.001	0.9	1026	23	1041	10	1037	7.8	1032	10	101
013d116	72 876	1137	64	0.07430	0.001	0.17374	0.002	1.77966	0.02	0.05207	0.001	0.91	1050	23	1033	10	1038	7.7	1026	10	98
015d118	43 620	736	59	0.07328	0.001	0.17525	0.002	1.77036	0.03	0.05247	0.001	0.74	1022	31	1041	11	1035	10	1034	11	102
017d1110	57 897	738	78	0.07438	0.001	0.17604	0.002	1.80533	0.03	0.05329	0.001	0.69	1052	31	1045	10	1047	10	1049	9.9	99
023d1111	67 284	1057	64	0.07455	0.001	0.17535	0.002	1.80227	0.02	0.05268	0.001	0.89	1056	24	1042	10	1046	8.0	1038	11	99
024d1112	68 705	930	74	0.07372	0.001	0.17175	0.002	1.74575	0.02	0.05152	0.0005	0.82	1034	25	1022	9.6	1026	8.0	1015	9.3	99
025d1113	43 200	852	51	0.07418	0.001	0.17129	0.002	1.75198	0.03	0.05217	0.001	0.75	1047	28	1019	10	1028	9.2	1028	10	97
026d1114	38 712	771	50	0.07398	0.001	0.17247	0.002	1.75920	0.02	0.05090	0.001	0.84	1041	26	1026	11	1031	8.8	1004	11	99
027d1115	76 004	1319	58	0.07407	0.001	0.18083	0.002	1.84688	0.03	0.05413	0.001	0.79	1044	27	1072	11	1062	9.5	1066	11	103
<i>Excluded - no <sup>207</sup>Pb/<sup>206</sup>Pb plateau</i>																					
008d111	57 716	968	60	0.09474	0.001	0.17670	0.002	2.30847	0.03	0.05309	0.001	0.77	1523	27	1049	11	1215	10.3	1046	11	69
009d112	65 478	1 155	57	0.08231	0.001	0.17815	0.002	2.02196	0.03	0.05251	0.001	0.74	1253	28	1057	11	1123	10.2	1034	10	84
010d113	65 379	1 180	55	0.07943	0.001	0.18002	0.002	1.97135	0.03	0.05358	0.001	0.84	1183	25	1067	11	1106	9.3	1055	11	90
016d119	57 789	835	69	0.17777	0.002	0.24028	0.003	5.88885	0.08	0.05344	0.001	0.89	2632	20	1388	15	1960	11.4	1052	12	53
014d117	54 737	901	61	0.09326	0.001	0.18627	0.002	2.39523	0.04	0.05263	0.001	0.7	1493	30	1101	11	1241	11.3	1037	10	74

<sup>a</sup> U and Pb concentrations and Th/U ratios are calculated relative to NIST610 glass.

<sup>b</sup> Corrected for background and within-run Pb/U fractionation and normalised to reference monazite USGS 44069 (ID-TIMS values/measured value); <sup>207</sup>Pb/<sup>235</sup>U calculated using (207Pb/206Pb)/(238U/206Pb × 1/137.88).

<sup>c</sup> Rho is the error correlation defined as the quotient of the propagated errors of the <sup>206</sup>Pb/<sup>238</sup>U and the <sup>207</sup>U/<sup>235</sup>U ratio.

<sup>d</sup> percent Concordance defined by agreement between <sup>206</sup>Pb/<sup>238</sup>U and <sup>207</sup>Pb/<sup>206</sup>Pb spot ages.



## C.1.3: SDORPB15-4B

## SD1ORPB15-4B

Analysis No	Th <sup>a</sup> (ppm)	U <sup>a</sup> (ppm)	Th/U <sup>a</sup>	Apparent spot ages (Ma)										2s %Conc <sup>d</sup>							
				<sup>207</sup> Pb/ <sup>206</sup> Pb <sup>b</sup>	2s <sup>206</sup> Pb/ <sup>238</sup> U <sup>b</sup>	2s <sup>207</sup> Pb/ <sup>235</sup> U <sup>b</sup>	2s <sup>208</sup> Pb/ <sup>232</sup> Th <sup>b</sup>	2s	r <sup>c</sup>	<sup>207</sup> Pb/ <sup>206</sup> Pb	2s <sup>206</sup> Pb/ <sup>238</sup> U	2s <sup>207</sup> Pb/ <sup>235</sup> U	2s <sup>208</sup> Pb/ <sup>232</sup> Th								
SD15-004B-1	37 069	1481	25	0.07257	0.001	0.14885	0.002	1.48890	0.02	0.05172	0.0005	0.73	1002	30	895	9.2	926	9.1	1019	10	89
SD15-004B-2	25 099	858	29	0.07242	0.001	0.14924	0.002	1.48993	0.02	0.05113	0.0005	0.78	998	28	897	9.5	926	8.9	1008	10	90
SD15-004B-3	29 053	937	31	0.07193	0.001	0.14814	0.002	1.46894	0.02	0.05067	0.0005	0.76	984	29	891	9.4	918	9.0	999	10	91
SD15-004B-4	90 008	2602	35	0.07283	0.001	0.16921	0.002	1.69897	0.02	0.04254	0.0005	0.83	1009	26	1008	11	1008	8.7	842	8.9	100
SD15-004B-5*	27 614	415	67	0.11645	0.002	0.30595	0.004	4.91197	0.08	0.09565	0.0011	0.77	1902	27	1721	19	1804	13	1846	20	90
SD15-004B-6*	68 682	1780	39	0.07994	0.001	0.13477	0.002	1.48522	0.02	0.04338	0.0005	0.82	1196	26	815	8.8	924	8.5	858	9.1	68
SD15-004B-7	29 402	1199	25	0.07306	0.001	0.15247	0.002	1.53527	0.02	0.05210	0.0005	0.75	1016	29	915	9.4	945	9.2	1027	10	90
SD15-004B-8	31 793	1225	26	0.07230	0.001	0.15002	0.002	1.49482	0.02	0.05107	0.0005	0.72	994	31	901	9.3	928	9.4	1007	9.9	91
SD15-004B-9	80 956	2511	32	0.07266	0.001	0.15817	0.002	1.58415	0.02	0.04391	0.0005	0.73	1004	30	947	9.9	964	9.6	869	9.0	94
SD15-004B-10	20 827	432	48	0.07345	0.001	0.15500	0.002	1.56937	0.03	0.05288	0.0006	0.66	1026	35	929	10	958	11	1042	11	91
SD15-004B-11	37 982	1666	23	0.07260	0.001	0.15142	0.002	1.51513	0.02	0.05248	0.0006	0.71	1003	31	909	9.6	937	9.7	1034	11	91
SD15-004B-12	25 793	1173	22	0.07329	0.001	0.15225	0.002	1.53832	0.02	0.05245	0.0006	0.74	1022	31	914	9.9	946	9.8	1033	11.0	89
SD15-004B-13	25 621	1120	23	0.07334	0.001	0.14083	0.002	1.42370	0.03	0.04936	0.0005	0.63	1024	37	849	9.3	899	11.1	974	10	83
SD15-004B-14	19 339	680	28	0.07250	0.001	0.15071	0.002	1.50602	0.03	0.05149	0.0005	0.59	1000	41	905	10.1	933	12	1015	10	90
SD15-004B-15	39 730	1141	35	0.07262	0.001	0.15206	0.002	1.52178	0.02	0.05169	0.0005	0.71	1003	31	913	9.5	939	9.6	1019	10	91
SD15-004B-16	27 636	1143	24	0.07187	0.001	0.15580	0.002	1.54392	0.03	0.05183	0.0006	0.66	982	37	933	11	948	12	1021	12	95
SD15-004B-17	30 463	1374	22	0.07271	0.001	0.14948	0.002	1.49846	0.03	0.05230	0.0006	0.69	1006	34	898	10	930	11	1030	12	89
SD15-004B-18	28 510	1099	26	0.07335	0.001	0.15230	0.002	1.54002	0.02	0.05229	0.0006	0.78	1024	28	914	9.9	947	9.2	1030	11	89
SD15-004B-19	62 064	1662	37	0.07176	0.001	0.15330	0.002	1.51599	0.02	0.04618	0.0005	0.71	979	31	919	9.6	937	9.7	912	9.2	94
SD15-004B-20	14 231	933	15	0.07234	0.001	0.15001	0.002	1.49608	0.03	0.05280	0.0006	0.68	996	34	901	9.8	929	10	1040	11	90
SD15-004B-22	26 163	1040	25	0.07288	0.001	0.15536	0.002	1.56108	0.03	0.05286	0.0006	0.68	1011	35	931	11	955	11	1041	11	92
SD15-004B-23	79 038	1874	42	0.07234	0.001	0.15076	0.002	1.50332	0.02	0.04481	0.0005	0.81	995	27	905	9.5	932	8.5	886	9.2	91
SD15-004B-24	35 353	1100	32	0.07283	0.001	0.15116	0.002	1.51783	0.02	0.05117	0.0006	0.76	1009	30	908	10	938	9.5	1009	11	90
SD15-004B-25	122 878	4222	29	0.07241	0.001	0.16771	0.002	1.67413	0.02	0.04516	0.0005	0.86	998	25	1000	10	999	8.4	893	9.4	100

<sup>a</sup> U and Pb concentrations and Th/U ratios are calculated relative to NIST610 glass.

<sup>b</sup> Corrected for background and within-run Pb/U fractionation and normalised to reference monazite USGS 44069 (ID-TIMS values/measured value); <sup>207</sup>Pb/<sup>235</sup>U calculated using (<sup>207</sup>Pb/<sup>206</sup>Pb)/(<sup>238</sup>U/<sup>206</sup>Pb × 1/137.88).

<sup>c</sup> Rho is the error correlation defined as the quotient of the propagated errors of the <sup>206</sup>Pb/<sup>238</sup>U and the <sup>207</sup>U/<sup>235</sup>U ratio.

<sup>d</sup> percent Concordance defined by agreement between <sup>206</sup>Pb/<sup>238</sup>U and <sup>207</sup>Pb/<sup>206</sup>Pb spot ages.

**C.1.4: SDORPB15-07D****SDORPB15-7D**

Analysis No	Th <sup>a</sup>	U <sup>a</sup>	Th/U <sup>a</sup>	Apparent spot ages (Ma)										2s %Conc <sup>d</sup>							
	(ppm)	(ppm)	<sup>207</sup> Pb/ <sup>206</sup> Pb <sup>b</sup>	2s <sup>206</sup> Pb/ <sup>238</sup> U <sup>b</sup>	2s <sup>207</sup> Pb/ <sup>235</sup> U <sup>b</sup>	2s <sup>208</sup> Pb/ <sup>232</sup> Th <sup>b</sup>	2s	r <sup>c</sup>	<sup>207</sup> Pb/ <sup>206</sup> Pb	2s <sup>206</sup> Pb/ <sup>238</sup> U	2s <sup>207</sup> Pb/ <sup>235</sup> U	2s <sup>208</sup> Pb/ <sup>232</sup> Th									
SD15-007D-1	177 332	9401	19	0.07239	0.001	0.17255	0.002	1.72218	0.02	0.04614	0.0005	0.89	997	32	1026	11	1017	8.3	912	9.8	103
SD15-007D-2	178 189	8634	21	0.07205	0.001	0.17055	0.002	1.69421	0.02	0.04584	0.0005	0.88	988	24	1015	11	1006	8.5	906	9.9	103
SD15-007D-3	126 570	4725	27	0.07297	0.001	0.17400	0.002	1.75084	0.02	0.04663	0.0005	0.85	1013	24	1034	11	1028	8.7	921	9.9	102
SD15-007D-4	130 982	4678	28	0.07264	0.001	0.17308	0.002	1.73315	0.03	0.04677	0.0005	0.8	1004	25	1029	12	1021	9.8	924	10	103
SD15-007D-5	94 957	3763	25	0.07252	0.001	0.17506	0.002	1.75045	0.02	0.04602	0.0005	0.88	1001	28	1040	11	1027	8.4	909	9.6	104
SD15-007D-6	201 418	12735	16	0.07209	0.001	0.16986	0.002	1.68796	0.02	0.04596	0.0005	0.86	988	24	1011	11	1004	8.9	908	10	102
SD15-007D-10	153 008	13631	11	0.07232	0.001	0.16859	0.002	1.68070	0.02	0.04602	0.0005	0.83	995	25	1004	11	1001	9.4	909	10	101
SD15-007D-11	145 735	12548	12	0.07211	0.001	0.16571	0.002	1.64741	0.02	0.04595	0.0005	0.86	989	18	988	10	989	8.1	908	9.2	100
SD15-007D-12	129 673	11443	11	0.07268	0.001	0.16942	0.002	1.69762	0.02	0.04575	0.0005	0.92	1005	24	1009	11	1008	8.0	904	9.5	100
SD15-007D-14	130 996	3746	35	0.07281	0.001	0.16690	0.002	1.67534	0.03	0.04560	0.0005	0.81	1009	30	995	11	999	9.5	901	10	99
SD15-007D-15	130 561	3501	37	0.07227	0.001	0.16950	0.002	1.68870	0.03	0.04558	0.0005	0.8	994	27	1009	11	1004	9.8	901	10	102
SD15-007D-17	130 971	3636	36	0.07219	0.001	0.16759	0.002	1.66793	0.03	0.04502	0.0005	0.78	991	28	999	11	996	9.9	890	10	101
<b>Inheritance - 1089 Ma</b>																					
SD15-007D-7	222 143	11748	19	0.07592	0.001	0.16850	0.002	1.76345	0.02	0.04057	0.0005	0.85	1093	26	1004	11	1032	9.1	804	9.0	92
SD15-007D-9	178 297	8415	21	0.07562	0.001	0.17247	0.002	1.79804	0.02	0.04544	0.0005	0.85	1085	24	1026	11	1045	8.6	898	9.2	95
SD15-007D-19	180 797	5043	36	0.07510	0.001	0.17808	0.002	1.84354	0.02	0.04603	0.0005	0.87	1071	32	1057	11	1061	8.8	910	9.8	99
<b>Inheritance - 1209 Ma</b>																					
SD15-007D-8	174 032	8403	21	0.08106	0.001	0.15935	0.002	1.78076	0.02	0.04447	0.0005	0.86	1223	25	953	10	1039	8.6	880	9.1	78
SD15-007D-13	133 365	10343	13	0.08020	0.001	0.15019	0.002	1.66106	0.03	0.03449	0.0004	0.72	1202	23	902	9.8	994	10	685	7.5	75
SD15-007D-16	145 251	3211	45	0.08021	0.001	0.16939	0.002	1.87319	0.03	0.04031	0.0005	0.79	1202	28	1009	11	1072	10	799	8.9	84

<sup>a</sup> U and Pb concentrations and Th/U ratios are calculated relative to NIST610 glass.

<sup>b</sup> Corrected for background and within-run Pb/U fractionation and normalised to reference monazite USGS 44069 (ID-TIMS values/measured value); <sup>207</sup>Pb/<sup>235</sup>U calculated using (<sup>207</sup>Pb/<sup>206</sup>Pb)/(<sup>238</sup>U/<sup>206</sup>Pb × 1/137.88).

<sup>c</sup> Rho is the error correlation defined as the quotient of the propagated errors of the <sup>206</sup>Pb/<sup>238</sup>U and the <sup>207</sup>U/<sup>235</sup>U ratio.

<sup>d</sup> percent Concordance defined by agreement between <sup>206</sup>Pb/<sup>238</sup>U and <sup>207</sup>Pb/<sup>206</sup>Pb spot ages.

**C.1.5: SDORPB15-9**

SDORPB15-9																					
Analysis No	Th <sup>a</sup>	U <sup>a</sup>	Th/U <sup>a</sup>	Apparent spot ages (Ma)																	
	(ppm)	(ppm)		<sup>207</sup> Pb/ <sup>206</sup> Pb <sup>b</sup>	2s	<sup>206</sup> Pb/ <sup>238</sup> U <sup>b</sup>	2s	<sup>207</sup> Pb/ <sup>235</sup> U <sup>b</sup>	2s	<sup>208</sup> Pb/ <sup>232</sup> Th <sup>b</sup>	2s	r <sup>c</sup>	<sup>207</sup> Pb/ <sup>206</sup> Pb	2s	<sup>206</sup> Pb/ <sup>238</sup> U	2s	<sup>207</sup> Pb/ <sup>235</sup> U	2s	<sup>208</sup> Pb/ <sup>232</sup> Th	2s	%Conc <sup>d</sup>
028dog91	74 936	5778	13	0.07170	0.001	0.16729	0.002	1.65379	0.02	0.05038	0.001	0.95	978	22	997	9.6	991	7.0	993	9.8	102
029dog92	80 255	6042	13	0.07114	0.001	0.16715	0.002	1.63961	0.02	0.05013	0.001	0.96	962	21	996	9.8	986	7.0	989	10	104
030dog93	86 561	5775	15	0.07227	0.001	0.16323	0.002	1.62642	0.02	0.04734	0.0005	0.95	994	21	975	9.6	981	7.0	935	9.5	98
031dog94	125 634	2007	63	0.07189	0.001	0.16942	0.002	1.67934	0.02	0.05080	0.0005	0.67	983	31	1009	9.1	1001	9.2	1002	8.8	103
032dog95	57 038	4609	12	0.07226	0.001	0.16772	0.002	1.67105	0.02	0.04906	0.0005	0.94	993	22	1000	9.7	998	7.1	968	9.6	101
038dog96	129 511	1840	70	0.07189	0.001	0.17217	0.002	1.70656	0.02	0.05071	0.001	0.9	983	23	1024	10	1011	7.6	1000	10	104
039dog97	151 571	2596	58	0.07316	0.001	0.17297	0.002	1.74477	0.02	0.04693	0.0005	0.93	1019	22	1028	10	1025	7.4	927	9.4	101
040dog98	100 183	6649	15	0.07152	0.001	0.16793	0.002	1.65598	0.02	0.05073	0.001	0.92	972	22	1001	9.7	992	7.1	1000	10	103
041dog99	84 606	5446	16	0.07116	0.001	0.16830	0.002	1.65111	0.02	0.05082	0.001	0.93	962	22	1003	10	990	7.4	1002	11	104
042dog910	78 602	6042	13	0.07191	0.001	0.16806	0.002	1.66627	0.02	0.05043	0.001	0.93	984	22	1001	9.7	996	7.1	994	9.9	102
043dog911	87 286	1461	60	0.07198	0.001	0.17117	0.002	1.69841	0.02	0.05124	0.001	0.83	985	26	1019	10	1008	8.4	1010	11	103
044dog912	81 008	1447	56	0.07232	0.001	0.16680	0.002	1.66274	0.03	0.04910	0.001	0.77	995	29	994	11	994	9.7	969	11	100
046dog914	125 626	1894	66	0.07202	0.001	0.16785	0.002	1.66673	0.02	0.05114	0.001	0.89	987	23	1000	9.7	996	7.5	1008	10	101

<sup>a</sup> U and Pb concentrations and Th/U ratios are calculated relative to NIST610 glass.

<sup>b</sup> Corrected for background and within-run Pb/U fractionation and normalised to reference monazite USGS 44069 (ID-TIMS values/measured value); <sup>207</sup>Pb/<sup>235</sup>U calculated using (<sup>207</sup>Pb/<sup>206</sup>Pb)/(<sup>238</sup>U/<sup>206</sup>Pb × 1/137.88).

<sup>c</sup> Rho is the error correlation defined as the quotient of the propagated errors of the <sup>206</sup>Pb/<sup>238</sup>U and the <sup>207</sup>U/<sup>235</sup>U ratio.

<sup>d</sup> percent Concordance defined by agreement between <sup>206</sup>Pb/<sup>238</sup>U and <sup>207</sup>Pb/<sup>206</sup>Pb spot ages.

## C.1.6: SDORPB16-4

## SDORPB16-4

Analysis No	Th <sup>a</sup> (ppm)	U <sup>a</sup> (ppm)	Th/U <sup>a</sup>	Apparent spot ages (Ma)										2s %Conc <sup>d</sup>							
				<sup>207</sup> Pb/ <sup>206</sup> Pb <sup>b</sup>	2s	<sup>206</sup> Pb/ <sup>238</sup> U <sup>b</sup>	2s	<sup>207</sup> Pb/ <sup>235</sup> U <sup>b</sup>	2s	<sup>208</sup> Pb/ <sup>232</sup> Th <sup>b</sup>	2s	r <sup>c</sup>	<sup>207</sup> Pb/ <sup>206</sup> Pb		2s	<sup>206</sup> Pb/ <sup>238</sup> U	2s	<sup>207</sup> Pb/ <sup>235</sup> U	2s	<sup>208</sup> Pb/ <sup>232</sup> Th	2s
SD16-004-1	65 898	2512	26	0.07238	0.001	0.14471	0.002	1.44407	0.02	0.04635	0.0005	0.84	997	25	871	8.9	907	7.9	916	9.2	87
SD16-004-2	72 278	1675	43	0.07237	0.001	0.14869	0.002	1.48343	0.02	0.04464	0.0005	0.8	996	27	894	9.2	924	8.4	883	8.9	90
SD16-004-3	82 636	2062	40	0.07227	0.001	0.14764	0.002	1.47115	0.02	0.04417	0.0005	0.84	994	25	888	9.2	919	8.0	874	8.9	89
SD16-004-4	57 780	2747	21	0.07237	0.001	0.15240	0.002	1.52013	0.03	0.05224	0.0006	0.66	996	38	914	11	939	12	1029	12	92
SD16-004-6	59 180	2254	26	0.07221	0.001	0.15029	0.002	1.49620	0.02	0.05178	0.0006	0.86	992	25	903	9.4	929	8.0	1020	10	91
SD16-004-7	51 568	2155	24	0.07170	0.001	0.15084	0.002	1.49106	0.02	0.05149	0.0006	0.82	977	27	906	9.7	927	8.6	1015	11	93
SD16-004-9	69 490	2728	25	0.07225	0.001	0.16315	0.002	1.62516	0.03	0.04695	0.0005	0.76	993	30	974	11	980	9.9	927	10	98
SD16-004-10	99 296	2466	40	0.07190	0.001	0.14822	0.002	1.46911	0.02	0.04466	0.0005	0.81	983	26	891	9.0	918	8.0	883	8.7	91
SD16-004-11	104 852	2612	40	0.07235	0.001	0.14806	0.002	1.47621	0.02	0.04433	0.0004	0.75	996	29	890	9.0	921	8.7	877	8.5	89
SD16-004-12	85 045	1875	45	0.07203	0.001	0.14641	0.002	1.45393	0.02	0.04398	0.0005	0.76	987	29	881	9.4	912	9.1	870	9.1	89
SD16-004-13	83 084	1823	46	0.07173	0.001	0.14532	0.002	1.43689	0.02	0.04365	0.0004	0.72	978	31	875	9.0	904	9.2	864	8.6	89
SD16-004-14	57 796	1748	33	0.07191	0.001	0.15135	0.002	1.50050	0.02	0.05235	0.0006	0.79	984	27	909	9.6	931	8.7	1031	11	92
SD16-004-15	75 265	1436	52	0.07295	0.001	0.14684	0.002	1.47652	0.02	0.04385	0.0004	0.74	1013	29	883	9.1	921	9.0	867	8.5	87
SD16-004-17	45 492	1871	24	0.07197	0.001	0.14678	0.002	1.45629	0.02	0.05136	0.0006	0.81	985	27	883	9.3	913	8.4	1012	11	90
SD16-004-18	65 277	1452	45	0.07235	0.001	0.14913	0.002	1.48758	0.02	0.04827	0.0005	0.75	996	30	896	9.8	925	9.4	953	10	90
SD16-004-21	84 019	1643	51	0.07278	0.001	0.14407	0.002	1.44574	0.03	0.04362	0.0005	0.69	1008	33	868	9.7	908	10	863	9.4	86
SD16-004-22	59 153	2390	25	0.07268	0.001	0.14848	0.002	1.48781	0.02	0.05132	0.0006	0.77	1005	28	893	9.5	925	8.9	1012	11	89
SD16-004-23	59 132	2330	25	0.07238	0.001	0.14623	0.002	1.45908	0.02	0.05091	0.0005	0.82	997	26	880	9.2	914	8.2	1004	10	88
SD16-004-24	100 323	2308	43	0.07258	0.001	0.15028	0.002	1.50332	0.02	0.04503	0.0005	0.73	1002	30	903	9.3	932	9.1	890	8.8	90
SD16-004-25	101 408	2375	43	0.07222	0.001	0.14990	0.002	1.49264	0.02	0.04529	0.0005	0.79	992	28	900	9.6	927	8.7	895	9.4	91
<i>Excluded - no <sup>207</sup>Pb/<sup>206</sup>Pb plateau</i>																					
SD16-004-5	79 296	1 449	55	0.07415	0.001	0.14445	0.002	1.47676	0.03	0.04373	0.0005	0.69	1046	33	870	9.7	921	10.5	865	9.2	83
SD16-004-8	67 421	2 320	29	0.07425	0.001	0.14513	0.002	1.48569	0.02	0.04685	0.0005	0.8	1048	27	874	9.5	925	8.8	926	9.9	83
SD16-004-16	76 810	1 378	56	0.07984	0.001	0.15017	0.002	1.65295	0.03	0.04414	0.0005	0.75	1193	29	902	9.8	991	9.8	873	9.3	76
SD16-004-20	81 011	1 512	54	0.07594	0.001	0.14489	0.002	1.51679	0.03	0.04446	0.0005	0.71	1093	33	872	10	937	11	879	9.7	80
SD16-004-19	42 991	1 103	39	0.08129	0.001	0.16136	0.002	1.80830	0.03	0.05165	0.0006	0.8	1229	26	964	10	1049	9.2	1018	11	78

<sup>a</sup> U and Pb concentrations and Th/U ratios are calculated relative to NIST610 glass.

<sup>b</sup> Corrected for background and within-run Pb/U fractionation and normalised to reference monazite USGS 44069 (ID-TIMS values/measured value); <sup>207</sup>Pb/<sup>235</sup>U calculated using (<sup>207</sup>Pb/<sup>206</sup>Pb)/(<sup>238</sup>U/<sup>206</sup>Pb × 1/137.88).

<sup>c</sup> Rho is the error correlation defined as the quotient of the propagated errors of the <sup>206</sup>Pb/<sup>238</sup>U and the <sup>207</sup>U/<sup>235</sup>U ratio.

<sup>d</sup> percent Concordance defined by agreement between <sup>206</sup>Pb/<sup>238</sup>U and <sup>207</sup>Pb/<sup>206</sup>Pb spot ages.

## C.1.7: SDORPB16-5

SDORPB16-5																					
Analysis No	Th <sup>a</sup>		U <sup>a</sup> Th/U <sup>a</sup>	207Pb/206Pb <sup>b</sup>	2s	206Pb/238U <sup>b</sup>	2s	207Pb/235U <sup>b</sup>	2s	208Pb/232Th <sup>b</sup>	2s	r <sup>c</sup>	Apparent spot ages (Ma)				2s	%Conc <sup>d</sup>			
	(ppm)	(ppm)											207Pb/206Pb	2s	206Pb/238U	2s			207Pb/235U	2s	208Pb/232Th
SD16-005-1	94 291	18246	5	0.07307	0.001	0.17413	0.002	1.75434	0.02	0.04677	0.0005	0.93	1016	22	1035	11	1029	7.9	924	9.8	102
SD16-005-2	107 668	14922	7	0.07342	0.001	0.17669	0.002	1.78855	0.02	0.04729	0.0005	0.92	1026	23	1049	11	1041	8.4	934	10	102
SD16-005-3	93 913	19149	5	0.07331	0.001	0.16137	0.002	1.63079	0.02	0.04637	0.0005	0.94	1023	22	964	10	982	7.6	916	9.6	94
SD16-005-5	18 629	280	66	0.07259	0.002	0.15385	0.002	1.53979	0.04	0.05103	0.0006	0.51	1002	53	923	12	946	16	1006	11	92
SD16-005-6	14 686	238	62	0.07216	0.002	0.15341	0.002	1.52627	0.05	0.05072	0.0006	0.48	991	60	920	12	941	18	1000	11	93
SD16-005-8	14 874	242	61	0.07250	0.002	0.15431	0.002	1.54217	0.04	0.05079	0.0006	0.51	1000	54	925	12	947	17	1001	11	93
SD16-005-9	15 028	237	63	0.07258	0.002	0.15245	0.002	1.52566	0.04	0.05003	0.0006	0.51	1002	52	915	11	941	16	987	11	91
SD16-005-11	13 225	222	60	0.07318	0.002	0.15296	0.002	1.54325	0.03	0.05040	0.0006	0.58	1019	43	918	11	948	13	994	11	90

<sup>a</sup> U and Pb concentrations and Th/U ratios are calculated relative to NIST610 glass.

<sup>b</sup> Corrected for background and within-run Pb/U fractionation and normalised to reference monazite USGS 44069 (ID-TIMS values/measured value); 207Pb/235U calculated using (207Pb/206Pb)/(238U/206Pb × 1/137.88).

<sup>c</sup> Rho is the error correlation defined as the quotient of the propagated errors of the 206Pb/238U and the 207U/235U ratio.

<sup>d</sup> percent Concordance defined by agreement between 206Pb/238U and 207Pb/206Pb spot ages.

## C.2: Pella Domain

## C.2.1: RPGV14

RPGV14																					
Analysis No	Th <sup>a</sup>	U <sup>a</sup>	Th/U <sup>a</sup>	Apparent spot ages (Ma)																	
	(ppm)	(ppm)		<sup>207</sup> Pb/ <sup>206</sup> Pb <sup>b</sup>	2s <sup>206</sup> Pb/ <sup>238</sup> U <sup>b</sup>	2s <sup>207</sup> Pb/ <sup>235</sup> U <sup>b</sup>	2s <sup>208</sup> Pb/ <sup>232</sup> Th <sup>b</sup>	2s	r <sup>c</sup>	<sup>207</sup> Pb/ <sup>206</sup> Pb	2s <sup>206</sup> Pb/ <sup>238</sup> U	2s <sup>207</sup> Pb/ <sup>235</sup> U	2s <sup>208</sup> Pb/ <sup>232</sup> Th	2s	%Conc <sup>d</sup>						
V14_1	51 929	13 082	4	0.07062	0.001	0.16429	0.002	1.59964	0.02	0.04939	0.0006	0.86	946	26	981	11	970	9.0	974	12	104
V14_2	60 560	5 181	12	0.07168	0.001	0.16544	0.002	1.63511	0.02	0.05015	0.0006	0.85	977	26	987	11	984	9.2	989	12	101
V14_3	56 388	8 433	7	0.07081	0.001	0.16263	0.002	1.58778	0.02	0.04934	0.0006	0.83	952	27	971	11	965	9.2	974	11	102
V14_4	41 158	10 062	4	0.07151	0.001	0.16214	0.002	1.59863	0.02	0.04939	0.0006	0.86	972	25	969	11	970	8.9	974	11	100
V14_5	67 860	5 964	11	0.07150	0.001	0.16286	0.002	1.60553	0.02	0.05055	0.0006	0.85	972	26	973	11	972	9.2	997	12	100
V14_6	52 832	10 503	5	0.07076	0.001	0.16487	0.002	1.60879	0.02	0.04955	0.0006	0.84	951	26	984	11	974	9.1	978	11	104
V14_7	45 099	11 371	4	0.07109	0.001	0.16234	0.002	1.59103	0.03	0.04951	0.0006	0.81	960	28	970	12	967	9.9	977	12	101
V14_8	40 192	14 053	3	0.07141	0.001	0.16296	0.002	1.60463	0.03	0.05004	0.0006	0.77	969	29	973	11	972	9.8	987	11	100
V14_9	50 484	9 497	5	0.07127	0.001	0.16311	0.002	1.60313	0.02	0.04921	0.0006	0.85	965	26	974	11	971	9.0	971	11	101
V14_11	46 656	8 754	5	0.07151	0.001	0.16262	0.002	1.60337	0.02	0.04957	0.0006	0.85	972	26	971	11	972	9.2	978	12	100
V14_12	39 895	5 923	7	0.07122	0.001	0.16257	0.002	1.59644	0.02	0.04953	0.0006	0.84	964	27	971	11	969	9.2	977	11	101
V14_13	52 209	13 917	4	0.07146	0.001	0.16264	0.002	1.60259	0.02	0.04939	0.0006	0.85	971	26	971	11	971	9.0	974	11	100
V14_14	64 394	8 668	7	0.07056	0.001	0.16307	0.002	1.58669	0.03	0.04970	0.0006	0.77	945	30	974	11	965	10	980	12	103
V14_16	60 974	11 402	5	0.07175	0.001	0.16504	0.002	1.63262	0.03	0.05155	0.0007	0.71	979	35	985	12	983	12	1016	13	101
V14_17	31 523	12 400	3	0.07154	0.001	0.16395	0.002	1.61727	0.02	0.05051	0.0006	0.82	973	27	979	11	977	9.4	996	12	101
V14_18	40 467	8 472	5	0.07167	0.001	0.16243	0.002	1.60554	0.02	0.05025	0.0006	0.83	977	27	970	11	972	9.3	991	12	99
V14_19	40 839	11 733	3	0.07162	0.001	0.16161	0.002	1.59603	0.02	0.05043	0.0006	0.8	975	28	966	11	969	9.6	994	12	99
V14_20	40 037	8 520	5	0.07172	0.001	0.16331	0.002	1.61519	0.03	0.05016	0.0006	0.79	978	29	975	11	976	9.8	989	12	100
V14_21	53 740	5 037	11	0.07225	0.001	0.16265	0.002	1.62035	0.03	0.04937	0.0006	0.8	993	29	972	11	978	10	974	12	98
V14_22	52 800	11 255	5	0.07179	0.001	0.16285	0.002	1.61207	0.03	0.04956	0.0006	0.8	980	29	973	11	975	9.9	978	12	99
V14_23	23 965	4 901	5	0.07149	0.001	0.16280	0.002	1.60497	0.03	0.04903	0.0006	0.77	971	30	972	11	972	10	968	11	100
V14_24	14 363	13 817	1	0.07210	0.002	0.16753	0.002	1.66550	0.04	0.05344	0.0007	0.58	989	42	999	12	996	14	1052	13	101
V14_25	54 035	5 886	9	0.07160	0.001	0.16427	0.002	1.62201	0.03	0.04966	0.0006	0.77	975	30	981	11	979	10	980	12	101
<b>Excluded</b>																					
V14_10	51 418	20 256	3	0.06755	0.001	0.17020	0.002	1.58530	0.02	0.05004	0.0006	0.87	855	26	1013	12	965	8.8	987	12	119
V14_15	49 492	1 966	25	0.07981	0.001	0.17000	0.002	1.87075	0.03	0.04879	0.0006	0.76	1192	30	1012	12	1071	11	963	12	85

<sup>a</sup> U and Pb concentrations and Th/U ratios are calculated relative to NIST610 glass.

<sup>b</sup> Corrected for background and within-run Pb/U fractionation and normalised to reference monazite USGS 44069 (ID-TIMS values/measured value); <sup>207</sup>Pb/<sup>235</sup>U calculated using (207Pb/206Pb)/(238U/206Pb × 1/137.88).

<sup>c</sup> Rho is the error correlation defined as the quotient of the propagated errors of the <sup>206</sup>Pb/<sup>238</sup>U and the <sup>207</sup>U/<sup>235</sup>U ratio.

<sup>d</sup> percent Concordance defined by agreement between <sup>206</sup>Pb/<sup>238</sup>U and <sup>207</sup>Pb/<sup>206</sup>Pb spot ages.

## C.2.2: RPGV16

RPGV16																					
Analysis No	Th <sup>a</sup> (ppm)	U <sup>a</sup> (ppm)	Th/U <sup>a</sup>	<sup>207</sup> Pb/ <sup>206</sup> Pb <sup>b</sup>	2s <sup>206</sup> Pb/ <sup>238</sup> U <sup>b</sup>	2s <sup>207</sup> Pb/ <sup>235</sup> U <sup>b</sup>	2s <sup>208</sup> Pb/ <sup>232</sup> Th <sup>b</sup>	2s	Apparent spot ages (Ma)												
									r <sup>c</sup>	<sup>207</sup> Pb/ <sup>206</sup> Pb	2s <sup>206</sup> Pb/ <sup>238</sup> U	2s <sup>207</sup> Pb/ <sup>235</sup> U	2s <sup>208</sup> Pb/ <sup>232</sup> Th	2s %Conc <sup>d</sup>							
V16_1	43 355	3 520	12	0.07189	0.001	0.16269	0.002	1.61296	0.03	0.05032	0.0006	0.74	983	31	972	11	975	10	992	12	99
V16_2	57 714	4 002	14	0.07148	0.001	0.16716	0.002	1.64760	0.03	0.05138	0.0006	0.75	971	31	996	12	989	11	1013	12	103
V16_3	74 581	3 288	23	0.07253	0.001	0.16701	0.002	1.67057	0.03	0.05157	0.0006	0.77	1001	30	996	11	997	10	1016	12	99
V16_4	104 246	3 900	27	0.07167	0.001	0.16744	0.002	1.65473	0.03	0.05177	0.0006	0.77	977	30	998	12	991	10	1020	12	102
V16_5	59 850	2 661	22	0.07143	0.001	0.16246	0.002	1.59994	0.03	0.04930	0.0006	0.72	970	34	970	12	970	11	973	12	100
V16_6	52 016	7 303	7	0.07148	0.001	0.16567	0.002	1.63316	0.03	0.05016	0.0006	0.81	971	28	988	11	983	10	989	12	102
V16_9	85 910	3 708	23	0.07266	0.001	0.16451	0.002	1.64806	0.03	0.05176	0.0007	0.67	1005	37	982	12	989	13	1020	13	98
V16_10	73 769	14 501	5	0.07165	0.001	0.16666	0.002	1.64666	0.03	0.05284	0.0006	0.67	976	34	994	11	988	11	1041	12	102
V16_11	98 197	4 039	24	0.07180	0.001	0.16515	0.002	1.63534	0.03	0.05208	0.0006	0.72	980	33	985	11	984	11	1026	12	101
V16_12	89 877	1 231	73	0.07223	0.002	0.17740	0.002	1.76757	0.04	0.05329	0.0007	0.58	993	45	1053	13	1034	15	1050	13	106
V16_15	47 208	3 212	15	0.07219	0.001	0.16385	0.002	1.63123	0.03	0.04982	0.0006	0.76	991	31	978	11	982	11	983	12	99
V16_16	91 251	3 263	28	0.07220	0.001	0.16598	0.002	1.65276	0.03	0.05231	0.0006	0.75	992	31	990	12	991	11	1031	12	100
V16_17	35 319	1 164	30	0.07235	0.002	0.17048	0.002	1.70100	0.05	0.05101	0.0006	0.46	996	59	1015	13	1009	19	1006	12	102
V16_18	84 374	3 455	24	0.07243	0.001	0.16857	0.002	1.68378	0.03	0.05208	0.0007	0.72	998	33	1004	12	1002	11	1026	12	101
V16_19	89 066	3 271	27	0.07187	0.001	0.16439	0.002	1.62936	0.03	0.05171	0.0006	0.74	982	31	981	11	982	11	1019	12	100
V16_20	40 884	3 699	11	0.07224	0.001	0.16191	0.002	1.61287	0.03	0.05009	0.0006	0.75	993	31	967	11	975	10	988	12	97
V16_21	106 521	3 502	30	0.07224	0.001	0.16651	0.002	1.65898	0.03	0.05177	0.0006	0.75	993	31	993	12	993	11	1020	12	100
V16_22	80 279	2 981	27	0.07196	0.001	0.16642	0.002	1.65153	0.03	0.05330	0.0007	0.74	985	32	992	12	990	11	1050	13	101
V16_25	80 445	1 212	66	0.07140	0.001	0.17508	0.002	1.72395	0.03	0.05348	0.0007	0.69	969	35	1040	12	1018	12	1053	13	107
<b>Inheritance</b>																					
V16_8	174 269	15 350	11	0.07630	0.001	0.16801	0.002	1.76743	0.04	0.05032	0.0007	0.67	1103	37	1001	12	1034	13	992	13	91
V16_13	42 494	4 225	10	0.07683	0.001	0.18979	0.002	2.01091	0.03	0.05748	0.0007	0.78	1117	29	1120	13	1119	11	1130	14	100
V16_14	73 713	3 052	24	0.07695	0.001	0.16533	0.002	1.75390	0.03	0.05173	0.0007	0.68	1120	36	986	12	1029	13	1019	13	88
V16_23	81 061	3 130	26	0.07572	0.001	0.15810	0.002	1.65095	0.03	0.04932	0.0006	0.74	1088	31	946	11	990	11	973	12	87
V16_24	71 791	2 941	24	0.07648	0.001	0.16705	0.002	1.76166	0.03	0.05182	0.0006	0.74	1108	31	996	12	1032	11	1021	12	90

<sup>a</sup> U and Pb concentrations and Th/U ratios are calculated relative to NIST610 glass.

<sup>b</sup> Corrected for background and within-run Pb/U fractionation and normalised to reference monazite USGS 44069 (ID-TIMS values/measured value); <sup>207</sup>Pb/<sup>235</sup>U calculated using (<sup>207</sup>Pb/<sup>206</sup>Pb)/(<sup>238</sup>U/<sup>206</sup>Pb × 1/137.88).

<sup>c</sup> Rho is the error correlation defined as the quotient of the propagated errors of the <sup>206</sup>Pb/<sup>238</sup>U and the <sup>207</sup>U/<sup>235</sup>U ratio.

<sup>d</sup> percent Concordance defined by agreement between <sup>206</sup>Pb/<sup>238</sup>U and <sup>207</sup>Pb/<sup>206</sup>Pb spot ages.

**C.2.3: SDORPB15-10****SDORPB15-10**

Analysis No	Th <sup>a</sup> (ppm)	U <sup>a</sup> (ppm)	Th/U <sup>a</sup>	<sup>207</sup> Pb/ <sup>206</sup> Pb <sup>b</sup>	2s	<sup>206</sup> Pb/ <sup>238</sup> U <sup>b</sup>	2s	<sup>207</sup> Pb/ <sup>235</sup> U <sup>b</sup>	2s	<sup>208</sup> Pb/ <sup>232</sup> Th <sup>b</sup>	2s	Apparent spot ages (Ma)								%Conc <sup>d</sup>	
												r <sup>c</sup>	<sup>207</sup> Pb/ <sup>206</sup> Pb	2s	<sup>206</sup> Pb/ <sup>238</sup> U	2s	<sup>207</sup> Pb/ <sup>235</sup> U	2s	<sup>208</sup> Pb/ <sup>232</sup> Th		2s
053dog10a1	157 361	3 284	48	0.07195	0.001	0.16848	0.002	1.67086	0.02	0.05050	0.0006	0.86	985	25	1004	11	998	8.4	996	11	102
054dog10a2	50 692	3 431	15	0.07296	0.001	0.16874	0.002	1.69744	0.02	0.05000	0.0005	0.91	1013	23	1005	10	1008	7.6	986	10	99
055dog10a3	46 849	1 412	33	0.07357	0.001	0.17010	0.002	1.72534	0.02	0.05071	0.0005	0.88	1030	23	1013	9.8	1018	7.7	1000	10	98
056dog10a4	55 249	5 117	11	0.07439	0.001	0.17438	0.002	1.78782	0.03	0.05174	0.0006	0.8	1052	28	1036	11	1041	9.6	1020	12	98
057dog10a5	124 718	3 042	41	0.07309	0.001	0.17083	0.002	1.72141	0.02	0.05198	0.0005	0.91	1016	23	1017	9.8	1017	7.4	1024	10	100
058dog10a6	155 569	2 458	63	0.07351	0.001	0.17410	0.002	1.76455	0.02	0.05109	0.0005	0.91	1028	23	1035	10	1033	7.5	1007	10	101
059dog10a7	201 609	7 354	27	0.07293	0.001	0.17193	0.002	1.72846	0.02	0.05193	0.0006	0.88	1012	24	1023	10	1019	8.0	1023	11	101
060dog10a8	174 770	6 487	27	0.07300	0.001	0.17213	0.002	1.73252	0.02	0.05164	0.0005	0.92	1014	22	1024	9.9	1021	7.3	1018	10	101
061dog10a9	229 071	5 122	45	0.07275	0.001	0.17011	0.002	1.70632	0.02	0.05147	0.0005	0.9	1007	23	1013	9.8	1011	7.4	1014	10	101
062dog10a10	142 987	2 753	52	0.07324	0.001	0.17136	0.002	1.72993	0.02	0.05161	0.0006	0.86	1021	25	1020	11	1020	8.3	1017	11	100
068dog10a11	110 263	3 994	28	0.07263	0.001	0.16472	0.002	1.64942	0.02	0.04957	0.0005	0.69	1004	30	983	9.2	989	9.3	978	9.0	98
070dog10a13	136 598	2 108	65	0.07263	0.001	0.17329	0.002	1.73513	0.02	0.05210	0.0006	0.88	1004	24	1030	10	1022	7.9	1027	11	103
072dog10a15	168 264	2 820	60	0.07307	0.001	0.17383	0.002	1.75122	0.02	0.05245	0.0006	0.9	1016	23	1033	10	1028	7.8	1033	11	102

<sup>a</sup> U and Pb concentrations and Th/U ratios are calculated relative to NIST610 glass.

<sup>b</sup> Corrected for background and within-run Pb/U fractionation and normalised to reference monazite USGS 44069 (ID-TIMS values/measured value); <sup>207</sup>Pb/<sup>235</sup>U calculated using (<sup>207</sup>Pb/<sup>206</sup>Pb)/(<sup>238</sup>U/<sup>206</sup>Pb × 1/137.88).

<sup>c</sup> Rho is the error correlation defined as the quotient of the propagated errors of the <sup>206</sup>Pb/<sup>238</sup>U and the <sup>207</sup>U/<sup>235</sup>U ratio.

<sup>d</sup> percent Concordance defined by agreement between <sup>206</sup>Pb/<sup>238</sup>U and <sup>207</sup>Pb/<sup>206</sup>Pb spot ages.



**C.2.4: SD2015-13****SD2015-13**

Analysis No	Th <sup>a</sup> (ppm)	U <sup>a</sup> (ppm)	Th/U <sup>a</sup>	<sup>207</sup> Pb/ <sup>206</sup> Pb <sup>b</sup>	2s <sup>206</sup> Pb/ <sup>238</sup> U <sup>b</sup>	2s <sup>207</sup> Pb/ <sup>235</sup> U <sup>b</sup>	2s <sup>208</sup> Pb/ <sup>232</sup> Th <sup>b</sup>	2s	Apparent spot ages (Ma)												
									r <sup>c</sup>	<sup>207</sup> Pb/ <sup>206</sup> Pb	2s <sup>206</sup> Pb/ <sup>238</sup> U	2s <sup>207</sup> Pb/ <sup>235</sup> U	2s <sup>208</sup> Pb/ <sup>232</sup> Th	2s %Conc <sup>d</sup>							
028d131	22 590	2 036	11	0.07162	0.001	0.16656	0.002	1.64476	0.02	0.05046	0.0005	0.92	975	23	993	10	988	7.6	995	10	102
029d132	23 621	1 942	12	0.07197	0.001	0.16868	0.002	1.67368	0.02	0.05101	0.0005	0.92	985	22	1005	10	999	7.2	1006	10	102
030d133	24 451	1 506	16	0.07361	0.001	0.17071	0.002	1.73241	0.02	0.05140	0.0005	0.92	1031	22	1016	10	1021	7.5	1013	10	99
032d135	25 145	1 135	22	0.07244	0.001	0.17012	0.002	1.69911	0.02	0.05132	0.0005	0.89	998	24	1013	10	1008	7.8	1012	10	101
038dh136	26 063	1 113	23	0.07365	0.001	0.16643	0.002	1.68960	0.02	0.05014	0.0005	0.71	1032	29	992	9.2	1005	9.0	989	8.8	96
041d139	35 645	751	47	0.07285	0.001	0.17058	0.002	1.71324	0.02	0.05117	0.0005	0.87	1010	24	1015	10	1014	7.8	1009	10	101
042d1310	30 432	955	32	0.07270	0.001	0.17003	0.002	1.70408	0.02	0.05081	0.0005	0.89	1006	23	1012	10	1010	7.7	1002	10	101
043dh1311	264 412	8 283	32	0.07299	0.001	0.16782	0.002	1.68887	0.03	0.05031	0.0005	0.59	1014	39	1000	11	1004	12	992	10	99
044dh1312	30 210	855	35	0.07384	0.001	0.16829	0.002	1.71325	0.03	0.05037	0.0005	0.65	1037	33	1003	10	1014	10	993	9.1	97
047d1315	31 546	950	33	0.07424	0.001	0.17145	0.002	1.75480	0.02	0.05071	0.0005	0.76	1048	28	1020	10	1029	9.1	1000	10	97
<b>Not used- no 7/6 plateau</b>																					
039d137	57 171	507	113	0.24163	0.003	0.28732	0.003	9.57140	0.11	0.05880	0.0006	0.94	3131	17	1628	15	2394	10.0	1155	11	52
040d138	259 928	7 979	33	0.08166	0.002	0.15568	0.002	1.75275	0.04	0.04820	0.0005	0.54	1237	44	933	11	1028	15.0	952	10	75
045d1313	36 655	855	42	0.11535	0.001	0.14345	0.002	2.28126	0.03	0.03804	0.0004	0.91	1885	20	864	8.5	1207	8.2	755	7.5	46
<b>Excluded</b>																					
046d1314	34 060	1 562	22	0.07257	0.001	0.15601	0.002	1.56091	0.02	0.05163	0.0005	0.73	1002	28	935	8.8	954.8	8.6	1018	9.3	93

<sup>a</sup> U and Pb concentrations and Th/U ratios are calculated relative to NIST610 glass.

<sup>b</sup> Corrected for background and within-run Pb/U fractionation and normalised to reference monazite USGS 44069 (ID-TIMS values/measured value); <sup>207</sup>Pb/<sup>235</sup>U calculated using (<sup>207</sup>Pb/<sup>206</sup>Pb)/(<sup>238</sup>U/<sup>206</sup>Pb × 1/137.88).

<sup>c</sup> Rho is the error correlation defined as the quotient of the propagated errors of the <sup>206</sup>Pb/<sup>238</sup>U and the <sup>207</sup>U/<sup>235</sup>U ratio.

<sup>d</sup> percent Concordance defined by agreement between <sup>206</sup>Pb/<sup>238</sup>U and <sup>207</sup>Pb/<sup>206</sup>Pb spot ages.

### C.3: LFROTZ

#### C.3.1: HS15HF1

HS15HF1																					
Analysis No	Th <sup>a</sup>	U <sup>a</sup>	Th/U <sup>a</sup>	Apparent spot ages (Ma)																	
	(ppm)	(ppm)		<sup>207</sup> Pb/ <sup>206</sup> Pb <sup>b</sup>	2s <sup>206</sup> Pb/ <sup>238</sup> U <sup>b</sup>	2s <sup>207</sup> Pb/ <sup>235</sup> U <sup>b</sup>	2s <sup>208</sup> Pb/ <sup>232</sup> Th <sup>b</sup>	2s	r <sup>c</sup>	<sup>207</sup> Pb/ <sup>206</sup> Pb	2s <sup>206</sup> Pb/ <sup>238</sup> U	2s <sup>207</sup> Pb/ <sup>235</sup> U	2s <sup>208</sup> Pb/ <sup>232</sup> Th	2s	%Conc <sup>d</sup>						
HF1_1	81 939	8 438	10	0.07106	0.001	0.16391	0.002	1.60552	0.02	0.05025	0.0006	0.79	959	29	979	11	972	9.7	991	11	102
HF1_2	122 022	10 777	11	0.07153	0.001	0.15755	0.002	1.55399	0.02	0.05030	0.0006	0.9	973	24	943	11	952	8.4	992	11	97
HF1_3	95 798	8 884	11	0.07117	0.001	0.16340	0.002	1.60350	0.02	0.05067	0.0006	0.9	962	25	976	11	972	8.6	999	12	101
HF1_4	109 818	11 330	10	0.07087	0.001	0.16060	0.002	1.56934	0.02	0.05051	0.0006	0.9	954	24	960	11	958	8.4	996	12	101
HF1_5	118 917	11 291	11	0.07134	0.001	0.16212	0.002	1.59458	0.02	0.05004	0.0006	0.9	967	24	969	11	968	8.6	987	11	100
HF1_6	104 097	17 837	6	0.07162	0.001	0.16411	0.002	1.62227	0.03	0.04987	0.0006	0.72	975	31	980	11	979	10	984	11	100
HF1_7	113 492	10 496	11	0.07142	0.001	0.16250	0.002	1.60016	0.02	0.05086	0.0006	0.89	969	24	971	11	970	8.6	1003	12	100
HF1_8	94 007	9 088	10	0.07117	0.001	0.16375	0.002	1.60687	0.02	0.05060	0.0006	0.85	962	26	978	11	973	8.9	998	11	102
HF1_9	85 890	15 916	5	0.07098	0.001	0.16075	0.002	1.57328	0.02	0.05062	0.0006	0.85	957	26	961	11	960	9.1	998	12	100
HF1_10	96 223	8 453	11	0.07062	0.001	0.16356	0.002	1.59277	0.02	0.05048	0.0006	0.84	946	26	977	11	967	8.9	995	11	103
HF1_11	109 789	18 498	6	0.07122	0.001	0.16086	0.002	1.57961	0.02	0.05013	0.0006	0.91	964	24	962	11	962	8.5	989	12	100
HF1_12	87 076	9 150	10	0.07139	0.001	0.16499	0.002	1.62425	0.02	0.05087	0.0006	0.89	969	24	984	11	980	8.6	1003	12	102
HF1_13	111 001	12 059	9	0.07132	0.001	0.16096	0.002	1.58264	0.02	0.05012	0.0006	0.86	967	26	962	11	963	8.8	989	11	100
HF1_14	89 428	11 432	8	0.07061	0.001	0.16350	0.002	1.59169	0.02	0.05022	0.0006	0.87	946	26	976	11	967	8.9	991	12	103
HF1_15	92 608	9 812	9	0.07196	0.001	0.16060	0.002	1.59314	0.02	0.05009	0.0006	0.82	985	27	960	11	968	9.2	988	11	97
HF1_16	116 741	11 272	10	0.07106	0.001	0.16320	0.002	1.59927	0.02	0.05129	0.0006	0.88	959	25	975	11	970	8.7	1011	12	102
HF1_17	101 126	9 104	11	0.07181	0.001	0.16369	0.002	1.62078	0.02	0.05032	0.0006	0.85	981	27	977	11	978	9.4	992	12	100
HF1_18	49 680	16 207	3	0.07098	0.001	0.16174	0.002	1.58291	0.02	0.04913	0.0006	0.87	957	25	967	11	964	8.7	969	11	101
HF1_19	94 268	8 946	11	0.07115	0.001	0.16381	0.002	1.60708	0.02	0.05088	0.0006	0.89	962	24	978	11	973	8.6	1003	12	102
HF1_20	98 323	12 356	8	0.07145	0.001	0.16260	0.002	1.60203	0.02	0.05173	0.0006	0.86	970	25	971	11	971	8.8	1020	12	100
HF1_21	93 479	18 939	5	0.07026	0.001	0.16332	0.002	1.58186	0.02	0.05098	0.0006	0.79	936	28	975	11	963	9.5	1005	11	104
HF1_22	95 497	9 642	10	0.07135	0.001	0.16228	0.002	1.59676	0.02	0.05028	0.0006	0.79	967	28	969	11	969	9.5	992	11	100
HF1_23	106 098	12 240	9	0.07083	0.001	0.16296	0.002	1.59157	0.02	0.05118	0.0006	0.88	953	25	973	11	967	8.7	1009	12	102
HF1_24	68 488	9 690	7	0.07077	0.001	0.16082	0.002	1.56923	0.02	0.05018	0.0006	0.87	951	25	961	11	958	8.8	990	12	101
HF1_25	89 222	11 257	8	0.07110	0.001	0.16206	0.002	1.58879	0.02	0.05088	0.0006	0.87	960	25	968	11	966	8.9	1003	12	101

<sup>a</sup> U and Pb concentrations and Th/U ratios are calculated relative to NIST610 glass.

<sup>b</sup> Corrected for background and within-run Pb/U fractionation and normalised to reference monazite USGS 44069 (ID-TIMS values/measured value); <sup>207</sup>Pb/<sup>235</sup>U calculated using (207Pb/206Pb)/(238U/206Pb × 1/137.88).

<sup>c</sup> Rho is the error correlation defined as the quotient of the propagated errors of the <sup>206</sup>Pb/<sup>238</sup>U and the <sup>207</sup>U/<sup>235</sup>U ratio.

<sup>d</sup> percent Concordance defined by agreement between <sup>206</sup>Pb/<sup>238</sup>U and <sup>207</sup>Pb/<sup>206</sup>Pb spot ages.

## C.3.2: SDORPB15-15c

## SDORPB15-15C

Analysis No	Th <sup>a</sup> (ppm)	U <sup>a</sup> (ppm)	Th/U <sup>a</sup>	<sup>207</sup> Pb/ <sup>206</sup> Pb <sup>b</sup>	2s <sup>206</sup> Pb/ <sup>238</sup> U <sup>b</sup>	2s <sup>207</sup> Pb/ <sup>235</sup> U <sup>b</sup>	2s <sup>208</sup> Pb/ <sup>232</sup> Th <sup>b</sup>	2s	Apparent spot ages (Ma)					2s %Conc <sup>d</sup>							
									r <sup>c</sup>	<sup>207</sup> Pb/ <sup>206</sup> Pb	2s <sup>206</sup> Pb/ <sup>238</sup> U	2s <sup>207</sup> Pb/ <sup>235</sup> U	2s <sup>208</sup> Pb/ <sup>232</sup> Th								
073d151	33 356	1 063	31	0.07242	0.001	0.16740	0.002	1.67167	0.03	0.05073	0.0005	0.72	998	31	998	10	998	9.9	1000	10	100
074d152	27 485	900	31	0.07200	0.001	0.15993	0.002	1.58642	0.03	0.04864	0.0004	0.62	986	34	956	8.9	965	10	960	8.5	97
075d153	34 427	1 152	30	0.07121	0.001	0.16672	0.002	1.63676	0.02	0.05011	0.0005	0.87	964	24	994	9.7	985	7.6	988	9.8	103
076d154	45 650	1 340	34	0.07137	0.001	0.16243	0.002	1.59826	0.02	0.04888	0.0005	0.88	968	24	970	9.5	970	7.5	965	9.6	100
077d155	96 204	2 431	40	0.07142	0.001	0.16468	0.002	1.62154	0.02	0.04950	0.0005	0.9	970	23	983	9.6	979	7.3	977	9.7	101
083d156	34 022	1 082	31	0.07211	0.001	0.16753	0.002	1.66535	0.02	0.04929	0.0005	0.84	989	25	999	9.6	995	7.8	973	9.4	101
084d157	36 071	1 180	31	0.07123	0.001	0.16463	0.002	1.61673	0.02	0.04968	0.0005	0.87	964	24	982	9.6	977	7.6	980	9.7	102
085d158	28 894	1 128	26	0.07114	0.001	0.16524	0.002	1.62060	0.02	0.04984	0.0005	0.86	961	24	986	9.6	978	7.6	983	9.7	103
087d1510	49 452	1 556	32	0.07162	0.001	0.16856	0.002	1.66425	0.02	0.05000	0.0005	0.81	975	26	1004	9.2	995	7.8	986	9.0	103
088d1511	71 815	1 973	36	0.07151	0.001	0.16446	0.002	1.62156	0.02	0.04981	0.0005	0.88	972	24	982	9.5	979	7.5	983	9.7	101
089d1512	40 305	1 986	20	0.07150	0.001	0.16391	0.002	1.61586	0.02	0.04936	0.0005	0.87	972	24	979	9.6	976	7.6	974	9.8	101
092d1515	36 729	1 346	27	0.07116	0.001	0.16566	0.002	1.62529	0.02	0.04983	0.0005	0.84	962	25	988	9.8	980	7.9	983	9.9	103
<b>Excluded</b>																					
090d1513	40 439	919	44	0.08161	0.001	0.17961	0.002	2.02093	0.02	0.05394	0.0005	0.85	1236	24	1065	10	1123	8.3	1062	10	86
091d1514	39 422	5 723	7	0.07045	0.001	0.19949	0.002	1.93743	0.03	0.05247	0.0005	0.74	941	28	1173	11	1094	9.1	1034	9.5	125

<sup>a</sup> U and Pb concentrations and Th/U ratios are calculated relative to NIST610 glass.

<sup>b</sup> Corrected for background and within-run Pb/U fractionation and normalised to reference monazite USGS 44069 (ID-TIMS values/measured value); <sup>207</sup>Pb/<sup>235</sup>U calculated using (<sup>207</sup>Pb/<sup>206</sup>Pb)/(<sup>238</sup>U/<sup>206</sup>Pb × 1/137.88).

<sup>c</sup> Rho is the error correlation defined as the quotient of the propagated errors of the <sup>206</sup>Pb/<sup>238</sup>U and the <sup>207</sup>U/<sup>235</sup>U ratio.

<sup>d</sup> percent Concordance defined by agreement between <sup>206</sup>Pb/<sup>238</sup>U and <sup>207</sup>Pb/<sup>206</sup>Pb spot ages.

## C.3.3: SDORPB16-06

## SDOPRB16-6

Analysis No	Th <sup>a</sup> (ppm)	U <sup>a</sup> Th/U <sup>a</sup> (ppm)	207Pb/206Pb <sup>b</sup>	2s 206Pb/238U <sup>b</sup>	2s 207Pb/235U <sup>b</sup>	2s 208Pb/232Th <sup>b</sup>	2s	Apparent spot ages (Ma)					2s %Conc <sup>d</sup>								
								r <sup>c</sup> 207Pb/206Pb	2s 206Pb/238U	2s 207Pb/235U	2s 208Pb/232Th	2s									
SD16-006-7	106 608	2 948	36	0.07155	0.001	0.16240	0.002	1.60231	0.02	0.04307	0.0005	0.86	973	25	970	10	971	8.2	852	8.9	100
SD16-006-11	137 747	6 374	22	0.07168	0.001	0.16554	0.002	1.63614	0.02	0.04400	0.0005	0.91	977	23	988	10	984	7.8	870	9.1	101
SD16-006-12	140 435	6 581	21	0.07179	0.001	0.16662	0.002	1.64934	0.02	0.04396	0.0005	0.89	980	24	994	11	989	8.2	870	9.3	101
SD16-006-13	144 335	7 028	21	0.07168	0.001	0.16696	0.002	1.65051	0.02	0.04420	0.0004	0.9	977	23	995	10	990	7.4	874	8.4	102
SD16-006-14	106 542	7 618	14	0.07164	0.001	0.16613	0.002	1.64121	0.02	0.04361	0.0005	0.93	976	22	991	10	986	7.4	863	8.8	102
SD16-006-15	107 586	7 713	14	0.07130	0.001	0.16748	0.002	1.64662	0.02	0.04429	0.0005	0.94	966	22	998	10	988	7.4	876	8.9	103
SD16-006-16	160 262	7 192	22	0.07166	0.001	0.16777	0.002	1.65817	0.02	0.04408	0.0004	0.86	976	24	1000	10	993	7.7	872	8.4	102
SD16-006-17	167 999	7 643	22	0.07222	0.001	0.16756	0.002	1.66883	0.02	0.04406	0.0005	0.93	992	22	999	10	997	7.4	872	8.8	101
SD16-006-18	151 071	7 369	21	0.07194	0.001	0.16706	0.002	1.65748	0.02	0.04380	0.0005	0.93	984	22	996	10	992	7.3	867	8.7	101
SD16-006-19	136 111	6 421	21	0.07200	0.001	0.16754	0.002	1.66346	0.02	0.04422	0.0005	0.92	986	22	999	10	995	7.4	875	8.8	101
SD16-006-22	102 616	2 778	37	0.07151	0.001	0.16631	0.002	1.63998	0.02	0.04356	0.0005	0.83	972	26	992	10	986	8.5	862	9.0	102
SD16-006-23	142 503	6 779	21	0.07116	0.001	0.16702	0.002	1.63863	0.02	0.04389	0.0005	0.89	962	24	996	11	985	8.2	868	9.3	104
SD16-006-24	147 487	7 064	21	0.07185	0.001	0.16918	0.002	1.67602	0.02	0.04455	0.0005	0.91	982	23	1008	11	1000	8.0	881	9.3	103
SD16-006-25	143 652	6 810	21	0.07181	0.001	0.16480	0.002	1.63174	0.02	0.04399	0.0005	0.86	981	25	983	11	983	8.6	870	9.4	100
<b>Inheritance</b>																					
SD16-006-5	38 128	791	48	0.07651	0.001	0.16055	0.002	1.69389	0.02	0.05628	0.0006	0.8	1108	26	960	10	1006	8.9	1107	11	87
SD16-006-6	62 820	1 296	48	0.07718	0.001	0.15782	0.002	1.67990	0.02	0.04830	0.0005	0.84	1126	25	945	10	1001	8.3	953	9.6	84
SD16-006-8	110 616	9 359	12	0.07679	0.001	0.18969	0.002	2.00873	0.02	0.04917	0.0005	0.94	1116	21	1120	11	1119	7.6	970	9.6	100
SD16-006-9	61 292	7 761	8	0.07748	0.001	0.19039	0.002	2.03437	0.02	0.05014	0.0005	0.94	1134	21	1124	11	1127	7.8	989	10	99
SD16-006-10	35 946	4 576	8	0.07684	0.001	0.18536	0.002	1.96411	0.02	0.05703	0.0006	0.93	1117	22	1096	11	1103	7.8	1121	11	98
<b>Excluded</b>																					
SD16-006-1	107767.29	4642	23	0.13672	0.002	0.15269	0.002	2.87878	0.04	0.02308	0.0003	0.83	2186	23	916	10	1376	10.4	461	5	42
SD16-006-2	78165.38	2369	33	0.10896	0.001	0.21071	0.002	3.16644	0.04	0.03528	0.0004	0.82	1782	24	1233	12	1449	10.4	701	7	69
SD16-006-3	190133.39	10273	19	0.13768	0.002	0.05986	0.001	1.13669	0.01	0.01012	0.0001	0.93	2198	19	375	4	771	6.3	204	2	17
SD16-006-4	266996.53	12728	21	0.15820	0.002	0.16936	0.002	3.69527	0.04	0.00892	0.0001	0.94	2437	18	1009	10	1570	9.4	180	2	41
SD16-006-20	108737.55	8978	12	0.14034	0.002	0.35213	0.004	6.81436	0.08	0.02118	0.0002	0.92	2231	19	1945	19	2088	11.0	424	5	87
SD16-006-21	155362.44	6607	24	0.15233	0.002	0.13471	0.002	2.82903	0.04	0.01568	0.0002	0.9	2372	20	815	9	1363.3	10	315	3	34

<sup>a</sup> U and Pb concentrations and Th/U ratios are calculated relative to NIST610 glass.

<sup>b</sup> Corrected for background and within-run Pb/U fractionation and normalised to reference monazite USGS 44069 (ID-TIMS values/measured value); 207Pb/235U calculated using (207Pb/206Pb)/(238U/206Pb × 1/137.88).

<sup>c</sup> Rho is the error correlation defined as the quotient of the propagated errors of the 206Pb/238U and the 207U/235U ratio.

<sup>d</sup> percent Concordance defined by agreement between 206Pb/238U and 207Pb/206Pb spot ages.

## C.3.4: SDORPB16-07b

## SDORPB16-7B

Analysis No	Th <sup>a</sup> (ppm)	U <sup>a</sup> (ppm)	Th/U <sup>a</sup>	<sup>207</sup> Pb/ <sup>206</sup> Pb <sup>b</sup>	2s	<sup>206</sup> Pb/ <sup>238</sup> U <sup>b</sup>	2s	<sup>207</sup> Pb/ <sup>235</sup> U <sup>b</sup>	2s	<sup>208</sup> Pb/ <sup>232</sup> Th <sup>b</sup>	2s	Apparent spot ages (Ma)							%Conc <sup>d</sup>		
												r <sup>c</sup>	<sup>207</sup> Pb/ <sup>206</sup> Pb	2s	<sup>206</sup> Pb/ <sup>238</sup> U	2s	<sup>207</sup> Pb/ <sup>235</sup> U	2s		<sup>208</sup> Pb/ <sup>232</sup> Th	2s
SD16-007B-1	113 631	6 905	16	0.07188	0.001	0.16670	0.002	1.65161	0.02	0.04432	0.0005	0.88	982	24	994	10	990	7.9	877	9.0	101
SD16-007B-2	103 931	6 131	17	0.07224	0.001	0.16520	0.002	1.64524	0.02	0.04406	0.0005	0.86	993	24	986	10	988	8.2	872	9.2	99
SD16-007B-4	80 240	4 946	16	0.07199	0.001	0.16766	0.002	1.66304	0.02	0.04455	0.0005	0.79	986	27	999	10	995	8.7	881	8.7	101
SD16-007B-5	83 903	4 966	17	0.07176	0.001	0.16780	0.002	1.66010	0.02	0.04528	0.0005	0.84	979	26	1000	11	993	8.9	895	9.9	102
SD16-007B-6	118 793	6 795	17	0.07193	0.001	0.16775	0.002	1.66335	0.02	0.04514	0.0005	0.88	984	24	1000	11	995	8.2	892	9.5	102
SD16-007B-7	88 896	7 243	12	0.07216	0.001	0.16646	0.002	1.65585	0.02	0.04408	0.0005	0.89	990	23	993	10	992	7.9	872	9.1	100
SD16-007B-8	87 112	6 748	13	0.07232	0.001	0.16742	0.002	1.66900	0.02	0.04469	0.0005	0.88	995	24	998	10	997	8.0	884	9.1	100
SD16-007B-9	117 924	6 459	18	0.07166	0.001	0.16878	0.002	1.66727	0.02	0.04518	0.0005	0.89	976	24	1005	10	996	7.9	893	9.3	103
SD16-007B-10	114 153	3 052	37	0.07209	0.001	0.16980	0.002	1.68764	0.03	0.04522	0.0005	0.78	988	29	1011	11	1004	9.6	894	9.8	102
SD16-007B-11	98 662	5 648	17	0.07089	0.001	0.16280	0.002	1.59015	0.02	0.04446	0.0005	0.82	954	26	972	10	966	8.3	879	8.8	102
SD16-007B-12	79 382	4 735	17	0.07258	0.001	0.16834	0.002	1.68439	0.02	0.04485	0.0005	0.83	1002	26	1003	11	1003	8.8	887	9.6	100
SD16-007B-13	65 016	8 213	8	0.07241	0.001	0.16839	0.002	1.68074	0.02	0.05087	0.0005	0.88	998	24	1003	10	1001	8.0	1003	10	101
SD16-007B-14	88 173	5 115	17	0.07205	0.001	0.16812	0.002	1.66972	0.02	0.04505	0.0005	0.89	987	24	1002	11	997	8.2	891	9.4	101
SD16-007B-15	132 367	8 345	16	0.07187	0.001	0.16622	0.002	1.64724	0.02	0.04500	0.0005	0.84	982	26	991	11	989	9.1	890	10	101
SD16-007B-16	83 534	4 371	19	0.07211	0.001	0.16858	0.002	1.67587	0.02	0.04482	0.0005	0.82	989	26	1004	11	999	8.8	886	9.4	102
SD16-007B-17	98 102	5 210	19	0.07192	0.001	0.16619	0.002	1.64745	0.02	0.04468	0.0005	0.86	984	25	991	10	989	8.2	884	9.1	101
SD16-007B-18	67 625	3 957	17	0.07218	0.001	0.16616	0.002	1.65274	0.02	0.04701	0.0005	0.8	991	27	991	10	991	8.8	929	9.6	100
SD16-007B-19	139 126	7 028	20	0.07253	0.001	0.17077	0.002	1.70731	0.02	0.04536	0.0005	0.89	1001	23	1016	11	1011	8.1	897	9.4	102
SD16-007B-20	127 004	8 522	15	0.07190	0.001	0.16716	0.002	1.65677	0.02	0.04506	0.0005	0.88	983	24	996	10	992	8.2	891	9.5	101
SD16-007B-21	86 650	5 696	15	0.07188	0.001	0.16467	0.002	1.63210	0.03	0.04518	0.0005	0.75	983	30	983	11	983	10	893	10	100
SD16-007B-22	71 128	3 908	18	0.07218	0.001	0.16650	0.002	1.65672	0.02	0.04482	0.0005	0.86	991	25	993	10	992	8.4	886	9.4	100
SD16-007B-23	78 116	4 202	19	0.07276	0.001	0.16981	0.002	1.70305	0.02	0.04483	0.0005	0.85	1007	25	1011	10	1010	8.4	886	9.2	100
SD16-007B-24	106 973	6 270	17	0.07293	0.001	0.16764	0.002	1.68528	0.02	0.04481	0.0005	0.88	1012	24	999	10	1003	8.2	886	9.3	99
SD16-007B-25	112 592	7 040	16	0.07252	0.001	0.16807	0.002	1.67938	0.02	0.04579	0.0005	0.82	1001	26	1002	10	1001	8.6	905	9.1	100
SD16-007B-26	115 387	7 538	15	0.07267	0.001	0.16488	0.002	1.65170	0.02	0.04494	0.0005	0.88	1005	24	984	10	990	8.2	889	9.5	98
SD16-007B-27	75 640	8 369	9	0.07196	0.001	0.16668	0.002	1.65328	0.02	0.04592	0.0005	0.87	985	24	994	10	991	8.1	907	9.4	101
SD16-007B-28	103 882	2 790	37	0.07287	0.001	0.16618	0.002	1.66946	0.03	0.04601	0.0005	0.75	1010	30	991	11	997	10.1	909	10	98
SD16-007B-29	74 908	4 660	16	0.07214	0.001	0.16804	0.002	1.67108	0.02	0.04547	0.0005	0.86	990	24	1001	11	998	8.4	899	9.6	101
SD16-007B-30	122 336	6 896	18	0.07265	0.001	0.16841	0.002	1.68668	0.02	0.04615	0.0005	0.83	1004	26	1003	11	1004	9.0	912	10	100

<sup>a</sup> U and Pb concentrations and Th/U ratios are calculated relative to NIST610 glass.

<sup>b</sup> Corrected for background and within-run Pb/U fractionation and normalised to reference monazite USGS 44069 (ID-TIMS values/measured value); <sup>207</sup>Pb/<sup>235</sup>U calculated using (<sup>207</sup>Pb/<sup>206</sup>Pb)/(<sup>238</sup>U/<sup>206</sup>Pb × 1/137.88).

<sup>c</sup> Rho is the error correlation defined as the quotient of the propagated errors of the <sup>206</sup>Pb/<sup>238</sup>U and the <sup>207</sup>U/<sup>235</sup>U ratio.

<sup>d</sup> percent Concordance defined by agreement between <sup>206</sup>Pb/<sup>238</sup>U and <sup>207</sup>Pb/<sup>206</sup>Pb spot ages.

## C.4: Kakamas Domain

### C.4.1: SDORPB15-17

SDORPB15-17																					
Analysis No	Th <sup>a</sup>	U <sup>a</sup>	Th/U <sup>a</sup>	Apparent spot ages (Ma)																	
	(ppm)	(ppm)		<sup>207</sup> Pb/ <sup>206</sup> Pb <sup>b</sup>	2s <sup>206</sup> Pb/ <sup>238</sup> U <sup>b</sup>	2s <sup>207</sup> Pb/ <sup>235</sup> U <sup>b</sup>	2s <sup>208</sup> Pb/ <sup>232</sup> Th <sup>b</sup>	2s	r <sup>c</sup>	<sup>207</sup> Pb/ <sup>206</sup> Pb	2s <sup>206</sup> Pb/ <sup>238</sup> U	2s <sup>207</sup> Pb/ <sup>235</sup> U	2s <sup>208</sup> Pb/ <sup>232</sup> Th	2s	%Conc <sup>d</sup>						
053d171	75 495	12 320	6	0.07272	0.001	0.16463	0.002	1.65055	0.02	0.05142	0.0005	0.94	1006	22	982	9.6	990	7.1	1013	10	98
054d172	73 296	20 082	4	0.07134	0.001	0.16224	0.002	1.59573	0.02	0.05108	0.0006	0.94	967	22	969	9.9	969	7.3	1007	11	100
055d173	74 601	11 375	7	0.07175	0.001	0.16619	0.002	1.64400	0.02	0.05100	0.0005	0.94	979	22	991	9.7	987	7.0	1005	10	101
056d174	69 526	9 604	7	0.07174	0.001	0.16197	0.002	1.60194	0.02	0.05016	0.0005	0.94	979	22	968	9.3	971	6.9	989	9.6	99
057d175	70 302	10 739	7	0.07247	0.001	0.16440	0.002	1.64258	0.02	0.05091	0.0005	0.94	999	22	981	9.6	987	7.0	1004	10	98
058d176	72 280	11 442	6	0.07190	0.001	0.16387	0.002	1.62451	0.02	0.05067	0.0005	0.94	983	22	978	9.5	980	7.0	999	9.9	100
059d177	65 571	14 951	4	0.07208	0.001	0.16310	0.002	1.62073	0.02	0.05127	0.0005	0.94	988	22	974	9.5	978	7.0	1011	10	99
060d178	61 872	14 028	4	0.07264	0.001	0.16469	0.002	1.64927	0.02	0.05198	0.0005	0.94	1004	22	983	9.6	989	7.1	1024	10	98
061d179	74 297	10 206	7	0.07188	0.001	0.16592	0.002	1.64436	0.02	0.05101	0.0005	0.94	983	22	990	9.6	987	7.1	1006	10	101
062d1710	74 538	12 523	6	0.07246	0.001	0.16536	0.002	1.65191	0.02	0.05115	0.0005	0.94	999	22	987	9.6	990	7.1	1008	10	99
068d1711	74 224	12 469	6	0.07201	0.001	0.16163	0.002	1.60467	0.02	0.05020	0.0005	0.93	986	22	966	9.4	972	7.0	990	9.8	98
069d1712	83 087	14 361	6	0.07177	0.001	0.16424	0.002	1.62507	0.02	0.05123	0.0005	0.93	979	22	980	9.5	980	7.1	1010	10	100
070d1713	42 815	16 994	3	0.07234	0.001	0.16163	0.002	1.61188	0.02	0.05134	0.0005	0.93	995	22	966	9.4	975	7.0	1012	10	97
071d1714	62 954	13 574	5	0.07227	0.001	0.16224	0.002	1.61644	0.02	0.05132	0.0005	0.93	993	22	969	9.4	977	7.1	1012	10	98
072d1715	77 741	13 348	6	0.07205	0.001	0.16340	0.002	1.62299	0.02	0.05090	0.0005	0.93	987	22	976	9.5	979	7.1	1004	10	99

<sup>a</sup> U and Pb concentrations and Th/U ratios are calculated relative to NIST610 glass.

<sup>b</sup> Corrected for background and within-run Pb/U fractionation and normalised to reference monazite USGS 44069 (ID-TIMS values/measured value); <sup>207</sup>Pb/<sup>235</sup>U calculated using (207Pb/206Pb)/(238U/206Pb × 1/137.88).

<sup>c</sup> Rho is the error correlation defined as the quotient of the propagated errors of the <sup>206</sup>Pb/<sup>238</sup>U and the <sup>207</sup>U/<sup>235</sup>U ratio.

<sup>d</sup> percent Concordance defined by agreement between <sup>206</sup>Pb/<sup>238</sup>U and <sup>207</sup>Pb/<sup>206</sup>Pb spot ages.

**C.4.2: SDORPB15-18****SDORPB15-18**

Analysis No	Th <sup>a</sup> (ppm)	U <sup>a</sup> (ppm)	Th/U <sup>a</sup>	<sup>207</sup> Pb/ <sup>206</sup> Pb <sup>b</sup>	2s <sup>206</sup> Pb/ <sup>238</sup> U <sup>b</sup>	2s <sup>207</sup> Pb/ <sup>235</sup> U <sup>b</sup>	2s <sup>208</sup> Pb/ <sup>232</sup> Th <sup>b</sup>	2s	Apparent spot ages (Ma)					2s %Conc <sup>d</sup>					
									r <sup>c</sup>	<sup>207</sup> Pb/ <sup>206</sup> Pb	2s <sup>206</sup> Pb/ <sup>238</sup> U	2s <sup>207</sup> Pb/ <sup>235</sup> U	2s <sup>208</sup> Pb/ <sup>232</sup> Th						
028dog181	100 594	2 066	49	0.07287	0.001 0.16822	0.002 1.69012	0.02 0.04963	0.0005	0.81	1010	26	1002	9.6	1005	8.1	979	9.5	99	
029dog182	119 365	3 454	35	0.07336	0.001 0.17192	0.002 1.73894	0.02 0.05006	0.0005	0.87	1024	24	1023	9.8	1023	7.7	987	9.8	100	
030dog183	104 725	2 059	51	0.07286	0.001 0.16898	0.002 1.69756	0.02 0.05013	0.0006	0.83	1010	26	1007	11	1008	8.7	989	11	100	
038dog186	140 917	5 632	25	0.07303	0.001 0.17132	0.002 1.72506	0.02 0.05135	0.0006	0.81	1015	26	1019	10	1018	8.7	1012	11	100	
039dog187	137 890	4 957	28	0.07300	0.001 0.17250	0.002 1.73467	0.03 0.05046	0.0006	0.71	1014	33	1026	12	1022	11.1	995	12	101	
<b>Excluded</b>																			
031dog184	158 762	4 686	34	0.12856	0.001 0.17696	0.002 3.13689	0.04 0.03546	0.0004	0.9	2078	20	1050	10	1442	8.9	704	7.1	51	
032dog185	122 595	4 125	30	0.07944	0.001 0.17366	0.002 1.90200	0.02 0.05048	0.0006	0.89	1183	23	1032	10	1082	8.1	995	11	87	
040dog188	157 776	6 046	26	0.08330	0.001 0.17493	0.002 2.00921	0.03 0.04983	0.0006	0.7	1276	31	1039	11	1119	12	983	11	81	

**C.4.3: SDORPB15-20****SDORPB15-20**

Analysis No	Th <sup>a</sup> (ppm)	U <sup>a</sup> (ppm)	Th/U <sup>a</sup>	<sup>207</sup> Pb/ <sup>206</sup> Pb <sup>b</sup>	2s <sup>206</sup> Pb/ <sup>238</sup> U <sup>b</sup>	2s <sup>207</sup> Pb/ <sup>235</sup> U <sup>b</sup>	2s <sup>208</sup> Pb/ <sup>232</sup> Th <sup>b</sup>	2s	Apparent spot ages (Ma)					2s %Conc <sup>d</sup>				
									r <sup>c</sup>	<sup>207</sup> Pb/ <sup>206</sup> Pb	2s <sup>206</sup> Pb/ <sup>238</sup> U	2s <sup>207</sup> Pb/ <sup>235</sup> U	2s <sup>208</sup> Pb/ <sup>232</sup> Th					
008dog201	73 873	5 442	14	0.07158	0.001 0.16523	0.002 1.63062	0.02 0.05014	0.0005	0.96	974	21	986	9.5	982	6.9	989	9.8	101
009dog202	71 722	5 306	14	0.07174	0.001 0.16667	0.002 1.64863	0.02 0.04989	0.0005	0.96	979	21	994	9.6	989	6.9	984	9.8	102
010dog203	81 691	5 529	15	0.07172	0.001 0.16610	0.002 1.64241	0.02 0.05045	0.0005	0.93	978	22	991	10	987	7.4	995	10	101
013dog206	83 135	4 335	19	0.07193	0.001 0.17032	0.002 1.68919	0.02 0.05106	0.0005	0.95	984	22	1014	9.9	1005	7.1	1007	10	103
014dog207	66 368	3 597	18	0.07248	0.001 0.16613	0.002 1.66022	0.02 0.05061	0.0005	0.95	1000	22	991	9.5	994	6.9	998	9.8	99
015dog208	89 270	5 658	16	0.07124	0.001 0.16295	0.002 1.60062	0.02 0.04953	0.0005	0.96	964	22	973	9.7	971	7.0	977	10	101
016dog209	39 592	2 893	14	0.07190	0.001 0.16903	0.002 1.67573	0.02 0.04956	0.0005	0.93	983	22	1007	10	999	7.3	978	10	102
017dog2010	75 228	3 487	22	0.07238	0.001 0.16934	0.002 1.68999	0.02 0.05087	0.0005	0.95	997	22	1009	9.8	1005	7.1	1003	10	101
023dog2011	93 053	5 011	19	0.07186	0.001 0.16911	0.002 1.67561	0.02 0.05125	0.0006	0.94	982	22	1007	10	999	7.3	1010	11	103
024dog2012	47 002	3 424	14	0.07207	0.001 0.16805	0.002 1.66983	0.02 0.05092	0.0005	0.91	988	23	1001	10	997	7.5	1004	10	101
025dog2013	49 403	3 280	15	0.07192	0.001 0.16695	0.002 1.65551	0.02 0.05159	0.0005	0.9	984	23	995	9.3	992	7.1	1017	9.7	101
026dog2014	74 449	4 545	16	0.07196	0.001 0.16677	0.002 1.65459	0.02 0.05053	0.0005	0.93	985	22	994	9.8	991	7.2	996	10	101
027dog2015	92 872	7 046	13	0.07182	0.001 0.16420	0.002 1.62593	0.02 0.05013	0.0005	0.95	981	22	980	9.8	980	7.1	989	10	100

<sup>a</sup> U and Pb concentrations and Th/U ratios are calculated relative to NIST610 glass.

<sup>b</sup> Corrected for background and within-run Pb/U fractionation and normalised to reference monazite USGS 44069 (ID-TIMS values/measured value); <sup>207</sup>Pb/<sup>235</sup>U calculated using (<sup>207</sup>Pb/<sup>206</sup>Pb)/(<sup>238</sup>U/<sup>206</sup>Pb × 1/137.88).

<sup>c</sup> Rho is the error correlation defined as the quotient of the propagated errors of the <sup>206</sup>Pb/<sup>238</sup>U and the <sup>207</sup>U/<sup>235</sup>U ratio.

<sup>d</sup> percent Concordance defined by agreement between <sup>206</sup>Pb/<sup>238</sup>U and <sup>207</sup>Pb/<sup>206</sup>Pb spot ages.

**C.4.4: SDORPB16-08****SDORPB16 8**

Analysis No	Th <sup>a</sup> (ppm)	U <sup>a</sup> (ppm)	Th/U <sup>a</sup>	<sup>207</sup> Pb/ <sup>206</sup> Pb <sup>b</sup>	2s <sup>206</sup> Pb/ <sup>238</sup> U <sup>b</sup>	2s <sup>207</sup> Pb/ <sup>235</sup> U <sup>b</sup>	2s <sup>208</sup> Pb/ <sup>232</sup> Th <sup>b</sup>	2s	Apparent spot ages (Ma)					%Conc <sup>d</sup>							
									r <sup>c</sup>	<sup>207</sup> Pb/ <sup>206</sup> Pb	2s <sup>206</sup> Pb/ <sup>238</sup> U	2s <sup>207</sup> Pb/ <sup>235</sup> U	2s <sup>208</sup> Pb/ <sup>232</sup> Th								
SD16-008-1	11 279	8 981	1	0.07206	0.001	0.16806	0.002	1.66957	0.02	0.05058	0.0006	0.92	988	23	1001	10	997	7.8	997	11	101
SD16-008-2	32 151	5 402	6	0.07203	0.001	0.16740	0.002	1.66230	0.02	0.05070	0.0005	0.9	987	23	998	10	994	7.9	1000	10	101
SD16-008-3	29 554	5 222	6	0.07156	0.001	0.16770	0.002	1.65379	0.02	0.05164	0.0005	0.83	974	26	999	10	991	8.4	1018	10	103
SD16-008-4	76 174	6 607	12	0.07221	0.001	0.16810	0.002	1.67329	0.02	0.04859	0.0005	0.87	992	24	1002	10	998	8.1	959	9.8	101
SD16-008-5	71 546	15 059	5	0.07153	0.001	0.16956	0.002	1.67203	0.02	0.04842	0.0005	0.92	973	23	1010	10	998	7.7	956	10	104
SD16-008-6	105 378	5 559	19	0.07219	0.001	0.17104	0.002	1.70265	0.02	0.04599	0.0005	0.84	991	26	1018	11	1010	9.3	909	10	103
SD16-008-7	95 844	5 188	18	0.07198	0.001	0.17001	0.002	1.68674	0.02	0.04578	0.0005	0.85	985	25	1012	10	1004	8.3	905	9.2	103
SD16-008-8	54 428	10 436	5	0.07179	0.001	0.16842	0.002	1.66718	0.02	0.05085	0.0006	0.85	980	26	1003	11	996	9.0	1003	11	102
SD16-008-11	152 998	13 453	11	0.07231	0.001	0.16345	0.002	1.62958	0.02	0.04382	0.0005	0.88	995	24	976	10	982	8.0	867	9.1	98
SD16-008-12	66 817	4 392	15	0.07270	0.001	0.16961	0.002	1.70029	0.03	0.04966	0.0006	0.79	1006	29	1010	11	1009	9.9	980	11	100
SD16-008-13	76 390	5 257	15	0.07268	0.001	0.16756	0.002	1.67910	0.02	0.04576	0.0005	0.86	1005	25	999	10	1001	8.3	904	9.5	99
SD16-008-14	99 937	6 403	16	0.07167	0.001	0.16853	0.002	1.66537	0.02	0.04569	0.0005	0.87	977	24	1004	10	995	8.2	903	9.5	103
SD16-008-15	107 053	7 135	15	0.07277	0.001	0.16974	0.002	1.70297	0.02	0.04568	0.0005	0.88	1008	24	1011	11	1010	8.2	903	9.5	100
SD16-008-16	85 794	5 622	15	0.07190	0.001	0.16719	0.002	1.65754	0.02	0.04495	0.0005	0.86	983	25	997	10	992	8.2	889	9.3	101
SD16-008-17	99 154	7 978	12	0.07216	0.001	0.16355	0.002	1.62714	0.02	0.04400	0.0005	0.87	990	25	977	10	981	8.1	870	9.1	99
SD16-008-20	108 738	8 978	12	0.07241	0.001	0.16512	0.002	1.64847	0.02	0.04484	0.0005	0.84	998	25	985	10	989	8.3	887	9.2	99
SD16-008-21	117 231	7 345	16	0.07236	0.001	0.16750	0.002	1.67080	0.03	0.04516	0.0005	0.77	996	29	998	11	998	9.8	893	9.8	100
SD16-008-22	110 308	6 141	18	0.07286	0.001	0.16508	0.002	1.65800	0.02	0.04470	0.0005	0.77	1010	29	985	11	993	9.5	884	9.6	98
SD16-008-23	115 845	7 149	16	0.07325	0.001	0.16926	0.002	1.70941	0.03	0.04580	0.0005	0.74	1021	30	1008	11	1012	10	905	9.8	99
SD16-008-25	91 650	3 158	29	0.07209	0.001	0.16382	0.002	1.62789	0.03	0.04376	0.0005	0.72	988	32	978	11	981	10	866	9.5	99
SD16-008-28	94 516	7 240	13	0.07263	0.001	0.16773	0.002	1.67938	0.02	0.04547	0.0005	0.76	1004	29	1000	10	1001	9.4	899	9.5	100
SD16-008-29	10 910	8 780	1	0.07267	0.001	0.16254	0.002	1.62823	0.03	0.04898	0.0005	0.65	1005	34	971	9.8	981	10	967	9.9	97
SD16-008-30	80 824	6 452	13	0.07199	0.001	0.16813	0.002	1.66854	0.03	0.04365	0.0005	0.63	986	37	1002	11	997	12	864	9.6	102
<b>Inheritance</b>																					
SD16-008-18	40 097	21 586	2	0.08035	0.001	0.15155	0.002	1.67904	0.02	0.05109	0.0006	0.81	1206	26	910	9.7	1001	9.1	1007	11	75
SD16-008-19	39 655	22 946	2	0.08116	0.001	0.14623	0.002	1.63632	0.02	0.05066	0.0005	0.85	1225	24	880	9.1	984	8.2	999	10	72
SD16-008-26	39 309	47 981	0.8	0.08096	0.001	0.15077	0.002	1.68281	0.02	0.05096	0.0006	0.81	1221	26	905	9.4	1002	8.8	1005	11	74
SD16-008-27	40 630	50 163	0.8	0.08105	0.001	0.14927	0.002	1.66782	0.02	0.05105	0.0005	0.78	1223	27	897	9.2	996	8.9	1006	10	73

<sup>a</sup> U and Pb concentrations and Th/U ratios are calculated relative to NIST610 glass.

<sup>b</sup> Corrected for background and within-run Pb/U fractionation and normalised to reference monazite USGS 44069 (ID-TIMS values/measured value); <sup>207</sup>Pb/<sup>235</sup>U calculated using (207Pb/206Pb)/(238U/206Pb × 1/137.88).

<sup>c</sup> Rho is the error correlation defined as the quotient of the propagated errors of the <sup>206</sup>Pb/<sup>238</sup>U and the <sup>207</sup>U/<sup>235</sup>U ratio.

<sup>d</sup> percent Concordance defined by agreement between <sup>206</sup>Pb/<sup>238</sup>U and <sup>207</sup>Pb/<sup>206</sup>Pb spot ages.



## C.4.5: SDORPB16-09

## SDORPB16-9

Analysis No	Th <sup>a</sup> (ppm)	U <sup>a</sup> (ppm)	Th/U <sup>a</sup>	<sup>207</sup> Pb/ <sup>206</sup> Pb <sup>b</sup>	Apparent spot ages (Ma)																
					2s <sup>206</sup> Pb/ <sup>238</sup> U <sup>b</sup>	2s <sup>207</sup> Pb/ <sup>235</sup> U <sup>b</sup>	2s <sup>208</sup> Pb/ <sup>232</sup> Th <sup>b</sup>	2s <sup>206</sup> Pb/ <sup>238</sup> U <sup>b</sup>	2s <sup>207</sup> Pb/ <sup>235</sup> U <sup>b</sup>	2s <sup>208</sup> Pb/ <sup>232</sup> Th <sup>b</sup>	2s %Conc <sup>d</sup>	r <sup>c</sup> <sup>207</sup> Pb/ <sup>206</sup> Pb	2s <sup>206</sup> Pb/ <sup>238</sup> U	2s <sup>207</sup> Pb/ <sup>235</sup> U	2s <sup>208</sup> Pb/ <sup>232</sup> Th	2s %Conc <sup>d</sup>					
SD16-009-1	80 754	22 652	4	0.07288	0.001	0.17105	0.002	1.71885	0.03	0.04601	0.0005	0.75	1011	29	1018	10	1016	9.4	909	9.1	101
SD16-009-2	85 130	22 866	4	0.07277	0.001	0.16980	0.002	1.70331	0.02	0.04565	0.0005	0.81	1008	26	1011	10	1010	8.7	902	9.1	100
SD16-009-3	71 839	19 198	4	0.07261	0.001	0.17083	0.002	1.71002	0.02	0.04693	0.0005	0.89	1003	24	1017	11	1012	8.2	927	9.9	101
SD16-009-4	83 012	10 535	8	0.07311	0.001	0.17137	0.002	1.72733	0.02	0.04608	0.0005	0.85	1017	25	1020	11	1019	8.9	911	10	100
SD16-009-5	84 860	16 845	5	0.07355	0.001	0.17216	0.002	1.74534	0.02	0.04653	0.0005	0.86	1029	24	1024	11	1025	8.5	919	9.7	100
SD16-009-6	103 216	9 078	11	0.07322	0.001	0.17448	0.002	1.76123	0.03	0.04787	0.0006	0.77	1020	30	1037	12	1031	10	945	11	102
SD16-009-7	74 430	19 626	4	0.07275	0.001	0.17028	0.002	1.70866	0.03	0.04495	0.0005	0.74	1007	30	1014	11	1012	9.9	889	9.4	101
SD16-009-8	114 825	9 247	12	0.07316	0.001	0.17159	0.002	1.73070	0.02	0.04688	0.0005	0.87	1018	24	1021	11	1020	8.4	926	9.8	100
SD16-009-9	120 806	8 169	15	0.07371	0.001	0.17533	0.002	1.78199	0.02	0.04673	0.0005	0.83	1034	25	1041	11	1039	8.7	923	9.4	101
SD16-009-10	70 154	17 988	4	0.07290	0.001	0.17122	0.002	1.72065	0.02	0.04787	0.0005	0.88	1011	24	1019	11	1016	8.1	945	9.8	101
SD16-009-11	89 245	13 649	7	0.07283	0.001	0.17150	0.002	1.72198	0.02	0.04661	0.0005	0.88	1009	24	1020	11	1017	8.2	921	9.6	101
SD16-009-13	109 371	10 084	11	0.07332	0.001	0.17187	0.002	1.73719	0.02	0.04627	0.0005	0.86	1023	25	1022	11	1022	8.6	914	9.8	100
SD16-009-14	111 461	8 498	13	0.07372	0.001	0.17088	0.002	1.73694	0.02	0.04555	0.0005	0.79	1034	27	1017	11	1022	9.2	900	9.3	98
SD16-009-15	117 927	10 859	11	0.07388	0.001	0.17362	0.002	1.76852	0.03	0.04616	0.0005	0.79	1038	28	1032	11	1034	9.7	912	10	99
SD16-009-16	113 501	10 352	11	0.07351	0.001	0.16942	0.002	1.71712	0.03	0.04646	0.0005	0.76	1028	29	1009	11	1015	9.9	918	10	98
SD16-009-17	94 514	10 658	9	0.07365	0.001	0.17242	0.002	1.75086	0.03	0.04654	0.0005	0.74	1032	30	1025	11	1028	10	919	9.5	99
SD16-009-19	118 518	15 362	8	0.07307	0.001	0.17191	0.002	1.73209	0.02	0.04648	0.0005	0.84	1016	26	1023	11	1021	8.8	918	10	101
SD16-009-20	98 363	17 409	6	0.07296	0.001	0.16659	0.002	1.67527	0.02	0.04638	0.0005	0.84	1013	25	993	10	999	8.6	916	9.7	98
SD16-009-21	80 738	22 692	4	0.07337	0.001	0.16791	0.002	1.69823	0.03	0.04600	0.0005	0.7	1024	31	1001	10	1008	10	909	9.2	98
SD16-009-22	95 821	10 251	9	0.07373	0.001	0.16993	0.002	1.72742	0.02	0.04651	0.0005	0.87	1034	24	1012	11	1019	8.4	919	9.7	98
SD16-009-23	99 478	14 606	7	0.07361	0.001	0.17267	0.002	1.75239	0.02	0.04629	0.0005	0.86	1031	24	1027	11	1028	8.4	915	9.5	100
SD16-009-25	71 595	15 481	5	0.07312	0.001	0.17123	0.002	1.72598	0.02	0.04674	0.0005	0.85	1017	25	1019	11	1018	8.4	923	9.6	100
SD16-009-26	102 677	16 310	6	0.07335	0.001	0.17299	0.002	1.74867	0.03	0.04651	0.0005	0.68	1024	33	1029	11	1027	11	919	9.6	100
SD16-009-27	115 621	4 250	27	0.07336	0.001	0.17250	0.002	1.74499	0.03	0.04705	0.0005	0.76	1024	29	1026	11	1025	9.9	929	10	100
~1203 Ma inheritance																					
SD16-009-1A	80 754	22 652	4	0.08038	0.001	0.15474	0.002	1.71446	0.02	0.04566	0.0005	0.88	1206	23	928	10	1014	8.3	903	9.7	77
SD16-009-2A	85 130	22 866	4	0.08008	0.001	0.15423	0.002	1.70229	0.02	0.04535	0.0005	0.86	1199	24	925	9.9	1009	8.6	896	9.6	77
SD16-009-21A	89 362	23 618	4	0.08049	0.001	0.15535	0.002	1.72378	0.02	0.47100	0.0005	0.86	1209	24	931	10	1017	8.7	903	9.6	77
SD16-009-12A	80 738	22 692	4	0.08006	0.001	0.15105	0.002	1.66752	0.02	0.04583	0.0005	0.81	1198	26	907	9.8	996	9.1	906	9.9	76
SD16-009-24A	67 302	21 413	3	0.08010	0.001	0.15045	0.002	1.66136	0.02	0.04999	0.0005	0.82	1199	26	904	9.6	994	8.8	986	10	75

<sup>a</sup> U and Pb concentrations and Th/U ratios are calculated relative to NIST610 glass.

<sup>b</sup> Corrected for background and within-run Pb/U fractionation and normalised to reference monazite USGS 44069 (ID-TIMS values/measured value); <sup>207</sup>Pb/<sup>235</sup>U calculated using (207Pb/206Pb)/(238U/206Pb × 1/137.88).

<sup>c</sup> Rho is the error correlation defined as the quotient of the propagated errors of the <sup>206</sup>Pb/<sup>238</sup>U and the <sup>207</sup>U/<sup>235</sup>U ratio.

<sup>d</sup> percent Concordance defined by agreement between <sup>206</sup>Pb/<sup>238</sup>U and <sup>207</sup>Pb/<sup>206</sup>Pb spot ages.

## C.4.6: SDORPB16-12

## SDORPB16-12

Analysis No	Th <sup>a</sup> (ppm)	U <sup>a</sup> (ppm)	Th/U <sup>a</sup>	<sup>207</sup> Pb/ <sup>206</sup> Pb <sup>b</sup>	2s	<sup>206</sup> Pb/ <sup>238</sup> U <sup>b</sup>	2s	<sup>207</sup> Pb/ <sup>235</sup> U <sup>b</sup>	2s	<sup>208</sup> Pb/ <sup>232</sup> Th <sup>b</sup>	2s	Apparent spot ages (Ma)					2s	%Conc <sup>d</sup>			
												r <sup>c</sup>	<sup>207</sup> Pb/ <sup>206</sup> Pb	2s	<sup>206</sup> Pb/ <sup>238</sup> U	2s			<sup>207</sup> Pb/ <sup>235</sup> U	2s	<sup>208</sup> Pb/ <sup>232</sup> Th
<b>~993 Crystallisation</b>																					
SD16-012-14	102 061	5 548	18	0.07197	0.001	0.16665	0.002	1.65372	0.02	0.04411	0.0005	0.89	985	23	994	10	991	7.7	872	8.8	101
SD16-012-20	96 489	5 367	18	0.07236	0.001	0.16686	0.002	1.66462	0.02	0.04389	0.0005	0.91	996	23	995	9.9	995	7.5	868	8.6	100
<b>~1 092 Ma Inheritance</b>																					
SD16-012-1	53 114	6 826	8	0.07578	0.001	0.18967	0.002	1.98179	0.02	0.05676	0.0006	0.93	1089	22	1120	11	1109	8.0	1116	11	103
SD16-012-2	51 877	7 033	7	0.07606	0.001	0.18618	0.002	1.95256	0.02	0.05602	0.0006	0.94	1097	22	1101	11	1099	7.7	1102	11	100
SD16-012-3	53 127	5 217	10	0.07534	0.001	0.18579	0.002	1.93007	0.02	0.05166	0.0005	0.93	1078	22	1099	11	1092	7.7	1018	10	102
SD16-012-8	57 682	1 231	47	0.07673	0.001	0.16270	0.002	1.72135	0.02	0.05179	0.0005	0.76	1114	28	972	9.9	1017	9.3	1021	10	87
SD16-012-10	59 251	308	192	0.07706	0.002	0.18156	0.002	1.92928	0.04	0.05259	0.0006	0.57	1123	43	1076	12	1091	15	1036	11	96
SD16-012-13	57 635	2 580	22	0.07747	0.001	0.16983	0.002	1.81413	0.02	0.05401	0.0006	0.89	1134	23	1011	10	1051	8.1	1063	11	89
SD16-012-19	25 531	668	38	0.07595	0.001	0.16427	0.002	1.72023	0.03	0.05646	0.0006	0.72	1094	30	981	10	1016	9.9	1110	11	90
SD16-012-23	49 243	2 572	19	0.07691	0.001	0.17231	0.002	1.82712	0.02	0.05615	0.0006	0.87	1119	24	1025	10	1055	8.2	1104	11	92
SD16-012-24	39 180	1 244	32	0.07540	0.001	0.17111	0.002	1.77873	0.02	0.05599	0.0006	0.79	1079	27	1018	10	1038	9.0	1101	11	94
SD16-012-25	36 110	774	47	0.07604	0.001	0.16492	0.002	1.72897	0.03	0.05687	0.0006	0.75	1096	29	984	10	1019	9.7	1118	11	90
<b>~1 144 Ma Inheritance</b>																					
SD16-012-4	42 486	2 732	16	0.07782	0.001	0.19733	0.002	2.11728	0.03	0.05880	0.0006	0.89	1142	23	1161	12	1154	8.7	1155	12	102
SD16-012-5	46 810	2 986	16	0.07814	0.001	0.19343	0.002	2.08408	0.02	0.05859	0.0006	0.91	1150	22	1140	11	1144	8.1	1151	11	99
SD16-012-7	46 464	2 489	19	0.07811	0.001	0.19435	0.002	2.09261	0.03	0.05968	0.0007	0.8	1150	28	1145	13	1146	10.6	1172	13	100
SD16-012-12	30 831	3 109	10	0.07726	0.001	0.19519	0.002	2.07936	0.02	0.05818	0.0006	0.91	1128	22	1149	11	1142	8.2	1143	11	102
<b>~1 200 Ma Inheritance</b>																					
SD16-012-6	39 486	4 524	9	0.07941	0.001	0.20046	0.002	2.19495	0.03	0.06038	0.0006	0.92	1183	22	1178	12	1179	8.3	1185	12	100
SD16-012-9	45 937	3 717	12	0.08028	0.001	0.19196	0.002	2.12487	0.03	0.05989	0.0006	0.9	1204	22	1132	11	1157	8.2	1176	11	94
SD16-012-11	47 268	1 234	38	0.07936	0.001	0.18254	0.002	1.99742	0.03	0.05878	0.0006	0.79	1181	28	1081	12	1115	10	1154	12	92
SD16-012-15	47 202	4 332	11	0.08038	0.001	0.20577	0.002	2.28053	0.03	0.06127	0.0006	0.93	1206	22	1206	12	1206	8.3	1202	12	100
SD16-012-16	50 205	3 046	16	0.07843	0.001	0.19787	0.002	2.13968	0.03	0.05590	0.0006	0.91	1158	22	1164	12	1162	8.4	1100	11	101
SD16-012-17	44 908	1 348	33	0.07947	0.001	0.17742	0.002	1.94401	0.03	0.06023	0.0007	0.8	1184	27	1053	11	1096	9.6	1182	12	89
SD16-012-18	44 417	1 579	28	0.08039	0.001	0.18379	0.002	2.03715	0.03	0.06167	0.0007	0.8	1207	27	1088	12	1128	10	1210	13	90

<sup>a</sup> U and Pb concentrations and Th/U ratios are calculated relative to NIST610 glass.

<sup>b</sup> Corrected for background and within-run Pb/U fractionation and normalised to reference monazite USGS 44069 (ID-TIMS values/measured value); <sup>207</sup>Pb/<sup>235</sup>U calculated using (207Pb/206Pb)/(238U/206Pb × 1/137.88).

<sup>c</sup> Rho is the error correlation defined as the quotient of the propagated errors of the <sup>206</sup>Pb/<sup>238</sup>U and the <sup>207</sup>U/<sup>235</sup>U ratio.

<sup>d</sup> percent Concordance defined by agreement between <sup>206</sup>Pb/<sup>238</sup>U and <sup>207</sup>Pb/<sup>206</sup>Pb spot ages.

## Appendix D: Monazite Sm-Nd isotope compositions

The Sm-Nd isotope measurements were taken on a Thermo-Finnigan Neptune multi-collector-ionised coupled plasma-mass spectrometer (MC-ICP-MS) coupled with a 193 nm HellEx Photon-Machine laser ablation system at the Laboratório de Geoquímica Isotópica (LOPAG), Universidade Federal de Ouro Preto (UFOP) in Brazil.

Two-stage depleted model ages were calculated using the formula:

$$T_{2DM} = \left( \frac{1}{\lambda_{Sm}} \right) \ln \left\{ \frac{1 + \left[ \left( \frac{^{143}Nd}{^{144}Nd} \right)_{sample} - \left( \frac{^{143}Nd}{^{144}Nd} \right)_{DM} - (e^{\lambda t}) \left[ \left( \frac{^{147}Sm}{^{144}Nd} \right)_{sample} - \left( \frac{^{147}Sm}{^{144}Nd} \right)_{CC} \right] \right]}{\left( \frac{^{147}Sm}{^{144}Nd} \right)_{sample} - \left( \frac{^{147}Sm}{^{144}Nd} \right)_{DM}} \right\}$$

(Liew *et al.*, 1988)

Where  $\left( \frac{^{143}Nd}{^{144}Nd} \right)_{DM} = 0.513151$ ;  $\left( \frac{^{147}Sm}{^{144}Nd} \right)_{DM} = 0.219$ ;  $\left( \frac{^{147}Sm}{^{144}Nd} \right)_{CC} = 0.12$ ;  $\lambda_{Sm} = 6.54 \times 10^{-12} \text{y}^{-1}$  (Liew *et al.*, 1988) and  $t$  = monazite crystallisation age of the sample

Epsilon units ( $\epsilon_{Nd}$ ) were calculated using the appropriate magmatic age for the individual pegmatite samples for  $t$ , using the formula:

$$\epsilon_{Nd} = \left\{ \frac{\left( \frac{^{143}Nd}{^{144}Nd} \right)_{sample}^t}{\left[ \left( \frac{^{143}Nd}{^{144}Nd} \right)_{CHUR} - \left( \frac{^{147}Sm}{^{144}Nd} \right)_{CHUR}^t \right] (e^{\lambda t})} \right\} \quad (\text{Depaolo } et al., 1976)$$

Where  $\left( \frac{^{143}Nd}{^{144}Nd} \right)_{CHUR} = 0.51264$  and  $\left( \frac{^{147}Sm}{^{144}Nd} \right)_{CHUR} = 0.1967$  (Jacobsen *et al.*, 1980) and  $t$  = monazite crystallisation age of the sample

## D.1: Vioolsdrif Domain

## D.1.1: SD2015-10

Sample	Spot #	Nd <sub>tot</sub> [ppm]	<sup>147</sup> Sm/ <sup>144</sup> Nd <sup>a</sup>	±2s <sup>b</sup>	βNd <sup>c</sup>	<sup>145</sup> Nd/ <sup>144</sup> Nd <sup>d</sup>	<sup>148</sup> Nd/ <sup>144</sup> Nd <sup>d</sup>	<sup>150</sup> Nd/ <sup>144</sup> Nd <sup>d</sup>	<sup>143</sup> Nd/ <sup>144</sup> Nd <sup>a</sup>	±2s <sup>b</sup>	<sup>143</sup> Nd/ <sup>144</sup> Nd <sub>t</sub> <sup>f</sup>	εNd <sub>0</sub> <sup>e</sup>	εNd <sub>t</sub> <sup>f</sup>	±2s <sup>b</sup>	f <sup>(Sm/Nd)</sup>	U-Pb Age <sup>g</sup> [Ma]	Age(Ga) <sup>g</sup> [Ga]	T <sub>1</sub> Dm [Ga]	T <sub>2</sub> Dm [Ga]
SD2015-010	spot83	36.1	0.22949	0.0007	-1.41	0.34836	0.24156	0.23729	0.51218	0.00002	0.51066	-9.0	-13.2	0.56	0.17	1010	1.01	-9.7	2.6
	spot84	34.7	0.20837	0.0018	-1.42	0.34837	0.24155	0.23720	0.51205	0.00002	0.51067	-11	-13.0	0.54	0.06	1010	1.01	29	2.6
	spot85	36.2	0.32124	0.0008	-1.43	0.34839	0.24154	0.23634	0.51272	0.00002	0.51059	1.6	-14.6	0.56	0.63	1010	1.01	-0.6	2.7
	spot86	33.9	0.28153	0.001	-1.44	0.34840	0.24154	0.23718	0.51246	0.00002	0.51059	-3.5	-14.5	0.50	0.43	1010	1.01	-1.6	2.7
	spot87	39.1	0.23667	0.0007	-1.44	0.34840	0.24156	0.23682	0.51219	0.00002	0.51062	-8.8	-14.0	0.47	0.20	1010	1.01	-6.5	2.6
	spot88	39.9	0.27713	0.0022	-1.44	0.34839	0.24154	0.23638	0.51244	0.00002	0.51060	-3.9	-14.3	0.55	0.41	1010	1.01	-1.7	2.6
	spot89	39.3	0.30037	0.0015	-1.44	0.34840	0.24153	0.23479	0.51258	0.00002	0.51059	-1.2	-14.6	0.50	0.53	1010	1.01	-1.0	2.7
	spot90	38.2	0.24401	0.001	-1.44	0.34840	0.24155	0.23682	0.51222	0.00002	0.51061	-8.1	-14.3	0.48	0.24	1010	1.01	-4.7	2.6
	spot91	34.3	0.32752	0.0021	-1.44	0.34840	0.24153	0.23706	0.51273	0.00002	0.51056	1.8	-15.2	0.55	0.67	1010	1.01	-0.6	2.7
	spot92	33.2	0.22203	0.0005	-1.43	0.34840	0.24156	0.23689	0.51208	0.00002	0.51061	-11	-14.1	0.50	0.13	1010	1.01	-21	2.6

## D.1.2: SD2015-11

Sample	Spot #	Nd <sub>tot</sub> [ppm]	<sup>147</sup> Sm/ <sup>144</sup> Nd <sup>a</sup>	±2s <sup>b</sup>	βNd <sup>c</sup>	<sup>145</sup> Nd/ <sup>144</sup> Nd <sup>d</sup>	<sup>148</sup> Nd/ <sup>144</sup> Nd <sup>d</sup>	<sup>150</sup> Nd/ <sup>144</sup> Nd <sup>d</sup>	<sup>143</sup> Nd/ <sup>144</sup> Nd <sup>a</sup>	±2s <sup>b</sup>	<sup>143</sup> Nd/ <sup>144</sup> Nd <sub>t</sub> <sup>f</sup>	εNd <sub>0</sub> <sup>e</sup>	εNd <sub>t</sub> <sup>f</sup>	±2s <sup>b</sup>	f <sup>(Sm/Nd)</sup>	U-Pb Age <sup>g</sup> [Ma]	Age(Ga) <sup>g</sup> [Ga]	T <sub>1</sub> Dm [Ga]	T <sub>2</sub> Dm [Ga]
SD2015-011	spot41	23.3	0.17488	0.0017	-1.39	0.34840	0.24155	0.24037	0.51219	0.00004	0.51100	-8.7	-5.8	0.78	-0.11	1038	1.04	3.7	2.0
	spot42	28.1	0.17468	0.0007	-1.40	0.34840	0.24155	0.23735	0.51217	0.00003	0.51098	-9.2	-6.3	0.65	-0.11	1038	1.04	3.8	2.1
	spot43	23.4	0.15116	0.0019	-1.41	0.34843	0.24155	0.24024	0.51195	0.00004	0.51092	-13	-7.4	1.09	-0.23	1038	1.04	2.9	2.2
	spot44	27.7	0.15008	0.0004	-1.40	0.34841	0.24155	0.23777	0.51191	0.00002	0.51088	-14	-8.1	0.52	-0.24	1038	1.04	3.0	2.2
	spot45	21.6	0.15643	0.0003	-1.39	0.34842	0.24154	0.23759	0.51193	0.00002	0.51086	-14	-8.5	0.57	-0.20	1038	1.04	3.2	2.2
	spot46	28.6	0.16365	0.0005	-1.39	0.34840	0.24155	0.23791	0.51207	0.00002	0.51096	-11	-6.7	0.53	-0.17	1038	1.04	3.3	2.1
	spot47	22.4	0.14506	0.001	-1.41	0.34840	0.24154	0.23859	0.51194	0.00002	0.51095	-14	-6.8	0.54	-0.26	1038	1.04	2.7	2.1
	spot48	17.9	0.14876	0.002	-1.40	0.34840	0.24152	0.24471	0.51199	0.00007	0.51098	-13	-6.3	1.61	-0.24	1038	1.04	2.7	2.1
	spot49	21.7	0.14815	0.002	-1.38	0.34842	0.24160	0.24022	0.51189	0.00005	0.51088	-15	-8.2	1.07	-0.25	1038	1.04	2.9	2.2
	spot50	29.7	0.15178	0.0006	-1.39	0.34840	0.24154	0.23784	0.51196	0.00002	0.51093	-13	-7.2	0.48	-0.23	1038	1.04	2.9	2.1

A.73

<sup>a</sup> Unweighted mean ratio corrected for inter-element fractionation using Steenkampskraal (Namaqualand; Liu et al, 2012)<sup>b</sup> Uncertainty in the corrected ratio (expressed at 95% confidence interval)<sup>c</sup> Mass bias correction factor using exponential law<sup>d</sup> Quadratic addition of measurement uncertainty and excess variance of Steenkampskraal RM (Lie et al, 2012)<sup>e</sup> Initial ratio corrected according to U-Pb age<sup>f</sup> t = calculated U-Pb age for the given sample in Ma<sup>g</sup> magmatic age of pegmatite sample, or where indicated age of inherited xenocrystic monaziteT<sub>1DM</sub> is the single-stage depleted mantle model age (in Ga)T<sub>2DM</sub> is the two-stage depleted model age (in Ga)

**D.1.3: SDORPB15-09**

Sample	Spot #	Nd <sub>tot</sub> <sup>147Sm/144Nd<sup>a</sup></sup> [ppm]	±2s <sup>b</sup>	βNd <sup>c</sup>	<sup>145Nd/144Nd<sup>d</sup></sup>	<sup>148Nd/144Nd<sup>d</sup></sup>	<sup>150Nd/144Nd<sup>d</sup></sup>	<sup>143Nd/144Nd<sup>a</sup></sup>	±2s <sup>b</sup>	<sup>143Nd/144Nd<sup>f</sup></sup>	εNd <sub>0</sub> <sup>e</sup>	εNd <sub>t</sub> <sup>f</sup>	±2s <sup>b</sup>	f <sup>(Sm/Nd)</sup>	U-Pb Age <sup>g</sup> [Ma]	Age(Ga) <sup>g</sup> [Ga]	T <sub>1</sub> Dm [Ga]	T <sub>2</sub> Dm [Ga]	
SDORPB15-09	spot31	30.8	0.50915	0.0046	-1.43	0.34840	0.24150	0.23582	0.51389	0.00003	0.51054	24	-16	0.69	1.59	1004	1.00	0.4	2.7
	spot32	30.3	0.54059	0.0011	-1.42	0.34840	0.24151	0.22586	0.51409	0.00002	0.51053	28	-16	0.56	1.75	1004	1.00	0.4	2.8
	spot33	35.1	0.50911	0.0038	-1.45	0.34840	0.24152	0.20172	0.51387	0.00002	0.51051	24	-16	0.61	1.59	1004	1.00	0.4	2.8
	spot34	31.1	0.55574	0.0108	-1.42	0.34841	0.24150	0.19701	0.51417	0.00006	0.51051	30	-16	1.31	1.83	1004	1.00	0.5	2.8
	spot35	29.9	0.53210	0.0086	-1.42	0.34841	0.24152	0.21943	0.51411	0.00004	0.51060	29	-15	0.88	1.71	1004	1.00	0.5	2.7
	spot36	31.2	0.53810	0.0016	-1.44	0.34840	0.24152	0.20947	0.51417	0.00003	0.51062	30	-14	0.67	1.74	1004	1.00	0.5	2.6
	spot37	34.5	0.51889	0.0027	-1.44	0.34839	0.24153	0.20271	0.51398	0.00003	0.51056	26	-15	0.64	1.64	1004	1.00	0.4	2.7
	spot38	33.2	0.52987	0.003	-1.45	0.34840	0.24153	0.20507	0.51400	0.00002	0.51051	27	-16	0.60	1.70	1004	1.00	0.4	2.8
	spot39	23.4	0.56270	0.0047	-1.41	0.34842	0.24154	0.23017	0.51424	0.00006	0.51053	31	-16	1.38	1.86	1004	1.00	0.5	2.8
	spot40	32.3	0.52655	0.0012	-1.41	0.34839	0.24152	0.21203	0.51399	0.00002	0.51052	26	-16	0.50	1.68	1004	1.00	0.4	2.8
	spot41	30.3	0.52213	0.0011	-1.42	0.34840	0.24151	0.23449	0.51396	0.00002	0.51052	26	-16	0.51	1.66	1004	1.00	0.4	2.8
	spot42	31.7	0.47051	0.0023	-1.43	0.34841	0.24153	0.23382	0.51367	0.00002	0.51057	20	-15	0.57	1.39	1004	1.00	0.3	2.7
	spot43	31.3	0.46244	0.001	-1.43	0.34839	0.24152	0.23641	0.51363	0.00002	0.51058	19	-15	0.52	1.35	1004	1.00	0.3	2.7
	spot44	30.0	0.45980	0.0051	-1.43	0.34839	0.24153	0.23689	0.51364	0.00003	0.51061	20	-14	0.62	1.34	1004	1.00	0.3	2.6
	spot45	32.4	0.48102	0.0054	-1.44	0.34840	0.24152	0.23240	0.51373	0.00004	0.51056	21	-15	0.84	1.45	1004	1.00	0.3	2.7
	spot46	32.8	0.47402	0.0028	-1.44	0.34840	0.24154	0.23082	0.51369	0.00002	0.51056	20	-15	0.61	1.41	1004	1.00	0.3	2.7
	spot47	31.9	0.43915	0.0148	-1.45	0.34840	0.24153	0.23679	0.51347	0.00008	0.51057	16	-15	1.60	1.23	1004	1.00	0.2	2.7
	spot48	33.7	0.45626	0.0024	-1.44	0.34839	0.24152	0.23185	0.51364	0.00002	0.51064	20	-14	0.57	1.32	1004	1.00	0.3	2.6

**D.2: Pella Domain****D.2.1: SD2015-13**

Sample	Spot #	Nd <sub>tot</sub> <sup>147Sm/144Nd<sup>a</sup></sup> [ppm]	±2s <sup>b</sup>	βNd <sup>c</sup>	<sup>145Nd/144Nd<sup>d</sup></sup>	<sup>148Nd/144Nd<sup>d</sup></sup>	<sup>150Nd/144Nd<sup>d</sup></sup>	<sup>143Nd/144Nd<sup>a</sup></sup>	±2s <sup>b</sup>	<sup>143Nd/144Nd<sup>f</sup></sup>	εNd <sub>0</sub> <sup>e</sup>	εNd <sub>t</sub> <sup>f</sup>	±2s <sup>b</sup>	f <sup>(Sm/Nd)</sup>	U-Pb Age <sup>g</sup> [Ma]	Age(Ga) <sup>g</sup> [Ga]	T <sub>1</sub> Dm [Ga]	T <sub>2</sub> Dm [Ga]	
SD2015-013	spot61	21.0	0.17711	0.001	-1.39	0.34841	0.24160	0.24070	0.51189	0.00003	0.51072	-15	-12	0.83	-0.10	1005	1.01	5.2	2.5
	spot62	26.3	0.17274	0.0007	-1.39	0.34841	0.24156	0.23770	0.51181	0.00002	0.51067	-16	-13	0.55	-0.12	1005	1.01	4.9	2.6
	spot63	26.6	0.17513	0.0004	-1.39	0.34841	0.24154	0.23738	0.51181	0.00002	0.51065	-16	-14	0.49	-0.11	1005	1.01	5.3	2.6
	spot64	22.3	0.17128	0.0004	-1.40	0.34843	0.24157	0.23720	0.51175	0.00001	0.51062	-17	-14	0.45	-0.13	1005	1.01	5.0	2.6
	spot65	23.2	0.18016	0.0005	-1.39	0.34841	0.24155	0.23999	0.51186	0.00002	0.51067	-15	-13	0.62	-0.08	1005	1.01	5.8	2.6
	spot66	27.0	0.17988	0.0004	-1.39	0.34841	0.24154	0.23750	0.51184	0.00002	0.51066	-15	-13	0.55	-0.09	1005	1.01	5.8	2.6
	spot67	22.9	0.16186	0.0004	-1.39	0.34840	0.24155	0.23717	0.51175	0.00002	0.51068	-17	-13	0.58	-0.18	1005	1.01	4.1	2.5
	spot68	21.9	0.17291	0.0016	-1.39	0.34840	0.24154	0.23824	0.51180	0.00002	0.51066	-16	-13	0.54	-0.12	1005	1.01	5.0	2.6
	spot69	28.5	0.14665	0.0004	-1.39	0.34841	0.24155	0.23776	0.51160	0.00002	0.51063	-20	-14	0.48	-0.25	1005	1.01	3.5	2.6
	spot70	22.6	0.14386	0.0004	-1.40	0.34840	0.24155	0.23763	0.51164	0.00002	0.51070	-19	-13	0.51	-0.27	1005	1.01	3.3	2.5

A.74

<sup>a</sup> Unweighted mean ratio corrected for inter-element fractionation using Steenkampskraal (Namaqualand; Liu et al, 2012)<sup>b</sup> Uncertainty in the corrected ratio (expressed at 95% confidence interval)<sup>c</sup> Mass bias correction factor using exponential law<sup>d</sup> Quadratic addition of measurement uncertainty and excess variance of Steenkampskraal RM (Lie et al, 2012)<sup>e</sup> Initial ratio corrected according to U-Pb age<sup>f</sup> t = calculated U-Pb age for the given sample in Ma<sup>g</sup> magmatic age of pegmatite sample, or where indicated age of inherited xenocrystic monaziteT<sub>1DM</sub> is the single-stage depleted mantle model age (in Ga)T<sub>2DM</sub> is the two-stage depleted model age (in Ga)

**D.2.2: SDORPB15-10**

Sample	Spot #	Nd <sub>tot</sub> [ppm]	<sup>147</sup> Sm/ <sup>144</sup> Nd <sup>a</sup>	±2s <sup>b</sup>	βNd <sup>c</sup>	<sup>145</sup> Nd/ <sup>144</sup> Nd <sup>d</sup>	<sup>148</sup> Nd/ <sup>144</sup> Nd <sup>d</sup>	<sup>150</sup> Nd/ <sup>144</sup> Nd <sup>d</sup>	<sup>143</sup> Nd/ <sup>144</sup> Nd <sup>a</sup>	±2s <sup>b</sup>	<sup>143</sup> Nd/ <sup>144</sup> Nd <sub>t</sub> <sup>f</sup>	εNd <sub>0</sub> <sup>e</sup>	εNd <sub>t</sub> <sup>f</sup>	±2s <sup>b</sup>	f <sup>(Sm/Nd)</sup>	U-Pb Age <sup>g</sup> [Ma]	Age(Ga) <sup>g</sup> [Ga]	T <sub>1</sub> Dm [Ga]	T <sub>2</sub> Dm [Ga]
SDORPB15-010	spot58	21.7	0.14166	0.0003	-1.43	0.34839	0.24155	0.23704	0.51156	0.00002	0.51062	-21	-14	0.5	-0.28	1016	1.02	3.3	2.6
	spot59	22.2	0.14012	0.0003	-1.43	0.34840	0.24155	0.23705	0.51155	0.00002	0.51062	-21	-14	0.59	-0.29	1016	1.02	3.3	2.6
	spot60	25.0	0.12206	0.0004	-1.43	0.34840	0.24157	0.23738	0.51142	0.00003	0.51061	-24	-14	0.62	-0.38	1016	1.02	2.9	2.6
	spot61	24.2	0.12762	0.0005	-1.42	0.34839	0.24156	0.23686	0.51160	0.00002	0.51075	-20	-11	0.49	-0.35	1016	1.02	2.7	2.4
	spot62	25.4	0.11740	0.0006	-1.43	0.34840	0.24156	0.23670	0.51138	0.00002	0.51059	-25	-14	0.53	-0.40	1016	1.02	2.8	2.7
	spot63	23.1	0.09463	0.0005	-1.43	0.34840	0.24157	0.23692	0.51119	0.00002	0.51056	-28	-15	0.52	-0.52	1016	1.02	2.5	2.7
	spot64	23.0	0.09905	0.0004	-1.43	0.34840	0.24156	0.23711	0.51127	0.00002	0.51061	-27	-14	0.52	-0.50	1016	1.02	2.5	2.6
	spot65	18.9	0.14907	0.0012	-1.45	0.34839	0.24154	0.24118	0.51169	0.00004	0.51070	-19	-12	0.81	-0.24	1016	1.02	3.4	2.5
	spot66	21.8	0.14667	0.0016	-1.43	0.34841	0.24157	0.23732	0.51160	0.00002	0.51063	-20	-14	0.5	-0.25	1016	1.02	3.5	2.6
	spot67	21.0	0.12357	0.0018	-1.43	0.34838	0.24154	0.24033	0.51149	0.00003	0.51067	-22	-13	0.73	-0.37	1016	1.02	2.8	2.5
	spot68	21.2	0.12004	0.0012	-1.43	0.34839	0.24159	0.23940	0.51150	0.00003	0.51070	-22	-12	0.7	-0.39	1016	1.02	2.7	2.5
	spot69	21.5	0.13479	0.0004	-1.43	0.34840	0.24157	0.23719	0.51156	0.00002	0.51066	-21	-13	0.54	-0.31	1016	1.02	3.1	2.6
spot70	20.9	0.14352	0.0005	-1.43	0.34841	0.24156	0.23771	0.51160	0.00002	0.51065	-20	-13	0.57	-0.27	1016	1.02	3.3	2.6	

**D.2.3: RPGV14**

Sample	Spot #	Nd <sub>tot</sub> [ppm]	<sup>147</sup> Sm/ <sup>144</sup> Nd <sup>a</sup>	±2s <sup>b</sup>	βNd <sup>c</sup>	<sup>145</sup> Nd/ <sup>144</sup> Nd <sup>d</sup>	<sup>148</sup> Nd/ <sup>144</sup> Nd <sup>d</sup>	<sup>150</sup> Nd/ <sup>144</sup> Nd <sup>d</sup>	<sup>143</sup> Nd/ <sup>144</sup> Nd <sup>a</sup>	±2s <sup>b</sup>	<sup>143</sup> Nd/ <sup>144</sup> Nd <sub>t</sub> <sup>f</sup>	εNd <sub>0</sub> <sup>e</sup>	εNd <sub>t</sub> <sup>f</sup>	±2s <sup>b</sup>	f <sup>(Sm/Nd)</sup>	U-Pb Age <sup>g</sup> [Ma]	Age(Ga) <sup>g</sup> [Ga]	T <sub>1</sub> Dm [Ga]	T <sub>2</sub> Dm [Ga]
RPGV14	spot23	25.2	0.11883	0.0004	-1.45	0.34840	0.24157	0.23687	0.51142	0.00002	0.51067	-24	-14	0.48	-0.40	973	0.97	2.8	2.6
	spot24	25.8	0.11840	0.0003	-1.45	0.34840	0.24156	0.23670	0.51142	0.00002	0.51066	-24	-14	0.51	-0.40	973	0.97	2.8	2.6
	spot25	24.8	0.11633	0.0002	-1.45	0.34841	0.24157	0.23715	0.51135	0.00002	0.51061	-25	-15	0.59	-0.41	973	0.97	2.8	2.7
	spot26	25.9	0.11464	0.0007	-1.45	0.34840	0.24156	0.23689	0.51139	0.00002	0.51066	-24	-14	0.6	-0.42	973	0.97	2.7	2.6
	spot27	27.2	0.12098	0.0011	-1.45	0.34841	0.24157	0.23663	0.51146	0.00002	0.51069	-23	-14	0.53	-0.38	973	0.97	2.8	2.6
	spot28	25.9	0.11769	0.0004	-1.45	0.34840	0.24156	0.23694	0.51137	0.00002	0.51062	-25	-15	0.53	-0.40	973	0.97	2.8	2.7
	spot29	26.4	0.12382	0.0003	-1.45	0.34839	0.24159	0.23717	0.51148	0.00003	0.51069	-23	-13	0.61	-0.37	973	0.97	2.8	2.6
	spot30	24.7	0.11913	0.0005	-1.45	0.34839	0.24158	0.23740	0.51140	0.00002	0.51064	-24	-15	0.58	-0.39	973	0.97	2.8	2.6
	spot31	27.0	0.12522	0.0003	-1.45	0.34840	0.24157	0.23706	0.51149	0.00002	0.51069	-22	-14	0.51	-0.36	973	0.97	2.9	2.6
	spot32	24.9	0.12149	0.0006	-1.45	0.34840	0.24158	0.23697	0.51138	0.00002	0.51061	-25	-15	0.62	-0.38	973	0.97	2.9	2.7
	spot33	26.0	0.11998	0.0003	-1.45	0.34841	0.24156	0.23727	0.51144	0.00002	0.51067	-23	-14	0.52	-0.39	973	0.97	2.8	2.6
	spot34	25.4	0.11936	0.0004	-1.45	0.34841	0.24156	0.23708	0.51145	0.00002	0.51069	-23	-14	0.54	-0.39	973	0.97	2.7	2.6
	spot35	25.5	0.12022	0.0005	-1.46	0.34840	0.24157	0.23707	0.51140	0.00002	0.51064	-24	-15	0.56	-0.39	973	0.97	2.8	2.6
	spot36	25.0	0.12307	0.0003	-1.45	0.34841	0.24157	0.23730	0.51139	0.00002	0.51061	-24	-15	0.55	-0.37	973	0.97	2.9	2.7
	spot37	25.8	0.12055	0.0007	-1.44	0.34841	0.24156	0.23719	0.51141	0.00002	0.51064	-24	-15	0.59	-0.39	973	0.97	2.8	2.6
	spot38	26.3	0.12294	0.0004	-1.44	0.34840	0.24156	0.23693	0.51143	0.00002	0.51065	-23	-14	0.57	-0.37	973	0.97	2.9	2.6

A.75

<sup>a</sup> Unweighted mean ratio corrected for inter-element fractionation using Steenkampskraal (Namaqualand; Liu et al, 2012)<sup>b</sup> Uncertainty in the corrected ratio (expressed at 95% confidence interval)<sup>c</sup> Mass bias correction factor using exponential law<sup>d</sup> Quadratic addition of measurement uncertainty and excess variance of Steenkampskraal RM (Lie et al, 2012)<sup>e</sup> Initial ratio corrected according to U-Pb age<sup>f</sup> t = calculated U-Pb age for the given sample in Ma<sup>g</sup> magmatic age of pegmatite sample, or where indicated age of inherited xenocrystic monaziteT<sub>1DM</sub> is the single-stage depleted mantle model age (in Ga)T<sub>2DM</sub> is the two-stage depleted mantle model age (in Ga)

**D.2.4: RPGV16**

Sample	Spot #	Nd <sub>tot</sub> [ppm]	<sup>147</sup> Sm/ <sup>144</sup> Nd <sup>a</sup>	±2s <sup>b</sup>	βNd <sup>c</sup>	<sup>145</sup> Nd/ <sup>144</sup> Nd <sup>d</sup>	<sup>148</sup> Nd/ <sup>144</sup> Nd <sup>d</sup>	<sup>150</sup> Nd/ <sup>144</sup> Nd <sup>d</sup>	<sup>143</sup> Nd/ <sup>144</sup> Nd <sup>a</sup>	±2s <sup>b</sup>	<sup>143</sup> Nd/ <sup>144</sup> Nd <sup>f</sup>	εNd <sub>0</sub> <sup>e</sup>	εNd <sub>t</sub> <sup>f</sup>	±2s <sup>b</sup>	f <sup>(Sm/Nd)</sup>	U-Pb Age <sup>g</sup> [Ma]	Age(Ga) <sup>g</sup> [Ga]	T <sub>1</sub> Dm [Ga]	T <sub>2</sub> Dm [Ga]
RPGV16	spot65	34.5	0.08966	0.0003	-1.43	0.34840	0.24156	0.23759	0.51121	0.00002	0.51063	-28	-14	0.48	-0.54	992	0.99	2.4	2.6
	spot66	26.1	0.14058	0.0008	-1.43	0.34841	0.24156	0.23750	0.51163	0.00001	0.51072	-20	-13	0.44	-0.28	992	0.99	3.1	2.5
	spot67	24.9	0.12918	0.0007	-1.44	0.34841	0.24156	0.23749	0.51154	0.00001	0.51070	-21	-13	0.46	-0.34	992	0.99	2.9	2.5
	spot68	25.2	0.13594	0.0005	-1.44	0.34840	0.24157	0.23739	0.51157	0.00002	0.51068	-21	-13	0.5	-0.31	992	0.99	3.1	2.5
	spot70	25.0	0.11486	0.0003	-1.43	0.34842	0.24158	0.23751	0.51147	0.00002	0.51072	-23	-12	0.49	-0.42	992	0.99	2.6	2.5
	spot71	24.1	0.08613	0.0002	-1.43	0.34840	0.24156	0.23737	0.51131	0.00002	0.51075	-26	-12	0.49	-0.56	992	0.99	2.2	2.5
	spot72	24.6	0.14268	0.0014	-1.42	0.34839	0.24157	0.23810	0.51165	0.00003	0.51072	-19	-12	0.67	-0.27	992	0.99	3.2	2.5
	spot73	21.2	0.19178	0.0006	-1.44	0.34841	0.24153	0.23741	0.51192	0.00002	0.51067	-14	-13	0.56	-0.02	992	0.99	8.4	2.6
	spot74	21.5	0.19418	0.0004	-1.43	0.34841	0.24156	0.23719	0.51192	0.00002	0.51065	-14	-14	0.53	-0.01	992	0.99	9.4	2.6
	spot75	23.7	0.12424	0.0007	-1.43	0.34840	0.24156	0.23720	0.51150	0.00002	0.51069	-22	-13	0.47	-0.37	992	0.99	2.8	2.5
	spot76	23.2	0.12456	0.0003	-1.43	0.34839	0.24155	0.23740	0.51149	0.00001	0.51068	-22	-13	0.46	-0.37	992	0.99	2.8	2.6
	spot77	23.6	0.13493	0.0003	-1.43	0.34841	0.24155	0.23725	0.51156	0.00002	0.51068	-21	-13	0.51	-0.31	992	0.99	3.1	2.6
	spot78	24.6	0.13448	0.0004	-1.43	0.34840	0.24155	0.23747	0.51160	0.00002	0.51073	-20	-12	0.56	-0.32	992	0.99	3.0	2.5
	spot79	23.0	0.13064	0.0003	-1.44	0.34841	0.24157	0.23705	0.51154	0.00002	0.51069	-22	-13	0.58	-0.34	992	0.99	2.9	2.5
spot69*	35.4	0.11695	0.0004	-1.43	0.34841	0.24156	0.23734	0.51195	0.00001	0.51119	-13	-3.3	0.44	-0.41	992	0.99	1.9	1.8	

**D.2.5: CM38-A**

Sample	Spot #	Nd <sub>tot</sub> [ppm]	<sup>147</sup> Sm/ <sup>144</sup> Nd <sup>a</sup>	±2s <sup>b</sup>	βNd <sup>c</sup>	<sup>145</sup> Nd/ <sup>144</sup> Nd <sup>d</sup>	<sup>148</sup> Nd/ <sup>144</sup> Nd <sup>d</sup>	<sup>150</sup> Nd/ <sup>144</sup> Nd <sup>d</sup>	<sup>143</sup> Nd/ <sup>144</sup> Nd <sup>a</sup>	±2s <sup>b</sup>	<sup>143</sup> Nd/ <sup>144</sup> Nd <sup>f</sup>	εNd <sub>0</sub> <sup>e</sup>	εNd <sub>t</sub> <sup>f</sup>	±2s <sup>b</sup>	f <sup>(Sm/Nd)</sup>	U-Pb Age <sup>g</sup> [Ma]	Age(Ga) <sup>g</sup> [Ga]	T <sub>1</sub> Dm [Ga]	T <sub>2</sub> Dm [Ga]
CM38-A	38A_spot14	22.1	0.13906	0.0005	-1.02	0.34840	0.24161	0.23715	0.51148	0.00002	0.51057	-23	-15	0.47	-0.29	994	0.99	3.4	2.7
	38A_spot15	21.8	0.12605	0.0005	-1.02	0.34839	0.24158	0.23695	0.51139	0.00002	0.51057	-24	-15	0.46	-0.36	994	0.99	3.0	2.7
	38A_spot16	22.4	0.13374	0.0008	-1.01	0.34840	0.24160	0.23705	0.51144	0.00001	0.51056	-23	-15	0.46	-0.32	994	0.99	3.2	2.7
	38A_spot17	21.9	0.13558	0.0005	-0.99	0.34839	0.24161	0.23721	0.51146	0.00001	0.51057	-23	-15	0.42	-0.31	994	0.99	3.3	2.7
	38A_spot18	23.0	0.13027	0.0004	-1.01	0.34838	0.24162	0.23730	0.51143	0.00001	0.51058	-24	-15	0.46	-0.34	994	0.99	3.1	2.7
	38A_spot19	23.5	0.13563	0.0004	-1.00	0.34839	0.24160	0.23726	0.51150	0.00001	0.51061	-22	-15	0.45	-0.31	994	0.99	3.2	2.7
	38A_spot20	22.6	0.12247	0.002	-0.99	0.34840	0.24159	0.23795	0.51140	0.00001	0.51061	-24	-15	0.41	-0.38	994	0.99	2.9	2.7
	38A_spot24	22.7	0.13762	0.001	-1.00	0.34838	0.24161	0.23713	0.51147	0.00001	0.51057	-23	-15	0.44	-0.30	994	0.99	3.3	2.7
	38A_spot27	21.1	0.14096	0.0006	-1.00	0.34839	0.24160	0.23706	0.51151	0.00001	0.51059	-22	-15	0.41	-0.28	994	0.99	3.4	2.7
	38A_spot28	21.4	0.13214	0.0006	-1.00	0.34839	0.24160	0.23681	0.51145	0.00001	0.51058	-23	-15	0.44	-0.33	994	0.99	3.2	2.7
	38A_spot29	18.5	0.12263	0.0003	-0.99	0.34839	0.24161	0.23714	0.51134	0.00002	0.51054	-25	-16	0.49	-0.38	994	0.99	3.0	2.8
	38A_spot30	14.0	0.13380	0.0008	-0.99	0.34839	0.24160	0.23772	0.51153	0.00002	0.51066	-22	-14	0.51	-0.32	994	0.99	3.1	2.6
	38A_spot31	21.3	0.14210	0.0003	-0.99	0.34839	0.24159	0.23713	0.51154	0.00002	0.51061	-21	-15	0.47	-0.28	994	0.99	3.4	2.7

A.76

<sup>a</sup> Unweighted mean ratio corrected for inter-element fractionation using Steenkampskraal (Namaqualand; Liu et al, 2012)<sup>b</sup> Uncertainty in the corrected ratio (expressed at 95% confidence interval)<sup>c</sup> Mass bias correction factor using exponential law<sup>d</sup> Quadratic addition of measurement uncertainty and excess variance of Steenkampskraal RM (Lie et al, 2012)<sup>e</sup> Initial ratio corrected according to U-Pb age<sup>f</sup> t = calculated U-Pb age for the given sample in Ma<sup>g</sup> magmatic age of pegmatite sample, or where indicated age of inherited xenocrystic monaziteT<sub>1DM</sub> is the single-stage depleted mantle model age (in Ga)T<sub>2DM</sub> is the two-stage depleted mantle model age (in Ga)

**D.2.6: CM13-B**

Sample	Spot #	Nd <sub>tot</sub> [ppm]	<sup>147</sup> Sm/ <sup>144</sup> Nd <sup>a</sup>	±2s <sup>b</sup>	βNd <sup>c</sup>	<sup>145</sup> Nd/ <sup>144</sup> Nd <sup>d</sup>	<sup>148</sup> Nd/ <sup>144</sup> Nd <sup>d</sup>	<sup>150</sup> Nd/ <sup>144</sup> Nd <sup>d</sup>	<sup>143</sup> Nd/ <sup>144</sup> Nd <sup>a</sup>	±2s <sup>b</sup>	<sup>143</sup> Nd/ <sup>144</sup> Nd <sub>t</sub> <sup>f</sup>	εNd <sub>0</sub> <sup>e</sup>	εNd <sub>t</sub> <sup>f</sup>	±2s <sup>b</sup>	f <sup>(Sm/Nd)</sup>	U-Pb Age <sup>g</sup> [Ma]	Age(Ga) <sup>g</sup> [Ga]	T <sub>1</sub> Dm [Ga]	T <sub>2</sub> Dm [Ga]
CM13-B	13_spot32	19.2	0.17955	0.0008	-0.98	0.34840	0.24164	0.24101	0.51180	0.00002	0.51067	-16	-14	0.56	-0.09	958	0.96	6.0	2.6
	13_spot33	22.6	0.17778	0.0004	-0.98	0.34840	0.24163	0.23696	0.51173	0.00001	0.51062	-18	-15	0.41	-0.10	958	0.96	5.9	2.7
	13_spot34	20.2	0.17989	0.0016	-0.96	0.34839	0.24163	0.24038	0.51176	0.00002	0.51063	-17	-15	0.6	-0.08	958	0.96	6.2	2.7
	13_spot35	19.4	0.17774	0.0008	-0.97	0.34839	0.24164	0.24098	0.51181	0.00002	0.51070	-16	-14	0.55	-0.10	958	0.96	5.6	2.6
	13_spot36	22.5	0.17195	0.0004	-0.98	0.34839	0.24161	0.23706	0.51173	0.00001	0.51065	-18	-15	0.43	-0.13	958	0.96	5.1	2.6
	13_spot37	22.4	0.16241	0.0004	-0.99	0.34840	0.24162	0.23718	0.51166	0.00001	0.51064	-19	-15	0.47	-0.17	958	0.96	4.4	2.6
	13_spot38	16.1	0.17579	0.0017	-0.98	0.34840	0.24162	0.23935	0.51177	0.00002	0.51067	-17	-14	0.49	-0.11	958	0.96	5.5	2.6
	13_spot39	16.8	0.16291	0.0009	-0.98	0.34839	0.24160	0.23964	0.51176	0.00002	0.51073	-17	-13	0.57	-0.17	958	0.96	4.1	2.5
	13_spot40	23.2	0.16221	0.0004	-0.98	0.34840	0.24160	0.23724	0.51167	0.00001	0.51065	-19	-15	0.42	-0.17	958	0.96	4.4	2.6
	13_spot41	23.4	0.16013	0.0005	-0.97	0.34839	0.24160	0.23708	0.51169	0.00001	0.51068	-18	-14	0.45	-0.19	958	0.96	4.1	2.6
	13_spot42	24.0	0.16146	0.0004	-0.97	0.34839	0.24162	0.23706	0.51166	0.00001	0.51064	-19	-15	0.43	-0.18	958	0.96	4.3	2.6
	13_spot43	25.4	0.16801	0.0004	-0.98	0.34840	0.24162	0.23706	0.51172	0.00001	0.51066	-18	-14	0.44	-0.15	958	0.96	4.7	2.6
	13_spot44	21.4	0.17288	0.0004	-0.98	0.34840	0.24161	0.23731	0.51174	0.00001	0.51066	-17	-15	0.41	-0.12	958	0.96	5.2	2.6
	13_spot45	21.9	0.16545	0.0004	-0.97	0.34839	0.24160	0.23733	0.51170	0.00001	0.51066	-18	-15	0.46	-0.16	958	0.96	4.5	2.6

**D.2.7: CP31-C**

Sample	Spot #	Nd <sub>tot</sub> [ppm]	<sup>147</sup> Sm/ <sup>144</sup> Nd <sup>a</sup>	±2s <sup>b</sup>	βNd <sup>c</sup>	<sup>145</sup> Nd/ <sup>144</sup> Nd <sup>d</sup>	<sup>148</sup> Nd/ <sup>144</sup> Nd <sup>d</sup>	<sup>150</sup> Nd/ <sup>144</sup> Nd <sup>d</sup>	<sup>143</sup> Nd/ <sup>144</sup> Nd <sup>a</sup>	±2s <sup>b</sup>	<sup>143</sup> Nd/ <sup>144</sup> Nd <sub>t</sub> <sup>f</sup>	εNd <sub>0</sub> <sup>e</sup>	εNd <sub>t</sub> <sup>f</sup>	±2s <sup>b</sup>	f <sup>(Sm/Nd)</sup>	U-Pb Age <sup>g</sup> [Ma]	Age(Ga) <sup>g</sup> [Ga]	T <sub>1</sub> Dm [Ga]	T <sub>2</sub> Dm [Ga]
CP31-C	31-c_spot58	21.2	0.10708	0.0007	-0.96	0.34840	0.24159	0.23717	0.51133	0.00001	0.51063	-25	-14	0.48	-0.46	1005	1.01	2.6	2.6
	31-c_spot59	23.5	0.10585	0.0002	-0.96	0.34840	0.24158	0.23687	0.51132	0.00002	0.51063	-26	-14	0.52	-0.46	1005	1.01	2.6	2.6
	31-c_spot60	24.6	0.10521	0.0002	-0.97	0.34839	0.24158	0.23712	0.51133	0.00001	0.51064	-25	-14	0.41	-0.46	1005	1.01	2.5	2.6
	31-c_spot61	22.8	0.10451	0.0003	-0.98	0.34841	0.24159	0.23708	0.51128	0.00001	0.51059	-26	-15	0.44	-0.47	1005	1.01	2.6	2.7
	31-c_spot62	24.7	0.10222	0.0002	-0.97	0.34840	0.24159	0.23692	0.51127	0.00001	0.51059	-27	-15	0.43	-0.48	1005	1.01	2.6	2.7
	31-c_spot63	22.7	0.10668	0.0005	-0.97	0.34840	0.24160	0.23736	0.51134	0.00002	0.51064	-25	-14	0.48	-0.46	1005	1.01	2.6	2.6
	31-c_spot64	21.0	0.10116	0.0006	-0.97	0.34840	0.24160	0.23768	0.51130	0.00001	0.51063	-26	-14	0.47	-0.49	1005	1.01	2.5	2.6
	31-c_spot65	22.9	0.10671	0.0003	-0.97	0.34841	0.24158	0.23666	0.51131	0.00001	0.51061	-26	-14	0.45	-0.46	1005	1.01	2.6	2.6
	31-c_spot66	23.1	0.10442	0.0005	-0.97	0.34840	0.24158	0.23706	0.51133	0.00001	0.51064	-25	-14	0.42	-0.47	1005	1.01	2.5	2.6
	31-c_spot67	22.9	0.10367	0.0004	-0.97	0.34840	0.24159	0.23678	0.51131	0.00001	0.51063	-26	-14	0.45	-0.47	1005	1.01	2.5	2.6

A.77

<sup>a</sup> Unweighted mean ratio corrected for inter-element fractionation using Steenkampskraal (Namaqualand; Liu et al, 2012)<sup>b</sup> Uncertainty in the corrected ratio (expressed at 95% confidence interval)<sup>c</sup> Mass bias correction factor using exponential law<sup>d</sup> Quadratic addition of measurement uncertainty and excess variance of Steenkampskraal RM (Lie et al, 2012)<sup>e</sup> Initial ratio corrected according to U-Pb age<sup>f</sup> t = calculated U-Pb age for the given sample in Ma<sup>g</sup> magmatic age of pegmatite sample, or where indicated age of inherited xenocrystic monaziteT<sub>1DM</sub> is the single-stage depleted mantle model age (in Ga)T<sub>2DM</sub> is the two-stage depleted mantle model age (in Ga)



**D.2.8: KG36**

Sample	Spot #	Nd <sub>tot</sub> [ppm]	<sup>147</sup> Sm/ <sup>144</sup> Nd <sup>a</sup>	±2s <sup>b</sup>	βNd <sup>c</sup>	<sup>145</sup> Nd/ <sup>144</sup> Nd <sup>d</sup>	<sup>148</sup> Nd/ <sup>144</sup> Nd <sup>d</sup>	<sup>150</sup> Nd/ <sup>144</sup> Nd <sup>d</sup>	<sup>143</sup> Nd/ <sup>144</sup> Nd <sup>a</sup>	±2s <sup>b</sup>	<sup>143</sup> Nd/ <sup>144</sup> Nd <sup>f</sup>	εNd <sub>0</sub> <sup>e</sup>	εNd <sub>t</sub> <sup>f</sup>	±2s <sup>b</sup>	f <sup>(Sm/Nd)</sup>	U-Pb Age <sup>g</sup> [Ma]	Age(Ga) <sup>g</sup> [Ga]	T <sub>1</sub> Dm [Ga]	T <sub>2</sub> Dm [Ga]
KG36	36_spot46	22.9	0.15504	0.0005	-0.99	0.34840	0.24162	0.23712	0.51161	0.00001	0.51060	-20	-15	0.43	-0.21	990	0.99	4.0	2.7
	36_spot47	23.0	0.15276	0.0004	-0.99	0.34839	0.24162	0.23701	0.51163	0.00001	0.51064	-20	-14	0.44	-0.22	990	0.99	3.8	2.6
	36_spot48	23.3	0.14700	0.0003	-0.99	0.34839	0.24161	0.23705	0.51158	0.00001	0.51062	-21	-14	0.43	-0.25	990	0.99	3.6	2.6
	36_spot49	24.0	0.14243	0.0003	-0.99	0.34840	0.24160	0.23705	0.51156	0.00001	0.51063	-21	-14	0.42	-0.28	990	0.99	3.4	2.6
	36_spot50	23.9	0.14847	0.0003	-0.99	0.34840	0.24160	0.23714	0.51161	0.00001	0.51065	-20	-14	0.43	-0.24	990	0.99	3.6	2.6
	36_spot51	24.0	0.15066	0.0003	-0.99	0.34840	0.24162	0.23705	0.51161	0.00001	0.51064	-20	-14	0.43	-0.23	990	0.99	3.7	2.6
	36_spot52	23.8	0.14850	0.0003	-0.99	0.34840	0.24159	0.23713	0.51159	0.00001	0.51063	-20	-14	0.42	-0.24	990	0.99	3.6	2.6
	36_spot53	22.8	0.15312	0.0003	-0.98	0.34840	0.24161	0.23719	0.51165	0.00002	0.51066	-19	-14	0.47	-0.22	990	0.99	3.7	2.6
	36_spot54	22.6	0.15412	0.0006	-0.98	0.34839	0.24160	0.23740	0.51165	0.00002	0.51065	-19	-14	0.49	-0.22	990	0.99	3.8	2.6
	36_spot55	20.8	0.17309	0.0004	-0.98	0.34840	0.24161	0.23780	0.51178	0.00001	0.51066	-17	-14	0.47	-0.12	990	0.99	5.1	2.6
	36_spot56	22.0	0.16002	0.0004	-0.97	0.34838	0.24161	0.23686	0.51170	0.00001	0.51066	-18	-14	0.43	-0.19	990	0.99	4.1	2.6
	36_spot57	8.7	0.16989	0.0009	-0.97	0.34841	0.24162	0.24178	0.51190	0.00002	0.51079	-14	-11	0.55	-0.14	990	0.99	4.3	2.4

**D.3: LFRÖTZ****D.3.1: HS15HF1**

Sample	Spot #	Nd <sub>tot</sub> [ppm]	<sup>147</sup> Sm/ <sup>144</sup> Nd <sup>a</sup>	±2s <sup>b</sup>	βNd <sup>c</sup>	<sup>145</sup> Nd/ <sup>144</sup> Nd <sup>d</sup>	<sup>148</sup> Nd/ <sup>144</sup> Nd <sup>d</sup>	<sup>150</sup> Nd/ <sup>144</sup> Nd <sup>d</sup>	<sup>143</sup> Nd/ <sup>144</sup> Nd <sup>a</sup>	±2s <sup>b</sup>	<sup>143</sup> Nd/ <sup>144</sup> Nd <sup>f</sup>	εNd <sub>0</sub> <sup>e</sup>	εNd <sub>t</sub> <sup>f</sup>	±2s <sup>b</sup>	f <sup>(Sm/Nd)</sup>	U-Pb Age <sup>g</sup> [Ma]	Age(Ga) <sup>g</sup> [Ga]	T <sub>1</sub> Dm [Ga]	T <sub>2</sub> Dm [Ga]
HS15HF1	spot51	29.5	0.19179	0.0007	-1.44	0.34841	0.24155	0.23741	0.51234	0.00002	0.51112	-5.9	-5.3	0.48	-0.02	967	0.97	5.6	1.9
	spot52	29.1	0.19839	0.0004	-1.44	0.34841	0.24154	0.23732	0.51239	0.00002	0.51113	-4.8	-5.1	0.52	0.01	967	0.97	7.5	1.9
	spot53	29.5	0.19030	0.0011	-1.43	0.34841	0.24156	0.23749	0.51231	0.00002	0.51110	-6.5	-5.7	0.50	-0.03	967	0.97	5.4	2.0
	spot54	24.6	0.21502	0.0008	-1.44	0.34839	0.24155	0.23777	0.51251	0.00002	0.51115	-2.5	-4.8	0.58	0.09	967	0.97	-92	1.9
	spot55	28.4	0.21480	0.0004	-1.43	0.34840	0.24156	0.23763	0.51250	0.00002	0.51113	-2.8	-5.0	0.51	0.09	967	0.97	-121	1.9
	spot56	28.4	0.19180	0.0004	-1.44	0.34840	0.24156	0.23724	0.51233	0.00001	0.51111	-6.0	-5.4	0.48	-0.02	967	0.97	5.7	2.0
	spot57	28.7	0.19165	0.0014	-1.44	0.34841	0.24156	0.23741	0.51232	0.00002	0.51110	-6.3	-5.7	0.51	-0.03	967	0.97	5.7	2.0
	spot58	26.7	0.19566	0.0008	-1.43	0.34840	0.24157	0.23862	0.51237	0.00002	0.51112	-5.3	-5.2	0.49	0.00	967	0.97	6.6	1.9
	spot59	27.9	0.19568	0.0009	-1.44	0.34840	0.24154	0.23781	0.51237	0.00002	0.51113	-5.2	-5.1	0.51	0.00	967	0.97	6.5	1.9
	spot60	27.4	0.20079	0.0011	-1.44	0.34840	0.24156	0.23747	0.51237	0.00002	0.51109	-5.3	-5.8	0.53	0.02	967	0.97	9.1	2.0
	spot61	29.3	0.18582	0.0008	-1.44	0.34841	0.24156	0.23729	0.51232	0.00002	0.51114	-6.3	-4.9	0.51	-0.05	967	0.97	4.5	1.9
	spot62	27.6	0.19873	0.0006	-1.44	0.34840	0.24156	0.23769	0.51238	0.00002	0.51112	-5.0	-5.2	0.54	0.01	967	0.97	7.7	1.9
	spot63	27.9	0.18400	0.0016	-1.44	0.34841	0.24156	0.23769	0.51230	0.00002	0.51113	-6.6	-5.1	0.47	-0.06	967	0.97	4.3	1.9
	spot64	25.5	0.20941	0.0009	-1.44	0.34841	0.24156	0.24239	0.51251	0.00003	0.51118	-2.5	-4.1	0.74	0.07	967	0.97	21.8	1.9

A.78

<sup>a</sup> Unweighted mean ratio corrected for inter-element fractionation using Steenkampskraal (Namaqualand; Liu et al, 2012)<sup>b</sup> Uncertainty in the corrected ratio (expressed at 95% confidence interval)<sup>c</sup> Mass bias correction factor using exponential law<sup>d</sup> Quadratic addition of measurement uncertainty and excess variance of Steenkampskraal RM (Lie et al, 2012)<sup>e</sup> Initial ratio corrected according to U-Pb age<sup>f</sup> t = calculated U-Pb age for the given sample in Ma<sup>g</sup> magmatic age of pegmatite sample, or where indicated age of inherited xenocrystic monaziteT<sub>1DM</sub> is the single-stage depleted mantle model age (in Ga)T<sub>2DM</sub> is the two-stage depleted mantle model age (in Ga)

**D.3.2: SDORPB15-15c**

Sample	Spot #	Nd <sub>tot</sub> <sup>147Sm/144Nd<sup>a</sup></sup> [ppm]	±2s <sup>b</sup>	βNd <sup>c</sup>	<sup>145Nd/144Nd<sup>d</sup></sup>	<sup>148Nd/144Nd<sup>d</sup></sup>	<sup>150Nd/144Nd<sup>d</sup></sup>	<sup>143Nd/144Nd<sup>a</sup></sup>	±2s <sup>b</sup>	<sup>143Nd/144Nd<sup>f</sup></sup>	εNd <sub>0</sub> <sup>e</sup>	εNd <sub>t</sub> <sup>f</sup>	±2s <sup>b</sup>	f <sup>(Sm/Nd)</sup>	U-Pb Age <sup>g</sup> [Ma]	Age(Ga) <sup>g</sup> [Ga]	T <sub>1DM</sub> [Ga]	T <sub>2DM</sub> [Ga]	
SDORPB15-015c	spot51	29.6	0.13237	0.0016	-1.40	0.34841	0.24156	0.23746	0.51210	0.00002	0.51124	-11	-2.5	0.52	-0.33	980	0.98	2.0	1.7
	spot52	29.0	0.12183	0.0024	-1.41	0.34841	0.24156	0.23728	0.51205	0.00002	0.51127	-12	-2.1	0.59	-0.38	980	0.98	1.8	1.7
	spot53	27.4	0.09475	0.001	-1.40	0.34841	0.24155	0.23715	0.51188	0.00002	0.51127	-15	-2.1	0.50	-0.52	980	0.98	1.6	1.7
	spot54	26.6	0.09430	0.0031	-1.40	0.34840	0.24155	0.23753	0.51189	0.00003	0.51128	-15	-1.8	0.69	-0.52	980	0.98	1.6	1.7
	spot55	26.4	0.08676	0.0013	-1.40	0.34840	0.24156	0.23731	0.51183	0.00002	0.51127	-16	-2.1	0.50	-0.56	980	0.98	1.6	1.7
	spot56	36.7	0.13429	0.0038	-1.40	0.34840	0.24156	0.23692	0.51212	0.00002	0.51126	-10	-2.3	0.55	-0.32	980	0.98	2.0	1.7
	spot57	37.7	0.15555	0.0009	-1.39	0.34840	0.24156	0.23752	0.51225	0.00002	0.51125	-7.5	-2.4	0.51	-0.21	980	0.98	2.3	1.7
	spot58	31.0	0.09009	0.0002	-1.39	0.34841	0.24156	0.23726	0.51183	0.00002	0.51125	-16	-2.4	0.51	-0.54	980	0.98	1.6	1.7
	spot59	31.9	0.08997	0.0004	-1.39	0.34841	0.24156	0.23733	0.51184	0.00002	0.51126	-16	-2.3	0.54	-0.54	980	0.98	1.6	1.7
	spot60	36.4	0.09688	0.0002	-1.41	0.34840	0.24156	0.23710	0.51189	0.00002	0.51127	-15	-2.1	0.49	-0.51	980	0.98	1.6	1.7

**D.4: Kakamas Domain****D.4.1: SDORPB15-17**

Sample	Spot #	Nd <sub>tot</sub> <sup>147Sm/144Nd<sup>a</sup></sup> [ppm]	±2s <sup>b</sup>	βNd <sup>c</sup>	<sup>145Nd/144Nd<sup>d</sup></sup>	<sup>148Nd/144Nd<sup>d</sup></sup>	<sup>150Nd/144Nd<sup>d</sup></sup>	<sup>143Nd/144Nd<sup>a</sup></sup>	±2s <sup>b</sup>	<sup>143Nd/144Nd<sup>f</sup></sup>	εNd <sub>0</sub> <sup>e</sup>	εNd <sub>t</sub> <sup>f</sup>	±2s <sup>b</sup>	f <sup>(Sm/Nd)</sup>	U-Pb Age <sup>g</sup> [Ma]	Age(Ga) <sup>g</sup> [Ga]	T <sub>1DM</sub> [Ga]	T <sub>2DM</sub> [Ga]	
SDORPB15-17	spot93	27.9	0.14519	0.0006	-1.43	0.34833	0.24159	0.23691	0.51217	0.00002	0.51123	-9.1	-2.6	0.54	-0.26	984	0.98	2.2	1.8
	spot94	28.5	0.14515	0.0004	-1.43	0.34840	0.24155	0.23665	0.51212	0.00002	0.51118	-10	-3.6	0.5	-0.26	984	0.98	2.3	1.8
	spot95	28.6	0.15665	0.0018	-1.43	0.34840	0.24155	0.23715	0.51217	0.00002	0.51116	-9.0	-4.0	0.51	-0.20	984	0.98	2.6	1.9
	spot96	28.0	0.14309	0.0004	-1.43	0.34839	0.24156	0.23716	0.51213	0.00002	0.51121	-10	-3.2	0.56	-0.27	984	0.98	2.2	1.8
	spot97	27.9	0.14090	0.0005	-1.43	0.34840	0.24156	0.23683	0.51208	0.00002	0.51117	-11	-3.8	0.52	-0.28	984	0.98	2.2	1.8
	spot98	27.5	0.14247	0.0011	-1.43	0.34841	0.24157	0.23668	0.51208	0.00002	0.51116	-11	-4.1	0.51	-0.28	984	0.98	2.3	1.9
	spot99	28.2	0.14300	0.0006	-1.43	0.34839	0.24155	0.23698	0.51208	0.00002	0.51116	-11	-4.1	0.52	-0.27	984	0.98	2.3	1.9
	spot100	26.4	0.14517	0.0003	-1.43	0.34839	0.24157	0.23694	0.51214	0.00002	0.51121	-10	-3.2	0.54	-0.26	984	0.98	2.2	1.8
	spot101	26.7	0.15130	0.0008	-1.43	0.34841	0.24156	0.23712	0.51217	0.00002	0.51119	-9.2	-3.5	0.52	-0.23	984	0.98	2.4	1.8
	spot102	26.6	0.15830	0.0005	-1.41	0.34835	0.24156	0.23679	0.51226	0.00002	0.51124	-7.4	-2.6	0.54	-0.19	984	0.98	2.4	1.8

A.79

<sup>a</sup> Unweighted mean ratio corrected for inter-element fractionation using Steenkampskraal (Namaqualand; Liu et al, 2012)<sup>b</sup> Uncertainty in the corrected ratio (expressed at 95% confidence interval)<sup>c</sup> Mass bias correction factor using exponential law<sup>d</sup> Quadratic addition of measurement uncertainty and excess variance of Steenkampskraal RM (Lie et al, 2012)<sup>e</sup> Initial ratio corrected according to U-Pb age<sup>f</sup> t = calculated U-Pb age for the given sample in Ma<sup>g</sup> magmatic age of pegmatite sample, or where indicated age of inherited xenocrystic monaziteT<sub>1DM</sub> is the single-stage depleted mantle model age (in Ga)T<sub>2DM</sub> is the two-stage depleted model age (in Ga)

**D.4.2: SDORPB15-18**

Sample	Spot #	Nd <sub>tot</sub> [ppm]	<sup>147</sup> Sm/ <sup>144</sup> Nd <sup>a</sup>	±2s <sup>b</sup>	βNd <sup>c</sup>	<sup>145</sup> Nd/ <sup>144</sup> Nd <sup>d</sup>	<sup>148</sup> Nd/ <sup>144</sup> Nd <sup>d</sup>	<sup>150</sup> Nd/ <sup>144</sup> Nd <sup>d</sup>	<sup>143</sup> Nd/ <sup>144</sup> Nd <sup>a</sup>	±2s <sup>b</sup>	<sup>143</sup> Nd/ <sup>144</sup> Nd <sup>f</sup>	εNd <sub>0</sub> <sup>e</sup>	εNd <sub>t</sub> <sup>f</sup>	±2s <sup>b</sup>	f <sup>(Sm/Nd)</sup>	U-Pb Age <sup>g</sup> [Ma]	Age(Ga) <sup>g</sup> [Ga]	T <sub>1</sub> Dm [Ga]	T <sub>2</sub> Dm [Ga]
SDORPB15-18	spot13	29.1	0.12323	0.0003	-1.44	0.34837	0.24160	0.23738	0.51206	0.00002	0.51124	-11	-1.7	0.62	-0.37	1015	1.02	1.8	1.7
	spot14	29.1	0.12265	0.0003	-1.45	0.34840	0.24156	0.23729	0.51208	0.00001	0.51126	-11	-1.3	0.46	-0.38	1015	1.02	1.8	1.7
	spot15	29.2	0.11999	0.0005	-1.45	0.34840	0.24157	0.23717	0.51204	0.00002	0.51124	-12	-1.7	0.55	-0.39	1015	1.02	1.8	1.7
	spot20	29.3	0.11999	0.0005	-1.45	0.34840	0.24156	0.23757	0.51207	0.00002	0.51127	-11	-1.2	0.49	-0.39	1015	1.02	1.8	1.7
	spot21	31.7	0.12006	0.0003	-1.45	0.34841	0.24158	0.23762	0.51204	0.00002	0.51124	-12	-1.7	0.53	-0.39	1015	1.02	1.8	1.7
	spot22	29.1	0.12149	0.0003	-1.45	0.34840	0.24157	0.23735	0.51210	0.00002	0.51129	-11	-0.79	0.57	-0.38	1015	1.02	1.7	1.6

**D.4.3: SDORPB15-20**

Sample	Spot #	Nd <sub>tot</sub> [ppm]	<sup>147</sup> Sm/ <sup>144</sup> Nd <sup>a</sup>	±2s <sup>b</sup>	βNd <sup>c</sup>	<sup>145</sup> Nd/ <sup>144</sup> Nd <sup>d</sup>	<sup>148</sup> Nd/ <sup>144</sup> Nd <sup>d</sup>	<sup>150</sup> Nd/ <sup>144</sup> Nd <sup>d</sup>	<sup>143</sup> Nd/ <sup>144</sup> Nd <sup>a</sup>	±2s <sup>b</sup>	<sup>143</sup> Nd/ <sup>144</sup> Nd <sup>f</sup>	εNd <sub>0</sub> <sup>e</sup>	εNd <sub>t</sub> <sup>f</sup>	±2s <sup>b</sup>	f <sup>(Sm/Nd)</sup>	U-Pb Age <sup>g</sup> [Ma]	Age(Ga) <sup>g</sup> [Ga]	T <sub>1</sub> Dm [Ga]	T <sub>2</sub> Dm [Ga]
SDORPB15-20	spot114	27.3	0.14257	0.0003	-1.44	0.34840	0.24156	0.23684	0.51217	0.00002	0.51125	-9.1	-2.3	0.48	-0.27	987	0.99	2.1	1.7
	spot115	28.5	0.11825	0.0003	-1.43	0.34839	0.24155	0.23685	0.51204	0.00002	0.51127	-12	-1.8	0.51	-0.40	987	0.99	1.8	1.7
	spot116	28.7	0.12069	0.0003	-1.42	0.34840	0.24156	0.23701	0.51205	0.00002	0.51126	-12	-2.0	0.5	-0.39	987	0.99	1.8	1.7
	spot117	28.3	0.12117	0.0003	-1.43	0.34840	0.24156	0.23716	0.51205	0.00001	0.51127	-11	-1.9	0.44	-0.38	987	0.99	1.8	1.7
	spot118	27.0	0.15761	0.0003	-1.43	0.34839	0.24156	0.23712	0.51226	0.00002	0.51124	-7.3	-2.4	0.53	-0.20	987	0.99	2.4	1.7
	spot119	27.3	0.15716	0.0003	-1.43	0.34839	0.24156	0.23714	0.51226	0.00002	0.51124	-7.4	-2.4	0.51	-0.20	987	0.99	2.4	1.7
	spot120	27.6	0.14389	0.0008	-1.43	0.34839	0.24156	0.23706	0.51221	0.00002	0.51128	-8.4	-1.7	0.55	-0.27	987	0.99	2.1	1.7
	spot121	28.9	0.13680	0.0019	-1.43	0.34839	0.24155	0.23716	0.51218	0.00002	0.51130	-8.9	-1.3	0.51	-0.30	987	0.99	1.9	1.7
	spot122	29.3	0.13162	0.0019	-1.43	0.34840	0.24156	0.23714	0.51213	0.00002	0.51128	-10	-1.8	0.51	-0.33	987	0.99	1.9	1.7
	spot123	27.9	0.14506	0.0013	-1.43	0.34840	0.24157	0.23714	0.51218	0.00002	0.51124	-8.9	-2.4	0.48	-0.26	987	0.99	2.1	1.7
	spot124	30.3	0.13269	0.0004	-1.43	0.34839	0.24155	0.23711	0.51216	0.00002	0.51130	-9.3	-1.2	0.54	-0.33	987	0.99	1.9	1.7
	spot125	29.6	0.12337	0.0006	-1.42	0.34836	0.24159	0.23720	0.51212	0.00002	0.51132	-10	-0.8	0.57	-0.37	987	0.99	1.7	1.6

A.80

<sup>a</sup> Unweighted mean ratio corrected for inter-element fractionation using Steenkampskraal (Namaqualand; Liu et al, 2012)<sup>b</sup> Uncertainty in the corrected ratio (expressed at 95% confidence interval)<sup>c</sup> Mass bias correction factor using exponential law<sup>d</sup> Quadratic addition of measurement uncertainty and excess variance of Steenkampskraal RM (Lie et al, 2012)<sup>e</sup> Initial ratio corrected according to U-Pb age<sup>f</sup> t = calculated U-Pb age for the given sample in Ma<sup>g</sup> magmatic age of pegmatite sample, or where indicated age of inherited xenocrystic monaziteT<sub>1DM</sub> is the single-stage depleted mantle model age (in Ga)T<sub>2DM</sub> is the two-stage depleted mantle model age (in Ga)

## Appendix E: Sm-Nd data for country rocks

Sm-Nd data sourced from literature was recalculated using  $(^{143}\text{Nd}/^{144}\text{Nd})_{\text{DM}}$ ,  $(^{147}\text{Sm}/^{144}\text{Nd})_{\text{DM}}$ ,  $(^{147}\text{Sm}/^{144}\text{Nd})_{\text{CC}}$ ,  $(^{143}\text{Nd}/^{144}\text{Nd})_{\text{CHUR}}$  and  $(^{147}\text{Sm}/^{144}\text{Nd})_{\text{CHUR}}$  used in calculating  $\epsilon\text{Nd}_t$  and 2-stage model ages for monazite from the sampled pegmatites. This was done to assure accurate interpretations when relating host country rock Sm-Nd compositions with the Sm-Nd compositions of the monazite from the pegmatite samples. The magmatic ages from U-Pb isotopic analysis that have been reported in the literature for the various country rocks, or the assumed geological age have been used for (t) in the various calculations.

Two-stage depleted model ages were calculated using the formula:

$$T_{2DM} = \left( \frac{1}{\lambda_{\text{Sm}}} \right) \ln \left\{ \frac{1 + [(^{143}\text{Nd}/^{144}\text{Nd})_{\text{sample}} - (^{143}\text{Nd}/^{144}\text{Nd})_{\text{DM}} - (e^{\lambda t}) [(^{147}\text{Sm}/^{144}\text{Nd})_{\text{sample}} - (^{147}\text{Sm}/^{144}\text{Nd})_{\text{CC}}]}{(^{147}\text{Sm}/^{144}\text{Nd})_{\text{sample}} - (^{147}\text{Sm}/^{144}\text{Nd})_{\text{DM}}} \right\}$$

(Liew *et al.*, 1988)

Where  $(^{143}\text{Nd}/^{144}\text{Nd})_{\text{DM}} = 0.513151$ ;  $(^{147}\text{Sm}/^{144}\text{Nd})_{\text{DM}} = 0.219$ ;  $(^{147}\text{Sm}/^{144}\text{Nd})_{\text{CC}} = 0.12$  and  $\lambda_{\text{Sm}} = 6.54 \times 10^{-12} \text{y}^{-1}$  (Liew *et al.*, 1988)

Epsilon units ( $\epsilon\text{Nd}_t$ ) were calculated using the appropriate magmatic age for the varying country rock lithologies for t, using the formula:

$$\epsilon\text{Nd}_t = \left\{ \frac{(^{143}\text{Nd}/^{144}\text{Nd})_{\text{sample}}^t}{[(^{143}\text{Nd}/^{144}\text{Nd})_{\text{CHUR}} - (^{147}\text{Sm}/^{144}\text{Nd})_{\text{CHUR}}^t] (e^{\lambda t})} \right\} \quad (\text{Depaolo } et al., 1976)$$

Where  $(^{143}\text{Nd}/^{144}\text{Nd})_{\text{CHUR}} = 0.51264$  and  $(^{147}\text{Sm}/^{144}\text{Nd})_{\text{CHUR}} = 0.1967$  (Jacobsen *et al.*, 1980)

Sources for the Sm-Nd isotope compositional data for the various country rocks are cited within the tables below.

Sample Number	Domain	Suite / Group	Unit	Rock Description	Age [Ma]	Sm ppm	Nd ppm	$^{147}\text{Sm}/^{144}\text{Nd}$	$^{143}\text{Nd}/^{144}\text{Nd}$	$\pm 2s$	$^{143}\text{Nd}/^{144}\text{Nd}_t$	$f^{(\text{Sm}/\text{Nd})}$	$\epsilon\text{Nd}_0$	$\epsilon\text{Nd}_t$	T2Dm [Ga]	Source
DRA-06E	Vioolsdrif	Orange River Group	Haib	Rhyolite	2085	8.70	48.90	0.108000	0.511418	-	0.511418	-0.45	-23.8	-0.2	2.52	Reid (1997)
DRA-05	Vioolsdrif	Orange River Group	Nous	Rhyolite	2085	6.66	36.20	0.111000	0.511444	-	0.511444	-0.44	-23.3	-0.5	2.55	Reid (1997)
DRA-06A	Vioolsdrif	Orange River Group	Nous	Rhyolite	2085	6.73	36.50	0.112000	0.511478	-	0.511478	-0.43	-22.6	-0.1	2.52	Reid (1997)
DRL-49	Vioolsdrif	Orange River Group	Nous	Basaltic andesite	2085	4.70	24.20	0.117800	0.511583	-	0.511583	-0.40	-20.6	0.4	2.48	Reid (1997)
DRL-7 1	Vioolsdrif	Orange River Group	Nous	dacite	2085	5.41	31.50	0.104000	0.511397	-	0.511397	-0.47	-24.2	0.4	2.47	Reid (1997)
DRI 125	Vioolsdrif	Orange River Group	Nous	Basaltic andesite	2085	6.01	31.20	0.116000	0.511562	-	0.511562	-0.41	-21.0	0.5	2.47	Reid (1997)
DRL-107	Vioolsdrif	Orange River Group	Nous	Rhyodacite	2085	5.66	33.20	0.103000	0.511394	-	0.511394	-0.48	-24.3	0.6	2.45	Reid (1997)
DRL-62	Vioolsdrif	Orange River Group	Nous	Andesite	2085	5.90	32.80	0.109000	0.511487	-	0.511487	-0.45	-22.5	0.9	2.44	Reid (1997)
DRL-92(Z)	Vioolsdrif	Orange River Group	Nous	Rhyodacite	2085	31.50	81.00	0.235000	0.513215	-	0.513215	0.20	11.3	1.0	2.44	Reid (1997)
DRL-50	Vioolsdrif	Orange River Group	Nous	Basaltic andesite	2085	4.23	27.60	0.092800	0.511338	-	0.511338	-0.53	-25.4	2.3	2.32	Reid (1997)
CHM275	Vioolsdrif	Orange River Group	Tsams Formation	Fine-grained metalatite	1882	4.67	25.90	0.108978	0.511479	-	0.510128	-0.45	-22.6	-1.6	2.47	Macey et al. (2014)
DC0397	Vioolsdrif	Vioolsdrif Suite	Goodhouse Subsuite	Ms-Bt augen granite gneiss (Cobooop type)	1875	3.30	24.60	0.082000	0.511072	-	0.511072	-0.58	-30.5	-3.1	2.59	Petterson et al (2009)
DRV-90	Vioolsdrif	Vioolsdrif Suite	Goodhouse Subsuite	tonalite	1998	7.30	38.80	0.114000	0.511541	-	0.511541	-0.42	-21.4	-0.3	2.46	Reid (1997)
DRV-90(P)	Vioolsdrif	Vioolsdrif Suite	Goodhouse Subsuite	tonalite	1998	0.25	2.28	0.066300	0.510935	-	0.510935	-0.66	-33.2	0.0	2.43	Reid (1997)
DRV-90(Z)	Vioolsdrif	Vioolsdrif Suite	Goodhouse Subsuite	tonalite	1998	18.10	65.60	0.167000	0.512271	-	0.512271	-0.15	-7.2	0.4	2.41	Reid (1997)
DRV-90(S)	Vioolsdrif	Vioolsdrif Suite	Goodhouse Subsuite	tonalite	1998	302.00	1645.00	0.111000	0.511545	-	0.511545	-0.44	-21.3	0.5	2.39	Reid (1997)
DRV-02(Z)	Vioolsdrif	Vioolsdrif Suite	Goodhouse Subsuite	granite	1998	25.50	115.00	0.134000	0.511855	-	0.511855	-0.32	-15.3	0.7	2.38	Reid (1997)
DRV-1 5(Z)	Vioolsdrif	Vioolsdrif Suite	Goodhouse Subsuite	Granodiorite	1998	32.00	81.30	0.238000	0.513218	-	0.513218	0.21	11.3	0.8	2.39	Reid (1997)
DRV-02	Vioolsdrif	Vioolsdrif Suite	Goodhouse Subsuite	granite	1998	7.49	42.70	0.106000	0.511504	-	0.511504	-0.46	-22.1	1.0	2.36	Reid (1997)
CHM280	Vioolsdrif	Vioolsdrif Suite	Khoromous Subsuite	Quartz monzonite gneiss	1885	5.31	30.94	0.103726	0.511412	-	0.510125	-0.47	-23.9	-1.6	2.47	Macey et al. (2014)
CHM288	Vioolsdrif	Vioolsdrif Suite	Ramansdrif Subsuite	Coarse-grained alkali granite	1885	4.36	23.18	0.113682	0.511471	-	0.510061	-0.42	-22.8	-2.8	2.58	Macey et al. (2015)
DRS- 100	Vioolsdrif	Vioolsdrif Suite	Vuurdood	troctolite	1998	0.39	1.21	0.195000	0.512600	-	0.512600	-0.01	-0.7	-0.3	2.48	Reid (1997)
DRS-83	Vioolsdrif	Vioolsdrif Suite	Vuurdood	Gabbro	1998	4.65	17.10	0.165000	0.512264	-	0.512264	-0.16	-7.3	0.8	2.38	Reid (1997)

Sample Number	Domain	Suite / Group	Unit	Rock Description	Age [Ma]	Sm ppm	Nd ppm	$^{147}\text{Sm}/^{144}\text{Nd}$	$^{143}\text{Nd}/^{144}\text{Nd}$	$\pm 2s$	$^{143}\text{Nd}/^{144}\text{Nd}_t$	$f^{(\text{Sm}/\text{Nd})}$	$\epsilon\text{Nd}_0$	$\epsilon\text{Nd}_t$	T2Dm [Ga]	Source
JM135058	Pella	Girtis Suite		Amphibolite	1220	5.44	23.57	0.139526	0.511641	-	0.510524	-0.29	-19.4	-10.6	2.68	Macey et al. (2014)
PM13018	Pella	Orange Falls Suite		Granitic augen gneiss (Orange Falls)	1210	5.68	30.78	0.111489	0.511327	-	0.510441	-0.43	-25.6	-12.4	2.83	Macey et al. (2014)
PM13027	Pella	Orange Falls Suite		Granitic augen gneiss (Orange Falls)	1220	9.92	62.27	0.096287	0.511217	-	0.510452	-0.51	-27.7	-12.1	2.81	Macey et al. (2014)
CL14001	Pella	Orange Falls Suite		Orange falls granitic gneiss	1238	2.43	15.47	0.094932	0.511200	-	0.510487	-0.52	-28.1	-12.0	2.81	Macey et al. (2015)
PM13001	Pella	Orange Falls Suite		Granitic augen gneiss (Orange Falls)	1212	6.53	43.80	0.090115	0.511189	-	0.510473	-0.54	-28.3	-11.8	2.78	Macey et al. (2014)
PM13019	Pella	Orange Falls Suite		Fine to medium grained	1212	4.35	29.92	0.087845	0.511192	-	0.510494	-0.55	-28.2	-11.4	2.74	Macey et al. (2014)
JM13TV38	Pella	Orange Falls Suite		Coarse-grained equigranular granite gneiss	1196	15.50	74.06	0.126497	0.511613	-	0.510608	-0.36	-20.0	-9.3	2.56	Macey et al. (2014)
PM13025	Pella	Vioolsdrif Suite	Goodhouse Subsuite	Hbl-Bt orthogneiss (Keimas area)	1885	4.01	20.54	0.117968	0.511552	-	0.510089	-0.40	-21.2	-2.3	2.53	Macey et al. (2014)
PM13151	Pella	Vioolsdrif Suite	Goodhouse Subsuite	Augen gneiss (Houms River area)	1885	9.15	57.02	0.096984	0.511332	-	0.510129	-0.51	-25.5	-1.5	2.47	Macey et al. (2014)
PM13052	Pella	Vioolsdrif Suite	Goodhouse Subsuite	Biotite granite augen gneiss	1885	5.48	34.17	0.096961	0.511334	-	0.510131	-0.51	-25.4	-1.5	2.47	Macey et al. (2014)
PM13235	Pella	Vioolsdrif Suite	Goodhouse Subsuite	Spotted Hbl-bt orthogneiss	1885	4.06	25.77	0.095217	0.511332	-	0.510151	-0.52	-25.5	-1.1	2.43	Macey et al. (2014)
PM13152	Pella	Vioolsdrif Suite	Ramansdrif Subsuite	Équigranular granite gneiss	1885	6.89	26.11	0.159510	0.512028	-	0.510050	-0.19	-11.9	-3.0	2.60	Macey et al. (2014)
PM13228	Pella	Vioolsdrif Suite	Ramansdrif Subsuite	Equigranular granite gneiss	1885	7.66	45.08	0.102696	0.511365	-	0.510091	-0.48	-24.8	-2.2	2.53	Macey et al. (2014)
PM13149	Pella	Warmbad Suite		Granite	1003	9.14	65.90	0.083821	0.511184	-	0.510634	-0.57	-28.4	-13.9	2.78	Macey et al. (2015)
PM13253	Pella	Warmbad Suite		Sheared granite	1003	6.66	42.16	0.095472	0.511321	-	0.510694	-0.51	-25.7	-12.8	2.69	Macey et al. (2015)
PM13225	Pella	Orange River Group	Guadom Gneiss	Biotite + Hornblende gneiss	1875	5.46	30.27	0.109017	0.511435	-	0.510083	-0.45	-23.5	-2.5	2.54	Macey et al. (2014)
JM13TV44	LFROT	Eendoorn Suite	Type 1	Porphyritic granodiorite (Eendoorn farm)	1230	12.01	65.88	0.110188	0.511726	-	0.510858	-0.44	-17.8	-4.2	2.17	Macey et al. (2014)
PM13063	LFROT	Eendoorn Suite	Type 1	Porphyritic granodiorite (Kum Kum Farm)	1200	7.11	35.59	0.120754	0.511867	-	0.510916	-0.39	-15.0	-3.4	2.08	Macey et al. (2014)
PM13103	LFROT	Eendoorn Suite	Type 2	Porphyritic granodiorite (Kinderzit farm)	1193	16.12	85.49	0.113967	0.511575	-	0.510677	-0.42	-20.7	-8.1	2.46	Macey et al. (2014)
MA14069	LFROT	Oupvlakte Complex	Felsic phase of Oupvlakte	Q-F gneiss	1210	9.30	62.16	0.090374	0.511315	17	0.510597	-0.54	-25.8	-9.4	2.58	Macey et al. (2015)
PM14137	LFROT	Oupvlakte Complex	Felsic phase of Oupvlakte	Q-F gneiss	1210	8.09	33.41	0.146283	0.512174	7	0.511012	-0.26	-9.0	-1.3	1.91	Macey et al. (2015)
JM13TV83	LFROT	Kum Kum Suite	Kum Kum Klippe	Gabbro, Kum Kum	1213	4.31	18.06	0.144087	0.511951	-	0.510796	-0.27	-13.4	-5.3	2.24	Macey et al. (2014)
JM13TV48	LFROT	Kum Kum Suite	Kum Kum Klippe	Gabbro, Kum Kum	1213	3.26	14.16	0.139034	0.511949	-	0.510836	-0.29	-13.4	-4.5	2.18	Macey et al. (2014)
JM13TV86	LFROT	Kum Kum Suite	Kum Kum Klippe	Gabbro, Kum Kum	1213	3.17	13.73	0.139735	0.511963	-	0.510843	-0.29	-13.2	-4.4	2.17	Macey et al. (2014)
JM13TV37	LFROT	Kum Kum Suite	Tantalite Valley Complex	Metagabbro, Tantalite Valley	1212	3.91	18.92	0.124909	0.511655	-	0.510654	-0.36	-19.2	-8.1	2.47	Macey et al. (2014)
JM13TV13	LFROT	Kum Kum Suite	Tantalite Valley Complex	Metagabbro, Tantalite Valley	1212	0.51	2.26	0.136399	0.511778	-	0.510685	-0.31	-16.8	-7.5	2.42	Macey et al. (2014)
JM13TV27	LFROT	Kum Kum Suite	Tantalite Valley Complex	Ultramafic, Tantalite Valley	1212	0.49	1.80	0.164551	0.512027	-	0.510708	-0.16	-11.9	-7.0	2.38	Macey et al. (2014)
JM13TV04	LFROT	Kum Kum Suite	Tantalite Valley Complex	Metagabbro, Tantalite Valley	1212	0.60	2.31	0.157004	0.511974	-	0.510716	-0.20	-13.0	-6.8	2.37	Macey et al. (2014)
JM13TV09	LFROT	Kum Kum Suite	Tantalite Valley Complex	Metagabbro, Tantalite Valley	1212	0.67	2.84	0.142601	0.511933	-	0.510791	-0.27	-13.8	-5.4	2.25	Macey et al. (2014)
PM13101	LFROT	Kum Kum Suite	Umies	Olivine gabbro (Umies satellite bodies)	1220	2.76	10.93	0.152637	0.511972	-	0.510749	-0.22	-13.0	-6.2	2.32	Macey et al. (2014)
PM13091	LFROT	Kum Kum Suite	Umies	Olivine gabbro (Umies satellite bodies)	1220	2.86	10.96	0.157737	0.512061	-	0.510797	-0.20	-11.3	-5.2	2.24	Macey et al. (2014)
PM13176	LFROT	Kum Kum Suite	Velloorkoppe	Olivine gabbro, Velloorkoppe	1220	2.92	9.64	0.183125	0.512679	-	0.511212	-0.07	0.8	2.9	1.57	Macey et al. (2014)
PM13044	LFROT	Sambok Suite	Keimasmund Complex	Granite dyke (Keimasmund)	1124	1.71	12.97	0.079830	0.511781	-	0.511192	-0.59	-16.7	0.0	1.73	Macey et al. (2014)
PM13061	LFROT	Sambok Suite	Kum Kum Klippe	Granite dyke (Kum-Kum)	1123	3.35	15.17	0.133474	0.511648	-	0.510663	-0.32	-19.3	-10.3	2.58	Macey et al. (2014)

Sample Number	Domain	Suite / Group	Unit	Rock Description	Age [Ma]	Sm ppm	Nd ppm	<sup>147</sup> Sm/ <sup>144</sup> Nd	<sup>143</sup> Nd/ <sup>144</sup> Nd	±2s	<sup>143</sup> Nd/ <sup>144</sup> Nd <sub>t</sub>	f <sup>(Sm/Nd)</sup>	εNd <sub>0</sub>	εNd <sub>t</sub>	T2Dm [Ga]	Source
Mkn4	Kakamas	Josling	Josling	fine grained, leucogranite gneiss	1217	5.40	29.80	0.108900	0.512030	9	0.511160	-0.45	-11.9	1.8	1.66	Baillie et al. (2017)
Mkn	Kakamas	Josling	Josling	fine grained, leucogranite gneiss	1217	4.20	27.30	0.092800	0.512000	6	0.511260	-0.53	-12.4	3.7	1.50	Baillie et al. (2017)
DC0398	Kakamas	Eendoorn Suite	Beenbreek	Bt megacrystic augen gneiss	1113	111.00	79.70	0.084400	0.511812		0.511812	-0.57	-16.1	-0.2	1.74	Petterson et al (2009)
PM14041	Kakamas	Eendoorn Suite	Twakputs Gneiss	Large porphyroclast granite gneiss	1200	11.51	55.94	0.124373	0.512016	8	0.511036	-0.37	-12.1	-1.1	1.88	Macey et al. (2014)
PM14048	Kakamas	Eendoorn Suite	Twakputs Gneiss	Large porphyroclast granite gneiss	1200	11.59	55.63	0.125936	0.512033	11	0.511040	-0.36	-11.8	-1.0	1.88	Macey et al. (2014)
DC0447	Kakamas	Witwater	Polisiehoek	Bt Granite gneiss	1203	6.44	23.10	0.168300	0.512374	-	0.512374	-0.14	-5.1	-0.8	1.86	Petterson et al (2009)
PM14055	Kakamas	Austerlitz	Schuidrift Gneiss	Bt augen (recrystallised) gneiss	1190	9.60	42.31	0.137174	0.512253	12	0.511181	-0.30	-7.5	1.5	1.66	Macey et al. (2015)
JM145 F064	Kakamas	Austerlitz	Yas	Leucogranite gneiss	1190	3.26	17.76	0.111023	0.511989	12	0.511121	-0.44	-12.7	0.3	1.76	Macey et al. (2015)
Mc8	Kakamas	Cyndas	Cyndas	monzogranite, variably grained	1159	15.10	82.20	0.111000	0.512050	10	0.511200	-0.44	-11.5	1.2	1.66	Baillie et al. (2017)
Cyn1	Kakamas	Cyndas	Cyndas	monzogranite, variably grained	1159	11.80	65.00	0.109400	0.512050	7	0.511220	-0.44	-11.5	1.4	1.64	Baillie et al. (2017)
Mcol3	Kakamas	Syn-tectonic Granites	Colston	potassic, peraluminous, granodiorite	1151	10.20	50.80	0.121700	0.512000	8	0.511070	-0.38	-12.4	-1.4	1.87	Baillie et al. (2017)
Col1	Kakamas	Syn-tectonic Granites	Colston	potassic, peraluminous, granodiorite	1151	10.30	47.80	0.130700	0.512150	7	0.511160	-0.34	-9.5	0.2	1.74	Baillie et al. (2017)
DC0391	Kakamas	Syn-tectonic Granites	Riemvasmaak	Bt granite augen gneiss	1156	152.00	70.90	0.129400	0.512181	-	0.512181	-0.34	-8.9	1.0	1.68	Petterson et al (2009)
DC0392	Kakamas	Syn-tectonic Granites	Riemvasmaak	Hbl granite gneiss	1151	183.00	91.90	0.120100	0.512204	-	0.512204	-0.39	-8.5	2.8	1.52	Petterson et al (2009)
DC0389	Kakamas	Syn-tectonic Granites	Vaalputs	Bt granite gneiss	1146	105.00	53.90	0.117400	0.512016	-	0.512016	-0.40	-12.1	-0.5	1.80	Petterson et al (2009)
Vaal	Kakamas	Syn-tectonic Granites	Vaalputs	monzogranite	1146	11.00	55.70	0.119600	0.512150	7	0.511250	-0.39	-9.5	1.7	1.61	Baillie et al. (2017)
PM13081	Gordonia	Syn-tectonic Granites	Keimasmund Complex	Sheared porphyritic granodiorite (Keimasmund)	1140	9.07	44.12	0.124222	0.511988	-	0.511071	-0.37	-12.7	-2.1	1.92	Macey et al. (2014)
PM13086	Gordonia	Syn-tectonic Granites	Keimasmund Complex	Sheared porphyritic granodiorite (Keimasmund)	1140	12.98	71.33	0.109993	0.511905	-	0.511093	-0.44	-14.3	-1.7	1.89	Macey et al. (2014)
PM14087	Kakamas	Komsberg Suite	Donkieboud Granodiorite	Porphyritic/porphyroclastic granite gneiss	1110	12.07	69.46	0.105036	0.511911	9	0.511146	-0.47	-14.2	-1.2	1.82	Macey et al. (2015)
CG14155	Kakamas	Komsberg Suite	Donkieboud Granodiorite	Porphyritic granite/gneiss	1110	9.01	57.73	0.094379	0.511887	13	0.511199	-0.52	-14.6	-0.2	1.73	Macey et al. (2015)
PM14072	Kakamas	Komsberg Suite	Naros Granite	C.g. Equigranular granite gneiss	1110	14.81	80.73	0.110890	0.511999	11	0.511191	-0.44	-12.5	-0.3	1.75	Macey et al. (2015)
RT14/01	Kakamas	Komsberg Suite	Naros Granite	Granite	1110	16.77	92.86	0.109163	0.511987	13	0.511191	-0.44	-12.7	-0.3	1.75	Macey et al. (2015)
PM14050	Kakamas	Komsberg Suite	Stolzenfels Enderbite	C.g. equigranular to weakly porphyritic enderbite	1110	16.73	92.45	0.109385	0.511967	7	0.511170	-0.44	-13.1	-0.7	1.78	Macey et al. (2015)
PM14076	Kakamas	Komsberg Suite	Warmbad Suid	Porphyritic/porphyroclastic granite gneiss	1110	12.49	80.91	0.093309	0.511895	9	0.511215	-0.53	-14.5	0.1	1.71	Macey et al. (2015)
DC0390	Kakamas	Keimoes Suite	Friersdale	Pyx-Hbl Bt Granite	1078	147.00	77.40	0.114400	0.511983	-	0.511983	-0.42	-12.8	-1.5	1.82	Petterson et al (2009)
OC0386	Kakamas	Keimoes Suite	Friersdale	Pyx-Hbl Bt Granite	1078	149.00	78.70	0.114300	0.512000	-	0.512000	-0.42	-12.4	-1.1	1.79	Petterson et al (2009)
S367	Kakamas	Keimoes Suite	Friersdale	monzogranite - granodioritic charnockite	1078	14.30	766.00	0.112900	0.512010	10	0.511210	-0.43	-12.3	-0.7	1.76	Baillie et al. (2017)
S815	Kakamas	Keimoes Suite	Friersdale	monzogranite - granodioritic charnockite	1078	14.40	78.80	0.110500	0.512010	9	0.511230	-0.44	-12.3	-0.4	1.73	Baillie et al. (2017)
S188	Kakamas	Keimoes Suite	Friersdale	monzogranite - granodioritic charnockite	1078	14.20	79.40	0.108200	0.512030	8	0.511270	-0.45	-11.9	0.3	1.67	Baillie et al. (2017)
Gems1	Kakamas	Keimoes Suite	Gemsbokbult	Bt granite	1103	14.00	77.90	0.093000	0.511984	12	0.511312	-0.53	-12.8	1.8	1.56	Baillie et al. (2011)b
Mka6	Kakamas	Keimoes Suite	Kanoneiland	Bt-rich monzogranite	1098	18.10	95.20	0.114600	0.512080	10	0.511250	-0.42	-10.9	0.6	1.66	Baillie et al. (2017)
Kan1	Kakamas	Keimoes Suite	Kanoneiland	Bt-rich monzogranite	1098	1.70	12.10	0.083500	0.511970	5	0.511360	-0.58	-13.0	2.8	1.48	Baillie et al. (2017)
Mkb6	Kakamas	Keimoes Suite	Keboes	potassic monzogranite	1105	4.30	21.10	0.124200	0.511980	14	0.511070	-0.37	-12.8	-2.6	1.93	Baillie et al. (2017)
Klp	Kakamas	Keimoes Suite	Klipkraal	Variable, granodiorite to monzogranite	1110	20.80	108.60	0.116000	0.511920	8	0.511080	-0.41	-14.0	-2.6	1.93	Baillie et al. (2017)
Mkl3	Kakamas	Keimoes Suite	Klipkraal	Variable, granodiorite to monzogranite	1110	108.60	576.80	0.113900	0.511970	10	0.511140	-0.42	-13.0	-1.3	1.83	Baillie et al. (2017)
Str1	Kakamas	Keimoes Suite	Straussburg	Bt-rich monzogranitic-granodioritic-granitic	1089	15.40	98.10	0.094900	0.511760	10	0.511080	-0.52	-17.1	-3.0	1.95	Baillie et al. (2017)
DC0381	Kaaien	Keimoes Suite	Straussburg	Bt granite gneiss	1089	116.00	58.00	0.120600	0.511967	-	0.511967	-0.39	-13.1	-2.5	1.91	Petterson et al (2009)
Klien01	Kakamas	Kleinbegin subsuite	Kleinbegin subsuite	leucocratic granodiorite	1099	13.70	88.70	0.118700	0.511643	8	0.510786	-0.40	-19.4	-8.5	2.41	Baillie et al. (2011)b
Kle1	Kakamas	Kleinbegin subsuite	Kleinbegin subsuite	leucocratic granodiorite	1101	7.40	37.50	0.119600	0.511700	7	0.510830	-0.39	-18.3	-7.5	2.33	Baillie et al. (2017)

Sample Number	Domain	Suite / Group	Unit	Rock Description	Age [Ma]	Sm ppm	Nd ppm	<sup>147</sup> Sm/ <sup>144</sup> Nd	<sup>143</sup> Nd/ <sup>144</sup> Nd	±2s	<sup>143</sup> Nd/ <sup>144</sup> Nd <sub>t</sub>	<i>f</i> <sup>(Sm/Nd)</sup>	εNd <sub>0</sub>	εNd <sub>t</sub>	T2Dm [Ga]	Source
ALP 14	Bushmanland	Bushmanland Gr	Kouboom; Gams Fm	graphitic, sulphidic sil-bt schist	1600	5.20	28.90	0.113790	0.511280	-	0.510080	-0.42	-26.5	-9.6	2.91	Baillie et al (2007)
ALP 40	Bushmanland	Bushmanland Gr	Kouboom; Gams Fm	graphitic, sulphidic sil-bt schist	1600	3.60	19.50	0.115130	0.511460	-	0.510250	-0.41	-23.0	-6.3	2.64	Baillie et al (2007)
ALP 12	Bushmanland	Bushmanland Gr	Kouboom; Gams Fm	sulphide-barite deposits schists	1600	7.70	41.80	0.116040	0.511470	-	0.510250	-0.41	-22.8	-6.3	2.64	Baillie et al (2007)
ALP 13	Bushmanland	Bushmanland Gr	Kouboom; Gams Fm	graphitic, sulphidic sil-bt schist	1600	5.20	29.10	0.113010	0.511440	-	0.510250	-0.43	-23.4	-6.3	2.64	Baillie et al (2007)
ALP 76	Bushmanland	Bushmanland Gr	Kouboom; Gams Fm	qtz-ms-grt-bt-sil schists	1600	8.70	50.00	0.109910	0.511430	-	0.510270	-0.44	-23.6	-5.9	2.60	Baillie et al (2007)
ALP 10	Bushmanland	Bushmanland Gr	Kouboom; Gams Fm	qtz-ms-grt-bt-sil schists	1600	7.60	42.50	0.113380	0.511470	-	0.510280	-0.42	-22.8	-5.8	2.59	Baillie et al (2007)
ALP 59	Bushmanland	Bushmanland Gr	Kouboom; Gams Fm	graphitic, sulphidic sil-bt schist	1600	6.60	36.70	0.112870	0.511470	-	0.510280	-0.43	-22.8	-5.7	2.59	Baillie et al (2007)
ALP 53	Bushmanland	Bushmanland Gr	Kouboom; Gams Fm	Bt gneiss	1600	7.30	40.80	0.112530	0.511470	-	0.510290	-0.43	-22.8	-5.6	2.58	Baillie et al (2007)
ALP 42	Bushmanland	Bushmanland Gr	Kouboom; Gams Fm	graphitic, sulphidic sil-bt schist	1600	12.20	69.80	0.110530	0.511450	-	0.511450	-0.44	-23.2	-5.6	2.58	Baillie et al (2007)
ALP 13	Bushmanland	Bushmanland Gr	Kouboom; Gams Fm	grt-sil-bt-ms schist	1600	9.30	53.10	0.111240	0.511460	-	0.510290	-0.43	-23.0	-5.5	2.57	Baillie et al (2007)
ALP 14	Bushmanland	Bushmanland Gr	Kouboom; Gams Fm	grt-sil-bt-ms schist	1600	9.90	53.70	0.116700	0.511520	-	0.510290	-0.41	-21.8	-5.5	2.57	Baillie et al (2007)
ALP 16	Bushmanland	Bushmanland Gr	Kouboom; Gams Fm	grt-sil-bt-ms schist	1600	10.20	56.00	0.115360	0.511510	-	0.510300	-0.41	-22.0	-5.4	2.56	Baillie et al (2007)
ALP 57	Bushmanland	Bushmanland Gr	Kouboom; Gams Fm	graphitic, sulphidic sil-bt schist	1600	6.10	34.20	0.112430	0.511480	-	0.510300	-0.43	-22.6	-5.4	2.56	Baillie et al (2007)
ALP 17	Bushmanland	Bushmanland Gr	Kouboom; Gams Fm	quartzite	1600	7.20	32.30	0.141550	0.511800	-	0.510310	-0.28	-16.3	-5.1	2.54	Baillie et al (2007)
ALP 43	Bushmanland	Bushmanland Gr	Kouboom; Gams Fm	qtz-ms-grt-bt-sil schists	1600	8.80	47.60	0.117310	0.511550	-	0.510320	-0.40	-21.2	-5.0	2.53	Baillie et al (2007)
ALP 17	Bushmanland	Bushmanland Gr	Kouboom; Gams Fm	grt-sil-bt-ms schist	1600	8.20	44.20	0.117810	0.511570	-	0.510330	-0.40	-20.8	-4.7	2.51	Baillie et al (2007)
ALP 52	Bushmanland	Bushmanland Gr	Kouboom; Gams Fm	qtz-ms-grt-bt-sil schists	1600	8.50	47.40	0.113540	0.511540	-	0.510350	-0.42	-21.4	-4.5	2.48	Baillie et al (2007)
ALP 40	Bushmanland	Bushmanland Gr	Namies Schist	bt-grt-sil schist	1600	4.40	24.30	0.115550	0.511480	-	0.510260	-0.41	-22.6	-6.0	2.61	Baillie et al (2007)
ALP 63	Bushmanland	Bushmanland Gr	Namies Schist	bt-grt-sil schist	1600	8.70	48.10	0.114380	0.511590	-	0.510390	-0.42	-20.4	-3.7	2.42	Baillie et al (2007)
ALP 12	Bushmanland	Bushmanland Gr	Namies Schist	bt-grt-sil schist	1600	8.80	49.20	0.113500	0.511620	-	0.510430	-0.42	-19.9	-2.9	2.35	Baillie et al (2007)
ALP 39	Bushmanland	Bushmanland Gr	Namies Schist	bt-grt-sil schist	1600	7.00	38.90	0.113150	0.511660	-	0.510470	-0.42	-19.1	-2.0	2.28	Baillie et al (2007)
ALP 44	Bushmanland	Bushmanland Gr	Broken Hill Quartzite Fm	dark quartzites; Bt-ms	1600	2.30	12.10	0.120730	0.511460	-	0.510190	-0.39	-23.0	-7.5	2.73	Baillie et al (2007)
ALP 43	Bushmanland	Bushmanland Gr	Pella quartzite Fm	Ms-mag-py-grt quartzites	1600	1.00	5.00	0.119680	0.511570	-	0.510310	-0.39	-20.8	-5.1	2.54	Baillie et al (2007)
ALP 67	Bushmanland	Bushmanland Gr	Pella quartzite Fm	Ms-mag-py-grt quartzites	1600	1.60	9.20	0.112240	0.511540	-	0.510360	-0.43	-21.4	-4.2	2.46	Baillie et al (2007)
ALP 12	Bushmanland	Bushmanland Gr	Pellitic Schist Fm	grt-sil-bt-ms schist	1600	5.50	20.00	0.173590	0.511930	-	0.510100	-0.12	-13.8	-9.1	2.87	Baillie et al (2007)
ALP 68	Bushmanland	Bushmanland Gr	Pellitic Schist Fm	grt-sil-bt-ms schist	1600	7.70	41.80	0.116040	0.511450	-	0.510230	-0.41	-23.2	-6.7	2.67	Baillie et al (2007)
ALP 41	Bushmanland	Bushmanland Gr	Pellitic Schist Fm	grt-sil-bt-ms schist	1600	7.50	40.40	0.117560	0.511530	-	0.510290	-0.40	-21.6	-5.5	2.57	Baillie et al (2007)
DC03109	Bushmanland	Little Namaqualand Suite	Modderfontein	Bt-Hbl granite gneiss	1199	3.40	18.10	0.113600	0.511774	-	0.511774	-0.42	-16.9	-4.2	2.14	Petterson et al (2009)
98082105N	Bushmanland	Little Namaqualand Suite	Nababeep Granite Gneiss	qtz--plag-bt augen gneiss	1212	6.54	32.80	0.120700	0.511591	12	0.511591	-0.39	-20.4	-8.7	2.52	Yuhara et al. (2001)
99082409N	Bushmanland	Little Namaqualand Suite	Nababeep Granite Gneiss	qtz--plag-bt augen gneiss	1212	17.40	79.30	0.132600	0.511755	10	0.511755	-0.33	-17.2	-7.3	2.41	Yuhara et al. (2001)
98082308	Bushmanland	Little Namaqualand Suite	Nababeep Granite Gneiss	qtz--plag-bt augen gneiss	1212	10.80	50.80	0.128300	0.511735	10	0.511735	-0.35	-17.6	-7.0	2.39	Yuhara et al. (2001)
98081903	Bushmanland	Little Namaqualand Suite	Nababeep Granite Gneiss	qtz--plag-bt augen gneiss	1212	10.60	56.10	0.114200	0.511667	12	0.511667	-0.42	-18.9	-6.2	2.31	Yuhara et al. (2001)
49	Bushmanland	Little Namaqualand Suite	Nababeep Granite Gneiss	augen gneiss	1212	9.09	47.29	0.116200	0.511694	8	0.511694	-0.41	-18.4	-6.0	2.30	Clifford et al. (1995)
48	Bushmanland	Little Namaqualand Suite	Nababeep Granite Gneiss	grt bearing augen gneiss	1212	5.98	31.18	0.115900	0.511703	16	0.511703	-0.41	-18.2	-5.8	2.28	Clifford et al. (1995)
52	Bushmanland	Little Namaqualand Suite	Nababeep Granite Gneiss	augen gneiss	1212	12.22	69.04	0.107000	0.511635	7	0.511635	-0.46	-19.6	-5.7	2.27	Clifford et al. (1995)
99082401A	Bushmanland	Little Namaqualand Suite	Nababeep Granite Gneiss	qtz--plag-bt augen gneiss	1212	13.30	71.90	0.111800	0.511685	11	0.511685	-0.43	-18.6	-5.5	2.26	Yuhara et al. (2001)
50	Bushmanland	Little Namaqualand Suite	Nababeep Granite Gneiss	augen gneiss	1212	10.74	55.37	0.117200	0.511746	6	0.511746	-0.40	-17.4	-5.1	2.23	Clifford et al. (1995)
8a	Bushmanland	Little Namaqualand Suite	Nababeep Granite Gneiss	augen gneiss	1212	8.89	50.15	0.107200	0.511669	6	0.511669	-0.45	-18.9	-5.1	2.22	Clifford et al. (1995)
51	Bushmanland	Little Namaqualand Suite	Nababeep Granite Gneiss	augen gneiss	1212	10.92	54.87	0.120200	0.511775	7	0.511775	-0.39	-16.8	-5.0	2.22	Clifford et al. (1995)





Sample Number	Domain	Suite / Group	Unit	Rock Description	Age [Ma]	Sm ppm	Nd ppm	$^{147}\text{Sm}/^{144}\text{Nd}$	$^{143}\text{Nd}/^{144}\text{Nd}$	$\pm 2s$	$^{143}\text{Nd}/^{144}\text{Nd}_t$	$f^{(\text{Sm}/\text{Nd})}$	$\epsilon\text{Nd}_0$	$\epsilon\text{Nd}_t$	T2Dm [Ga]	Source
DC03106	Bushmanland	Spektakel Suite	Rietberg type	Burtonspits	1060	6.20	31.90	0.117600	0.512067		0.512067	-0.40	-11.1	-0.4	1.72	Petterson et al (2009)
98082205AY	Bushmanland	Spektakel Suite	Rietberg type	Garies Granite	1080	15.30	90.40	0.102302	0.511898	12	0.511977	-0.48	-14.4	-1.4	1.81	Yuhara et al. (2001)
99082407	Bushmanland	Spektakel Suite	Rietberg type	Garies Granite	1080	17.80	108.00	0.099623	0.511900	12	0.512012	-0.49	-14.4	-1.0	1.78	Yuhara et al. (2001)
98082301Y	Bushmanland	Spektakel Suite	Rietberg type	Garies Granite	1080	16.20	91.60	0.106903	0.511977	10	0.511990	-0.46	-12.9	-0.5	1.74	Yuhara et al. (2001)
98082301	Bushmanland	Spektakel Suite	Rietberg type	Garies Granite	1080	13.70	76.30	0.108535	0.511990	12	0.511891	-0.45	-12.6	-0.5	1.74	Yuhara et al. (2001)
98082205A	Bushmanland	Spektakel Suite	Rietberg type	Garies Granite	1080	16.50	98.90	0.100845	0.511951	11	0.511900	-0.49	-13.4	-0.2	1.71	Yuhara et al. (2001)
99082406	Bushmanland	Spektakel Suite	Rietberg type	Garies Granite	1080	34.50	200.00	0.104271	0.512012	12	0.511898	-0.47	-12.2	0.5	1.65	Yuhara et al. (2001)
cdb1122	Bushmanland	Spektakel Suite	Rietberg type	Jakkalshoek Granite	1062	14.33	67.23	0.129252	0.512180	7	0.512180	-0.34	-8.9	0.2	1.67	Macey et al. (2018)
pm11031	Bushmanland	Spektakel Suite	Rietberg type	Kalkvlei Granite	1065	4.78	26.71	0.107073	0.512056	9	0.512056	-0.46	-11.4	0.8	1.62	Macey et al. (2018)
98082302A	Bushmanland	Spektakel Suite	Rietberg type	Kliphoek Granite	1078	1.72	11.10	0.093662	0.511862	14	0.511758	-0.52	-15.1	-1.0	1.77	Yuhara et al. (2001)
98082302B	Bushmanland	Spektakel Suite	Rietberg type	Kliphoek Granite	1078	0.93	7.30	0.076589	0.511758	11	0.512267	-0.61	-17.2	-0.7	1.75	Yuhara et al. (2001)
cdb755	Bushmanland	Spektakel Suite	Rietberg type	Strandfontein Granite	1073	18.10	96.29	0.113936	0.512080	8	0.512080	-0.42	-10.9	0.4	1.66	Macey et al. (2018)
pm11011	Bushmanland	Ibequas	Ibequas	Ibequas Leucogranite	1074	1.79	8.17	0.132486	0.512205	7	0.512205	-0.33	-8.4	0.3	1.66	Macey et al. (2018)